

One Atom, One to Two Photons

DISSERTATION

zur Erlangung des akademischen Grades
d o c t o r r e r u m n a t u r a l i u m
(Dr. rer. nat.)
im Fach Physik

eingereicht an der
Mathematisch-Naturwissenschaftlichen Fakultät
der Humboldt-Universität zu Berlin

von

M.Phys. Luke Masters

Präsidentin der Humboldt-Universität zu Berlin:
Prof. Dr. Julia von Blumenthal

Dekanin der Mathematisch-Naturwissenschaftlichen Fakultät:
Prof. Dr. Caren Tischendorf

Promotionsausschuss:

Vorsitzender: Prof. Dr. Olaf Hohm
Gutachter: Prof. Dr. Arno Rauschenbeutel
Gutachter: Prof. Dr. Stephan Reitzenstein
Gutachter: Prof. Dr. Kai Müller
Mitglied: Prof. Dr. Oliver Benson

Tag der mündlichen Prüfung: 8. Juli 2025

Abstract

The interaction between light and a single two-level emitter is the most fundamental process in quantum optics, forming the basis for many applications in quantum information science and technology. Achieving strong light–matter interaction is central to harnessing this phenomenon, and can be facilitated by coupling an emitter to a single photon that is stored within a high-quality microresonator. Whispering-gallery-mode microresonators are an outlying class of resonator types that offer chiral light–matter interaction, enabling a variety of novel optical devices and protocols for the generation and processing of quantum light. Recent advancements in optically trapping a single atom that is strongly-coupled to a whispering-gallery-mode has brought experiments using these resonators on par with their more conventional Fabry-Pérot resonator counterparts.

This thesis describes the design and construction of an updated experimental apparatus aimed at deterministically coupling single trapped atoms to a fibre-integrated whispering-gallery-mode bottle microresonator. It incorporates a positionable optical dipole trap for single atoms as a key element. In a first experiment using this set-up, single trapped atoms are coherently driven by an external laser field, and their fluorescence light collected using a high numerical-aperture lens. A measurement of its photon statistics reveals strong photon antibunching – a distinctive feature of the light scattered by an isolated quantum emitter. Such photon anticorrelations are commonly associated with the fact that a single two-level emitter can only absorb and emit single photons. However, it can also be understood as an interference phenomenon between the two-photon components of the coherently and incoherently scattered fields, which perfectly cancel to preserve the single photon characteristics of the fluorescence light. To experimentally validate this picture, a narrow-band notch filter is introduced, that acts to suppress only the contribution of the coherently scattered field. As a consequence, the photon statistics of the filtered fluorescence are drastically modified. When maximal suppression is achieved, the remaining fluorescence light is predominantly comprised of the incoherently scattered component, and the measured photon statistics exhibit a strong time-symmetric bunching behaviour. This observation signifies the presence of simultaneously propagating pairs of photons that have been scattered by the atom, and further demonstrates that antibunching in resonance fluorescence relies on the delicate balance between the coherently and incoherently scattered two-photon components.

The experimental platform developed in this thesis represents a significant step towards realising deterministic quantum protocols that rely on a strong and stable interaction between a single atom and light confined inside a whispering-gallery-mode microresonator. The initial results obtained using this apparatus offer fundamental insights into the interaction that occurs between light and matter at the quantum level, and validate a counterintuitive picture of interfering quantum amplitudes in resonance fluorescence.

Zusammenfassung

Die Wechselwirkung zwischen Licht und einem einzelnen Zwei-Niveau-Emitter ist der grundlegendste Prozess in der Quantenoptik und bildet die Grundlage für viele Anwendungen in der Quanteninformationswissenschaft und -technologie. Die Erzielung einer starken Licht-Materie-Wechselwirkung ist von zentraler Bedeutung für die Nutzung dieses Phänomens und kann durch die Kopplung eines Emitters an ein einzelnes Photon, welches in einem optischen Resonator mit hohem Güte-Faktor gespeichert ist, erreicht werden. Als Resonator bieten sich Flüstergalerie-Mikroresonatoren an die eine chirale Licht-Materie-Wechselwirkung bieten und eine Vielzahl neuartiger optischer Geräte und Protokolle für die Erzeugung und Verarbeitung von Quantenlicht ermöglichen. Jüngste Fortschritte beim optischen Einfangen einzelner Atome, welcher stark an einen Flüstergalerieresonator gekoppelt sind, haben dazu geführt, dass Experimente mit diesen Resonatoren mit den konventionellen Fabry-Pérot-Resonatoren vergleichbar sind.

In dieser Arbeit wird der Entwurf und die Konstruktion eines aktualisierten Versuchsgeräts beschrieben, das darauf abzielt, einzelne gefangene Atome deterministisch an einen in eine Faser integrierten Flüstergalerie-Flaschen-Mikroresonator zu koppeln. Ein Schlüsselement ist eine positionierbare optische Dipol-Falle für einzelne Atome. In einem ersten Experiment werden einzelne gefangene Atome durch ein externes Laserfeld kohärent angetrieben, und ihr Fluoreszenzlicht wird mit einer Linse hoher numerischer Apertur gesammelt. Die gemessene Photonenstatistik zeigt ein starkes Photonen-Antibunching – ein charakteristisches Merkmal isolierter Quantenemitter. Solche Photonen-Antikorrelationen werden gemeinhin dadurch erklärt, dass ein einzelner Zwei-Niveau-Emitter nur einzelne Photonen absorbieren und emittieren kann. Sie können jedoch auch als Interferenzphänomen zwischen den Zwei-Photonen-Komponenten der kohärent und inkohärent gestreuten Felder verstanden werden, die sich perfekt aufheben. Um dieses Bild experimentell zu bestätigen, wird ein schmalbandiger Notchfilter eingeführt, der nur das kohärent gestreute Feld unterdrückt. Dies hat zur Folge, dass die Photonenstatistik der gefilterten Fluoreszenz drastisch verändert wird. Wenn die maximale Unterdrückung erreicht ist, besteht das verbleibende Fluoreszenzlicht überwiegend aus der inkohärent gestreuten Komponente, und die gemessene Photonenstatistik zeigt ein starkes zeitsymmetrisches Bunching-Verhalten. Diese Beobachtung deutet auf das Vorhandensein von sich gleichzeitig ausbreitenden Photonenpaaren hin, die vom Atom gestreut wurden, und zeigt außerdem, dass das Antibunching in der Resonanzfluoreszenz auf dem Gleichgewicht zwischen den kohärent und inkohärent gestreuten Zwei-Photonen-Komponenten beruht.

Die in dieser Arbeit entwickelte experimentelle Plattform stellt einen bedeutenden Schritt auf dem Weg zur Realisierung deterministischer Quantenprotokolle dar, die auf einer starken und stabilen Wechselwirkung zwischen einem einzelnen Atom und Licht beruhen, das in einem Mikroresonator im Flüstergalerie-Modus eingeschlossen ist. Die ersten Ergebnisse, die mit dieser Apparatur erzielt wurden, bieten grundlegende Einblicke in die Wechselwirkung zwischen Licht und Materie und bestätigen ein kontraintuitives Bild von interferierenden Quantenamplituden in der Resonanzfluoreszenz.

Hidden, then revealed
A path that once was shared
Beyond the quantum veil
Where solitude pairs.

for Kieran Shaw

Contents

Title Page	i
Abstract	iii
Zusammenfassung	v
List of Figures	xiii
List of Tables	xvii
Acronyms	xix
1 Introduction	1
1.1 Opening Remarks	1
1.2 Development of the Work in this Thesis	5
1.3 Organisation of the Thesis	8
2 Cavity Quantum Electrodynamics with the Bottle Microresonator	9
2.1 Cavity Quantum Electrodynamics with a Single Emitter	10
2.1.1 Rubidium as a Quantum Emitter	14
2.2 CQED with Whispering-Gallery Mode Microresonators	16
2.2.1 Optical WGMs	16
2.2.2 Optical Nanofibres	18
2.2.3 The Bottle Microresonator	20
2.2.4 Chiral CQED	23
2.3 Experimental Milestones	30
2.3.1 Strong Coupling of Single Atoms	30
2.3.2 Nonlinear π Phase Shift of Single Photons	33
2.3.3 Non-reciprocal Devices	34
2.4 Strong Coupling of Single <i>Trapped</i> Atoms	38
2.4.1 Optical Dipole Potentials	39
2.4.2 The Trapping Scheme	43
2.4.3 Compensation of the Trap-induced Light Shifts	44
2.4.4 Main Results	47
2.5 Critical Conclusions	53

3	Experimental Design	55
3.1	Words of Motivation	55
3.2	Design Goals	58
3.2.1	Key Elements of the <i>CQED 1.0</i> Experiment	59
3.2.2	Major Improvements in the <i>CQED 2.0</i> Experiment	61
3.3	The Science Chamber	63
3.3.1	Resonator Mount	63
3.3.2	Nanofibre Mounts	67
3.3.3	In-vacuum Lens Mount	70
3.3.4	Vibration Isolation	72
3.3.5	Chamber Assembly	77
3.4	Double Magneto-Optical Trap	82
3.4.1	MOT Working Principle	83
3.4.2	Lower MOT	88
3.4.3	Upper MOT	91
3.4.3.1	Optical Molasses Geometry	91
3.4.3.2	Magnetic Field Coils	92
3.4.3.3	Camera Imaging	95
3.4.4	Atomic Fountain	95
3.5	Ultra-High Vacuum Set-up	99
3.5.1	System Design	99
3.5.2	System Build	102
3.5.3	System Pump-down and Bake-out	105
3.6	Optical Dipole Trap Design	108
3.6.1	Loading Mechanisms	109
3.6.2	Envisioned Operation	114
3.7	Laser Systems	116
3.7.1	Cooling Laser	116
3.7.2	Repumping Laser	118
3.7.3	Resonator Laser	119
3.7.4	Trapping Laser	119
3.7.5	Subordinate Laser Systems	120
3.8	Control and Data Acquisition	122
3.9	Closing Remarks	123
4	Theory of Selective Resonance Fluorescence	125
4.1	Historical Developments	127
4.2	Semiclassical Light–Matter Interaction	128
4.3	The Scattered Field	135
4.3.1	Coherent and Incoherent Scattering	139

4.3.2	Second-order Correlation	144
4.4	Wavefunction Description of the Scattered Field	149
4.4.1	Photon Statistics of Each Component	153
4.4.2	Two-photon Spectra	158
4.5	Modifying the Photon Statistics	160
4.5.1	Defining a Two-Photon Filter Function	161
4.5.2	Filter Action on the Two-photon Component	165
4.5.3	Second-order Correlation Function of the Modified Field	167
4.5.4	Multi-line Filtering	172
4.6	To Conclude	174
5	Observation of Two-Photon Emission from a Single Atom	177
5.1	Experimental Methods	180
5.1.1	Trapping and Detecting Single Atoms	180
5.1.1.1	Focussing Lens Characterisation	183
5.1.1.2	Collection Efficiency	185
5.1.1.3	Trap Characteristics	188
5.1.2	Spectral Filtering	194
5.1.2.1	The Fibre-Ring Resonator	194
5.1.2.2	Characterisation	197
5.1.2.3	Frequency Stabilisation	199
5.1.3	Measurement of the Second-Order Correlation Function	204
5.1.3.1	Treatment of the Raw Data	206
5.2	Results	207
5.2.1	Modelling the Measured Second-Order Correlation Function	210
5.2.1.1	Data Normalisation	211
5.2.1.2	Trapped Atom Energy Distribution	214
5.2.1.3	Residual Filter–Laser Detuning	221
5.3	Discussion and Interpretation	224
5.3.1	A Competitive Photon-Pair Source	227
5.3.2	Filtering the Incoherent Component	230
5.3.3	Time-Domain Interpretation	233
5.4	Final Thoughts	236
6	Conclusions and Perspectives	239
6.1	Summary	239
6.2	Outlook	241
	References	247

Appendix A Documenting images	275
Appendix B Part drawings	279
Appendix C Procedure for exchanging in-vacuum components	293
C.1 Important Guidelines	293
C.2 Required Tools and Parts	294
C.3 Procedure	295
Appendix D Calculation of the UHV system conductances	303
Appendix E Calculating the second-order correlation function in the wavefunction description	305
E.1 Calculation	306
E.1.1 Calculating $\langle a_t^\dagger a_t \rangle_t$	306
E.1.2 Calculating $\langle a_t^\dagger a_{t+\tau}^\dagger a_{t+\tau} a_t \rangle_t$	308
E.1.3 Calculating $g^{(2)}(\tau)$	309
E.2 Some Sanity Checks	310
E.2.1 Calculating $\langle a_t \rangle_t$	310
E.2.2 Comparison to the Expected Scattering Rates	311
E.2.3 State Normalisation	311
Acknowledgements	315
End Matter	319

List of Figures

1.1	Broken nanofibre	6
2.1	Textbook CQED	11
2.2	Rubidium 85	15
2.3	Whispering-Gallery Mode resonators	17
2.4	Nanofibre–resonator coupling	19
2.5	Bottle microresonator mode	21
2.6	Polarisation properties of the WGM	25
2.7	Dressed state eigenenergies	26
2.8	Chiral light–matter interaction	29
2.9	Photon counts measured during single atom transits through the WGM	31
2.10	Transmission spectrum of the coupled atom–resonator system	32
2.11	Reconstructed density matrices of the transmitted two-photon state	33
2.12	Optical devices with the bottle microresonator and a single atom	35
2.13	Single atom optical isolator	36
2.14	Optical dipole trap	41
2.15	Light shifts on a two-level atom	42
2.16	Retroreflected optical dipole trap	45
2.17	Dual-colour magic wavelength trapping principle	46
2.18	Measurement of the trapping lifetime	48
2.19	Energy distribution of atoms in the trap	51
2.20	Transmission spectra of the trapped atom–resonator system	52
3.1	Resonator mount assembly	64
3.2	Finite Element Analysis of the resonator mount design	66
3.3	Nanofibre mounts assembly	68
3.4	In-vacuum lens assembly	71
3.5	Design of the Vibration Isolation System	75
3.6	Transfer function of a model mass-spring system	76
3.7	Composite Science chamber assembly	78
3.8	Working principles of laser cooling and the Magneto-Optical Trap	84
3.9	Working principles of laser cooling and the Magneto-Optical Trap (cont.)	86

LIST OF FIGURES

3.10	Composite Mot chamber assembly	89
3.11	Lower Magneto-Optical Trap	90
3.12	Magnetic field generation for the upper MOT	93
3.13	Upper Magneto-Optical Trap	96
3.14	MOT transfer with an Atomic Fountain	98
3.15	Schematic of the pumping system	100
3.16	Full pumping systems	104
3.17	Completed experimental system	106
3.18	System bake-out procedure	107
3.19	Proposed methods for single atom transport	110
3.20	Simulation of a transversally-displaced retroreflected trap beam	112
3.21	Envisioned trapping optics	115
3.22	Laser optical assemblies	117
4.1	The setting of resonance fluorescence	126
4.2	Steady-state solutions of the optical Bloch equations	131
4.3	Time-dependent solutions of the optical Bloch equations for exact resonance	133
4.4	General time-dependent solutions of the optical Bloch equations	134
4.5	Time-dependent solutions of the optical Bloch equations for a low and detuned drive	135
4.6	The Mollow triplet in resonance fluorescence	141
4.7	The detuned Mollow triplet	142
4.8	Scattering rates of the resonance fluorescence components	144
4.9	Photon statistics of light fields	145
4.10	Second-order correlation function in resonance fluorescence	148
4.11	Two-photon scattering processes in resonance fluorescence	152
4.12	Second-order correlation functions of the coherently and incoherently scattered components	156
4.13	Second-order correlation function with an attenuated coherent component	157
4.14	Spectrum of the scattered two-photon component	159
4.15	Two-photon spectrum subject to a suitable filter function	161
4.16	Centre-frequency dependence of the two-photon transmission function .	163
4.17	Linewidth dependence of the two-photon transmission function	164
4.18	Filtered two-photon spectrum	166
4.19	Sweep of the two-photon transmission function across the two-photon spectrum	168
4.20	Removing the coherently scattered two-photon component	169
4.21	Suppressing the incoherently scattered two-photon component	170
4.22	Removing the incoherently scattered two-photon component	171
4.23	Bunched photon statistics under multiple filtering lines	174

5.1	Artist’s visualisation of the simultaneous scattering of two photons by a single two-level atom	179
5.2	The confocal microscope	181
5.3	Collection of the resonance fluorescence from a single atom	187
5.4	Calculated collection efficiency	188
5.5	View of the tweezer beam	189
5.6	Detection of single trapped atoms	190
5.7	Lifetime of trapped atoms	191
5.8	Trapping frequencies measurement	193
5.9	Fibre-Ring Resonator schematic	195
5.10	Characterisation of the Fibre-Ring Resonator	199
5.11	Passive stability of the Fibre-Ring Resonator	201
5.12	Stabilising the resonance of the Fibre-Ring Resonator	202
5.13	Experimental set-up	205
5.14	Measured second-order correlation functions for different filter settings	209
5.15	Long-term behaviour of the second-order correlation function	212
5.16	The thermally occupied dipole trap	220
5.17	Considerations for the light-shifted atomic transition	220
5.18	Transmission through the filter with a residual detuning from the laser	223
5.19	Correlations at zero time delay as a function of the filter setting	226
5.20	Off-resonant filtering	232
5.21	Partial filtering of the incoherent component	232
5.22	The Fibre-Ring Resonator in the time-domain	235
6.1	Enhancing atomic emission with the WGM bottle microresonator	244
A.1	From Vienna to Berlin	275
A.2	Gold-plated copper block	276
A.3	Coupling set-up	276
A.4	Construction of CQED 2.0	276
A.5	System bake-out	277
A.6	Double MOT construction	277
A.7	A view on the Science chamber	278
A.8	The operational lab	278
C.1	Parts required for the experiment lift structure	294
C.2	Schematic for venting and pumping the entire experiment	296
C.3	Science chamber top flange	297
C.4	Partial lift structure to copper block	298
C.5	Removing the coupling set-up with the lift structure	299
C.6	Colour-coded view of the coupling set-up assembly	300

List of Tables

2.1	Retroreflected trap parameters	44
3.1	Viewport usage	80
3.2	Feedthrough usage	81
3.3	Upper MOT coil parameters	94
3.4	Results of the UHV system flow analysis	102
3.5	Maximum temperature ratings of selected UHV components	107
5.1	Confocal microscope spot sizes	185
5.2	Optical dipole trap parameters	189
5.3	Summary of the Fibre-Ring Resonator characteristics	198
5.4	Summary of the measurement settings and results	207
5.5	Characteristics of the slow bunching in each data set	213
B.1	List of part drawings	280
C.1	Important controller channels	295
D.1	Conductance values	304

Acronyms

AF	Atomic Fountain
AHH	anti-Helmholtz
AOD	Acousto-Optic Deflector
AOI	Angle of Incidence
AOM	Acousto-Optic Modulator
ASTM	American Society for Testing and Materials
BC	Before Christ
CAD	Computer-Aided Design
CCD	Charge-Coupled Device
CCW	Counter-Clockwise
CF	ConFlat TM
CMOS	Complementary Metal-Oxide-Semiconductor
CNC	Computer Numerical Control
CoQuS	The Vienna Doctoral Program on Complex Quantum Systems
CPU	Central Processing Unit
CQED	Cavity Quantum Electrodynamics
Cs	Caesium
CW	Clockwise
DAQ	Data Acquisition
DN	Diameter Nominal
DPT	Differential Pumping Tube
ECDL	External-Cavity Diode Laser
EFL	Effective Focal Length
FEA	Finite Element Analysis
FM	Frequency Modulation
FP	Fabry-Pérot
FPGA	Field Programmable Gate Array
FRR	Fibre-Ring Resonator
FSR	Free Spectral Range
FTL	Focus Tunable Lens
FWHM	Full Width at Half Maximum

Acronyms

HBT	Hanbury Brown and Twiss
HDD	Hard Disk Drive
HDL	Hardware Description Language
HH	Helmholtz
HOM	Hong-Ou-Mandel
HV	High Vacuum
HWHM	Half Width at Half Maximum
HWP	Half-Wave Plate
IO	Input/Output
IUVSTA	International Union for Vacuum Science, Technique and Applications
MEMS	Microelectromechanical Systems
MFD	Mode Field Diameter
MOT	Magneto-Optical Trap
NA	Numerical Aperture
NASA	National Aeronautics and Space Administration
OFHC	Oxygen-Free High thermal Conductivity
PBS	Polarising Beamsplitter
PD	Photodiode
PDH	Pound-Drever-Hall
PGC	Polarisation Gradient Cooling
PhD	Doctor of Philosophy
PID	Proportional, Integral, Derivative
PM	Polarisation Maintaining
PMT	Photomultiplier tube
PSF	Point Spread Function
PTFE	Polytetrafluoroethylene
QED	Quantum Electrodynamics
Rb	Rubidium
RF	Radio Frequency
RMS	Root Mean Square
SFWM	Spontaneous Four-Wave-Mixing
SLM	Spatial Light Modulator
SPCM	Single Photon Counting Module
SPDC	Spontaneous Parametric Down-Conversion
TA	Tapered Amplifier
TE	Transverse Electric
TEM	Transverse Electromagnetic
TM	Transverse Magnetic
TTL	Transistor-Transistor Logic
UHV	Ultra-High Vacuum

VCO	Voltage Controlled Oscillator
VHG	Volume-Holographic-Grating
VIS	Vibration Isolation System
WGM	Whispering-Gallery Mode
WQED	Waveguide Quantum Electrodynamics

1

Introduction

Exceptional claims demand exceptional evidence.

C. Hitchens, 2008 [1]

1.1 Opening Remarks

A basic process of the scientific method is the rigorous testing and evaluation of an informed hypothesis, against empirical observation derived from the results of experimentation. Fundamentally and historically driven simply by curiosity, science thus not only provides an ever-evolving understanding of the universe in which we live, but uniquely offers advances in technological innovation by an exploitation of the harnessed laws of nature. While this has held true in all areas of science, the advancement of knowledge alongside technological growth is undoubtedly best illustrated by the natural science of *physics* – where the roots of most modern technologies that permeate everyday life can be traced back to advances in physics, such as personal computers and world-wide communication enabled by the mastery of electromagnetism and solid-state physics (to give but one example). It is therefore no overstatement to posit that, beyond the driving curiosity to understand the strange behaviour present at the smallest scales thus-far reached, *quantum mechanics* – the newest branch of physics – promises to also dramatically transform the technologies at our disposal. We are currently well beyond the cusp of such a revolution, both in the breadth of knowledge and the fledgling applications.

1. Introduction

The advent of modern quantum mechanics shortly after the turn of the 20th century ushered in a completely new way to think about the nature of the universe, famously replacing the notions of determinism and continuity with a randomness and discreteness seemingly inherent to reality. This foundational disruption was born out of the marriage between experimental and theoretical physics, where perplexing physical phenomena such as blackbody radiation, the photoelectric effect, and spectral emission patterns, necessitated an entirely new description of light and matter and their mutual interaction [2]. The emergence of quantum theory, in which energy itself is treated as being quantised, gradually found success in accurately describing these until-then unexplained problems, thus rectifying many of the failings of classical physics at the (sub-) atomic scale [3–6]. Despite much Nobel-prize winning recognition [7–10], the early pioneers making use of such quanta were not always proponents however, as the strange new theory that took form began to show radical and unsettling consequences under its application – such as wave-particle duality, superposition states, or entangled states uniting multiple particles. Modern physicists are typically not afforded this early scepticism, and have instead had to accept the unease that accompanies quantum theory as its predications consistently prove experimentally verifiable time and time again [11]. As such, quantum physics is now an indisputably invaluable cornerstone of natural science that has blossomed into an expansive and active field of research with numerous technological applications, encompassing sub-fields such as quantum metrology [12], quantum sensing [13], quantum simulation [14], quantum communication [15], and quantum computation [16]. Recently, the field has even bridged the multidisciplinary border, giving rise to emergent and exciting frontiers such as quantum biology [17–19].

At the heart of quantum physics, since its origins, lies the question of how quantised light and matter behave and interact [20–22], from which many of the aforementioned fundamental investigations and technological applications are derived. The experimental study of this setting has made a considerable leap forward in the latter half of the last century, with thanks, in part, to the availability of coherent and near-monochromatic laser light sources [23, 24], alongside the ability to prepare, isolate, and control individual constituents of matter. A major advancement in this endeavour is the research field of **Cavity Quantum Electrodynamics (CQED)**, dedicated to studying and engineering light–matter interaction within the confines of a well-defined enclosure: a so-called cavity, or resonator. Dating back to 1946, where it was theoretically shown that the emission rate of a quantum emitter strongly depends on the environment in which it resides [25], experimental **CQED** emerged in the 1980’s with successful demonstrations of the enhancement [26–28] or inhibition [28–31] of atomic decay rates when subject to the boundary conditions imposed by a cavity. Other studies with Rydberg atoms situated inside a superconducting microwave cavity showed – for the first time – the reversible exchange of energy quanta between the atoms and the field [32–34], ultimately leading to direct evidence of field quantisation [35] as well as providing insights into

the effects of the measurement process on a quantum state [36]. The field of **CQED** has since been propelled forward by advances in nanofabrication technology, that has enabled the production of a variety of micro-scale resonator structures that aim to miniaturise the containment volume while ever increasing possible storage times for the light confined within them. The various types that are now available and regularly employed in **CQED** platforms [37] – including **Fabry-Pérot (FP)** resonators, photonic crystal cavities, and **Whispering-Gallery Mode (WGM)** microresonators – have been pioneering the development of novel quantum technologies for the distribution and processing of quantum information [38]. By situating single quantum emitters inside an optical resonator that acts to concentrate the electromagnetic field strength at the position of the emitter, and by exploiting the resulting strong light–matter interaction that can be engineered, demonstrations such as photon–photon [39] and nonlocal [40] quantum gates have paved the way towards the realisation of large-scale quantum networks [41, 42]. To date, a variety of different quantum emitters have been successfully coupled to microcavity fields, including ions [43], quantum dots [44], single molecules [45], and neutral atoms [46]; all of which together expand the possible experimental configurations that are available. Of the different types of optical cavities employed in such works, **WGM** resonators are set apart due to the way in which the light is stored and emitters are coupled. Structurally monolithic and with a microscopic circular cross-section, light in **WGM** resonators is contained by circumferentially circulating at the dielectric boundary via the principal of continuous total internal reflection. In this way, the resonator exhibits a strong evanescent field that can then be utilised for in vivo sensing applications [47], for coupling to quantum emitters that are placed at the vicinity of its surface [48], even granting access to the strong coupling regime of **CQED** with only a single emitter [49]. Furthermore, by interfacing this class of resonators with tapered optical fibres, a near-lossless in- and out-coupling of light is enabled by the principal of frustrated total internal reflection, rendering them worthy candidates for direct integration into fibre-based networks. This method of accessing the stored light further boosts the interest in **WGM** resonators as extremely low-loss and fibre-integrated platforms for the routing and processing of light down to the quantum level of single photons. Finally, and above all, it has been found that the confinement of circulating light in a **WGM** resonator gives rise to a phenomenon known as *spin–momentum locking* [50], in which the polarisation properties of the field are inherently linked to the propagation direction of the light [51, 52]. Such a directionality in the light field has profound consequences on the light–matter interaction that can be realised, facilitating a range of novel protocols and functionalities that are possible with platforms of this type [53]. This so-called *chiral* light–matter interaction has led to experimental demonstrations of; photon routing [54, 55] and direct photon–photon interactions [56] controlled by a single atom, optical devices featuring a new type of non-reciprocity [57, 58], as well as photon–atom state transfer operations [59].

1. Introduction

Since free-falling emitters are typically coupled to the evanescent part of the resonator field, i.e., on the outside of its structure, **WGM** resonators have – until most recently – suffered from a limited emitter interaction time, in addition to a probabilistic operation and time-dependent coupling strength. In order to mitigate these shortcomings, the latest major milestone in the advancement of **CQED** with **WGM** resonators was achieved, in the optical trapping of single atoms that are strongly coupled to the resonator field [60]. The tackling of this long-standing goal was realised by tightly focussing a laser onto the surface of a so-called bottle microresonator [61], in order to capture single atoms in real-time as they traverse through, and couple to, its **WGM**. With respect to free-flying atoms, this proof-of-principle trapping demonstration dramatically increases the interaction time, while also better localising the atom, leading to a more well-defined coupling strength. This feat thus constitutes the ultimate technical state-of-the-art for **WGM** resonators, and will be an all-important addition for future developments in **CQED** platforms of this type, with further applicability to experiments with emitters situated close to nanophotonic structures.

Although often dissimilar in practice and diverse in the approaches towards technological goals, the realisation of experiments centralised on emitter–photon interfaces with nanophotonic devices of various kinds [62] all share a commonality in that a plethora of sophisticated apparatus, all operating in tandem, are required. Modern set-ups seamlessly meld together efficient photonic engineering with highly-specialised vacuum, laser, measurement, and control technologies, each of which assuming indispensable integrants of a whole machine. These constituents, belonging to the class of so-called *enabling technologies*, can, nowadays, often be commercially sourced from research-focussed industry. Part of the art in designing such an experiment is to be familiar with the available options suited to each necessary division, while also envisioning their synchronous operation in a completed setting. This approach, coupled with an awareness of the inner workings of similar existing machines within the field, can result in an experimental set-up that boasts a broad horizon in its future explorations and technological promises.

In maintaining the spirit of this introduction – that of technological progress as a product of exploring fundamental questions, this thesis documents a small body of work in the same vein, contributing to the development of an updated **CQED** platform with **WGM** bottle microresonators, alongside the study of a counter-intuitive effect observed in light–matter interaction at the quantum scale. The latter, as is often the case in scientific exploration, unexpectedly arose during pursuit of the former.

1.2 Development of the Work in this Thesis

This thesis chronologically documents an important transitional chapter in the lifespan of the bottle microresonator **CQED** experiment. The origins of the experiment actually pre-date its initial construction in 2011 at the *Technische Universität Wien*, where the development of bottle microresonators as a **CQED** platform took place within the few years prior at the *Johannes Gutenberg-Universität Mainz*. Across the following 8 years, the growing set-up developed into one of the leading platforms employed to investigate the coupling of single atoms to a **Whispering-Gallery Mode** microresonator with the goal of engineering light–matter interaction at the quantum scale. During this time, it hosted a variety of researchers leading to the successful completion of around 13 Bachelor projects, 7 Master projects, 5 **PhD** theses and 3 Postdoctoral fellowships. In total, over 10 publications in peer-reviewed journals resulted from the important experimental findings [50, 53, 54, 56, 58, 63–68]. Of these, one of the most impactful results ushered in a new sub-genre of **CQED** – that of a *chiral* light–matter interaction – which opened the way for novel quantum devices to exploit this demonstrated feature. This chiral nature of the cavity field is exclusively offered by **WGM**-type microresonators due to their microscopic confinement of light that gives rise to exotic polarisation properties, thereby firmly setting them apart from other microresonator types. Still, one shortfall of these **WGM** microresonators is that an extended interaction between a single emitter and the **WGM** is technically challenging to realise, owing to the experimental difficulties associated with trapping the former in the evanescent field of the latter. The last remaining years of the bottle microresonator experiment in Vienna were dedicated to surmounting this obstacle, and much work was undertaken to implement a scheme for the *optical trapping* of single atoms within its **WGM** subject to the boundaries of the existing set-up.

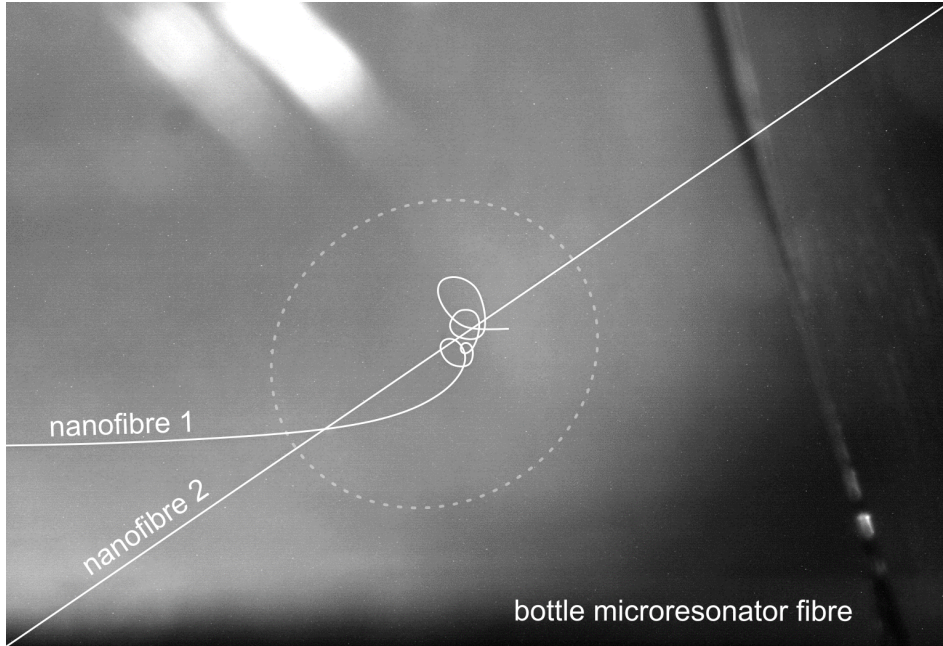


Figure 1.1. Broken nanofibre. A view into the unopened vacuum chamber that housed the bottle microresonator and its two coupling nanofibres, taken shortly after arrival in Berlin. Clearly, the primary nanofibre did not survive the transit, evident by the fact that it was found severed and coiled around the secondary nanofibre. The crossed nanofibres have been sketched over in white to aid in visibility, while the near-vertical fibre hosting the bottle microresonator is seen out of focus on the right.

It is at this point where this thesis begins. The successful demonstration of the strong coupling of trapped atoms to the WGM of the bottle microresonator [60] was achieved shortly before the entire experimental apparatus, and group, were relocated to the *Humboldt-Universität zu Berlin* in mid-2019. Movement took place by – quite literally – packing the entire experiment into boxes, loading them onto a truck, and bridging the ~ 700 km distance with a careful drive*. Upon arrival in Berlin, the unpacking and rebuilding of the experiment immediately commenced, with the idea of *picking up from where it was left off*. However, it was soon found out that one key component of the set-up had not survived the transit, as depicted in Figure 1.1. This unfortunate discovery of a broken nanofibre in fact presented itself as an opportunity to make some fundamental changes to the experimental apparatus, with the notion of improved atom trapping at the forefront. As such, the redesign process began with a particular focus in mind to address a number of limitations present in the previous design, which had not been initially planned out for atom-trapping over a decade ago. At the same time, a number of quality of life improvements could be implemented, such as a much more straightforward method for exchange of components within the vacuum system.

*The specialised transport company *Neumaier Logistics GmbH* aided in this endeavour.

Upon reaching a revised design to ensure the longevity of the apparatus, all the necessary components were ordered and assembly of the new set-up shortly began thereafter. This challenging task involved a list of over 50 new parts and devices, along with over 2000 assembling bolts. Initial construction was performed without the addition of in-vacuum fibres (i.e., the two nanofibres and bottle microresonator fibre), in order to fully realise a number of technical prerequisites, such as **Magneto-Optical Trap** alignment and the free-space optical dipole trapping of single atoms. It was during this stage that the research direction slightly detoured, due to the readily available source of single trapped atoms and efficient access to their scattered field. As such, measurements on the spectral filtering of the resonance fluorescence of these two-level atoms commenced, resulting in the observation of simultaneously scattered photon pairs [69]. This counterintuitive outcome shed new light on the interaction of light with matter at the fundamental level, and concluded a first experiment performed with the newly constructed apparatus – albeit without the bottle microresonator.

While at this stage the work presented in this thesis concludes, it should be mentioned that – at the time of writing – preparations for adding the fibres into the set-up are well underway. The aim is to insert an ultra-high quality bottle microresonator, in addition to its dual coupling nanofibres, into the newly constructed apparatus. Thus can begin explorations into the envisioned loading of a single optically trapped atom into the **WGM** of the bottle microresonator, to finally *pick up from where it was left off* prior to the move...

1.3 Organisation of the Thesis

This thesis chronologically accounts the work undertaken across a, broadly speaking, non-standard PhD period – where movement of the entire lab from Vienna* to Berlin† in 2019 acted as both a disruptor to ongoing progress and an opportunity for the implementation of new ideas. Due to this division in lab environments, the contents of the lab presently located in Berlin will be referred to throughout this thesis as the all-encompassing term: *CQED Experiment*, where the extensions 1.0 and 2.0 respectively refer to the original experiment moved from Vienna and its subsequent redesign in Berlin.

Accordingly, this thesis is structured as follows: after a presentation of some key concepts applicable to the experimental setting, Chapter 2 will present the theory underlying atom–light interaction in WGM resonators, as well as some major milestones of the CQED 1.0 experiment. A particular focus on the realisation of strongly coupling single optically trapped atoms to the Whispering-Gallery Mode of the bottle microresonator, that was accomplished shortly before the move to Berlin, concludes the discussion. The techniques employed and valuable lessons learned in the undertaking of this long-standing goal motivates that which is subsequently presented in Chapter 3: the design of the CQED 2.0 experiment upon arrival in Berlin. This Chapter contains exhaustive documentation on all aspects of the design, including its process and selected ongoing accomplishments, and is written primarily as reference material to aid future researchers working on the experiment, to thereby ensure its operational longevity. The next two Chapters 4 and 5 present a first experiment performed with the CQED 2.0 apparatus: concerning the spectral filtering of resonance fluorescence originating from a single two-level atom. By upsetting the delicate balance between the coherently and incoherently scattered components of the fluorescence light, it is shown that the antibunching present in the photon statistics only arises due to a fully destructive interference phenomena between the two-photon components in these two scattering processes. The complete removal of the coherent component leads to the observation of photon bunching, which, counterintuitively, indicates the presence of photon pairs that have been simultaneously scattered by the two-level atom. Chapter 4 will provide the theoretical background required for the understanding of the main experimental results presented in Chapter 5. The thesis concludes in Chapter 6, which provides a summary of the work, and more importantly, a discussion of the near- and long-term future prospectives in the redesigned *bottle microresonator CQED experiment*.

*Atominstitut, Technische Universität Wien, Stadionallee 2, 1020 Vienna, Austria.

†Institut für Physik, Humboldt-Universität zu Berlin, 10099 Berlin, Germany.

2

Cavity Quantum Electrodynamics with the Bottle Microresonator

Our resonator design seems particularly suited to be combined with a surface trap in order to couple trapped cold atoms to the resonator mode.

Y. Loyer, D. Meschede, and A. Rauschenbeutel, 2005 [61]

The goal of this Chapter is to introduce the *bottle microresonator* Cavity Quantum Electrodynamics (CQED) experiment and provide an overview of its rich and recent history. As specified at the closing of the opening Chapter in Section 1.3, the so-called *CQED experiment* is hereby referenced by two distinct time periods beginning from its conception: *CQED 1.0* encompasses all that was performed in Vienna since the experiment's initial construction, while *CQED 2.0* opens with the re-imagined experimental design upon moving to Berlin in 2019. Thus, an outline of the key concepts that underpin the experiment, along with a discussion of selected milestones throughout its former life so far, will help to contextualise the additions to the system within the framework of this thesis. For this, an introduction to single-emitter CQED and its relevance to the bottle microresonator platform will allow a delineation of the major milestones accomplished with this system along with its contextualisation within the field as a whole. A particular focus will be paid to the latest achievement performed with CQED 1.0 shortly before moving – the demonstration of strong coupling of a single optically trapped atom to the bottle microresonator, which has been published as an article in a peer-reviewed journal:

[60] E. Will, L. Masters, A. Rauschenbeutel, M. Scheucher, and J. Volz. Coupling a Single Trapped Atom to a Whispering-Gallery-Mode Microresonator. *Physical Review Letters* **126**, 233602 (2021),

and otherwise rigorously documented in the PhD thesis [70] preceding this work. The discussion of these specific results will provide the basis for justification of many of the design elements that make up the second generation of experiment in CQED 2.0, as will be subsequently presented in detail throughout Chapter 3.

2.1 Cavity Quantum Electrodynamics with a Single Emitter

While there are numerous ways to motivate the established field of Cavity Quantum Electrodynamics (CQED), many of which being application specific as outlined in Chapter 1, the first Nobel-Prize winning technique [71] to be encountered in this work is perhaps best summarised by the idea of wanting to study the interaction of light and matter, *at the most fundamental level*. In this endeavour, the most fundamental QED setting that can possibly be conceived is that of a single massive particle interacting with a single massless photon. While particles with mass, such as single atoms, can be located at very precise positions in space and time, single photons instead propagate through vacuum at the universal speed limit of c and can populate a continuum of spatio-temporal modes. The probability of interaction between the two, in free-space, is thus extraordinarily small. In order to render this interaction strong enough for study, both theoretically and experimentally, the main idea at the heart of CQED is to constrain the continuum of free-space photon modes to a discrete set, by employing a so-called *cavity* or *resonator*. Such a storage device for the photon thereby enhances the probability of its interaction with a quantum emitter that can be placed inside.

The commonly presented textbook example of an optical resonator [72, 73] suitable for a CQED setting, is a so-called *Fabry-Pérot (FP) cavity*, and is showcased in Figure 2.1. As depicted in Figure 2.1(a), it simply consists of two opposing and commensurate highly-reflective surfaces, which together define the spatial extension of the stored photon mode. The volume provided is also available for a quantum emitter to occupy, to then interact with the confined photon. Due to the boundary conditions imposed by the FP cavity structure as indicated in Figure 2.1(b), only light modes for which an integer number of half wavelengths, λ , is equal to the separation distance between the inner surfaces, d , are supported. The optical frequency, $\nu = c/\lambda$, of each of these so-called *resonances* take values expressed as

$$\nu_n = n \frac{c}{2d} \tag{2.1}$$

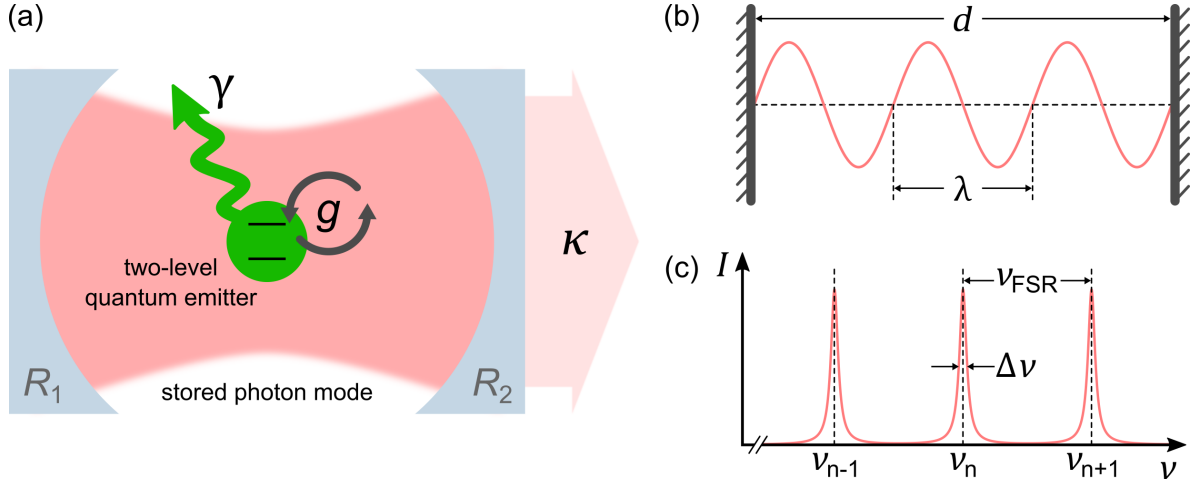


Figure 2.1. Textbook CQED. (a) Illustration of a typical CQED setting, comprising a single quantum emitter situated within the optical mode of a Fabry-Pérot cavity. A coherent energy exchange between the stored field and the emitter can take place at a rate g , with energy loss rates occurring via the cavity at a rate κ or irreversibly via the emitter at a rate γ – with these parameters characterising the system. (b) A simplified planar FP cavity supports an integer number of half wavelengths within a mirror separation of d . (c) An illustration of the intra-cavity intensity as a function of the optical frequency, highlighting the supported resonance frequencies of ν_n , that each have a spectral width of $\Delta\nu$ and are separated by ν_{FSR} .

with $n \in \mathbb{N}$. Adjacent resonances are separated by the *Free Spectral Range (FSR)*, $\nu_{\text{FSR}} = c/2d$, and can be tuned by the parameter d . In a realistic scenario, the surfaces making up the cavity do not have a perfect reflectivity, which gives rise to a leakage of light out of the resonator mode as depicted in Figure 2.1(a) and 2.1(c). This limited $1/e$ photon lifetime, τ_{photon} , consequently has the effect of broadening the otherwise infinitely narrow resonances, to a spectral width of

$$\Delta\nu = \frac{1}{2\pi\tau_{\text{photon}}} = \frac{\nu_{\text{FSR}}}{\mathcal{F}}. \quad (2.2)$$

Here, a key parameter for optical resonators, $\mathcal{F} = \nu_{\text{FSR}}/\Delta\nu$, is introduced on the right hand side: the *finesse*. It can be interpreted as the number of roundtrips that the light can perform within the cavity before being irreversibly lost by leakage through one of the surfaces, and is given by

$$\mathcal{F} = \frac{\pi(R_1 R_2)^{1/4}}{1 - \sqrt{R_1 R_2}}. \quad (2.3)$$

Each of the two surface reflectivities are denoted R_1 and R_2 , and typically have values close to unity.

A related parameter that is used to quantify the performance of resonators, is the *quality factor* Q . It compares the photon lifetime in the resonator to its optical period $T_{\text{opt}} = 2\pi/\omega$ as

$$Q = 2\pi \frac{\tau_{\text{photon}}}{T_{\text{opt}}} = \frac{\omega}{\Delta\omega}. \quad (2.4)$$

2. Cavity Quantum Electrodynamics with the Bottle Microresonator

The quality factor and finesse, together with the specific resonator mode of angular frequency $\omega = 2\pi\nu$, provide a convenient way to express the properties of a cavity. The two are related by the expression $Q = \omega d\mathcal{F}/\pi c$, which illustrates that, for **FP** cavities, Q is effectively unbound as it is explicitly dependent on the roundtrip length, $2d$, which can in principle be arbitrarily enlarged without introducing further cavity losses. Although often equally important in many applications, Q is the parameter typically used for resonators in which losses accumulate with increased roundtrip length, such as **WGM** resonators, while \mathcal{F} can be used for resonators where losses are roundtrip length-independent, such as **FP** resonators [74]. Both the quality factor and the finesse, in their respective applicabilities, indicate the degree to which light can be temporally stored inside a resonator: the larger Q or \mathcal{F} , the longer a photon remains inside the resonator mode, and the narrower the spectral width of the resonant mode. State of the art **FP** microresonators reach values of $\mathcal{F} > 10^6$ [75, 76], and **WGM** counterparts achieve Q 's in the range $10^8 - 10^{11}$ [63, 74, 77, 78], with corresponding resonance linewidths of only several (tens of) megahertz.

Besides the figure of merit for the temporal confinement of light inside a given resonator, the second key parameter is the spatial confinement, which is characterised by the mode volume V . It is given by the spatial integral over the normalised intensity distribution [61]

$$V = \int n^2(\mathbf{r}) \frac{I(\mathbf{r})}{I_{\max}} d\mathbf{r}, \quad (2.5)$$

where $n(\mathbf{r})$ and $I(\mathbf{r})$ are the refractive index and mode intensity at position \mathbf{r} , with I_{\max} being the peak intensity. In general, stronger confinement of the light leads to an enhancement of the mode intensity. This explains the motivation behind the term *microresonator*, which have geometries on the micrometre scale, enabling truly microscopic mode volumes down to the order of λ^3 * [79, 80].

Together, the mode volume and quality factor combine as a crucial performance indicator of microresonators for **CQED** applications, for which their ratio, Q/V , should be maximised [37]. This becomes evident by considering how a single atom inserted into the resonator interacts with a single resonator mode that coincides with the atomic transition frequency. Under this condition, the emitter and the cavity can exchange photons, where the strength of this interaction, g_0 , is governed by the field per photon at the position of the atom along with the electric dipole moment of the transition under investigation. For an atom under the two-level approximation, the latter is given by the dipole matrix element, $d_{ge} = \langle g | \hat{d} | e \rangle$, between the ground state $|g\rangle$ and the excited state $|e\rangle$. The position-dependent coupling strength is then [81]

$$g(\mathbf{r}) = \sqrt{\frac{d_{ge}^2 \omega}{2\epsilon_0 \hbar V}} \Psi(\mathbf{r}) = g_0 \Psi(\mathbf{r}), \quad (2.6)$$

*Note that these ultra small mode volumes typically come at the expense of reduced quality factors.

with the resonator mode function, $\Psi(\mathbf{r})$, defined by the mode volume such that $V = \int |\Psi(\mathbf{r})|^3 d\mathbf{r}$. The coupling strength above defines the rate at which coherent energy exchange can occur within the coupled atom-resonator system, in successive absorption and emission cycles of a single photon from and into the resonator mode by the atom. It is an important parameter when defining the well-known coupling regimes of **CQED** [72]. Of utmost importance for the practical observation of such cyclic energy exchange, the coupling strength must far outweigh all of the dissipative loss rates present in the system: which can result in reaching the so-called *strong-coupling regime* of **CQED**. The first loss channel arises from the finite lifetime of a photon in the resonator mode, τ_{photon} , which signifies that a photon emitted into the resonator mode by the atom has a chance to be *irreversibly* lost before it can be reabsorbed. This loss is typically expressed as the total resonator loss rate

$$\kappa = \frac{\omega}{2Q}, \quad (2.7)$$

which is equal to the modal linewidth (cf. eq. (2.4)). The second loss channel stems from an intrinsic property of the atom itself, in that, emission of photons into free space occurs isotropically at a rate given by the spontaneous emission rate [82]

$$\gamma = \frac{d_{ge}^2 \omega_0^3}{12\pi\epsilon_0 \hbar c^3}, \quad (2.8)$$

where the excited state lifetime of the atom is $\tau = 1/2\gamma$. Hence, there is a probability that the excited atom decays and emits a photon into the continuum rather than the resonator mode, in another *irreversible* process. Reaching the strong-coupling regime ensures that a *reversible* process between the single photon and single atom can occur before the aforementioned irreversible processes interrupt, and is thus defined by

$$g \gg \{\kappa, \gamma\}. \quad (2.9)$$

Due to the local reduction in the density of photonic (or vacuum) states at the position of the atom by the presence of the resonator, the resonant atom will experience an enhanced emission rate into the resonator mode by a factor $C\gamma$. Introducing the parameter *single-atom cooperativity*, C , as [25]

$$C = \frac{3\lambda^3 Q}{4\pi^2 V}, \quad (2.10)$$

the definition of the strong coupling regime can then be restated as

$$\frac{g^2}{2\kappa\gamma} = C \gg 1. \quad (2.11)$$

By comparison of equations (2.10) and (2.11), it is apparent that the attainment of strong coupling between the atom and resonator mode is effectively determined by

the properties of the resonator alone, Q/V . Advances in manufacturing techniques of nanoscale chip-based **FP** cavities has enabled Q/V ratios of up to $10^5\lambda^{-3}$ [83], while the largest values of Q/V have been obtained with **WGM** microresonators, exceeding $10^6\lambda^{-3}$ [84]. The bottle microresonator belongs to this latter class, for which its general introduction in Section 2.2 follows a brief visit into the specific type of single emitter employed in this **CQED** experiment.

2.1.1 Rubidium as a Quantum Emitter

The **CQED** experiment has traditionally been continuously operating with **Rubidium (Rb) 85** as the emitter of choice, for a variety of reasons as shall now be outlined in brief, particularly for relevance to the upcoming discussions of the milestones achieved with the apparatus.

The alkali metals, of which **Rb** is a member, are a particularly important class of elements from group 1A of the periodic table that are attractive for quantum optics experiments with neutral atoms. This is due to the fact that, in general, they possess one valence electron in an outer s^* shell, with all remaining inner orbitals filled. Thus, they behave as quasi-one-electron atoms and can be effectively treated as such[†]. In particular, the strong D-lines exhibited by this class of atoms can offer closed sub-transitions that are suitable for optical cooling and are easily addressed by current laser technologies. This has enabled a number of these species – besides **Rb** [85] – to be cooled to quantum degeneracy; including Lithium [86], Sodium [87], Potassium [88][‡], and **Cs** [89]. Francium, on the other hand, possesses the highest mass of all the alkalis and has no stable isotope. It instead alludes to being a promising candidate for tests of parity non-conservation [90]. **Rb** and **Cs** are perhaps the most abundantly utilised alkalis, due to their D-line transitions being accessible by inexpensive semiconductor laser diodes, respectively at wavelengths around 780 nm and 852 nm. ¹³³**Cs** is the primary atomic frequency standard, providing the modern day definition of time [91]. However, ⁸⁵**Rb** was chosen at the time of **CQED 1.0**'s construction simply due to the commercial availability of semiconductor diode lasers along with highly efficient optical components and detectors at the transition wavelength, and – more importantly – due to the expectation of reaching the strong coupling regime with the bottle microresonator [92, 93]. As such, it is sensible to retain this historical decision upon redesign of the experiment (see Chapter 3).

At room temperature, **Rb** metal is a soft solid composed of the two naturally occurring isotopes ⁸⁵**Rb** (72.2%) and ⁸⁷**Rb** (27.8%), that conveniently melts at around 39.5 °C with a vapor pressure of several 10^{-6} mbar [94]. In its ground state, its full electron

* s is the spectroscopic notation for an orbital state with angular momentum quantum number $l = 0$.

[†]However, unlike a true one-electron atom (i.e., Hydrogen), the gross energy of the valence electron in the alkalis depend both on the principal and orbital quantum numbers, n and l .

[‡]Note that this was achieved by sympathetic cooling with ⁸⁷**Rb**.

configuration is $1s^2 2s^2 p^6 3s^2 p^6 d^{10} 4s^2 p^6 5s^1$, with the first excited state of the outermost single valence electron in short denoted as $[\text{Kr}] 5p^{1*}$. As a result of the interaction between the magnetic field generated by the orbital motion of the valence electron and the magnetic dipole of its own spin – so called *spin-orbit coupling* [95] – its $5S \rightarrow 5P$ transition is split into two fine structure components that make up the well-known D-line doublet of Rb [96]. A hyperfine level structure on each of these D_1 and D_2 transitions are also present due to interaction between the electron and nuclear total angular momenta [95], as indicated in Figure 2.2 exclusively for ^{85}Rb . In particular, the $F = 3 \rightarrow F' = 4$ cycling transition of the D_2 line is of relevance for optical cooling and trapping (see Sections 3.4 and 2.4.1 for further discussions). Finally, each hyperfine F level consists of $2F + 1$ degenerate magnetic m_F sublevels, whose degeneracy can be lifted by application of an external weak magnetic field [97]. As shall be seen in the upcoming Sections, a number of particular transitions within this so-called Zeeman substructure (and their relative strengths) are important for the realisation of a variety of novel and non-reciprocal devices with the bottle microresonator platform. This, in particular, led to the advent of *chiral quantum optics*, which is the topic of Section 2.2.4.

Figure 2.2 showcases a selection of important properties intrinsic to ^{85}Rb that are of relevance to the CQED experiment, and are included as a reference for much of the work presented throughout this thesis.

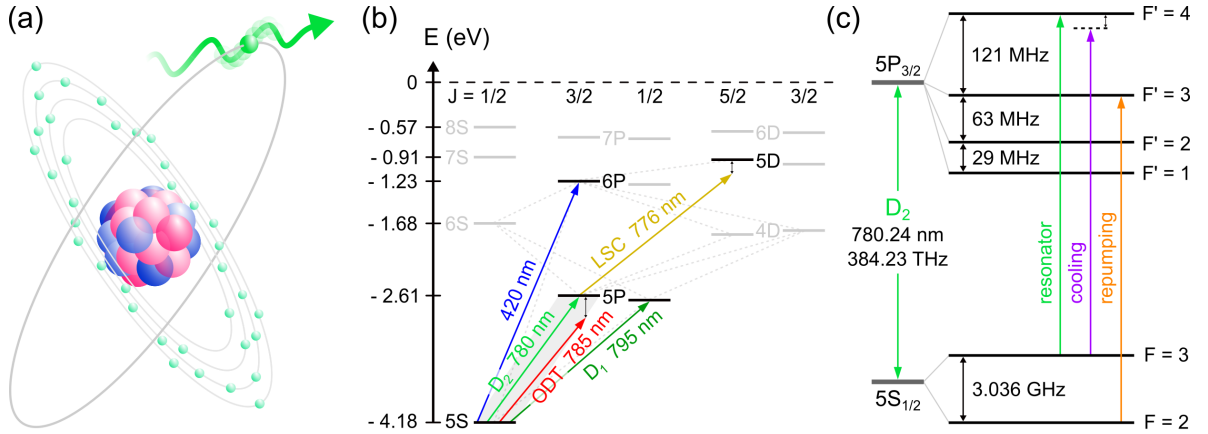


Figure 2.2. Rubidium 85. (a) A Bohr-like representation of the Rb atom, with the outer most valence electron and its response to resonant light pictorially indicated. (b) An energy level diagram of ^{85}Rb , with vacuum wavelengths of relevant transitions indicated. (c) A zoom on the D_2 transition depicted in (b), showcasing the hyperfine structure of this transition. Note that laser lines of relevance are included as coloured arrows, and that these diagrams are not to scale.

* p is the spectroscopic notation for an orbital state with angular momentum quantum number $l = 1$.

2.2 CQED with Whispering-Gallery Mode Microresonators

A brief overview concerning the active research field of single-emitter CQED was given in Section 2.1, mainly within the common textbook example of FP resonators (cf. Figure 2.1) while general WGM resonators were only briefly touched upon. Following the introduction of ^{85}Rb as the single emitter of choice for the CQED experiment in the preceding Section, an in-depth look at the specific type of WGM resonator that is utilised – the so-called *bottle microresonator* – is now warranted. An introduction to the general concepts of the WGM class of microresonators precedes a presentation of the bottle microresonator, including its fabrication and near-lossless in- and out-coupling of light, before its lead role in the advent of *chiral* CQED is discussed. It is this last feature of the bottle microresonator, and of WGM resonators in general, that firmly sets it apart from conventional FP-type resonators.

2.2.1 Optical WGMs

Whispering-Gallery Modes are running-wave eigenmodes that exist within resonators possessing a (quasi-)cylindrical or spherical geometry, and gain their namesake from the acoustic domain phenomenon witnessed inside St. Paul’s Cathedral and first described by John William Strutt (Lord Rayleigh) in the early 20th century [98, 99]. Remarkably, vocal whispers at the interior wall of the dome structure are audible at any other point along its circumference, and even directly across the grand 32 m diameter of the so-called *Whispering Gallery* at St Paul’s. This curious effect was explained as a refocussing of the travelling sound waves by the curved surface, and it was further postulated that such propagation modes would exist for electromagnetic waves too. Indeed, the optical equivalent of these acoustic WGMs can be excited inside numerous dielectric WGM microresonator structures that feature a principle circular cross section, as depicted in Figure 2.3. These modes are most-easily understood as consisting of closed-trajectory rays that are radially confined by a series of specular reflections at the interface between the optically thicker medium of the resonator material (refractive index n_1) and its (vacuum, refractive index n_2) surroundings. The condition for such *total internal reflection* of the rays occurs when the initial angle of incidence at the boundary, Θ (which fixes the angle of each subsequent reflection), is greater than the critical angle, Θ_c , by application of Snell’s law

$$\Theta > \Theta_c = \arcsin\left(\frac{n_2}{n_1}\right). \quad (2.12)$$

Thus, all rays fulfilling the above condition will be equatorially guided, for which an example trajectory is depicted in Figure 2.3(a). In the limit of glancing incidence, where

$\Theta \approx \pi/2$, the distance between two consecutive reflections, given by $d = 2R_0 \sin 2\Theta$, tends to zero. The ray is then radially confined at the radius of the resonator R_0 , and the roundtrip length is then equal to the resonator circumference of $2\pi R_0$. As similarly seen for the case of **FP** resonators in Section 2.1, resonances occur in **WGM** microresonators when the roundtrip length is equal to an integer number of half wavelengths.

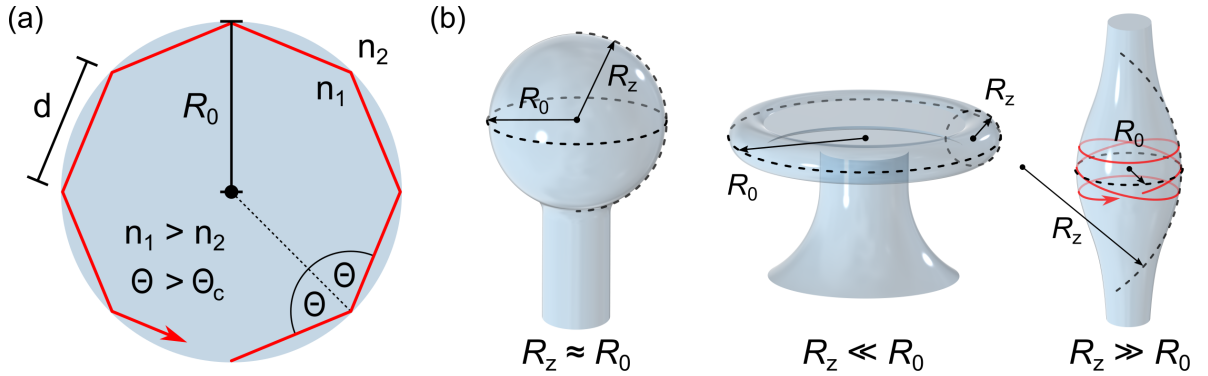


Figure 2.3. Whispering-Gallery Mode resonators. (a) A cross-sectional schematic of an example ray path wave that is guided and radially confined, via total internal reflection, within a circular resonator structure of equatorial radius R_0 and refractive index n_1 . (b) Examples of different **WGM** microresonator geometries, from left to right: microspheres, microtoroids, and microbottles. Each, in turn, is characterised by the relationship between R_0 and the axial radius of curvature, R_z , as denoted. An example spiral ray path is illustrated for the bottle microresonator.

In contrast to conventional **FP** resonators that support standing wave modes, the modes supported by **WGM** resonators are running waves. By extending the presented ray path picture into the third dimension and applying an axial radius of curvature, R_z , such running wave rays can spiral back and fourth along this axis before closing. A selection of **WGM** microresonator geometries supporting these extended roundtrips are depicted in Figure 2.3(b), including largely spherical microspheres where $R_z \approx R_0$ [100, 101], disk-like microtoroids with $R_z \ll R_0$ [77, 102, 103], and the highly prolate-spheroid bottle microresonator for which $R_z \gg R_0$ [104]. The emergence of evanescent fields that are tightly bound to the surface is a feature shared by all **WGMs** of these microresonator geometries. It enables the in-coupling of light into the resonator via *frustrated* total internal reflection with the use of prisms [101, 105], angle-polished fibres [106], or from so-called *tapered optical fibres* that have the added benefit of near-lossless coupling in a fibre-integrated setting [107]. It is for this latter coupling method that a focussed discussion follows in the next Sections.

2.2.2 Optical Nanofibres

Tapered optical fibres are cylindrically-symmetric waveguides that are fabricated from standard optical glass fibres using a *heat-and-pull* process [108]. Of these, *nanofibres* in particular feature a waist-section with a constant diameter of only a few hundred nanometres, that is sandwiched between two adiabatic taper transitions that bridge the axial variation in the radius between the nominal fibre diameter of $\sim 125\ \mu\text{m}$ and the $< 1\ \mu\text{m}$ -diameter nanofibre waist. Remarkably, by careful design of these transitions [109, 110] and with use of a dedicated fibre-pulling rig* [111], a near lossless transmission of light can be achieved, *even when the wavelength of the guided field is larger than the waist diameter*. In this case, a considerable part of the intensity exists in free space around the nanofibre, and is guided as a radially-decaying evanescent wave by the index jump between the glass and surrounding environment of usually vacuum or air. The access gained to this part of the fibre-guided field from the outside has meant that optical nanofibres are widely utilised in a diverse range of (quantum optics) applications [112], and particularly constitute an attractive tool for the efficient coupling of light to (arrays of [113]) single quantum emitters [114–116].

When the evanescent field of the guided nanofibre mode overlaps that of a microresonator's **WGM**, the nanofibre acts as an extremely efficient coupling waveguide for which almost 100% of the light can be transferred from the guided mode into the **WGM** [107]. By controlling the separation between the two structures, a widely tunable coupling scheme can be realised due to the exponential decay of each evanescent field [117]. Such coupling tunability is not typically possible for **FP** resonators, where access to the sustained cavity mode is given by the initial design and fabrication of the incoupling mirror. Thus, the nanofibre constitutes a near-perfect method for tunably coupling light into and out of the bottle microresonator. A schematic of the nanofibre and its use as a coupling device is shown in Figure 2.4.

The introduction of the nanofibre as a tunable coupling device for a **WGM** microresonator provides access to three different coupling regimes, that can be simply controlled by the fibre–resonator separation. As illustrated in the zoom of Figure 2.4, the coupling rate between the nanofibre and the resonator is denoted as κ_{ext} , with the intrinsic resonator loss rate κ_0 , such that the total resonator losses are $\kappa = \kappa_{\text{ext}} + \kappa_0$. Transmission through the coupling fibre thus depends on the interference between the incoming guided light, and that which is outcoupled from the resonator mode. In the absence of a coupled atom, the evanescent coupling between the resonator and the

*The fibre-pulling rig acts to linearly translate an uncoated fibre along its axis relative to a fixed heat source that originates from either a hydrogen-oxygen flame or a focussed CO_2 laser spot. In doing so, the heated fibre is simultaneously elongated by pulling on each end. By a combination of precise calibration of the rig and computer control of the pulling and heating processes, the axial radius variation of the fibre can be set as desired.

nanofibre waveguide depends on the relation between κ_{ext} and κ_0 , and can thus be distinguished by

Under-coupling ($\kappa_{\text{ext}} < \kappa_0$). Since the intrinsic resonator loss dominates over the nanofibre coupling rate, outcoupled light from the resonator only partially destructively interferes with the incoming light. The nanofibre transmission is therefore non-zero for large separation distances.

Critical coupling ($\kappa_{\text{ext}} = \kappa_0$). At the point of critical coupling, and on resonance, the magnitudes of the incoming light and the outcoupled light are equal but π out of phase. The two fields therefore fully destructively interfere, resulting in zero transmission through the nanofibre. All the incident light power is therefore coupled into the resonator, and dissipated therein.

Over-coupling ($\kappa_{\text{ext}} > \kappa_0$). Since the nanofibre coupling rate now dominates over the intrinsic resonator loss, the outcoupled light is larger in magnitude than the incoming light resulting in its destructive interference. The residual π -shifted outcoupled light leads to a non-zero transmission in the nanofibre for small separation distances.

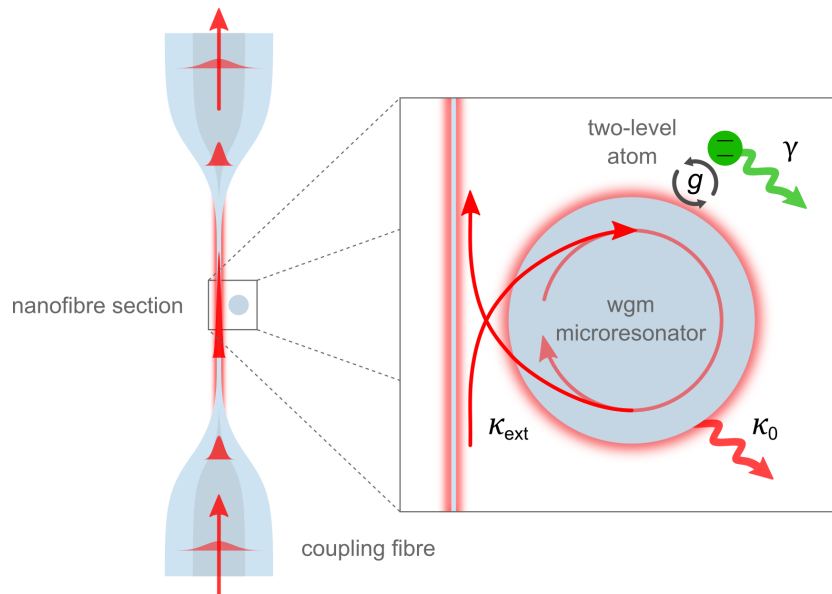


Figure 2.4. Nanofibre–resonator coupling. A schematic of a tapered optical nanofibre, illustrating the transition between the standard optical fibre to a nanofibre waist section and back again (left). The core-guided mode, depicted by its cross-sectional Gaussian intensity distribution, is propagating upwards. It is spatially compressed by the adiabatic reduction in the fibre-diameter, before propagating with an appreciable evanescent wave through the nanofibre section. A reversal of the taper ensures almost unity transmission. The zoom (right) depicts excitation of a **WGM** via evanescent coupling between the nanofibre guided mode and a **WGM** microresonator with intrinsic losses κ_0 , that occurs at a rate κ_{ext} . A two-level atom within the **WGM** can couple at a rate g , but has a spontaneous emission into free-space at a rate γ . Figure not to scale.

The point of critical coupling is of particular interest: on resonance, the transmission through the coupling fibre is zero. An atom entering the resonator field then adds an additional loss mechanism at the rate γ , thereby destroying the perfect destructive interference between the incoming and outcoupled field resulting in a non-zero fibre transmission. By continuously monitoring the transmission through the critically-coupled nanofibre, a strong increase in its transmission can be used to signify the coupling of individual atoms to the resonator **WGM**. This detection method will be outlined in more detail in Section 2.3.

2.2.3 The Bottle Microresonator

The bottle microresonator is produced in a fashion similar to nanofibre fabrication (cf. previous Section 2.2.2), but rather in a *two-step* heat-and-pull process [118]. The standard optical glass fibre is first tapered to a thickness of the desired microresonator diameter, $2R_0$, before a local heating at two axially separated spots – alongside a simultaneous pulling – generates two microtapers. The ultra-smooth bulge that remains in between is the *bottle* shape of the bottle microresonator, with a curvature determined by the positions and dimensions of the microtapers. The resonator used in the **CQED** 1.0 experiment featured microtapers separated by around $150\ \mu\text{m}$, resulting in an axial curvature of $\Delta k = 0.014\ \mu\text{m}^{-1}$ and central radius of $R_0 \approx 18.5\ \mu\text{m}$ [92, 93].

The zoom of Figure 2.4 schematically illustrates the evanescent coupling between a nanofibre and the **WGM** (bottle) microresonator in 2D, while Figure 2.3(b) depicts a simplified example of a closed ray path spiral along the axial direction of the bottle microresonator in 3D. The radial confinement is due to circumferential total internal reflection (cf. 2.3(a)), while the axial confinement is imposed by a parabolic potential for the light that arises from the prolate structure of the bottle. Such axial spiralling of the light between two turning points – the so-called *caustics* – results in an axial standing wave structure with a large intensity at each caustic. The three-dimensional structure of an example bottle mode is represented in Figure 2.5, which illustratively shows the spatial profile of the excited **WGM** in both the axial and radial directions. In order to gain insight into the full mode structure and polarisation properties of such an excited **WGM**, in addition to their spectral attributes, a model of the electromagnetic field distribution around the dielectric boundary is necessary. While there exists a direct analytic solution for microsphere **WGM** resonators due to their spherical symmetry [119], an approximate solution for the prolate spheroidal bottle microresonator can still be theoretically obtained despite its axial radius-dependence [61]. The main points out of a full derivation of the bottle microresonator **WGM** structure [93, 118] is outlined in the following.

The bottle microresonator is most intuitively described in a cylindrical coordinate basis, for which the radial, azimuthal, and axial components are respectively given by

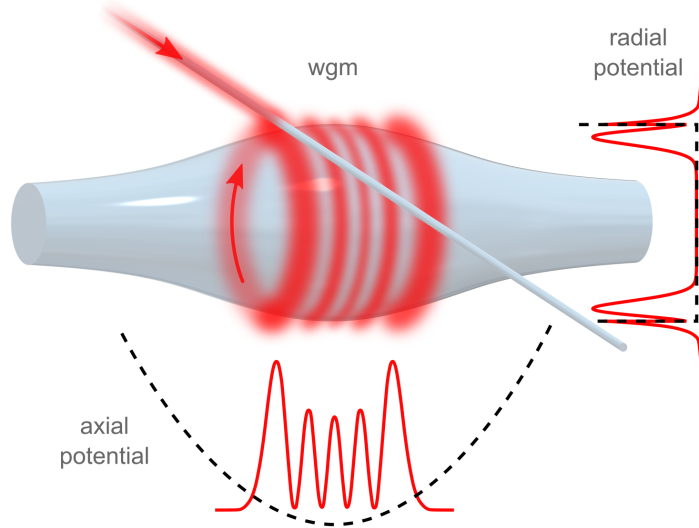


Figure 2.5. Bottle microresonator WGM. An example three-dimensional spatial mode structure of the critically-coupled bottle microresonator, with the axial and radial intensity distributions indicated respectively underneath and to the right in an illustrative fashion. The axial parabolic potential for the light confines the $q = 4$ excited mode between two caustics, while the lowest order $p = 0$ radial mode experiences a discontinuity at the resonator border for a **TM**-polarised mode. The coupling nanofibre is positioned at the left-most caustic.

$\{r, \phi, z\}$. The central bottle profile of the resonator is approximated as being parabolic along z , such that the axial variation in the radius is described by

$$R(z) \approx R_0 \left(1 - \frac{(\Delta k z)^2}{2} \right), \quad (2.13)$$

with $R_0 = R(z = 0)$ as the nominal (maximal) radius, and Δk the bottle curvature that is further assumed to be small and fulfilling $dR/dz \ll 1$. Under this approximation, the radial component, k_r , of the **WGM** wavevector, $\mathbf{k} = \{k_r, k_\phi, k_z\}$, can be neglected [61]. Thus, the slight axial dependence of \mathbf{k} , for which $|\mathbf{k}| = k \approx \sqrt{k_\phi^2 + k_z^2}$ is contained within $k_\phi = 2\pi n R_c / \lambda_0 R(z)$, where R_c is the radius at which the turning point (caustic) lies where k_z vanishes. This then allows for the construction of a separable* wavefunction for describing the eigenmodes of the bottle microresonator, $\Psi(r, \phi, z) = \mathcal{R}(r, R(z)) \cdot Z(z) \cdot \Phi(\phi)$, which must obey the Helmholtz equation [73]

$$(\nabla^2 + k^2)\Psi = 0. \quad (2.14)$$

Due to the cylindrical symmetry of the problem, the azimuthal part of the wave equation can be independently solved, yielding solutions of the form $e^{(im\phi)}$, with the azimuthal quantum number $m \in \mathbb{Z}$ counting the number of wavelengths around the circumference of the resonator. With this, the Helmholtz equation above separates into two differential

*The radial part still has a weak z -dependence due to the small axial variation of the radius.

equations

$$\left(\partial_r^2 + \frac{1}{r} \partial_r + k_\phi^2 - \frac{m^2}{r^2} \right) \mathcal{R} = 0, \quad (2.15)$$

$$\left(\partial_z^2 + k^2 - k_\phi^2 \right) Z = 0, \quad (2.16)$$

which can each be independently solved to obtain the radial and axial parts of Ψ . As the radial equation (2.15) has the form of a Bessel differential equation, the solutions consist of linear combinations of Bessel functions, J_m , and Hankel functions, Y_m . By restricting to modes that are well localised at the resonator surface, the possible solutions take the form [93]

$$\mathcal{R}_l(r, z) = \begin{cases} A_l \cdot J_m(k_\phi(z) \cdot r), & \text{for } r \leq R(z) \\ B_l \cdot Y_m(k_\phi(z) \cdot r), & \text{for } r > R(z), \end{cases} \quad (2.17)$$

where the index l represents the respective vectorial component of the electromagnetic field. The constants A_l and B_l are constrained by the boundary conditions imposed for a given polarisation at the dielectric–vacuum interface, along with the resonance condition for λ_0 and R_c [93, 108]. Specifically, the axial (\mathcal{E}_z and \mathcal{H}_z) and azimuthal (\mathcal{E}_ϕ and \mathcal{H}_ϕ) field components are parallel to the resonator interface at $r = R(z)$, and therefore must be continuous across it. Conversely, the radial (\mathcal{E}_r and \mathcal{H}_r) field components can be discontinuous at the interface in line with the boundary conditions for electric fields at normal incidence. Satisfactory solutions can then be labelled with the radial quantum number, $p \in \mathbb{Z}$, that counts the number of intensity nodes along the radial direction.

The axial equation (2.16), on the other hand, assumes the form of a differential equation for a harmonic oscillator due to the assumed parabolic profile of the resonator. It therefore has the well-known solution given by

$$Z_{m,q}(z) = \sqrt[4]{\frac{\Delta E_m}{\pi 2^{2q+1} (q!)^2}} \cdot H_q \left(\sqrt{\frac{\Delta E_m}{2}} \cdot z \right) e^{-\frac{\Delta E_m}{4} z^2}, \quad (2.18)$$

where H_q is a Hermite polynomial with axial quantum number $q \in \mathbb{Z}$ that counts the number of intensity nodes along the axial distribution. These axial eigenmodes each have a discrete energy eigenvalue given by $E_{mq} = (q+1/2)\Delta E_m$, where $\Delta E_m = 2m\Delta k/(c_r R_0)$, and corresponding wave numbers of the form

$$k_{m,q} = \sqrt{\frac{m^2}{(c_r R_0)^2} + \left(q + \frac{1}{2} \right) \frac{2m\Delta k}{c_r R_0}} \quad (2.19)$$

where a correction factor, c_r , that accounts for the radial intensity distribution of the modes has been used [93, 118].

Together, equations (2.17) and (2.18) allow for an accurate calculation of the spatial intensity distribution of a **WGM** with quantum numbers (p, m, q) that is supported by

a bottle microresonator of a given geometry. Furthermore, equation (2.19) allows for an estimation of the azimuthal and axial FSRs in the limit of low curvatures as [61]

$$\Delta\nu_m = \frac{c}{2\pi n} \cdot (k_{m+1,q} - k_{m,q}) \approx \frac{c}{2\pi n} \frac{1}{c_r R_0}, \quad (2.20)$$

$$\Delta\nu_q = \frac{c}{2\pi n} \cdot (k_{m,q+1} - k_{m,q}) \approx \frac{c}{2\pi n} \Delta k. \quad (2.21)$$

Clearly, the spectral attributes of the bottle microresonator are defined by its structural properties, R_0 , Δk and n . Thus, the tuning of these parameters will correspondingly tune the resonance frequencies of each WGM, by virtue of a geometrical change in the optical path lengths. This poses an attractive feature offered by the bottle microresonator, in that, tuning of a resonance frequency can easily be accomplished by simply pulling on each end of the bottle fibre. Such a mechanical *strain-tuning* elastically deforms the bottle microresonator structure, and can thus be used to bridge an axial FSR [118] or to actively stabilise its resonance frequency [64, 92].

2.2.4 Chiral CQED

When experimentally investigating the interaction of single (^{85}Rb) atoms with a resonant WGM supported by the bottle microresonator, the initially unexpected observations could only be explained by considering the full vectorial nature of the evanescent field [50, 93]. The response of the coupled atom–resonator system was observed to depend qualitatively on the polarisation properties of the excited WGM. This spectacular and rare demonstration of *Yhprum’s law** brought fourth the advent of *chiral*, i.e., direction-dependent, CQED present in WGM resonators, and paved the way for many interesting applications within the framework of chiral quantum optics [53, 68]. In the following, the polarisation properties of a WGM microresonator will be presented, before leading into the consequences of this for the light–matter interaction.

The bottle microresonator can fundamentally support two types of polarisation modes (arising from the two sets of solutions from the radial equation (2.17)), for which the electric field vector either lies parallel (Transverse Electric (TE) mode) or perpendicular (Transverse Magnetic (TM) mode) to the resonator axis. The electromagnetic field of a TE mode is thus described by the components \mathcal{H}_r , \mathcal{H}_ϕ , and \mathcal{E}_z – while conversely – only \mathcal{E}_r , \mathcal{E}_ϕ and \mathcal{H}_z are non-vanishing for a TM mode. It is for this latter class of WGMs that both a transverse (\mathcal{E}_r) and a longitudinal (\mathcal{E}_ϕ) electric field component occur, rendering their description in the standard paraxial approximation invalid [68]. In particular, this longitudinal component is comparable in magnitude to the transverse component due to a strong confinement of the mode, but has its direction intrinsically linked to the azimuthal circulation-direction of the WGM [93]. Since the resonator additionally supports a set of two degenerate running wave modes – one which circulates *Clockwise*

*The colloquial inverse of the epigram *Murphy’s law*.

(CW) in the $-\phi$ -direction, and one Counter-Clockwise (CCW) in the $+\phi$ -direction – the longitudinal component respectively lies along either $\mathcal{E}_{\pm\phi}$. By defining the orthogonal polarisation basis states of $\mathbf{e}_{\sigma^\pm} = (\mathbf{e}_r \pm i\mathbf{e}_\phi)/\sqrt{2}$ and $\mathbf{e}_\pi = \mathbf{e}_z$ for the quantisation axis chosen along the resonator axis (z), the overlap of the polarisation for each of the CW and CCW TM modes with pure σ^\pm circular polarisations close to the resonator surface can be computed as [120]

$$\frac{|\mathcal{E}^{ccw} \cdot \mathbf{e}_{\sigma^+}^*|^2}{|\mathcal{E}^{ccw}|^2} = \frac{|\mathcal{E}^{cw} \cdot \mathbf{e}_{\sigma^-}^*|^2}{|\mathcal{E}^{cw}|^2} = 0.97, \quad (2.22)$$

$$\frac{|\mathcal{E}^{ccw} \cdot \mathbf{e}_{\sigma^-}^*|^2}{|\mathcal{E}^{ccw}|^2} = \frac{|\mathcal{E}^{cw} \cdot \mathbf{e}_{\sigma^+}^*|^2}{|\mathcal{E}^{cw}|^2} = 0.03. \quad (2.23)$$

Together, the magnitude and direction of the longitudinal electric field component gives rise to a local polarisation that is almost perfectly circularly polarised, where the handedness, or local spin vector, is determined by the propagation-direction in a phenomenon known as the *spin-momentum locking* of light [51, 52]. This is schematically illustrated in Figure 2.6, where for the case of a TM-polarised WGM as shown in Figure 2.6(b), the CCW (CW) leads to a σ^+ (σ^-) polarisation of the evanescent field close to the surface cf. equation (2.22). Again, for the TE-polarised case as shown in Figure 2.6(a), the evanescent field is linearly polarised along the quantisation axis everywhere. Figure 2.6(c) demonstrates how these polarisation properties of the specifically excited WGM will drive specific transitions in the Zeeman substructure of an atom placed within the mode. It is this direction—dependence of the polarization of the counter-propagating TM WGMs that translates into a *chiral light-matter interaction*, as shall be discussed in the following.

In general, a full quantum mechanical description of the coherent interaction between a single atom and a single mode of the electromagnetic field was first provided by Jaynes and Cummings in 1963 [121]. The aptly named *Jaynes-Cummings Model* considers a two-level atom that exists either in its ground state $|g\rangle$ or its excited state $|e\rangle$, along with the quantised field mode that is characterised by the number of photons it contains $|n\rangle$. The full system, including their mutual interaction, is then described by the Jaynes-Cummings Hamiltonian

$$\hat{H}_{\text{JC}} = \hat{H}_{\text{A}} + \hat{H}_{\text{L}} + \hat{H}_{\text{I}}, \quad (2.24)$$

where the three parts respectively describe the free atom, the free field, and their interaction. The first term

$$\hat{H}_{\text{A}} = \frac{1}{2}\hbar\omega_{\text{A}}\hat{\sigma}_z, \quad (2.25)$$

contains the transition frequency of the atom, ω_{A} , and the atomic inversion operator, $\hat{\sigma}_z = |e\rangle\langle e| - |g\rangle\langle g|$. The factor $1/2$ arises from choosing the zero point in energy to lie between the two atomic energy levels that are separated by $\hbar\omega_{\text{A}}$ [122]. The second term

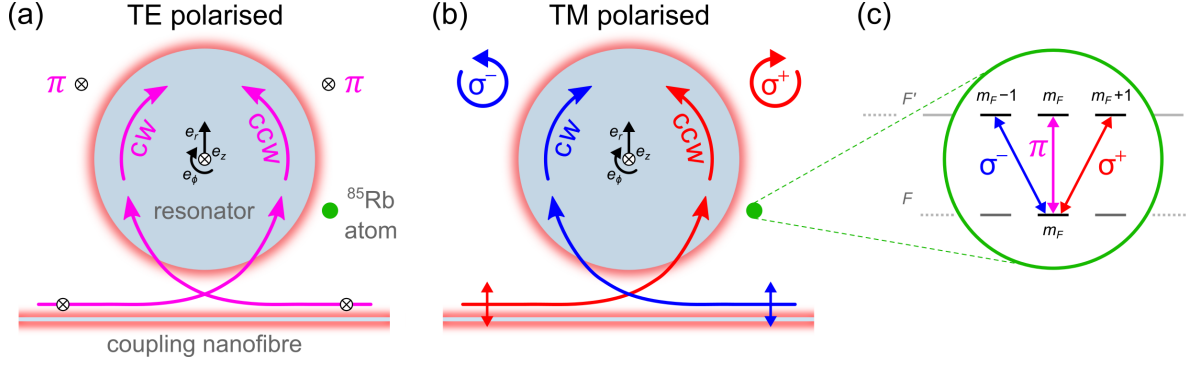


Figure 2.6. Polarisation properties of the WGM. A schematic representation of the local polarisation properties in the evanescent field of (a) a TE-polarised and (b) a TM-polarised WGM. For TE-polarisation, the electric field points along the quantisation (resonator) axis everywhere, and so both the Clockwise (CW) and Counter-Clockwise (CCW) WGMs have identical linear polarisation. In the case of TM-polarisation however, a longitudinal field component that is inherently linked to the direction of circulation occurs, which means that mutually orthogonal polarisations of the evanescent field, σ^- and σ^+ , are respectively realised for the CW and CCW propagating modes. (c) A depiction of the internal Zeeman substructure present in the hyperfine ground (m_F) and excited ($m_{F'}$) states of a ^{85}Rb atom. When such an atom is placed within the WGM as indicated in (a) and (b), its coupling strength to the resonator guided mode is dependent on both its internal state and the polarisation of the WGM. As shown, a transition driven by linear polarisation does not change the m_F state, while σ^\pm polarisation drives transitions for which the m_F state changes by ± 1 .

of equation (2.24) is given by

$$\hat{H}_L = \hbar\omega_L \hat{a}^\dagger \hat{a}, \quad (2.26)$$

where the frequency of the light is ω_L , with the bosonic operators \hat{a}^\dagger and \hat{a} respectively acting to create and destroy a photon from the quantised mode. The n -photon Fock state, $|n\rangle = (\hat{a}^\dagger)^n / \sqrt{n!} |0\rangle$, is obtained by application of the creation operator n times to the vacuum state. Furthermore, since it does not contribute to the dynamics, the zero-point energy of $1/2 \hbar\omega_L$ is set to zero in equation (2.26) [122]. The final term in equation (2.24) describes the interaction between the field and the atom, and within the dipole and rotating-wave approximations, can be written as

$$\hat{H}_I = \hbar g (\hat{a}^\dagger \hat{\sigma}_- + \hat{a} \hat{\sigma}_+). \quad (2.27)$$

Here, $\hat{\sigma}_+ = |e\rangle \langle g|$ and $\hat{\sigma}_- = |g\rangle \langle e|$ are the atomic raising and lowering operators respectively, while the atom–light coupling strength, g , was introduced in Section 2.1 as the field strength per photon at the position of the atom (cf. equation (2.6)).

For the case of an uncoupled system where $g = 0$, the atom and field both remain ‘free’. The eigenstates of \hat{H}_{JC} are then the so-called *bare states*, that correspond to the product of $n + 1$ (n) photons in the mode with the atom in its ground (excited) state, given by $|g, n + 1\rangle = |g\rangle \otimes |n + 1\rangle$ ($|e, n\rangle = |e\rangle \otimes |n\rangle$).

2. Cavity Quantum Electrodynamics with the Bottle Microresonator

Since the Hamiltonian \hat{H}_{JC} only couples the states $|g, n+1\rangle \leftrightarrow |e, n\rangle$, new eigenstates of the coupled system for $g \neq 0$ can be obtained [122]. Doing so results in the so-called *dressed states*

$$\begin{aligned} |n, +\rangle &= \sin(\Phi_n/2) |g, n+1\rangle + \cos(\Phi_n/2) |e, n\rangle, \\ |n, -\rangle &= \cos(\Phi_n/2) |g, n+1\rangle - \sin(\Phi_n/2) |e, n\rangle, \end{aligned} \quad (2.28)$$

where $\Phi_n = \tan^{-1}(2g\sqrt{n+1}/\Delta_{AL})$ with the detuning between the atomic transition and the light field given by $\Delta_{AL} = \omega_A - \omega_L$. The corresponding energy associated with each dressed state is given by the eigenvalues

$$E_{n,\pm} = \left(n + \frac{1}{2}\right) \hbar\omega_L \pm \frac{1}{2} \hbar\Omega_n(\Delta_{AL}), \quad (2.29)$$

where here, the detuning-dependent *Rabi frequency* $\Omega_n(\Delta_{AL}) = \sqrt{4g^2(n+1) + \Delta_{AL}^2}$ has been introduced.

Figure 2.7 displays both the dressed state ($g > 0$) and bare state ($g = 0$) eigenenergies as a function of the atom–light detuning, according to equation (2.29). For larger detunings, the dressed state energies asymptotically approach those of the corresponding bare states due to the diminishing light–matter interaction. On resonance however ($\omega_L = \omega_A$), the dressed states clearly differ from the bare states and exhibit a so-called *avoided crossing*. The energy splitting here is given by $\Omega_n(\Delta_{AL} = 0) = 2g\sqrt{n+1}$, which for the lowest excitation ($n = 0$), amounts to $2g$. This latter scenario is referred to as *vacuum-Rabi splitting*, signifying that the atom can still undergo Rabi oscillations that are stimulated by the electromagnetic vacuum state [123].

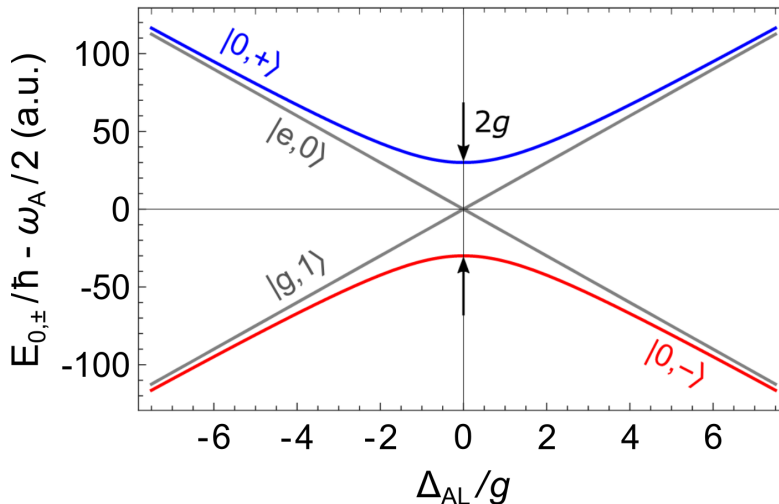


Figure 2.7. Dressed state eigenenergies. Energy eigenvalues, $E_{n,\pm}$, of the lowest two dressed states $|n, -\rangle$ (red) and $|n, +\rangle$ (blue) for the case of $n = 0$, as a function of the atom–light detuning Δ_{AL} . The $|g, 1\rangle$ and $|e, 0\rangle$ bare state eigenenergies are displayed for comparison (grey). At zero detuning, the dressed states undergo an avoided crossing with the splitting width given by $2g$.

The Jaynes-Cummings model, as presented, constitutes a simple yet powerful theory for describing the basics of light–matter interaction at the quantum level in a CQED setting, where the single quantised mode can be experimentally provided by a cavity [122]. The model has since been extended and generalised [124] to better describe situations involving – for example – multiple atoms interacting with a single field mode [125], atoms with a multi-level structure [126], multiple field modes [127], or even for multiple emitters coupled to multiple cavity modes [128]. However, the idealised setting for the Jaynes-Cummings model does not contain the dissipation mechanisms that are present in a real system that inevitably interacts with its environment. In order to fully describe the atom–WGM interaction, the introduction of such irreversible processes, as presented in Section 2.1, must also be accompanied by a controlled external coupling channel to the environment, as outlined in Section 2.2.2. The approach to tackle such an *open quantum system* which has both these losses and driving, involves extending the Jaynes-Cummings description using the so-called *master equation approach* [129].

A comprehensive presentation of the master equation approach specific to CQED 1.0’s setting of ^{85}Rb coupling to the WGM bottle microresonator can be found in [93, 120], while a glancing description that highlights the chiral aspect of the light–matter interaction is included in the following. Here, the open quantum system can be modelled as a system of interest, the dissipation of which occurs via coupling to an external reservoir. The density matrix of the composite system–reservoir, $\hat{\rho}_{SR}$, temporally evolves according to the von-Neumann equation, $d\hat{\rho}_{SR}/dt = -i/\hbar [\hat{H}_{SR}, \hat{\rho}_{SR}]$. By assuming only a weak coupling of the system to the reservoir (Born approximation), and that correlations within the reservoir are short-lived (Markov approximation), the dynamics of the system alone can be obtained by tracing out over the many degrees of freedom of the reservoir as $\hat{\rho}_S(t) = \text{Tr}_R [\hat{\rho}_{SR}(t)]$. Then, within the *Born-Markov approximation* [129], the master equation describing the system evolution reads

$$\frac{d\hat{\rho}_S}{dt} = -\frac{i}{\hbar} [\hat{H}_S, \hat{\rho}_S] + \mathcal{L}\hat{\rho}_S, \quad (2.30)$$

where $\hat{H}_S = \hat{H}_{\text{JC}} + \hat{H}_{\text{D}}$ is the total system Hamiltonian that includes the Jaynes-Cummings Hamiltonian (cf. equation (2.24)) extended with the controlled driving term \hat{H}_{D} . Furthermore, \mathcal{L} is the *Lindblad superoperator* that contains the dissipative part of the dynamics via the weak reservoir coupling, and is given by [120]

$$\begin{aligned} \mathcal{L}\hat{\rho}_S = & \kappa(2\hat{a}\hat{\rho}_S\hat{a}^\dagger - \hat{a}^\dagger\hat{a}\hat{\rho}_S - \hat{\rho}_S\hat{a}^\dagger\hat{a} + 2\hat{b}\hat{\rho}_S\hat{b}^\dagger - \hat{b}^\dagger\hat{b}\hat{\rho}_S - \hat{\rho}_S\hat{b}^\dagger\hat{b}) \\ & + \gamma(2\hat{\sigma}_-\hat{\rho}_S\hat{\sigma}_+ - \hat{\sigma}_+\hat{\sigma}_-\hat{\rho}_S - \hat{\rho}_S\hat{\sigma}_+\hat{\sigma}_-). \end{aligned} \quad (2.31)$$

As previously outlined (cf. Figure 2.6), a WGM microresonator supports two degenerate counter-propagating running-wave modes that can each be individually excited with antiparallel external driving through the coupling nanofibre. Including these two modes,

2. Cavity Quantum Electrodynamics with the Bottle Microresonator

$\hat{a} \equiv \text{CCW}$ and $\hat{b} \equiv \text{CW}$, the total system Hamiltonian, in a frame rotating at the drive frequency ω_D , can then be constructed as

$$\begin{aligned} \hat{H}_S/\hbar = & \Delta_{\text{AD}}\hat{\sigma}_+\hat{\sigma}_- \\ & + \Delta_{\text{RD}}(\hat{a}^\dagger\hat{a} + \hat{b}^\dagger\hat{b}) + (h\hat{a}^\dagger\hat{b} + h^*\hat{b}^\dagger\hat{a}) \\ & + (g_a^*\hat{a}^\dagger\hat{\sigma}_- + g_a\hat{a}\hat{\sigma}_+) + (g_b\hat{b}^\dagger\hat{\sigma}_- + g_b^*\hat{b}\hat{\sigma}_+) \\ & + i\epsilon_a(\hat{a} - \hat{a}^\dagger) + i\epsilon_b(\hat{b} - \hat{b}^\dagger), \end{aligned} \quad (2.32)$$

where the detunings between the atom(resonator) and drive field have been included as $\Delta_{\text{A(R)D}} = \omega_{\text{A(R)}} - \omega_D$. Equation (2.32) contains many terms. The first two lines respectively describe the free atom and free field (cf. equations (2.25) and (2.26)), where the latter has been extended to include the additional resonator mode, along with the possibility of symmetric coupling between these modes \hat{a} and \hat{b} at a rate of h [130]. The third line describes the interaction between the atom and the two modes (cf. equation (2.27)), where coupling can occur to mode \hat{a} (\hat{b}) at a rate $g_{a(b)}$. The last line is the driving extension to the modified \hat{H}_{JC} , where each of the resonator modes can be coherently driven from the outside at a rate $\epsilon_s = \sqrt{2\kappa_{\text{ext}}}\langle\hat{s}_{\text{in}}\rangle$, with \hat{s}_{in} as the amplitude of the incident field that drives mode $\hat{s} \in \{\hat{a}, \hat{b}\}$. The same channel used for driving the system can also be employed to analyse the light that leaves the system. The field amplitude in the output mode, \hat{s}_{out} , is given by a superposition of the input drive field with the outcoupled resonator mode, as $\hat{s}_{\text{out}} = \hat{s}_{\text{in}} - i\sqrt{2\kappa_{\text{ext}}}\hat{s}$ [131]. Computation of the resonator field mode $\langle\hat{s}\rangle$ then allows for a determination of the steady-state transmission through the coupling fibre by $T_s = |\langle\hat{s}_{\text{out}}/\hat{s}_{\text{in}}\rangle|^2$. This can be achieved by solving the master equation (2.30) in the steady-state, i.e., $d\hat{\rho}_S/dt = 0$ [120].

This versatile model can provide analytic expressions for T_s across a number of interesting scenarios through an appropriate setting of the various contained parameters. For example, in the absence of coupling between the modes ($h = 0$), power transmission through the coupling fibre in the forward direction is found as

$$T_a = \left| \frac{g_a^2 + (\gamma + i\Delta_{\text{AD}})(\kappa_0 - \kappa_{\text{ext}} + i\Delta_{\text{RD}})}{g_a^2 + (\gamma + i\Delta_{\text{AD}})(\kappa_0 + \kappa_{\text{ext}} + i\Delta_{\text{RD}})} \right|^2, \quad (2.33)$$

while in the backwards direction, T_b is obtained by exchanging the coupling strength to mode \hat{a} , with g_b . It has previously been shown that due to the spin-momentum locking of light for a **TM**-polarised drive (cf. equation (2.22)), the evanescent field of mode \hat{a} is almost exclusively σ^+ -polarised, while mode \hat{b} dons the orthogonal σ^- -polarisation. Thus, an atom with a polarisation-dependent transition strength can unequally couple to each mode ($g_a \neq g_b$), as illustrated in Figure 2.8 for the extreme case of $g_a \gg g_b \approx 0$. It becomes clear that such a situation results in a chiral light-matter interaction, where the steady-state transmission through the coupling fibre is dependent on both the direction of driving as well as the internal m_F state of

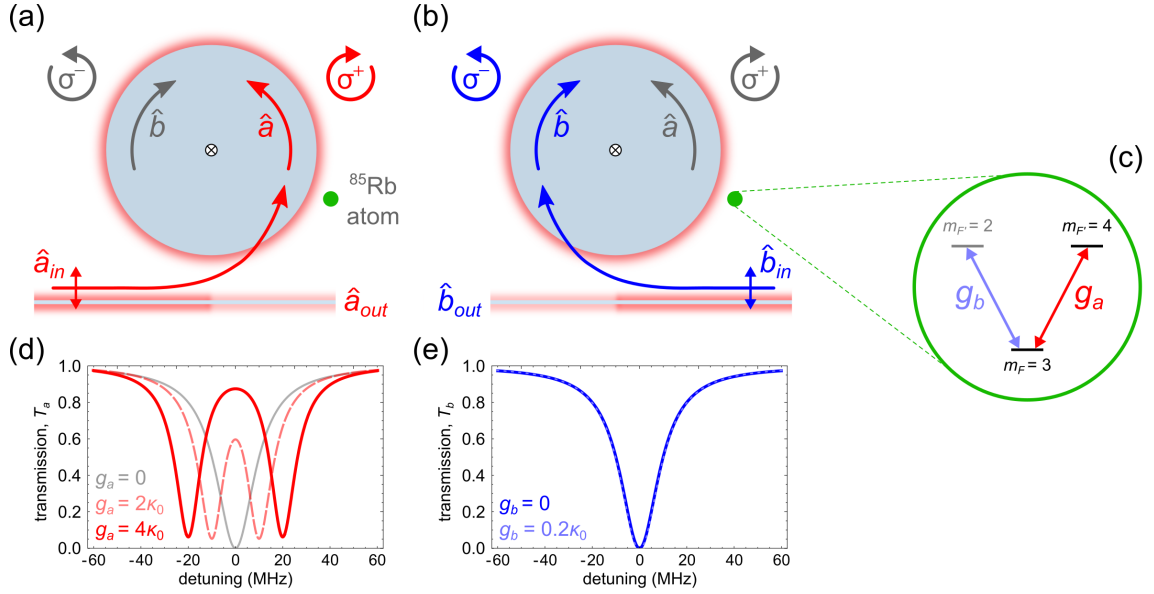


Figure 2.8. Chiral light–matter interaction. (a) Schematic of the coupling between a single atom and the WGM \hat{a} , that is driven by a TM-polarised input field through the coupling nanofibre from the left. (b) Same as (a), but for the WGM \hat{b} , when driven with a TM-polarised input field from the right. (c) Scheme of the internal V-like level structure of the coupled atom. When the strengths of the two transitions differ significantly, this level structure effectively collapses to a two-level system, and the coupling strength to mode \hat{b} , g_b , can be neglected. (d) Calculated transmission spectra as a function of the detuning ($\Delta = \Delta_{AD} = \Delta_{RD}$) according to equation (2.33) for the case illustrated in (a), with three different coupling strengths, g_a , considered. Here, a critical coupling of the resonator is assumed with $\kappa_{\text{ext}} = \kappa_0 = 2\pi \times 5$ MHz, and the spontaneous decay rate of ^{85}Rb taken as $\gamma = 2\pi \times 3$ MHz [96]. A vacuum Rabi splitting of magnitude $2g_a$ is apparent. (e) Same as in (d) but for the case displayed in (b). Here, since coupling to the mode \hat{b} is negligible, the spectrum resembles that of empty resonator.

the coupled atom (see Figure 2.6). For the case of an atom prepared in its outermost Zeeman substate of the hyperfine groundstate, i.e., $m_F = F$ as depicted in Figure 2.8(c), the resonator field drives a V-like level structure. However for alkali atoms, the strength of the $(m_F = F) \rightarrow (m_{F'} = F - 1)$ cycling transition is significantly lower than the $(m_F = F) \rightarrow (m_{F'} = F + 1)$ counterpart [96], resulting in an (almost) exclusive coupling of the atom to mode \hat{a} . Hence if mode \hat{b} is driven, for which $g_b \approx 0$ and $h = 0$, the system behaves almost like an empty resonator. Probing such a system through mode \hat{a} thus realises the ideal Jaynes-Cummings model, where an effective two-level atom couples to only one resonator mode. Figure 2.8(d) and (e) respectively illustrate these two scenarios, that manifest as an on-resonance non-zero or (near-)zero transmission through the coupling nanofibre in the combined atom–resonator system. The response of the system, as described, clearly depends on the propagation direction of the input light-field – constituting the chiral nature of the light–matter interaction present in the system.

This qualitative discussion presented so far, covers enough ground to understand the major milestones, and quantum devices, realised with such a system. These are outlined in the following Section 2.3, before a discussion of atom trapping in the WGM is presented in Section 2.4.

2.3 Experimental Milestones

In the following, a chronological selection of prior key achievements demonstrated by the CQED 1.0 experiment are presented, with the aim of their contextualisation in order to motivate the latest milestone of atom trapping at the bottle microresonator (see Section 2.4), in addition to the redesign to CQED 2.0 (see Chapter 3). Within the framework of the strong coupling of single ^{85}Rb atoms to the WGM bottle microresonator, the parameters of the resonator, its frequency stabilisation, stabilisation of its evanescent coupling, and a number of realised nanophotonic optical devices, are respectively delineated. All of the results contained within this Section are recorded and discussed in detail within the PhD theses [92, 93, 120].

2.3.1 Strong Coupling of Single Atoms

Following the procedure for its fabrication as outlined in Section 2.2.3, the bottle microresonator installed in the CQED 1.0 set-up featured a nominal diameter of $2R_0 = 37 \mu\text{m}$ with curvature $\Delta k = 0.014 \mu\text{m}^{-1}$ [92, 93], and boasted a quality factor of $Q \approx 5 \times 10^7$ that remained approximately constant across its ~ 10 years of employment under UHV [70]. Having been glued to a specialised mount hosting shear piezos, and interfaced by a set of two positionable nanofibres, this coupling set-up of CQED 1.0 afforded active stabilisation of the bottle microresonator via strain-tuning [64], along with an active (or passive) stabilisation of its evanescent coupling to a nanofibre [67]. Together, this allows the resonator to be stably operated in the critically coupled regime, and further locked to the D_2 transition of ^{85}Rb .

The delivery of single atoms to the evanescent field of a WGM microresonator is typically performed by releasing a cold cloud of atoms prepared in a Magneto-Optical Trap (MOT) that is located close to the resonator structure, such that the atoms traverse through the evanescent field with a relatively low velocity [49, 132]. A related method involves delivery of a dilute cold atomic cloud to the WGM of the resonator via the Atomic Fountain (AF) principle [133–135]. This latter approach was adopted in the CQED 1.0 set-up, where preparation of an ^{85}Rb MOT took place within a separate UHV chamber, before the atom cloud was ballistically launched to the location of the bottle microresonator through a Differential Pumping Tube linking the two vertically-displaced chambers. The long-time preservation of the high resonator Q -factor is attributed to this

two-chamber design, where potential Q -degrading contaminants that can originate from MOT preparation are mostly isolated from the resonator housing. Upon activation of the AF, where the launch parameters are set such that the turning point of the trajectory coincides roughly with the position of the bottle microresonator, detection of single-atom transits through the evanescent field of a WGM is registered by a transmission increase in the critically coupled nanofibre. This detection scheme corresponds to the situation displayed in Figure 2.8(a) and (d), when both the driving field and WGM are resonant to the transiting atom. Thus, the initially approximately zero transmission without an atom will jump to a non-zero value during an atom transit. The observation of an increase in the photon countrate through the coupling nanofibre signifies such a coupling event, and can be registered by assigning a threshold countrate. This was typically set, using a running time-window, to 6 or more counts in $1.28 \mu\text{s}$. A selection of such photon detection events during single atom couplings, alongside an average over many coupling events, is displayed in Figure 2.9. The latter shows that the average interaction time between a single atom and the WGM bottle microresonator is around $2 \mu\text{s}$. The asymmetry in the peak distribution is attributed to both the averaging over dissimilar atom transits, in addition to the mostly asymmetric nature of the trajectory.

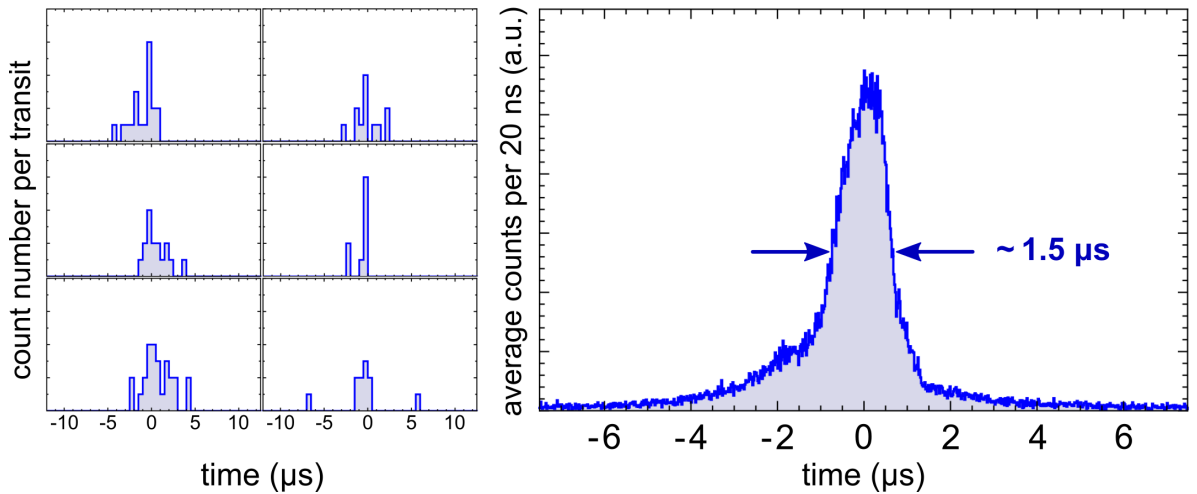


Figure 2.9. Photon counts measured during single atom transits through the WGM. Reproduced from [93]. The collection of six plots on the left display a random selection of the typical countrates observed through the critically coupled nanofibre when a single atom transits through the evanescent field of a TM-polarised WGM. The zero of the time-axis corresponds to the timestamp of a successful atom-coupling event, defined here as the observation of 6 or more photon counts in $1.28 \mu\text{s}$. The plot on the right displays the average nanofibre transmission across 3420 of these atom transit events, indicating an average interaction time of around $2 \mu\text{s}$. Its asymmetrical profile around zero is attributed to the averaging over many different types of coupled atom trajectories, in which an abrupt end to the interaction occurs for a substantial fraction of events where the atom passes too close to the resonator surface.

The successful registration of a single atom transit with this method allowed for a subsequent ~ 500 ns probing phase, that was typically followed by a second detection phase for the same atom (with the same method) in order to post-select successful experimental runs with a strongly-coupled atom. Such a scheme necessitated ultra-fast reaction times and optical switching, which was aided by an **Field Programmable Gate Array (FPGA)**-based detection and control scheme [92, 136].

With suitable redetection and post-selection, transmission spectra could be obtained in order to characterise the coupled atom–resonator system. For this, the transmission through the coupling nanofibre during the probing phase was averaged across ~ 1000 atom-coupling events and repeated in a step-wise scan of the resonator-drive detuning across a range of ± 60 MHz. Figure 2.10 displays the result of this spectroscopy performed with the coupled atom–resonator system. The grey data points show the empty resonator spectrum, with a Lorentzian fit yielding a **FWHM** of $2\kappa/2\pi = 20$ MHz at critical coupling. The blue data points, obtained in the presence of coupled atoms, reveal a vacuum Rabi splitting where the on-resonance transmission increase amounts to around 70%. The theoretical fit here takes into account the full polarisation properties of the evanescent field as well as the Zeeman substructure of the hyperfine transition $F = 3 \rightarrow F' = 4$, in addition to a time-varying coupling strength arising from the transiting nature of each atom coupling event [93]. It yields an average coupling strength of $\bar{g} \approx 2\pi \times 17$ MHz, corresponding to a mean distance of the atoms from the resonator surface of around 125 nm [70]. By comparing the obtained coupling strength with the system losses (cf. equation 2.11), the cooperativity is determined to be $C = g^2/2\kappa\gamma \approx 4.8$, which demonstrates that the atom–resonator system operates in the strong coupling regime.

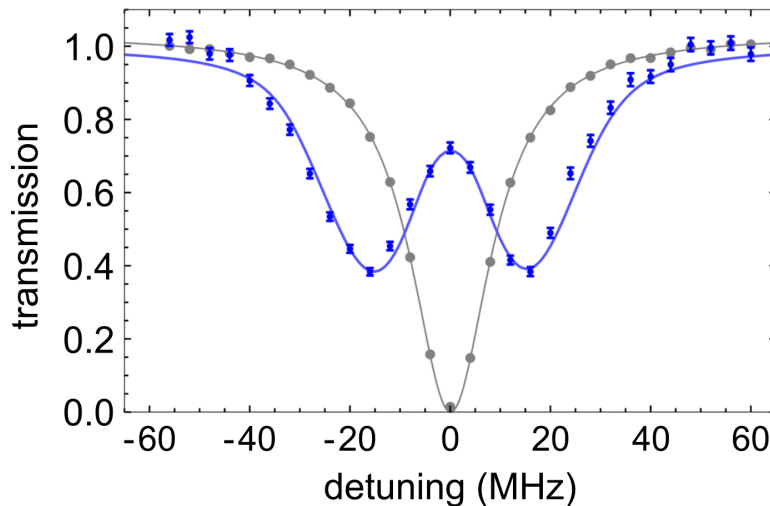


Figure 2.10. Transmission spectrum of the coupled atom–resonator system. Reproduced from [50]. The empty resonator spectrum (grey) shows its Lorentzian lineshape, while in the presence of atoms, the measured spectrum (blue) exhibits a vacuum Rabi splitting of $\bar{g} \approx 2\pi \times 17$ MHz as a clear signature of their strong coupling.

2.3.2 Nonlinear π Phase Shift of Single Photons

The single atom acts as a saturable absorber, and its strong coupling to the **WGM** bottle microresonator realises a fibre-integrated optical medium for which the transmission properties of single photons depend on their number [56]. Single, resonant photons arriving at the empty resonator – set to operate in the overcoupled regime – are transmitted with a phase shift of π due to their interaction with the resonator mode. This property results from the destructive interference between the part of the photon that remains in the coupling fibre, which acquires zero phase shift, and the part that is outcoupled from the resonator, where the latter is larger in amplitude and phase shifted by π (see Section 2.2.2). When a single atom is strongly coupled to the resonator, the atom–resonator system operates in the undercoupled regime due to the additional loss rate added by virtue of the resonator-enhanced atom. The amplitude of the light in the coupling fibre is thus greater than that outcoupled from the resonator, and single photons are consequently transmitted with zero phase shift.

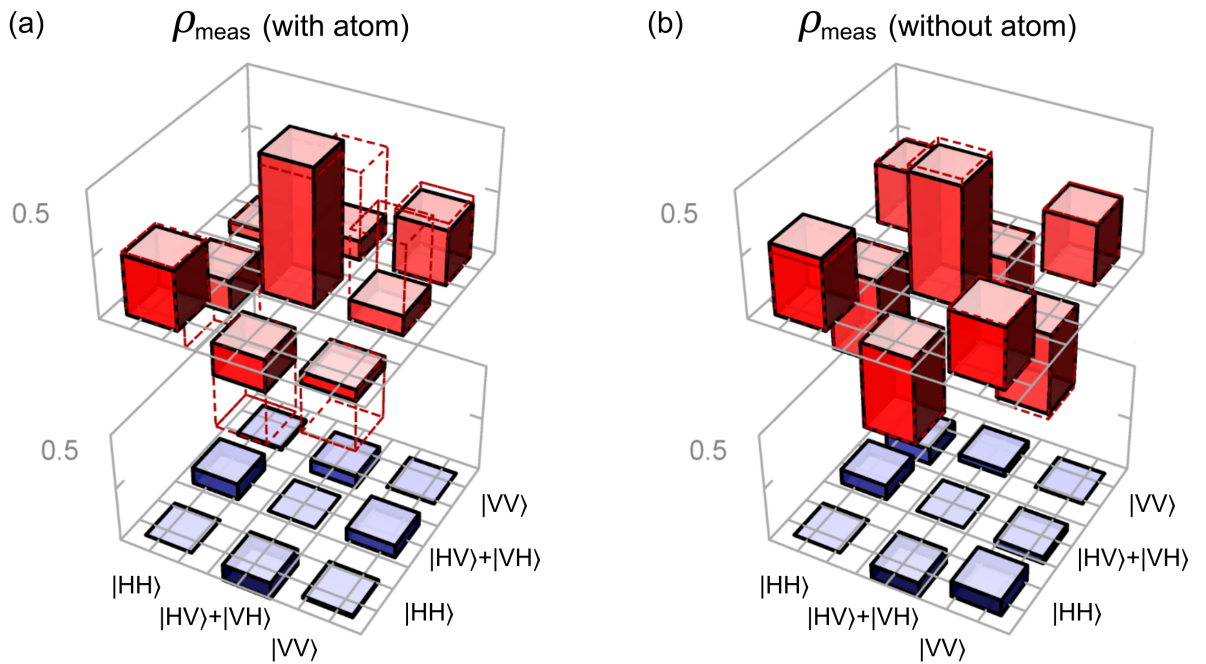


Figure 2.11. Reconstructed density matrices of the transmitted two-photon state. Reproduced from [56]. The real (red) and imaginary (blue) parts of the reconstructed measured density matrix, ρ_{meas} , obtained in the case where (a) a single atom is coupled to the resonator and (b) no atom is coupled. These results were obtained by measuring photon coincidences in the light transmitted past the resonator, when measuring in complementary polarisation bases. Here, H and V are respectively the horizontal and vertical polarisation components. In both (a) and (b), the dashed lines indicate the density matrix obtained with an ideal, i.e., lossless, atom–resonator system [120].

The situation changes dramatically when two photons are incident on the coupled atom–resonator system. In this case, the strong field enhancement within the resonator enables a complete saturation of the coupled atom by only one of the photons, while the second cannot be absorbed. Consequently, the amplitude of the two-photon wavefunction inside the resonator is much larger than that remaining in the coupling fibre, and its dominance upon outcoupling results in the transmitted two-photon wavefunction acquiring an additional phase shift of π . This ultra-strong nonlinear response of the system at the single-photon level arises only from the enhancement of the nonlinearity, owed to the resonator-enhanced atom*. Furthermore, through their interaction with the coupled atom–resonator system, this effect can be used to generate entanglement between the initially uncorrelated coincident photons. By measuring the coincidences of the two photons in different polarisation bases after transmission through the coupled atom–resonator system, the density matrix of the full two-photon polarisation state can be reconstructed [56, 120]. These findings are reproduced in Figure 2.11. The results show that the nonlinear phase shift of π , applied to the two-photon state, generates a non-separable state of light in which the polarisation correlations cannot be classically accounted for. The generation of such an entanglement in an effective photon–photon interaction, where the polarisation of one photon is maximally flipped conditional on the state of the other, can be employed to perform high-fidelity quantum logic operations [120]. Its demonstration in an optical fibre-based architecture makes the system scaleable and suitable for integration into photon-based quantum networks.

2.3.3 Non-reciprocal Devices

The **WGM** bottle microresonator platform lends itself to the realisation of integrated nanophotonic devices suitable for the processing and routing of optical signals [137]. When strongly and *chirally* coupling a single atom to the resonator, as represented in Figure 2.12(a), the drastic change induced in the system can be used to produce devices that are *controlled* by a single atom, enabling an operation even at the single photon level. Furthermore, exploitation of the chiral light–matter interaction that is available in the system allows for the realisation of non-reciprocal, i.e., *direction-dependent*, devices. Demonstrations of this kind open up the route towards scalable architectures for fibre-integrated quantum optical networks, and constitute an important application of the bottle microresonator system beyond its explorations into the fundamental interaction between light and matter. These devices are outlined in the following, schematically illustrated in Figure 2.12, and bring this Section on the experimental milestones (without atom trapping) to a close.

*Note that Figure 2.12(b) illustrates a schematic representation of the nonlinear π phase shift for single photons interacting with the resonator-enhanced atom.

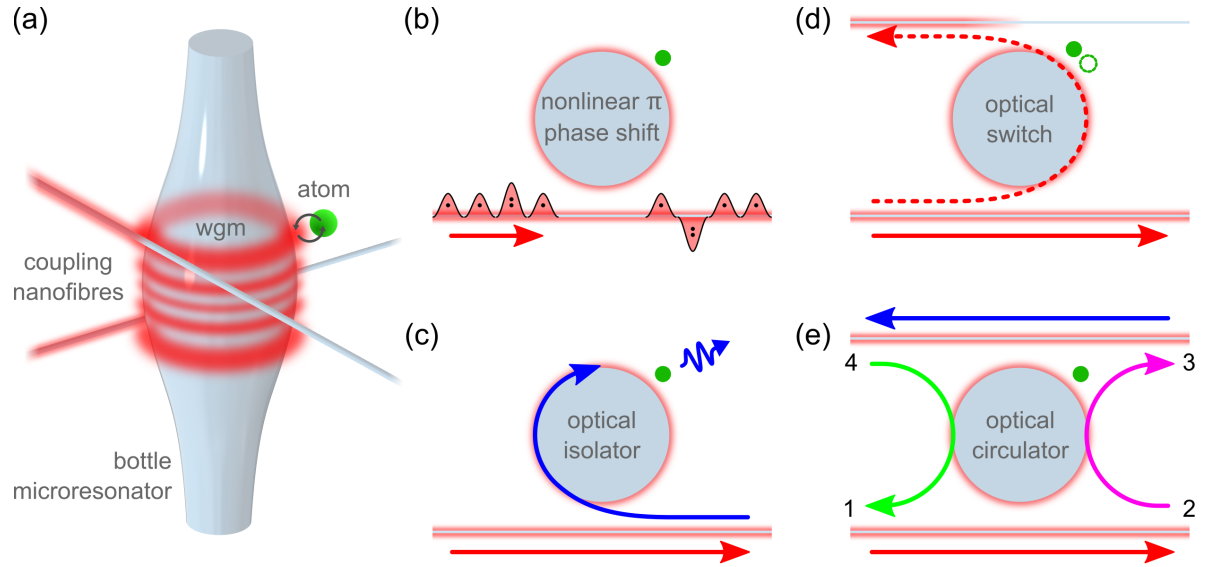


Figure 2.12. Optical devices with the bottle microresonator and a single atom.

(a) An illustration of resonator-mediated coupling between two nanofibre waveguides, that can be controlled by a single atom strongly coupled to the resonator’s **WGM**. Schematics of the various devices that can and have been realised with this setting are shown in (b) – (e). See text for details.

Single atom optical isolator [57]. An optical isolator, or equivalently optical diode, is a non-reciprocal device that enables a high transmission of light along only one direction. It can be characterised by its isolation, $\mathcal{I} = 10|\log(T_b/T_a)|$, where $T_{a(b)}$ is the transmission in the forwards(backwards) direction. For the critically coupled empty bottle microresonator, when held on resonance, the transmission in both the forward and backward directions through the coupling nanofibre is effectively zero – due to coupling of the light into the resonator mode and it being dissipated therein. However, when a single atom strongly couples to the resonator mode as schematically presented in Figure 2.12(c) and previously illustrated in Figure 2.8, i.e., under chiral excitation, the situation radically changes. Transmission in the forward direction now takes a finite value that explicitly depends on the coupling strength to the excited **WGM**, g_a (cf. equation (2.33) and Figure 2.8(d) for $\Delta = \Delta_{AD} = \Delta_{RD} = 0$). Due to the chiral light–matter interaction, transmission in the backward direction remains low due to the negligible coupling strength g_b . This is illustrated in Figure 2.13, which shows the calculated non-reciprocal transmission in both the forward and backward directions as a function of κ_{ext} according to equation (2.33). Here, the chirally coupled atom is assumed to be in its outermost Zeeman substate of the hyperfine ground state, such that it couples to the forward excited **WGM** with strength $g_a = 2\pi \times 17$ MHz and the backward excited **WGM** with strength $g_b = 2\pi \times 2.9$ MHz [57]. The isolation is also displayed, which exceeds 40 dB at the point of critical coupling. The experimentally obtained values of $T_a = 0.72$ and $T_b = 0.03$ at this point lead to a measured isolation of $\mathcal{I} = 13$ dB, which arises due to the finite overlap of the **WGM** with perfect circular

polarisation alongside the technical fluctuations present in the system. Finally, this realised device offers the possibility of being programmable through preparation of the atom in a defined Zeeman ground state. The example presented here illustrates isolation along the forwards direction, but a reverse operation is feasible when the atom is instead prepared in the innermost Zeeman substate $m_F = -3$, where $g_b \gg g_a$.

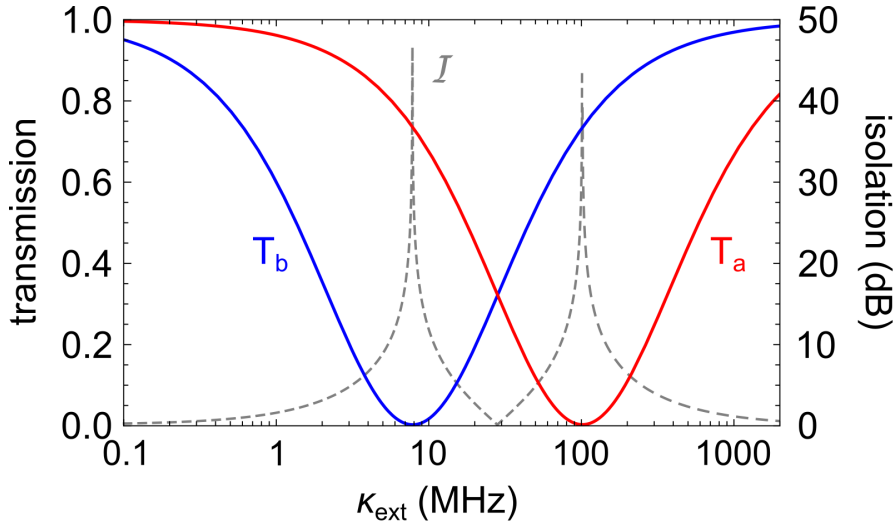


Figure 2.13. Single atom optical isolator. Reproduced from [57]. Calculated non-reciprocal transmission of light (red solid line: forwards, blue solid line: backwards), and corresponding isolation (grey dashed line), through the chirally-coupled atom-resonator system as a function of the nanofibre-resonator coupling rate. Here, the transmission is determined according to equation 2.33 by assuming coupling strengths of a single spin-polarised atom to the forward (backward) excited WGM of $g_a = 2\pi \times 17$ MHz ($g_b = 2\pi \times 2.9$ MHz).

Single atom optical switch [54]. The optical isolator, as previously discussed, is a device based on losses through the coupled atom-resonator system, where a high transmission is made possible due to the dissipation introduced by the atom. A particular advantage of the bottle microresonator platform, owing to its elongated cylindrical geometry, is the ability to interface two optical nanofibre waveguides at the same time and prevent the dissipated light being irreversibly lost into free-space. Doing so creates an all-fibre setting for the efficient in- and out-coupling of light to the resonator via each of the so-called *bus* and *drop* waveguides, gaining the ability to access and direct light into their two different ports as schematically represented in Figure 2.12(d). The transmission between the nanofibre waveguide ports in this so-called *add-drop* configuration is tunable by controlling the evanescent coupling between each fibre and the resonator, characterised by the coupling constants κ_{bus} and κ_{drop} . A resonator-mediated coupling between the two fibres is then feasible, where a critical tuning enables the light entering the bus fibre to resonantly excite the WGM, before exiting through the drop fibre. This situation can be assigned as the "ON" state of the

device, and is experimentally obtained by setting the fibre positions with respect to the resonator such that the critical coupling condition, $\kappa_{\text{bus}} = \kappa_0 + \kappa_{\text{drop}}$, is fulfilled. The strong coupling of a single atom to the **WGM** then modifies this critical coupling condition with the introduction of an additional loss mechanism. Here, the atom prevents the build-up of the resonator field, in which case the light mostly remains in the bus fibre. This redirection of the light controlled solely by the presence of an atom that strongly couples to the resonator field corresponds to the device's "OFF" state. The maximum switching contrast is obtained when the light is resonant to the resonator-enhanced atom, and amounts to a 10 dB increase from the bus to the drop port. With a demonstrated switching fidelity of 0.62, in conjunction with around a 79% probability of recovering an input photon, this device therefore realises an efficient single atom-controlled switch for optical signals containing much less than one photon per resonator lifetime, rendering it highly suitable for quantum communication protocols with atoms and photons [54]. Furthermore, due to the saturable nature of the atom, the "OFF" state of the switch exhibits a photon-number-dependent routing for higher input powers: two photon states are preferentially coupled into the resonator, leading to a bunching behaviour in the drop port transmission, while single photons remain in the bus fibre, yielding an antibunching in the photon statistics of the add port transmission. This capability in particular allows for the preparation and distribution of non-classical states of light, which again, takes place in an optical fibre-integrated setting.

Single atom optical circulator [58]. The aforementioned single atom optical switch controls the flow of light between two separate nanofibre waveguides via the **WGM** of the bottle microresonator in an add-drop configuration, using only one port as an input for the light. As schematically depicted in Figure 2.12(e), each port of the switch configuration can also be employed as an input to realise a non-reciprocal 4-port device – the optical circulator – for which control over its mode of operation is afforded by a single strongly coupled atom. The chiral coupling of an atom to the bottle microresonator, where the coupling strength depends on the circulation direction of the **WGM**, results in a directional bias for the flow of light. The routing of light therefore depends on both the input port as well as the internal state of the atom. Each of the bus (with port 1 and port 2) and drop (with port 3 and port 4) nanofibres are adjusted to realise a critical coupling to the resonator, where $\kappa_{\text{bus}} \approx \kappa_{\text{drop}} \gg \kappa_0$. When resonant light is injected into port 1, the **CCW WGM** is excited, which strongly couples to an atom in its $m_F = 3$ ground state. This coupling prevents a build-up of the resonator field, and the light is transmitted directly to port 2. However, as in the case of the single atom optical isolator, light injected into port 2 excites the **CW WGM** which does not strongly couple to the same atom (cf. Figure 2.8). The resonator-mediated fibre coupling results in light being directed into port 3. This same situation occurs for light injected into port 3, which is transmitted to port 4, and from port 4 via the

resonator back to port 1 – thus completing the circulation. The opposite direction of circulation can be realised when the atom is in its $m_F = -3$ ground state, whereby it strongly (weakly) couples to the CW (CCW) WGM instead. Light injected into port 1 will therefore be directed to port 4, then from port 4 to port 3, from port 3 to port 2, and from port 2 to port 1. For an optimum circulator performance, the measured operational fidelity of 0.72 with a 73% photon survival probability demonstrates its efficient routing capabilities [58]. As the circulator is programmable by the state of the coupled atom, a critical aspect of its functionality is the quantum control that this enables, in addition to its operation at the single photon level. Akin to the single atom optical switch, the circulator exhibits a photon number-dependent routing capability due to saturation of the strongly-coupled atom by only a single photon. While individual photons are transmitted through their original fibre, simultaneously arriving photons are instead preferentially transferred to the second fibre. The ability to route photons in this way provides a versatile tool that is fully fibre-integrated, and thus suitable for application into fibre-based optical circuits and networks. Beyond this, linear arrays of such quantum-controlled circulators are promising candidates for realising photon lattices in quantum computation [138].

2.4 Strong Coupling of Single *Trapped* Atoms

All of the experiments and proof-of-principle devices demonstrated with the CQED 1.0 system outlined so far in Section 2.3 were performed with free-flying atoms, and therefore suffered from a limited interaction time with a time-varying coupling strength, in addition to an overall probabilistic experiment operation. To overcome these shortfalls, and also to bring the class of WGM microresonators up to date with the more conventional FP resonator counterparts, trapping of the emitter within the WGM of the microresonator has been a paramount task. This Section will outline the steps taken, in part, for the realisation of this long-standing goal, and therefore further provides the backdrop necessary for the literal building on of this work throughout the remainder of the thesis. Note that this work is thoroughly documented in [70], and so only selected key points will be highlighted and described in the upcoming Sections. The following introduction to optical dipole potentials merits a more in-depth presentation, due to its relevance for the experiments performed and contained within Chapter 5.

2.4.1 Optical Dipole Potentials

Optical traps, in general, refer to the interaction of light with microscopic objects in order to spatially confine and manipulate them. A variety of different techniques for the trapping of small particles with the use of light has been developed over the course of a rich recent history with thanks, in part, due to the numerous configurations attained both with free-space and guided lasers. Optical trapping is based on the fundamental principle that a polarisable particle subject to an external electric field will gain an induced electric dipole moment, leading to a subsequent attraction or repulsion of the particle to regions of high intensity [139, 140]. This Nobel-Prize winning technique [141], coined *optical tweezers*, first found applications in manipulating micron-sized biological systems [142, 143] before revolutionising single-atom optical manipulation [144]. The optical dipole trapping of neutral atoms is now commonplace across experiments that require the localisation of atoms and is the method of choice due to its relative ease of implementation, versatility, and well-understood working principle [145]. A number of models exist for describing – in particular – how a realistic particle interacts with a light field, in which either the former or latter can be treated classically, quantum mechanically, or somewhere in between. A non-comprehensive presentation of the most relevant and applicable descriptions, concerning the interaction of a multilevel neutral atom with a classical light field, is outlined in the following.

Classical model of the dipole force. A fully classical treatment of both the field and atom, while succeeded by more accurate and comprehensive quantum mechanical descriptions, still provides a solid foundation for an intuitive understanding, and approximate description, of the resulting dipole force on the atom.

For this, a monochromatic classical electric field (originating from a laser for example) with an angular frequency of ω , spatially dependent field amplitude of $\mathcal{E}(\mathbf{r})$, and polarisation given by the unit vector \mathbf{u} , is described by the temporally oscillating function

$$\mathbf{E}(\mathbf{r}, t) = \mathcal{E}(\mathbf{r})\mathbf{u} e^{-i\omega t} + c.c. \quad (2.34)$$

The neutral atom, on the other hand, is approximated as a harmonic oscillator consisting of a single electron of mass m_e and charge $-e$, that is elastically bound to the atomic nucleus of mass $M \gg m_e$ and charge $+e$. The oscillating dipole exhibits damping at a rate of Γ , by continuous dipole radiation. The electric field of eq. (2.34), when subject to such a *Lorentz*-like atom, induces an electric dipole moment in the atom of $\mathbf{d}(\mathbf{r}, t) = \alpha(\omega)\mathbf{E}(\mathbf{r}, t)$ which harmonically oscillates at the driving frequency. The frequency-dependent proportionality factor, $\alpha(\omega)$, is the complex *atomic polarisability*, and it is in knowing this quantity that the response of the classical system can be understood. It is obtained by solving the equation of motion for the driven electron

given by

$$\ddot{\mathbf{x}} + \Gamma_\omega \dot{\mathbf{x}} + \omega_0^2 \mathbf{x} = -e\mathbf{E}(\mathbf{r}, t), \quad (2.35)$$

where

$$\Gamma_\omega = \frac{e^2 \omega^2}{6\pi\epsilon_0 m_e c^3} \quad (2.36)$$

is *Larmor's formula* for the radiated power of an accelerated charge [146, 147] and relates to the on-resonance damping rate as $\Gamma \equiv \Gamma_{\omega_0} = (\omega_0/\omega)^2 \Gamma_\omega$, where ω_0 is the atomic resonance. The stationary solution of eq. (2.35), together with eq. (2.36), then yields the polarisability, $\alpha(\omega)$, via $-e\mathbf{x}(t) = \alpha(\omega)\mathbf{E}(t)$ as

$$\alpha(\omega) = 6\pi\epsilon_0 c^3 \frac{\Gamma/\omega_0^2}{\omega_0^2 - \omega^2 - i(\omega^3/\omega_0^2)\Gamma}. \quad (2.37)$$

The interaction energy of the induced dipole in the applied classical electric field can then be found by

$$U_{\text{dip}} = -\frac{1}{2} \langle \mathbf{d} \cdot \mathbf{E} \rangle = -|\mathcal{E}\mathbf{u}|^2 \text{Re}(\alpha), \quad (2.38)$$

where the angular brackets denote a time average over one period of the time-dependent electric field, the factor of 1/2 reflects the fact that the dipole is induced rather than permanent, and the real part of the polarisability describes the component of the dipole moment that oscillates in phase with the external field. By substituting eq. (2.37) into the right hand side of the above equation, together with the spatial field intensity expression $I(\mathbf{x}) = 2\epsilon_0 c |\mathcal{E}\mathbf{u}|^2$, the compact form of the dipole potential becomes

$$U_{\text{dip}}(\mathbf{x}) = \frac{3\pi c^2}{2\omega_0^3} \frac{\Gamma}{\Delta} I(\mathbf{x}). \quad (2.39)$$

This simple expression is brought about by applying the so-called *rotating wave approximation* [82] in the realistic case of the detuning $\Delta = \omega - \omega_0 \ll \omega_0$, where the counter-rotating terms oscillating at $\omega + \omega_0$ are discarded. Equation (2.39) illustrates that a dipole trapping potential can be formed by an appropriately shaped intensity distribution – a focussed Gaussian laser as depicted in Figure 2.14, where the intensity becomes maximal in the focal region, is the perfect and most basic configuration. However, the sign of the atom–light detuning, Δ , matters. When Δ is negative with respect to the atomic frequency, in a so-called *red-detuned* trap where the laser frequency is smaller than the atomic resonance frequency, neutral atoms are attracted to regions of intensity maxima where U_{dip} is minimal. Conversely, for positive Δ in a so-called *blue-detuned* trap, atoms are repelled by intensity maxima. The corresponding force on the dipole is given by the gradient of the dipole potential as $\mathbf{F}_{\text{dip}}(\mathbf{x}) = -\nabla U_{\text{dip}}(\mathbf{x})$.

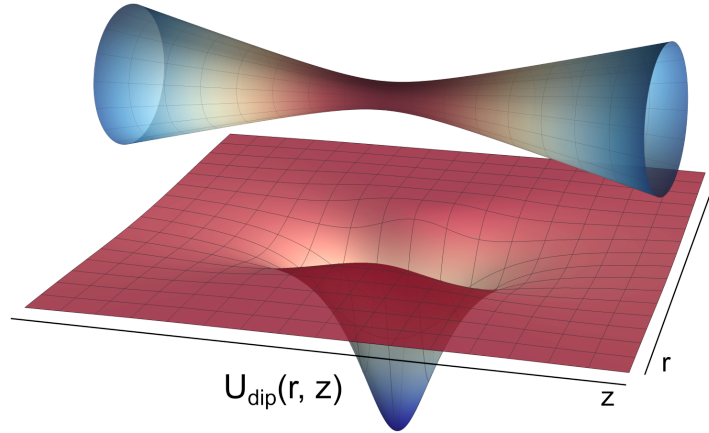


Figure 2.14. Optical dipole trap. A representative illustration of a three-dimensional trapping potential (lower surface), generated by a red-detuned focussed Gaussian beam (upper surface).

Semiclassical model. It is interesting to note that in a semiclassical approach, whereby the external motion of the atom is treated as classical and the internal dynamics assigned quantised energy states, the above results of the classical model only require minor modifications. For a two-level quantum emitter with transition frequency ω_0 , driven by a (near-)resonant classical field, spontaneous emission from the populated excited state is now the energy decay rate and can no longer be determined from Larmor’s formula. The damping rate is instead calculated by considering the transition dipole matrix element between the ground and excited state [145]. In contrast to the classical Lorentz atom however, very high driving intensities of the classical field can saturate the excited state population of the quantised emitter, rendering eq. (2.37) no longer valid. Saturation effects however, typically do not concern dipole trap configurations as the trapping light fields are far-detuned from resonance and have low scattering rates. Consequently, equation (2.39) can be applied in these situations. A more comprehensive presentation of the theory for semiclassical light–matter interaction will be given in Section 4.2 of Chapter 4, in the context of resonance fluorescence.

Quantum mechanical approach. The most complete description of the dipole force arises from a fully quantum treatment of both the atom and the light field, along with their combined interaction in a so-called *dressed-state* picture [148, 149]. In this treatment, the energy eigenstates of the free atom are replaced by the combined states of the atom plus quantised trapping field, where the new eigenstates of the combined system are shifted in energy due to the mutual interaction. Here, the energy shift of the i th state is given by [145]

$$\Delta E_i = \sum_{j \neq i} \frac{|\langle j | \hat{H}_{\text{int}} | i \rangle|^2}{\epsilon_i - \epsilon_j} \quad (2.40)$$

that uses the interaction Hamiltonian defined as $\hat{H}_{\text{int}} = -\hat{\mathbf{d}}\hat{\mathbf{E}}$, and the energy of the unperturbed state $|i\rangle$ given by ϵ_i . In the dressed state picture, this energy amounts to $\epsilon_g = n\hbar\omega$ for the example of a two-level atom in its ground state $|g\rangle$ and the field consisting of n photons with frequency ω . When the atom is excited to the state $|e\rangle$ by absorbing a single photon from the field, the new unperturbed energy of the atom–photon system is given by $\epsilon_e = \hbar\omega_0 + (n-1)\hbar\omega = -\hbar\Delta_{ge} + n\hbar\omega$, using $\Delta_{ge} = \omega - \omega_0$ as the detuning of the light field relative to the atomic transition frequency. Equation (2.40) thus reduces to

$$\Delta E_{g|e} = \pm \frac{|\langle e|\hat{\mathbf{d}}|g\rangle|^2}{\Delta_{ge}} |E|^2 = \pm \frac{3\pi c^2}{2\omega_0^3} \frac{\Gamma}{\Delta_{ge}} I \quad (2.41)$$

where the plus and minus sign respectively corresponds to the energy shift of the ground and excited state. The above expression has the same form as equation (2.39) that describes the dipole potential resulting from the classical approach. Here, it is exactly this optically induced energy shift – the so-called *light shift* – of the ground state that corresponds to the dipole potential for the two-level atom. While the excited state is shifted by the same amount, but in the opposite direction, the relevant trapping potential is that of the ground state for the practical case of low saturation (where the atom mostly remains in its ground state). This situation is depicted in Figure 2.15 for the case of a two-level atom subject to a red-detuned ($\Delta_{ge} < 0$) light field, and illustrates how the position dependent energy shift of the dressed states in a spatial intensity distribution can give rise to a trapping potential. For multi-level atoms featuring transition substructure, such as ^{85}Rb , this treatment can still be applied when considering all dipole matrix elements $\mathbf{d}_{ij} = \langle g_i|\hat{\mathbf{d}}|e_j\rangle$ from the relevant transitions $|g_i\rangle \rightarrow |e_j\rangle$ [70, 145], and will be employed in Section 5.2.1.2 of Chapter 5 in order to calculate the average detuning of a light-shifted trapped atom with respect to an excitation frequency.

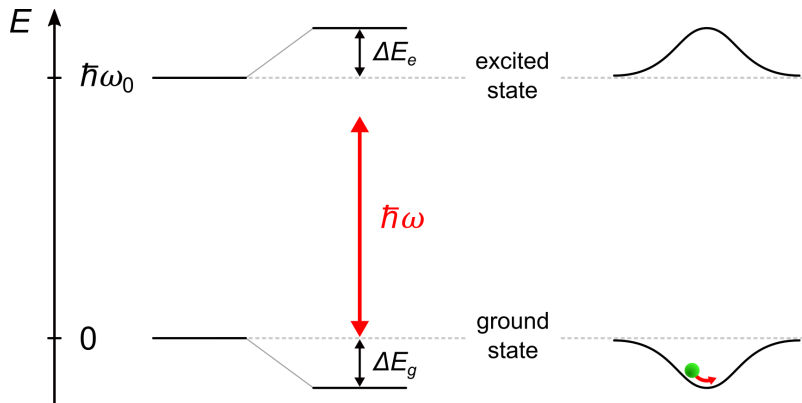


Figure 2.15. Light shifts on a two-level atom. A sketch of the ground and excited state energies (left) that are respectively shifted by an amount ΔE_g and ΔE_e , according to equation (2.41), when subject to a red-detuned ($\Delta_{ge} < 0$) light field (centre). A spatially inhomogeneous field, such as a beam with a Gaussian intensity profile, can produce a trapping potential out of the ground state (right).

This presentation covering the basic physics of optical dipole trapping illustrates the key ingredients necessary to realise attractive or repulsive potentials for neutral atoms: namely, a light field of appropriately chosen power and detuning (with respect to an atomic transition), that features a desired spatial intensity distribution. Since engineering of these parameters is readily achievable with free-space lasers and interference patterns, a myriad of possible configurations have been successfully realised within the context of few-atom optical traps [145]. These concepts are also applicable to more exotic trapping geometries that rely on the dipole forces originating from evanescent waves [150–152], whereby multiple optical potentials can be generated to within a few hundred nanometres from dielectric waveguide structures by multiple guided fields [113, 153]. Alternative schemes that enable the trapping of atoms at similar sub-wavelength distances away from dielectrics are based upon an external beam retroreflected tweezer trap [80, 154]. Interference between the incoming beam and from that which is reflected from the surface generates a partial standing wave pattern that features an array of optical potentials along the beam axis. It is with this scheme that loading of single atoms within the first trapping site closest to the surface of the bottle microresonator and their strong coupling was successfully realised [60]. An explanation of this feat is presented across the following Sections.

2.4.2 The Trapping Scheme

In order to extend the interaction time of atoms in the **WGM** of the bottle microresonator, an optical dipole trap for single atoms, located within the **WGM**, was chosen. Its operation is described in the following. Initial transfer of single atoms to the bottle resonator **WGM** is performed in the same manner as previously described, in that, a laser-cooled cloud of ^{85}Rb atoms is brought to the resonator location via an **Atomic Fountain**. The characteristic burst of photons registered in transmission of the critically-coupled bottle microresonator signifies the presence of a single atom traversing the evanescent field of the **WGM**. Following such a real-time detection event, a sub-microsecond reaction time is required in order to attempt optical trapping of the same free-flying atom before it exits the **WGM** again to be lost into free space. For this purpose, a dedicated **Field Programmable Gate Array (FPGA)**-based electronics that initially tags the atom coupling event subsequently acts to trigger the switching of a free-space trapping laser, the total time of which is suitably minimised to be less than $0.3\ \mu\text{s}$, including all of the light and electrical signal propagation timings. The trapping laser, which is focussed to a spot size of around $3.5\ \mu\text{m}$ by optics located outside of the vacuum chamber, has its waist positioned on the surface of the resonator. In doing so, with its wavelength red-detuned to the D_2 transition of ^{85}Rb , a partial standing wave optical potential for the atoms is generated due to interference between the incident and back-reflected beam.

2. Cavity Quantum Electrodynamics with the Bottle Microresonator

An atom located in the vicinity of the potential minimum closest to the surface of the resonator, at the moment of capture, will be confined to a region that is only ~ 200 nm away from the surface, where it experiences appreciable coupling to the resonator's **WGM** of about $g \approx 2\pi \times 10$ MHz. Figure 2.16 illustrates this described scheme where 2.16(a) depicts its schematic, 2.16(b) shows the calculated spatial optical potential compared to the position-dependent coupling strength, and 2.16(c) displays a general experimental sequence as a reference for the measurements to be presented in Section 2.4.4. Table 2.1 summarises the parameters used for the realised retroreflected dipole trap, in addition to key figures of merit as will be outlined in the next Sections.

wavelength	783.68 nm
detuning to D_2	$2\pi \times 1.68$ THz
power	19 mW
waist	3.5 μ m
depth	$U_0/k_B = 2.7$ mK
light shift [70]	$\delta_g \approx -2\pi \times 91$ MHz
<hr/>	
trap loading efficiency	$\eta_0 \approx 0.7\%$
trap lifetime	$\tau \approx 2$ ms
trapped atom temperature	$E_0/k_B \approx 1.8$ mK
coupling strength	$\bar{g} \approx 2\pi \times 9.3$ MHz

Table 2.1. Retroreflected trap parameters. Lower panel: measured figures of merit for the successfully implemented dual-colour magic wavelength trap for single atoms that are strongly coupled to the **WGM** bottle microresonator [60].

Upon application of the trapping light field however, the ground and excited state energies of a **Rb** atom confined in the optical trap will be strongly shifted in opposite directions, resulting in a substate- and position-dependent atomic transition frequency. This has the detrimental effect of inducing a large detuning of the atom with respect to the resonator **WGM**, to the extent that coupling of the two is no longer easily visible. Thus, the trap-induced light shifts have to be compensated for – the discussion of which is presented in the next Section.

2.4.3 Compensation of the Trap-induced Light Shifts

For a fixed power and detuning of the trapping field, the $5S_{1/2}$ ground state of an atom located in the trap centre ($\mathbf{r} = 0$) is maximally scalar shifted to a lower energy by an amount δ_g , while the $5P_{3/2}$ excited state manifold undergoes scalar *and* tensor light shifts towards higher energies. The resulting fine structure and Zeeman substate-dependant atomic transition frequency is thus given by $\omega_a(F', m_{F'}) = \omega_0 + \delta_g + \delta_e(F', m_{F'})$, where

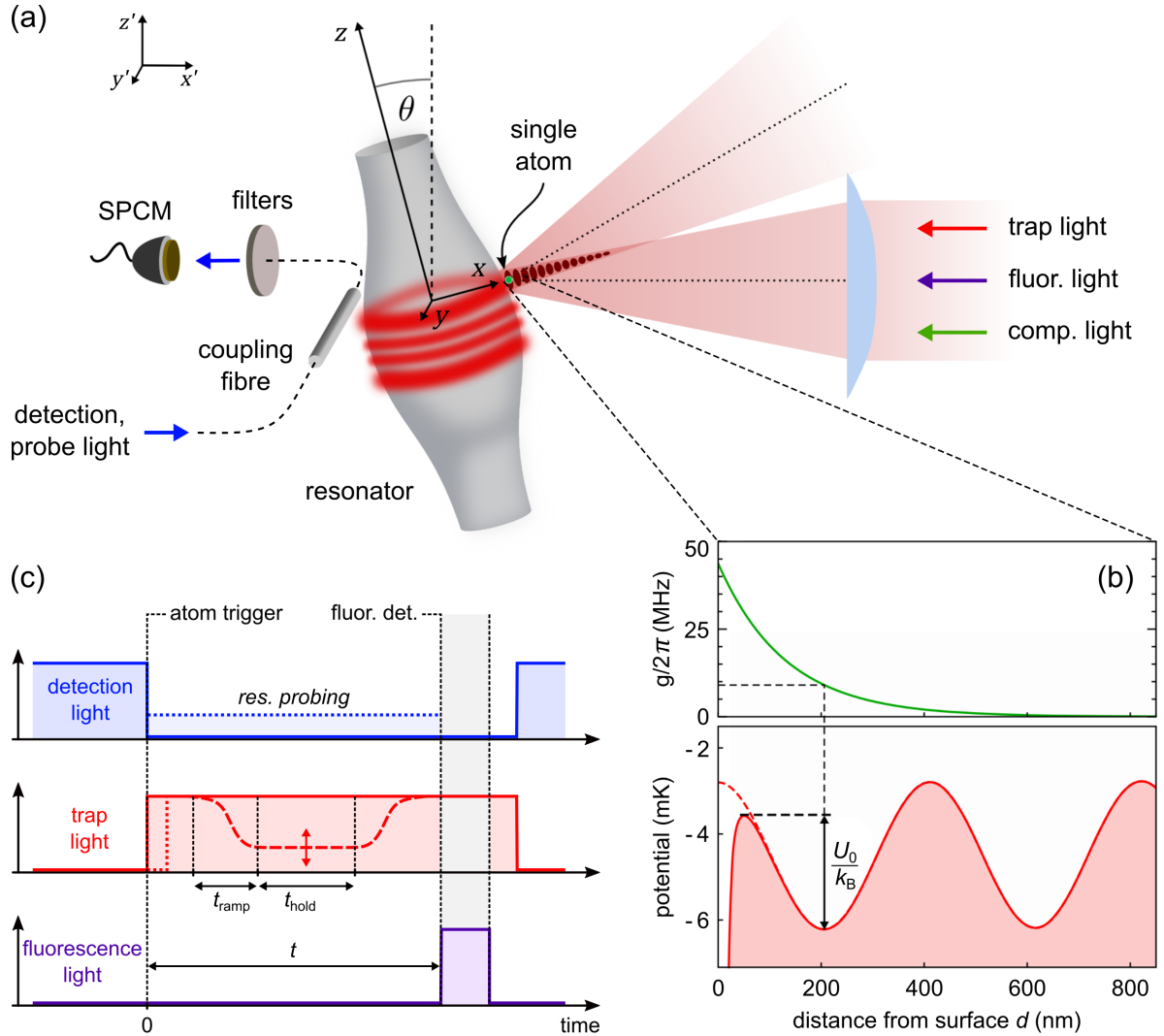


Figure 2.16. Retroreflected optical dipole trap. Reproduced from [60]. (a) Diagram of the experimental set-up used for the trapping of individual ^{85}Rb atoms that are strongly coupled to the bottle microresonator's **WGM**. (b) Expected coupling strength, g (upper panel), and calculated optical trap potential (lower panel) along the x direction. The trapping potential steeply drops within ~ 50 nm of the resonator surface due to attractive surface forces. (c) General experimental sequence. Immediately upon detection of an atom coupling to the **WGM**, the detection (trap) light is switched off (on). Following this, a fluorescence detection pulse is sent through the trap optics to test the presence of an atom inside the trap. Between the initial atom trigger and the subsequent fluorescence detection, and depending on the type of measurement performed, the trap light can be modulated to change the depth of the trap, or probing of the trapped atom via the resonator can be performed. See text (Section 2.4.4) for details.

2. Cavity Quantum Electrodynamics with the Bottle Microresonator

ω_0 is the vacuum frequency of the unperturbed ($5S_{1/2}, F = 3, m_F = 3$) \rightarrow ($5P_{3/2}, F' = 4, m_{F'} = 4$) atomic cycling transition to which the resonator is stabilised (cf. green laser line in Figure 2.2(c)), and $\delta_e(F', m_{F'})$ is the shift of the excited substate with ($F', m_{F'}$). Note that this is also relevant to other transitions, and is accessible by redefining ω_0 [70]. Due to the finite temperature of the atom inside the trap, motion away from $\mathbf{r} = 0$ means that it explores the three-dimensional intensity distribution of the trapping field and consequently, all of the aforementioned quantities except ω_0 are dependent on the atomic position \mathbf{r} . Therefore, in order to realise $\omega_a(\mathbf{r}) = \omega_0$ for all positions \mathbf{r} , the light shift compensation must operate across the spatial extent of the trap, and particularly for the (F, m_F) \rightarrow ($F', m_{F'}$) resonator transition of interest. Doing so ensures that the trapped atom is resonant with, and can thus be coupled to, the WGM.

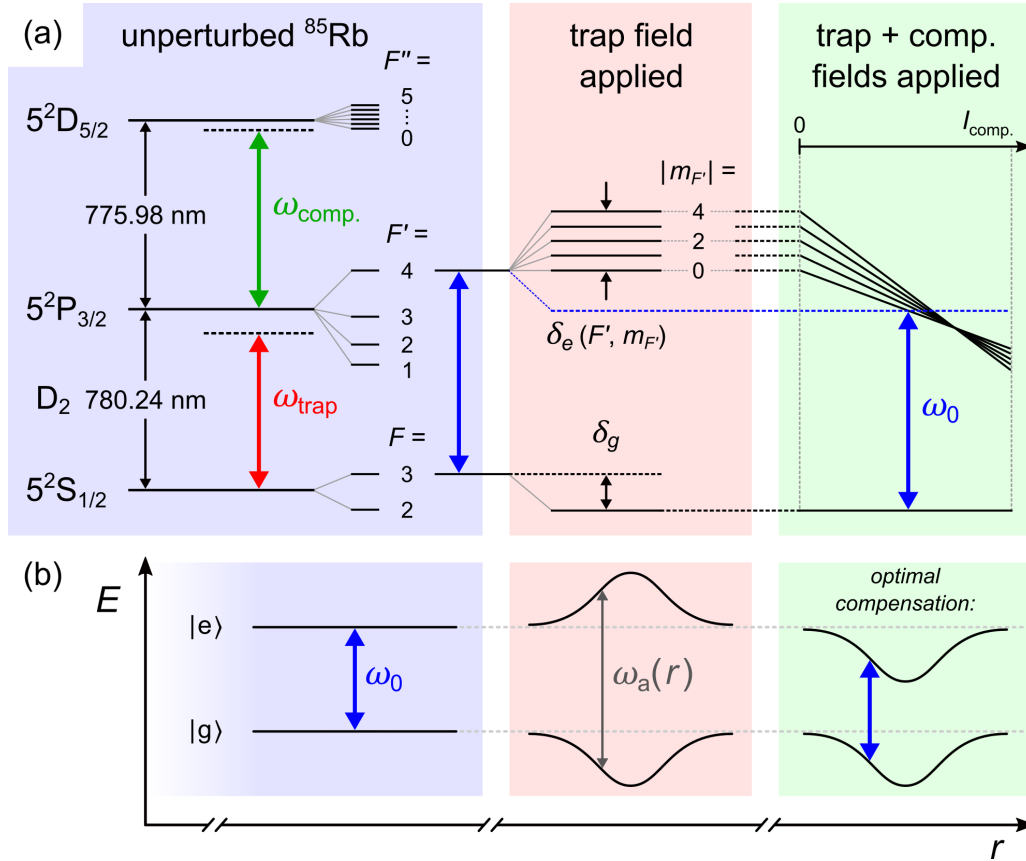


Figure 2.17. Dual-colour magic wavelength trapping principle. Reproduced from [70]. (a) A simplified energy level schematic of the relevant transitions of ^{85}Rb : in free space (left panel), for a fixed intensity and detuning of the trapping field with frequency ω_{trap} (middle panel), and under this applied trapping field in combination with the compensation field (right panel). The latter scenario depicts how, when increasing the intensity of the compensation field at a fixed detuning (frequency $\omega_{\text{comp.}}$), the $F' = 4$ Zeeman substates can be tuned into resonance with the resonator, at frequency ω_0 . (b) An illustration of the positional energy dependence of the ground state, $|g\rangle$, and excited state, $|e\rangle$, of a representative two-level atom for the three different situations depicted in (a). Here, a Gaussian intensity profile along the spatial coordinate r is assumed.

Although the D_2 transition of **Rb** does not offer a so-called *magic wavelength** for a red-detuned trap field unlike a number of other atomic species [155–157], compensation of the trap-induced light shifts is still possible by adopting a so-called *dual-colour* magic wavelength scheme [158], whereby a second light field is superposed with that of the optical trap. This additional *compensation* field is near-resonant to the $5P_{3/2} \rightarrow 5D_{5/2}$ higher-lying transition of ^{85}Rb as indicated in Figures 2.2(b) and 2.17. Much like the light shift of the $5S_{1/2}$ ground state caused by the trapping field, the compensation field imparts an additional light shift on the $5P_{3/2}$ (intermediate) excited state manifold while leaving the ground state mostly unaffected, as schematically illustrated in Figure 2.17(a). For an optimal choice of power and detuning of the compensation field, both the scalar and tensor light shifts of the $F' = 4$ state can be matched to the trap-induced scalar shift of the ground state, thereby restoring the unperturbed transition frequency, ω_0^\dagger . Furthermore, the position-dependency of the atomic transition frequency is effectively removed for a perfectly mode-matched spatial intensity distribution of both fields, as illustrated in Figure 2.17(b).

In order to realise such a dual-colour trapping scheme, the compensation light field is focussed onto the resonator surface alongside the trapping field, as shown in Figure 2.16(a). As the wavelengths of these two fields (respectively $\lambda \approx \{783, 776\}$ nm) are very close, the first antinode of each of the generated standing waves roughly coincide. Operating together, single atoms can then be captured in this dual-colour magic wavelength trap and simultaneously brought into resonance with the **WGM** of the bottle microresonator by virtue of the light shift compensation mechanism. The characteristics of this trapping scheme, and a measurement of the vacuum Rabi splitting in the coupled trapped atom–resonator system spectrum, will conclude in the next Section.

2.4.4 Main Results

Implementation of the dual-colour resonator trapping scheme as described in the previous Sections 2.4.2 and 2.4.3 (cf. Figure 2.16) enables the coupling of single *trapped* atoms to the **Whispering-Gallery Mode** of the bottle microresonator. In order to verify such a coupling event, it is paramount that detection of the atom contained within the trap occurs *via the resonator* – thereby ensuring that the atom is located within the potential minimum closest to its surface and indeed experiencing coupling to the exponentially decaying evanescent field of the **WGM** (cf. Figure 2.16(b)). Therefore two distinct – but not entirely dissimilar – detection methods are employed. The primary method

*An optical trap operating at a magic wavelength has the desirable effect of shifting both the ground and excited states by the same amount, leading to an unmodified transition frequency of the trapped atom.

†Note that however, due to the presence of tensor light shifts, compensation cannot be achieved for all $F' = 4$ Zeeman substates simultaneously.

involves the standard detection via resonant probing through the coupling nanofibre, as performed for the initial triggering of the trap (see Section 2.4.2). However, this method heavily relies on a resonant atom–resonator interaction, and so cannot be applied when the atom is largely detuned to the resonator, as in the absence of an optimal light shift compensation for example. The secondary method combats this disadvantage by directly detecting the fluorescence of a trapped atom that is coupled into the resonator with use of an external resonant excitation. For this, a high power pulse of light with a centre frequency equal to the **WGM** resonance is sent onto the trapped atom through the same trap optics, as shown in Figures 2.16(a) and (c). The pulse has a duration of 20 μs . Despite the large trap-induced detuning between the atomic transition and the **WGM** (in the absence of light shift compensation), the trapped atom elastically scatters photons from this *fluorescence detection* pulse, of which a fraction is coupled into the resonator, picked up by the coupling nanofibre, to then be detected in transmission and used as a signature of a successful detection. The intensity and duration of the pulse can be further tuned to enable a high-fidelity but destructive detection of the atom within the trap, or a lower-fidelity but non-destructive detection [70]. This method carries the additional advantage that *only* a trapped atom contributes to the fluorescence detection signal. These detection methods, in various combinations, allow for a characterisation of the whole trapping scheme alongside a measurement of the coupling between trapped atoms and the bottle microresonator, as summarised in the lower panel of Table 2.1 and described in the following.

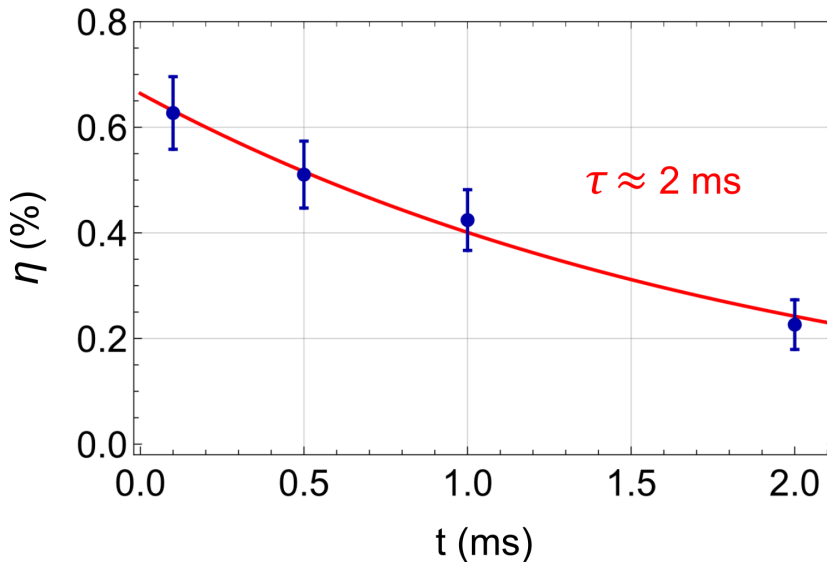


Figure 2.18. Measurement of the trapping lifetime. Reproduced from [60]. Measurement of the probability for finding a given detected single atom in the trap as a function of the waiting time, t , yielding a trap lifetime of around 2 ms.

Lifetime. By registering an atom coupling event via detection through the nanofibre – which also triggers the switching on of the trap – the fluorescence detection method can be subsequently employed after a variable waiting time, t , following the initial detection (see Figure 2.16(c)). This yields the survival probability of the atom in the trap, the results of which are displayed in Figure 2.18. By fitting an exponential decay of the form $\eta(t) = \eta_0 e^{-t/\tau}$ (red line) to the measured data (blue data points), the probability for trapping an initially detected atom, $\eta_0 \approx 0.7\%$, and the trapping lifetime, $\tau \approx 2$ ms, can be extracted. This rather low trapping efficiency is expected when considering that the trapping mechanism is triggered for every single atom coupling event. These can occur at any trajectory through the WGM within ~ 250 nm from the cylindrical surface of the resonator, while the trap is only located at a fixed position within the WGM. As only atoms located close to the potential minimum at the moment of capture can be trapped, the value of $\eta_0 \lesssim 1\%$ is expected given the finite overlap of the trap volume with respect to the resonator WGM [70]. The lifetime of several milliseconds, on the other hand, constitutes a 1000-fold increase in the interaction time of a single atom with the resonator mode when compared to the free-falling case of only a few microseconds (see Figure 2.9). While this result is a major step forwards for WGM resonators in general in establishing the first trapping of atoms in a WGM, the measured lifetime is significantly shorter when compared to free-space standing wave optical dipole traps for single atoms [159] and is around an order of magnitude lower than atoms trapped close to dielectrics [113, 114, 153, 160]. This contrast is mainly attributed to the fact that, on average, trapped atoms have a high initial temperature due to the trap loading mechanism and can therefore be quickly lost from the trap due to scattering-induced heating [70]. This is verified in a separate measurement that is performed in order to estimate the energy distribution of single atoms contained within the trap.

Energy distribution. During the trapping sequence, after an initial atom trigger event, the power of the trapping laser is ramped down to an adjustable level, held at this power for a certain time, before time-reversing the ramp to reach the original power value again. This is followed by a fluorescence detection pulse, as shown in Figure 2.16(c). Doing so has the effect of reducing the trap depth from its initial value U_0 to a new value U_{low} , such that atoms with an energy larger than this lowered depth are ejected. By repeating for various values of U_{low} , a measurement of the fraction of atoms surviving in the lowered trap can be performed, from which the average energy distribution can be extracted. It is important that the temporal modification of the trap depth, $U(t)$, conforms to a number of technical constraints in order to yield a reliable estimate of the survival probability as a function of U_{low} . Firstly, the depth must be lowered (and subsequently raised) *adiabatically* such that the total energy of the atom is reduced from its initial energy E_0 to a E , and only lost if $U_{\text{low}} < E$. This condition ensures that the action of the atom within the trap is conserved across the

variation $U(t)$, and that the atom remains in a well-defined energy eigenstate of the trapping potential with the desired consequence that there is a one-to-one mapping of these energies E to E_0 [70, 159]. Secondly, the holding time between the power ramps must be suitably chosen. It should be longer in duration than the period of all trapping frequencies, such that the atom has enough time to leave the trap, but much shorter than the measured trapping lifetime. Doing so ensures that only atoms with an energy $E \leq E_{\max} \equiv U_{\text{low}}$ will contribute to the fluorescence detection signal after this procedure. Implementation of this measurement as described reveals that the energy distribution is peaked towards higher energies out of the initial potential depth, from which the average energy of $E_0 \approx 2/3U_0 = k_{\text{B}} \times 1.8$ mK is obtained. These results are displayed in Figure 2.19. This high-temperature result, while sub-optimal, can be easily understood on account of the trap loading mechanism where atoms are captured from free-fall. A single atom, at the moment of initial detection, has a mean kinetic energy of around $k_{\text{B}} \times 0.5$ mK arising due to its free-fall during the AF launch. Further to this, the position of the atom with respect to the trap centre at the moment of capture determines its initial potential energy. This contributes in most cases since trapped atoms are likely to be displaced from the trap centre upon initial capture, in part due to the reactional time delay of ~ 250 ns when switching on the trap following the trigger by an atom detection event. Ultimately, this high average temperature of the trapped atoms leaves them susceptible to a pronounced heating out of the trap in a short amount of time. The dominant heating effect originates from the strongly repulsive dipole force in the excited state that imparts a large energy increase each time the atom scatters a trap photon, which fundamentally limits the lifetime of the demonstrated trap to only several milliseconds [70].

Atom–resonator coupling. Even with these initially hot captured atoms, a measurement of the average coupling strength between single trapped atoms and the WGM resonator can still be accomplished within the measured lifetime. To observe this resonant interaction during trapping, a transmission spectrum of the coupled atom–resonator system is taken. This is achieved by measuring the transmission of a probing pulse sent through the coupling nanofibre following an initial atom detection, and varying its detuning around the WGM (and compensated atomic) resonance. The data collected during successful trapping and survival events, signified with the use of a fluorescence detection succeeding the half-millisecond probing period, are subsequently analysed. Figure 2.20 displays two such transmission spectra resulting from the described measurement procedure, both with (blue data) and without (purple data) the aid of the light shift compensation technique that was introduced in the previous Section 2.4.3. The plot on the left shows a spectrum resembling the empty resonator spectra (grey data in each plot), indicating that atoms trapped in the WGM are not strongly coupled to the resonator in the absence of light shift compensation

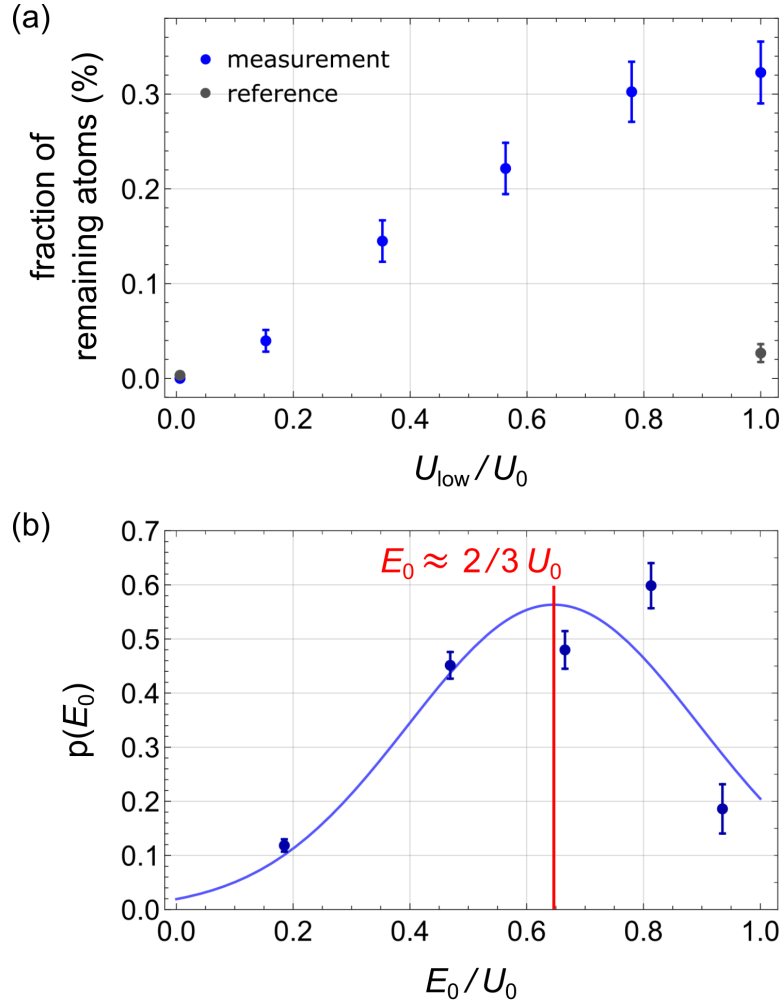


Figure 2.19. Energy distribution of atoms in the trap. Reproduced from [70]. (a) Measured fraction of atoms that survive a lowering of the trapping potential to a depth of U_{low} . (b) Measurement of the energy distribution of the trapped atoms, with a Gaussian fit showing the peak at an energy of $E_0 \approx 2/3 U_0 = k_B \times 1.8$ mK.

due to the substantial detuning of the atomic transition induced by the trapping field. As the average atom–resonator detuning here is large, but still finite, the spectrum shows a small dispersive shift of the resonator resonance. Furthermore, for large positive detunings of the probing light, deviations from a pure Lorentzian lineshape are visible and can be attributed to the coupling of atomic transitions other than the intended $F = 3 \rightarrow F' = 4$ cycling transition, which are light-shifted closer to resonance [70]. Strikingly, but perhaps unsurprisingly, the plot on the right – where the atoms were trapped in a potential with the light shift compensation – shows a spectrum that exhibits a clear vacuum Rabi splitting. This observation illustrates the strong and resonant coupling between these single trapped atoms and the **WGM** of the bottle microresonator, as brought about by virtue of the dual-colour magic wavelength trap. A model of the data (solid line), which takes into account the atomic motion within the trap together with the position-dependent coupling strength (cf. Figure 2.16(b)), yields a mean trapped atom–resonator coupling strength of $\bar{g}/2\pi = 9.3$ MHz. Finally,

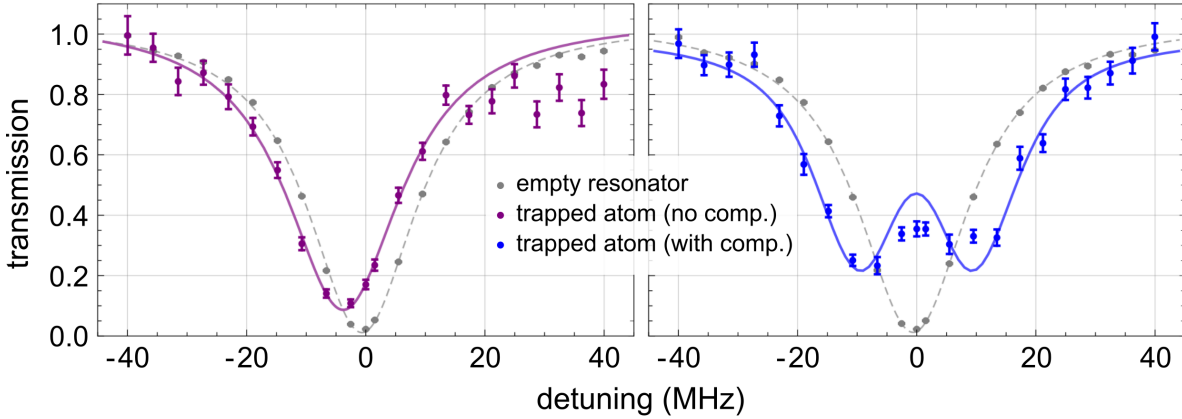


Figure 2.20. Transmission spectra of the trapped atom–resonator system. Reproduced from [60]. The plot on the left shows that the measured spectrum without compensation of the trap-induced light shift (purple) resembles the empty resonator spectrum (grey), albeit with a slight dispersive shift of the resonance due to the finite detuning of the atomic transition with respect to the **WGM**. The plot on the right shows that the measured spectrum, with the addition of light shift compensation (blue), clearly differs from the empty resonator spectrum (grey). This vacuum Rabi splitting, of mean strength $\bar{g} = 2\pi \times 9.3$ MHz, is a clear signature of a strong atom–resonator coupling with trapped atoms.

it is informative to compare the vacuum Rabi spectra for the cases of trapped atoms as displayed in Figure 2.20 to that of the transiting (untrapped) atoms in Figure 2.10, since both measurements were undertaken with use of the same **WGM**. The difference between the extracted mean coupling strengths, where $\bar{g}_{\text{transit}} \approx 2\bar{g}_{\text{trapped}}$, therefore indicates that the transiting atoms pass closer to the surface of the resonator than the trapped atoms on average. This exemplifies the necessity to provide a stable interaction at the smallest distance possible due to the exponential decay of the electric field of the **WGM** in its evanescent field.

This latter main result succinctly encapsulates all techniques described throughout this Chapter thus far: the integration of the **Whispering-Gallery Mode** bottle microresonator with single atoms in a unique **Cavity Quantum Electrodynamics** platform, the optical trapping of these atoms within its **WGM** and a compensation of the trap-induced light shift to ensure mutual resonance, where a verification of the strong and resonant coupling with trapped atoms solves a long-standing goal within this class of resonators. The opportunity for critical retro-reflection on these milestones enables a well-informed plan for the future of the experiment to materialise, the discussion of which will close this Chapter in the next Section.

2.5 Critical Conclusions

The introduction of the **WGM** bottle microresonator at the beginning of this Chapter has signified its role as a novel **CQED** platform that offers a variety of advantageous and attractive properties. In particular, near-lossless in- and out-coupling of light via evanescent coupling with the use of positionable optical nanofibres allows for a tunable excitation of a desired **WGM**. Ultra-high quality factors in combination with microscopic mode volumes made possible by a controlled and reliable manufacturing process of the bottle microresonator, enables access to the strong-coupling regime of **CQED** when coupling single emitters to the resonator. The chiral nature of certain **WGMs** realises the ideal situation of a single two-level emitter interacting with a single cavity mode, and further opens up a new range of applications in fibre-integrated nanophotonic devices that can control the flow of light with only a single atom. The resonator's favourable geometry grants precise and wide-range adjustment of its resonance frequency solely by axial strain, and can be hence actively stabilised to the transition of the emitter of choice. The latest milestone in the achievement of interfacing the resonator with strongly coupled atoms for extended periods of time by virtue of optical trapping at sub-micron distances from its surface, tops off the list of demonstrated capabilities offered by this system.

It is from this latter result, and the lessons learned from it, that drives the development in improvements to the overall design of the experimental apparatus. By making improvements to the technical merits of atom confinement at the resonator, all previously demonstrated milestones will additionally benefit from the (i) longer atom–resonator interaction time, (ii) better defined coupling strength, (iii) optimised experimental cycle, and (iv) deterministic atom control. So far, with the demonstrated trapping scheme, points (i) and (ii) suffered from the high-temperature of the atoms at the moment of coupling, while points (iii) and (iv) have not been addressable due to the loading and capture mechanism dictated by the design of the **CQED** 1.0 apparatus.

In order to improve the demonstrated trapping scheme, one major requirement would be to start with colder atoms. The central idea for the **CQED** 2.0 apparatus is thus to recapture atoms from the **Atomic Fountain** in a second **MOT** stage located in the vicinity of the bottle microresonator housing. From there, single atoms could be picked up in a movable optical tweezer and brought towards the bottle resonator to be subsequently confined within its **WGM**. Together, this would ideally enable a near-deterministic loading of cold atoms into the resonator–surface trap, thereby realising all the aforementioned points (i)-(iv). The next Chapter 3 focusses on the re-design of the experimental set-up, beginning with an outline of the specific design goals that will enable the set-up to initially perform everything presented thus far.

3

Experimental Design

And now for something completely different...

Monty Python

Achtung! This Chapter contains an overkill of technical information concerning the workings of the CQED 2.0 experiment. Its contents are therefore aimed at future experimentalists working with this platform, or for extremely curious readers...

3.1 Words of Motivation

The opening chapter of Karl Jousten's *Handbook of Vacuum Technology* [161] begins with the account of the Greek philosopher *Democritus*, who together with his teacher *Leucippus* in around 400 BC, coined the term *atomos* to describe the small indivisible particles that they supposed to make up all matter in the world. By this reasoning, they assumed, in addition, that the space between these so-called 'atoms' would be unoccupied – culminating the first concept of a *vacuum*. This empty void then becomes a necessary requirement for the uninhibited movement of atoms, such that they can freely arrange themselves en masse to produce the diversity visible in our macroscopic world. Surprisingly, these ancient philosophical considerations have stood the test of time, subject to fervent debate and experimentation across the following centuries, and even surviving the period of Aristotle-inspired *horror vacui* around the 1300s [162]. A back-of-the-envelope calculation reveals that the average (visible) matter density in the universe to be less than one atom per cubic metre, indicating that there can be appreciable volumes (between galaxies, for example) without any massive particles,

3. Experimental Design

typically referred to today as *absolute* vacuum. Modern quantum mechanics, however, now stipulates that even absolute vacuum is not empty – the quantum vacuum state has a non-zero minimum energy, in which momentary virtual particle pairs are continuously popping in and out of existence [163, 164].

It is not necessary to remain in Ancient Greece in order to follow the advancements in modern vacuum physics, which arguably dates back to the more recent 1909, when *Knudsen* divided gaseous flows at different pressures into three regimes [165]. Inside a container at high pressures (~ 1 bar), a gas behaves as a continuum in which the particles constantly mutually collide, continuously exchanging momentum and energy in a so-called *viscous* flow. For sufficiently low enough pressures ($\lesssim 10^{-2}$ mbar), the mean free path of the particles becomes much greater than the dimensions of the container such that these mutual collisions hardly occur, resulting in a so-called *molecular* flow. The intermediate regime, characterising the transition between a viscous and molecular flow, is known as a *Knudsen* flow. While vacuum science is a whole vast discipline in and of itself, the wealth of modern vacuum technology spawned from such considerations can all be categorised predominantly by in which of these flow regimes they operate. From everyday examples like food preservation, filament bulbs, and thermal insulation that exploit a rough vacuum, to high vacuum usage in major automated industrial machine processes such as vacuum-aided gripping and positioning, vacuum environments are an essential commodity underpinning a surprising amount of modern living. Notably, the development and manufacture of microelectronics and semiconductor technology is made possible through high vacuum environments for physical and chemical vapour deposition.

These examples all share the commonality in that the “...*vacuum itself is maybe not so important – it’s what you do with it that’s important. Vacuum is an enabler...*”^{*} for other technological applications. It unequivocally demonstrates how advances in industry have traditionally gone hand-in-hand with advances in scientific research, and vice versa. A prime example of this symbiosis is the relationship between vacuum technology and quantum science, with improvements in one discipline practically enabling furtherments in the other. A large technological hurdle in the latter is to generate a readily available source of quantum matter, from which a sample (e.g., from one to several billion atoms) can be selected and utilised for experimentation. Successes in this endeavour strictly require a reliable, controllable, and reproducible test environment in order to isolate the sample from the ambient background – for which an **Ultra-High Vacuum (UHV)** is, mostly, the only contender. Modern byproducts of the marriage between industry and research along this direction have resulted in the commercial availability of pre-assembled **Magneto-Optical Trap** units, for a plug-and-play route towards quantum matter. Another example is the 3D printing of vacuum components, including chambers, driven by a

^{*}Quote from *Lars Montelius* 2018 – president of the **International Union for Vacuum Science, Technique and Applications (IUVSTA)**.

necessity for portability as well as size and weight constraints in space applications. Here, the design of a **UHV** environment must revolve around the central **CQED** setting of a nanofibre-coupled **WGM** bottle-microresonator, that can interface – and strongly couple – to single ^{85}Rb atoms. In this case, the **UHV** environment principally enables cold atom preparation, but additionally provides robust conditions in order to avoid a short-term degradation of the microresonator’s quality factor. The specialised atom–waveguide coupling via the bottle-microresonator necessitates a custom-made coupling apparatus away from what is currently available on the market, while still integrating commercial industry products where appropriate. Creating such an experiment completely from scratch thus requires an extensive background knowledge on the technologies that can enable the vision, not only on the experiment which is to be performed in the end. Centring on **UHV**, and generally speaking, the important tasks in this process can be summarised in the following steps: design of the apparatus, manufacture/ordering of the components making up the design, the system assembly (including **UHV**-compatibility treatment), its evacuation (from ambient down to **UHV** pressures), preparation of cold atoms, and only then onto experimentation with the sample. Arguably the most challenging out of the aforementioned is to devise an appropriate design, which, if carefully performed, can render the apparatus somewhat future-proof and expandable while maintaining its versatility as a **WGM** microresonator **CQED** platform. For this crucial step, it was not necessary to begin completely from scratch, as experience with the **CQED** 1.0 experimental apparatus allowed for informed design goals to be outlined for the transition to **CQED** 2.0.

The aim of this Chapter is thus predominantly twofold: to provide a comprehensive documentation on the entire experimental apparatus in its design and construction, and, in doing so, to serve as a reference material for future generations of researchers building on the work presented here. Opening with a specification of the design goals, the constructed apparatus that meets these criteria will then be introduced. The milestones achieved, including the procedures undertaken in the process, will accompany brief overviews of specific relevant concepts as they arise in the context. This Chapter also provides the necessary information on the set-up used, for an understanding of the experimental results presented in Chapter 5. Additional and complementary information relevant to this Chapter can be found in Appendices A and B. Appendix A contains a selection of images that document various stages of the **CQED** 2.0 experiment, while Appendix B consists of technical drawings and information for the various designed and used parts.

3.2 Design Goals

As discussed in Chapter 2, the heart of the **Cavity Quantum Electrodynamics (CQED)** experiment should essentially comprise a whispering-gallery-mode bottle microresonator and its coupling nanofibre(s), with the former strongly coupled to a single quantum emitter. Of course, experimentation and novel devices cannot be realised with just these three ingredients alone. As such, while the design of the entire experiment revolves around this central setting, all auxiliary design elements are carefully chosen with consideration of this foundational framework in mind. The primary goal of the re-design of the experiment can be succinctly stated as: **CQED 2.0** should be able to accomplish all that **CQED 1.0** could perform; *plus much more*. While the key milestones of the original experiment have been outlined in Section 2.3, the latter aim requires an elaboration. In particular, the most recent achievement of optically trapping a single atom that is strongly-coupled to the **WGM** of the bottle microresonator [60] has been a driving factor in the improvement of the experiment. The knowledge gained through experience with the strengths and shortcomings of the implemented trapping scheme has allowed for planning exactly around this higher-order objective. As stressed in Section 2.4, the stable coupling and long interaction enabled by optical trapping of the atom in the evanescent field of the **WGM** microresonator is a requisite for bringing this class of resonators in line with the more conventional **Fabry-Pérot (FP)** resonator counterparts.

In the following, the main goals of the upgraded design are listed alongside the justifications for each design choice. These are split into a hierarchy of importance, with the goals representing the capabilities of **CQED 1.0** (Section 3.2.1) preceding the goals to realise major improvements and extensions to the set-up in the form of **CQED 2.0** (Section 3.2.2). A final disclaimer should be noted in that, the design process presented here can be written up as a series of well-informed decisions that are cleanly separated and that follow a logical ordering. However, the reality has been that the task of designing such an experiment is a highly entangled one, where these decisions are not actually so well separated. In fact, the choice of solution for each goal greatly affects the available solutions for the remainder, in a cascading network of possibilities. For example, the choice of method for atom preparation and loading to the resonator dictates the optical access requirements, which in turn influences the geometry of the resonator–nanofibre(s) mounting, and therefore the choice of **UHV** housing, which can successively put limitations on the access, field coil dimensions, and so on *ad infinitum*. What is presented in the following is a convergence on the best possible solution that was found for meeting the design goals of the aptly coined **CQED 2.0** experiment.

3.2.1 Key Elements of the *CQED 1.0* Experiment

The upgraded-design of the experiment should not sacrifice any capabilities of the former design, and should therefore include;

1. *An ultra-high quality ($Q \gtrsim 10^8$) **Whispering-Gallery Mode** bottle microresonator with a tunable resonance frequency.*

The fibre on which the bottle microresonator is fabricated should be affixed to shear piezos for strain-tuning of its resonance frequency. These are, in turn, mounted upon a specialised base to maximise the stability of this tuning. See Section 3.3.1.

2. *Two coupling nanofibres for exciting the **WGMs** of the bottle microresonator, in either a singular-loaded or add-drop configuration.*

Each nanofibre should be affixed to its own holder that incorporates a bending piezo for axial elongation in order to enable control over the spatial coupling point. Importantly, each nanofibre should also be positionable along and perpendicular to the resonator axis, while remaining independent from one another in three dimensions. See Section 3.3.2.

3. *A high vibration isolation for maximal nanofibre–resonator coupling stability.*

In order to maintain a fixed coupling rate between the resonator and both nanofibres, the respective coupling gaps must be stable to within around ten nanometres [92]. Thus, the independent mounts upon which each of the three fibres are fixed should be attached to a large vibration sink, which is itself isolated from the internal walls of the vacuum chamber by using a suitable damping material. This internal **Vibration Isolation System (VIS)** should minimise the transmittance of mechanical vibrations that may otherwise excite string modes in the nanofibres that ruin the coupling. See Section 3.3.4.

4. *Single ^{85}Rb atoms at the vicinity of the resonator surface for **CQED** experiments.*

The atoms should be prepared in a **Magneto-Optical Trap (MOT)**, and launched towards the resonator from below via an **Atomic Fountain (AF)**. The fact that the atoms are loaded into the **MOT** from commercially available **Rb** dispensers, which can emit potential contaminants [166] that may coat the resonator and degrade its quality factor over time [167], necessitates a two-chamber design in which the dispensers are well separated from the resonator to preserve the lifetime of the latter. The alternative would be to house everything in a single **UHV** chamber that could potentially greatly simplify the overall design. However, the cost in experiment down-time to replace the resonator (and both nanofibres)

3. Experimental Design

every few months adds unnecessary complications to its continuous operation, not to mention the slow drop in its quality over time, which would inhibit the consistency of measurements. Both of these shortfalls can be avoided by adopting the proven two-chamber design: indeed, the previous resonator was kept under **UHV** for around a decade, with no noticeable decrease of its quality factor across this duration. This feat was attributed to the maintenance of a 'clean' **UHV** environment due to the containment of the alkali dispensers in a separate chamber. See Section 3.4.2.

5. *An optical dipole trap for single atoms at the resonator surface.*

In order to gain strong and stable coupling of a single atom to a **WGM** of the resonator for extended periods of time, the atom must be held – in free-space – as close as possible to the surface of the resonator. As demonstrated in [60], this can be achieved by positioning the tight focus of an optical tweezer onto the resonator's surface, such that a potential minimum is generated at a distance of $\sim \lambda_{\text{trap}}/4$ due to interference with the back-reflected beam. Details of this trapping scheme have been presented in Section 2.4, while the planned upgrades to this scheme will be outlined in Section 3.6 of this Chapter. Still, an unobstructed view onto the resonator (see Section 3.3.5, Table 3.1) is required for such a trapping scheme, regardless of the chosen trap loading method.

6. *Optical access for resonator heating via an external laser.*

This design goal has two purposes: firstly, the tight focusing of an intense laser onto the resonator (e.g., for generation of the single atom dipole trap) will cause a frequency shift of the resonator mode due to absorption of some fraction of the incident power, which changes both the resonator diameter and its material refractive index. This detrimental heating effect can be compensated for with the addition of a second, far-off-resonant (i.e., non-interacting with **Rb**), focussed beam, whose purpose is to keep the resonator at a constant temperature and therefore stable mode frequency. It would have the inverse on/off switching pattern to that of the dipole trap beam [70]. Secondly, the possibility to cleanse the resonator surface of adsorbed **Rubidium** and other undesired contaminants via their thermal evaporation is desirable. For both the aforementioned purposes, illumination of the resonator with light at a wavelength of around ten micrometres would suffice due to the fact that silica is highly absorbing at mid-infrared wavelengths [168]. A CO_2 laser is suitable for this task, but non-standard **UHV** viewports must be considered for its transmission at typical wavelengths and at potentially such high intensities. See Section 3.3.5.

3.2.2 Major Improvements in the *CQED 2.0* Experiment

CQED 2.0 has a number of upgrades incorporated into its design based upon experience with the *CQED 1.0* version of the experiment. Issues encountered along with the designed-in solutions are listed and discussed in the following;

1. **Issue:** In the previous version of the set-up, atoms were probabilistically loaded into the surface trap after a period of thermal expansion dictated by the transfer characteristics of the *Atomic Fountain (AF)*. The initially cold cloud of atoms ($T \approx 6 \mu\text{K}$) after the *MOT* and *Polarisation Gradient Cooling* stages underwent roughly a quarter of a second of ballistic free fall before reaching the resonator, during which no cooling force was present. This consequently meant that single atoms had a temperature greater than one millikelvin at the time of strong coupling, making their capture in the resonator trap challenging and trapping lifetime limited.

Upgrade: *Colder atoms at the vicinity of the resonator, in order to yield a higher trap loading efficiency and increased trapping lifetime.*

The idea is to add an additional cooling stage by recapturing the free-flying atom cloud after the *AF* launch in a second *MOT* stage that is located within the same *UHV* chamber as the resonator. This scheme would provide a reservoir of cold atoms that are readily available for near-deterministic transfer towards the resonator surface trap, while simultaneously preserving the clean *UHV* environment necessary for maintenance of an ultra-high resonator quality factor for as long as possible. This requires the standard constituents for the realisation of a *MOT* also inside the Science chamber, i.e., optical access for three pairs of counterpropagating cooling beams, along with magnetic field confinement, typically generated by pairs of current-carrying coils of wire in an *anti-Helmholtz (AHH)* configuration. Additional coils pairs in a *Helmholtz (HH)* configuration are required to produce bias fields for centring the magnetic field zero and also for the compensation of external stray fields. With proper design, the latter can also be used to produce offset fields along arbitrary directions. See Section 3.4.3.

2. **Issue:** The previous version of the experiment was not initially designed with the idea of optically trapping single atoms close to the resonator surface in mind. As such, the *ad hoc* solution demonstrated in [60] consisted of adding the optics required for the dipole trap beam *outside* of the vacuum chamber. This consequently set a lower limit on the focal length of the focusing lens which, in turn, restricted the *Numerical Aperture (NA)* of the system along with the size of the tweezer waist. This rendered collection of the single trapped atom's fluorescence via the trap optics challenging, and was indeed never observed. Furthermore, tight focusing of the beam through the front viewport of the *UHV* chamber introduced a number of unwanted effects, namely, chromatic aberrations and polarisation disturbance due to stress-induced

3. Experimental Design

birefringence of the transmitting viewport [70].

Upgrade: *Relocate the trap focusing lens closer to the resonator, i.e., inside the vacuum chamber.*

This would potentially counter or resolve all previously mentioned shortfalls, where, upon proper selection of lens: the **NA** would substantially increase and the tweezer waist would reduce, to enable improved single-atom localisation, detection and coupling. The higher **NA** would also improve the collection efficiency of fluorescence photons from the atom, to enable detection of a trapped atom via the trap optics. At the same time, the incident beams could pass through the viewport collimated, thus avoiding unwanted distortions to the beam properties. Such a lens has to be attached to an independent 3D-positioner in order to position its focus on the resonator surface. This solution opens the possibilities for a range of near-*deterministic* loading methods of the resonator surface trap. See Sections 3.3.3 and 3.6.

3. **Issue:** The design of the **CQED** 1.0 experiment meant that exchange of any components within the **UHV** environment was an extremely difficult, tedious, and time-consuming exercise (not to mention the induced stress when undertaking such a delicate and important task). It was so much so that compromises on the measured quality factor of the resonator had to be taken, in order to avoid repeating the procedure indefinitely. This was not helped by the fact that a number of the feedthroughs, both electrical and optical, were located at inaccessible locations and even on different **UHV** components entirely.

Upgrade: *Carefully factor this inescapable procedure into the new design to make the chamber internals 'easily' exchangeable, or at least in an effort to minimise the complication.*

Opening of the **UHV** system can always be a necessity, especially in the cases where a component under **UHV** may unexpectedly fail. A particularly relevant example is the replacement of a fibre component: either of the nanofibres, or the **WGM** resonator. Other examples include the upgrading of outdated vacuum technologies, or the replacement of alkali dispensers. If, for whatever reason, the chamber must be opened, particularly when installing the resonator for the first time, the entire procedure should be carried out quickly – but cautiously – and as smoothly as possible to minimise the potential of resonator degradation from deposited contaminants due to air exposure and risk of leakage. This can be achieved by gathering all of the feedthroughs into one component for convenience, and such that only a single flange has to be opened to gain access to the housed set-up. See Section 3.3.5 (Appendix C additionally provides extensive instructional documentation on the entire procedure). Finally, the

two-chamber design can also be refined with insertion of a segmenting gate-valve such that each system maintains its isolated pumping. Closure of said valve would enable replacement of parts in either chamber with minimal induced disturbance to the other. See Section 3.4.4.

4. A final consideration for an optimised design would be to maximise the optical access onto the centrally-located resonator itself. As outlined in the above, a number of the design goals require unhindered optical access to the general location of the resonator. Ideally, the UHV chamber itself would be concentric with the geometry of the resonator and made entirely of glass, with anti-reflection coatings suitable for near-lossless transmission of light at the desired wavelengths for different applications, i.e., a so-called *glass-cell*. Such a solution has been successfully utilised for other nanofibre experiments in our group, and is a popular design choice for numerous cold atom experiments in general. However, the use of a custom glass-cell to prioritise optical access would be incompatible with almost all other design goals outlined previously, particularly with the mounting of the fibres on 3D-positioners that are to be fixed to a VIS. A suitable glass-cell design would be extremely difficult to manufacture, worrysomey fragile, and not to mention expensive. As such, a preferable choice is the more conventional steel chamber variant with ConFlat™ (CF) flange technology that are commercially readily available and offer a multitude of ports for optical access. See Section 3.3.5.

3.3 The Science Chamber

This Section will detail and justify all design elements that have gone into the construction of the experimental heart: the resonator and coupling nanofibre(s) assembly and their housing in a UHV chamber, accordingly named the *Science Chamber*.

3.3.1 Resonator Mount

The holder of the resonator is designed to take advantage of the fact that the bottle structure itself is fabricated directly on a standard optical fibre, which can allow for frequency adjustment of a WGM resonator by so-called *strain-tuning* [63]. This elegant method of tuning – by simply pulling on the fibre ends to elastically deform the resonator’s geometry – takes precedence over other methods such as laser lock-in [169] and electrical thermo-optic heating [170, 171] due to its large tuning range (several hundred GHz) and stabilisation bandwidth (several hundred kHz) [63]. Furthermore, an active stabilisation of a desired resonator resonance is possible with use of the Pound-Drever-Hall (PDH) locking technique [172], whereby an error signal is generated from a frequency-modulated field transmitted past the resonator before a PID servo loop provides feedback onto the strain-tuning process. Such a lock was first demonstrated in [64] for the bottle resonator

3. Experimental Design

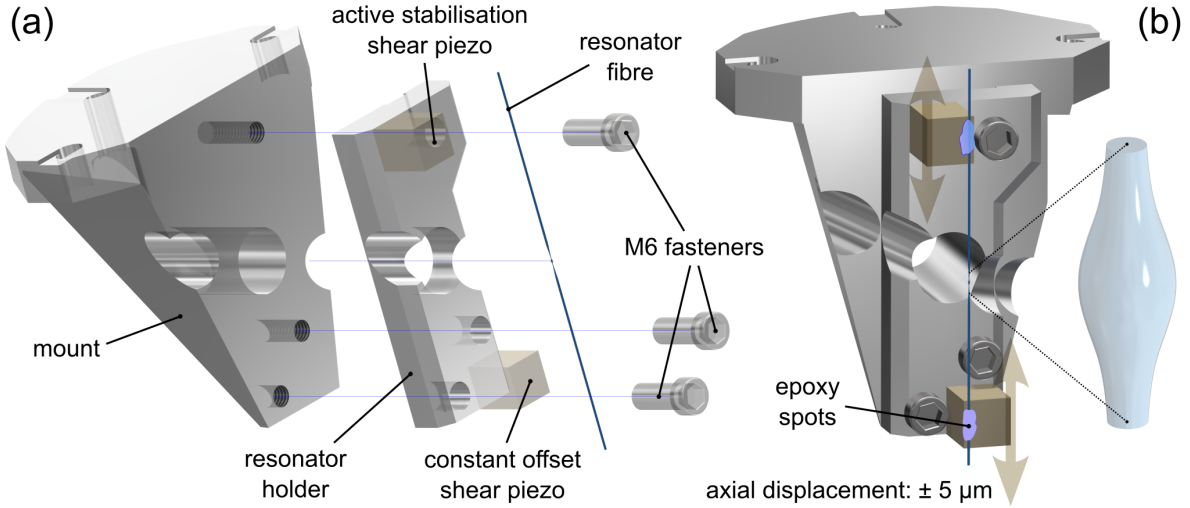


Figure 3.1. Assembly of the resonator mount design. (a) Exploded-view rendering. The mount’s depicted inclination to the vertical is 22° , in line with the final fully-constructed experiment. (b) Assembled-view rendering. Translucent arrows indicate the direction of motion of each shear piezo onto which the resonator fibre is affixed, thereby enabling strain-tuning of the resonator by axial pulling. Inset: zoom on the bottle structure, fabricated at the centre of the resonator fibre.

by feedback onto the fibre’s elongation with use of a bending piezo. To optimise the feedback, the bending piezo was upgraded to a pair of shear piezos (one at each fibre end) to apply axial strain only, making this method paramount for all other milestones in the **CQED** experiment (see Chapter 2), where the mode was typically actively stabilised to the frequency of the $(5S_{1/2}, F = 3, m_F = 3) \rightarrow (5P_{3/2}, F' = 4, m_{F'} = 4)$ cycling transition of ^{85}Rb . As such, this proven method of tuning has been retained and factored into the final design of the updated resonator holder, which is displayed in Figure 3.1.

The resonator fibre is fixed at each end, using a strong binding **UHV**-compatible (**NASA** low outgassing standard **ASTM E595** [173]) two-component epoxy (*EPO-TEK H77*, *Epoxy Technology, Inc.*), to the top plate of a multi-layer shear piezo actuator (*P141.10*, *PI Ceramic GmbH*) with a travel range of $10\ \mu\text{m}$. The presence of the capping plates ensures that the resonator fibre can be removed again without damaging the piezos. Each **UHV**-compatible shear piezo is bonded, using electrically conducting silver-filled epoxy (*EPO-TEK H21D*, *Epoxy Technology, Inc.*), to **PTFE**-coated wire leads for its high-voltage operating supply ($-250\ \text{V}$ to $+250\ \text{V}$), which are directed to the corresponding electrical vacuum feedthrough (see Section 3.3.5, Table 3.2). Each shear piezo stack is further affixed, with the same **UHV**-compatible epoxy, to a custom holder which is itself rigidly connected to a triangular supporting structure with use of three vented M6 bolts. Both are machined from a **UHV**-compatible aluminium alloy (*EN AW-6061*), and are appropriately bored to maximise optical access to the bottle resonator structure. As can be seen in Figure 3.1, care was also taken to avoid

UHV-destroying trapped pockets of gas (so-called *virtual leaks*) at the meeting faces and threadings of the screws.

The assembled mounting structure has an irregular tetrahedron (truncated half-pyramidal) geometry, which was specifically selected for its favourable mechanical resonance properties. It is necessary to adopt such a form in order to push the natural frequencies of mechanical vibration into the several kHz regime to ensure optimal stability of the whole mounting system. While passive stability is important, more critical is to confirm stability during active stabilisation of the resonator, i.e., during use of the shear piezos, where their principle operation direction is indicated in Figure 3.1(b). Therefore, all the assembled components were optimised with use of the **Computer-Aided Design (CAD)** program *Autodesk Inventor 2018*, which has a built-in suite to perform a **Finite Element Analysis (FEA)** of the user-specified system. Such a simulation, in which the designed parts are spatially discretised to numerically solve the macroscopic behaviour of the system [174], was performed in order to obtain the natural resonant frequencies of the designed bottle resonator holding structure. Figure 3.2 shows the results of this study for the final design, where the first six resonances that occur primarily around the shear piezos are displayed. The assembled holder seen in Figure 3.2(a) is shown vertically inverted to best illustrate the grounded fixed constraint, see Section 3.3.4. Furthermore, the relative deformation of the holder is graphically exaggerated for visibility and is also colour coded for clarity, where blue (red) indicates the minimum (maximum) displacement from equilibrium. The simulated vibrations at each frequency in Figure 3.2 (b)-(g) occur in different directions, as can be clearly seen from the closed contours of the undeflected system. By choosing only the lower shear piezo for active stabilisation and the upper for application of a constant (offset) voltage, an evaluation of the significance of each of these modes of vibration can then be undertaken. In doing so, it becomes clear that the first four resonances (Figure 3.2(b)-(e)) should not be strongly excited under normal operation as the upper shear piezo will be static, and can thus be neglected (assuming a high quality external mechanical vibration isolation, see Section 3.3.4 for details). The mechanical 'twist' motion indicated in the fifth resonance (Figure 3.2(f)) is not in the direction in which either shear piezo acts (see Figure 3.1) and therefore should also not get excited. The sixth resonance at around 20 kHz, however, exhibits deflection primarily along the direction of the piezo motion and is particularly strong for the lower active stabilisation one. As the chosen shear piezos have a specified mechanical resonance frequency of 100 kHz, this result thereby sets an upper limit on the achievable stabilisation bandwidth. It should be noted that the performed **FEA** is not without some limitations, namely that the assembled components under consideration are assumed to be made of the same material (the desired 6061 aluminium alloy), despite the fact that the shear piezos are manufactured from piezo ceramic type *PIC255* and are glued to the aluminium surface as previously described. Nevertheless, the simulated resonance frequencies, both in magnitude and modal type, should not significantly differ

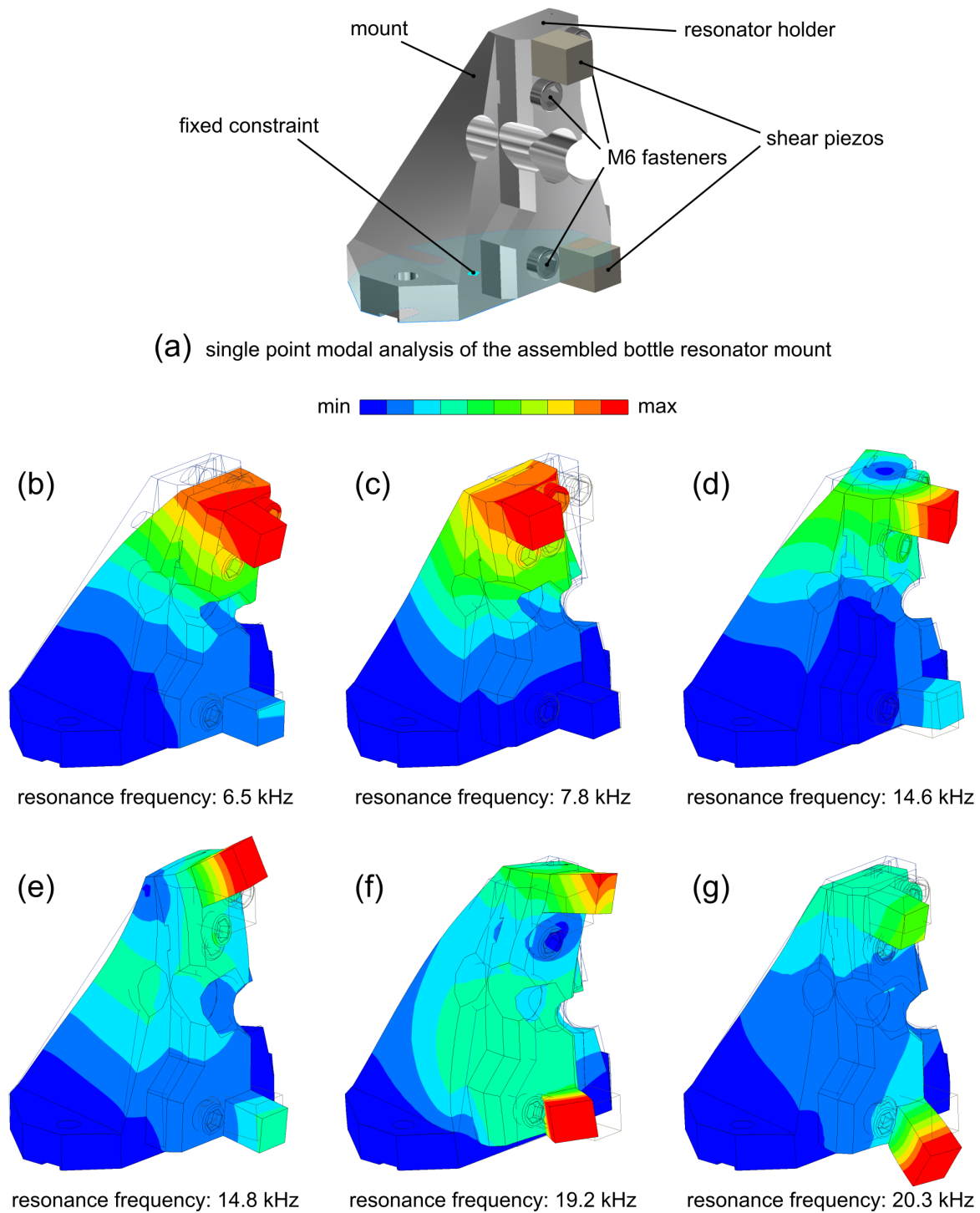


Figure 3.2. Finite Element Analysis of the resonator mount design. (a) The construction under consideration, where the fixed constraint plane is indicated. (b - g) Results of the FEA for the six lowest mechanical modes of vibration, respectively, labelled with the magnitude of each resonance frequency. The relative deformation of the resonator mount for each mode is colour coded and exaggerated for visibility.

from the reality [175]. Finally, this analysis still indicates an improvement on the entire mounting design with respect to the magnitude of its natural modes of vibration when compared to those of that presented in [92], despite the removal of $\sim 10\%$ of the volume for optical access. This can be attributed to the redistribution of the centre-of-mass of the mount to being closer to the vibration sink, thereby increasing the frequency magnitude of all comparable natural mechanical vibration modes.

3.3.2 Nanofibre Mounts

Evanescent coupling of light into the resonator requires a stable overlap of a **WGM** of the resonator with the evanescent field of a nanofibre-guided mode. For the excitation and maintenance of a specific mode, this overlap should be both controllable and anchored, respectively. To exploit the full potential of the bottle microresonator, two nanofibres are made available for simultaneous in- and out-coupling of light in an add-drop configuration. As described in the preceding Section 3.3.1, since the position of the bottle resonator fibre is fixed in space for maximum stability of its resonance, the coupling fibres themselves must be independently positionable in two dimensions with respect to the bottle structure in order to interface each of them to the desired **WGM**. Crucially, this tuning of the nanofibre positions should be extremely precise and accurate down to approximately one nanometre.

For this purpose, a specially designed mounting system was constructed for each coupling nanofibre, where the final designs of which are displayed in Figure 3.3. In both cases, each coupling fibre is manufactured from standard single-mode step-index optical glass fibres (*F-SF*, *Newport Corporation*) and feature a nanofibre section with a minimal diameter of 500 nm across a length of 5 mm, that is sectioned between two tapered regions each of length ~ 40 mm that connect the nanofibre to the 125 μm -diameter unprocessed fibre. The four fibre ends will be directed out of the vacuum system via a fibre-feedthrough [176] (see Section 3.3.5, Table 3.2). Spots of the unprocessed sections of the fibres are fixed, using the same low-outgassing epoxy introduced in Section 3.3.1 (*EPO-TEK H77*, *Epoxy Technology, Inc.*), at one end to a 6061 aluminium L-shaped custom fibre holder and at the other to a **UHV**-compatible **PTFE**-capped bending piezo that is itself rigidly clamped to the fibre holder with a pair of vented M2.5 fasteners. These bending piezos have a specified travel range of ± 100 μm (*PL112.10*, *PI Ceramic GmbH*) and are, again, bonded to **PTFE**-coated wire leads for their operating voltage supply (0 V to 60 V) which are directed to the corresponding electrical vacuum feedthrough (see Section 3.3.5, Table 3.2). While the fibres are glued under pre-tension, the bending piezos are necessary for additional tensioning, which has two important purposes: Firstly, application of an axial-strain can appropriately tune the mechanical resonant frequencies in order to reduce the amplitude of string-mode vibrations, thereby enhancing the overall coupling stability. Secondly, by positioning the beginning of the

3. Experimental Design

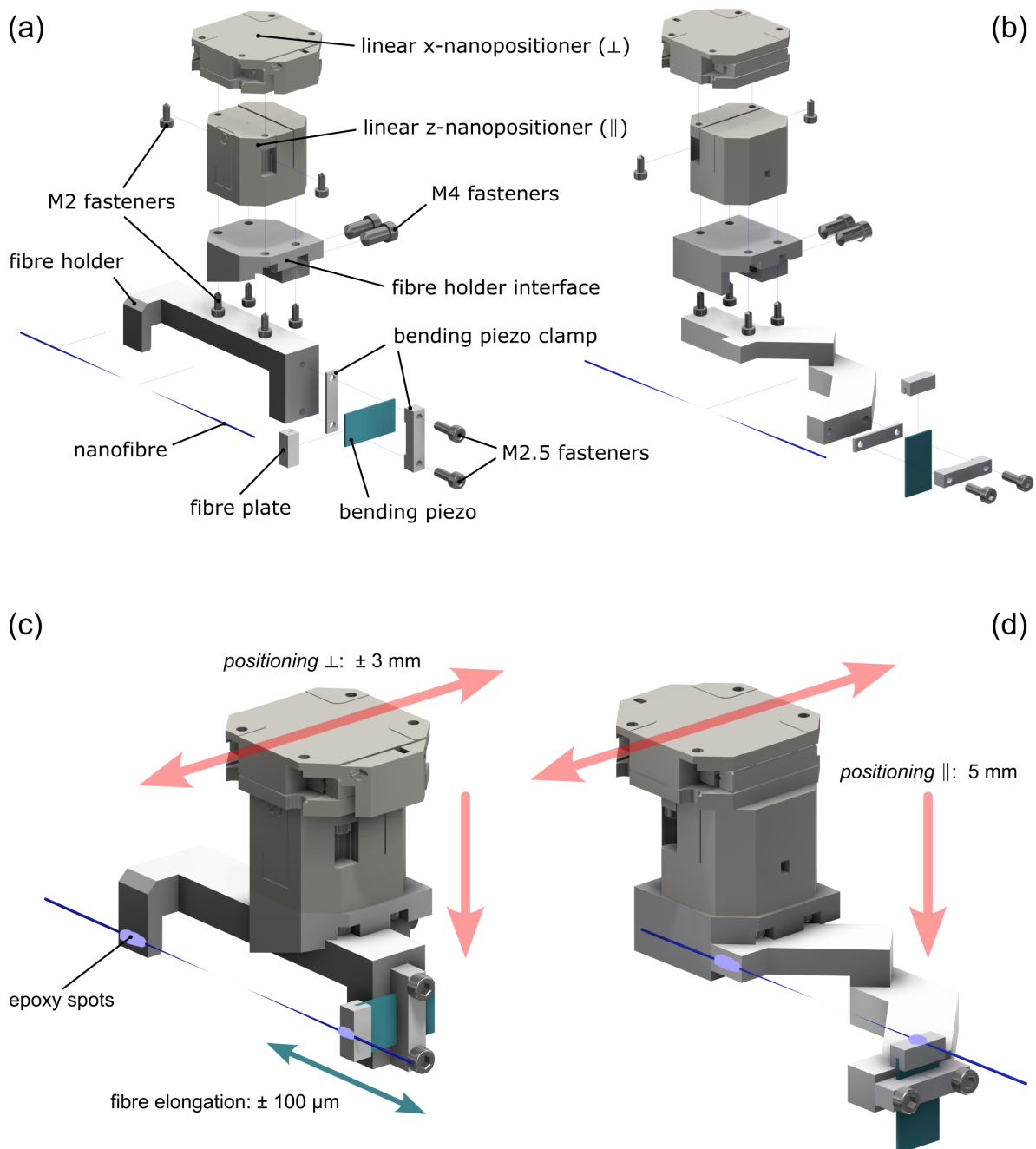


Figure 3.3. Assembly of the mounting and positioning designs for both coupling nanofibres. (a) Exploded-view rendering of the primary nanofibre mount. (b) Exploded-view rendering of the secondary nanofibre mount. Unlabelled parts are concurrent with that displayed in (a). (c) Assembled-view rendering of the positioning system for the primary nanofibre. Translucent arrows indicate the direction of motion of the positioning components. (d) Same as (c), but for the secondary nanofibre positioning system instead.

taper-transition at the resonator, an optimisation of the resonator coupling can be performed by pulling on the fibre which changes the effective diameter of the coupling fibre at the coupling point, thereby tuning the overlap of the two evanescent fields. The latter effectively allows a fine positioning of the nanofibre section to the bottle structure along the coupling fibre axis. To finely position the coupling fibre in the remaining two dimensions (i.e., parallel and perpendicular to the resonator axis), the fibre holder is mounted on a stack of two UHV-compatible, titanium, piezo-based nanopositioners. The first of these is a linear z-nanopositioner (*ANPz101/RES/UHV, attocube systems AG*) which allows for vertical motion over a total range of 5 mm, while the second is a linear x-nanopositioner (*ANPx311/HL/RES/UHV, attocube systems AG*) that has a range of 6 mm but in the horizontal direction instead. The copper insulated twisted pair of wires from each nanopositioner comes pre-assembled and are connected to their corresponding vacuum-feedthrough (see Section 3.3.5, Table 3.2) to interface with a dedicated controller (*AMC300, attocube systems AG*). The assembly of these and their respective directions of motion are shown in Figure 3.3(c) and (d). Due to the exponential decay of the evanescent fields, the nanofibre is effectively completely decoupled from the resonator for a separation larger than only a few microns, rendering the full travel ranges of both nanopositioners across several millimetres useful only for an initial coarse alignment. The long-range movement is only possible in one of the two operational modes of the nanopositioners – the *slip-stick* mode – in which the linear motion is performed in discrete steps up to a maximum velocity of 3 mm/s. This mode is particularly useful for ‘unsticking’ the coupling nanofibre from the resonator fibre in the unlikely event that they come into contact, where a large step size of a few micrometres can be set in order to pull them apart in one movement. The minimum step-size, however, is larger than 50 nm and therefore does not allow for an extremely fine positioning of the coupling fibre. Furthermore, the discrete nature of the motion under this mode of operation can excite mechanical vibrations of the nanofibre that can be up to several micrometres in amplitude, depending on the fibre tensioning. It is therefore necessary and favourable to use the second operational mode of the nanopositioners – the *scanning* mode – in which a continuous linear motion over a range of 5 μm with sub-nanometre resolution is possible by application of a voltage on the piezo elements of each positioner. Finally, the chosen nanopositioner models offer a closed-loop positioning control where a feedback loop integrated into the control electronics acts to minimise the difference between the specified target position and a measured position. The latter is acquired by a built-in resistive encoder based on a potentiometer, that features a sensor resolution of ~ 1 nm and a repeatability of ~ 50 nm.

Both the previously described modes of each nanopositioner piezo operation, together with the fibre-tensioning bending piezo, allow for full tunability of the spatial coupling point with respect to the bottle resonator structure using two nanofibres, see Section 3.3.5. Experience with the chosen nanopositioners additionally guarantees the stability

3. Experimental Design

of their set position – and therefore also spatial coupling point – which typically does not drift by more than 500 nm over the duration of one week. This is, of course, provided that external disturbances of the housing chamber are minimised; the topic of which will be discussed in the upcoming Section 3.3.4.

3.3.3 In-vacuum Lens Mount

One of the first major improvements to the design of the CQED experiment is to add a multipurpose lens inside of the vacuum chamber as part of a confocal microscope, the final design of which is displayed in Figure 3.4. Its primary purpose is to tightly focus an incident laser beam and create an optical dipole trap for single atoms, located in the vicinity of the resonator surface. It should also act as a high-efficiency collection optic for the fluorescence of trapped atoms. Since the resonator is fixed in space, the optical axis of the lens must be adjustable in order to align it with respect to the resonator. Once aligned, it should then remain stable over time. Therefore, the chosen lens is affixed to a 3D-positioner similar to those required for the coupling nanofibres (see Section 3.3.2). However, as indicated in Figure 3.4(a), the size of the lens itself is geometrically constrained – mainly by the preservation of optical access for cooling laser beams that must intersect within its focal region (see Section 3.4.3), but also by limitations on the available space due to the other mounting structures of the coupling set-up. As such, the lens diameter and Effective Focal Length (EFL) are chosen in order to maximise the Numerical Aperture (NA) while also accommodating these restrictions.

A single aspheric lens is the natural choice, as it minimises spherical aberrations or other optical defects [177]. It also means a more complex multi-lens system is not required [178], thus simplifying the overall design and reducing the bulk. The utilisation of a single lens for focusing does, however, put utmost importance on the quality of its manufacture in order to reach a spot size in its focus limited only by diffraction. Consequently, a lot of effort was spent in characterising the optical focii of a range of commercially available aspheres, the details of which are outlined in [179]. This investigation employed three separate measurement techniques to map out the focussed beam spatial intensity profile, with the aim of finding the optimal quality of focus for the lens sizes imposed by the geometrical constraints of the coupling set-up design. Contrasting the so-called *knife-edge* technique [180, 181] to that of a microscope imaging of the *point-spread function* (see Section 5.1.1) [182], in addition to a newly developed method based on scanning a nanofibre probe (both with and without a core Erbium dopant [183]) through the beam, meant that a well-informed choice of lens could be made. Indeed, for the imposed lens dimensions, it was found that a number of aspheres (e.g., precision-series CNC-polished both from *Thorlabs, Inc.* and *Edmund Optics, Ltd.*) introduced large wavefront errors in the measured beam which could potentially inhibit the optical trapping, and subsequent detection, of single atoms.

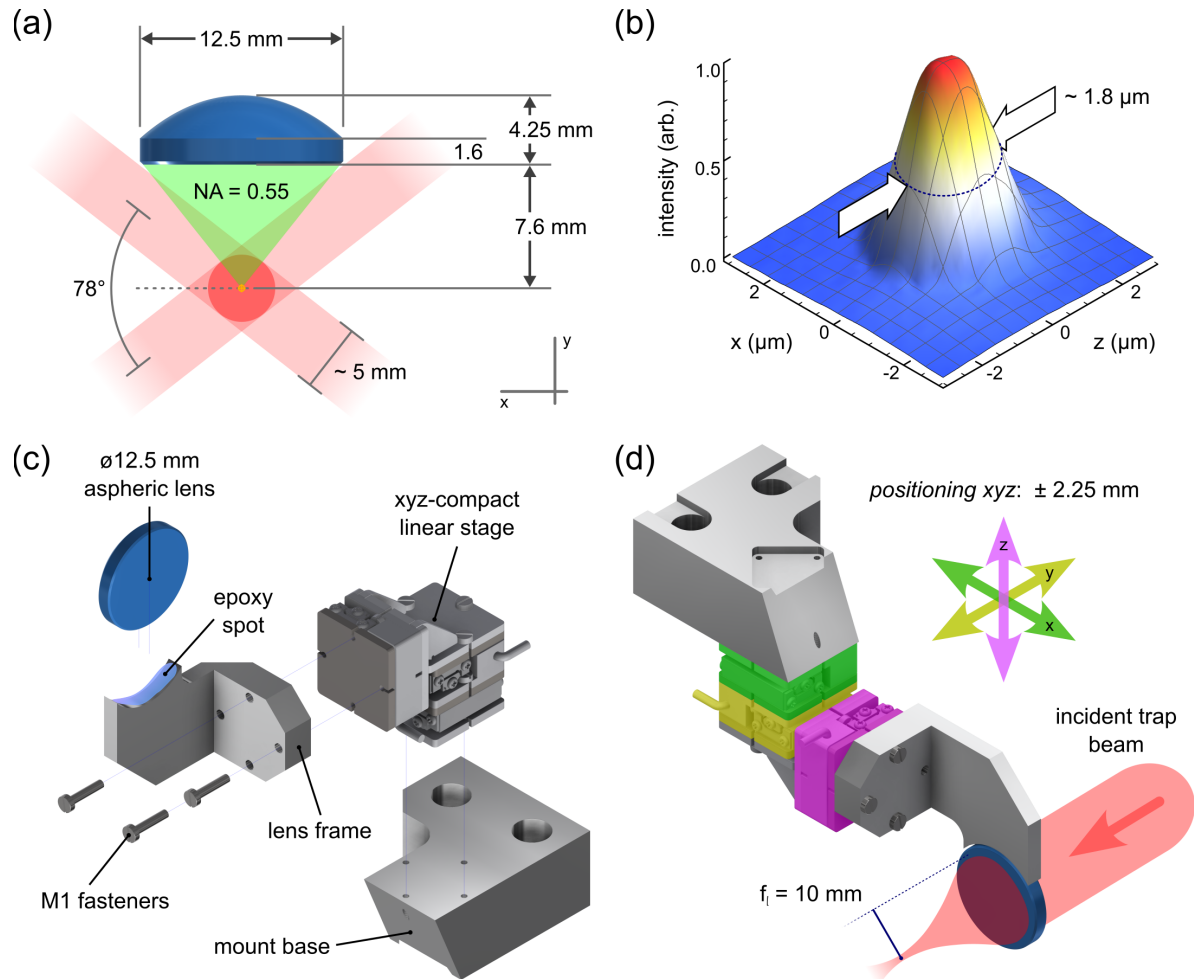


Figure 3.4. Assembly of the mounting and positioning designs for the in-vacuum high-NA lens. (a) Dimensioned schematic of the chosen lens ($\text{NA} = 0.55$) in the experiment's horizontal plane, with an illustration of the cooling beam geometry for the upper MOT (see Section 3.4.3). (b) Example measurement of the intensity distribution measured in the focal plane of the chosen aspheric lens. The arrows demonstrate a microscopic waist size of $w_0 = 1.8 \pm 0.2 \mu\text{m}$ (Section 5.1.1 provides more details). (c) Exploded-view rendering of the aspheric lens mounting. (d) Assembled-view rendering of the positioning system for the mounted lens. Colour coded arrows indicate the direction of motion of each linear positioner. An example incident beam is focussed beyond the planar face of the lens.

Figure 3.4(b) shows a sample characterisation of the focus spot achieved with the chosen aspheric lens (*AHL12-10-U-U-780*, *asphericon GmbH*), displaying a 3D surface interpolation plot of the measured intensity distribution in the focal plane. It illustrates a waist size of $\sim 1.8 \mu\text{m}$ (for more details on the focal spot size characterisation, see Section 5.1.1 in Chapter 5, where this lens is responsible for generating an optical dipole trap for single atoms). This diffraction-limited asphere has a diameter of $D = 12.5 \text{ mm}$, an EFL of $f = 10 \text{ mm}$ (with a reasonable working distance of $w_d = 7.6 \text{ mm}$), resulting in a high Numerical Aperture of $\text{NA} = 0.55$. Furthermore, its S-LAH64 substrate is anti-reflection coated for near-infrared to ensure minimal reflection losses at wavelengths around 780 nm ($R_{780} \sim 0.3 \%$ reflectance [184]) and together are UHV-compatible* and

3. Experimental Design

bakeable up to 150 °C*. Importantly, the CNC manufacturing procedure of the lens includes a high-end magnetorheological finishing step that serves as a final correction for ultra-precise surface finishing [185]. The manufacturer-quoted wavefront error of $\text{RMS} \leq 78$ nm and measured focus indicates that a diffraction-limited spot size can be achieved.

Figure 3.4(c) and (d) illustrate the custom mounting design for the chosen lens. The lens is glued (*EPO-TEK H77*, *Epoxy Technology, Inc.*) to a lightweight 6061 aluminium frame whose bore is concentric to the lens' diameter, thereby ensuring an ease of installation and stability of the affixation. The frame is secured with M1 fasteners to an assembly of three rotated ultra-compact linear positioners (*SL-0610*, *SmarAct GmbH*) that realises a miniature multi-axis translation stage. Each piezo-based positioner offers a travel range of ± 2.25 mm around their neutral position as indicated in Figure 3.4(d) and an open-loop resolution of less than one nanometre with use of the accompanying pre-configured control system (*MCS2*, *SmarAct GmbH*). They, similarly to the nanopositioners for each nanofibre, offer a *slip-stick* and *scanning* mode of operation as outlined in Section 3.3.2. The pre-assembled kapton-insulated stranded wires for the voltage supply features an all-metal LEMO connector which is fed to the corresponding vacuum-feedthrough (see Section 3.3.5, Table 3.2). A final advantage of placing the in-vacuum lens on such a 3D-positioner system is that the resonator surface can be mapped out by performing a 2D-scan of the lens position, and therefore also the focus position (which is always approximately located on the lens' optical axis for small displacements), with respect to an incident beam. By covering a plane of area $\approx 50 \mu\text{m} \times 50 \mu\text{m}$ centred around the bottle structure, the high-NA of the lens could enable collection of a portion of the light reflected by the resonator (or coupled into a nanofibre via the resonator [70]), which would be maximal under normal-incidence (tangential-incidence). Such a scheme enables fine-positioning, to within a fraction of a micrometre, of the focus position on the resonator surface. This flexible and future-proof design opens up a myriad of possibilities for experiments and protocols utilising single atoms that are stably coupled to a WGM of the bottle microresonator (see Section 6.2).

3.3.4 Vibration Isolation

The designs of the mechanical mounting and positioning systems for the bottle resonator and pair of coupling nanofibres, along with the in-vacuum lens, are outlined in the preceding Sections respectively (see Sections 3.3.1, 3.3.2 and 3.3.3), where the necessity of the set-up to facilitate flexible – but extremely stable – coupling was highlighted. To enable the latter, these mounts, in turn, must be themselves affixed to a sturdy structure within the UHV chamber. Such a stage, however, has to also be carefully designed in order to prevent the transmission of mechanical and acoustical vibrations

*Confirmed in a private communication with *asphericon GmbH* technical assistance.

from external noise sources through the vacuum chamber set-up (see Section 3.5) to the resonator coupling set-up, which must be stable to within ten nanometres (particularly at critical coupling). A useful consequence of placing the whole coupling set-up under **UHV** (primarily for the preparation of cold atoms and preservation of the resonator quality) is that acoustic vibrations transmitted through the air are insignificant and can therefore be neglected. However, due to the absence of air that would normally provide damping of excited fibre-vibrations, the latter will instead exhibit an increase of the quality factor of these mechanical vibration modes. The design and choice of a **Vibration Isolation System (VIS)** that highly suppresses transmission of mechanical noise from the vacuum chamber to the coupling set-up across a broad frequency range (single-digit to thousands of hertz) is therefore critical. In the following, details of a composite **VIS** that is used for this purpose are outlined.

Low-frequency noise A common practice in optics labs is to make use of commercial optical tables that are specifically manufactured to feature passive damping of low-frequency noise – typically less than 100 Hz – that arises from sources such as the vocals and movements of lab personnel (including the slamming of lab entrances...), nearby equipment, to floor and building resonances. Part of the chosen **VIS** is thus to build the entire experiment on such a device. The selected optical bench system (*RS4000 Optical Table Top and S-2000A Stabilisers, Newport Corporation*) upon which the vacuum set-up housing the main experiment sits, features a trussed-honeycomb core tabletop with six tuned dampers for optimum dynamic rigidity, sat over four self-leveling pneumatic supports for mechanical decoupling from the building (in this low frequency regime). The Mot chamber and its **UHV** system is mounted directly upon the optical table, while a raised breadboard is held aloft by a total of eighteen steel posts (*Ø1.5" pillars, Thorlabs, Inc.*) and hosts the vertically displaced Science chamber along with its own **UHV** system (see Section 3.5 for further details), thereby also connecting it to the optical table. The custom-made breadboard features a support frame with tuned dampers on its underside to aid in its stability [92]. A **CAD** model of the entire constructed experiment calculates the centre-of-mass point to be central to the tabletop at less than 15 cm from the surface, thus ensuring a decent overall stability.

High-frequency noise While sources of high-frequency mechanical noise – usually above 100 Hz – are typically not of a large amplitude, it is still paramount to implement a passive damping to interrupt the efficient transfer (i.e., via the metal-to-metal interfaces) of these vibrations to the coupling set-up. Driven by the sensitivity and stability requirements of scanning probe surface analysis techniques [186], a variety of platforms for this purpose have been developed; including magnetic eddy current damping [187], tuned mass dampers [188], shunted

3. Experimental Design

piezoelectric materials [189], shape memory alloys [190] and hysteretic damping [191]. The latter method, under correct choice of material, is particularly suited for applications requiring **UHV** due to its relatively simple implementation and effectivity. Essentially, in such an approach, a relatively incompressible viscoelastic material (i.e., it possesses both viscous and elastic behaviour) is employed as a damping medium, which acts to convert mechanical energy into heat under an applied strain. It does so as the long molecular chains of the polymer that these classes of elastomers consist of are in a semi-rigid and semi-flow state, allowing for both a macroscopic stress deformation and also for internal frictional effects, resulting in the occurrence of high energy losses. Therefore, the second part of the **VIS** design is to attach the coupling set-up to a massive rigid body that sandwiches an appropriate elastomeric dampener against the inside of the **UHV** chamber walls in order to isolate the former from the potential source of high-frequency mechanical vibrations of the latter. Choice of the properties of the aforementioned components is crucial for a number of reasons, as shall be delineated in the following; note that the referred-to system architecture is showcased in Figure 3.5:

Rigid Body: The $m = 6.2$ kg so-called *copper block* is produced from an **Oxygen-Free High thermal Conductivity (OFHC)** copper, as it has a relatively high density but can be easily machined, with an acceptable outgassing rate [192]. To improve the **UHV** suitability and to protect the surface from oxidisation (under the conditions of vacuum baking for example, see Section 3.5.3), it is further coated with a nickel-free gold-plating [193]. This mass is designed to be broadly of a cylindrical geometry with its principal axis aligned along the vertical direction. Its height is chosen to yield the target weight for a suitable dampener (see below), while its radius is smaller (but comparable) to the clear aperture of the chamber in which it is mounted for the purpose of controlled extraction from the chamber. A pair of M6 threads in the upper surface enables attachment of a lifting structure to aid in this procedure, see Section 3.3.5 and Appendix C for a detailed explanation and accompanying instructions. The flat perimeter on the underside of the mass then constitutes a platform upon which it, along with the attached coupling set-up, can rest within the chamber atop the dampener. The underside also features a complex extrusion profile for the mounting of the various positioners and holders of the coupling set-up. Furthermore, a central hole penetrates through the entire copper block which allows optical access along the central vertical axis that links both chambers via the **DPT**. This access is paramount for one of the beam pairs of the upper **MOT** that are aligned along this direction, see Section 3.4.3. Finally, as copper is an excellent conductor, a radial slice-through section breaks the rotational symmetry

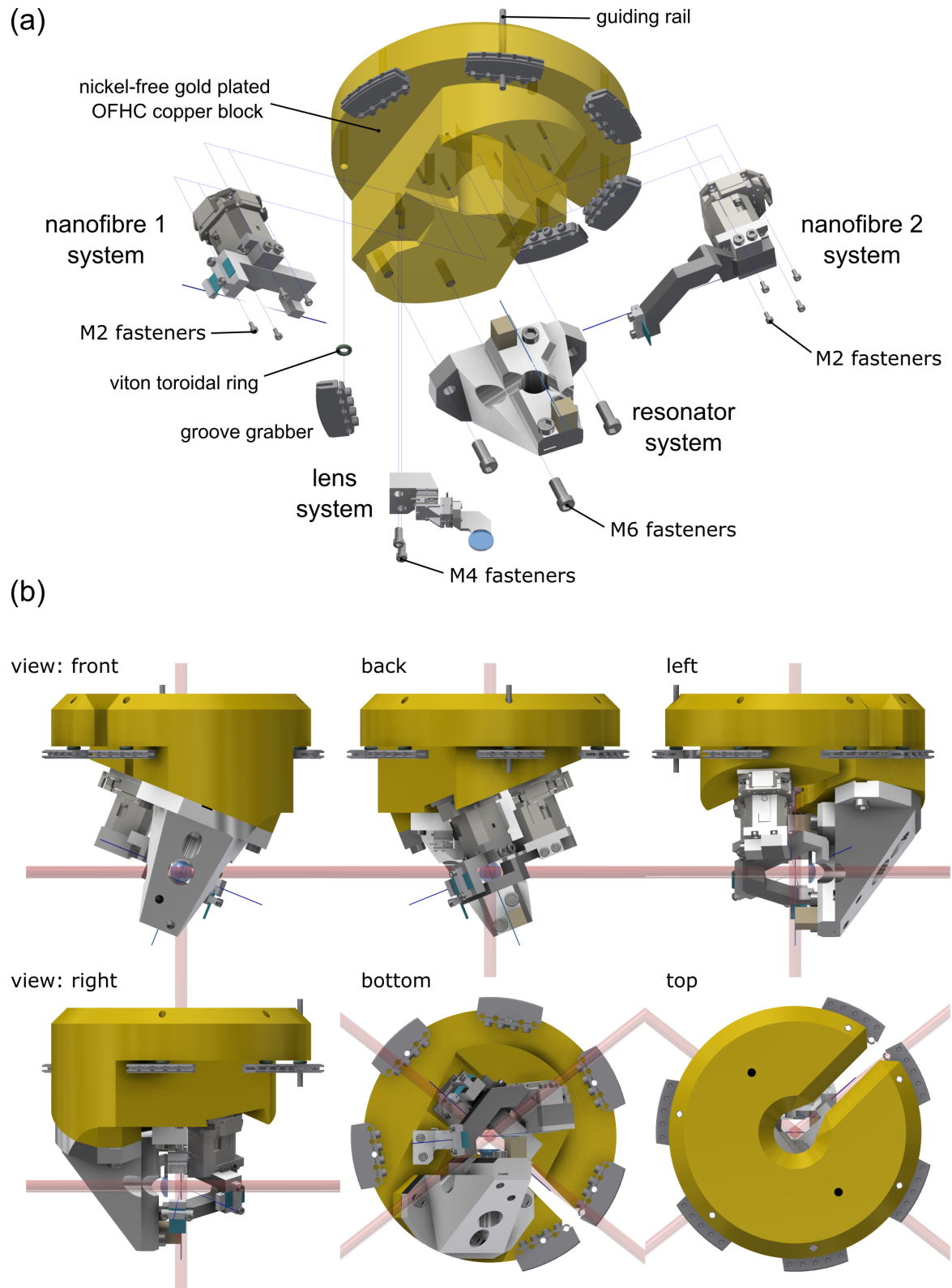


Figure 3.5. Design of the Vibration Isolation System. (a) Exploded-view render illustrating how the various sub-systems comprising the coupling set-up are mounted to the gold-plated copper block, which is displayed in a semi-transparent gold colour to better illustrate its geometry. (b) Various rendered views of the completed assembly, highlighting the optical access along these principal directions (cooling beams for the upper MOT as an example – see Section 3.4.3 – are displayed as semi-transparent red cylinders).

3. Experimental Design

about the principal axis, thereby preventing the formation of magnetic fields from eddy currents in response to a changing applied magnetic flux [146] (e.g., arising from the switching of the field coils necessary for the upper MOT, see Section 3.4.3). This gap additionally allows for all cabling and fibre ends originating from the coupling set-up to freely pass upwards to meet their respective feedthroughs, see Section 3.3.5.

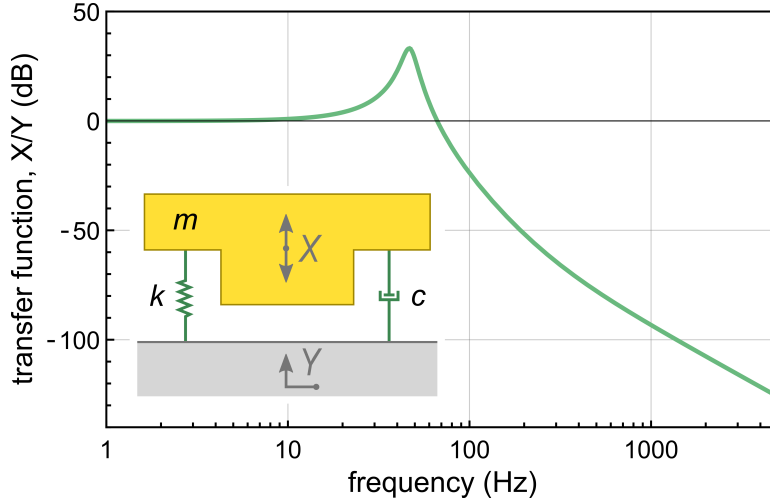


Figure 3.6. Transfer function of a model mass-spring system. According to equation (3.2), the frequency response of a mass m on a spring with spring constant k and damping constant c in 1D (inset) exhibits a mechanical resonance at around 45 Hz, with a reduction in external perturbations by over five orders of magnitude above 1 kHz. The plot is generated with the final chosen parameters of $m = 6.2$ kg, $k = 5 \times 10^5$ N/m, and $c = 340$ Ns/m [194].

Dampener: The copper block, as just described, must rest upon a suitable dampener within the UHV chamber that acts as an interface between the coupling set-up and the UHV system for satisfactory vibration isolation. Commercially available viton toroidal *O-rings* are a viable option due to their mechanical properties and UHV compatibility. While the specific choice of this viscoelastic material is governed mainly by its outgassing rate, the dimensions, which partially determine its stiffness and damping coefficients, must be carefully considered. The analysis in the following was performed for rings with a thickness of 2.4 mm and inner diameter of 13.3 mm (*OR2401330-V70G1, Sahlberg GmbH*). Such a ring of viton can be modelled as a spring with a length-dependent spring constant, k , and a damping constant, c , that depends on an applied load of mass m . By assuming one degree of freedom for this simple mass-spring system as depicted in the inset of Figure 3.6, its oscillatory response $Xe^{i\omega t}$ following an external perturbation $Ye^{i\omega t}$ is

governed by Newton's second law [195]

$$(k + i\omega c)Y = X(k + i\omega c - \omega^2 m), \quad (3.1)$$

which upon rearrangement yields the frequency response of the system by the transfer function

$$dB = 20 \log \left[\sqrt{\text{Re}(X)^2 + \text{Im}(X)^2} / Y \right]. \quad (3.2)$$

This equation can then be used to calculate the isolation provided for a given mass, when suitably choosing the elastomer properties determined from a length of viton, i.e., number of rings. By measuring the displacements of a load applied to a single ring, a verification of Hooke's law yields a value of $k = 82 \times 10^3$ N/m for the spring constant, which is in agreement with literature [194]. Similarly, a damping constant of around $c \approx 50$ Ns/m per ring is assumed [194]. A total of six of these viton rings ($l = 0.3$ m) supporting a mass of $m = 6.2$ kg yields the transfer function displayed in Figure 3.6. It features a mechanical resonance at around 45 Hz, with a significant roll-off greater than 50 dB/decade beyond 100 Hz. At ~ 4 kHz, the system suppresses mechanical noise transferral by 120 dB, i.e., reduces the amplitude of external perturbations by a factor of 10^{-6} . This is mostly effective in the vertical direction of motion as set by the problem geometry, but is also partially effective in the lateral direction [92]. Vibrations originating from within the coupling set-up should also be suitably attenuated due to their attachment to the massive copper block.

As displayed in Figure 3.5, a single viton ring sits upon a *groove grabber* which is mechanically clamped to the inside chamber wall to form a ledge. The copper block, from which hangs the entire coupling set-up, rests upon a total of six of these to yield the desired damping effect illustrated in Figure 3.6. A further explanation of its assembly and situation with the Science chamber is provided in the next Section.

3.3.5 Chamber Assembly

To conclude this Chapter Section concerning the *Science chamber* (of which this term also encompasses all of its housed internal set-up), a focus on the improvements afforded by the updated construction are presented, in accordance with that outlined in the design goals 3.2.2.

Figure 3.7 exhibits the referred-to architecture. The chamber itself is actually a revised version of a commercially available multi-CF hardware that was successfully

3. Experimental Design

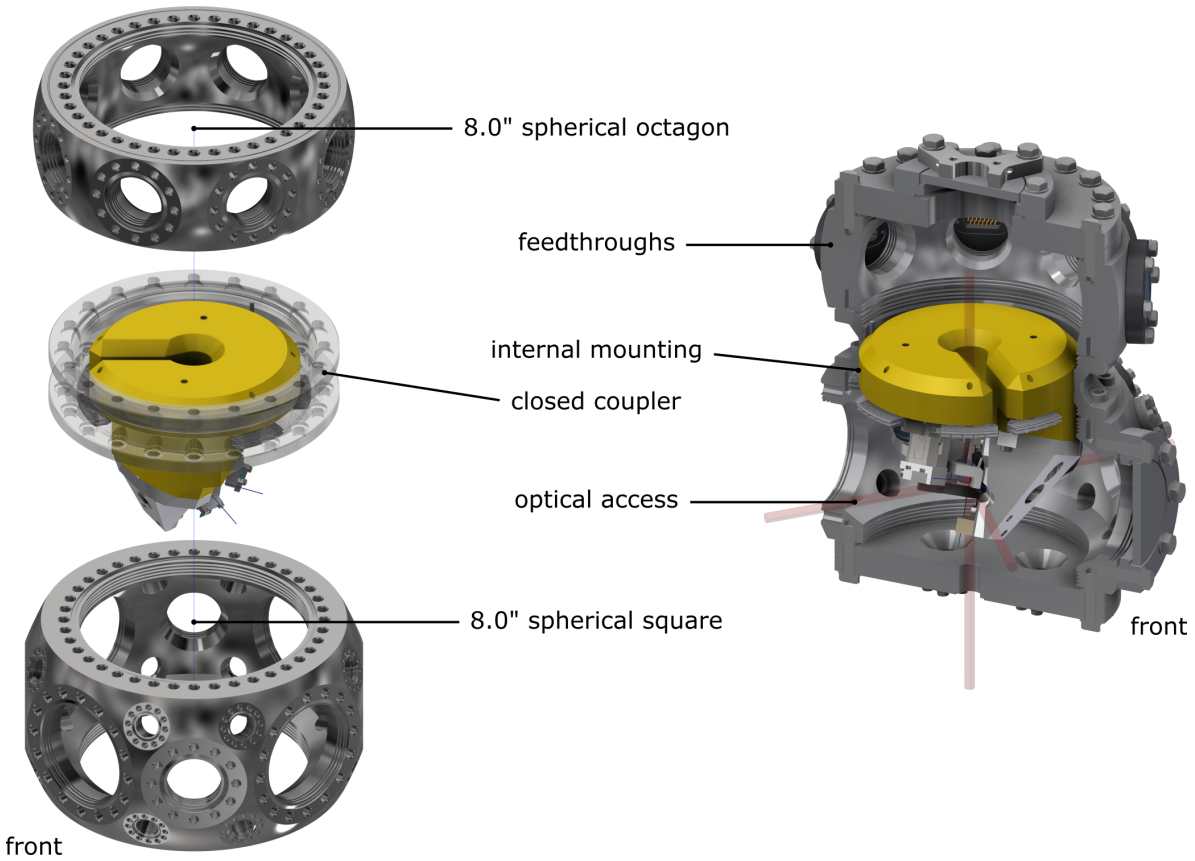


Figure 3.7. Composite Science chamber assembly. An exploded-view rendering of the Science chamber design is shown on the left, while a slice-through assembled view rendering is shown on the right. In both cases, the VIS and its attachment to the closed coupler piece are visible. The right-most half-sphere of the assembled chamber contains a subset of the flanged viewports and feedthrough components.

utilised in CQED 1.0 [92], albeit now rotated by 90° around the horizontal axis and extended with additional UHV hardware. For compatibility purposes, the opportunity to make the 'jump' from imperial to metric threading was also eagerly undertaken at this stage of the design process. The chosen vacuum chamber (*MCF800-SphSq-G2E4C4A16*, Kimball Physics) is CNC milled from a monolith of 316LN non-magnetic stainless steel and features an extended spherical-square geometry to maximise the interior functional volume (~ 3.8 L) while minimising the external footprint. All surfaces have a mirror finish. Several of its design features and extended construction are detailed in the following (for the evacuation design, see Section 3.5);

Optical access: The main chamber boasts, in total, twenty-six (thirteen pairs of) CF flange ports of various sizes as shown in Table 3.1. The arrangement is such that the cylindrical axis of each flange pair share a common intersection point which is located at the chamber centre, with opposite flanges being equidistant from this point. Thus, positioning the resonator at this location ensures that by looking antiparallel along any flanged viewport normal, a direct line of sight onto the resonator is available.

As such, the plan of the coupling set-up (see Sections 3.3.1 - 3.3.4) factored in these sight-lines to minimise their obstruction so that they can be used for various imaging optics and free-space laser beams. As previously stated, a similar chamber model was employed in CQED 1.0 and so an evaluation of the improvement to both the direct and throughput views onto the centrally-located resonator can be undertaken. In summary, the availability of flanges for viewports was increased from 38% to 70%, with throughput views quadrupled from two to eight. These results are tabulated in Table 3.1. Each hermetically-sealed viewport (*VPZL-[size (in inches)]LDIO*, Kurt J. Lesker Company) window is produced from quartz (*HPFS 7980 Fused Silica*, Corning Incorporated) and has an anti-reflective coating on both sides that is optimised for transmission of wavelengths around 780 nm ($R_{780} < 0.25$ % reflectance per surface [196]). This holds for all bar a pair of opposing DN16CF flanges, which are fitted with Zinc-Selenide viewports (*VPZL-133UZC*, Kurt J. Lesker Company) that are optimised for transmission of wavelengths in a range of 8 – 12 microns, and have a broadband anti-reflective coating on both surfaces to cover this range ($R_{1064} < 1$ % reflectance per surface [197]). This chosen throughput view can be used to freely pass a CO₂ laser beam at a wavelength of around 10.6 μm in order to heat the resonator and evaporate unwanted adsorbed contaminants, thereby cleaning its surface to prevent the degradation of its quality factor. To provide further views onto the resonator from below, the lower port of the main chamber is sealed with a custom-made 8.0" to 1.33" (DN160CF to DN16CF) zero-length reducer flange which has four additional off-centre conical bores in a quincunx formation (Kurt J. Lesker Company). While the centre bore attaches the Differential Pumping Tube (DPT) to interface the Mot chamber (see Sections 3.4.4 and 3.4.2), the remainder are sealed with viewports. Two of the 8× DN16CF ports on the main chamber that cannot offer views onto the resonator (see Table 3.1) are fitted with dual copper-conductor alumina-insulated electrical feedthroughs (*EFT0123052*, Kurt J. Lesker Company), while the rest are sealed with blank flanges (*F0133N000NLN*, Kurt J. Lesker Company). These electrical feedthroughs are rated up to 27 A each, and are therefore more than capable of housing two Rb dispensers in parallel (*RB/NF/7/25FT10+10*, SAES Getters S.p.A.) that are fixed across them on the inside with the use of beryllium copper inline barrel connectors (*FTAIBC094*, Kurt J. Lesker Company). These dispensers in the main chamber are only for alignment steps of the upper MOT (see Section 3.4.3), and thus have their emission cone directed towards the chamber wall [166].

The improved optical access is also due, in part, to both the revised internal mounting of the VIS (which lifts the copper piece upwards out of view-obstruction) and the gathering of all feedthroughs into an independent chamber piece (which frees up the main chamber flanges solely for viewport usage). These two design choices were also made for the original goal of easier exchange of in-vacuum components, as will be detailed respectively in the following.

3. Experimental Design

available chamber ports	viewports flanged in:	
	CQED 1.0	CQED 2.0
2× DN160CF (8.00")		[]]
4× DN63CF (4.50")	[]]	[]] []]
4× DN35CF (2.75")		[]] []]
16× DN16CF (1.33")	[]]	[]] []] []]

Table 3.1. Viewport usage: A breakdown list of the available port sizes offered by the extended spherical-square main chamber, and a comparison of the available views onto the resonator between the old and new design of the experiment. Each tally mark represents a count of an unobstructed sight-line to the centrally-located resonator, with bracketed pairs indicating a throughput view offered by a pair of opposing ports.

Internal mounting: The chamber features internal circumferential channels that are machined concentrically with all flanges larger than DN16CF, referred to as *grabber grooves*. Their purpose is to interface with aptly-named *groove grabbers* – a mounting accessory consisting of a split-axial clamping mechanism that generates a small platform transverse to the port axis by mechanical gripping. Fixing screws are gold-plated for lubrication. Five of these (*MCF800-GroGrb-C01*, *Kimball Physics*) are utilised on the centre grabber grooves of an 8.0" (DN160CF) close coupler (*MCF800-ClsCplr-G1r1*, *Kimball Physics*), which is itself attached to the top of the main chamber, see Figure 3.7. As outlined in Section 3.3.4, a single viton ring rests centrally on each of the six groove grabbers, upon which the 6.2 kg gold-plated copper block is situated. The height is such that the coupling set-up supported by the copper block ‘hangs’ into the main chamber, with the resonator located at its centre. Three of the groove grabbers in a triangular formation hold guiding rails of a 3.2 mm diameter that penetrate 4 mm bores in the block, thereby aiding in the rotational alignment of the entire coupling set-up around the vertical centre line. This is required in particular for the correct orientation of the tilted resonator axis with respect to the axes of optical access. Finally, care was taken in the design of all components to avoid the formation of virtual leaks, especially at meeting faces and threaded bores. The exclusive use of vented screws under UHV aids in this endeavour.

Feedthroughs: A rotationally symmetric spherical-octagon chamber (*MCF800-SphOct-G2C8*, *Kimball Physics*) is connected to the top port of the close coupler, and has eight radial DN35CF flange ports which are utilised as feedthroughs for the various electrical and optical connections required for the coupling set-up. Electrical cabling originating from the seven positioners (two per coupling fibre, plus three for the lens) and the four piezos (two resonator fibre shear piezos, plus one bending piezo per coupling

fibre), along with the four coupling fibre ends, are directed upwards and tidily gathered above the copper mass before connecting to their respective feedthrough. The fibre ends are, instead, all fed through a single custom-made feedthrough that has four 1/8" *Swagelok* connectors each sealed by a locking nut. By clamping on a teflon ferrule through which the fibre concentrically passes, a UHV-tight seal is created [176]. Details of the chosen feedthroughs are summarised in Table 3.2. Particular care is taken to avoid the crossing of cabling into free-space optical paths, and to ensure that the fibre ends do not have too small bending radii which could result in transmission losses. Finally, the feedthrough chamber is enclosed at the very top with an 8.0" to 2.75" (DN160CF to DN35CF) zero-length reducer flange (*RF800X275M*, *Kurt J. Lesker Company*), which is topped off with a viewport that hosts a custom-made adapter plate for the mounting of additional optics (see Section 3.4.3).

connector type	used by	part number
10-pin LEMO	lens positioner	<i>ALB-VF-10-CF40</i>
15-pin Sub-D	nanofibre positioners	<i>IFDGG151053</i>
2× 9-pin Sub-C	nanofibre bending piezos	<i>IFDGG091053</i>
9-pin Sub-D	resonator fibre shear piezos	<i>IFDJG181053</i>
4× 1/8" Swagelok	fibre ends	<i>custom design: FLG-SPL809</i>

Table 3.2. Feedthrough usage. Documentation of the various feedthroughs utilised in the upper spherical-octagon feedthrough chamber. A description of the feedthrough type is followed by its application, before the part number is given. All the listed components are of a DN35CF flange size and manufactured by *Kurt J. Lesker Company*, apart from the feedthrough for the lens positioner which hails from *SmarAct GmbH*.

(Cumulating in the) In-vacuum component exchange: The main purpose of gathering all of the various feedthroughs into a dedicated chamber is to address one major design goal of the updated experiment: an 'easy' exchange of the in-vacuum components, particularly the resonator. The design of the internal VIS has also influenced the chamber choice and its subsequent orientation (and vice versa), with the large DN160CF port axis aligned along the vertical to gain accessibility to the copper block and the entire attached coupling set-up. As such, the procedure for part-exchange in CQED 2.0 has been greatly simplified with respect to CQED 1.0, in that only the top-most flange has to be removed. Prior to opening, it is paramount that the entire vacuum system be vented with an inert gas rather than ambient air to avoid the deposition of unwanted contaminants that are carried in the air. At best, flooding with air can lead to extended evacuation and reduction in the achievable base pressure, and at worst, can lead to the destruction of UHV-components (e.g., transmission-destroying dust on a nanofibre). Pure argon gas is therefore most appropriate in this case as it is denser than

3. Experimental Design

air, and consequently remains in the chamber when opened from the top (as opposed to the more commonly used pure nitrogen). Once the top flange is opened, dedicated M6 threads milled into the top face of the copper block then allow for the attachment of a specially made lift apparatus that enables, in a controllable fashion, its raising out of the chamber to expose the coupling set-up on its underside. The relatively quick exchange of any components – including the resonator and/or coupling nanofibre(s) – can subsequently take place, before a reversal of the procedure brings the modified coupling set-up safely back into **UHV**. On account of the fact that this entire course of action – while designed to be as straightforward as possible and completed in only a few hours (including preparation but excluding pump-down to **UHV**) – is still an arduous task, a full comprehensive documentation and instructions for its successful completion is included in Appendix **C**.

3.4 Double Magneto-Optical Trap

Explorations into the strong coupling of *single* atoms to the **WGM** bottle microresonator is the ultimate *raison d'être* for the **CQED** (2.0) experiment. In the preceding section, a thorough explication of the experimental design for the bottle microresonator coupling set-up was laid out. This Section will accordingly then focus on the other aspect, and describe the approach taken to prepare and deliver cold atoms towards the vicinity of the resonator – a pre-requisite for their eventual strong-coupling. As outlined in the design goals Section 3.2, this broadly consists of a double-**MOT** stage where several 10^7 ^{85}Rb atoms are captured and cooled with a combination of near-resonant laser light and magnetic fields in one **MOT**, before being transferred to a second via an **Atomic Fountain**. The **Magneto-Optical Trap** is a Nobel-Prize winning technique [198] involving the capture of room temperature atoms from a dilute vapour and their subsequent cooling and ensemble confinement to sub-millikelvin temperatures, while the **Atomic Fountain** extends this technique to ballistically launch the ensemble. The latter is a technique commonly utilised in modern atomic clocks [199], as it allows for a deterministic transfer of cold atoms from their initial preparation region in a **MOT**, to an interrogation zone separated from external hindrances to the exact measurement of a frequency standard. Prior to this, since its first experimental demonstration [200], **Magneto-Optical Trapping** is now commonplace in the majority of cold and ultracold atom laboratories, and has thus evolved to cater for a variety of technical needs over the following years. Examples of interesting configurations and exotic geometries include $2D^+$ **MOTs** as a source of slow atoms [201], *mirror* **MOTs** bringing the advent of *atom chips* [202, 203], miniaturisation in the form of *pyramidal* [204] and *tetrahedral* [205] **MOTs**, along with *grating* **MOT** varieties made accessible by recent advances in nanofabrication technologies [206–208].

Today, even commercial MOT-based cold atom sources are available for off-the-shelf purchase. Due to this wide-ranging implementation, its working principle shall only be briefly described in the following, before a more relevant and comprehensive presentation of the double-MOT and transfer technical implementation is given.

Practically, the standard MOT is easily implemented with a pair of current-carrying coils of wire in an anti-Helmholtz (AHH) configuration, along with three pairs of circularly-polarised counter-propagating beams that are mutually orthogonal and tuned to cool on the $(5^2S_{1/2}, F = 3) \rightarrow (5^2P_{3/2}, F' = 4)$ transition of the ^{85}Rb atom. These beams are all sent towards the point of zero magnetic field that is located in the centre of the quadrupole field generated by the AHH coils. A technical necessity is the addition of a so-called *repump* field that is tuned on the $(5^2S_{1/2}, F = 2) \rightarrow (5^2P_{3/2}, F' = 3)$ transition, the purpose of which is to excite atoms in the dark $F = 2$ ground state in order to bring them back into the cooling cycle. The laser systems that satisfy these requirements will be detailed in Section 3.7, while the mechanical design and characteristics of each of the separate MOTs will be outlined in the following.

3.4.1 MOT Working Principle

The operation of a MOT can be understood, in brief, by considering the concepts which chronologically arose over the course of its historical development [97, 209]. That is, Doppler cooling, sub-Doppler cooling, mechanisms such as Polarisation Gradient Cooling, and finally the combination of these laser cooling methods with an inhomogeneous magnetic field. Figures 3.8 and 3.9 exemplify a graphic selection of some concepts related to the discussion presented in the following.

In general, the process of laser cooling is based upon the principle of momentum exchange between single atoms and single photons, across numerous absorption and emission cycles, as depicted in Figure 3.8(a). When an atom absorbs a photon, it receives a momentum kick equal to the photon's momentum in the direction of the photon's propagation. Conversely, upon re-emission, the atom's momentum kick is in a random direction but equal and opposite to that of the emitted photon. An atom that moves against a beam of photons in one dimension, i.e., in a counter-propagating laser, will therefore have its velocity reduced since the momentum kicks from absorption will accumulate, but those from the spontaneous emission cycles average out to zero. This *scattering force*, also referred to as *radiation pressure*, is an effective method for reducing the atom's velocity spread in momentum space, as it occurs, for large beam intensities, close to the scattering rate:

$$\mathbf{F}_{sc} = \hbar\mathbf{k} \cdot \frac{\Gamma}{2} \cdot \frac{I/I_{sat}}{1 + I/I_{sat} + (2\Delta_v/\Gamma)^2}. \quad (3.3)$$

Here, each photon is part of a single laser beam with intensity I , has a momentum of

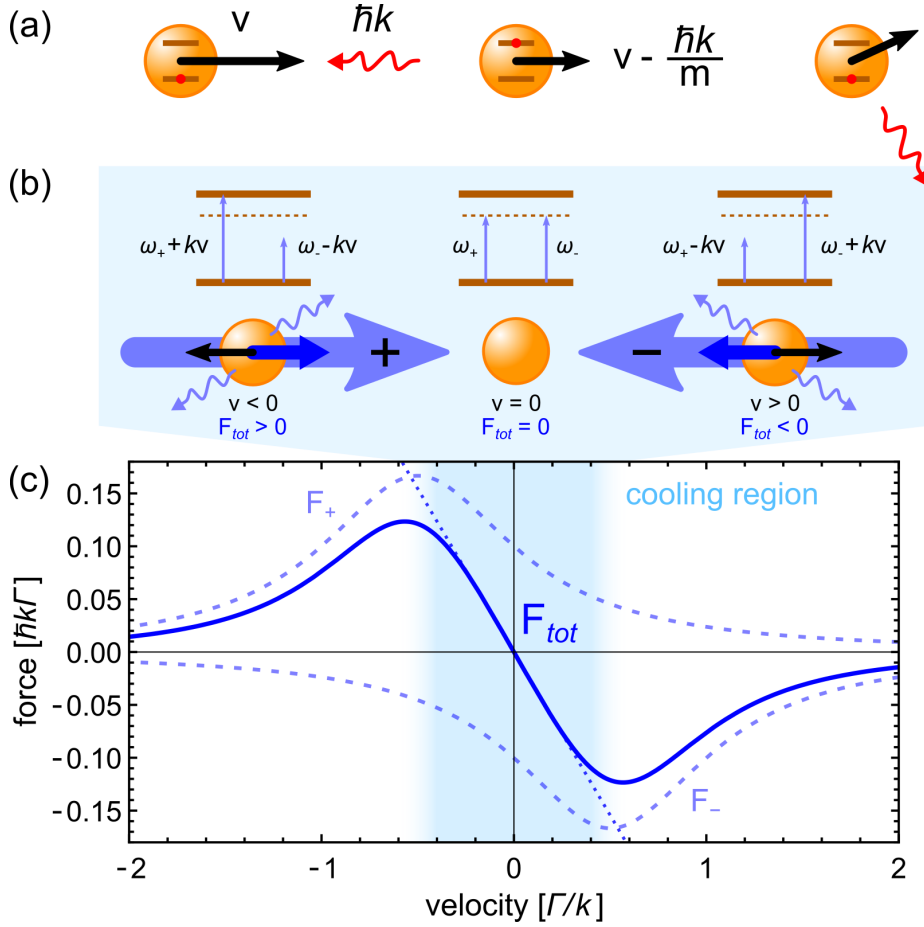


Figure 3.8. Working principles of laser cooling and the Magneto-Optical Trap. (a) Concept of radiation pressure in one dimension. An atom moving towards the right with velocity v can absorb a counter-propagating photon with momentum $\hbar k$. The direction of spontaneous emission of a photon is random, and so the averaging of many such absorption and emission processes results in a net reduction of the atomic velocity in 1D. (b) One dimensional Doppler cooling. An atom at rest (centre) experiences no net force from two counter-propagating beams that are mutually red-detuned from the atomic resonance, due to an equal absorption of each. A velocity-dependent imbalance in the atomic absorption of the two beams arises due to the Doppler effect, where a preferential scattering of the beam that is Doppler-shifted closer to resonance occurs. The net light force on the atom is therefore positive for an atom moving towards the left (left of centre) and negative for an atom moving towards the right (right of centre). (c) A plot of the total light force on the atom according to equation (3.4) (blue solid line) as a sum of the force contributions from each of the two red-detuned counter-propagating beams (blue dashed lines) as illustrated in (b), for $I/I_{sat} = 0.5$ and $\Delta = -\Gamma/2$. The total force within the central cooling region (shaded light blue) features a negative linear gradient whereby the atom experiences a velocity dependent restoring force.

magnitude $\hbar k$, is detuned from atomic resonance (with a **FWHM** linewidth Γ) by Δ such that $\Delta_v = \Delta - \mathbf{k} \cdot \mathbf{v}$ includes the Doppler shift of light in the frame of an atom with velocity \mathbf{v} . k is the wavenumber of the light and I_{sat} is the saturation intensity of the atom, i.e., the intensity at which, for resonant light, it spends a quarter of the time in its excited state.

As the velocity-dependent detuning of the laser, Δ_v , enters in equation (3.3), the most conceptually simple method of cooling with use of this velocity-dependent scattering force is *Doppler cooling*. In a 1D arrangement such as that depicted in Figure 3.8(b), illumination of the atom using two counter-propagating laser beams that are detuned slightly below resonance ($\Delta < 0$), the atom will preferentially scatter light that is shifted closer to resonance due to the Doppler effect, i.e., from a beam that it moves into. The total force on the atom is then the sum of the scattering forces from each beam as

$$\mathbf{F}_{tot} = \mathbf{F}_+ + \mathbf{F}_-, \quad (3.4)$$

with

$$\mathbf{F}_{\pm} = \pm \hbar \mathbf{k} \frac{\Gamma}{2} \frac{I/I_{sat}}{1 + I/I_{sat} + (2(\Delta \mp \mathbf{k} \cdot \mathbf{v})/\Gamma)^2} \quad (3.5)$$

using equation (3.3). This restoring force is plotted in Figure 3.8(c) for the red-detuned case considered here. Around zero velocity, the total force on the atom has a negative linear gradient over a restricted velocity range, leading to a damping effect in this region. This mechanism does not, however, allow cooling to zero temperature. A fundamental limit exists, called the *Doppler temperature*, that is due to the stochastic nature of the photon absorption and emission cycles which lead to a fluctuation of the atomic momentum around its steady-state value $\langle \mathbf{p} \rangle = 0$ [210, 211]. For the D_2 transition of ^{85}Rb , with a natural linewidth of $\Gamma = 2\pi \times 6.1$ MHz, the Doppler temperature amounts to $T_D = \hbar\Gamma/2k_B = 145.6$ μK [96].

The simple discussion presented so far has neglected the multilevel structure of real atoms in addition to the polarisation state of the cooling light, both of which can lead to temperatures far below the Doppler temperature. These so-called *sub-Doppler* cooling mechanisms are important and can actually reduce this lower limit by two orders of magnitude [212]. The one dimensional combination of counter-propagating cooling beams can lead to a complex spatial intensity and polarisation modulation. A multilevel atom that moves through such a field pattern can experience spatially varying light shifts of its energy levels, and therefore a polarisation state dependent optical pumping between the hyperfine structure and the lifted degeneracy of the magnetic substructure. The first energy loss mechanism in such a **Polarisation Gradient Cooling (PGC)** as depicted in Figure 3.9(a), aptly named the *Sisyphus effect*, occurs due to the preferential excitation of the atom when it is located around potential maxima as it traverses a sinusoidally varying potential landscape. Subsequent decay into a potential minima

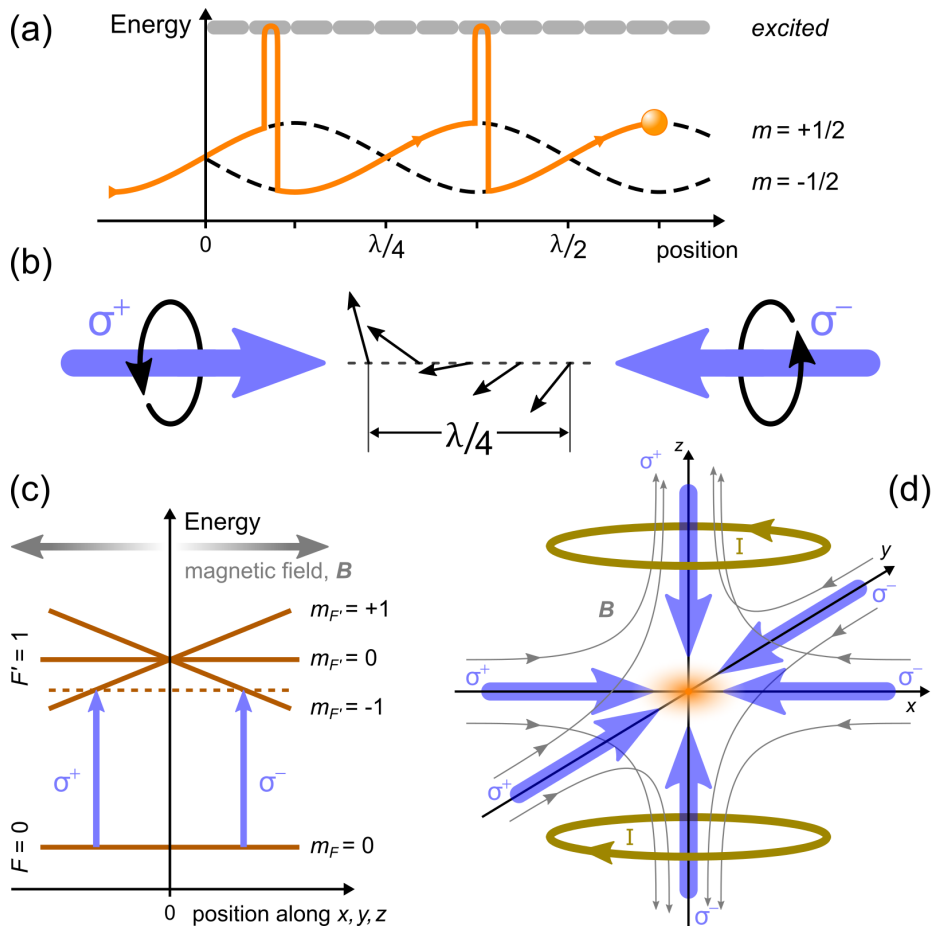


Figure 3.9. Working principles of laser cooling and the Magneto-Optical Trap (cont.). (a) Sisyphus cooling in brief. An atom that moves through a light field featuring a polarisation gradient will experience a spatially varying state dependent light shift (grey dashed lines). When traversing through such a standing wave of polarisation (orange trajectory), an atom initially in the $m = +1/2$ ground state sublevel must climb the potential landscape. As the polarisation of the light field changes, the $m = +1/2$ sublevel becomes less strongly coupled and the atom's kinetic energy is converted to potential energy until it is optically pumped to the $m = -1/2$ ground state. The gain in potential energy is radiated away in the spontaneous emission of a photon with a higher energy to that initially absorbed. This **Polarisation Gradient Cooling** process repeats until the atomic kinetic energy is too low to traverse over a potential hill. (b) A counter-propagating beam pair in a $\sigma^+\sigma^-$ -configuration combine to form a linearly-polarised beam, in which the electric field rotates around the propagation axis with a periodicity equal to its wavelength, λ . (c) Sketch of the spatially-dependent atomic resonance for a $F = 0 \rightarrow F' = 1$ transition that is subject to a quadrupole magnetic field. A preferential scattering of either a σ^+ or σ^- polarised cooling beam for an atom that is respectively negatively or positively displaced from the origin results in a restoring force towards the trap centre. (d) Scheme for the production of a 3D **MOT**, where the intersection region of three sets of mutually orthogonal counter-propagating red-detuned cooling beam pairs (blue arrows) is aligned to the zero-point of a quadrupole magnetic field (grey lines) that can be generated by a pair of coils in an **anti-Helmholtz** configuration (gold circles). Laser cooled atoms can accumulate in the trap centre (orange cloud).

ensures that kinetic energy is lost, with an emitted photon of slightly higher frequency to that initially absorbed carrying the energy difference. The second mechanism in **PGC** takes place for an atom moving through a special case of pure linear polarisation that instead rotates around the axis of propagation. As shown in Figure 3.9(b), this helical field oscillation can be thought of, and realised by, a pair of counter-propagating beams with opposite circular polarisation in a so-called $\sigma^+\sigma^-$ -configuration. Optical pumping induces a velocity-dependent ground state population difference, and thereby an imbalanced radiation pressure, which leads to an efficient frictional damping. Both aforementioned processes now reach temperatures that are close to the fundamental limit of laser cooling associated with the energy of one photon recoil, which for ^{85}Rb is $T_r = \hbar^2 k^2 / 2k_B m_{\text{Rb}} = 370.5 \text{ nK}$ [96].

So far, the discussion has been restricted to the interaction of light with atoms in one dimension. Extending this arrangement to 3D, with the addition of counter-propagating beam pairs along each Cartesian axis for example, leads to a three dimensional reduction in the atom's kinetic energy. The analogy of such a light field acting as a viscous fluid for the atoms in the overlap region has been termed *optical molasses*, and while this scenario provides cooling by the strongly dissipative velocity-dependent force, there is no spatial confinement. The addition of a spatially inhomogeneous magnetic field in combination with the 3D optical molasses cooling provides a position-dependent restoring force, i.e., the trapping of a **Magneto-Optical Trap**. As illustrated in Figure 3.9(c), a quadrupole magnetic field along one axis is zero at the origin and varies linearly with the position. Away from the origin, the non-zero magnetic field lifts the degeneracy of the excited state manifold via the Zeeman effect, as illustrated for a $F = 0 \rightarrow F' = 1$ transition. This position-dependent excited state shift translates into a position-dependent detuning from the $\sigma^+\sigma^-$ -configuration cooling beam pair, by an amount

$$\Delta_B = \frac{\mu}{\hbar} B, \quad (3.6)$$

where $\mu = (g_{F'} m_{F'} - g_F m_F) \mu_B$ is the effective magnetic moment between the excited and ground states, with the constant g_F the Landé factor and μ_B the Bohr magneton. Each of the σ_+ and σ_- cooling beams preferentially couple to the $m_{F'} = +1$ and $m_{F'} = -1$ excited states, respectively. An atom that is displaced from the origin will therefore become more resonant with the beam that it moves against, due to the selection rules of $\Delta m_F = \pm 1$ for a beam with σ_{\pm} polarisation. As such, the total force experienced by the atom is now dependent on its position as well as its velocity, and is given by equation (3.4) with the force from each beam as

$$\mathbf{F}_{\pm} = \pm \hbar \mathbf{k} \frac{\Gamma}{2} \frac{I/I_{\text{sat}}}{1 + I/I_{\text{sat}} + (2(\Delta \mp \mathbf{k} \cdot \mathbf{v} \pm \Delta_B)/\Gamma)^2}. \quad (3.7)$$

3. Experimental Design

Figure 3.9(d) shows a schematic of the basic ingredients necessary for generating a real MOT: namely, the quadrupole magnetic field generated by a pair of coils in the AHH configuration, in conjunction with a $\sigma^+\sigma^-$ -configuration 3D optical molasses. Alignment of the intersection point of the six cooling beams with the position of zero magnetic field defines the trap centre, where laser-cooled atoms can accumulate in a cloud-like structure.

3.4.2 Lower MOT

The lower Magneto-Optical Trap is labelled so due to its vertical alignment *underneath* the resonator location, and follows most of the design of CQED 1.0's original MOT set-up [92, 93, 213]. It is housed in a separate expanded spherical cube UHV-chamber (MCF275-ESC608, Kimball Physics) that has mechanical properties akin to that of the Science chamber, albeit at a tenth of the internal volume (~ 0.4 L). The six DN35CF (2.75") flange ports achieve a port alignment precision of less than 0.1° , and are each closed with the same anti-reflection coated viewports detailed in Section 3.3.5 (VPZL-275LDIO, Kurt J. Lesker Company). Opposing throughput views are each used for transmission of an optical molasses beam-pair in the $\sigma^+\sigma^-$ -configuration. The chamber is oriented to realise a so-called (1, 1, 1)-configuration of the 3D molasses, whereby each DN35CF port-axis meets the vertical at an angle of 54.7° . The remaining eight DN16CF (1.33") ports are utilised in a variety of ways: two on the side house electrical feedthroughs for a pair of Rubidium dispensers in the same manner as detailed for the Science chamber (see Section 3.3.5), the lower and upper provide mechanical support around a viewport and connection to the Science chamber respectively (see Section 3.4.4), the one at the rear is connected to vacuum pumping apparatus (see Section 3.5), with the remainder having viewports for MOT imaging and transmission of the repumper light (see Section 3.7.2).

Surrounding the chamber is a six-piece custom-made *cage system* that supports both the beam optomechanics and the AHH coils. Manufactured from black-anodised aluminium, the cage is completely detached from the UHV-chamber that allows for: passive cooling of the coils by acting as a heat sink, a correct macroscopic orientation of the whole MOT set-up with respect to the UHV-chamber, and an independent alignment capability of the six individual cooling beams. A selected-component view is displayed in Figure 3.10.

The optomechanics for each beam path comprises a modular unit made up of a fibre collimator with an integrated quarter-wave plate (60FC-Q780-4-M150-37, Schäfter + Kirchoff GmbH) that generates a collimated free-space beam with a circular polarisation and Gaussian intensity profile of diameter 27 mm [92]. For beam steering, the collimator is attached to two kinematic right-angle mirror mounts (KCB2, Thorlabs, Inc.) that each house a 50 mm diameter broadband mirror with a high, and equal, reflectivity

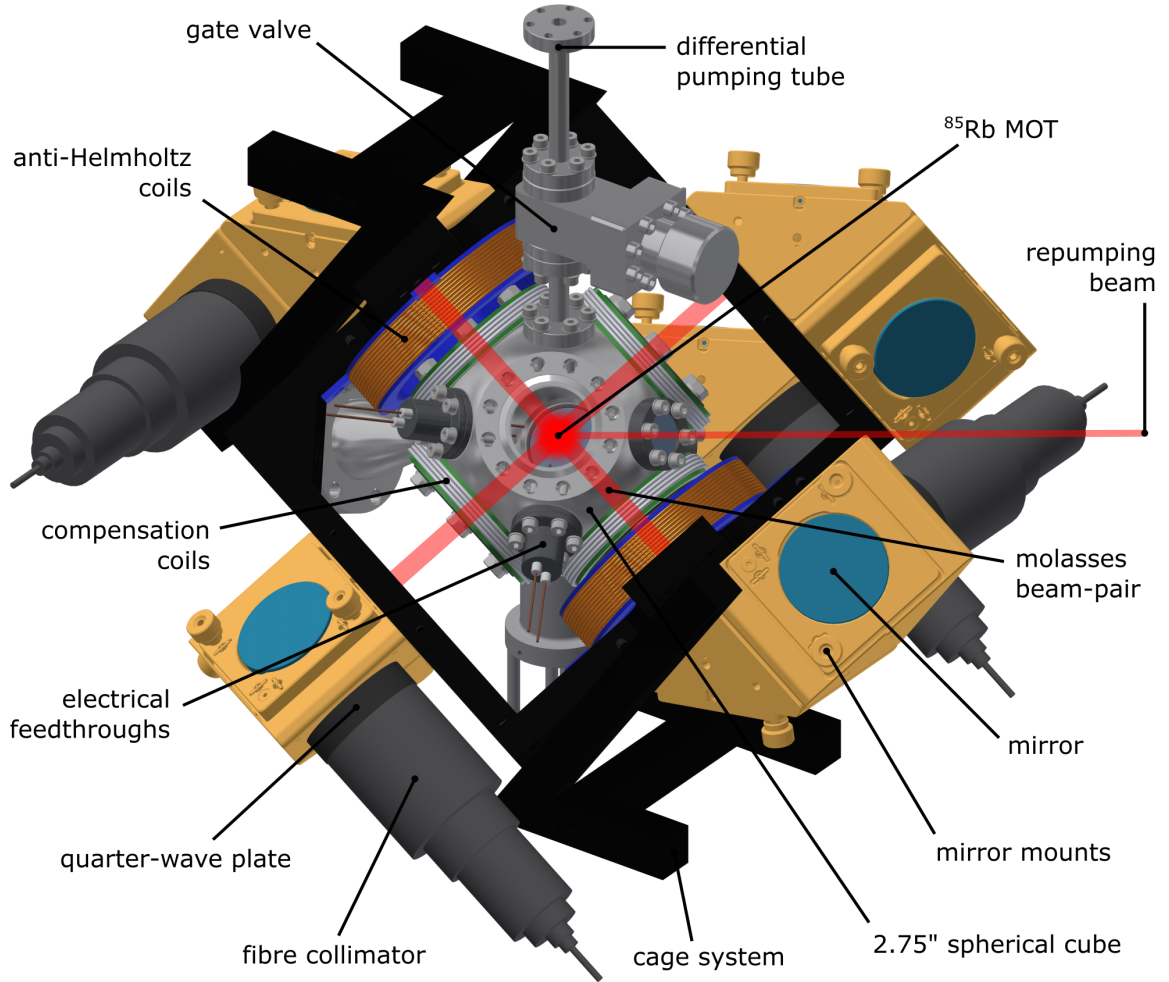


Figure 3.10. Composite Mot chamber assembly. A selected-component rendering of the Mot chamber design, including the assembled cage system that hosts the **AHH** coil pair and beam optomechanics necessary for the generation of an ^{85}Rb MOT. A beam-path overlay illustrates the intersection point at the chamber centre, where the components obstructing this view have been omitted.

for s - and p -polarisations (*MirHR780, Lens Optics*). Each of the six units are fed with fibre-guided laser light originating from a set of two $1 \rightarrow 3$ fibre port clusters (*48-FPC-1-3-780, Schäfter + Kirchoff GmbH*), see Section 3.7.1 for further details.

The pair of **AHH** coils are each constructed from 1.5 mm diameter enamel-coated copper wire that is wound around an aluminium former with a 94 mm inside diameter. The wire is affixed with a thermal adhesive for heat dissipation (*ASTA-7G, Arctic Silver, Inc.*), and each coil former is attached to the inside of the cage and separated along their shared cylindrical axis by 130 mm symmetric around the chamber centre. Each coil contains 60 windings, and together, are capable of generating linear magnetic field gradients in the chamber centre of 10(5) G/cm along(perpendicular to) the coil axis for 13 A of current [213]. When continuously applying this value of current, the coils themselves heat up to around 43 °C, which is acceptable especially when considering

3. Experimental Design

their normal operation is typically at less than 50% of this amperage. A highly stable power supply (*TOE 8815, TOELLNER Electronic Instrumente GmbH*) provides current to both coils, which can be quickly shut-off on the microsecond timescale with use of a homemade switching circuit in series [92]. Finally, three additional pairs of bias coils in a **HH** configuration are arranged symmetrically around the chamber with windings concentric to each **DN35CF** viewport. A thin **PTFE** former of 72 mm inside diameter clasps the steel surface of each viewport, and hosts a strip of ribbon cable to total 15 windings. Each coil pair is independently controlled with its own current supply (*EA-PS 3016-10B, EA Elektro-Automatik GmbH & Co. KG*) and are used to compensate external (stray) fields in order to centre the zero of the **AHH** quadrupole field in the chamber.

Upon synergistic construction, alignment, and operation of all previously described ingredients (for details on the **UHV** and laser aspects, see Sections 3.5 and 3.7.1 respectively), an approximately spherical cloud of ^{85}Rb atoms can routinely be trapped in the lower **MOT**. A camera image obtained with a **CMOS** sensor (*ELP-USBGS720P02-L36, Ailipu Technology Co., Ltd.*) of a first realisation, along with the relevant experimental parameters, is given in Figure 3.11.

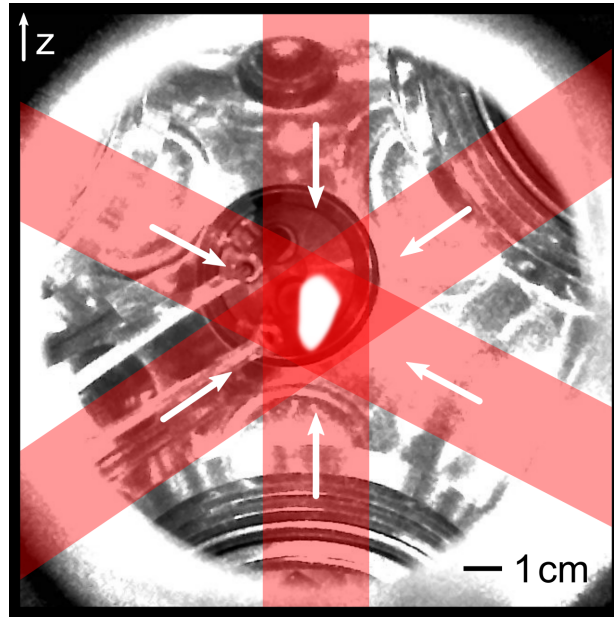


Figure 3.11. Lower Magneto-Optical Trap. A false colour **CCD** camera image of a first realisation of laser-cooled ^{85}Rb atoms, visible as a glowing cloud with a diameter of approximately ~ 1 cm, confined in the lower **MOT**. A current of 10 A supplied to the **AHH** coil pair (resulting in a magnetic field gradient of ~ 5 G/cm in the trap centre), with each cooling beam set to a power of 1 mW and 16 MHz detuning, was used in the capture of this image. A power of 1 mW was used for the single-beam repumper. The cooling beam paths have been sketched over in red, with the cloud of atoms superimposed for clarity. The rough orientation of the apparatus is indicated in the upper left, and an approximate scale bar is included in the lower right.

3.4.3 Upper MOT

As outlined in the design goals Section 3.2.2, a major upgrade of CQED 2.0 is the addition of a second Magneto-Optical Trap stage centrally-located within the Science chamber that houses the resonator, hence its namesake *upper MOT*. It was also stressed – particularly in Section 3.3 – that the design of the Science chamber and its constituents factored in the containment of this MOT, which in turn affected the route to realisation of the latter. While the beam paths for cooling light require only a brief initial discussion, the highly-constrained design of the magnetic field coils geometry is subsequently presented in depth.

3.4.3.1 Optical Molasses Geometry

An optimisation of the available optical access to the Science chamber centre ensures that the standard six-beam MOT geometry, comprising three pairs of mutually orthogonal circularly polarised beams, can be utilised. For the upper MOT, a caveat is that the two beam-pairs in the horizontal plane intersect at an angle of $\sim 78^\circ$ in order to bypass the high-NA in-vacuum lens (see Figure 3.4(a)), which is also situated in the horizontal plane. The remaining beam pair is aligned along the vertical direction, and traverses both UHV-chambers via the DPT, see Section 3.4.4. A similar modular design to that presented for the lower MOT is chosen for the optomechanics (see Section 3.4.2), namely; rigid pedestals that surround the chamber, hosting a pair of right-angle mirror mounts (*KCB1C/M*, *Thorlabs, Inc.*) that hold a miniaturised fibre collimator (*F810APC-780*, *Thorlabs, Inc.*) at the input side with a quarter-wave plate and adjustable iris at the output. The units for the vertical beam-pair are attached to the top of the Science chamber and the bottom of the Mot chamber with use of custom-made viewport-to-mirror mounts. The collimator on each unit produces a free-space Gaussian intensity profile of 7.5 mm diameter, which can be truncated with use of the iris in order to minimise stray light inside the Science chamber. All units are fed with fibre-guided laser light, where the horizontal beams originate from a $1 \rightarrow 4$ fibre port cluster (*48-FPC-1-4-780*, *Schäfter + Kirchhoff GmbH*) and the vertical beams each have a dedicated fibre coupling, see Section 3.7.1 for further details.

Coarse alignment of all beams was performed by flooding the Science chamber with Rb from the temporary dispensers and using CMOS cameras from multiple directions to observe the ‘glowing’ beam paths*. The vertical beams are most easily aligned by using the DPT as a reference, while custom diaphragms with a 3 mm hole fitted upon each viewport aids in ensuring collinearity of the horizontal beam pairs. Figure 3.5 in Section 3.3.4 illustrates the realised beam paths that bypass all elements of the coupling set-up to intersect in the Science chamber centre.

*By constantly running both dispensers at ~ 5 A, a high enough density of Rubidium renders each beam visible on an infrared-sensitive camera when exciting the D_2 transition.

3.4.3.2 Magnetic Field Coils

With the choice of Science chamber fixed (see Section 3.3.5), the minimum inside radius and separation of the AHH coil arrangement becomes 102 mm and 124 mm respectively, assuming direct contact with the outside of the chamber. Furthermore, bias coils in a HH configuration that are also located outside the chamber should ideally have a radius equal to their separation for maximum field homogeneity along their shared axis. These limitations on compactness imposed by the chamber put a restriction on the achievable field-gradient and offset-field magnitudes in the chamber centre, and so was used as a starting point for a realistic coil design [214]. However, these geometrical constraints merge with a number of other design restrictions. Importantly, none of the coils should block any available optical access while producing the static field gradients required for loading of the upper MOT. The zero of the generated quadrupole field should also be positionable in 3D, at least to within half a cubic centimetre, to allow for fine alignment with respect to both the resonator and the six-beam optical molasses. Furthermore, the whole coil arrangement should thermalise to an acceptable temperature. Finally, in the long term, the application of strong homogeneous magnetic fields* in arbitrary directions (e.g., along the tilted resonator axis) is required, which necessitates a current switching capability.

Therefore, to aid the iterative design process, a pre-construction simulation of the 3D field distribution for a given coil geometry was imperative. For this, the *Radia* software package which interfaces to the *Wolfram Mathematica* Front-End was utilised [215, 216]. This application has the advantage of accurate and fast computation of a magnetostatic field, even at arbitrary distances from a user-defined field-producing object geometry, thanks to its usage of analytical formulas. As such, a relatively simple final design was reached, and after subsequently spooling all coils, the resulting magnetic fields were measured and cross-checked with the simulation.

The simulated coil geometry, a CAD representation of the mechanical construction around the chamber, along with measurements of the obtained 3D B-field and its comparison to the simulation, are displayed in Figure 3.12. As shown in Figure 3.12(b), a self-supporting six-piece aluminium frame assembly, that was also factored into the simulation of the final design as depicted in Figure 3.12(a), compresses cylindrical L-shaped teflon spacers against the DN160CF flanges of the Science chamber and is formed to house the correct winding structures of all coils. Measurements of the magnetic field strength were performed by injecting current into the completed coil system and recording the readout of a hall sensor (*MF100, FLIR Systems Inc.*) at various positions along each coil-pair axis when set in either a HH or AHH configuration. Figure 3.12(c) shows the strength of the homogeneous B-field at the centre of the chamber measured for when each coil pair is individually operated in a HH-configuration. A linear fit to

*Homogeneity on the scale of the interaction WGM, i.e., across several tens of microns.

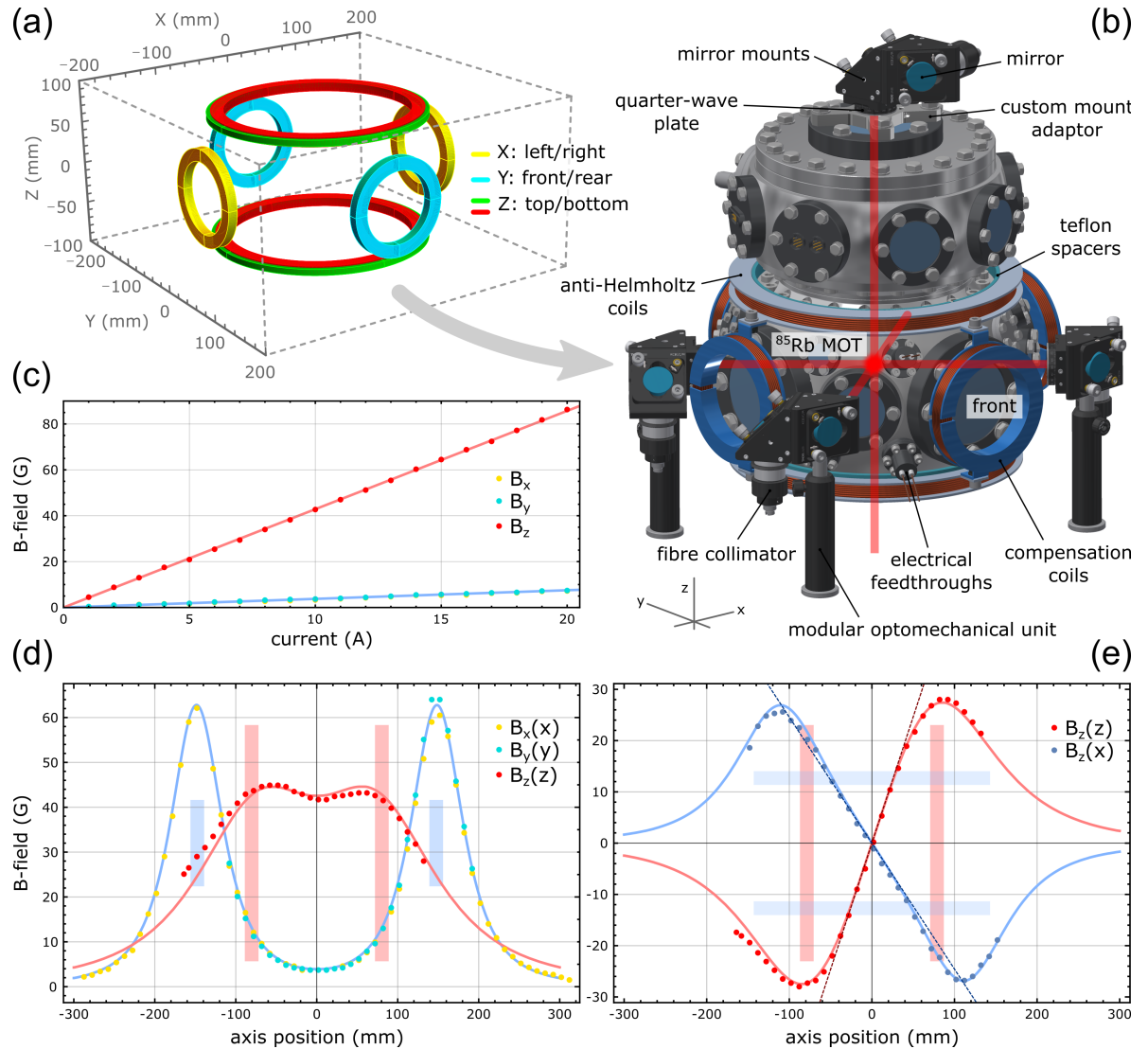


Figure 3.12. Magnetic field generation for the upper MOT. (a) The coil geometry designed and simulated with the *Radia* software package. (b) A rendered view of the designed coil system and beam optomechanics surrounding the Science chamber for the generation of an ^{85}Rb MOT. A beam-path overlay illustrates the intersection point at the chamber centre, where the upper MOT is located. The optomechanical unit for the underside vertical beam has been omitted. (c) Measurement of the magnetic field strength in the chamber centre at position $\{0, 0, 0\}$ as a function of the current applied to a HH-configuration coil pair (data points). A linear fit to the data (solid lines) yields 4.3 G/A along the z-direction (red) and 0.4 G/A along the x- and y- directions (yellow and blue respectively). (d) Measurement of the on-axis magnetic field generated by the constructed design for 10 A supplied to each HH-configuration coil pair as a function of axial position (data points). The expected B-field distribution computed with the Radia simulation (solid lines) concurs with the data, see text for details. The coloured boxes indicate the approximate coil positions with respect to the measured data. (e) Same as (d), but for 10 A supplied to the z-axis coil pair in an AHH-configuration. Linear fits around the origin yield magnetic field gradients of 5.2(2.6) G/cm along (perpendicular to) the z-axis.

3. Experimental Design

the obtained data results in a variation of the field strength with the applied current by 4.3 G/A for the vertical coil pair and 0.4 G/A for the horizontal coil pairs. Figures 3.12(d) and (e) show the spatial variation of the B-field when measured on axis for each coil pair, respectively for 10 A of applied current in a **HH** and **AHH** configuration. In both cases, the solid lines result from the Radia simulation and have an excellent agreement with the measured data when scaling the current density in the simulated geometry by 78.5%. This figure corresponds exactly to the ratio of cross-sectional areas between the simulated solid mass and realistic grid-packed wires of each coil. Fits to the data in Figure 3.12(e) yield magnetic field gradients of 5.2(2.6) G/cm along (perpendicular to) the direction of the vertical molasses beam. A summary of all the optimised coil parameters, in design and results, are recorded in Table 3.3.

coil pair	X: <i>left/right</i> , Y: <i>front/rear</i>	Z: <i>top/bottom</i>
dimensions (mm)	{42.0, 56.4, 10.8}	{107.0, 126.2, 18.0}
wire radius (mm)	0.9	0.9
windings	48	64
separation (mm)	297	147
cable length (m)	12.67	43.03
resistance (mΩ)	86	291
inductance (H)	12.7	43.0
B/I (G/A)	0.4	4.3
$\frac{dB}{dz \cdot I} \left(\frac{G}{cm \cdot A} \right)$	-	0.52
$\frac{dB}{dx \cdot I} \left(\frac{G}{cm \cdot A} \right)$	-	0.26

Table 3.3. Upper MOT coil parameters. A summary of the relevant parameters for each of the three coil pairs shown in Figure 3.12. Dimensions of each coil are recorded as {*inner radius, outer radius, thickness*}, with the number of windings populating the resulting solid volume. The separation of the coil pair is given as the distance between each coil centre, while the cable lengths, resistances and inductances are calculated. B-field values are recorded on axis between the two coils.

During construction, a liberal amount of heat conducting paste based on a high temperature resistant two-component epoxy adhesive (*Loctite EA 9492, Henkel Corp.*) was applied between each layer of windings (*Damid200-Gr3, Dahrén Group*), which acts to provide mechanical stability and thermal dissipation (being rated up to 180 °C). Operation of the upper **MOT** coil cage under semi-realistic conditions, i.e., ~ 10 A continuously applied to the **AHH** pair, reveals that it heats up to around 55 °C after several hours. Thanks to the teflon spacers however, heat transfer to the Science chamber is minimal, which remains around room temperature itself.

3.4.3.3 Camera Imaging

Observation through the left-most viewport of the Science chamber (see Figure 3.12(b)) offers an unobstructed view on the cloud of ^{85}Rb atoms contained within the upper MOT, that is typically suspended between the mechanical mounts of the coupling set-up around half a centimetre from the planar face of the high-NA lens. Figure 3.13(a) displays a false colour image of the described view, taken with a CMOS camera (*ELP-USBGS720P02-L36, Ailipu Technology Co., Ltd.*). When replacing the camera with a Photomultiplier tube (PMT) (*H6780-20, Hamamatsu Photonics GmbH*), atomic fluorescence originating from the upper MOT can be monitored. Figure 3.13(b) displays a time trace of the PMT signal after switching on all cooling beams at time zero, with the Rb dispensers and fixed magnetic field permanently activated. A simple fit to the fluorescence data signal using $s(t) = S \cdot (1 - e^{-t/\tau})$ [217], where S is the steady-state fluorescence signal for $t \gg 0$, indicates a loading time of $\tau \approx 1$ s. The relatively slow MOT build-up observed in this example configuration is attributed to the assumed low density of Rb background gas, where the dispensers of the Science chamber were operated at a current of only 2.5 A in order to avoid unnecessary deposition within the coupling set-up.

While this method of *fluorescence imaging* can yield approximate values for the cloud size and its loading speed, an alternative technique such as *absorption imaging* [218] would give quantitative values for the number of atoms contained within the cloud along with their temperature. This important – but not crucial – characterisation step was skipped due to the quick observation of single atoms loaded into the optical dipole trap directly from the realised upper MOT, see Section 5.1.1 in Chapter 5.

3.4.4 Atomic Fountain

At the time of writing, this work is still ongoing. Therefore, only a brief introduction to the working principle, design, capabilities, and some early successes of the Atomic Fountain will be presented.

In the CQED 2.0 experiment, the AF is the chosen method for transferral of the cooled cloud of atoms from the lower to the upper chamber due to its relative ease of implementation and versatility of the transfer characteristics [134]. After the cloud of cold atoms is produced in the lower MOT, an optical molasses for the cloud is generated by removal of the magnetic confinement. Shortly after, by red and blue detuning opposing beams, a subsequent imbalance in the radiation pressure will accelerate the cloud and transfer it into a frame of reference that co-moves with cloud. This frame possesses the velocity in which the Doppler-shifted molasses beams all have the same detuning. The magnitude of the initial launch velocity is proportional to the magnitude of the detuning applied, while its direction is determined by that of the resultant force vector arising from the radiation pressures of each various beam pair. The initial launch

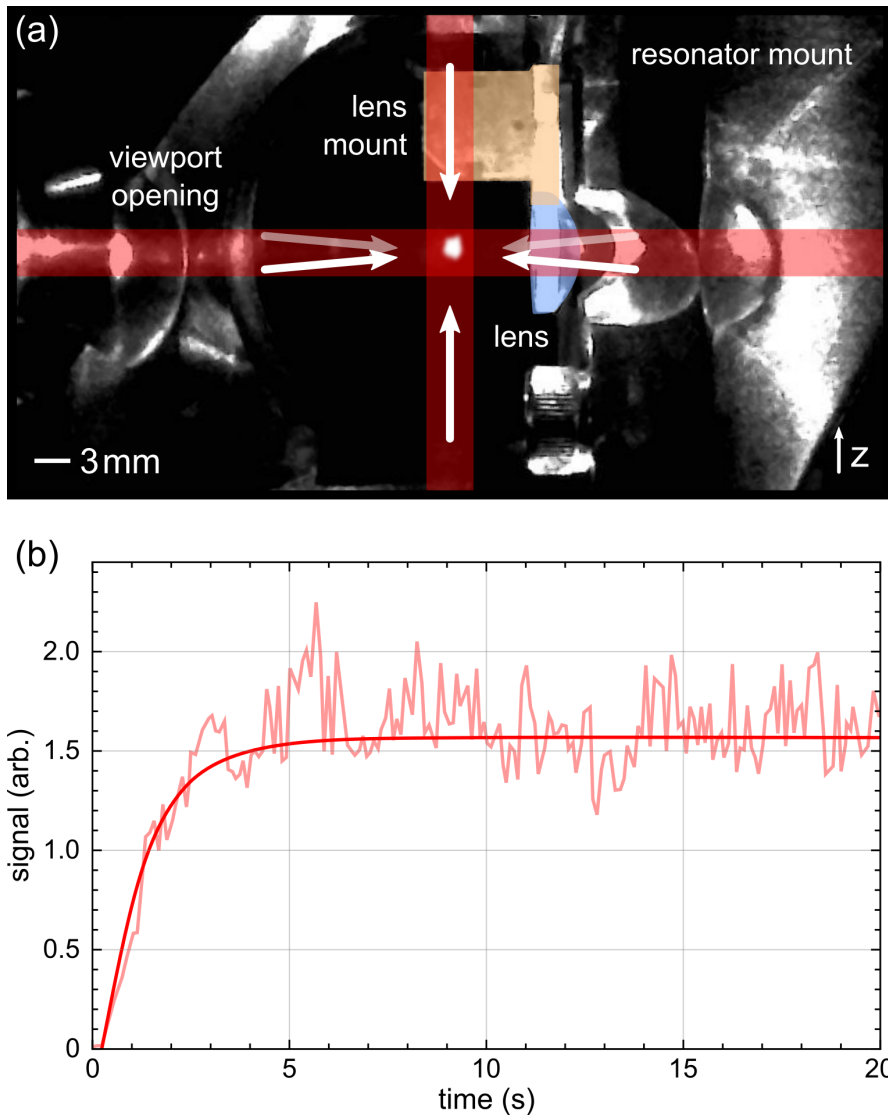


Figure 3.13. Upper Magneto-Optical Trap. (a) A camera image of a cloud of laser-cooled ^{85}Rb atoms confined within the constructed upper MOT, visible as a glowing cloud of ~ 2 mm diameter. A magnetic field gradient of ~ 6.5 G/cm was used, with powers of 1 mW and 16.3 MHz detuning set for each cooling beam. A power of 1 mW was used for the repumping beam, and equally split along the two vertical paths. Various components of interest in close proximity to the cloud are sketched over and labelled accordingly, including the cooling beam paths. An approximate scale bar is included in the bottom left, and the vertical direction indicated in the bottom right. (b) A typical loading curve of the upper MOT, obtained by abruptly switching on the cooling beams at $t = 0$ and recording the fluorescence signal (light-red line) on a Photomultiplier tube set in place of the camera. A fit to the data (red line) yields a loading time of approximately 1 s.

parameters thereby govern the parabolic flight trajectory which the atomic cloud's centre-of-mass traverses. As displayed in Figure 3.14(a), the (1, 1, 1)-configuration of the lower MOT molasses beams (see Section 3.4.2) enables this trajectory to lie along the vertical direction when simultaneously blue (red) detuning the lower (upper) sets of cooling beams. In CQED 1.0, the initial velocity of the cloud was chosen such that its turning point coincided roughly with the location of the resonator, around 30 cm above the lower MOT. The centre of the chambers (and therefore the distance between the lower MOT and the resonator) has been kept constant across the redesign. However, due to the modified Science chamber, the inner diameter of the Differential Pumping Tube (DPT) had to be re-evaluated as a result of its reduced overall length. Ultimately, the DPT must accommodate two competing constraints to reach a satisfactory trade-off between them: a long and narrow-bore tube ensures the low gas conductance necessary for maintenance of a 'clean' UHV environment in the Science chamber (as opposed to the higher pressure due to the alkali vapour present in the Mot chamber), while a short and wide-bore tube enables larger-diameter clouds of atoms to pass through unhindered. As such, an evaluation [213] of the functional dependence of the DPT's inner diameter and overall length on the resulting pressure difference between the two chambers and initial temperature of the cloud of atoms has been undertaken. The results are plotted in Figure 3.14(b), where the upper blue (lower purple) shaded curves are the constraints imposed by the initial cloud temperature (differential pressure ratio). The chosen DPT dimensions are displayed, and are compatible with initial cloud temperatures of around 10 μK and a pressure ratio between the two chambers of around 600 or less [92].

With these dimensions, the DPT is realised by a custom-made DN16CF full nipple piece with the desired overall length and inside diameter (*FN-SPL1570*, Kurt J. Lesker Company), and vertically connects the top of the Mot chamber to the bottom of the Science chamber as illustrated in Figure 3.14(c). A notable design feature of the new DPT is the addition of an all-metal manual gate valve (*SG0063MCCFM*, Kurt J. Lesker Company) just under halfway between the two chambers. When closed, its safe withstanding of ~ 1 bar pressure difference across the gate enables either of the upper or lower chamber systems to be brought to atmospheric pressure while the other remains at UHV, thereby streamlining maintenance work on either system (e.g. replacing dispensers in the Mot chamber).

Due to the updated addition of the upper MOT in the Science chamber, the current set-up offers alternative methods of atom transfer from the lower to the upper MOT. Since the vertical beams of the upper MOT traverse both chambers and have an individual switching capability, the possibility of using a 2D^+ MOT configuration is opened up, whereby the AF launch is aided by a vertically-oriented 'push' beam. Most recently, this approach enabled observation of single atoms loaded into the dipole trap without activation of the atomic dispensers in the Science chamber, indicating a successful transferral of the lower MOT to the upper.

3. Experimental Design

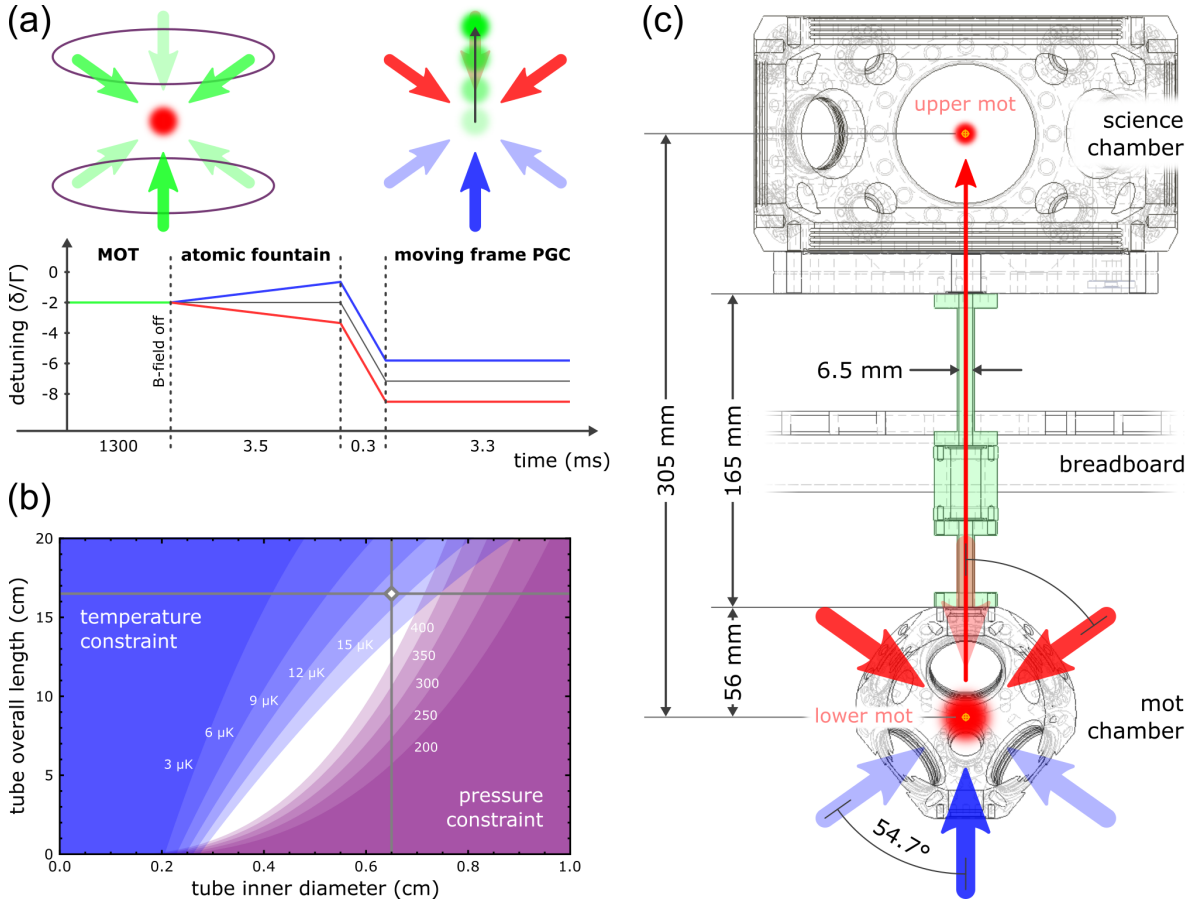


Figure 3.14. MOT transfer with an Atomic Fountain. (a) Pictorial representation of the **Atomic Fountain** (upper right) following the preparation of a **MOT** cloud (upper left), including the typical temporal sequence of its operation (lower middle). The **MOT** cloud is initially prepared before the magnetic confinement is switched off, and the lower (upper) molasses beam sets are blue-detuned (red-detuned) with respect to the initial cooling frequency. The imbalance in radiation pressure transfers the cloud into a moving molasses, in a reference frame that moves with a velocity where the Doppler-shifted cooling beams have the same detuning. An additional **PGC** stage in the moving frame is added following the **Atomic Fountain** launch, such that the cloud is continuously cooled until it exits the beams [213]. Figure adapted from [70]. (b) Competing constraints on the designed **Differential Pumping Tube** arising from the initial **MOT** cloud temperature (blue contours) and the differential pressure ratio between the chambers (purple contours). The dimensions of the **DPT** are set to a 165 mm overall length and 6.5 mm inner bore diameter (marked point) in order to support uninhibited passage of a cloud of atoms cooled to around 10 μK with a 3 mm initial diameter, while maintaining a differential pressure ratio of around 600 between the two chambers. (c) Wire-frame view of the designed connection between the Science and Mot chambers established by the **DPT**. The relevant dimensions in the design are correspondingly labelled, and an illustration of the transfer trajectory depicted.

3.5 Ultra-High Vacuum Set-up

The two vertically-aligned Science and Mot chambers are rigidly connected via the **Differential Pumping Tube**. Each requires a sophisticated permanent apparatus for their evacuation, as well as for the measurement and maintenance of the desired **Ultra-High Vacuum** environment. A stable and good quality **UHV** in each chamber is paramount for a variety of reasons, but especially necessary when working with cold dipole-trapped atoms that are easily expelled from the trap by collisions with the remaining room temperature background gas – an undesirable process which limits the trapping lifetime. The two-chamber design offers the advantage of maintaining a pressure difference between the chambers, whereby the Mot chamber can sustain a relatively high background gas pressure of **Rb** atoms for efficient generation of the lower **MOT** ($\sim 10^{-8}$ mbar), while low conductance to the Science chamber by virtue of the **DPT** (see Section 3.4.4) ensures a lower background gas pressure ($< 10^{-9}$ mbar). In the following, the design considerations of the set-up are first outlined, based upon an estimation of the gas conductance within the proposed system [213, 219], before a description of the build and pumping process is presented.

3.5.1 System Design

The proposed assembly of the vacuum hardware required for **CQED** 2.0 follows the overall structure of that used for **CQED** 1.0, albeit with a number of upgrades as will be outlined in the next Section 3.5.2. As such, a number of vacuum hardware components were reused due to their continuing functionality. A starting point for the most basic structure, considering the designs of the Science and Mot Chambers (see Sections 3.3 and 3.4.2 respectively) can then be planned out, a simplified schematic of which is shown in Figure 3.15. The Science and Mot chambers, joined by the **DPT**, each have an independent pump that is connected via appropriate piping. The pressures, P , and suction powers (volume flowrates), $S = dV/dt$, of each vacuum component hardware are denoted by the subscripts $A(B)$ and $PA(PB)$ for the Science (Mot) chamber reservoirs and pumps respectively Figure 3.15. The conductances along each of the numbered connecting pieces, C_n , along with the mass flowrates towards each pumping system, Q_A and Q_B , are also indicated. To ensure good conductance to the pumping systems throughout the design, an analysis of the flow processes is necessary [161, 219].

A number of approximations are used that simplify the analysis, rendering the results useful as an indication of the lower bound in achievable pressures, while still providing a relatively accurate simulation of the final build. The model assumes the molecular flow regime [161], whereby the mass flow rates are constant. This assumption is valid when considering that, in practice, the pumping systems in the calculation are used to maintain a **UHV** pressure only after evacuating with a separate pumping system.

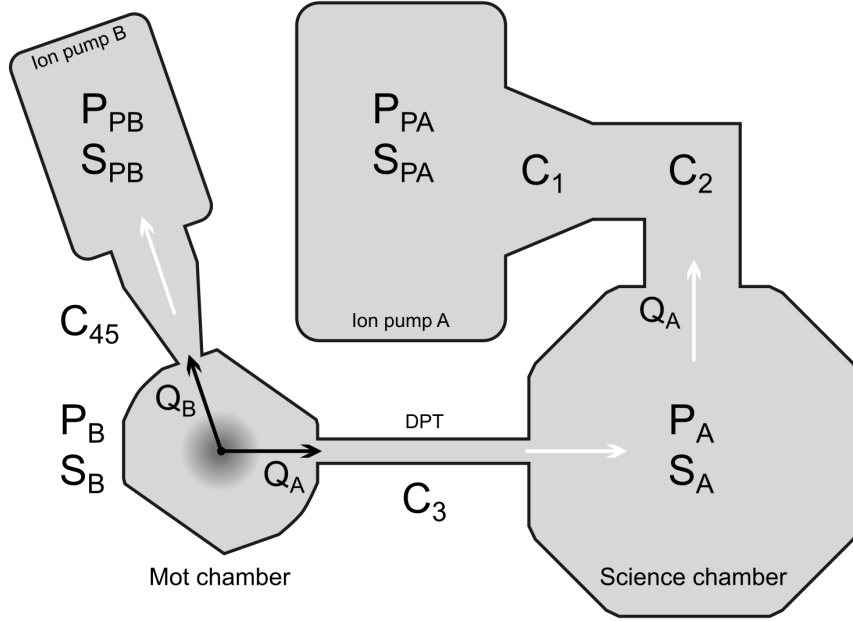


Figure 3.15. Schematic of the pumping system used to estimate the achievable base pressures within each of the Mot and Science chambers. The two chambers are rigidly connected via the **Differential Pumping Tube**, and each has an individual ion pump joined by conductive piping. It is assumed that the Mot chamber housing **Rb** dispensers is the source of all mass flows, as depicted. See text for details.

Therefore, the additional components outside of the major flow paths are neglected, and a constant background pressure corresponding to the residual pressure in the absence of mass flow, $P_{A(B)}^0$, is assigned for the upper (lower) system. Under the aforementioned assumptions, the following mass flowrates at each connection can be listed as [161]

$$Q_A = \begin{cases} (P_{PA} - P_A^0)S_{PA} \\ C_{12}(P_A - P_{PA}) \\ (P_A - P_A^0)S_A \\ C_3(P_B - P_A) \\ (P_B - P_A^0)S_B \end{cases} \quad (3.8)$$

and

$$Q_B = \begin{cases} (P_{PB} - P_B^0)S_{PB} \\ C_{45}(P_B - P_{PB}) \\ (P_B - P_B^0)S_B. \end{cases} \quad (3.9)$$

Here, the conductance of multiple pieces connected in series is the sum over the reciprocals, i.e.,

$$\frac{1}{C_{nm}} = \sum_{k=n}^m \frac{1}{C_k}, \quad (3.10)$$

where the conductance through a singular piece is given by C_k . Values for these parameters are calculated according to the specific geometry of each connecting piece, the details of which are outlined in Appendix D. By assuming that the Mot chamber will be flooded with Rb gas from the atomic dispensers used to load the lower MOT, the simplifying assumption that all mass flows Q_A and Q_B originate from the Mot chamber and are in the direction of their respective pumping systems can be made. Thus, from equations (3.8) and (3.9), the expected pressure and suction power values in each chamber can be obtained as

$$P_A = \frac{P_{PA} - P_A^0}{C_{12}} S_{PA} + P_{PA} \quad (3.11)$$

$$S_A = C_{12} \frac{P_A - P_{PA}}{P_A - P_A^0} \quad (3.12)$$

and

$$P_B = \frac{P_A - P_A^0}{C_3} S_A + P_A \quad (3.13)$$

$$S_B = C_3 \frac{P_B - P_A}{P_B - P_A^0}. \quad (3.14)$$

By choosing manufacturer-specified values for the pumping speeds of each of the upper ($S_{PA} = 300$ (200) L/s for air (Rb)) and lower ($S_{PB} = 40$ (17) L/s for air (Rb)) pumps, in addition to assuming residual background pressures in each pumping system of $P^0 = 2.3$ (10) $\times 10^{-10}$ mbar for air (Rb) [213], equations (3.11)–(3.14) can be evaluated for the cases of a primary background gas of air or Rb. The results of this analysis are contained within Table 3.4. As a comparison, the values obtained for the pressure P'_B and suction power S'_B in the Mot chamber by consideration of the flow Q_B , are also displayed* (see Appendix D for further details). It is clear that despite a substantial throttling of the ion pump suction powers at each chamber due to the non-optimal conductances C_{12} and C_{45} , the pressure expected in the Science (Mot) chamber amounts to a factor of only roughly four (six) times that in the upper (lower) ion pump. This would still yield UHV pressures in the range 10^{-9} mbar, suitable for Magneto-Optical Trapping as well as for the capture of single atoms in a dipole trap. Notably, when considering only suction from the upper ion pump, the intentional conductance throttling of C_3 via the DPT results in a pressure ratio between the chambers of $P_B/P_A > 300$ – thereby ensuring that a high Rb background pressure in the Mot chamber for efficient loading of the lower MOT can be maintained, while preserving a lower pressure in the Science chamber for protection of the bottle microresonator.

*These values are obtained with equations analogous to (3.13) and (3.14), resulting from the rearrangement of equation (3.9).

	air	Rb
P_A (mbar)	4.2×10^{-9}	8.1×10^{-9}
S_A (L/s)	66.0	39.6
P_B (mbar)	1.3×10^{-6}	2.5×10^{-6}
S_B (L/s)	0.2	0.1
P'_B (mbar)	5.8×10^{-9}	2.7×10^{-8}
S'_B (L/s)	6.4	3.5

Table 3.4. Results of the UHV system flow analysis: for the Science (*system A*) and Mot (*system B*) chambers, for the cases of air and Rb. A realistic pressure at each ion pump of $P_P = 10^{-9}$ mbar is assumed for the calculations using equations (3.11)–(3.14) and (D.4)–(D.5) [213].

3.5.2 System Build

With the flow analysis of the proposed UHV system in the preceding Section 3.5.1 yielding satisfactory expected pressures in both chambers, its assembly can be undertaken. CAD models of the final set-up for both the upper and lower pumping systems are shown in Figure 3.16, and provide a clear display of the real-life build. In general, each chamber is connected at its rear to an individual ion getter pump (cf. Figure 3.15) in addition to a turbomolecular (or turbo) pump that can be isolated behind a gate valve. This scheme allows for the individual pumping of each of the upper and lower systems from ambient pressure (10^3 mbar) down to the HV regime ($\sim 10^{-7}$ mbar) with use of turbo and roughing pumps connected in series (see the next Section 3.5.3 for further details), before each ion getter pump can take over to reduce and maintain the pressure within the UHV regime ($< 10^{-8}$ mbar). Assembly of the full system takes place while strictly adhering to recommended practices when working with vacuum hardware intended for the generation and maintenance of UHV [220]. In short, this amounts to a thorough inspection and cleaning of each piece prior to assembly, and subsequent appropriate handling when flanging connecting pieces. Most importantly, the components to be placed inside the UHV undergo an additional cleaning process with use of an ultrasonic bath where appropriate*. All system components are of a ConFlat™ port variety, allowing for a UHV-tight sealing between connections with use of appropriately sized copper gaskets† and connecting bolts kits. All bolts are silver-plated to prevent seizing, and must be incrementally tightened to a nominal torque value in a star-shaped pattern,

*All custom mounting structures of the coupling set-up, in addition to the assembling screws, are cleaned in this manner. Commercial components such as the various nanopositioners are pre-cleaned by the manufacturer, thus requiring only a careful handling.

†A so-called *knife-edge* on each port opening will bite into the malleable copper gasket sandwiched between components, ensuring a metal-to-metal interface.

depending on the port size [220]. A detailed description of each assembled system is outlined in the following, referenced to that respectively shown in Figure 3.16 (a) and (b);

Upper System for the Science chamber: A standard symmetric 4-way cross (*C-0450S*, Kurt J. Lesker Company) is connected at the rear of the Science chamber, and is sealed with a viewport (*VPZL-450LDIO*, Kurt J. Lesker Company) for optical access to the coupling set-up along this direction. To the right, the cross connects to the ion getter pump (*VacION Plus Starcell 300*, Agilent Technologies Inc.) via a conical reducer nipple (*CRN600X450*, Kurt J. Lesker Company) and a zero-length reducing flange (*RF800X600M*, Kurt J. Lesker Company). The remaining port of the cross on the left is connected to a second asymmetric 4-way reducer cross (*C-0450-275*, Kurt J. Lesker Company) that houses a pirani/cold cathode pressure gauge (*PKR 251*, Pfeiffer Vacuum GmbH) for pressure monitoring. This cross piece also provides connection to the turbo pump (*TMU 071 P*, Pfeiffer Vacuum GmbH) behind an all-metal manual gate valve (*SG0250MCCFM*, Kurt J. Lesker Company) that can sever the connection to the turbo pump when UHV is reached. The turbo pump itself is part of a pump-stand unit (*TSU-071E*, Pfeiffer Vacuum GmbH) which can be interfaced to an associated diaphragm roughing pump (*MVP 015-2*, Pfeiffer Vacuum GmbH). The assembled system rests upon custom mounts fixed to the raised breadboard that each include viton buffer material for additional precaution against mechanical vibration transmittance. Furthermore, the orientation of each piece is chosen to minimise the overall lateral footprint of the system, to enable a more efficient usage of the available breadboard space (with respect to the CQED 1.0 design [213]).

Lower System for the Mot chamber: This system is analogous to the upper system as outlined above. A small conical reducer nipple (*CRN275X133*, Kurt J. Lesker Company) extrudes from a rear DN16CF port of the Mot chamber and is connected to a custom-made asymmetric 4-way reducer cross, which in turn is connected to an ion getter pump (*VacION Plus Starcell 40*, Agilent Technologies Inc.) directly behind the Mot chamber. At a right angle to the latter, an all-metal manual angle valve (*54.1 series*, VAT Group AG) allows for isolation of a dry turbo pump unit (same models as used in the upper system) that is connected in series. Again, custom mounts fixed to the optical table support the entire system and, in particular, provide the correct orientation of the ion pump that is rigidly connected to the Mot chamber.

3. Experimental Design

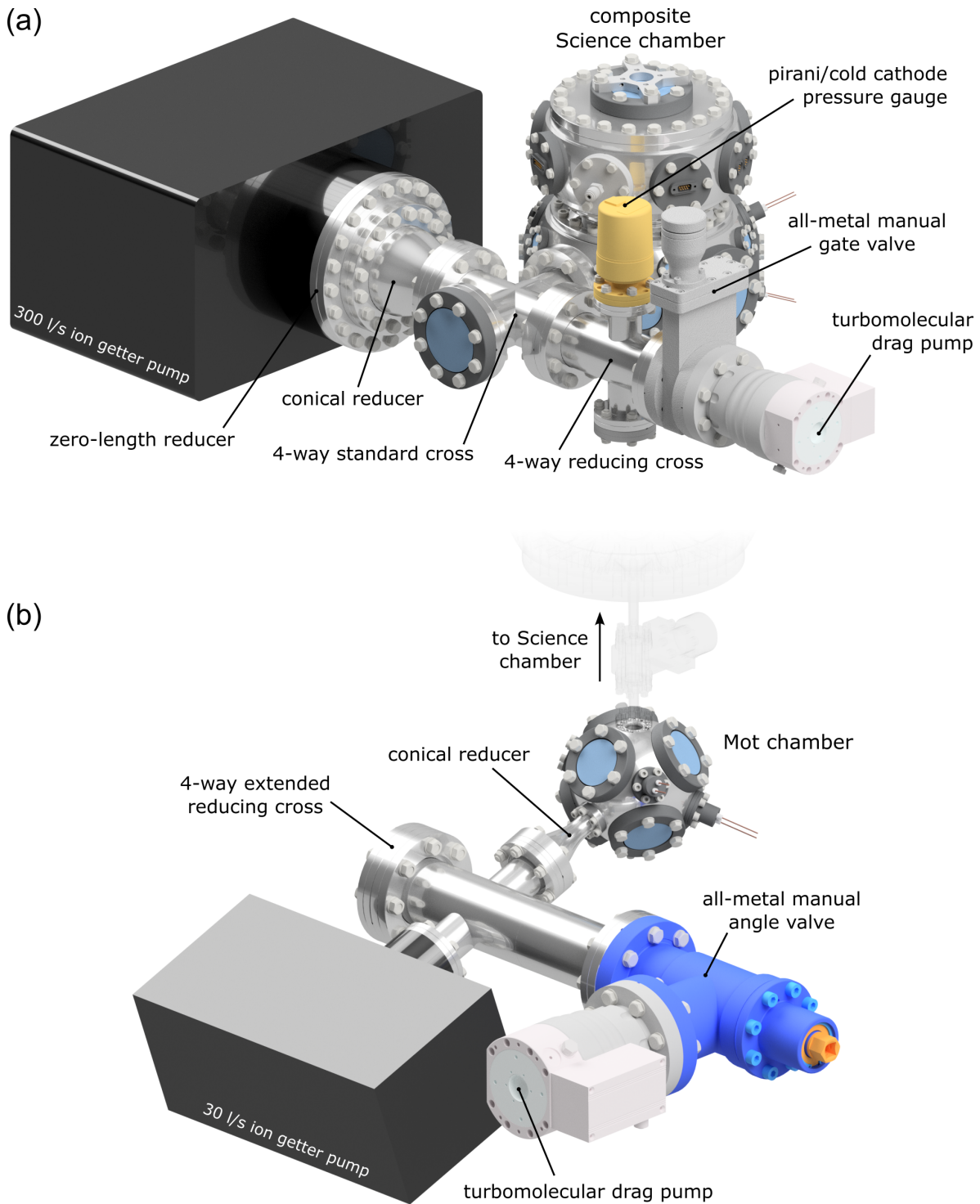


Figure 3.16. Full pumping systems (a) Assembled view render of the Science chamber upper pumping system, with notable components labelled. (b) Same as (a), but instead for the Mot chamber lower pumping system.

3.5.3 System Pump-down and Bake-out

Upon completion of the entire system assembly as described in the preceding Section 3.5.2 and shown in Figure 3.17, the next important stages for generating UHV are the *pumping down* and *baking out* of the system(s). These two procedures typically operate in tandem, whereby the latter aids the former in reaching lower base pressures via removal of contaminants (mainly water vapour) adsorbed on the inner surfaces by a controlled heating of the assembled system across a duration of many hours. In general, baking dramatically increases the outgassing rates of contaminants within the system, and ideally, hotter temperatures will eventually yield lower base pressures due to a reduction and evacuation of any adsorbed contaminants. Practically, the temperature for baking is limited by the maximum temperature ratings of the various sensitive instruments that comprise the system – for which a selection of relevant values of importance are included in Table 3.5. Further to this, to avoid irreparable damage to the viewports (for example), the temperature should not be ramped faster than 20 °C/h, and should also ideally remain uniform across the whole system to avoid both subjecting a single component to large temperature gradients or leaving cold spots where outgassed material can condense. Finally, all Rb dispensers were activated after initial pumping, but prior to the bake, such that any undesired contaminants emitted during the activation could be removed. Along the lines of the aforementioned, a brief description of the procedures performed are documented in the following. Note that these were carried out with the partial coupling set-up in place, i.e., all components apart from the fibres themselves were included.

With all three UHV valves within the system open, initial pumping is carried out by the roughing pumps connected behind each turbo pump, before initiating the latter. After baking and reaching the regime of HV, as monitored on the pressure gauges, the roughing and turbo pumps are further left running for some time. Finally, each of the ion pumps are switched on and left to operate alongside the turbo pumps before eventually sealing the isolating gate valves and switching off the latter. From that moment on, the UHV is solely maintained by the two ion pumps. Baking is performed during the initial pumping stage, and the temperature parameters were chosen according to the lowest maximum temperature rating (cf. Table 3.5). For this, the whole system is wrapped in several layers of UHV aluminium foil (*FOILA24, Kurt J. Lesker Company*), taking care to avoid direct contact across each viewport and other sensitive components, before winding a number of heating tapes around each chamber (*IT-S45/3, Thermocoax Isopad GmbH*) followed by additional foil over the top. The temperature of the tapes are set by an automatic temperature switch (*TS1000, H-TRONIC GmbH*) and monitored with an eight-channel data logger (*TC-08, Pico Technology*) that reads out thermocouple-based

3. Experimental Design

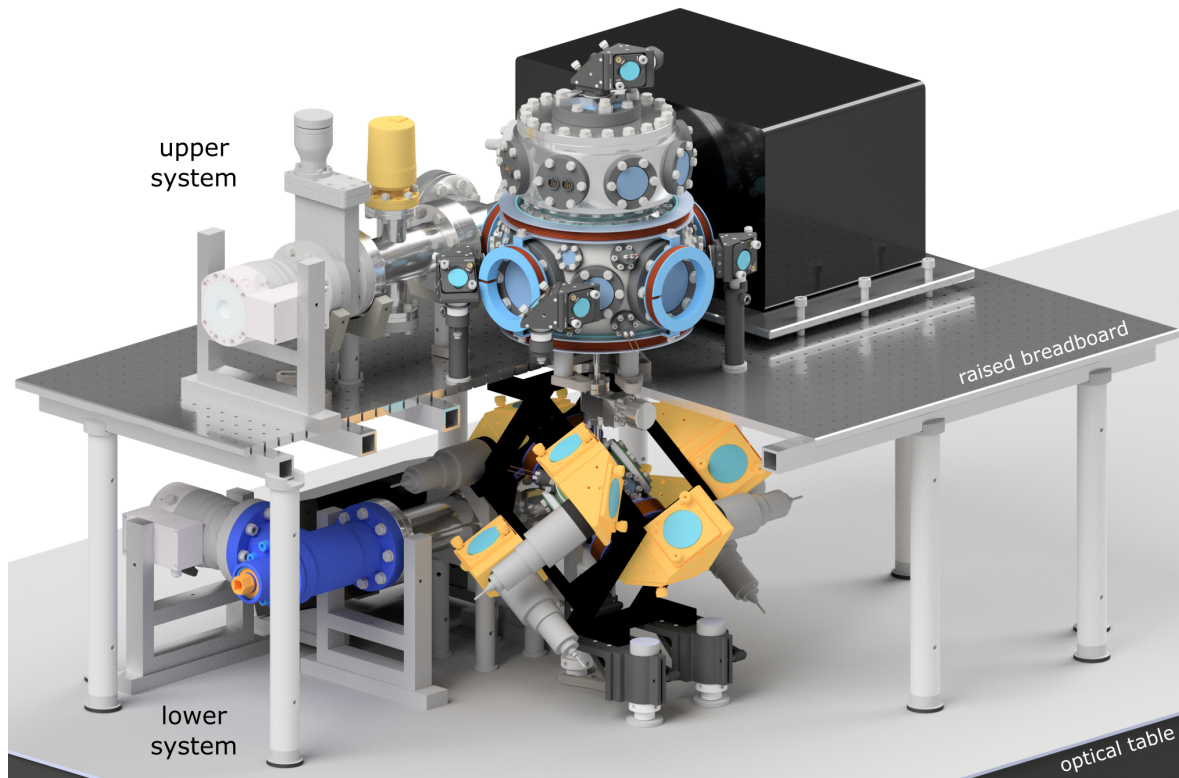


Figure 3.17. Completed experimental system. A render of the completed **CQED 2.0** experiment, illustrating how the entire upper system is raised above the lower system and centrally connected via the **DPT**. The composite breadboard used for this purpose has a section cut-out for visualisation purposes.

temperature probes that are fixed at various points of interest across the system*. With this, the bake-out procedure recorded in Figure 3.18 was performed across a duration totalling almost three weeks: an incremental increasing of the temperature of the system by no more than 5 °C/h from room temperature to a maximum of ~ 145 °C (measured at the Science chamber) was followed by a period of holding at this maximum temperature, before a controlled reversal of the temperature ramp cooled the system back to room temperature. The measured pressure at the upper ion pump, initially stable at 6.3×10^{-7} mbar, underwent pressure spikes of up to $\sim 10^{-5}$ mbar during the temperature ramp due to outgassed material. The subsequent prolonged hold-out period, lasting for approximately ten days, compensates to some extent the fact that the system cannot be baked to temperatures higher than 150 °C. During this time, the pressure steadily dropped to 3.0×10^{-7} mbar with the continued outgassing and removal of material via pumping. The most dramatic drop in pressure of almost two orders of magnitude occurred during the cooling procedure, likely due to the gradual removal or adsorption of the outgassed material without its replenishment from a continued heating.

*Multiple probes placed in direct contact with each chamber ensure an accurate monitoring of the applied heating.

component	maximum temperature rating (°C)
nanofibre positioners	150
lens positioner	150
piezos	150
viton	150
viewports	200
kapton insulated wiring	220
feedthroughs	250
gold-plating	250
steel	450
Rubidium dispensers	500

Table 3.5. Maximum temperature ratings of selected UHV components. Commercially available components that are intended for use under UHV are typically rated to temperatures > 100 °C for the purposes of vacuum baking. A selection of manufacturer-defined values are provided for the most sensitive equipment comprising the Science chamber set-up, along with other components of interest for comparison purposes. The maximum bake-out temperature should then accommodate these constraints, and was accordingly chosen as no more than 140 °C.

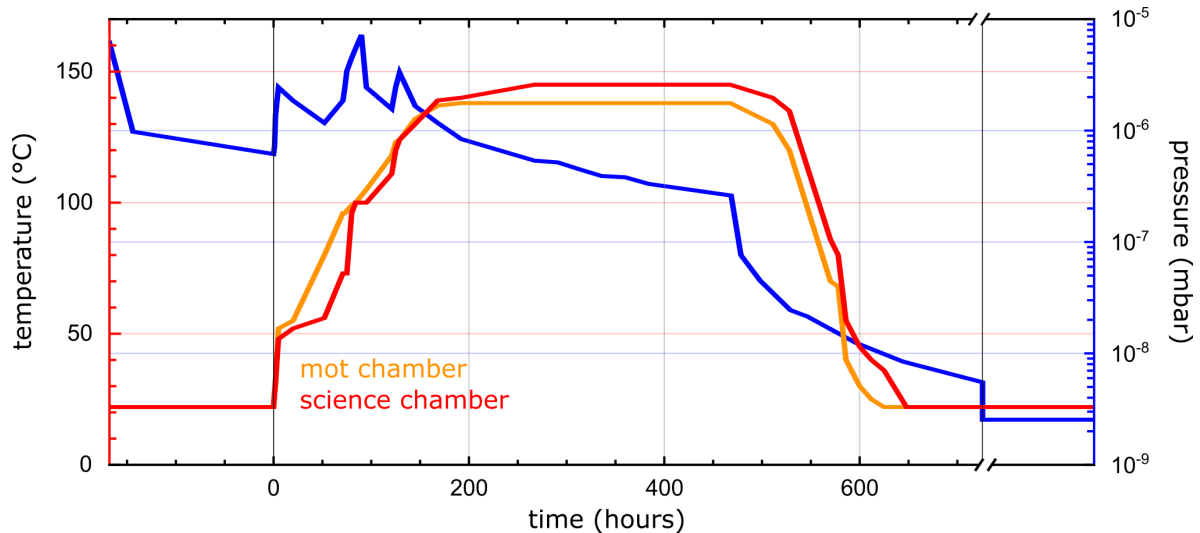


Figure 3.18. System bake-out procedure. A dual-axis graph of the temperature (red y-axis, left) recorded at the surfaces of the Science (red line) and Mot (orange line) chambers across a duration of around one month surrounding a system bake-out. The pressure at the upper ion pump, displayed on a logarithmic scale (blue y-axis, right), was also monitored throughout this time (blue line).

3. Experimental Design

Upon completion of the bake-out and pumping procedures, the system reached pressures of $P_{PA}^{\text{meas.}} = 2.3 \times 10^{-9}$ mbar ($P_{PB}^{\text{meas.}} = 6.1 \times 10^{-9}$ mbar) as measured at the upper (lower) ion pump, corresponding to a pressure in the Science (Mot) chamber of $P_A^{\text{meas.}} = 8.7 \times 10^{-9}$ mbar ($P_B^{\text{meas.}} = 1.2 \times 10^{-8}$ mbar) according to the analysis performed in Section 3.5.1. The measured values are roughly a factor of two higher than the expected values presented in Table 3.4, which can potentially be attributed to the presence of the coupling set-up in the Science chamber which may act as an additional source of mass flow not accounted for in the analysis performed in Section 3.5.1. Nevertheless, the measured values obtained are suitable for continuation of the experiment in the development of a MOT within each chamber (presented in Sections 3.4.2 and 3.4.3 respectively), as well as for a consideration of the optical dipole trap design to enable transport of single atoms from the upper MOT to the WGM of the bottle microresonator – to be outlined in the next Section.

3.6 Optical Dipole Trap Design

In CQED 1.0, strongly coupled atoms flying freely through the WGM of the bottle microresonator triggered an optical dipole trap in the vicinity of the resonator surface, in which a small fraction could be captured [60, 70] (see Section 2.4). One of the main goals in the design of CQED 2.0 is to improve upon the single atom delivery to such a trap, in order to further increase the interaction time between the atom and the WGM, as well as to move towards a more deterministic operation of the experiment (see Section 3.2.2). Here, following the procedure of loading the upper MOT from the lower MOT via the Atomic Fountain operation, a single atom should be collected and subsequently transported to the bottle microresonator. Of particular relevance to the overall design of the CQED 2.0 experiment, is a consideration of the transport mechanism that would enable a (near-)deterministic strong coupling of single atoms to the WGM. The intentional addition of a positionable high-NA lens inside the Science chamber (see Section 3.3.3) affords the possibility of generating an optical dipole trap situated inside the upper MOT, into which a single atom can be cooled, trapped, and detected. From there, a number of alternative methods for a controllable loading of the resonator surface trap are feasible. In the following, a speculative but critical qualitative discussion of these are presented. In order to complete the long-term vision for the operation of the CQED 2.0 experiment, a proposal for the trapping optics required for the most suitable envisioned transport mechanism is also subsequently outlined.

3.6.1 Loading Mechanisms

The location of the bottle microresonator is designed to be in the exact centre of the Science chamber. Accordingly, the in-vacuum lens is situated at a distance equal to its focal length ($f_l = 10$ mm) in front of the resonator, where its focus can be positioned to lie on the resonator surface through use of its mounted positioning system. Between the two resides the upper MOT, which contains a cleanly-produced source of cold ^{85}Rb atoms loaded from the lower MOT, wherefrom a single atom can be loaded into the optical dipole trap created by the lens when positioned inside the MOT cloud (see Figure 3.4 in Section 3.3.3). It is worth noting that, due to the close proximity of the upper MOT to the resonator, it is likely that single-atom coupling events would be achieved by simply releasing the cloud of laser-cooled atoms. By launching the cloud towards the resonator in a second AF-like stage*, the number of coupling events per release would be increased. In both of these cases, the dipole trap, positioned at the resonator surface, could be triggered upon each coupling event in following the trapping procedure demonstrated in CQED 1.0 [60]. Although the updated geometry in this scheme is favourable (i.e., atoms would be arriving in the WGM from the same side as the location of the trapping volume), which would allow for a comparatively improved trap loading efficiency, trapping such free-flying atoms would still be *probabilistic* in operation.

Afforded by the design of CQED 2.0, transporting a single optically trapped atom from free space to the resonator surface trap in a *deterministic* manner can potentially be attempted in a few different ways. By considering experimental demonstrations of (single-)atom optical transport in free space and towards dielectric structures from the literature, an evaluation of the method and its suitability for application in the CQED 2.0 apparatus can be performed. These are briefly presented in the following, organised in an ascending order of suitability. Figure 3.19 displays illustrations of each of these considered schemes, with 3.19(a) showing the starting point ingredients.

Optical conveyor [154, 221, 222]. By superimposing a second trapping beam counter-propagating to that created by the in-vacuum lens, a quasi-1D standing wave optical lattice along the shared beam-axis would be created due to an interference between the two beams, into which single atoms could be directly loaded from the upper MOT. In free-space, a mutual detuning of both beams axially moves the interference pattern. Atoms contained within the lattice can therefore be transported across macroscopic distances, while still remaining trapped. In this way, controlling the time-variation of the standing wave dipole trap allows for a precise movement of single

*In such a scheme, the horizontal plane cooling beams of the upper MOT that are directed towards the resonator from the front (back) side would be simultaneously blue(red)-detuned. By initially positioning the upper MOT slightly below the bottle microresonator, the vertical cooling beams could also be used to set the turning point of the ballistic flight at the resonator. See Section 3.4.4.

3. Experimental Design

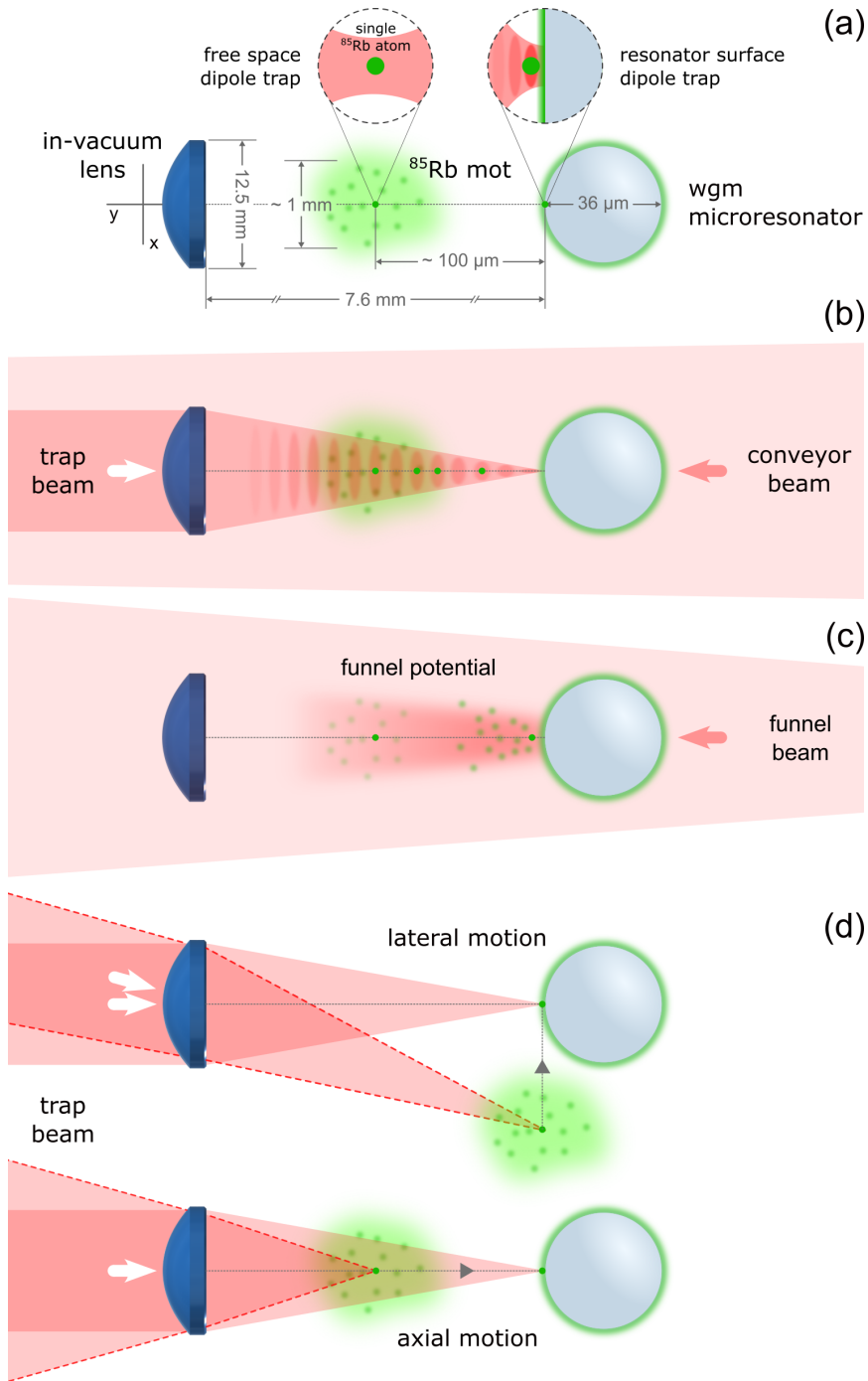


Figure 3.19. Proposed methods for single atom transport towards the resonator.

Figures *not-to-scale*: for illustrative purposes only. (a) A top-view of the fixed experimental setting, consisting of the in-vacuum lens at its focal length away from the resonator, with the prepared ^{85}Rb MOT situated between. A single atom must be brought from the MOT location to the resonator surface trap (insets). (b) A conveyor beam generates a standing wave lattice upon interference with the trap beam, in which single atoms can be loaded. Time-variation of the standing wave can transport lattice-trapped atoms towards the resonator. (c) A funnel beam, diffracting through the resonator, can generate a guiding potential towards its surface that features a strong transverse confinement in the near-field for atoms released from the MOT. (d) Transport based on a movable optical dipole trap. On the top (bottom), the trap position is swept transversally (axially) to the optical axis.

atoms, in a tool known as an *optical conveyor belt*. As illustrated in Figure 3.19(b), this technique could be employed to bring atoms out of the MOT region and towards the resonator. However, the second beam of the lattice would have to be focussed through the rear-most viewport of the 4-way cross behind the Science chamber (see Figure 3.16 for reference), as well as through the bottle microresonator fibre. While the optical access to the upper MOT from the rear (that was not available in CQED 1.0) enables its implementation, focussing through the resonator fibre would lead to beam distortions that disturb the interference pattern, potentially severely inhibiting a controlled transportation. Furthermore, it is paramount that interferometric stability between the counter-propagating lattice beams is maintained during such a transport, which would be experimentally challenging across the ~ 430 mm free-space separation between the front and rearmost viewports, even despite its designed-in minimisation.

Optical funnel [223]. In a scheme similar to the aforementioned optical conveyor technique, an *optical funnel* configuration can be realised by sending a far-off resonant red-detuned beam towards the MOT, again from the rear-direction, that is loosely focussed at the position of the resonator. As illustrated in Figure 3.19(c), this would generate a tapered guiding potential for atoms released from the MOT, that would then begin in motion towards the resonator. Within a few micrometres from its surface, the beam diffracted through the resonator could potentially create the funnel structure with a strong transverse confinement for a precise guiding to its surface. The addition of a slightly blue-detuned WGM would act as a method of detection for atoms as they arrive and couple to the resonator, while simultaneously acting to 'plug' the funnel by providing a repulsive barrier from the surface. Upon such a detection event, the nominal dipole trap positioned at the resonator surface, as created by the in-vacuum lens, could be activated to freeze-out the atomic motion in the axial direction. Here, single atoms initially inside the funnel would be loaded into various potential minima of the generated partial standing-wave dipole trap, where the atom that triggered the activation would have a high chance of being captured in the trap site closest to the surface. A successful transfer of the atom from the guiding funnel to the desired potential minimum of the retroreflected trap could be easily verified by a resonant probing of the atom via the resonator. An unsuccessful transfer would not necessitate to start over, as switching back to the funnel beam and blue-detuned WGM combination would again guide atoms that were captured in sites further away from the resonator towards its surface, for a re-try of the transfer into the desired trap site. Such a protocol for loading the resonator surface trap is near-deterministic, as it can be repeated multiple times upon each MOT-release phase until the atoms within the funnel have been exhausted.

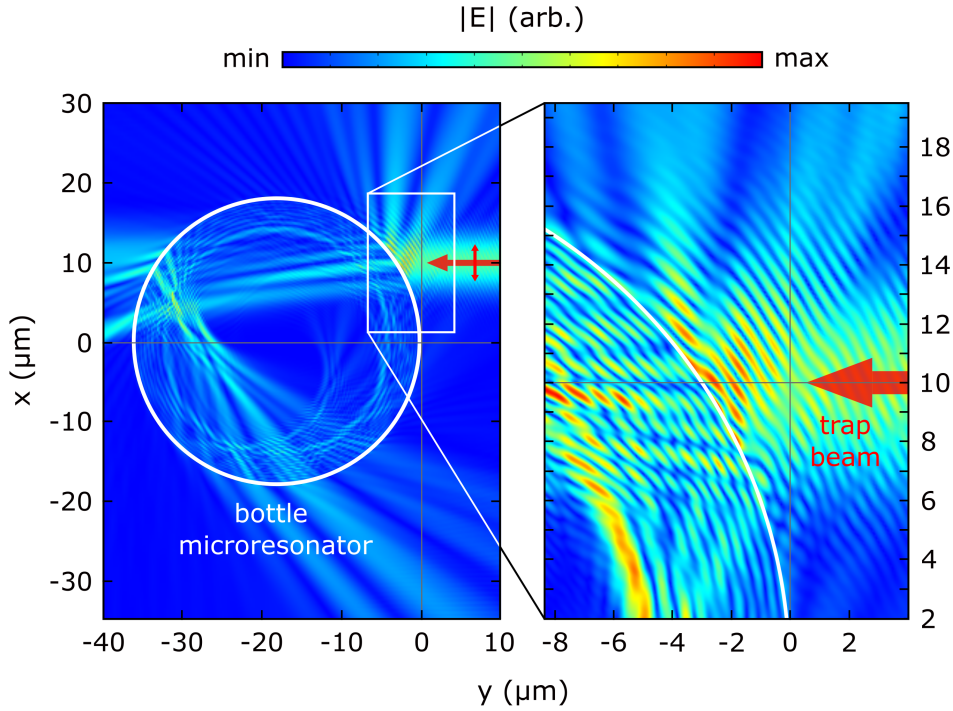


Figure 3.20. Simulation* of a transversally-displaced retroreflected trap beam. In this snapshot example, the incident Gaussian trapping beam is displaced by $10\ \mu\text{m}$ from the optical axis ($x = 0$), with its focus lying transverse to the extremity of the **WGM** microresonator's surface ($y = 0$). The plot on the right is a zoom on the boxed region displayed in the plot on the left. Chaotic interference appears to inhibit the maintenance of a stable trapping potential during transverse beam displacement.

Movable optical tweezer [80, 224, 225]. To reach a fully deterministic loading protocol, it is envisioned that a single atom captured in the dipole trap, loaded from the upper **MOT**, can be brought directly to the surface of the resonator by employing a *movable* optical tweezer. Two potential options for this scheme exist, as illustrated from top to bottom in Figure 3.19(d). The first involves a *lateral* sweeping of the focus position of the trapping beam along a path transverse to the lens' optical axis, which can be accomplished with use of an **Acousto-Optic Deflector** prior to the in-vacuum lens. However, the circular cross-sectional geometry of the bottle microresonator poses a particular challenge to the success of this method, where refraction of the beam as it impinges on the resonator – in combination with its multiple reflections – chaotically interferes with the incoming beam, resulting in an unstable trapping potential during the motion. Indeed, an initial simulated investigation* revealed that a closed trajectory between the free-space potential minimum to that of the surface trap, did not exist. Figure 3.20 displays a single setting of this investigation as an example, in which the incident trapping beam is transversally displaced by $10\ \mu\text{m}$ from the optical axis. The second, and more promising option, involves an *axial* motion of the focus position of the trapping beam along the optical axis of the in-vacuum lens, which is set to be

*Using the *COMSOL Multiphysics* software package.

normal to the resonator surface. While this could be performed by physically moving the focussing lens towards the resonator with use of its y -axis nanopositioner (as part of the full lens positioning system, see Section 3.3.3), such a slip-stick-based mechanical movement has the potential to introduce an unwanted resonant heating of the atom during the transport, and is also limited by the manufacturer-defined maximum velocity of 10 $\mu\text{m}/\text{ms}$. An alternative solution would be to tune the collimation of the trapping beam incident on the in-vacuum lens: by slightly (de)focussing, the position of the trap will be moved (further from) closer to the lens. This can be achieved with the addition of a so-called **Focus Tunable Lens (FTL)** as the last optical element before the in-vacuum lens, which would act to initially position the trap within the **MOT** in order to capture a single atom, before smoothly moving the occupied trap towards the resonator. However, as the focus position reaches the resonator, a build up in the contrast of the partial standing wave generated by the interference between the incident and back-reflected trap beams will inevitably occur. Transport of the atom in this way is therefore not subject to a completely uninhibited movement directly to the surface of the resonator, as the atom can remain trapped in a potential minimum that is located further away, where the coupling strength is negligibly low. A simple workaround to this undesired effect could be implemented in performing multiple back-and-forth movements of the trap position at the vicinity of the resonator surface, in order to continuously switch between a high-contrast and low-contrast standing wave trap. In this case, the trapped atom would be shuffled between the potential minima of the standing wave, with a net movement towards the resonator surface. This protocol could be repeated indefinitely (within the trapping lifetime) until the atom is detected via the resonator, where it can then be held in the surface trap.

A completely uninhibited transport using the trapping beam focussed on the resonator surface would necessitate its back-reflected beam to not give rise to high-contrast interference fringes. This would require a spatial dephasing between the two beams to occur on the scale of the trap extent, which cannot be achieved with the standard Gaussian intensity profile dipole trap that has so far been considered. A recent proposal [225] instead suggests the use of spatially structured light to generate the dipole trap [226–228], which can lead to both an improved atom-localisation by a reduction in the trapping volume, as well as an improved single-atom delivery to nanophotonic structures by a suppression of the interference fringe contrast. Here, the example of superpositions of purely radial Laguerre-Gauss beams feature a rapid spatial variation of the Guoy phase [229, 230] in the focal region, such that the input and reflected beams rapidly dephase to result in a suppression of both the contrast and spatial extent of near-field interference when compared to unstructured (Gaussian) light. This strategy can be combined with the aforementioned axially-translating optical tweezer using the **FTL**, promising a potential route towards deterministic delivery of single optically trapped atoms to the bottle microresonator. An investigation of this loading mechanism requires

3. Experimental Design

an additional optical element in order to generate the desired structured intensity profile in the trapping beam, for which a single **Spatial Light Modulator (SLM)** is suitable [231–233]. In the next Section, a route towards combining these techniques is proposed. Finally, to state an (extreme) long-term ambition that could be realised with the application of an **SLM**, would be the generation of multiple trapping sites [234, 235] – potentially enabling the simultaneous coupling of more than one atom to the bottle microresonator [236].

3.6.2 Envisioned Operation

Considering all of the potential methods for transport of a single optically trapped atom to the surface of the bottle microresonator, as explored in the previous Section, the most promising candidate involves an axially-movable and spatially-structured optical tweezer. The optics required for the generation of such a dipole trap must therefore combine an **FTL** for tuning the position of the trap, in conjunction with an **SLM** for imprinting a desired spatial intensity distribution. For its implementation and trial in the updated **CQED 2.0** apparatus, a number of practical additions to the optical set-up beyond these core elements must also be considered. These include additional beam paths for the purposes of; compensating for trap-induced light shifts by conversion to a dual-colour magic wavelength trap (see Section 2.4.3 in Chapter 2), probing and detecting single atoms inside the trap on either the D_1 or D_2 transitions, and transferral into a shorter-wavelength dipole trap to facilitate stronger coupling (see Section 3.7.5). Further to these, a method for inspecting the combination of all beam focii, alongside a positioning system to align the combined beam paths with respect to the resonator (via the in-vacuum lens), are also paramount to realise. The design of an optical assembly that incorporates all of these elements, importantly, must fit into the available space in front of the Science chamber (see Figure 3.17 for reference). A proposal for a set-up meeting these criteria is presented in Figure 3.21, which concludes the overall design considerations for the **CQED 2.0** experiment in its goal of deterministically delivering single optically trapped atoms to the **WGM** of the bottle microresonator. Note that this presented set-up functioned as a target when constructing the realised assembly used for single atom trapping and detecting as outlined in Section 5.1.1.

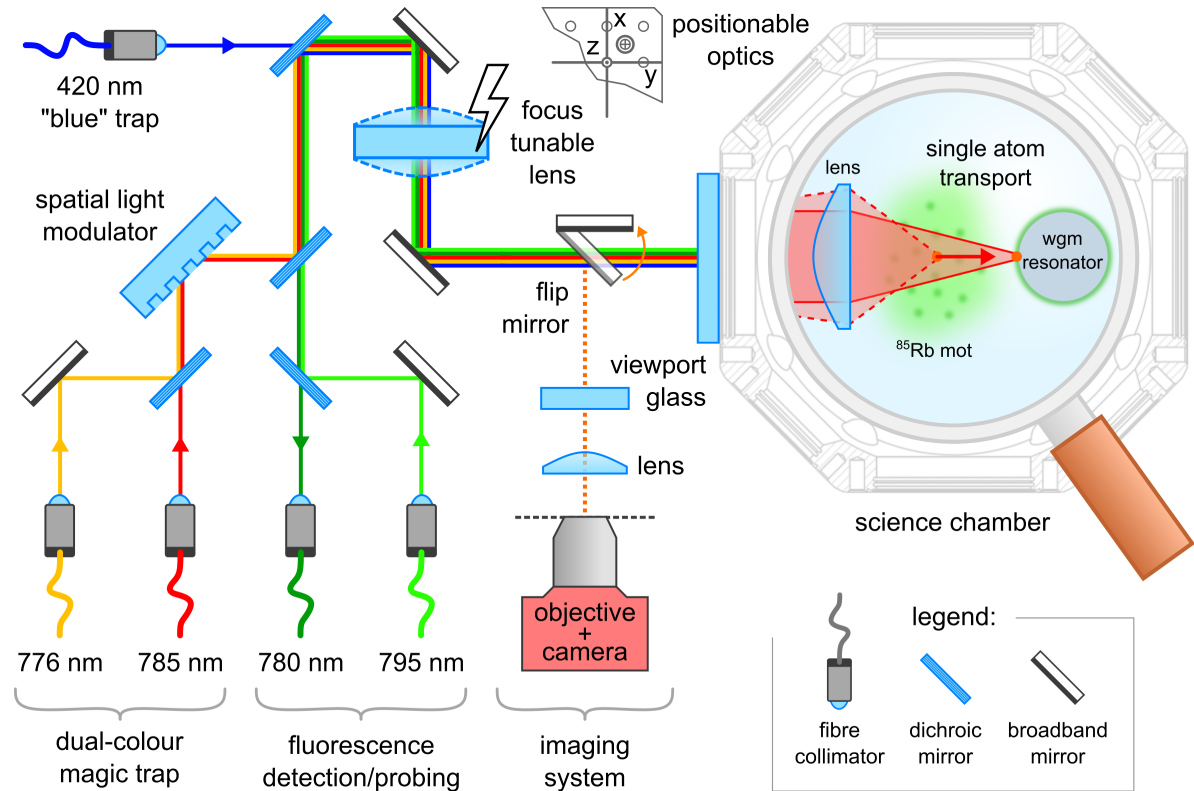


Figure 3.21. Envisioned trapping optics. A highly simplified schematic of the optical assembly required for axially transporting a single optically trapped atom, loaded from the upper MOT, to the surface of the WGM microresonator. This set-up combines beam paths for a dual-colour magic wavelength dipole trap, as well as for the fluorescence detection and probing of trapped atoms on both the D_1 and D_2 lines. The trapping beams pass via a Spatial Light Modulator for their spatial structuring, and all beams are sent through a vertically-oriented Focus Tunable Lens. The electrically-controlled FTL tunes the beam diameter incident on the in-vacuum lens, allowing to axially tune the focal position. Additional beam paths for a shorter wavelength dipole trap and an alignment arm are indicated. The entire set-up is affixed to a positionable optical breadboard for adjustment of the combined beam paths with respect to the in-vacuum lens. A zoom into the centre of the Science chamber illustrates the atom transport scheme.

3.7 Laser Systems

A narrow-band source of resonant coherent light is required for the study of optical interactions with a single atom (via the resonator). A semiconductor diode laser is the perfect candidate due to its coherence, tunability, stability, commercial availability, reliability and out-of-the-box ease of use. In actual fact, multiple laser systems are necessary in order to realise such studies: for the preparation, manipulation and probing of **Rubidium**, in addition to enabling stabilisation of the resonator frequency and its coupling fibre.

This Section provides documentation on all laser optical assemblies relevant to the **CQED** experiment, primarily for completeness, but also for reference with respect to the experiment presented in Chapter 5. Figure 2.2 in Chapter 2 (Section 2.1.1) schematically illustrates the ^{85}Rb transitions of interest along with a depiction of the associated laser lines. All laser set-ups are built upon aluminium breadboards to assist in stability and portability, which are, in turn, each affixed on an optical bench (*CleanTop series, AMETEK TMC*) for passive vibration isolation (see Section 3.3.4 for further details). For laser safety purposes, the optical bench is surrounded by a suspended enclosure, featuring openable panels manufactured from a suitable barrier material (*BM0M7P065PM1, laservision GmbH & Co. KG*). The enclosure doubles as a sealant for a humidity- and temperature-controlled microclimate* with a downwards laminar airflow (*TFM-Deckenmodul/600x900, Trox GmbH*), that ensures long-term stable operation of the laser systems and their optical assemblies. Note that a similar structure is used for the second optical bench that houses the main experimental set-up.

3.7.1 Cooling Laser

Currently available commercial laser sources offer powerful solutions to the modern experimentalists requirements. All twelve cooling beams for both the upper and lower ^{85}Rb MOTs are provided by a single **Tapered Amplifier (TA)** laser system in a so-called *master-slave* configuration, that has an output power of up to 2 W at a wavelength around 780 nm (*TA pro, TOPTICA Photonics AG*). It consists of an **External-Cavity Diode Laser (ECDL)** as the master that is frequency-stabilised to the $(5S_{1/2}, F = 3) \rightarrow (5P_{3/2}, F' = 3, 4)$ crossover transition of $^{85}\text{Rb}^\dagger$, which seeds the chip-based **TA** slave for amplification at the desired frequency. The stabilisation, based on **Frequency Modulation (FM)** of the master, is implemented with the use of a commercial Doppler-free absorption saturation spectroscopy unit (*CoSy, TEM Messtechnik GmbH*) that provides the spectroscopy signal from which the error signal for locking is generated

*Temperature stability < 0.1 °C, humidity stability < 2%.

†Chosen due to its strong absorption line.

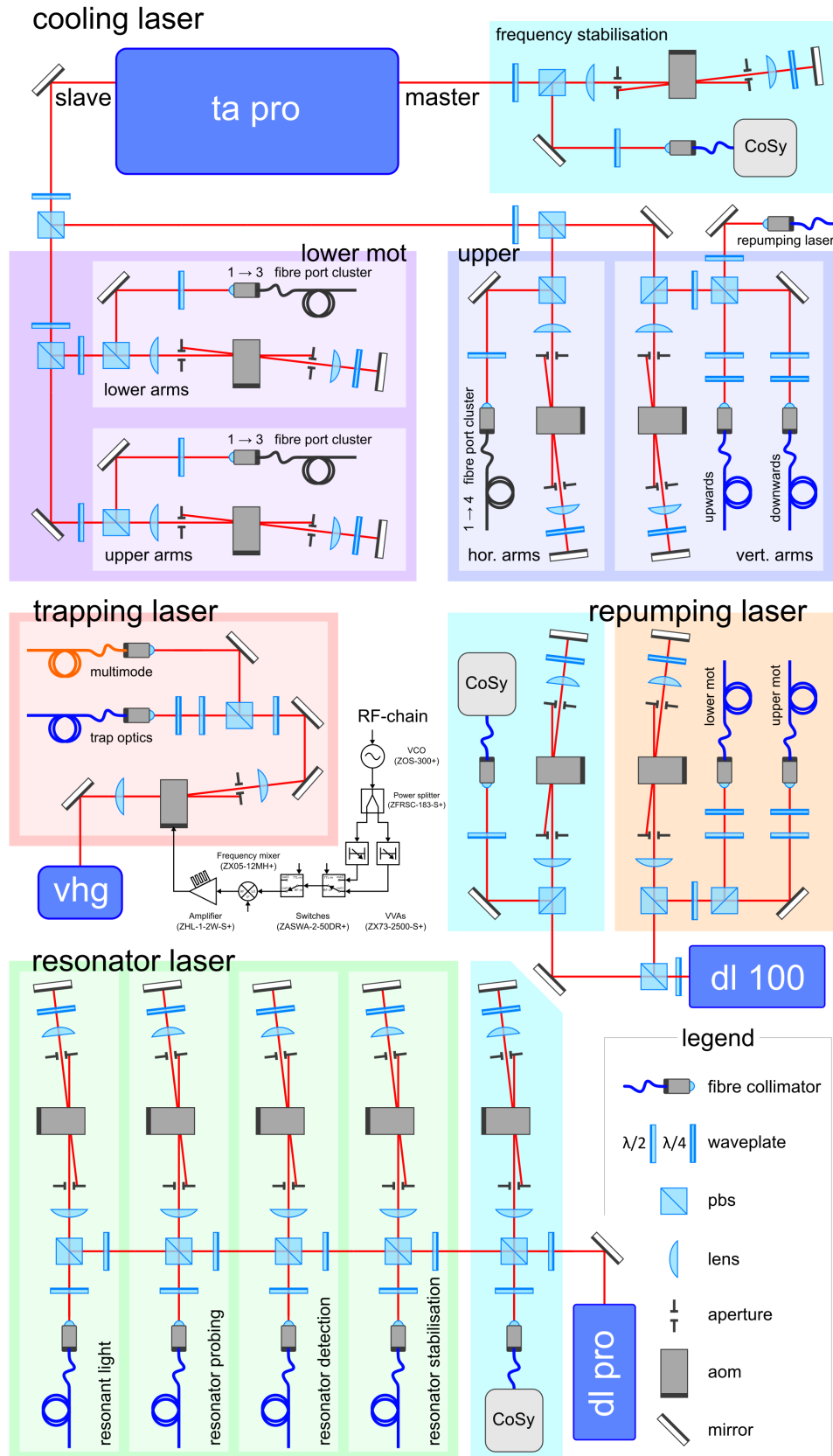


Figure 3.22. Simplified schematics of the main laser optical assemblies. Displayed clockwise from the top half: cooling laser (Section 3.7.1), repumping laser (Section 3.7.2), optical component legend, resonator laser (Section 3.7.3), trapping laser (Section 3.7.4). The sub-set-ups on each laser schematic are coloured for distinction – see the corresponding Sections for details. Note that for clarity, around only $\sim 60\%$ of the total optical elements required for proper beam path alignment are presented.

3. Experimental Design

[92]. The upper half of Figure 3.22 displays a simplified schematics of the full cooling laser system set-up. It consists of five similarly designed double-pass **Acousto-Optic Modulator (AOM)** set-ups: one for the frequency stabilisation of the master, and one for each beam set of the upper and lower **MOTs** that are coupled into **Polarisation Maintaining (PM)** fibres for distribution to the main experiment. These are highlighted in Figure 3.22 respectively with the colours: turquoise, blue and purple. The use of a double-pass **AOM** system allows for independent frequency and power adjustment of each of the individual beam sets by respectively changing the frequency and amplitude of the **RF**-signal supplied to each **AOM**, and features the major advantage of maintaining efficient fibre-coupling during frequency sweeps [237]. The power for each **AOM** set-up is adjusted by utilising a rotary **Half-Wave Plate (HWP)** and **Polarising Beamsplitter (PBS)** combination, enabling a precise control of power distribution without sacrificing beam path alignment. Minimisation of the entire optical assembly for the twelve **MOT** beams is made possible by the employment of modular optomechanical units – so-called *fibre port clusters* – each of which comprising a cascade of **HWPs**, **PBSs**, polarisers, and fibre-couplers in a rugged and compact housing that reliably splits the intensity of one **PM** fibre input equally into a number of output **PM** fibres. A $1 \rightarrow 3$ version is used for each of the lower and upper three beams of the lower **MOT**, while a $1 \rightarrow 4$ version is used for the four beams in the horizontal plane of the upper **MOT**. These fully **PM** fibre-coupled fibre port clusters also contain an internal photodiode that monitors a fraction of the input power, the signal of which can be used for intensity stabilisation by feedback onto the amplitude input of the corresponding **AOM** driver. The remaining two beams for the upper **MOT** along the vertical direction additionally have light from the repumping laser coupled into their **PM** guiding fibre, the source of which is presented in the next Section 3.7.2.

3.7.2 Repumping Laser

As outlined in Section 3.4.1, generation of a **MOT** for ^{85}Rb requires, in addition to light on the $F = 3 \rightarrow F' = 4$ cooling transition, light stabilised on the $F = 2 \rightarrow F' = 3$ transition of the D_2 line in order to prevent the accumulation of atoms in the dark state that cannot be addressed by the cooling lasers. For this, a dedicated grating-stabilised **ECDL** running at 780 nm is utilised (*DL 100, TOPTICA Photonics AG*). Its simplified optical assembly schematics is displayed on the middle-right of Figure 3.22, highlighted in orange. Similar to the set-up of the cooling laser, it consists of two **AOM** double-pass set-ups: one for frequency stabilisation and the other for fibre-coupled distribution to the main experiment. The frequency stabilisation here is performed with a side-of-fringe locking, whereby the spectroscopy signal itself, originating from a commercial Doppler-free absorption saturation spectroscopy unit (*CoSy, TEM Messtechnik GmbH*), serves as the error signal for feedback on the laser grating. The output of the distribution

set-up is split into two **PM** fibre-couplings. The first is guided to the Mot chamber, where it is directed at the intersection region of the cooling beams through a **DN16CF** viewport after expansion with a fibre collimator. The second is out-coupled into the beam path of the cooling laser set-up for the vertical beams of the upper **MOT**. In this way, the repumper can also be used for fluorescence detection during **Atomic Fountain** launch diagnostics or to enable more sophisticated launch schemes, see Section 3.4.4.

3.7.3 Resonator Laser

An **ECDL** (*DL pro*, *TOPTICA Photonics AG*) that is locked to the $(5S_{1/2}, F = 3) \rightarrow (5P_{3/2}, F' = 4)$ transition provides the light required for active stabilisation of the resonator. Light fields through which the single atoms can be detected via the resonator and then subsequently addressed and probed are also derived from this source. The lower half of Figure 3.22, highlighted in green, displays a simplified schematics of the set-up. Along with the previously introduced laser set-ups, the resonator laser optical assembly consists of a number of **AOM** double-pass set-ups for the independent manipulation of each required near-resonant light field. After the laser head output, the first **AOM** set-up is responsible for the laser locking with use of a commercial Doppler-free absorption saturation spectroscopy unit (*CoSy*, *TEM Messtechnik GmbH*) that provides the spectroscopy signal from which the error signal is generated. The second, third and fourth dispense fields used for resonator stabilisation, and detection and probing of atoms via the resonator, respectively. The fifth and final provides a source of resonant light for, e.g., alignment tasks. Each beam is coupled into a **PM** fibre for direction to the main experiment table.

3.7.4 Trapping Laser

The final main laser system is responsible for generation of the light used to create the optical dipole trap for a single atom, where a single-frequency operation with several milliwatts of output power is desirable. As such, the so-called *trapping* laser consists of a **Volume-Holographic-Grating (VHG)**-stabilised diode (*LD785-SEV300*, *Thorlabs, Inc.*) housed in a dedicated temperature-controlled mount (*LDM90/M with LDMXY*, *Thorlabs, Inc.*) which operates at a centre wavelength of 785 nm with a maximum output power of 300 mW. The **VHG** incorporated in the diode is manufactured to ensure that only the desired wavelength of light satisfying the Bragg condition is reflected back, resulting in a narrow-linewidth emission below 10 MHz and stable continuous wave operation. A simplified schematic of the optical assembly is shown on the middle-left of Figure 3.22 and is highlighted by the colour red. The diode's output is steered through an optical isolator before making a single pass through an **AOM**, where the -1^{st} diffraction order is coupled into a **PM** fibre for guiding to the trapping optics set-up in front of the Science chamber, see Section 5.1.1. The **RF**-signal supplied to the **AOM**

3. Experimental Design

originates from a dedicated chain of **RF**-components (*Mini-Circuits*[®]) that allows for, via control voltage and **TTL** inputs, a fast command over the power coupled into the output fibre. Its simplified scheme, where the individual components are labelled with their model names and numbers, is depicted alongside the trapping laser schematics of Figure 3.22. Importantly, the presence of the frequency mixer allows the **RF**-signal produced by the **VCO** to undergo a time-varying attenuation by application of a suitable temporal voltage, while the **RF**-switch allows for abrupt switching of the power on a fraction of a μs timescale. These available features are beneficial when characterising the optical trap (see Section 5.1.1), or when capturing free-falling atoms as in **CQED** 1.0.

3.7.5 Subordinate Laser Systems

In addition to the principal laser systems previously outlined, a number of others exist in the lab that have either already been used in the **CQED** 1.0 experiment, or plans for their near-future implementation within **CQED** 2.0 are in place. In the following, a brief overview of these subsidiary laser systems is provided in a chronological order.

Resonator Heating Laser This infrared (wavelength: 980 nm) laser diode (*RLT980-150GS*, *Roithner Lasertechnik GmbH*) has been successfully utilised to demonstrate the maintenance of a constant temperature – and therefore resonance condition – of the resonator, necessitated by the heating of the resonator from the tight focusing of a high-power trapping beam onto the resonator surface [70]. Importantly, due to its large detuning from both the D_1 and D_2 lines, along with its 'loose' focusing on the resonator of $\sim 50 \mu\text{m}$ waist, it applied negligible optical forces on the atoms and thus did not affect the detection and subsequent trapping of single atoms at the resonator surface [60]. Optical access, from a number of directions (see Section 3.3.5), is available for its direction at the resonator in **CQED** 2.0 should it be necessary. With implementation of the upgraded trapping scheme (compared to that of [60]), where single atoms are loaded from the upper **MOT** rather than being captured directly from free fall (see Section 3.6), trapped atoms will be a factor of roughly 10^3 colder even after a period of transportation from the **MOT** region towards the resonator. As such, the trap depth can be substantially lowered, thereby reducing the resonator heating effect and thus the stringency of its required compensation.

Light Shift Compensation Laser A widely tunable **ECDL** (*New Focus Velocity TLB-6700*, *Newport Corporation* – to be replaced by *DL pro*, *TOPTICA Photonics AG*) is frequency locked to the $5P_{3/2} \rightarrow 5D_{5/2}$ transition at a wavelength around 776 nm [70, 238, 239]. The presence of this laser alongside the dipole trap, in a mode-matched configuration (across the trapping volume), is paramount for the compensation of large position-dependent shifts of the atomic transition induced

by the trapping field, and realises a so-called *dual-colour magic-wavelength trap* [158]. The laser applies a strong and controllable light shift on the excited state of the trapped atom, while having a negligible effect on its ground state, and was imperative for bringing the trapped atoms back into resonance with the resonator to enable the successful demonstration of their strong coupling [60]. Due to this non-negligible trap-induced light shift, the new generation of trapping optics must factor in the use of this laser when coupling a single trapped atom to the resonator.

Blue Trapping Laser A long-term goal of the **CQED** experiment is to work with stably trapped atoms that are *strongly* coupled to a **WGM** of the bottle resonator. The trapping scheme successfully demonstrated in **CQED** 1.0 and improved upon in design for the upgraded experiment has the fundamental limitation that the trapping site closest to the resonator surface (i.e., the first intensity maximum of the partial standing wave built up by retroreflecting the trap beam from the surface) is located at a distance of approximately $\lambda_{trap}/4$ away, thereby fixing the coupling strength. As the **WGM** exponentially decays into free space, a reduction in the atom–resonator separation significantly enhances the coupling strength. This can be accomplished by reducing the wavelength of the trapping light field. For this purpose, an **ECDL** with a wavelength close to 420 nm (*DL pro*, *TOPTICA Photonics AG*) is available. This laser can be set red-detuned to the $5S \rightarrow 6P$ transition in order to realise an optical dipole trap. As such, the distance between the resonator surface and the trapped atom is roughly halved, and the coupling strength consequently increased by a factor of three or more. A prospective loading scheme for such a trap would be an adiabatic transfer of atoms between the two surface traps at the resonator: by simultaneously reducing the intensity of the 785 nm trapping field while ramping the intensity of the 420 nm trapping field. The design of the new trapping optics factors in the use of such a beam, which requires that the optical elements along with their anti-reflective coatings are designed to also work for shorter wavelengths than those of the typically used near-infrared versions.

D₁ Laser The latest addition to the ammunition of light for **Rubidium** is an **ECDL** for interrogation of atoms on the D₁ line, at a wavelength of 795 nm (*DL pro*, *TOPTICA Photonics AG*). Through use of a spectroscopy set-up in the same manner as for the master of the cooling laser (see Section 3.7.1), the laser is locked on the $5S_{1/2} \rightarrow 5P_{1/2}$ transition. In the experiment, this allows for resonance fluorescence collection at a wavelength well-separated from 780 nm, thereby providing an alternative atom detection method that may prove necessary when integrating the trapped atom with the resonator.

3.8 Control and Data Acquisition

As part of the overhaul work for the **CQED** experiment, an effort has gone into streamlining the experimental control, for which a brief note on this is included in the following. **CQED** 1.0 had a multilayered control system, foundationally consisting of a custom control software written in *LabWindows/CVI** that allowed for the playing of a pre-programmed sequence controlling the voltage output cycles of a pair of computer-interfaced **DAQ** cards with a timing resolution as low as $2\ \mu\text{s}$ [92]. The available total of twelve analogue and forty digital outputs controlled and triggered various devices in the lab during an experimental cycle. On top of this, the triggering of secondary and tertiary **FPGA**- and LabView-based control sequences that had to further communicate or interrupt the main cycle, dramatically increased the operational complexity and rendered the whole hierarchy error-prone. The opportunity to reform and simplify the working of the experimental control was therefore undertaken. The chosen control system, due to its successful employment in other adjacent labs in the group, is the *ADwin* hardware system (*ADwin-Pro II*, *Jäger Computergesteuerte Messtechnik GmbH*). A real-time **CPU** controls optional sub-systems that are housed in the modular structure, which allows for their interchange and extension. So far the lab control modules are a pair of digital **IO** cards each with $8\times$ digital **IOs**, an analogue **IO** card with $8\times$ analogue **IOs**, and a 32-bit counter card with $8\times$ **TTL** inputs. The software now includes a proven *python*-based user interface as a toplevel for the *ADbasic* home software [240], which operates on a dedicated *control* desktop computer. Most importantly, ADwin combines the possibility to play pre-programmed sequences with real-time reaction and control in the same operational system.

When running a typical experimental cycle, the main measurement signals are photons scattered by a single atom, which are then collected, relayed into different ports, and distributed to **Single Photon Counting Modules** (*Count-50N-FC*, *Laser Components GmbH*). For each detected photon, the **SPCM** produces a short electronic pulse of 3 V amplitude and ~ 15 ns duration that is sent to a dedicated *timetagging unit* based on an **FPGA** (*XEM3005*, *Opal Kelly, Inc.*), which assigns a timestamp to each rising edge it receives with a sub-nanosecond resolution. Each timetag consists of the channel number which registered the click, plus the absolute time of the click stored as a 32-bit number in picoseconds. All recorded data is continuously written to a binary file and saved locally on a dedicated *analysis* desktop computer for post-analysis. An advantage of the chosen **FPGA**-based timetagger is that it can be re-configured to suit a desired functionality based on a user-programmed software developed in *Vivado Design Suite* using the **HDL Verilog** (*AMD-Xilinx, Inc.*). In **CQED** 1.0 with free-falling atoms, this feature was heavily relied on to reduce the data volume, by saving only the photon

*This software has its origins in Professor Dr. Dieter Meschede's *Quantum Technologies* group (Institut für Angewandte Physik, Rheinische Friedrich-Wilhelms-Universität Bonn).

timestamps that lie within a window of $\pm 25 \mu\text{s}$ relative to an atom arrival event [92, 93, 136]. This time window was extended to several milliseconds when probing the atom–resonator system with trapped atoms [70], and so far for CQED 2.0 it has been left permanently running for recording of the resonance fluorescence of a continually loaded optical trap (see the measurements presented in Chapter 5).

3.9 Closing Remarks

This Chapter has extensively presented the re-design and upgrading of the entire experiment, from CQED 1.0 to CQED 2.0, along with accompanying justifications for each of the specified design choices. This included the vacuum hardware which houses the main experimental set-up: a WGM bottle microresonator evanescently coupled to two optical nanofibres, that can interface to strongly-coupled single atoms. Work towards realising the full potential of the set-up is ongoing, and will continue for some time to come. As such, the plan has been to design a somewhat future-proof experiment, which can be both robust in its operation and versatile in its exploration possibilities. Notable features in enabling the aforementioned, *a.k.a an insurance policy*, is the fact that the design of the Science chamber grants a relatively simple – and inexpensive* – replacement and/or re-upgrade of the coupling set-up. Isolation of the upper and lower pumping systems afforded by the gate valve within the Differential Pumping Tube allows for such maintenance work to be carried out with minimal complication. The introduction of a second MOT in the Science chamber to recapture atoms after the Atomic Fountain launch provides a new, and *cleanly*-produced, reservoir of cold atoms close to the resonator from which single atoms can be optically trapped and eventually transported to the resonator structure.

To return to the initial overarching goal of the redesign as outlined in Section 3.2: "CQED 2.0 should be able to perform all that CQED 1.0 could; *plus much more*" – the carefully thought-out plan, in practice, is beginning to come to fruition. In retaining all the capabilities of the 'old' experiment into the 'new', the research direction remains broadly unchanged[†], while the various improved-upon systems ensures the longevity of the set-up and opens new avenues to explore. The next remaining Chapters introduce a first application of the constructed set-up (in the absence of fibres), concerning the spectral filtering of fluorescence originating from a single optically trapped atom.

*All custom-designed mechanical mounting structures, including non-standard materials and finishes, could be manufactured for less than 1000 € in total (FACTUREE, *cwmk GmbH*).

[†]See the following Chapters for a minor detour in the research direction.

4

Theory of Selective Resonance Fluorescence

Resonance fluorescence is the *drosophila* of quantum optics.

E. Z. Casalengua, E. del Valle, and F. P. Laussy, 2023 [241]

The term *resonance fluorescence* has so-far not been explicitly defined, and yet its concept has permeated much of the work presented thus-far: it is the term used to describe the radiation originating from a single two-level quantum emitter, such as an isolated atom, that is driven by a monochromatic field at a frequency equal or close to the natural frequency of the emitter. As depicted in Figure 4.1, a portion of the scattered field can be collected and observed, revealing that it consists solely of antibunched single photons due to the saturable nature of the emitter and the associated single photon absorption and emission cycle. The setting of resonance fluorescence thereby constitutes the most fundamental process in quantum optics, which, on the one hand, is of great interest for the understanding and modelling of light–matter interaction at the quantum scale, while on the other, provides the mechanism for its technological prospects as a source of Fourier-limited single photons (for example). While these fundamental theoretical aspects date back to the origin of QED [21], its experimental implementations were delayed by only several decades, as the technological advances in coherent light sources, single emitter isolation, and the measurement of single photons became feasible. Modern experimental set-ups now readily utilise resonance fluorescence to generate single photons, which are themselves a highly sought-after resource for quantum technologies that take advantage of photonic qubits [15, 16, 242–245].

4. Theory of Selective Resonance Fluorescence

More recently, the setting of resonance fluorescence has garnered attention in the unexpected regime of multiphoton emission. Here, the distinctive single photon emission characteristic associated with resonance fluorescence is seen as the interplay between two types of multiphoton scattering processes – coherent and incoherent – that usually perfectly cancel to preserve the expected antibunched photon statistics. However, when selected and examined *individually*, each of these processes exhibit photon statistics fundamentally distinct from that of their combination. It is this notion that revives the setting of resonance fluorescence as providing further insight into the fundamental interaction of light with matter, while also providing novel routes towards the generation of highly non-classical light fields for state-of-the-art quantum technologies.

As such, this Chapter opens with a description of the historical developments of resonance fluorescence, followed by a selection of its models relevant to this work. The latter includes a visit of the semiclassical interaction between a quantised emitter and a classical field in the context of the *optical Bloch equations*, and how these give rise to the two components of the scattered field. A modification of the optical Bloch equations in order to quantise the field is also provided. By truncating the quantised coherent input field at the two-photon Fock state, the nature of these components at the two-photon level is highlighted. Following this, an introduction into the experimentally obtainable coherence functions of resonance fluorescence precedes a presentation of their modification by frequency filtering, the results of which conclude this Chapter in the theoretical demonstration of the simultaneity of two-photon scattering.

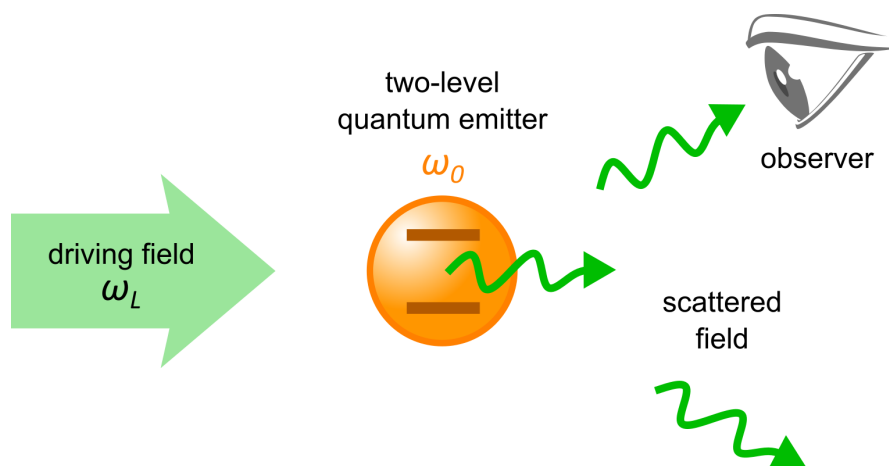


Figure 4.1. The setting of resonance fluorescence. Observation of the field scattered by a single two-level quantum emitter of resonance frequency ω_0 , driven by a monochromatic coherent light field at frequency $\omega_L = \omega_0 + \Delta$, where Δ denotes the detuning.

4.1 Historical Developments

A comprehensive detailing of the developments in describing the phenomenon of resonance fluorescence, including notable controversies along the way, can be found in [241] – much of the following description aligns with this presentation, while many of the mentioned topics will be expanded upon throughout the body of this Chapter.

The treatment of the resonance fluorescence problem unfolded somewhat backwards, in the sense that an initial quantum approach preceded a semiclassical one, in which the latter reigned superior in providing an accurate description until fully quantised models that incorporated multiphoton effects took precedence. Early theoretical developments included those of Weisskopf, who examined scattering off atomic ground and excited states [246, 247], and Heitler, whose analysis demonstrated that the radiation’s lineshape is determined by the driving source rather than the natural lineshape of the emitter [248]. Heitler further highlighted the role of two-photon processes in scattering, in that the atom *retains memory* of the absorbed quantum, before relaxing in a re-emission process. However, initial quantising at the one-photon level by Stroud [249] led to inaccurate predictions of the complex triplet structure that was observed in the spectrum of resonance fluorescence [250–252]. This so-called *Mollow triplet* gains its namesake from the pioneer of its successful theoretical description when using a semiclassical approach, in which the field was not quantised [253]. It pointed to the fact that for high-driving – the so-called *Mollow regime* – the triplet arises from nonlinear interactions whereby multiple degenerate photons from the drive are redistributed into different energies by the emitter. Mollow did, however, extend the (incorrect, as noted by Carmichael and Walls [254]) fully quantised model of Smithers and Freedhoff that had attempted to build on Stroud’s work [255] to include multiphoton contributions to the scattering, that ultimately resolved this QED method [256]. Following this, a perturbative scattering approach within the context of a new dressed-state picture of the atom was presented by Cohen-Tannoudji and co-workers [257–259]. These key contributions provided a framework indicating that fluorescence photons originate from a spontaneous emission cascade down the ladder of dressed-state eigenstates of the coupled atom–field system, accounting for the spectral lineshape of the Mollow triplet, and many of the correlations found to exist between the peaks. In particular, it intuitively explained the observation of bunched and time-ordered emission when cross correlating the well-separated side peaks of the triplet [260–262].

The study of the statistical properties of filtered light [263] has recently gained traction in the context of resonance fluorescence with frequency-resolved photon correlations [264–266]. This has led to a resurgence in the consideration of the two-level system as a multiphoton emitter, with the potential to tune the photon statistics of its emission conditioned on the disruption of interfering quantum amplitudes [267, 268]. Indeed, when removing the incoherently scattered light from the resonance fluorescence of a

two-level quantum dot by filtering [269, 270], the demonstrated loss of all correlations in the remaining coherently scattered light supports the view that antibunching – a two-photon observable – relies on the presence of incoherent emission. For extremely low driving strengths, deep in the so-called *Heitler regime*, the incoherent component vanishes in one-photon observables and yet *rules* the photon statistics [241].

The investigation of the incoherent component in the resonance fluorescence of a two-level atom undertaken here (presented in detail, together with the experimental results, in Chapter 5), follows along in this vein, adding to the experimental confirmation in the theoretical consideration that antibunching can be viewed as an interference phenomenon between coherent and incoherent two-photon scattering processes. It thereby contributes to the rich history in the understanding of the problem of resonance fluorescence, and paves the way for the technological harnessing of the demonstrated effect.

4.2 Semiclassical Light–Matter Interaction

In the following, the phenomenon of resonance fluorescence is introduced in a manner not entirely dissimilar to that of the Jaynes-Cummings model outlined in Chapter 2 (Section 2.2.4) in a CQED setting. As before, a density matrix for the two-level atom is defined, in addition to an interaction Hamiltonian, where instead here the light field is classically defined. This will enable for a construction of the optical Bloch equations, which provide time-dependent expressions for the amplitudes of the atomic states and coherences of the excitation process. Further examination of the scattered field can illustrate the spectral properties of resonance fluorescence for different regimes of optical driving strengths.

Again, the two-level atom is characterised as consisting of a ground and excited state, $|g\rangle = \begin{pmatrix} 0 \\ 1 \end{pmatrix}$ and $|e\rangle = \begin{pmatrix} 1 \\ 0 \end{pmatrix}$ respectively, which are both eigenstates of the free atomic Hamiltonian and separated by an energy $\hbar\omega_A$. As such, the time evolution of the free atomic state is a coherent superposition of these basis states as

$$|\psi(t)\rangle = c_g(t) |g\rangle + c_e(t) |e\rangle, \quad (4.1)$$

and is normalised with

$$|c_g|^2 + |c_e|^2 = 1 \quad (4.2)$$

where c_g and c_e carry all the time dependence of the atomic state, that are to be determined*. The density matrix of the atom is given by

$$\begin{aligned}\hat{\rho} &= |\psi\rangle\langle\psi| \\ &= \rho_{gg} |g\rangle\langle g| + \rho_{ge} |g\rangle\langle e| + \rho_{eg} |e\rangle\langle g| + \rho_{ee} |e\rangle\langle e| = \begin{pmatrix} \rho_{gg} & \rho_{ge} \\ \rho_{eg} & \rho_{ee} \end{pmatrix},\end{aligned}\quad (4.3)$$

with these matrix elements defined by

$$\rho_{gg} = c_g^* c_g, \quad \rho_{ee} = c_e^* c_e, \quad \rho_{ge} = c_g^* c_e, \quad \rho_{eg} = \rho_{ge}^*, \quad \text{and} \quad \rho_{gg} + \rho_{ee} = 1. \quad (4.4)$$

The diagonal elements are known as *populations*, and give the probability for finding the atom in either the ground or excited state, while the off-diagonal elements are referred to as *coherences*, and describe the ensemble-averaged optical dipole and provide information on the relative phase between each atomic basis state.

The temporal evolution of these coefficients result from solving the Schrödinger equation for the two-level system interacting with the classical field of frequency ω_L , $i\hbar\partial_t |\psi\rangle = \hat{H} |\psi\rangle$, where $\hat{H} = \hat{H}_A - \mathbf{d} \cdot \mathbf{E}(t)$. Both \hat{H}_A and $\mathbf{E}(t)$ have previously been defined in Chapter 2 (equations (2.25) and (2.34) respectively), within the context of a fully quantum or fully classical treatment of the light–matter interaction. The Schrödinger equation then reads

$$\partial_t c_g |g\rangle + \partial_t c_e |e\rangle = -i\omega_A c_e |e\rangle - i\frac{\Omega}{2} e^{i\omega_L t} c_e |g\rangle - i\frac{\Omega}{2} e^{-i\omega_L t} c_g |e\rangle, \quad (4.5)$$

which, upon projecting with $\langle g|$ and $\langle e|$, results in a pair of coupled differential equations of the form

$$\begin{aligned}\partial_t c_g &= i\frac{\Omega_0}{2} e^{i\Delta t} c_e \\ \partial_t c_e &= i\frac{\Omega_0}{2} e^{-i\Delta t} c_g.\end{aligned}\quad (4.6)$$

By absorbing the time-dependence (i.e., defining $\tilde{c}_g = c_g e^{-i\Delta t}$ and $\tilde{c}_e = c_e e^{i\Delta t}$), this pair can be written in a compact matrix notation as

$$\begin{pmatrix} \partial_t \tilde{c}_g \\ \partial_t \tilde{c}_e \end{pmatrix} = \frac{i}{2} \begin{pmatrix} -\Delta & \Omega_0 \\ \Omega_0 & \Delta \end{pmatrix} \begin{pmatrix} \tilde{c}_g \\ \tilde{c}_e \end{pmatrix}. \quad (4.7)$$

In order to reach this result, the rotating-wave approximation has been applied which eliminates the fast oscillating sum-frequency terms that contribute negligibly to the dynamics. Here, the Rabi frequency $\Omega_0 = \frac{E_0}{\hbar} d_{ge}$ is introduced, that contains the dipole matrix element d_{ge} that is the projection of the transition dipole moment along the field direction \mathbf{E} .

*Note that the damping effect of spontaneous emission will be included phenomenologically, by inserting additional terms into the equations of motion that govern the atomic state evolution

4. Theory of Selective Resonance Fluorescence

By combining equations (4.4) and (4.7), with the phenomenological introduction of damping terms to account for spontaneous emission from the excited state that decays at a rate γ (with the coherences decaying at a rate $\gamma/2$), the *optical Bloch equations* can be constructed as

$$\begin{aligned}
 \partial_t \rho_{gg} &= i \frac{\Omega_0}{2} (\tilde{\rho}_{ge}^* - \tilde{\rho}_{ge}) + \gamma \rho_{ee} \\
 \partial_t \rho_{ee} &= i \frac{\Omega_0}{2} (\tilde{\rho}_{ge} - \tilde{\rho}_{ge}^*) - \gamma \rho_{ee} \\
 \partial_t \tilde{\rho}_{ge} &= i \frac{\Omega_0}{2} (\rho_{ee} - \rho_{gg}) - \left(\frac{\gamma}{2} + i\Delta \right) \tilde{\rho}_{ge} \\
 \partial_t \tilde{\rho}_{eg} &= i \frac{\Omega_0}{2} (\rho_{ee} - \rho_{gg}) - \left(\frac{\gamma}{2} - i\Delta \right) \tilde{\rho}_{eg}.
 \end{aligned} \tag{4.8}$$

They fully describe the temporal dynamics of the ground and excited state amplitudes, and coherences, of the two-level atom driven by a near-resonant excitation field, including the effect of spontaneous emission. An atom driven in this way will cycle between its two states at a rate of Ω_0 and emit a photon every time it decays. This emission can occur either spontaneously, or by stimulated emission back into the mode of the driving field. It is now conducive to solve the optical Bloch equations depending on the excitation strength of the driving field, in order to view the temporal behaviour of both the populations ρ_{gg} and ρ_{ee} and the coherences $\tilde{\rho}_{ge}$ and $\tilde{\rho}_{eg}$.

A starting point is to consider the dynamics for long timescales (i.e., $t \rightarrow \infty \gg 1/\gamma$), where the driven atom has reached a dynamic equilibrium with the excitation field. In this so-called *steady-state* case, the time derivatives of the density matrix elements are all zero, and the optical Bloch equations (4.8) can be solved by setting the left-hand-sides to zero. In doing so, the expressions

$$\rho_{ee}^{(ss)} = \frac{1}{2} \frac{S}{1+S}, \tag{4.9}$$

$$\rho_{gg}^{(ss)} = 1 - \rho_{ee}^{(ss)}, \tag{4.10}$$

$$\tilde{\rho}_{eg}^{(ss)} = \frac{i}{2} \frac{\sqrt{S}}{1+S} \frac{\gamma}{\Omega_0} \left(1 + \frac{2i\Delta}{\gamma} \right), \tag{4.11}$$

are obtained, where the *saturation parameter* $S = \frac{2\Omega_0^2/\gamma^2}{1+4\Delta^2/\gamma^2}$ has been introduced to give these compact solutions. By their inspection, it can be seen that the excitation linearly increases with S until saturating around $S = 1$. For much larger values of S , the limiting value of $\rho_{ee} \rightarrow 1/2$ is reached, corresponding to an equal probability for the atom to be in either of its two states. The coherence, on the other hand, scales with \sqrt{S} for small excitations and slowly reaches zero as $S \rightarrow \infty$. This is illustrated in Figure 4.2(a), which plots these steady-state solutions to the optical Bloch equations as a function of S . Spontaneous emission from the excited state randomises the atomic dipole, preventing inversion of the population in the steady-state. The rate of spontaneously emitted

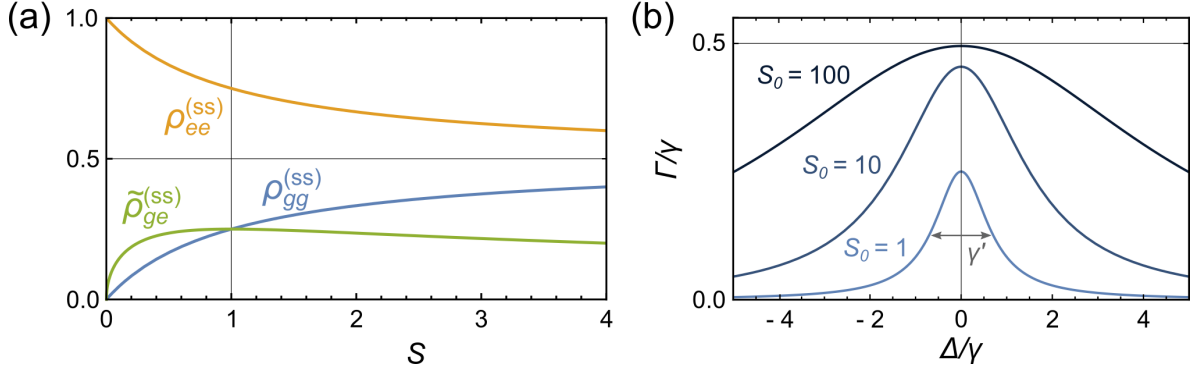


Figure 4.2. Steady-state solutions of the optical Bloch equations. (a) Plots of $\rho_{ee}^{(ss)}$, $\rho_{gg}^{(ss)}$, and $\tilde{\rho}_{ge}^{(ss)}$ as a function of the saturation parameter S , according to equations (4.9), (4.10), and (4.11) respectively. (b) The photon scattering rate $\Gamma/\gamma = \rho_{ee}^{(ss)}$ according to equation (4.12), for different values of the on-resonance saturation parameter S_0 , features a Lorentzian lineshape with a **FWHM** of $\gamma' = \gamma\sqrt{1+S_0}$.

photons for a given S is simply the product of the excited state population with the decay rate, as

$$\Gamma = \gamma\rho_{ee}^{(ss)} = \frac{\gamma}{2} \frac{S_0}{1 + S_0 + 4\Delta^2/\gamma^2}, \quad (4.12)$$

where the *on-resonance saturation parameter* $S_0 = S(\Delta = 0) = 2(\Omega_0/\gamma)^2$ has been introduced. This has the form of a Lorentzian lineshape with detuning, where the **FWHM** given by $\gamma' = \gamma\sqrt{1+S_0}$ is dependent on both the driving strength and decay rate. In the limiting case of low excitation, where $\Omega_0 \ll \gamma$, the system is Fourier limited and the linewidth is fundamentally lifetime limited with $\gamma' \approx \gamma = 1/\tau$. As the driving strength is increased, so too does the linewidth, in an effect known as *power broadening* of the transition. This occurs due to the fact that the scattering rate near resonance is limited by saturation. Again, a maximum scattering rate of $\gamma/2$ is obtained at resonance as $S_0 \rightarrow \infty$, which is expected for a saturated atom. These considerations are illustrated in Figure 4.2(b), which displays the scattering rate in units of γ around resonance, for different values of S_0 .

While the steady-state solutions to the optical Bloch equations highlight a few important properties of the continuously driven system across longer timescales, the transient dynamics occurring at short timescales are of particular interest for a full understanding of resonance fluorescence. The optical Bloch equations given by (4.8) are a set of closed differential equations, for which general solutions of the temporal populations $\rho_{ii}(t)$ and coherences $\rho_{ij}(t)$ are difficult to obtain. The problem can be simplified to some extent by employing the *Laplace transform* method, which transforms differential equations into algebraic ones via

$$\mathcal{L}[\dot{\rho}_{ij}](s) = s\tilde{\rho}_{ij}(s) - \rho_{ij}(0), \quad (4.13)$$

4. Theory of Selective Resonance Fluorescence

where $\tilde{\rho}_{ij}(s) = \mathcal{L}[\rho_{ij}](s)$ is the Laplace transform of the matrix element ρ_{ij} , and the dot-notation has been adopted for the time-derivative. By considering the exemplary case of an atom initiated in its ground state, and under exact resonance of the driving field, $\Delta = 0$, the Laplace transform of the excited state population assumes the form [82]

$$\tilde{\rho}_{ee}(s) = \frac{\Omega_0^2}{2s \left(s^2 + \frac{3}{2}\gamma s + \frac{3}{2}\gamma^2 + \Omega_0^2 \right)}, \quad (4.14)$$

which has the three solutions s_j . It can therefore be expressed as the sum of three fractions

$$\tilde{\rho}_{ee}(s) = \Omega_0^2 \sum_{j=1}^3 \frac{1/\prod_{i \neq j=1}^3 (s_j - s_i)}{s - s_j}. \quad (4.15)$$

In this latter form, the inverse Laplace transform

$$\mathcal{L}^{-1} \left[\sum_i \frac{c_i}{s - s_i} \right] (t) = \sum_i c_i e^{s_i t}, \quad (4.16)$$

can be applied to obtain the corresponding expression in the time domain, $\rho_{ee}(t)$. By inserting the values for s_j and c_j , simplifying the terms, and repeating this procedure for the coherences, the final expressions

$$\rho_{ee}(t) = \frac{\Omega_0^2}{\gamma^2 + 2\Omega_0^2} \left[1 - \frac{p+q}{2q} e^{-(p-q)t} + \frac{p-q}{2q} e^{-(p+q)t} \right] \quad (4.17)$$

$$\rho_{ge}(t) = \frac{i\gamma\Omega_0}{\gamma^2 + 2\Omega_0^2} \left[1 + \frac{d-q}{2q} e^{-(p-q)t} - \frac{d+q}{2q} e^{-(p+q)t} \right] \quad (4.18)$$

are reached. Here, the substitutions

$$\begin{aligned} p &= \frac{3}{4}\gamma \\ q &= i\sqrt{\Omega_0^2 - \left(\frac{\gamma}{2}\right)^2} \\ d &= \frac{\Omega_0^2}{\gamma} - \frac{\gamma}{4} \end{aligned} \quad (4.19)$$

simplify these time-dependent solutions. A consistency check reveals that in the limit of $t \rightarrow \infty$, the expressions (4.17) and (4.18) match the respective steady-state solutions of (4.9) and (4.11) for the case of zero detuning where $S(\Delta = 0) = S_0$. By utilising Euler's formula, the exponentials in equation (4.17) can be expressed in terms of sine and cosine functions, which leads to

$$\rho_{ee}(t) = \frac{1}{2} \frac{S_0}{1 + S_0} \left[1 - e^{-\frac{3}{4}\gamma t} \left(\cos \left(\frac{\gamma}{2} \sqrt{2S_0 - 1} t \right) + \frac{3}{2\sqrt{2S_0 - 1}} \sin \left(\frac{\gamma}{2} \sqrt{2S_0 - 1} t \right) \right) \right]. \quad (4.20)$$

Figure 4.3 illustrates the population difference making use of this result, for different values of S_0 . In all cases, it is evident that the long-time behaviour reaches an equilibrium and again approaches equal populations of the two atomic states for large driving as expected from the steady-state analysis. While at low driving the equilibrium is exponentially reached, an oscillatory behaviour in the population emerges at shorter timescales as the driving is increased, resulting from the coherent field driving Rabi oscillations that outweigh the damping. This is evident from the form of $\rho_{ee}(t) \sim 1/\gamma$ in equation (4.20), where the arguments of the sine and cosine functions take the form $\Omega't$ with $\Omega' = \sqrt{\Omega_0^2 - (\gamma/2)^2}$ identified as the *modified Rabi frequency*. These are damped by the multiplicative exponential term with a time constant proportional to $1/\gamma$.

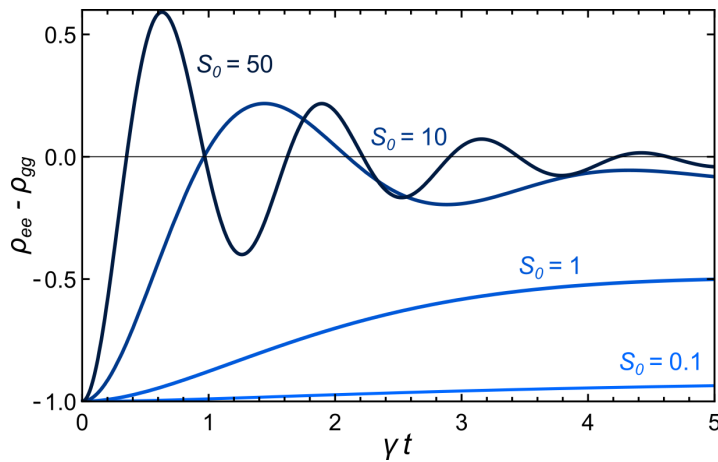


Figure 4.3. Time-dependent solutions of the optical Bloch equations for exact resonance. A plot of the time-dependent population difference, $\rho_{ee}(t) - \rho_{gg}(t)$ in units of γt , according to equation (4.20). When increasing the value of the on-resonance saturation parameter S_0 , oscillatory behaviour emerges as Rabi cycles compete with damping.

The same method of employing Laplace transforms, as previously outlined for the case of exact resonance, can also be performed for the detuned case where $\Delta \neq 0$. Doing so results in an expression for $\rho_{ee}^{(\Delta)}(t)$ adopting a form similar to that presented for resonance in equation (4.20), i.e., a summation of sine and cosine functions that is multiplied by an exponential damping term. The pre-factors and arguments of each are all Δ -dependent, and far too cumbersome to include here (see [271, 272] instead, for example, that provide analytic solutions of the optical Bloch equations for arbitrary $\{\Omega, \Delta\} \neq 0$). Still, Figure 4.4 illustrates the resulting population behaviour for a given driving strength of $S = 10$ and different non-zero detunings using the result of this method. In general, it is evident that faster Rabi oscillations with a smaller amplitude are driven as the value of detuning is increased, and occur close to the *generalised Rabi frequency* of $\Omega = \sqrt{\Omega_0^2 + \Delta^2 - (\gamma/2)^2}$. Similarly, the excited state population decreases until the driving field is too far from resonance with the atom, at which point excitation no longer occurs at all.

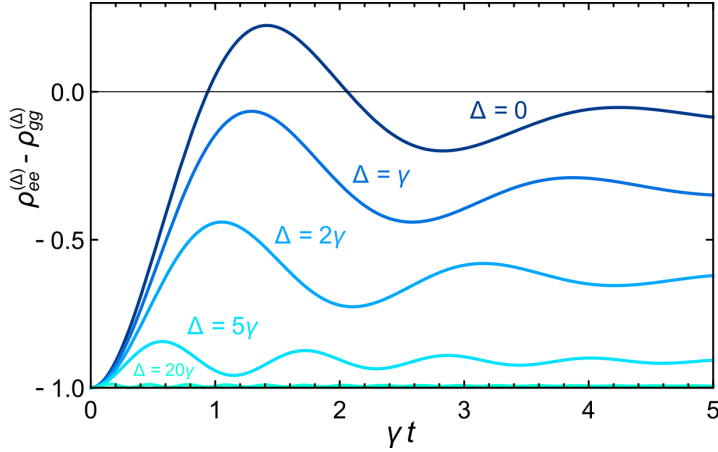


Figure 4.4. General time-dependent solutions of the optical Bloch equations.

A plot of the time-dependent population difference, $\rho_{ee}^{(\Delta)}(t) - \rho_{gg}^{(\Delta)}(t)$ in units of γt , for a fixed $S = 10$. When increasing the detuning of the driving field Δ , the probability of excitation decreases and faster oscillations, close to the detuning-dependent generalised Rabi frequency, occur.

The parameter regimes that are typically used for illustrating the dynamics described by the optical Bloch equations are exact resonance ($\Delta = 0$) or strong driving ($\Omega \gg \gamma$), as the solutions significantly simplify under these conditions [273]. The situation corresponding to a large and detuned driving ($\Delta \neq 0$ and $S > 1$) was described above, although the complicated general solutions [271, 272] were only used to produce Figure 4.4 and have not been explicitly included. These solutions do, however, somewhat simplify once more in the final case to consider: that of a weak and detuned drive ($\Delta \neq 0$ and $S \ll 1$). Here, the assumption of $|\Delta| \gg \Omega_0$ can be exploited such that $\Omega \approx \Delta$, yielding a simplified expression for the excited state population as

$$\rho_{ee}^{(S \ll 1)}(t) \approx \frac{1}{2} + \frac{S(\gamma^2 + 4\Delta^2)}{S\gamma^2 + 4(2+S)\Delta^2} \left(1 + e^{-\gamma t} + e^{-\frac{1}{2}\gamma t} \cos(\Delta t)\right). \quad (4.21)$$

Figure 4.5 displays the time-dependent population difference according to the above equation, for a fixed saturation parameter of $S = 0.01$ and different values of detuning. The behaviour is similar to the previously considered detuned but high-driving case (see Figure 4.4), in that Rabi oscillations are present and the excitation probability decreases as the detuning is increased. However, the oscillations now occur at the frequency $\sim \Delta$, and the overall population in the excited state is close to zero, even for small detunings, which results from driving in the very weak excitation regime.

The discussion of resonance fluorescence thus far using the optical Bloch equations formalism allows for the internal temporal dynamics of a two-level atom, coherently driven near resonance, to be fully described. In order to relate how the field scattered by the atom is related to its internal dynamics, the discussion is continued in the next Section with an introduction to correlation functions. These are an invaluable tool in

the analysis of the scattered field, from which arises information about the spectrum of the fluorescence and its photon statistics. The latter is of particular importance as an experimentally measurable quantity.

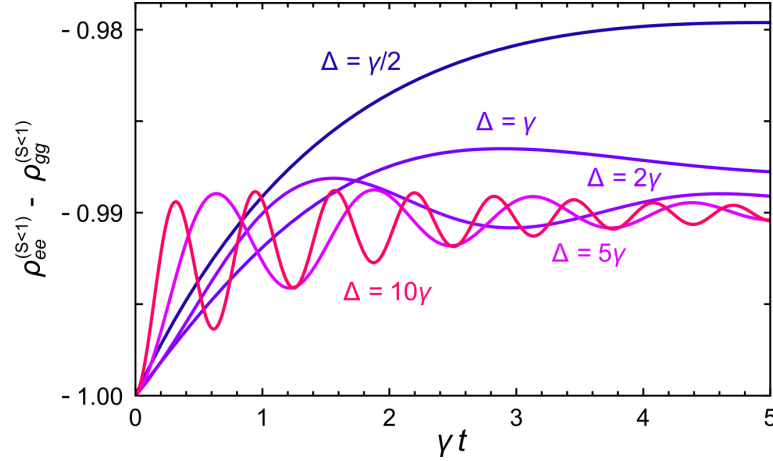


Figure 4.5. Time-dependent solutions of the optical Bloch equations for a low and detuned drive. A plot of the time-dependent population difference, $\rho_{ee}^{(S<1)}(t) - \rho_{gg}^{(S<1)}(t)$ in units of γt , for a weak drive of $S = 0.01$. When increasing the detuning of the driving field Δ , the probability of excitation decreases and oscillations at the frequency Δ occur. Note the scale of the y -axis, that indicates a low excitation probability independent of the detuning value, since $S \ll 1$.

4.3 The Scattered Field

The properties of the field scattered by a two-level atom provide a direct signature of the non-classical nature of resonance fluorescence. They are a direct consequence of the emitter being modelled as a saturable absorber with one level of excitation, in that, a photon is only emitted upon decay from the excited state to the ground state. The probability of this emission is therefore proportional to the probability of the excited state occupation, i.e., ρ_{ee} that was introduced in the last Section. Furthermore, successive emission events must be separated in time by an absorption event [256], which gives rise to so-called *antibunched* statistics of the single photons comprising the scattered field. This is a purely quantum phenomenon, which requires quantisation of the field in order to be fully described. This is tackled in the following.

Returning to the formalism of open quantum systems within the Born-Markov approximation [129] as introduced in Chapter 2 for the context of CQED with the WGM bottle microresonator, the electric field can be written in terms of the operators of the external reservoir as

$$E(\mathbf{r}, t) = i \sum_k \hat{\epsilon}_k e^{i\mathbf{k}\cdot\mathbf{r}} \sqrt{\frac{\hbar\omega_k}{2\varepsilon_0 V}} a_k(t), \quad (4.22)$$

4. Theory of Selective Resonance Fluorescence

where the reservoir is assumed to be in a vacuum state of the quantum electromagnetic field. Here, $a_k^{(\dagger)}$ is the annihilation (creation) operator for a photon mode in the reservoir of wave-vector \mathbf{k} , frequency ω_k and polarisation mode of $\hat{\epsilon}_k$. These field modes are coupled to the atom via the reservoir, and undergo evolution according to the Heisenberg equations of motion

$$\dot{a}_k = -i\omega_k a_k - i\zeta_k^* \sigma_-, \quad (4.23)$$

where $\sigma_- = |g\rangle\langle e|$ ($\sigma_+ = |e\rangle\langle g|$) is the Pauli matrix operator for atomic raising (lowering), that is coupled to the field modes defined by the constant

$$\zeta_k = -ie^{i\mathbf{k}\cdot\mathbf{r}_0} \sqrt{\frac{\omega_k}{2\hbar\epsilon_0 V}} \epsilon_k \cdot \mathbf{d} \quad (4.24)$$

with \mathbf{r}_0 the position of the atom and \mathbf{d} its dipole moment. Equation (4.23) can then be solved as

$$\tilde{a}_k(t) = a_k(0) - i\zeta_k^* \int_0^t dt' \tilde{\sigma}_-(t') e^{i(\omega_k - \omega_0)t'} \quad (4.25)$$

where $\tilde{a}_k = a_k e^{i\omega_k t}$ and $\tilde{\sigma}_- = \sigma_- e^{i\omega_0 t}$ have been defined. By inserting the above result into equation (4.22) that describes the quantised field, it is clear that it takes the form of $E(\mathbf{r}, t) = E_f + E_s$, with each of the two components corresponding respectively to the evolution of the *free* and *scattered* fields. In order to isolate the portion of the field that arises due to scattering from the two-level atom, consider the first- and second-order correlation functions,

$$G^{(1)}(t, t + \tau) = \langle E^\dagger(t) E(t + \tau) \rangle \quad (4.26)$$

$$G^{(2)}(t, t + \tau) = \langle E^\dagger(t) E^\dagger(t + \tau) E(t + \tau) E(t) \rangle, \quad (4.27)$$

which respectively characterise field–field and intensity–intensity correlations at two times t and τ . Due to the statistical averaging over the empty reservoir, denoted by $\langle \dots \rangle$, the free field portion E_f does not affect these correlation functions as the average photon number $a_k^\dagger(0)a_k(0) = 0$. With this in mind, and in the steady-state where the total field is in equilibrium with the dipole, the expressions for $G^{(1)}(t, t + \tau)$ and $G^{(2)}(t, t + \tau)$ of the scattered field become

$$G^{(1)}(\tau) = \langle \sigma_+(0) \sigma_-(\tau) \rangle \quad (4.28)$$

$$G^{(2)}(\tau) = \langle \sigma_+(0) \sigma_+(\tau) \sigma_-(\tau) \sigma_-(0) \rangle \quad (4.29)$$

where the limit of $t \rightarrow \infty$ has been adopted in order to consider τ as the only variable. Importantly, these two equations relate the dipole operators governing the dynamics of the two-level atom to the operators of the scattered field, where evaluating the expectation values of the former provide information on the latter.

By recalling the elements of the atomic density matrix as defined in (4.4), the expectation values of the dipole operators are then

$$\langle \sigma_- \rangle = \tilde{\rho}_{eg} \quad (4.30)$$

$$\langle \sigma_+ \rangle = \tilde{\rho}_{ge} \quad (4.31)$$

$$\langle \sigma_z \rangle = \rho_{ee} - \rho_{gg} \quad (4.32)$$

with σ_z introduced as the population difference. The on-resonance solutions of the optical Bloch equations given by (4.17) and (4.18) can then be employed to write

$$\langle \sigma_z \rangle = -\frac{\gamma^2}{\gamma^2 + 2\Omega_0^2} \left(1 + \frac{2\Omega_0^2}{\gamma^2} \left(\frac{p+q}{2q} e^{-(p-q)t} - \frac{p-q}{2q} e^{-(p+q)t} \right) \right), \quad (4.33)$$

with the notation p and q assuming the definitions as per (4.19). With this, the first order correlation function (4.28) can be evaluated by

$$G^{(1)}(\tau) = \langle \langle \sigma_+ \rangle_{ss} \langle \sigma_- \rangle_{ss} \rangle + \langle \delta\sigma_+(0) \delta\sigma_-(\tau) \rangle, \quad (4.34)$$

where the Pauli matrices have been decomposed into fluctuations around their steady-state values as $\sigma_i = \langle \sigma_i \rangle_{ss} + \delta\sigma_i$. The first term of equation (4.34) can be straightforwardly obtained using equation (4.11), while the second term requires employment of the *quantum regression theorem* to evaluate [274, 275].

In brief, when starting from a master equation of the form $\dot{\rho} = \mathcal{L}\rho$ that describes a system weakly interacting with a reservoir (cf. equation (2.30)), the quantum regression theorem states the equivalence of equations of motion for the expectation values of system operators and their correlation functions, thereby providing a method for computing the two-time correlator of interest, as [129]

$$\frac{d}{d\tau} \langle \delta\sigma_+(0) \delta\sigma(\tau) \rangle = \mathcal{M} \langle \delta\sigma_+(0) \delta\sigma(\tau) \rangle \quad (4.35)$$

with

$$\mathcal{M} = \begin{bmatrix} -\gamma/2 & 0 & -i\Omega_0/2 \\ 0 & -\gamma/2 & i\Omega_0/2 \\ -i\Omega_0 & i\Omega_0 & -\gamma \end{bmatrix} \quad (4.36)$$

being the evolution matrix relevant to the on-resonance resonance fluorescence problem [82]. The vector $\delta\sigma$ has the fluctuations of each of the three Pauli matrices as its components, that is,

$$\sigma = \langle \sigma \rangle_{ss} + \delta\sigma \quad (4.37)$$

with

$$\langle \boldsymbol{\sigma} \rangle_{ss} = \begin{bmatrix} -\frac{i\Omega_0\gamma}{\gamma^2+2\Omega_0^2} \\ \frac{i\Omega_0\gamma}{\gamma^2+2\Omega_0^2} \\ -\frac{\gamma^2}{\gamma^2+2\Omega_0^2} \end{bmatrix}, \quad (4.38)$$

$$\boldsymbol{\delta\sigma} = \begin{bmatrix} \delta\sigma_- \\ \delta\sigma_+ \\ \delta\sigma_z \end{bmatrix}.$$

The solution for equation (4.35) is obtained by diagonalisation of the matrix \mathcal{M} , which can be achieved using $(\Lambda^T)^{-1} \mathcal{M} \Lambda^T = \boldsymbol{\lambda}$, for which Λ is a matrix composed of the eigenvectors of \mathcal{M} , and $\boldsymbol{\lambda}$ is the diagonal matrix containing the eigenvalues of \mathcal{M} . Then

$$\frac{d}{d\tau} (\Lambda^T)^{-1} \langle \delta\sigma_+(0) \boldsymbol{\delta\sigma}(\tau) \rangle = \left((\Lambda^T)^{-1} \mathcal{M} \Lambda^T \right) (\Lambda^T) \langle \delta\sigma_+(0) \boldsymbol{\delta\sigma}(\tau) \rangle, \quad (4.39)$$

from which it follows that

$$\langle \delta\sigma_+(0) \boldsymbol{\delta\sigma}(\tau) \rangle = \Lambda^T e^{\boldsymbol{\lambda}\tau} (\Lambda^T)^{-1} \langle \delta\sigma_+ \boldsymbol{\delta\sigma} \rangle_{ss}. \quad (4.40)$$

The right-hand-side can be calculated from the steady-state solutions to the optical Bloch equations given in equations (4.9)–(4.11). In matrix notation, it is given by [129]

$$\begin{aligned} \langle \delta\sigma_+ \boldsymbol{\delta\sigma} \rangle_{ss} &= \begin{bmatrix} \langle \sigma_+ \sigma_- \rangle_{ss} - \langle \sigma_+ \rangle_{ss} \langle \sigma_- \rangle_{ss} \\ \langle \sigma_+ \sigma_+ \rangle_{ss} - \langle \sigma_+ \rangle_{ss}^2 \\ \langle \sigma_+ \sigma_z \rangle_{ss} - \langle \sigma_+ \rangle_{ss} \langle \sigma_z \rangle_{ss} \end{bmatrix} \\ &= \begin{bmatrix} \frac{1}{2}(1 + \langle \sigma_z \rangle_{ss}) - \langle \sigma_+ \rangle_{ss} \langle \sigma_- \rangle_{ss} \\ -\langle \sigma_+ \rangle_{ss}^2 \\ -\langle \sigma_+ \rangle_{ss}(1 + \langle \sigma_z \rangle_{ss}) \end{bmatrix} \\ &= \left(\frac{\Omega_0}{\gamma^2 + 2\Omega_0^2} \right)^2 \begin{bmatrix} 2\Omega_0^2 - \gamma^2/2 \\ \gamma^2 \\ 2i\gamma\Omega_0 \end{bmatrix}, \end{aligned} \quad (4.41)$$

where the relations $\sigma_{\pm}\sigma_{\mp} = \frac{1}{2}(1 \pm \sigma_z)$ and $\sigma_{\pm}\sigma_z = \mp\sigma_{\pm}$ have been used.

Insertion of the above equation (4.41) into equation (4.40), together with the results of equation (4.37), allows construction of $G^{(1)}(\tau)$ as defined by equation (4.28). In doing so, the final expression describing the on-resonance *first-order correlation function for resonance fluorescence* reads

$$G^{(1)}(\tau) = \left(\frac{\gamma}{\Omega_0} \tilde{\rho}_{ge}^{(ss)} \right)^2 + \frac{\tilde{\rho}_{ge}^{(ss)}}{4} e^{-\frac{\gamma}{2}\tau} + C_+ e^{-(p-q)\tau} + C_- e^{-(p+q)\tau}, \quad (4.42)$$

with the coefficients C_+ and C_- given by

$$C_{\pm} = \gamma \left(\frac{\tilde{\rho}_{ge}^{(ss)}}{4\Omega_0} \right)^2 \left(2 \pm \frac{\gamma}{2q} \right) (d \mp q) \quad (4.43)$$

and $\{p, q, d\}$ assuming the definitions provided in equation (4.19). This expression can be easily grouped into two contributions that are either dependent or independent of τ as

$$G^{(1)}(\tau) = G_{\text{coh}}^{(1)} + G_{\text{inc}}^{(1)}(\tau) \quad (4.44)$$

where the subscripts of the first and second terms respectively stand for *coherent* and *incoherent*. These labels are chosen to reflect the fact that these contributions to the first-order correlation function arise from two different scattering processes – *coherent scattering* and *incoherent scattering* – which will be the topic of discussion in the following Section.

4.3.1 Coherent and Incoherent Scattering

In making use of the quantum regression theorem to obtain an explicit expression for the first-order correlation function of resonance fluorescence (performed for the exemplary case of zero detuning), the dipole operator $\hat{\sigma}$ was expanded as the sum of the average dipole in the steady-state, $\langle \hat{\sigma} \rangle$, and its instantaneous difference from the average value, $\delta\hat{\sigma}$, such that $\delta\hat{\sigma} = \hat{\sigma} - \langle \hat{\sigma} \rangle$. The $G^{(1)}(\tau)$ recorded in equation (4.42), that describes the field scattered by a two-level quantum emitter under resonant excitation, can thus be decomposed into two parts: consisting of a coherent and an incoherent contribution, that are each labelled as such to reflect their respective ability and inability to interfere with the driving field. The first term, $G_{\text{coh}}^{(1)}$, arises from the averaged dipole, that oscillates in phase with the driving to thereby emit a correlated field. The first-order correlation function therefore always decays to a τ -independent finite value for long times. The fluctuating part of the dipole, on the other hand, represents the nonlinear response of the two-level emitter to the field, and is responsible for the second τ -dependent term in equation (4.44), $G_{\text{inc}}^{(1)}(\tau)$. These two scattering processes can be further examined by considering the spectrum of resonance fluorescence $\mathcal{S}(\omega_s)$, which can be directly obtained from the Fourier transform of $G^{(1)}(\tau)$ via the *Wiener-Khintchine theorem* [276]. Doing so, using equation (4.42), inevitably leads to a spectrum which is also separated into contributions from these two coherent and incoherent scattering processes as

$$\mathcal{S}(\omega) = \mathcal{S}_{\text{coh}}(\omega) + \mathcal{S}_{\text{inc}}(\omega_s), \quad (4.45)$$

4. Theory of Selective Resonance Fluorescence

where,

$$\mathcal{S}_{\text{coh}}(\omega_s) = \frac{1}{2\pi} \int_{-\infty}^{\infty} G_{\text{coh}}^{(1)} e^{i(\omega_s - \omega_L)\tau} d\tau \quad (4.46)$$

$$= \frac{1}{2\pi} \left(\frac{\gamma}{\Omega_0} \rho_{ee}^{(\text{ss})} \right)^2 \delta(\omega_s - \omega_L) \quad (4.47)$$

and

$$\mathcal{S}_{\text{inc}}(\omega_s) = \frac{1}{2\pi} \int_{-\infty}^{\infty} G_{\text{inc}}^{(1)}(\tau) e^{i(\omega_s - \omega_L)\tau} d\tau \quad (4.48)$$

$$\begin{aligned} &= \frac{1}{4\pi} \frac{\gamma}{(\omega_s - \omega_L)^2 + (\gamma/2)^2} \\ &+ \frac{\gamma}{16\pi} \frac{3\Omega'(\Omega_0^2 - \gamma^2/2) + (5\Omega_0^2 - \gamma^2/2)(\omega_s - \omega_L + \Omega')}{\Omega'(\Omega_0^2 + \gamma^2/2) ((\omega_s - \omega_L + \Omega')^2 + (3\gamma/4)^2)} \\ &+ \frac{\gamma}{16\pi} \frac{3\Omega'(\Omega_0^2 - \gamma^2/2) - (5\Omega_0^2 - \gamma^2/2)(\omega_s - \omega_L - \Omega')}{\Omega'(\Omega_0^2 + \gamma^2/2) ((\omega_s - \omega_L - \Omega')^2 + (3\gamma/4)^2)}. \end{aligned} \quad (4.49)$$

The above result can be generalised to the case of non-zero detuning [253, 277, 278], and somewhat compactified by expressing in terms of the saturation parameter, to yield

$$\mathcal{S}_{\text{coh}}(\omega_s) = \frac{S}{2\pi(1+S)^2} \delta(\omega_s - \omega_L) \quad (4.50)$$

and

$$\begin{aligned} \mathcal{S}_{\text{inc}}(\omega_s) &= \frac{S_0}{8\pi\gamma} \frac{S}{1+S} \\ &\times \frac{1 + \frac{S_0}{4} + \left(\frac{\omega_s - \omega_L}{\gamma}\right)^2}{\left[\frac{1}{4} + \frac{S_0}{4} + \left(\frac{\Delta}{\gamma}\right)^2 - 2\left(\frac{\omega_s - \omega_L}{\gamma}\right)^2 \right]^2 + \left(\frac{\omega_s - \omega_L}{\gamma}\right)^2 \left[\frac{5}{4} + \frac{S_0}{2} + \left(\frac{\Delta}{\gamma}\right)^2 - \left(\frac{\omega_s - \omega_L}{\gamma}\right)^2 \right]^2}. \end{aligned} \quad (4.51)$$

As seen in both equation (4.47) and (4.50), the coherent part of the scattered spectrum consists of a perfectly defined spectral peak located at the driving frequency $\omega_s = \omega_L$, defined by the δ -function. This result is not surprising, as the Fourier transform of the constant "dc" term of $G^{(1)}(\tau)$ leads to a delta function in frequency space. The incoherent part of the spectrum, as seen in equation (4.49) and (4.51), instead has a more complicated structure and comprises a triplet set of approximately Lorentzian peaks. That is, it is spread over a range of frequencies, with the central peak spectrally located at $\omega_s = \omega_L$ and the satellite peaks surrounding it being separated by the generalised Rabi frequency of Ω , with each located at $\omega_s = \omega_L \pm \Omega^*$. The **FWHM** of the central incoherent peak is γ , while that of the side peaks is $3/2\gamma$. The side peaks have a third of the height with respect to the central. Figure 4.6(a) illustrates this spectral character of

*For the case of zero detuning, $\Delta = 0$, the separation is given by the modified Rabi frequency Ω' .

the emission for the case of resonance ($\Delta = 0$), and further showcases the behaviour of the incoherent triplet with respect to the driving strength in Figure 4.6(b). For vanishing driving strengths, the coherent scattering process dominates and the emission spectrum retains the spectral profile of the excitation light (assumed monochromatic). As the driving strength increases, but remains small such that $\Omega_0 \ll \gamma$ and Ω' is imaginary, the incoherent scattering process takes place and all components are centred at the resonance frequency. The incoherent process dominates with driving beyond this weak-field limit, and the side peaks separate from the central line by an amount corresponding to the modified Rabi frequency $\Omega' \approx \Omega_0$. Integrating across the spectrum reveals that half of the total power is contained in the central peak, while the remaining half is equally shared between the two side peaks.

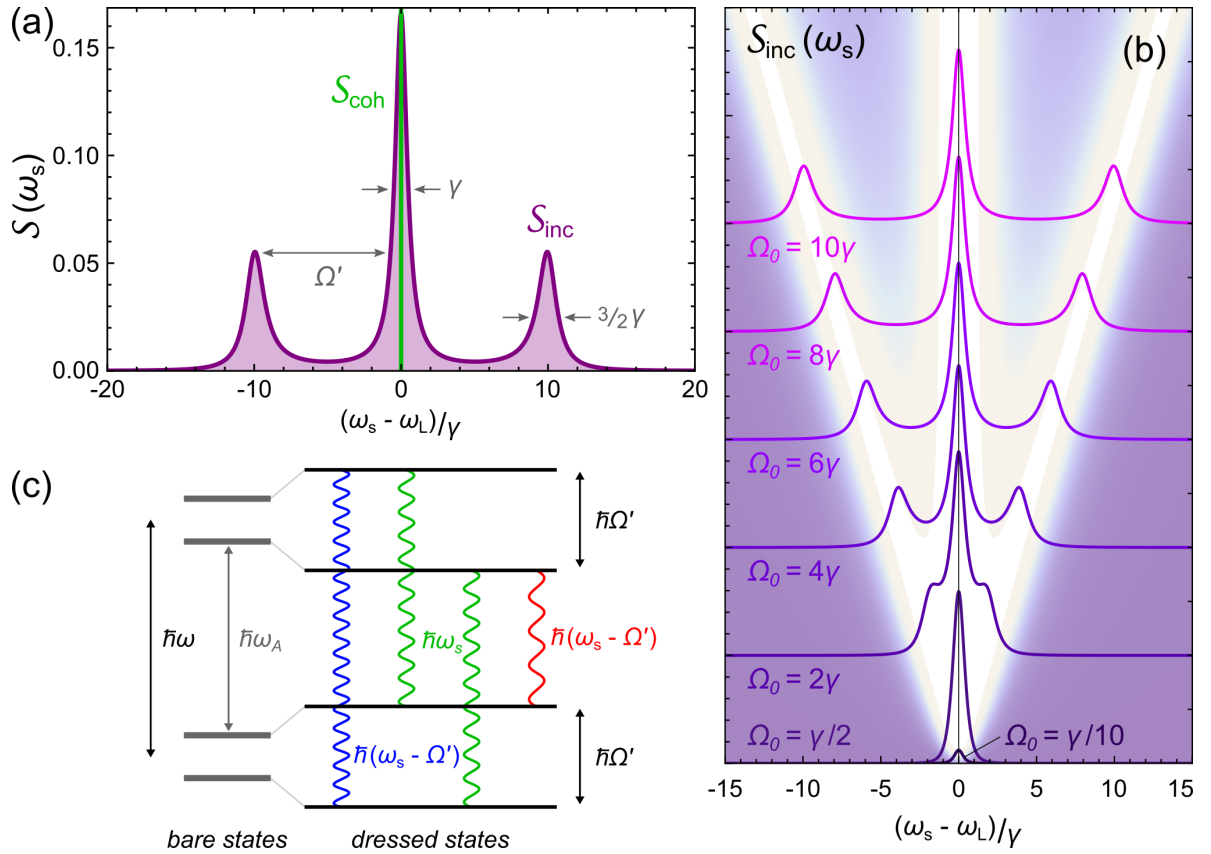


Figure 4.6. The Mollow triplet in resonance fluorescence. (a) An example of the characteristic emission spectrum resulting from equation (4.45), showcasing the three distinct Lorentzian peaks of the incoherent component that are centred with the δ -like coherent component at the driving frequency $\omega_s = \omega_L$ ($\Delta = 0$). The relative peak heights and FWHM of the incoherent triplet are respectively 1:3:1 and 3:2:3, where the sidebands are each separated from the centre by an amount given by the modified Rabi frequency Ω' . (b) The evolution of the incoherent component according to equation (4.49) with $\Delta = 0$, plotted as a function of the resonant driving strength $S_0 = 2\Omega_0^2/\gamma^2$. As the excitation increases, the triplet structure emerges and spectrally broadens. (c) A simplified schematic of the light-dressed atomic states that illustrate the fluorescence cascade down the dressed-state ladder, giving rise to the Mollow triplet spectrum.

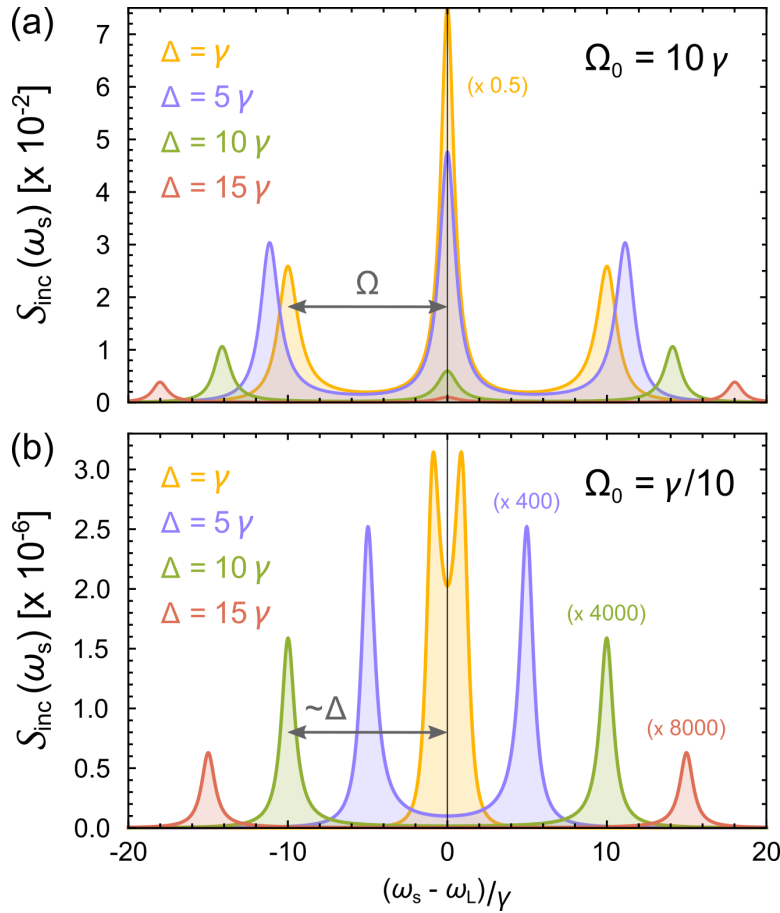


Figure 4.7. The detuned Mollow triplet. (a) The case of high driving, $S_0 = 200$, for different detunings Δ (see colour-coded key). The triplet structure is visible throughout, with the side peaks separated from the central peak by the generalised Rabi frequency, $\Omega \approx \sqrt{\Omega_0^2 + \Delta^2}$. The saturation parameter for each value of detuning, $\Delta/\gamma = \{1, 5, 10, 15\}$, is respectively given by $S = \{40, 2, 0.5, 0.2\}$. (b) The case of low driving, $S_0 = 0.02$, for different detunings Δ (see colour-coded key). The central peak is suppressed compared to the high driving (or resonant) case, and the side peaks are separated from the driving frequency by $\Omega \approx |\Delta|$. The saturation parameter for each value of detuning is now given by $S = \{40, 2, 0.5, 0.2\} \times 10^{-4}$. In both (a) and (b), some of the curves have been scaled for visibility purposes and indicated where applicable.

For the off-resonance case ($\Delta \neq 0$), a few special scenarios can be illustratively described. In the case of large detuning or driving ($\Delta \vee \Omega_0 \gg \gamma$), the splitting between the peaks is given by the (reduced) generalised Rabi frequency $\Omega \approx \sqrt{\Omega_0^2 + \Delta^2}$. In the case of large detuning and weak excitation ($|\Delta| \gg \Omega_0$), the splitting is now approximately given by the detuning Δ . Correspondingly, the vanishingly small central peak lies at the laser frequency ω_L along with the delta-peak of the coherent component, with the sidebands spectrally located at $\omega_s = \omega_L \pm \Delta$. Figure 4.7 displays the described behaviour of the detuned triplet spectrum in the limits of strong and weak driving strengths, respectively in 4.7(a) and 4.7(b). In both cases, the spectra are centred about the laser frequency, at which both the coherent delta peak and incoherent central peak lie. The latter reduces in amplitude as the detuning is increased, and is vanishingly small in the

regime of weak driving. This is highlighted in the particular scenario of when the driving is weak and the detuning large, where the triplet structure of the incoherent component appears to reduce to a doublet of separation $2|\Delta|$. Figure 4.7 further illustrates that in general, the spectral density (height of the peaks) increases with driving strength and/or closer to resonance. In the limit of low driving, the central peak height is proportional to $(1 + S_0)S^3$ and the side peak heights to S^2 .

As mentioned in Section 4.1, the triplet structure of the incoherent emission was first described by Mollow [253], and so is commonly referred to as the *Mollow triplet* of resonance fluorescence. As the excited state population – and therefore the emission probability – is modulated by Rabi oscillations, this triplet spectrum can thus be understood qualitatively as that of a driven oscillator featuring sidebands that are displaced from the carrier by the modulation frequency. In the dressed-state picture [257, 276], the spectrum can alternatively be intuitively understood as an emission cascade down the ladder of light-dressed atomic states. In this picture, as illustrated in Figure 4.6(c), each atomic bare state is split into two dressed states that have an energy spacing proportional to the Rabi frequency. In this case, three possible decay channels are present in the dressed atom eigenstates, that map to the spectral distribution of the Mollow triplet frequencies.

Returning to equation (4.12) that introduced the total scattering rate as the product of the excited state population in the steady-state with the amplitude decay rate, it is now possible to consider what fraction of coherent to incoherent scattering makes up this rate. Again, the total scattering rate $R_{\text{sc}}^{(\text{tot})}$ as a function of S is given by

$$R_{\text{sc}}^{(\text{tot})} = \gamma \rho_{ee}^{(\text{ss})} = \frac{\gamma}{2} \frac{S}{1 + S}, \quad (4.52)$$

the coherent portion of which reads

$$R_{\text{sc}}^{(\text{coh})} = \gamma \left| \tilde{\rho}_{ge}^{(\text{ss})} \right|^2 = \frac{\gamma}{2} \frac{S}{(1 + S)^2}. \quad (4.53)$$

The incoherent portion is thus the remaining difference given by

$$R_{\text{sc}}^{(\text{inc})} = R_{\text{sc}}^{(\text{tot})} - R_{\text{sc}}^{(\text{coh})} = \frac{\gamma}{2} \frac{S^2}{(1 + S)^2} \quad (4.54)$$

with

$$\frac{R_{\text{sc}}^{(\text{inc})}}{R_{\text{sc}}^{(\text{coh})}} = S. \quad (4.55)$$

Figure 4.8 displays the behaviour of these two components of the total scattering rate against the driving strength characterised by S . The coherent contribution to the scattering process is dominated by the incoherent contribution as the saturation parameter exceeds unity. A zoom on the low saturation regime for $S < 0.25$ highlights

4. Theory of Selective Resonance Fluorescence

the linear growth of the coherent component with the drive, while the incoherent component grows quadratically instead. It demonstrates that for vanishing S , the coherent scattering is the prevalent process and indicates why the contribution from the incoherent scattering to the total scattering rate is typically neglected.

The Mollow spectrum has been experimentally observed and studied in several physical systems that realise the setting of resonance fluorescence; including atoms, molecules, quantum dots, superconducting qubits, and even a hybrid spin-nanomechanical system [262, 279–283]. Its characteristic triplet structure further opens the possibility to study correlations between the different composite frequency components, for which the *second-order correlation function* is an invaluable tool. The following Section is dedicated to its introduction and discussion within this context.

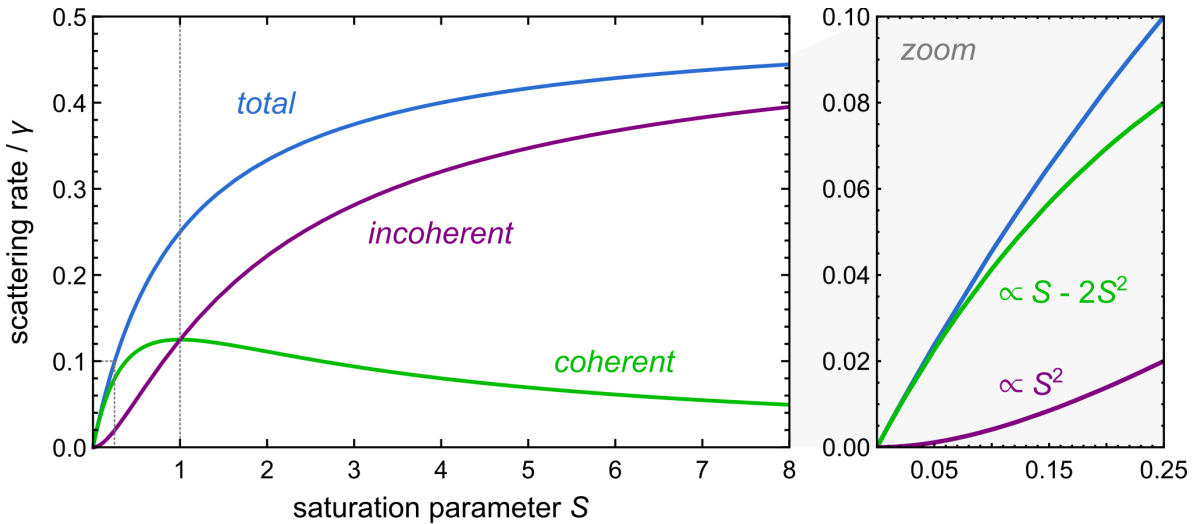


Figure 4.8. Scattering rates of the resonance fluorescence components. Dependence of the coherent and incoherent scattering rates in units of γ , as a function of the saturation parameter S . A zoom on the low saturation regime for $S < 0.25$ is shown on the right, illustrating the respective linear and quadratic growth of the coherent and incoherent components with the drive strength.

4.3.2 Second-order Correlation

The second-order correlation function is a key analysis tool in quantum optics, and in general, can be used to examine the degree of coherence that a (fluctuating) field has. It notably provides information on the statistical properties of a light field, such as how its photons are distributed in space or time, that can give insight into whether its source behaves as a classical or quantum emitter. The second-order correlation function therefore aids in the classification of a light field, depending on its specific statistical distribution of photons. In general, there are three possible cases that can be distinguished: a field that exhibits sub-Poissonian, super-Poissonian or Poissonian

photon statistics. Examples of these are displayed in Figure 4.9, and an explanation of each is outlined in the following.

Coherent light fields exhibit *Poissonian* photon statistics, where the temporal separation between photons is completely random and number fluctuations are negligible compared to the total. The quantum description of such a field is that of a coherent state, that can be written in the basis of Fock states as

$$|\alpha\rangle = \sum_{n=0}^{\infty} \frac{\alpha^n}{\sqrt{n!}} e^{-|\alpha|^2/2} |n\rangle. \quad (4.56)$$

The probability to find n photons is found by projecting onto the Fock state $|n\rangle$ as $P_n = |\langle n|\alpha\rangle|^2$, yielding

$$P_n = \frac{|\alpha|^{2n}}{n!} e^{-|\alpha|^2} = \frac{\langle n \rangle^n}{n!} e^{-\langle n \rangle}, \quad (4.57)$$

which is the function for a Poissonian distribution in which the average photon number is equal to the variance as $\langle n \rangle = \Delta n^2$. Such a distribution gives a flat second-order correlation function, corresponding to an equal probability at any time to find n photons. An example of such a light source is that of an idealised single-frequency laser. However,

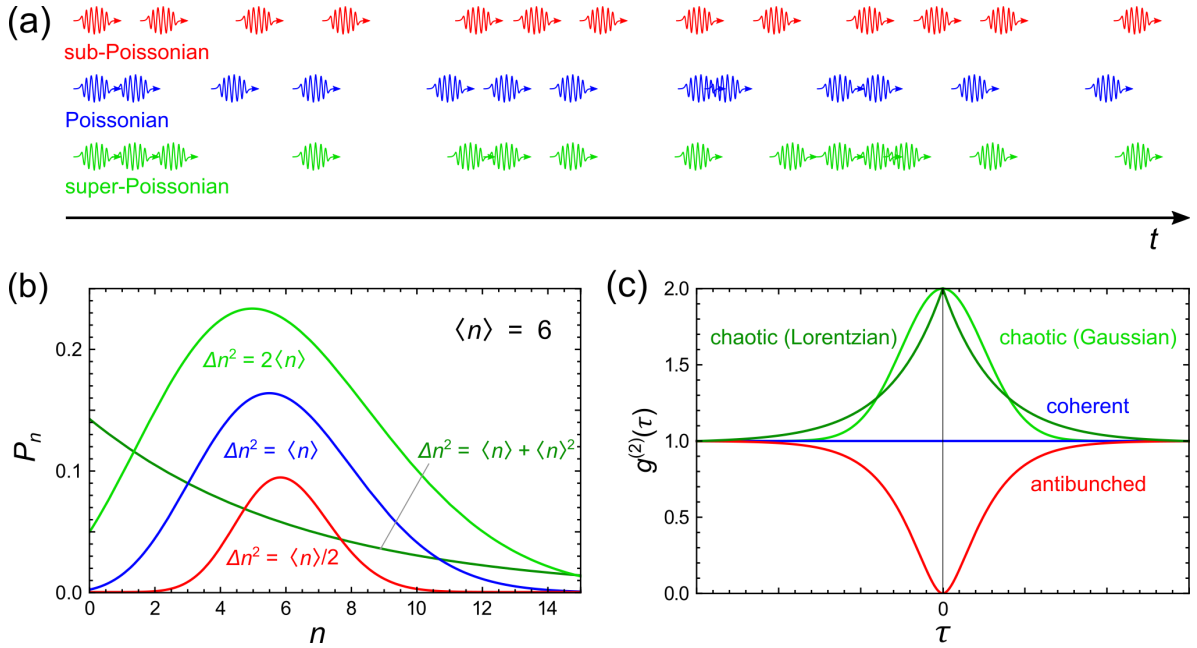


Figure 4.9. Photon statistics of light fields. (a) A representation of photon distributions in time that follow sub-Poissonian (red), super-Poissonian (green), and Poissonian (blue) statistics. (b) Examples of the statistical distributions depicted in (a) according to equation (4.57), for a mean photon number $\langle n \rangle = 6$. For comparison, a Bose-Einstein distribution with the same mean photon number for a thermal light source is included (dark green). (c) The corresponding second-order correlation function, $g^{(2)}(\tau)$, for the four cases depicted in (a). Each respectively shows a clear antibunching with $g^{(2)}(0) < g^{(2)}(\tau)$ (red), bunching with $g^{(2)}(0) > g^{(2)}(\tau)$ (green), or flat with $g^{(2)}(0) = g^{(2)}(\tau)$ (blue).

4. Theory of Selective Resonance Fluorescence

the idealised case of perfectly coherent light is atypical to most realistic light sources, which instead obey *super-Poissonian* photon statistics where $\langle n \rangle < \Delta n^2$. Known as *thermal*, or *chaotic* light, the large fluctuations in intensity arise from the randomness in the emission processes of a collection of largely independent emitters. A characteristic of such light sources is that the second-order correlation function shows a *bunching* effect, where $g^{(2)}(0) > g^{(2)}(\tau)$. Photons of the field are thus more likely to arrive with a short temporal spacing rather than completely at random. A hot glowing filament or spectral lamp are respective examples of such thermal or chaotic light sources.

Lastly, and most importantly, is a light field that follows *sub-Poissonian* photon statistics, for which $\langle n \rangle > \Delta n^2$. In contrast to the previous two cases, such a source cannot be described classically or semi-classically and instead requires quantisation of the electromagnetic field, i.e., single photons. Its second-order correlation function exhibits an *antibunching* effect, where $g^{(2)}(0) < g^{(2)}(\tau)$. Here, photons are more likely to arrive with a regular temporal separation rather than random. For perfect photon antibunching, $g^{(2)}(0) = 0$, and the light never contains simultaneously propagating photons. An example of such a so-called *single-photon source*, is that which has permeated the discussion so far: the resonance fluorescence of a two-level quantum emitter.

As the first-order correlation function quantifies the temporal fluctuations of the electric field amplitude, the second-order correlation function, $G^{(2)}$, analogously does so instead for its intensity fluctuations, as evident by equations (4.26) and (4.27). In a particle picture, of photons in this case, the $G^{(2)}(\tau)$ can be interpreted as the probability of detecting a photon at time τ , conditioned on an initial detection of a photon at time zero. Normalisation of this function by the steady-state probability of photon detection yields $g^{(2)}(\tau)$, which equals one for $|\tau| \gg 0$. Written in terms of the atomic dipole operators in equation (4.29), the second-order correlation function can be used to relate the internal dynamics of the two-level atom with the (measured) photon statistics of its scattered field.

Obtaining an expression for $G^{(2)}(\tau)$ for the fluorescence of a single atom is similar to that performed for obtaining $G^{(1)}(\tau)$, as presented in Section 4.3. Equation (4.29) can be expanded using the relation $\sigma_+ \sigma_- = \frac{1}{2}(1 + \sigma_z)$ into [129]

$$G^{(2)}(\tau) = \frac{1}{2} (\langle \sigma_+ \sigma_- \rangle_{\text{ss}} + \langle \sigma_+(0) \sigma_z(\tau) \sigma_-(0) \rangle_{\text{ss}}). \quad (4.58)$$

The second term of the above expression is again calculated by using the quantum regression theorem [129, 274, 275], for the standard initial conditions of the atom in its ground state, i.e., $\rho(0) = |g\rangle \langle g|$. This ultimately yields

$$G^{(2)}(\tau) = \frac{1}{2} \langle \sigma_+ \sigma_- \rangle_{\text{ss}} (1 + \langle \sigma_z(\tau) \rangle), \quad (4.59)$$

enabling insertion of equations (4.33) and (4.41) to obtain the final expression for the *on-resonance* second-order correlation function for resonance fluorescence as

$$g^{(2)}(\tau) = 1 - e^{-\frac{3}{4}\gamma|\tau|} \left(\cos(\Omega'|\tau|) + \frac{3\gamma}{4\Omega'} \sin(\Omega'|\tau|) \right) \quad (4.60)$$

which has been normalised to unity at long times by multiplication with $(\langle\sigma_+\sigma_-\rangle_{\text{ss}})^{-2}$. For the off-resonance case, the above has to be performed using the solutions to the optical Bloch equations obtained for $\Delta \neq 0$, which are themselves lengthy expressions [271, 272] and not recorded here. Doing so can yield analytical forms of the second-order correlation function, which, in general, appear similar to equation (4.60) albeit with significantly more complicated prefactors and arguments to the exponential and trigonometric functions [284]. The expression simplifies under special scenarios, of which exact resonance (above) is one such case. To state the another result for the special case of weak driving, the *detuned* second-order correlation function for resonance fluorescence is [278, 284]

$$g^{(2)}(\tau) = 1 + e^{-\gamma|\tau|} - 2e^{-\frac{1}{2}\gamma|\tau|} \cos(\Delta|\tau|). \quad (4.61)$$

These resultant expressions behave similar to the temporal evolution of the excited state population, which, in the case of resonance and for an atom initially in its ground state, is given by equation (4.20). Under this initial condition, the second-order correlation function therefore begins at zero and shows damped oscillations towards a steady-state, the exact form of which is dependent on the excitation properties. This is due to the fact that the probability of a second photon detection conditioned on a first, as measured in the $g^{(2)}(\tau)$, is directly proportional to the population dynamic of the atom: since the atom is projected into its ground state after a photon emission and its initial detection event.

To illustrate this, Figure 4.10 displays results using the expressions (4.60) and (4.61) for the second-order correlation function in resonance fluorescence. Figure 4.10(a) shows the case of resonance, for different values of the driving strength S_0 , and Figure 4.10(b) shows the case of weak excitation but off-resonance, with different detunings Δ . The first obvious distinction between the curves in each plot is evident for $|\tau| > 0$, where more frequent oscillations are apparent as either the excitation intensity or detuning is increased, that respectively occur at the modified Rabi frequency Ω' or approximately at the detuning $\sim |\Delta|$. Both are damped on the timescale of $2/\gamma$. The position of the peaks in both plots correspond to the times at which there is a higher probability of a second photon emission after the first, arising from the local maxima in the excited state populations (cf. Figures 4.3 and 4.5). This behaviour is symmetric in time around $\tau = 0$. For all of the cases depicted in Figure 4.10, it is clear that at this time, $\tau = 0$, the second-order correlation function assumes a value of $g^{(2)}(0) = 0$, that highlights the fact that the scattered field is comprised of single photons that are separated in time. This

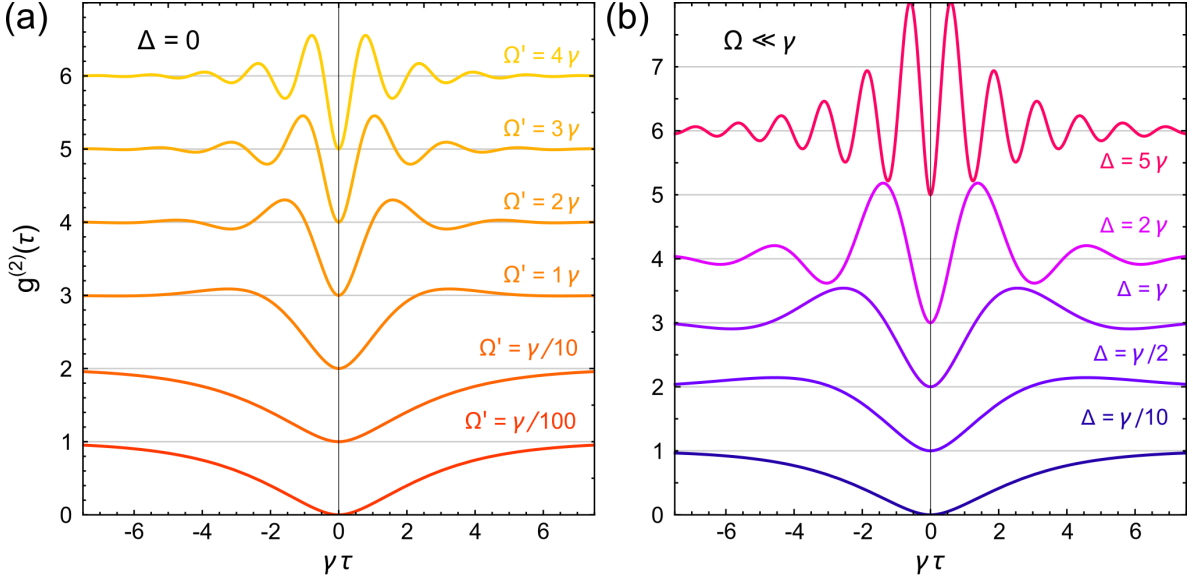


Figure 4.10. Second-order correlation function in resonance fluorescence. (a) The on-resonance $g^{(2)}(\tau)$ according to equation (4.60) for various driving strengths, plotted as a function of the two-photon separation, τ , in units of $1/\gamma$. (b) The off-resonance and weak-driving $g^{(2)}(\tau)$ according to equation (4.61) for various detunings, also plotted as a function of τ in units of $1/\gamma$. In both (a) and (b), respectively for ascending Ω' and Δ , is offset along the y-axis and have the same vertical scale. All cases clearly show antibunching at $\tau = 0$, i.e., $g^{(2)}(0) = 0$, interpreted as a zero probability for the scattered field to contain simultaneously propagating photons. This characteristic of resonance fluorescence remains as the driving strength or detuning increases, where the emergence of Rabi oscillations for $|\tau| > 0$ becomes evident above $\Omega' \vee \Delta \approx \gamma$ in either case. These are damped on the timescale $2/\gamma$.

behaviour turns out to be a clear violation of the *Cauchy-Schwartz inequality*, that sets the boundary for classical and non-classical light in stating that $g^{(2)}(0) \geq g^{(2)}(\tau) \forall \tau$ [278]. The antibunching present in the second-order correlation of the scattered field in resonance fluorescence, i.e., that $g^{(2)}(0) < g^{(2)}(\tau)$, is thus a *purely quantum phenomenon*. It points to the sub-Poissonian statistics of the light, further indicating that two photons cannot be simultaneously detected in the resonance fluorescence of a two-level atom.

With these results in mind, it is instructive to next consider the interaction of two photons with the single two-level atom, that can occur both coherently and incoherently. For this, these two processes are explicitly defined in a wavefunction description of the scattered field, as outlined in the next Section.

4.4 Wavefunction Description of the Scattered Field

As outlined in Section 4.2, the interaction of a classical light source with a single two-level quantum emitter is described by the optical Bloch equations. They model the practical scenario of a two-level atom (for example) being excited by a coherent laser beam, where the field scattered by the atom can be obtained from the time evolution of the atomic raising and lowering operators. As highlighted in Section 4.3.1, this scattered field comprises both a coherent and incoherent component, the ratio of which is given by the saturation parameter of the driving field

$$S = \frac{1}{2} \frac{(\Omega/\gamma)^2}{1 + (\Delta/\gamma)^2}. \quad (4.62)$$

Here again, $\Delta = \omega_L - \omega_0$ is the detuning of the excitation laser with respect to the atomic transition, γ is the amplitude decay rate of the excited state, and Ω is the Rabi frequency of the drive that is proportional to the driving laser field amplitude. The coherent and incoherent scattering rates of the atom are respectively given by

$$n_{\text{coh}} = \gamma \frac{S}{(1+S)^2} \approx \gamma(S - 2S^2) \quad (4.63)$$

and

$$n_{\text{inc}} = \gamma \frac{S^2}{(1+S)^2} \approx \gamma S^2, \quad (4.64)$$

where the right-hand-side of each of the above expressions is the Taylor expansion of the left-hand-side up to second order in S . This low saturation approximation is applied throughout the following in order to obtain a simple theoretical description of the scattered light field containing only a few photons, and as shall be shown in Chapter 5, is experimentally achievable by setting $S \ll 1$.

In this *low saturation regime*, the driving field can be modelled by decomposition into its photon number components, which occupy a mode with a rectangular temporal profile of total duration T . This duration is sufficiently long such that transient features at the start and the end of the pulse can be neglected, while remaining short enough to ensure that the mean number of photons it contains is much less than one. It thus fulfils the condition that $1/\gamma \ll T \ll 1/\gamma S$. The photon number (Fock) states of such a pulse are then defined as

$$|n\rangle_\omega = \left(\frac{1}{\sqrt{T}} \int_{-T/2}^{T/2} dt e^{i\omega t} a_t^\dagger |0\rangle \right)^{\otimes n}, \quad (4.65)$$

4. Theory of Selective Resonance Fluorescence

with the photon creation and annihilation operators given by

$$a_{\omega}^{\dagger} |n\rangle_{\omega} = \sqrt{n+1} |n+1\rangle_{\omega}, \quad (4.66)$$

$$a_{\omega} |n\rangle_{\omega} = \sqrt{n} |n-1\rangle_{\omega}, \quad (4.67)$$

that respectively create or destroy a photon at the frequency ω . The latter are related by

$$a_{\omega}^{\dagger} = \frac{1}{\sqrt{T}} \int_{-T/2}^{T/2} dt e^{i\omega t} a_t^{\dagger} \quad (4.68)$$

$$a_t^{\dagger} = \sqrt{T} \int_{\infty}^{\infty} d\omega e^{-i\omega t} a_{\omega}^{\dagger} \quad (4.69)$$

that maps their frequency representation to time, with a_t^{\dagger} (a_t) as the operator for creating (annihilating) a photon at time t . With this, the frequency modes given by a_{ω}^{\dagger} can be approximated to possess a δ -like spectrum.

The coherently scattered part of the field can then be represented as a coherent state, that is written out as

$$|\alpha\rangle = e^{-|\alpha|^2/2} \left(1 + \alpha a_{\omega}^{\dagger} + \frac{\alpha^2}{2} a_{\omega}^{\dagger} a_{\omega}^{\dagger} + \dots \right) |0\rangle \quad (4.70)$$

$$\approx |0\rangle + \alpha |1\rangle + \frac{\alpha^2}{\sqrt{2}} |2\rangle. \quad (4.71)$$

Here, α is assumed real, and defines the mean photon number by $\alpha^2 = n_{\text{coh}}T$ with n_{coh} given by equation (4.63). Using equation (4.68), the two photon component of the coherently scattered state becomes

$$\frac{\alpha^2}{\sqrt{2}} |2\rangle = \iint_{-T/2}^{T/2} dt_1 dt_2 \underbrace{\frac{\alpha^2}{2T} a_{t_1}^{\dagger} a_{t_2}^{\dagger}}_{\alpha^{(2)}} |0\rangle, \quad (4.72)$$

where the amplitude of the two photon wavefunction, $\alpha^{(2)} = n_{\text{coh}}/2$, has been introduced.

In addition to this coherently scattered light $|\alpha\rangle$, defined in equation (4.71), the atom also scatters an incoherent light field, $|\phi\rangle$. In the low saturation limit, it consists solely of energy–time entangled photon pairs [285–288] and the state in the time domain can be written as

$$|\phi\rangle = \iint_{-T/2}^{T/2} dt_1 dt_2 \phi^{(2)}(t_2 - t_1) a_{t_1}^{\dagger} a_{t_2}^{\dagger} |0\rangle. \quad (4.73)$$

By introducing the temporal photon separation, $\tau = t_2 - t_1$, and imposing the normalisation condition that both the coherently and incoherently scattered fields must have the same amplitude at $\tau = 0$, the temporal envelope of this two photon state

is given by

$$\phi^{(2)}(\tau) = -\frac{n_{\text{coh}}}{2} e^{-(\gamma-i\Delta)|\tau|}, \quad (4.74)$$

which denotes the probability amplitude for finding two photons within a time delay τ . This amplitude is maximum at $\tau = 0$, and exponentially decays within the time interval $|\tau| \sim 1/\gamma$. In contrast to this, the corresponding amplitude of the coherently scattered two-photon wavefunction is time-independent, resulting in a delta function spectrum, spectrally located at the driving frequency ω_L . The frequency representation of the incoherently scattered two photon state is, similarly, obtained by Fourier transform, resulting in a spectral distribution consisting of a pair of Lorentzian-shaped lines, each with a **FWHM** of γ and centred at the frequencies $\omega = \omega_L \pm \Delta^*$. This result has a similar form to that obtained with the optical Bloch equations in the regime of low driving with a non-zero detuning (see Section 4.3.1).

The total scattered field is given by the sum of both the coherently and incoherently scattered components as

$$|\psi\rangle = |\alpha\rangle + |\phi\rangle, \quad (4.75)$$

for which its two-photon component takes the form

$$|\psi^{(2)}(\tau)\rangle = \frac{n_{\text{coh}}}{2} \iint_{-T/2}^{T/2} dt_1 dt_2 \left[1 - e^{-(\gamma-i\Delta)|t_2-t_1|} \right] a_{t_1}^\dagger a_{t_2}^\dagger |0\rangle \quad (4.76)$$

with the temporal two photon amplitude

$$\psi^{(2)}(\tau) = \frac{n_{\text{coh}}}{2} \left(1 - e^{-(\gamma-i\Delta)|\tau|} \right). \quad (4.77)$$

The two distinct two-photon scattering processes in this considered setting of resonance fluorescence are depicted in 4.11(a), for the case of a red-detuned drive ($\Delta < 0$) [259]. It illustrates that the coherent process comprises two independent Rayleigh scattering events, leading to two uncorrelated photons that possess the same frequency as the drive. Such a two-photon scattering, consisting of a pair of single-photon scatterings, accounts for the constant amplitude of $\alpha^{(2)}(\tau)$, whereby the scattered photons have an equal probability for any temporal separation τ as a consequence of the coherent drive in which the two input photons also have an equal probability for any temporal separation. In contrast, the incoherent process involves a three-photon transition to the excited state via an intermediate virtual state, such that the scattered photons are respectively red- and blue-detuned to the drive. The latter process occurs when the two drive photons arrive at the two-level emitter within its excited state lifetime, i.e., $|\tau| \lesssim 1/\gamma$, exchanging energy in the process via interaction with the emitter

*Explicit expressions for these spectra are given and discussed in detail in Section 4.4.2.

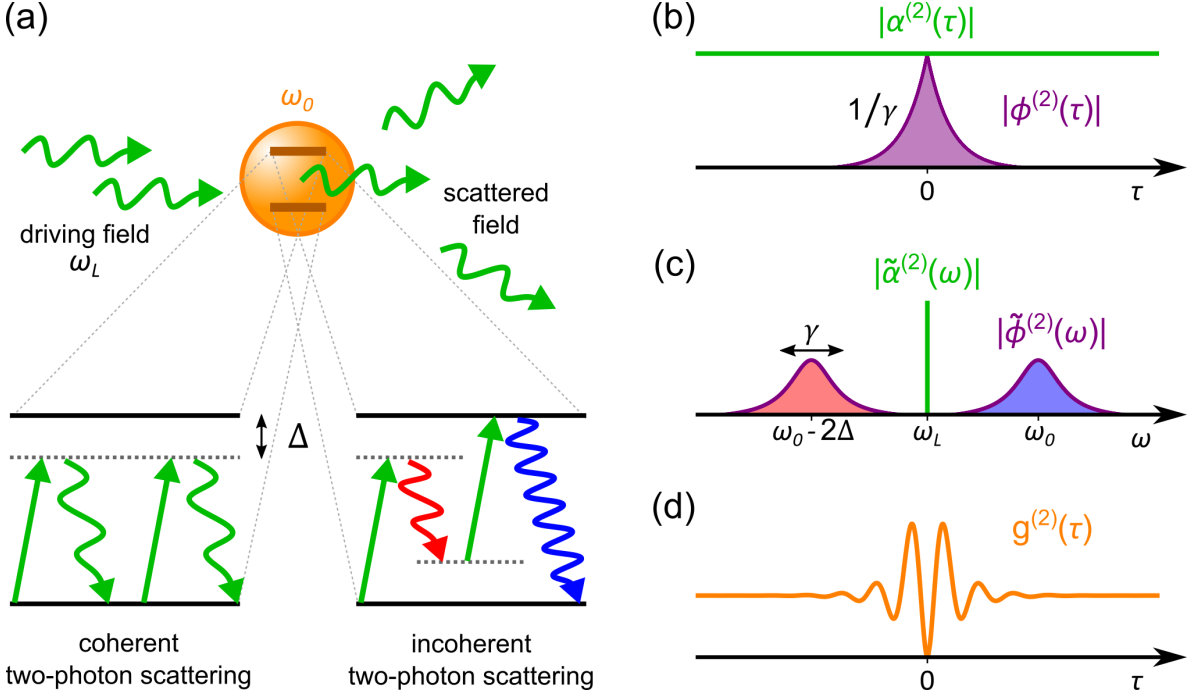


Figure 4.11. Two-photon scattering processes in resonance fluorescence. (a) Illustration of the setting of resonance fluorescence in the low driving regime, with a zoom on the coherent and incoherent two-photon scattering processes. (b) The two-photon wavefunction of the incoherent component (purple), $\phi^{(2)}(\tau)$, is a double exponential with decay constant $1/\gamma$, while the coherent component (green), $\alpha^{(2)}$, is a constant in time. At $\tau = 0$, $\phi^{(2)}(0) = -\alpha^{(2)}$. (c) In the frequency domain, related by the Fourier transform of the temporal two-photon wavefunctions, the coherent component is a delta function centred at the driving frequency (green), while the incoherent component is given by a double Lorentzian at $\omega_L \pm \Delta$ (purple). (d) The second-order correlation function, resulting from the interference between the coherent and incoherent two-photon wavefunctions, exhibits perfect photon antibunching at $\tau = 0$ where they fully destructively interfere. In the case of $\Delta \neq 0$ as shown explicitly in (c), Rabi oscillations for $|\tau| > 0$ are apparent.

and leading to an energy(frequency)–time entanglement between them. The amplitudes of both the coherently and incoherently scattered two photon wavefunctions are displayed in Figure 4.11(b) for the time domain, and in Figure 4.11(c) for the frequency domain. This respectively shows that the coherent (incoherent) scattering process is constant (exponentially decaying) in τ while being equal in amplitude at $\tau = 0$, and the spectrum of which assuming a delta function (pair of Lorentzians) at (separated by $\pm\Delta$ from) the driving field frequency. Importantly, by construction, the coherently and incoherently scattered two-photon components have equal amplitudes but are exactly π out of phase with respect to each other at zero time delay ($\tau = 0$). Consequently, they both perfectly destructively interfere such that $\psi^{(2)}(\tau = 0) = 0$ and the probability for the scattered light field to contain two simultaneously propagating photons is zero. This result, arising from the presented description, concurs with the expectation of antibunched photon statistics of the scattered light field, obtained by measurement of the second-order correlation function. An expression for $g^{(2)}(\tau)$, introduced in Section 4.3 and written out

explicitly in terms of the atomic dipole operators (cf. equation (4.27)), was obtained in Section 4.3.2 using the optical Bloch formalism (cf. equation (4.60)). It can equivalently be written in terms of the photon creation and annihilation operators as

$$g^{(2)}(\tau) = \frac{\langle a_t^\dagger a_{t+\tau}^\dagger a_{t+\tau} a_t \rangle_t}{\langle a_t^\dagger a_t \rangle_t^2} \quad (4.78)$$

where $\langle \dots \rangle_t = 1/T \int dt \langle \dots \rangle$ represents the time-averaged expectation value. In this low saturation regime of resonance fluorescence, only the two-photon component of the scattered field will contribute to the numerator of the above expression. Using equations (4.74) and (4.76), it thus simplifies to

$$\begin{aligned} g^{(2)}(\tau) &= \frac{\langle \psi^{(2)} | a_t^\dagger a_{t+\tau}^\dagger a_{t+\tau} a_t | \psi^{(2)} \rangle_t}{\langle \psi | a_t^\dagger a_t | \psi \rangle_t^2} \\ &\approx \left| 1 + \phi^{(2)}(\tau) \right|^2. \end{aligned} \quad (4.79)$$

Figure 4.11(d) displays an example $g^{(2)}(\tau)$ for the considered case of a driving field with $\Delta = -2\gamma$. As expected, the function is zero at $\tau = 0$ due to the full destructive interference between the two-photon components of the coherently and incoherently scattered light. Rabi oscillations occurring at a frequency $\Omega \approx |\Delta|$ due to the non-zero detuning of the drive are apparent for $|\tau| > 0$, which arises due to a beating between the two components as the phase of the incoherent component oscillates at the frequency $|\Delta|$. Note that the above expression has the same form as that obtained in the optical Bloch formalism (cf. equation (4.61)), which can be seen explicitly by expanding the second line in equation (4.79) as

$$\left| 1 + \phi^{(2)}(\tau) \right|^2 \approx 1 - 2 e^{-\gamma|\tau|} \underbrace{\text{Re} \left[e^{i\Delta|\tau|} \right]}_{\cos(\Delta|\tau|)} + e^{-2\gamma|\tau|}, \quad (4.80)$$

which demonstrates the validity of the treatment.

Returning to Figure 4.11 as a reference, it is clear that the coherently and incoherently scattered two-photon components each have distinct temporal and spectral distributions. This feature thereby enables an examination of the photon statistics of each individually, by selectively modifying or removing one via application of an appropriate spectral separation. This idea will be treated and discussed throughout the next Sections.

4.4.1 Photon Statistics of Each Component

The two-photon component of the scattered field in resonance fluorescence can be decomposed into a coherently and incoherently scattered contribution, in which each exhibits distinct spectral and temporal characteristics. As a function of the temporal two-photon separation, τ , the coherently scattered two photon component $\alpha^{(2)}$ features

4. Theory of Selective Resonance Fluorescence

a constant two-photon amplitude (is time-independent, c.f. equation (4.72)). The incoherently scattered two-photon component $\phi^{(2)}(\tau)$, in contrast, has an amplitude that exponentially decays in $|\tau|$ at a time constant of $1/\gamma$ (c.f. equation (4.74)). Importantly, at zero time-delay ($\tau = 0$), both of these components have an equal amplitude but are exactly π out of phase. This results in a perfect destructive interference between the two when taken together, ensuring that the total two-photon component of the scattered field $|\psi^{(2)}(\tau)\rangle = |\alpha^{(2)}\rangle + |\phi^{(2)}(\tau)\rangle$ exhibits precisely a zero probability for containing two simultaneously propagating photons that have a temporal separation of $\tau = 0$ (c.f. equation (4.77)). It is this interpretation of interfering quantum amplitudes between the higher photon-number scattered components that accounts for single photon emission – antibunching in the photon statistics – in the resonance fluorescence of a two-level quantum emitter.

When taken individually however, both the coherently and incoherently scattered two-photon components have a finite amplitude at zero time delay, i.e., $|\alpha^{(2)}| = |\phi^{(2)}(\tau = 0)| = n_{\text{coh}}/2$, reflecting the fact that each features a non-zero probability for containing two simultaneously propagating photons. This fact is best illustrated by considering the temporal statistical distribution of the two photons within each component separately, made concrete by an examination of the second-order correlation function that is obtained in either case. As introduced in Section 4.3.2, the $g^{(2)}(\tau)$ is given by equation (4.78), and quantifies the fluctuations in a statistical distribution of photons within a field compared to the average value (in a given time window). It is normalised to unity at long times in order to compare the probability of detecting a photon at time τ , conditioned on an initial detection at time $t = 0$. When the field under examination is comprised of – at most – only two photons, as is the case for the components of resonance fluorescence in the considered regime of low saturation, correct normalisation of $g^{(2)}(\tau)$ is not always possible. The second-order correlation functions obtained for the coherently and incoherently scattered fields, along with their combination, are presented and discussed in the following.

Consider first the photon statistics of the coherently scattered field $|\alpha\rangle$, which under the assumption of $S \ll 1$, contains a negligible three-photon component. Using equations (4.71) and (4.78), the second-order correlation function of the truncated coherent state $|\alpha\rangle$ reads

$$\begin{aligned}
 g^{(2)}(\tau) \Big|_{|\alpha\rangle} &= \frac{\langle \alpha | a_t^\dagger a_{t+\tau}^\dagger a_{t+\tau} a_t | \alpha \rangle_t}{\langle \alpha | a_t^\dagger a_t | \alpha \rangle_t^2} \\
 &= \frac{e^{-|\alpha|^2} \frac{|\alpha|^4}{2} \langle 2 | a_t^\dagger a_{t+\tau}^\dagger a_{t+\tau} a_t | 2 \rangle_t}{e^{-2|\alpha|^2} (|\alpha|^2 \langle 1 | a_t^\dagger a_t | 1 \rangle_t + \frac{|\alpha|^4}{2} \langle 2 | a_t^\dagger a_t | 2 \rangle_t)^2} \\
 &= \frac{e^{|\alpha|^2} |\alpha|^4}{(|\alpha|^2 + |\alpha|^4)^2}, \tag{4.81}
 \end{aligned}$$

which is time-independent but only correctly normalised for $|\alpha| \ll 1$ [289]*. Under this assumption, $g^{(2)}(\tau) \big|_{|\alpha\rangle} \rightarrow |\alpha|^4/|\alpha|^4 = 1$ as $|\alpha| \rightarrow 0$, for all times. This result clearly illustrates that the second-order correlation function of the coherently scattered portion exhibits Poissonian photon statistics, where the photon arrival times are uncorrelated. In the considered limit of weak driving, the truncated coherent state therefore behaves like the ideal coherent state (that does not have a truncated Fock state expansion), and retains a classical-like second-order correlation behaviour.

In a similar fashion, the photon statistics of the incoherently scattered portion is obtained using the state $|\phi\rangle$ instead (given by equation (4.73)), as

$$\begin{aligned} g^{(2)}(\tau) \big|_{|\phi\rangle} &= \frac{\langle \phi | a_t^\dagger a_{t+\tau}^\dagger a_{t+\tau} a_t | \phi \rangle_t}{\langle \phi | a_t^\dagger a_t | \phi \rangle_t^2} \\ &= \frac{(\gamma T)^2 e^{|\alpha|^2 - 2\gamma|\tau|}}{(|\alpha|^2)^2} \\ &= S^{-2} e^{-2\gamma|\tau|}, \end{aligned} \tag{4.82}$$

where the last line uses α in terms of S and γT (see Appendix E for further details). As with the second-order correlation function obtained for the coherently scattered portion, this result is only valid in the limit of weak driving ($S \ll 1$). In contrast however, $g^{(2)}(\tau) \big|_{|\phi\rangle}$ is time-dependent, exhibiting a bunching behaviour with its maximum situated at $\tau = 0$. Furthermore, $g^{(2)}(\tau) \big|_{|\phi\rangle}$ decays to zero for $|\gamma\tau| \gg 1$. This second-order correlation function is therefore not properly normalised (so that it settles to unity for $|\tau| \rightarrow \infty$), and has a bunching amplitude that scales with $1/S^2$ (resulting in a divergence of $g^{(2)}(0) \big|_{|\phi\rangle}$ as $S \rightarrow 0$). Both of these traits are, however, expected for the considered state $|\phi\rangle$ since it consists of a single photon pair that jointly propagates within a time interval of $\tau \approx 1/\gamma$.

These results discussed above are contained in Figure 4.12. Figure 4.12(a) shows a plot of the second-order correlation functions obtained for both $|\alpha\rangle$ and $|\phi\rangle$, determined respectively using equations (4.81) and (4.82). As expected, the $g^{(2)}(\tau)$'s functionally resemble the temporal distributions of the two-photon component of each part of the scattered field, cf. Figure 4.11(b), since $g^{(2)}(\tau) \big|_{|x\rangle} \propto |x^{(2)}(\tau)|^2$ for a given state $|x\rangle$. That is, while each component yields a temporally symmetric $g^{(2)}(\tau)$ around $\tau = 0$, the coherently scattered field gives a constant in τ while the incoherently scattered field exponentially decays in $|\tau|$. Both independently show a non-zero value of the second-order correlation function at zero time-delay, exemplifying that each field has a finite probability to contain two simultaneously propagating photons. However, while this probability is constant for any temporal separation between the two photons for the coherent component, it is maximum for the incoherent component exactly at $\tau = 0$. This reflects the fact that the coherently scattered component assumes the uncorrelated

*This is expected for a truncated coherent state.

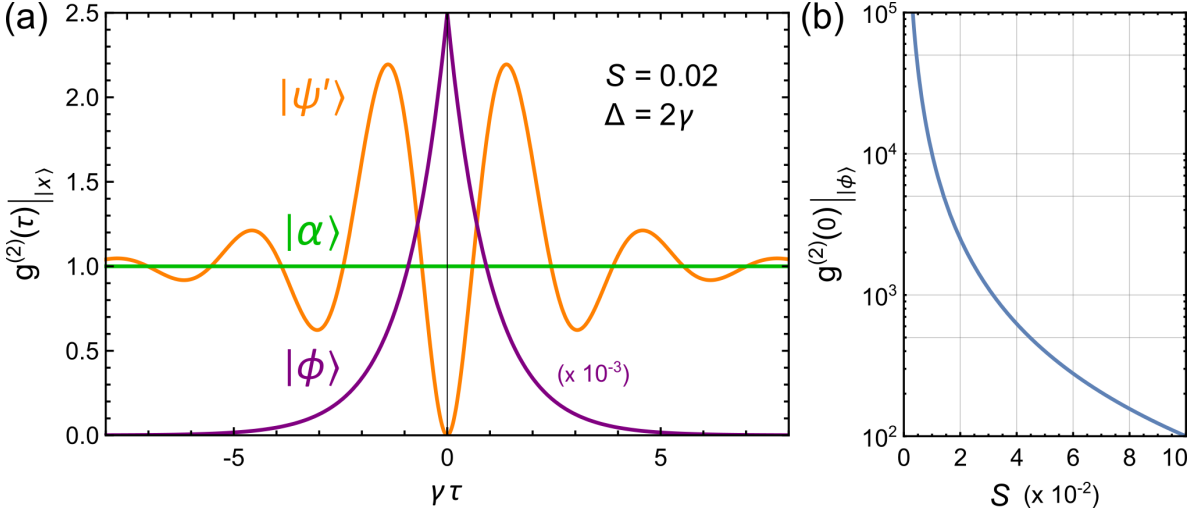


Figure 4.12. Second-order correlation functions of the coherently and incoherently scattered components. (a) The coherently scattered component (green), given by equation (4.81), is time-independent and normalised to unity. The incoherently scattered component (purple), given by equation (4.82), is time-dependent and exponentially decays to zero in $|\tau|$. The combined state (orange), given by equation (4.85), produces the expected behaviour for the parameters used (note that $t_{\text{coh}} = 1$ here). For all curves, $S = 0.02$ and $\Delta = 2\gamma$. (b) The amplitude of $g^{(2)}(\tau = 0)_{|\phi\rangle}$ as a function of the saturation parameter, S , in the weak-driving limit of $S \ll 1$. Note the logarithmic scale.

photon statistics of the driving laser, while the incoherently scattered component has highly correlated photon statistics due to the interaction with the two-level atom. Figure 4.12(b) shows the bunching amplitude of $g^{(2)}(\tau = 0)_{|\phi\rangle}$, as a function of S , in the weak driving limit of $S \ll 1$.

A plot of the second-order correlation function, $g^{(2)}(\tau = 0)_{|\psi\rangle}$, obtained with the total scattered field, $|\psi\rangle = |\alpha\rangle + |\phi\rangle$, is also shown in Figure 4.12(a). It clearly features the expected antibunching behaviour (along with Rabi oscillations at $\Omega \approx \Delta$ due to the weak and detuned drive), that results from the complete cancellation of the two-photon components in $|\alpha\rangle$ and $|\phi\rangle$ at $\tau = 0$, and their interference for $0 < |\tau| \lesssim 2/\gamma$. With this, it is relatively straightforward to study the transition from an antibunching to bunching behaviour in the photon statistics of the total field, by removal of the coherently scattered contribution to the total field $|\psi\rangle$. To do so, the parameter $t_{\text{coh}} \in [0, 1]$ is introduced, that acts to attenuate only the amplitude of $|\alpha\rangle$. The scattered field then has the quantum state

$$|\psi'\rangle = (|t_{\text{coh}}\alpha\rangle + |\phi\rangle), \quad (4.83)$$

which can be used to obtain an expression for the second-order correlation function as

$$g^{(2)}(\tau)_{|\psi'\rangle} = \frac{\langle \psi' | a_t^\dagger a_{t+\tau}^\dagger a_{t+\tau} a_t | \psi' \rangle_t}{\langle \psi' | a_t^\dagger a_t | \psi' \rangle_t^2}. \quad (4.84)$$

Evaluation of the above expression requires calculation of the expectation values $\langle a_t^\dagger a_t \rangle_t$ and $\langle a_t^\dagger a_{t+\tau}^\dagger a_{t+\tau} a_t \rangle_t$, using the normalised state $|\psi'\rangle$ given in equation (4.83). The full calculations of these are contained in Appendix E for reference. In doing so, the final expression for $g^{(2)}(\tau) \big|_{|\psi'\rangle}$ reads

$$g^{(2)}(\tau) \big|_{|\psi'\rangle} = \left(\frac{|t_{\text{coh}}^2 - e^{-(\gamma-i\Delta)|\tau|}|}{t_{\text{coh}}^2 + S(1 - 2t_{\text{coh}}^2)} \right)^2. \quad (4.85)$$

Figure 4.13 displays an investigation of the second-order correlation function obtained, using equation (4.85), under attenuation of the coherently scattered component $|\alpha\rangle$. Figure 4.13(a) shows line plots, for different (low-driving) S values, of $g^{(2)}(\tau) \big|_{|\psi'\rangle}$ at $\tau = 0$ and $\tau > 0$ when t_{coh} is reduced from 1 to 0. For large τ , the second-order

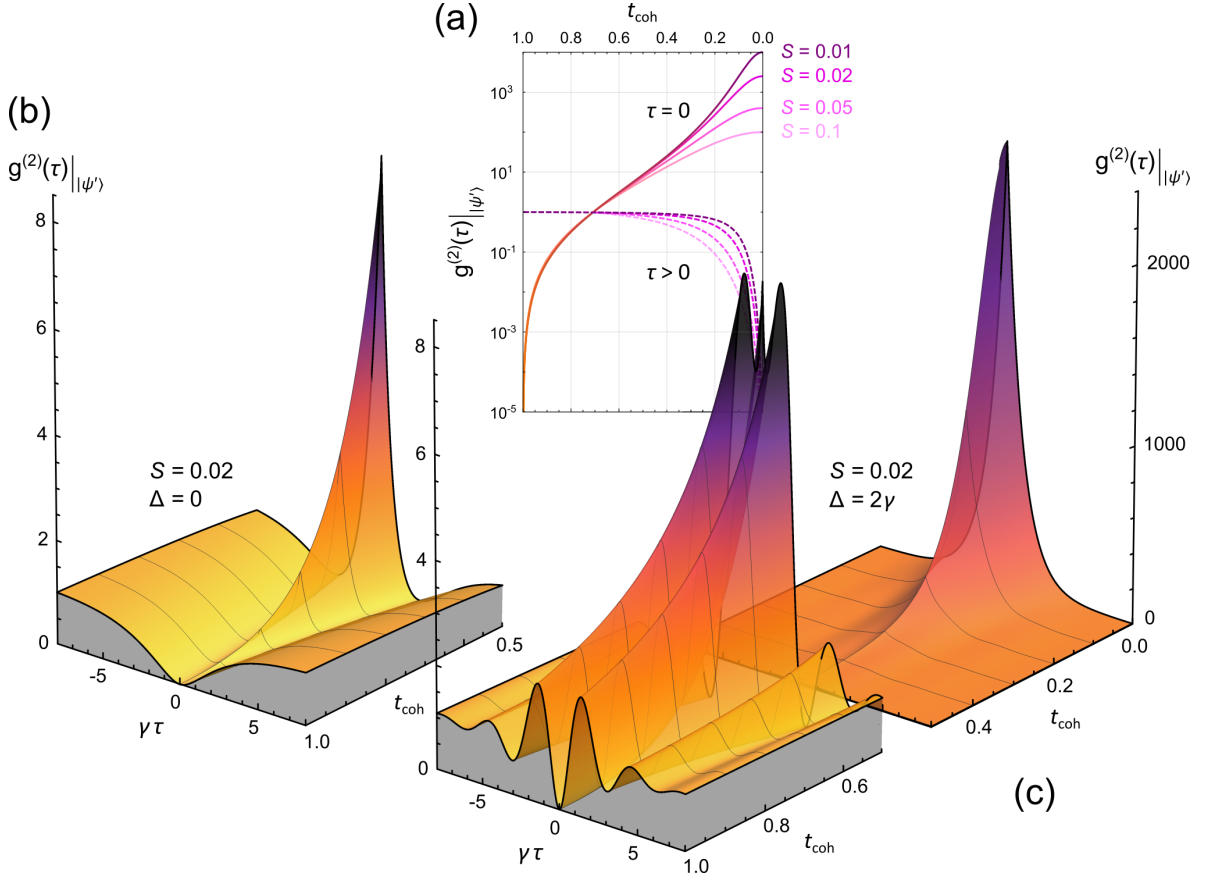


Figure 4.13. Second-order correlation function with an attenuated coherent component. (a) A plot of $g^{(2)}(\tau) \big|_{|\psi'\rangle}$ as a function of the attenuation applied to the coherent component, t_{coh} , according to equation (4.85). Curves for different S are displayed, with the solid lines using $\tau = 0$ and the dashed lines for $\tau = 10^5/\gamma$. The y -axis has a logarithmic scale. (b) A surface plot $g^{(2)}(\tau) \big|_{|\psi'\rangle}$ as a function of τ and t_{coh} . The latter is displayed from 1.0 to 0.5. Here, $S = 0.02$ and $\Delta = 0$. (c) The same as shown in (b), but for $\Delta = 2\gamma$. The back-right plot is a continuation of the front-left plot, with t_{coh} further reduced from 0.5 to 0.0. The vertical axes are accordingly scaled.

correlation function remains approximately normalised to unity until $t_{\text{coh}} \sim 0.5$, after which it asymptotically approaches zero. This behaviour is due to the gradual isolation of the incoherent component (cf. Figure 4.12(a)), which for lower S , occurs at greater attenuation of the coherent component due to its relative dominance. At $\tau = 0$, the amplitude of $g^{(2)}(0) \Big|_{|\psi'\rangle}$ exponentially increases with the attenuation of $|\alpha\rangle$, to a maximum corresponding to the S -dependent $g^{(2)}(0) \Big|_{|\phi\rangle}$ (cf. Figure 4.12(b)). Figures 4.13(b) and 4.13(c) display surfaces of $g^{(2)}(\tau) \Big|_{|\psi'\rangle}$ in the case of zero and non-zero detuning respectively, both showing a continuous transition from antibunching ($t_{\text{coh}} = 1$, $|\psi'\rangle = |\psi\rangle$) to bunching ($t_{\text{coh}} \rightarrow 0$, $|\psi'\rangle \approx |\phi\rangle$).

By artificially separating the scattered field into its coherent and incoherent contribution, the photon statistics of each – which are ruled by the two-photon component – are found to exhibit distinct temporal distributions. In the following Section, the spectrum of each of these components is computed, which paves the way for defining a practical method for their *spectral* separation. This will allow for a realistic investigation into modification of the photon statistics, as briefly explored in the latter part of this Section.

4.4.2 Two-photon Spectra

In the time domain, the two-photon component of the scattered field is given by the wavefunction

$$\begin{aligned}\Psi(\tau) &= \alpha + \phi(\tau) \\ &= A \left(1 - e^{-(\gamma - i\Delta)|\tau|} \right)\end{aligned}\tag{4.86}$$

where the arbitrary amplitude $A \approx \gamma(S - 2S^2)$ (assumed small), has been introduced. Here, and throughout the following, the superscripts of ⁽²⁾ are dropped for the brevity of notation. Equation (4.86) encapsulates the interplay between the coherently and incoherently scattered portions of the resonance fluorescence, respectively α and $\phi(\tau)$. Importantly, due to the phase shift of π between α and $\phi(0)$, the amplitude of Ψ is zero at $\tau = 0$ and as such, in accordance with antibunched photon statistics, the scattered field never contains two simultaneously propagating photons. The complementary frequency domain spectrum of the two-photon component of resonance fluorescence is obtained by taking the Fourier transform of the above expression, as

$$\begin{aligned}\tilde{\Psi}(\omega) &= \frac{1}{\sqrt{2\pi}} \int_{-\infty}^{\infty} \Psi(\tau) e^{i\omega\tau} d\tau \\ &= \tilde{A} \left(\delta(\omega) - \frac{1}{\pi} \frac{\gamma - i\Delta}{\omega^2 + (\gamma - i\Delta)^2} \right),\end{aligned}\tag{4.87}$$

where the factors of $\sqrt{2\pi}$ have been absorbed into the amplitude prefactor \tilde{A} . The first term, a Dirac delta function at frequency ω , stems from the Fourier transform of the coherent two-photon component α , which is a constant in time. In the excitation laser

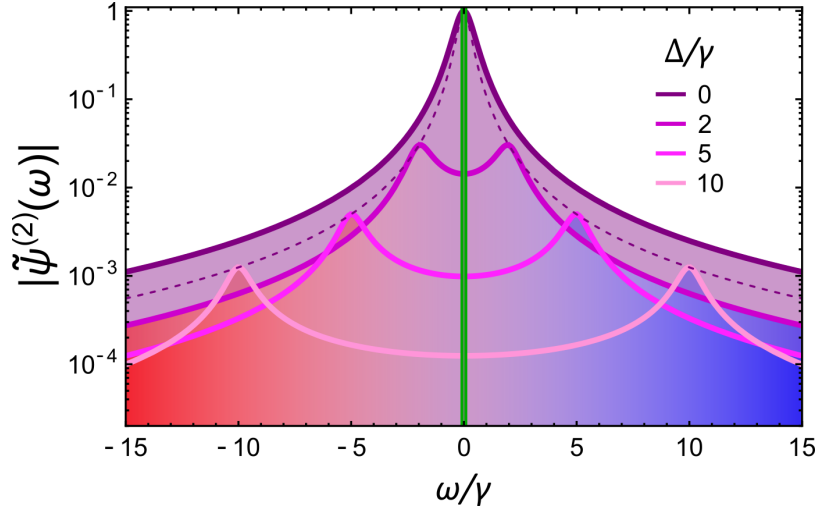


Figure 4.14. Spectrum of the scattered two-photon component. In the frame of the driving laser field, $\omega = \omega_L \equiv 0$, the incoherently scattered component $|\tilde{\phi}(\omega)|$ consists of a pair of spectrally symmetric Lorentzian lines centred at the frequencies $\omega = \pm\Delta$ (solid purple curves). $|\tilde{\phi}(\omega = \Delta)|$ is also displayed (dashed purple curve). The coherently scattered component $|\tilde{\alpha}|$, on the other hand, is a delta function at the frequency of the driving field (green vertical line). The plot is displayed with a logarithmic y-axis (arbitrary scale) and for different magnitudes of atom–drive detunings $|\Delta|$.

frame, this lies at the driving frequency ω_L : all coherently (Rayleigh) scattered photons, by definition, do not change energy and thus preserve the frequency of the drive photon upon each scattering event. The second term instead describes a pair of Lorentzian lines, each of width γ , which are separated by $\pm\Delta$ from ω_L . Corresponding to the incoherent two-photon component $\tilde{\phi}(\omega)$, it results from taking the Fourier transform of the double exponentially decaying function in $|\tau|$ as given by equation (4.74). When incoherently scattered, the two-photon component of the drive, where each photon is initially at the driving frequency, is thus redistributed into a pair of respectively blue- (ω_B) and red-detuned (ω_R) photons centred at the frequencies ω_0 and $\omega_0 - 2\Delta$. Furthermore, as is the case for the coherent two-photon scattering process, energy must be conserved across the incoherent two-photon scattering process, such that $2\hbar\omega_L = \hbar(\omega_B + \omega_R)$. As a result of this interaction with the emitter, the incoherently scattered two-photon component is thus a pair of energy–time entangled photons (c.f. equation (4.74)). As illustrated in Figure 4.14, the spectrum of the two-photon component of the scattered field, $\tilde{\Psi}(\omega)$, thus resembles the expected Mollow triplet that contains contributions from both the coherent and incoherent two-photon scattering processes (depicted in Figure 4.11(a)). The coherent and incoherent two-photon portions of the scattered field are clearly distinctive, and in the case of $2\gamma < |\Delta| \ll \omega_0$ (i.e., a detuning of the driving field larger than the width of the Lorentzians given in equation (4.87), but still small enough to yield efficient scattering), are spectrally separated. It is this combination of the spectral uniqueness between the two components, together with the detuned

setting of resonance fluorescence to enable their spectral separation, that provides a neat configuration for modifying the photon statistics of the scattered field – simply by the application of a spectral filter. This insight, and its consequences, will be investigated throughout the remainder of this Chapter.

4.5 Modifying the Photon Statistics

Modification of the photon statistics of the scattered field – a two-photon observable – can be achieved by upsetting the balance between the two-photon component in the coherently and incoherently scattered light, which have each been found to possess different frequency distributions (see Figures 4.11(c) and 4.14). The introduction of a suitable spectral discriminator – characterised by the complex frequency-dependent transmission coefficient $\tilde{t}(\omega)$ – should therefore ideally attenuate only one of the two scattered components, while not significantly affecting the other. In the time domain, an investigation with such an amplitude attenuation parameter, t_{coh} , was already used (equation (4.83)) to conveniently examine the transformation of the photon statistics of the scattered field when only reducing the amplitude of the coherent contribution. This approach, however, leads to an unphysical filtering configuration in which the frequency-domain t_{coh} , \tilde{t}_{coh} , consists of a delta(-like)-function at the excitation frequency (i.e., $\tilde{t}_{\text{coh}} = 0$ for $\omega \neq \omega_L$). For a more realistic applicability, an approach that takes into account the spectral spread of both $\tilde{\Psi}(\omega)$ and a suitable $\tilde{t}(\omega)$, is necessary. Due to the triplet structure of the total scattered two-photon wavefunction in the case of finite detuning, transmitting it through a notch-like band-pass (band-block) spectral filter that is centred at the driving frequency will selectively attenuate the incoherent (coherent) component. For a perfect transmittance outside of the finite bandwidth filter, and for a spectrum in which the coherently and incoherently scattered components are well separated, the filter can be set up to attenuate only one of the components, while leaving the other approximately unaffected.

Figure 4.15 illustrates a desired configuration that makes use of a Lorentzian-shaped band-block filter that features control over its spectral position, blocking width, and attenuation. This arrangement is described by defining the transmission function

$$\tilde{t}_F(\omega) = \frac{\kappa_0 - \kappa_{\text{ext}} + i(\omega - \omega_c)}{\kappa + i(\omega - \omega_c)} \quad (4.88)$$

which features a bandwidth of $\kappa = \kappa_0 + \kappa_{\text{ext}}$ and spectral location of ω_c^* . Such a configuration realises the generalisation of applying the attenuation parameter t_{coh} , in which $\tilde{t}_{\text{coh}} = \tilde{t}_F(\omega_L, \omega_c = \omega_L)$ in the limit of $\kappa \rightarrow 0$ ($\kappa_{\text{ext}} = \kappa_0$), where $\tilde{t}_F(\omega)$ instead has a finite spectral width and affords control over its spectral location (as well as the

*Note that equation (4.88) is written using ring-resonator notation, where $\kappa_{0(\text{ext})}$ is the intrinsic loss (external coupling) rate and ω_c its resonance frequency. See Section 5.1.2 for further details.

attenuation at ω_c via tuning of the ratio $\kappa_{\text{ext}}/\kappa_0$). Similarly, by using $1 - \tilde{t}_F(\omega)$, the inverse Lorentzian-shaped band-pass filtering configuration is defined (see Figure 4.15). Both situations can be experimentally realised by employing a resonator [269, 270, 290] (see Section 5.1.2 for further details).

In the following, the act of applying such a spectral filter to the scattered field in the detuned and weak-driving setting of resonance fluorescence is examined, by first defining the two-photon filter function, before exploring its impact on the photon statistics of the filtered field for a range of different settings.

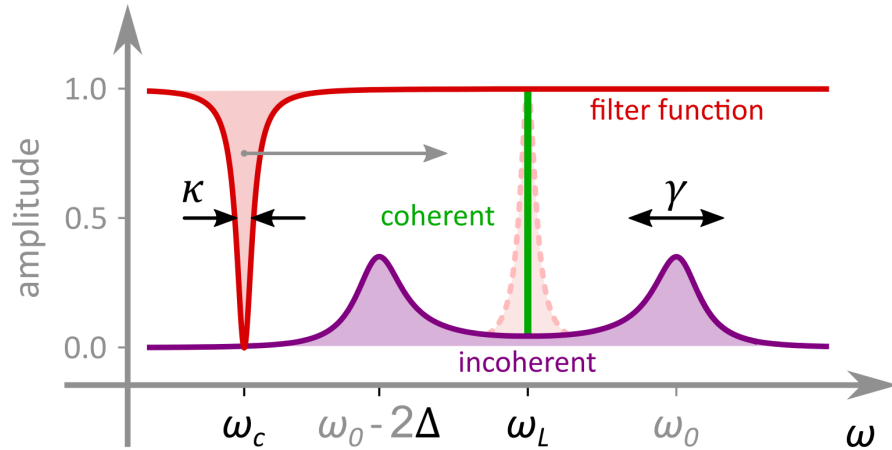


Figure 4.15. Two-photon spectrum subject to a suitable filter function. The spectrum of the two-photon part of the scattered field is comprised of a coherent component (green delta function at ω_L) and an incoherent component (purple Lorentzian pair, each of width γ , and centred at $\omega_L \pm \Delta$). The spectral uniqueness of these two components affords the possibility to discriminate them, with the addition of a suitable "filter" function. A narrowband and notch-like Lorentzian, centred at the tunable frequency ω_c and featuring a **FWHM** linewidth of 2κ (red solid line), can be employed as such a spectral discriminator. It has a nominal amplitude of unity, with a variable suppression of between one and zero at the frequency $\omega = \omega_c$. Set at $\omega_c = \omega_L$, it can be used to attenuate the amplitude of the coherent component while leaving the incoherent component mostly unaffected. For comparison, its band-pass inverse is displayed (red dashed line), that can realise the opposite effect of attenuating the incoherent component while leaving the coherent component unaffected.

4.5.1 Defining a Two-Photon Filter Function

The relative amplitudes of $\tilde{\alpha}(\omega) = \delta(\omega_L)$ and $\tilde{\phi}(\omega)$ can be tuned between zero and one by subjecting them to a suitable frequency-dependent "filter" function, for which a highly-tunable Lorentzian notch-like setting, $\tilde{t}_F(\omega)$, is given by equation (4.88). Such a filtering configuration can be used to spectrally modify the two-photon part of the scattered field – and in doing so – disturb the interference between the coherent and incoherent components. The photon statistics of the field that remains after filtering can then be subsequently analysed. For this, it is necessary to consider the filtering action on

4. Theory of Selective Resonance Fluorescence

the two-photon component of the scattered field, i.e., how application of the two-photon spectral filter function $\tilde{t}(\omega_1, \omega_2) = \tilde{t}_F(\omega_1)\tilde{t}_F(\omega_2)$ (equation (4.88)) modifies the spectral components of $\tilde{\Psi}(\omega_1, \omega_2) = \tilde{\alpha}(\omega_1, \omega_2) + \tilde{\phi}(\omega_1, \omega_2)$ (equation (4.86)), and how this would then manifest in the temporal dynamics of the second-order correlation function. In particular, if one photon from either of the coherent or incoherent two-photon component is removed through filtering, the remaining photon no longer contributes a $|\tau| \lesssim \gamma$ coincidence event to the photon statistics (a two-photon observable). In order to describe this, and by exploiting the fact that the two-photon spectrum is symmetric around ω_L in the laser frame, the joint spectral filter $\tilde{t}(\omega_1, \omega_2)$ can be written in terms of the single relative variable ω . This results in the complex-valued *two-photon transmission function* as

$$\begin{aligned} \tilde{t}(\omega) &= \left(\frac{\kappa_0 - \kappa_{\text{ext}} + i(\omega - \omega_c)}{\kappa + i(\omega - \omega_c)} \right) \cdot \left(\frac{\kappa_0 - \kappa_{\text{ext}} - i(\omega + \omega_c)}{\kappa - i(\omega + \omega_c)} \right) \\ &= \frac{\omega^2 + (\kappa - 2\kappa_{\text{ext}} - i\omega_c)^2}{\omega^2 + (\kappa - i\omega_c)^2}, \end{aligned} \quad (4.89)$$

which describes a set of two combined notch-like Lorentzians centred at the relative frequencies $\omega = \pm\omega_c$, each with a **WHM** of $\kappa = \kappa_0 + \kappa_{\text{ext}}$. The two-photon filtering function $\tilde{t}(\omega)$ ensures that both photons in each component are subject to the same transmission factor, providing a two-photon transmission that is independent of the filter's spectral location ω_c (relative to ω_L). This form therefore accounts for the filtering of the correlated frequencies in the incoherent component.

In order to illustrate this, Figure 4.16 displays density plots of the real $\text{Re}[\tilde{t}(\omega)]$ and imaginary $\text{Im}[\tilde{t}(\omega)]$ parts of equation (4.89) (left column), as well its absolute value $\text{Abs}[\tilde{t}(\omega)]$ and argument $\text{Arg}[\tilde{t}(\omega)]$ (right column), all as a function of ω_c . As illustrated in the corresponding 1D line-cut plots (lower part of Figure 4.16), each Lorentzian is fixed with a linewidth of $\kappa = 1$ and with $\kappa_0 = \kappa_{\text{ext}}$, ensuring that the transmission at ω_c reaches zero, i.e., $|\tilde{t}(\omega_c)|^2 = 0$. While the real part and absolute value of \tilde{t} showcase the desired spectrum that consists of the Lorentzian lines each centred at $\pm\omega_c$ (coinciding exactly for $\omega_c = 0$), the imaginary part and argument illustrates how the spectrum undergoes a sign flip with $\text{sgn}(\omega_c)$. In particular, the argument expressed in units of π corresponds to the phase response of \tilde{t} . By defining that the phase of the two Lorentzians in $\tilde{t}(\omega)$ perfectly cancel at the spectral location of $\omega_c \equiv 0$, both $\text{Arg}[\tilde{t}(\omega, \omega_c = 0)] = \text{Im}[\tilde{t}(\omega, \omega_c = 0)] = 0 \forall \omega$. By setting this spectral location at the driving laser frequency, the two-photon filter function can be used to completely suppress all coherently scattered photons, while imparting zero phase to the remaining incoherently scattered two-photon spectrum.

In the same vein as in Figure 4.16, Figure 4.17 displays density plots of the spectrum of $\tilde{t}(\omega)$, but instead as κ_{ext} is varied. The illustrative case of $\omega_c \neq 0$ is considered. The amplitude of both the real and imaginary parts of \tilde{t} , as well as its absolute value and argument, are clearly dependent on the parameter κ_{ext} . The two notch-like regions of

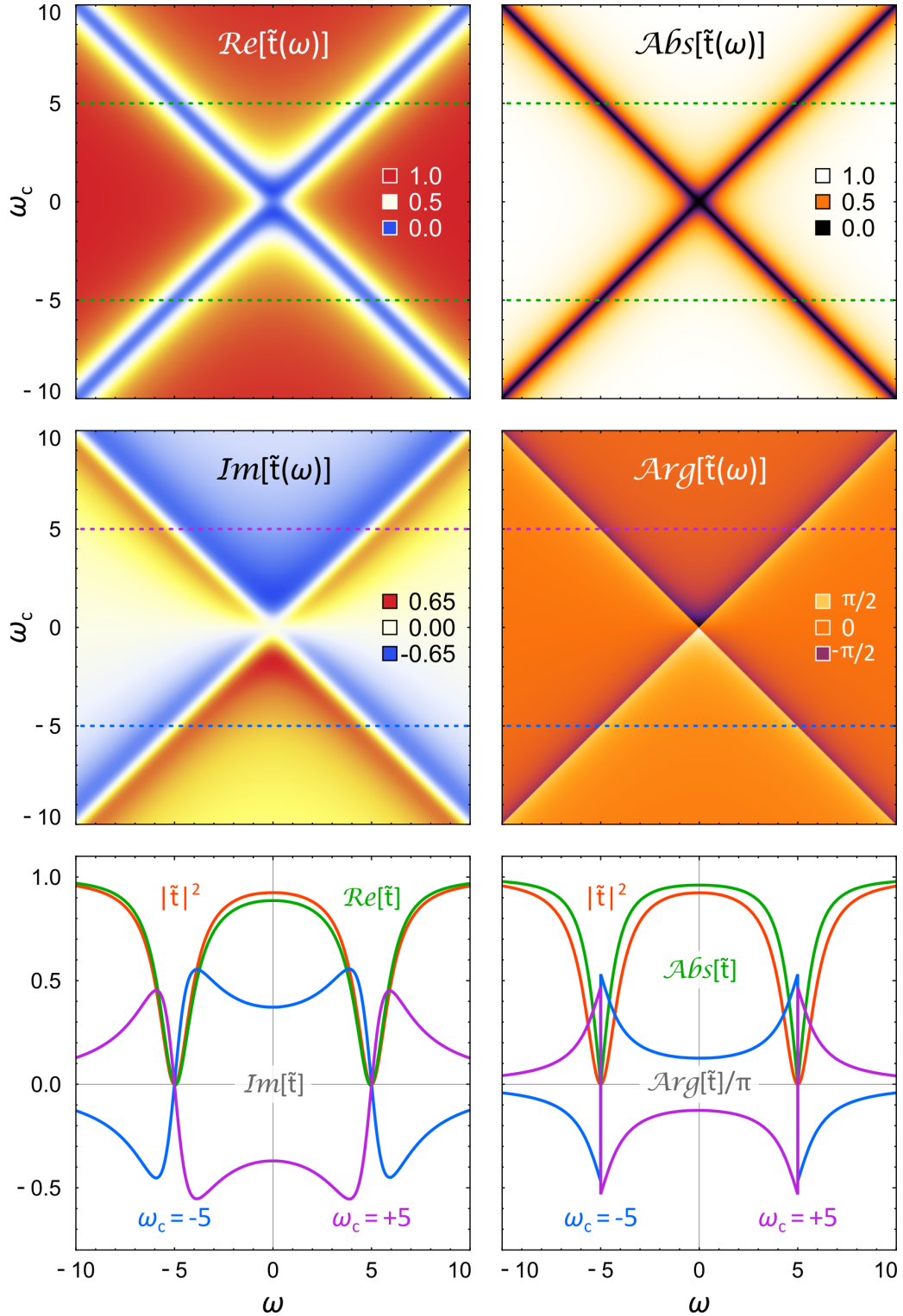


Figure 4.16. Centre–frequency dependence of the two-photon transmission function. Left column: density plots of the real (top) and imaginary (middle) part of the spectrum $\tilde{t}(\omega)$ (equation (4.89)), as a function of the Lorentzian centre frequency ω_c . These spectra at $\omega_c = \pm 5$ (horizontal dotted lines) are displayed, using corresponding colours, in a separate plot (bottom). $|\tilde{t}(\omega)|^2$ is also included here. Right column: same as the left column, but instead for the absolute value (top) and argument (middle) of $\tilde{t}(\omega)$ as a function of ω_c . Parameters used: Lorentzian linewidth of $\kappa = 1$, with $\kappa_0 = \kappa_{\text{ext}}$ such that $|\tilde{t}(\omega_c)|^2 = 0$.

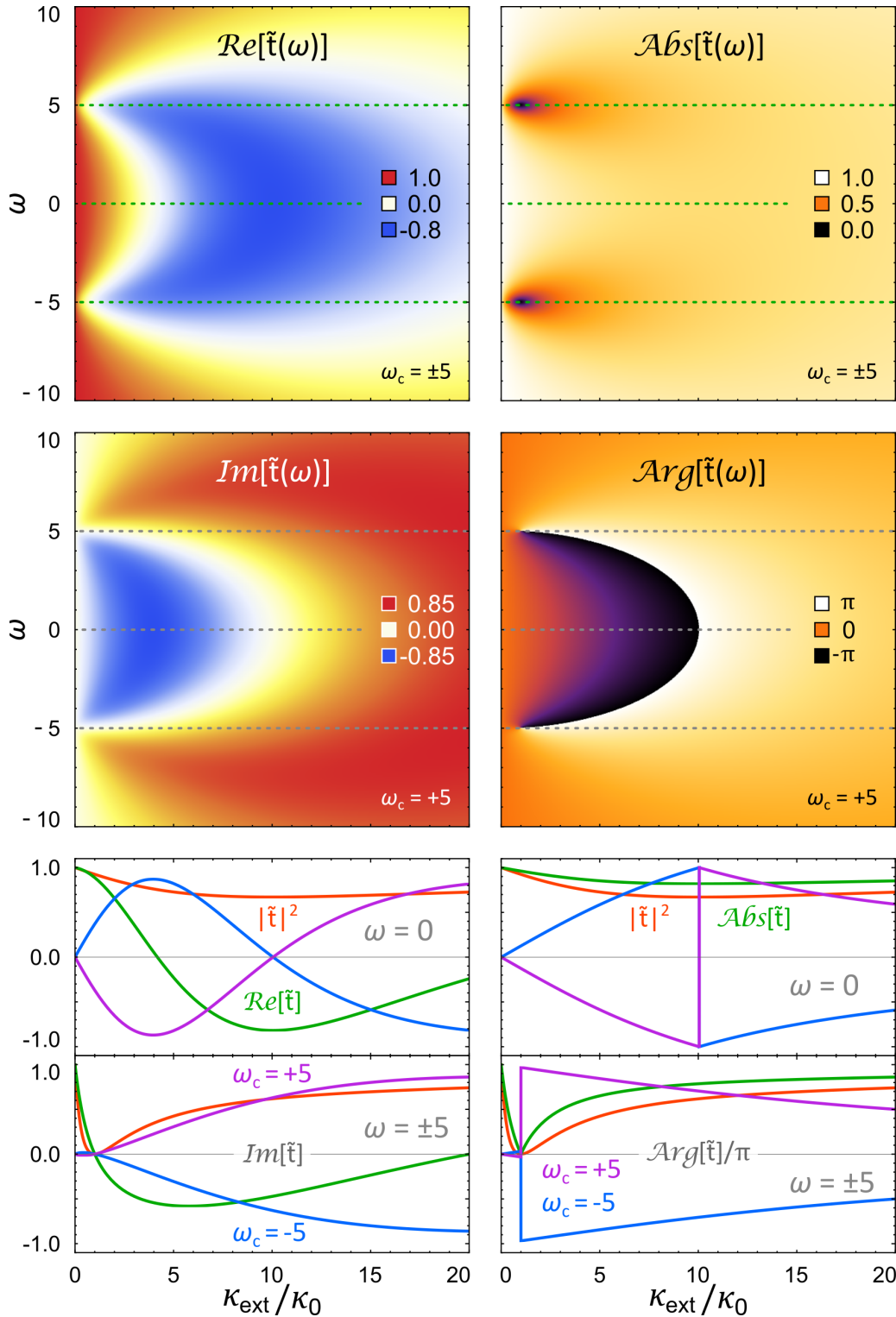


Figure 4.17. Linewidth dependence of the two-photon transmission function. Left column: density plots of the real (top) and imaginary (middle) part of the spectrum $\tilde{t}(\omega)$ (equation (4.89)), as a function of the linewidth set by the parameter κ_{ext} . The pair of (bottom) plots respectively display the cuts (horizontal dotted lines) at $\omega = \{0, \pm 5\}$ in the corresponding colours, along with $|\tilde{t}(\kappa_{ext})|^2$. Right column: same as the left column, but instead for the absolute value (top) and argument (middle) of $\tilde{t}(\omega)$ as a function of κ_{ext} . Parameters used: $\kappa_0 = 1/2$, with $\omega_c = +5$ throughout. Note that for $\omega_c = -5$, the signs of both $Im[\tilde{t}(\omega)]$ and $Arg[\tilde{t}(\omega)]$ flip, amounting to an inversion of the displayed density plot colour-scale (as indicated in the corresponding cyan and magenta curves contained in the bottom plots).

suppression are centred symmetrically around $\omega = 0$ at $\pm\omega_c$, and broaden as κ_{ext} is increased. The two-photon transmission at ω_c similarly evolves as $|\tilde{t}(\omega_c)| = |\kappa_0 - \kappa_{\text{ext}}/\kappa|^2$. The real part can become negative (is negative for $\omega = \omega_c$ and $\kappa_{\text{ext}} > \kappa_0$) and the imaginary part, again, flips sign depending on $\text{sgn}(\omega_c)$. Likewise, the argument also flips sign depending on $\text{sgn}(\omega_c)$, and takes values between $\pm\pi$ over the linewidth κ . These phase changes appear as bands or gradients near $\omega = \pm\omega_c$, that shift and broaden as κ_{ext} is increased. As shown in the line cuts, the transmission $|\tilde{t}(\omega)|^2$ at $\omega = |\omega_c|$ can be fully tuned between one (for $\kappa_{\text{ext}} = 0$ or $\kappa_{\text{ext}} \rightarrow \infty$) and zero (when $\kappa_{\text{ext}} = \kappa_0$).

The next Section explores how this two-photon transmission function modifies the two-photon spectrum, paying attention to the particular filtering parameters that characterise its spectral location with respect to the coherent component, as well as its linewidth and centre attenuation.

4.5.2 Filter Action on the Two-photon Component

When the spectrum of the two-photon wavefunction, $\tilde{\Psi}(\omega)$, is subject to the filtering function, $\tilde{t}(\omega)$, a modified spectrum, $\tilde{\Psi}^t(\omega) = \tilde{t}(\omega) \cdot \tilde{\Psi}(\omega)$, is obtained. It now features a frequency-dependent phase and amplitude that depends not only on the resonance fluorescence parameters γ and Δ , but also on the parameters set within the filter function: $\tilde{t}(\omega; \omega_c, \kappa_0, \kappa_{\text{ext}})$. As such, the relative amplitudes of the coherent and incoherent components of the two-photon spectrum, along with the phase imparted upon each, can be spectrally modified by tuning both the centre frequency and linewidth of \tilde{t} . Density plots of the modified two-photon spectrum (for a fixed non-zero atom–light detuning and filter linewidth), as a function of the filter centre ω_c , are showcased in Figure 4.18 for a selection of parameters of interest. These are broken down into its real $\text{Re}[\tilde{\Psi}^t(\omega)]$ and imaginary $\text{Im}[\tilde{\Psi}^t(\omega)]$ parts (left column), alongside the absolute value $\text{Abs}[\tilde{\Psi}^t(\omega)]$ and argument $\text{Arg}[\tilde{\Psi}^t(\omega)]$ of $\tilde{\Psi}^t(\omega)$ (right column). They clearly illustrate how the modified two-photon spectrum is the product between the unmodified two-photon spectrum, $\tilde{\Psi}(\omega)$ (cf. Figure 4.14), and the filter function, $\tilde{t}(\omega)$ (cf. Figure 4.16). The amplitude of the former is cut into and reduced by the latter in the vicinity of the filtering lines, while the phase is accordingly altered. Notably, as depicted in the 1D line cuts for a constant $\omega_c = \pm|\Delta|$ (bottom row), the phase of the modified two-photon spectrum explicitly depends on $\text{sgn}(\omega_c)$.

Choosing the notch-like form of filter function $\tilde{t}(\omega)$, as defined in equation (4.89), enables an amplitude reduction of the coherent component when placed at $\omega_c = \omega_L$, that is tuned solely by the parameter κ_{ext} for a given κ_0 . For an atom–laser detuning much larger than both the filter linewidth and the excited state decay rate, $|\Delta| \gg \{\kappa, \gamma\}$, the incoherent component lies in the unity transmission band and thus remains largely unaffected. This situation is shown in Figure 4.18 for constant $\omega_c = 0$. Conversely, placing the filter at $\omega_c = \pm|\Delta|$ and setting $\kappa \gg \gamma$ reduces the amplitude of the incoherent

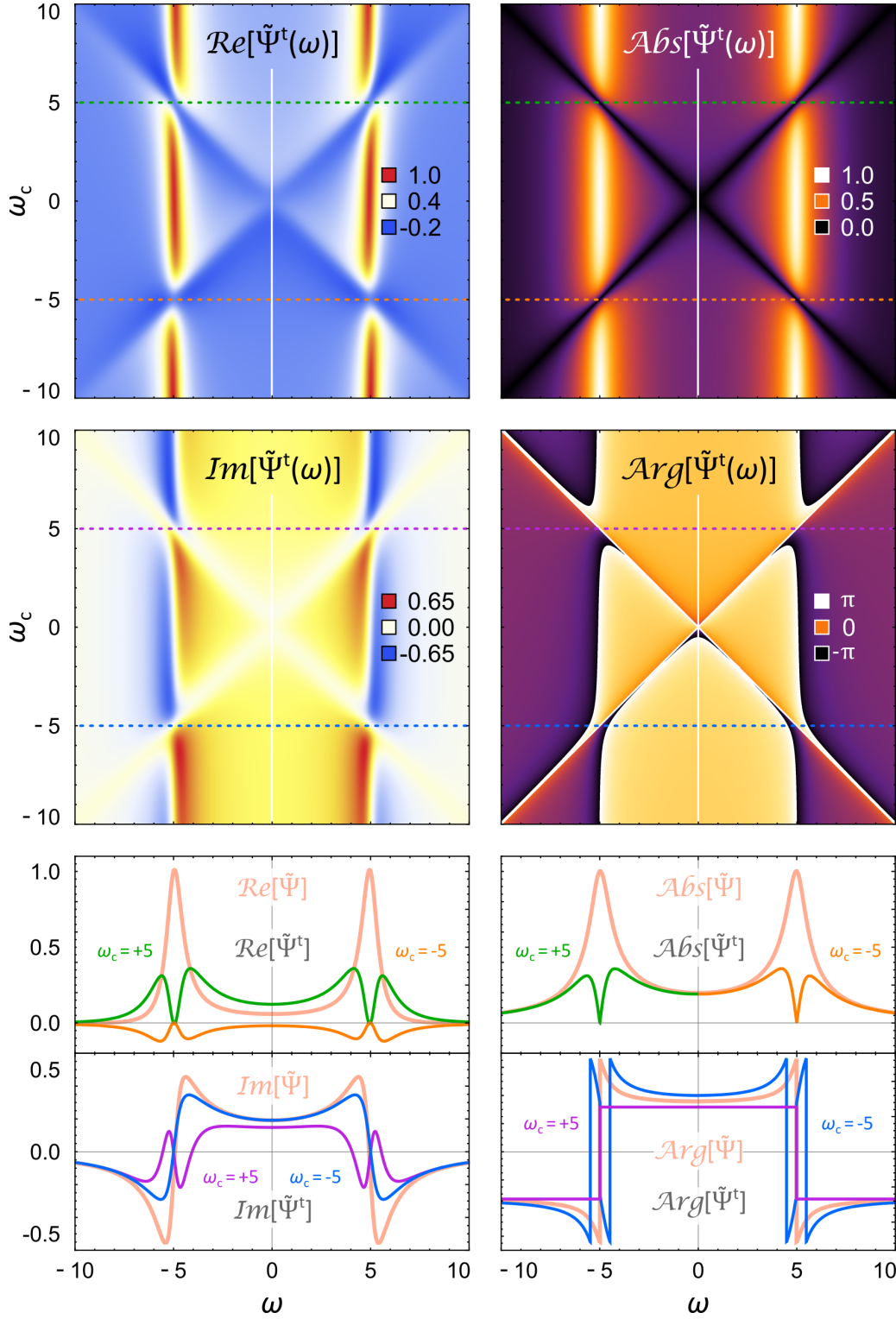


Figure 4.18. Filtered two-photon spectrum. Left column: density plots of the real (top) and imaginary (middle) part of the two-photon spectrum, $\tilde{\Psi}^t(\omega)$, that is subject to the two-photon filter function, $\tilde{t}(\omega)$ (equation (4.89)), as a function of the Lorentzian centre frequency ω_c . These spectra at $\omega_c = \pm 5$ (horizontal dotted lines) are displayed, using corresponding colours, in a separate plot (bottom). The unfiltered spectra, $\text{Re}[\tilde{\Psi}(\omega)]$ and $\text{Im}[\tilde{\Psi}(\omega)]$, are also included here. Right column: same as the left column, but instead for the absolute value (top) and argument (middle) of $\tilde{t}(\omega)$ as a function of ω_c . Parameters used: $\Delta = -5\gamma$, $\kappa_0 = \kappa_{\text{ext}} = \gamma/2$.

component. However, due to the finite Lorentzian-lineshape filter of linewidth κ acting on the spectrally broad, and also Lorentzian-shaped γ (in contrast to the coherent delta-peak), a non-uniform spectral suppression across the incoherent component will result, inhibiting its complete removal. What remains still leads to an interference between the two. An alternative to the latter situation would be to choose a narrow band-pass type filter function centred at the coherent component, i.e., $1 - \tilde{t}(\omega)$ with $\omega_c = \omega_L$, and fixing the linewidth $\kappa_{\text{ext}} = \kappa_0$ such that $|1 - \tilde{t}(\omega_c)|^2 = 1$. In this case, for $|\Delta| \gg \kappa$, only the incoherent component will have its amplitude effectively reduced to zero.

Access to the photon statistics of this modified scattered field requires the time-dependent two-photon wavefunction following the filtering. This is obtained by taking the inverse Fourier transform of the two-photon spectrum after the filter, as

$$\begin{aligned}\Psi^t(\tau) &= \frac{1}{\sqrt{2\pi}} \int_{-\infty}^{\infty} \tilde{\Psi}^t(\omega) e^{-i\omega\tau} d\omega \\ &= \Psi(\tau) * t(\tau)\end{aligned}\tag{4.90}$$

where the last line illustrates that the product of the two frequency domain functions, $\tilde{\Psi}(\omega)$ and $\tilde{t}(\omega)$, corresponds to the convolution of their time-domain counterparts, respectively $\Psi(\tau)$ and $t(\tau)$. This yields the total two-photon component of the scattered field that is transmitted past the well-defined filter function, in the time domain, which can be modified by the filter parameters. By defining $\omega_L \equiv \omega = 0$ to work in the frame of the laser, the photon statistics of the filtered field can be straightforwardly analysed for the interesting cases of tuning either the filter centre ω_c or its linewidth κ (and centre-frequency transmission $(\kappa_0 - \kappa_{\text{ext}})^2/\kappa^2$). These investigations are presented in the next Section.

4.5.3 Second-order Correlation Function of the Modified Field

The time-dependent two-photon component of the scattered and filtered field is given by $\Psi^t(\tau)$ (equation (4.90)), for which its probability density allows to compute the unnormalised second-order correlation function according to $G^{(2)}(\tau) = |\Psi^t(\tau)|^2$. Normalisation of $G^{(2)}(\tau)$ is achieved by division with the square of the mean photon flux following the filtering as

$$g^{(2)}(\tau) = \frac{|\Psi^t(\tau)|^2}{\left(|\tilde{t}(\omega = \omega_L)| n_{\text{coh}} + \underbrace{|\tilde{t}(\omega = \Delta)|}_{\approx 0} n_{\text{inc}} \right)^2},\tag{4.91}$$

where $|\tilde{t}(\omega)|$ is the transmission coefficient at the frequency ω (equation (4.88)) with n_{coh} and n_{inc} the S -dependent scattering rates of the coherent and incoherent two-photon

4. Theory of Selective Resonance Fluorescence

components (equations (4.63) and (4.64), respectively). Note that for $S \ll 1$, the second term in the denominator is negligible as indicated. This equation therefore ensures that $g^{(2)}(\tau)$ settles to unity for $|\tau| \gg 0$, and can be used for a comprehensive study of the second-order correlation function of the filtered resonance fluorescence under various configurations of the filtering and excitation parameters contained within $\Psi^t(\tau)$. In particular, large parameter sweeps of the filter settings ($\{\kappa, \omega_c\}$) – for a given two-photon spectrum ($\{\omega_L \equiv 0, S, \Delta\}$) – can reveal the evolution of the photon statistics between filtering arrangements of interest.

Figures 4.19, 4.20, and 4.21 display three selected investigations into the photon statistics of the filtered resonance fluorescence, encapsulated in equation (4.91), with each focussing on a particular parameter sweep. In order to limit the parameter space under investigation to only the filter parameters, the fluorescence spectrum (prior to filtering) is appropriately fixed. The considered setting of resonance fluorescence is thereby chosen to use a fixed driving strength and detuning, respectively as $S = 0.02$ and $\Delta = -4\gamma$, such that the coherently and incoherently scattered two-photon components

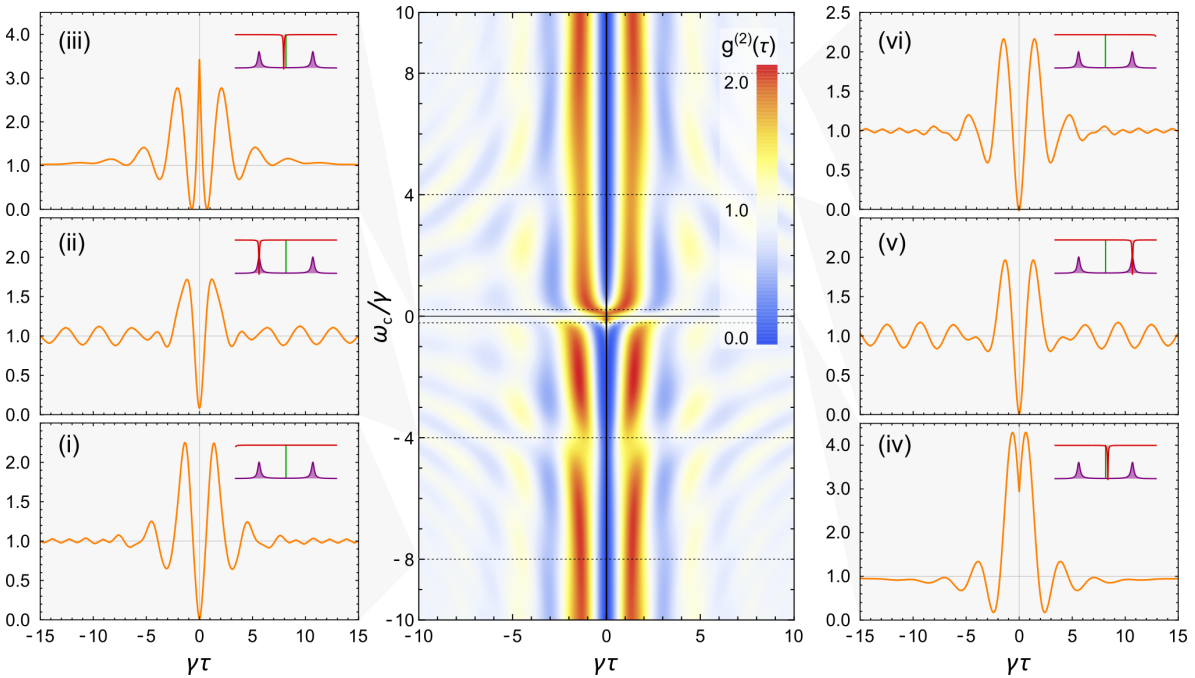


Figure 4.19. Sweep of the two-photon transmission function across the two-photon spectrum. The centrally-located density plot displays the relative modification of the second-order correlation function, according to $g^{(2)}(\tau) = 1 + |\Psi^t(\tau)|^2 - |\Psi^t(|\tau| \gg 0)|^2$, as the centre frequency of $\tilde{t}(\omega)$ is varied. Plots of the cuts (horizontal dotted lines) along constant values of the centre frequency, using equation (4.91), are displayed for $\omega_c/\gamma =$ (i) -4 , (ii) -2 , (iii) -0.1 , (iv) $+0.1$, (v) $+2$, (vi) $+4$. Each of these includes an inset to illustrate the spectral locations of the coherent two-photon component $\tilde{\alpha}$ (green), the incoherent component $\tilde{\phi}(\omega)$ (purple), and $\tilde{t}(\omega_c)$ (red). Parameters used: laser frame $\omega_L \equiv 0$, detuning $\Delta = -4\gamma$, filter linewidth of $2\kappa = \gamma/3$ with $\kappa_0 = \kappa_{\text{ext}}$.

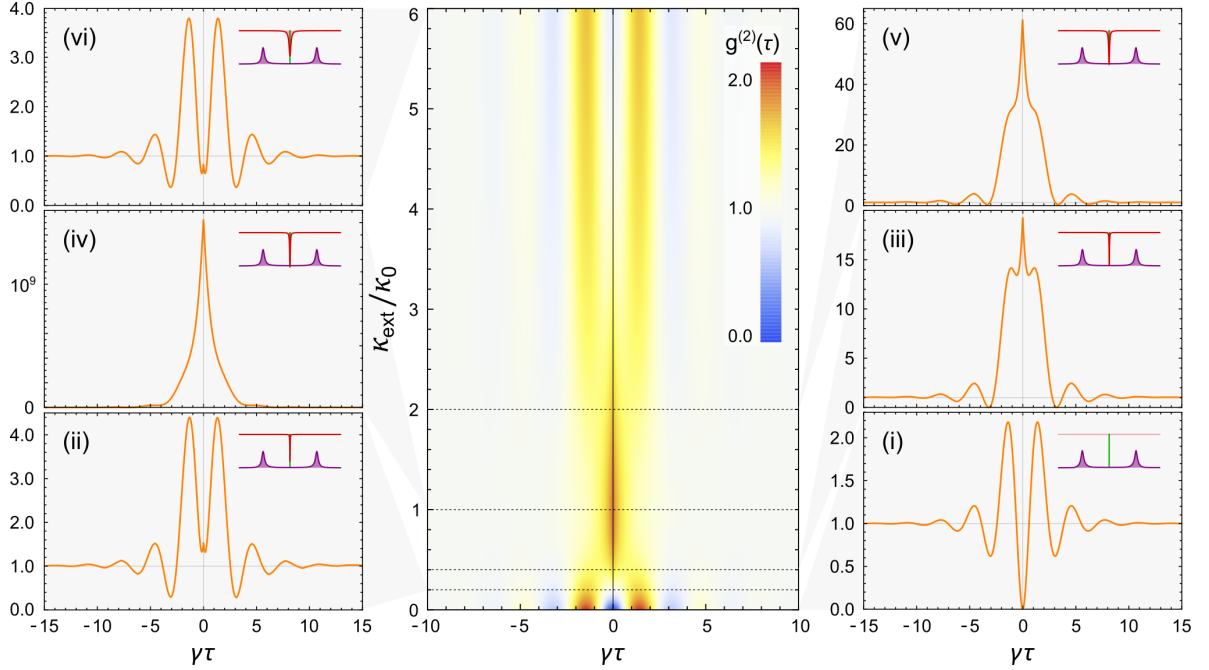


Figure 4.20. Removing the coherently scattered two-photon component.

The centrally-located density plot displays the relative modification of the second-order correlation function, according to $g^{(2)}(\tau) = 1 + |\Psi^t(\tau)|^2 - |\Psi^t(|\tau| \gg 0)|^2$, as the amplitude of the coherent component is varied – controlled by setting $\tilde{t}(\omega_c = \omega_L)$ and varying the parameter κ_{ext} . Plots of the cuts (horizontal dotted lines) along constant values of $\kappa_{\text{ext}}/\kappa_0$, using equation (4.91), are displayed for $\kappa_{\text{ext}}/\kappa_0 =$ (i) 0, (ii) 0.2, (iii) 0.4, (iv) 1, (v) 2, (vi) 6. Each of these includes an inset to illustrate the spectral locations of the coherent two-photon component $\tilde{\alpha}$ (green), the incoherent component $\tilde{\phi}(\omega)$ (purple), and $\tilde{t}(\kappa_{\text{ext}})$ (red). Parameters used: laser frame $\omega_L \equiv 0 = \omega_c$, detuning $\Delta = -4\gamma$, filter linewidth at $\kappa_0 = \kappa_{\text{ext}}$ of $2\kappa = \gamma/3$.

are spectrally well-separated. Furthermore, excitation in the laser frame is considered, such that $\omega_L \equiv \omega = 0$. With this, the centre position of the filter, ω_c , and its linewidth, κ , are both respectively tuned. Figure 4.19 displays the case of a fixed filter linewidth ($2\kappa = \gamma/3$), where the filter centre is swept across the fluorescence spectrum. Figures 4.20 and 4.21 consider a fixed filter centre, respectively at $\omega_c = \omega_L$ and $\omega_c = \pm|\Delta|$, while sweeping the filter linewidth (and therefore the transmission coefficient at ω_c). All three Figures contain a density plot of $g^{(2)}(\tau)$ as the relevant parameter is varied, along with line cuts at specific constant values of the parameter as indicated. The former are calculated using $g^{(2)}(\tau) = 1 + G^{(2)}(\tau) - G^{(2)}(|\tau| \gg 0)$ in order to compress the out-of-plane scale (for visualisation purposes), while the latter are calculated according to equation (4.91) to show the expected τ -dependent $g^{(2)}(\tau)$ amplitude. Furthermore, each of the line cuts contain an inset that depicts the two-photon and filter transmission spectra for reference.

The plots displayed in Figures 4.19, 4.20, and 4.21, all demonstrate how the antibunching behaviour that is expected for this setting of resonance fluorescence ($g^{(2)}(\tau = 0) = 0$ with damped Rabi oscillations at $\Omega \approx |\Delta|$ for $|\tau| > 0$) can be easily

4. Theory of Selective Resonance Fluorescence

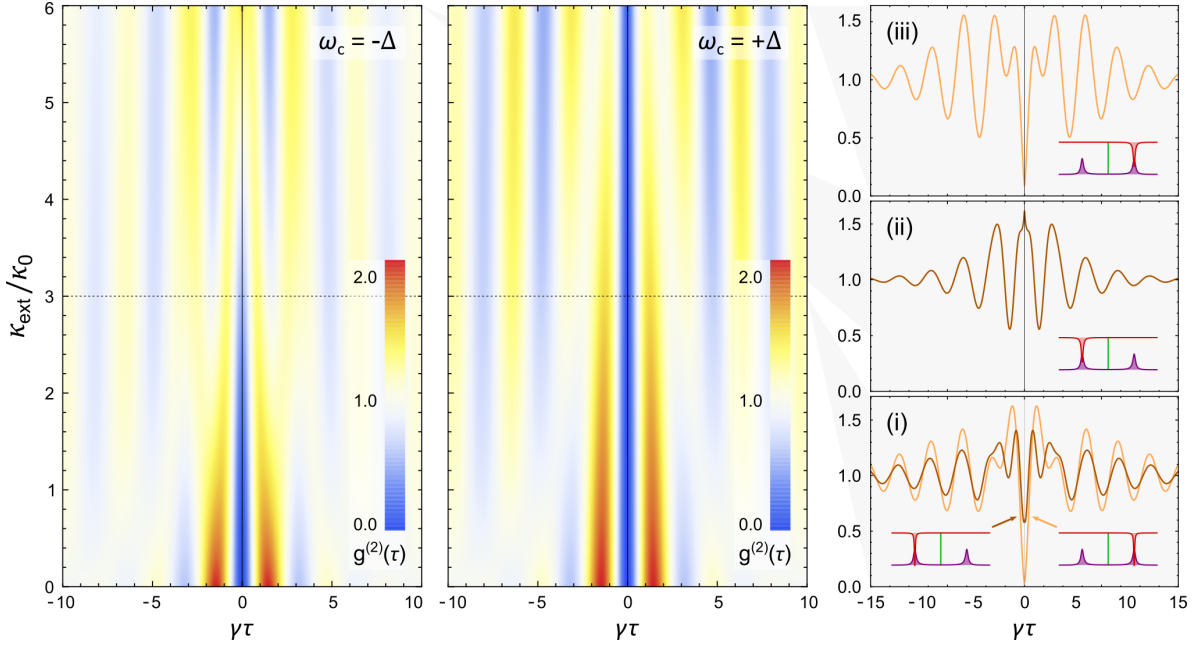


Figure 4.21. Suppressing the incoherently scattered two-photon component.

A pair of density plots display the relative modification of the second-order correlation function, according to $g^{(2)}(\tau) = 1 + |\Psi^t(\tau)|^2 - |\Psi^t(|\tau| \gg 0)|^2$, as the amplitude of the incoherent component is varied – controlled by respectively setting $\tilde{t}(\omega_c = \pm|\Delta|)$ and varying the parameter κ_{ext} . Plots of the cuts (horizontal dotted lines) along constant values of $\kappa_{\text{ext}}/\kappa_0$, using equation (4.91) are displayed for $\kappa_{\text{ext}}/\kappa_0 =$ (i) 0, (ii) 3, (iii) 6. Each of these includes an inset to illustrate the spectral locations of the coherent two-photon component $\tilde{\alpha}$ (green), the incoherent component $\tilde{\phi}(\omega)$ (purple), and $\tilde{t}(\kappa_{\text{ext}})$ (red). Parameters used: laser frame $\omega_L \equiv 0 = \omega_c$, detuning $\Delta = -4\gamma$, filter linewidth at $\kappa_0 = \kappa_{\text{ext}}$ of $2\kappa = \gamma/3$.

spoiled upon filtering, as the interference condition between the two-photon components of the coherently and incoherently scattered light is modified. In the extreme cases of $\kappa_{\text{ext}} \ll \kappa_0$ or $|\omega_c| \gg |\Delta|$, antibunching is trivially preserved since $\tilde{t}(\omega) \approx 1$ such that $\tilde{\Psi}^t(\omega) \approx \tilde{\Psi}(\omega)$. As soon as the amplitude of either component is reduced by the filter, which occurs for $-\Delta \lesssim \omega_c \lesssim \Delta$ and $\kappa_{\text{ext}}/\kappa_0 > 0$, the two components no longer perfectly destructively interfere (at $\tau = 0$), and a perfect antibunching in the photon statistics of the remaining light is no longer apparent ($g^{(2)}(\tau = 0) > 0$). In the incidences where the amplitude of the coherent component is significantly attenuated with respect to the incoherent component (i.e., when $\tilde{t}(\pm\Delta) \approx 1$ and $\tilde{t}(\omega_L) < 1$), the antibunching is not only spoiled, but is transformed into a bunching peak ($g^{(2)}(\tau = 0) > 1$). The most drastic departure from an antibunched dip occurs for the situation in which the coherent component is maximally removed, when $|\tilde{t}(\omega_L)| = 0$ and $\omega_c = \omega_L$, where the isolated incoherent component ensures that the bunching peak is maximised. Due to the finite width of the filter, in conjunction with the finite atom–laser detuning, the spectrum of the filtered incoherent component is slightly modified with respect to the unfiltered spectrum (i.e., the presence of the filter removes a small but finite portion of

the incoherent spectrum around ω_L). This manifests in the photon statistics as noticeable oscillations in the bunching peak of $g^{(2)}(|\tau| > 0)$, when compared to the idealised case of removing the coherent component with a delta-like spectral filter to leave the incoherent component unaffected, in which such oscillations are not present. This latter case was addressed in Section 4.4.1 (cf. Figures 4.12 and 4.13). The modified interference between the two components through filtering persists for $|\tau| > 0$, where the damped Rabi oscillations present in the unmodified fluorescence can be either enhanced or diminished in frequency or amplitude. This behaviour of the modified photon statistics at both $\tau = 0$ and $|\tau| > 0$ is highlighted when comparing the line cut plots, where it becomes evident that the temporal shape additionally depends on the sign of ω_c , i.e., whether the detuning of the filter centre with respect to the laser frequency is positive or negative (cf. Figure 4.18). In this way, a tuning of the filtering parameters enables a full manipulation of the photon statistics of the quantum light source – from fully antibunched to fully bunched, to almost anywhere in between.

Finally, for comparison to the notch-like filter case presented thus far, the case of filtering the resonance fluorescence with a band-pass filter centred at the laser frequency (see Figure 4.15) can also be examined: by replacing $\tilde{t}(\omega)$ with $1 - \tilde{t}(\omega)$ in equation (4.90) onwards. Figure 4.22 displays the resulting second-order correlation functions obtained for this latter filtering scenario, using different filter widths κ . Figure 4.22(a) displays $g^{(2)}(\tau)$ for both a zero and non-zero atom–laser detuning (respectively to the left and right of $\tau = 0$), while Figure 4.22(b) plots the corresponding $g^{(2)}(\tau = 0)$

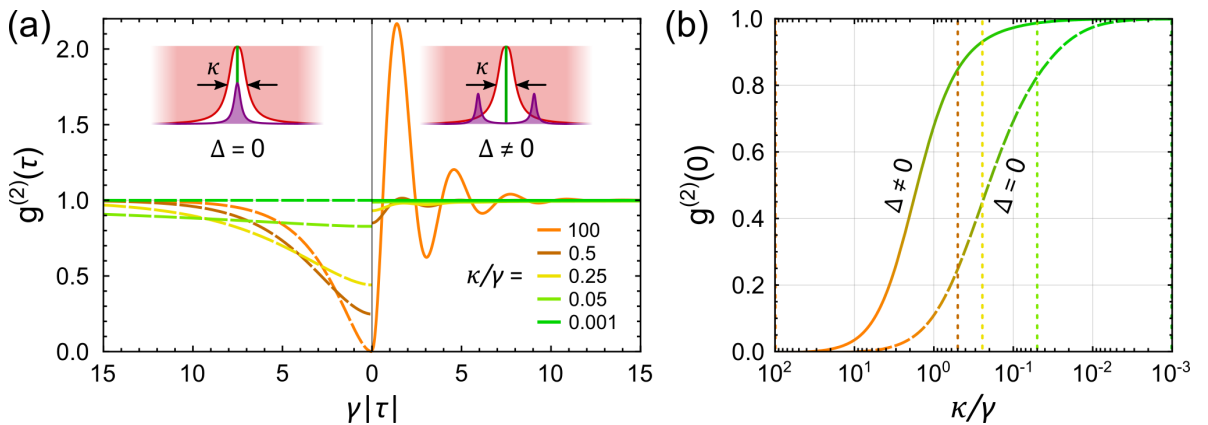


Figure 4.22. Removing the incoherently scattered two-photon component. (a) Second-order correlation functions of the filtered resonance fluorescence, using a band-pass filter centred at the laser frequency, for different filtering widths. The cases of zero detuning ($\Delta = 0$) and non-zero detuning ($\Delta = -4\gamma$) are both displayed, respectively to the left (dashed lines) and right (solid lines) of the origin. Insets: the spectral locations of the coherent component (green), the incoherent component (purple), and the band-pass filter (red). (b) $g^{(2)}(\tau = 0)$ as a function of the band-pass filtering width, for the cases of zero detuning ($\Delta = 0$) and non-zero detuning ($\Delta = -4\gamma$). The vertical dotted lines are colour-coded with respect to the curves shown in (a).

amplitude as a function of the band-pass filter width. Here, the coherently scattered component is gradually isolated by reducing κ (see insets), and the antibunching that is initially present for $\kappa \gg \gamma + |\Delta|$, is continuously lost. In the limit of $\kappa \ll \gamma$, the incoherent component is almost entirely removed, and the photon statistics exhibit a loss of all temporal correlations. For the case of a non-zero detuning, the fluorescence spectrum is broader than the resonance spectrum, in which the coherent and incoherent components are both aligned at the laser (and atomic) frequency. As such, narrower filtering is required to reach the same reduction in antibunching when compared to the detuned case. Regardless of detuning, and under a suitably narrow filter linewidth, the band-pass filtering configuration can remove the incoherent component much more efficiently than the band-block filter (cf. Figure 4.21). Conversely, the band-block filtering configuration is much more suited to isolation of the incoherent component (cf. Figure 4.20). This brief investigation into band-pass filtering therefore complements the focus of this Section (notch-like filtering), and further solidifies that antibunched photon statistics in resonance fluorescence arises from interference between the coherently and incoherently scattered components of the light, and that these components each exhibit distinct photon correlations. Isolation of the coherent fraction leads to Poissonian photon statistics [269, 270], and as previously demonstrated, isolation of the incoherent fraction leads to strongly bunched photon statistics.

4.5.4 Multi-line Filtering

Explorations into the modification of the photon statistics of resonance fluorescence has so far been carried out by 'filtering' the two-photon component of the field scattered by a two-level atom. The two-photon filter function employed for this task, $\tilde{t}(\omega)$ (defined in equation (4.89)), is characterised by a pair of Lorentzian lines located at $\omega = \pm\omega_c$. Given the fact that the finite spectral width of each line, κ , can impart non-negligible frequency-dependent phase shifts upon the unmodified two-photon spectrum (see Figure 4.18), having far-reaching consequences on the photon statistics of the filtered light (see Figures 4.19 – 4.21), it is instructive to consider the effect of filtering under multiple, spectrally separated lines.

For this, the filter function defined by

$$\tilde{t}_n(\omega, \omega_c) = \prod_{i=0}^{n-1} \tilde{t}(\omega, \omega_c \pm i \cdot \omega_{\text{FSR}}) \quad (4.92)$$

generates $n = 2i + 1$ duplicates of $\tilde{t}(\omega)$, spectrally located at the centre frequencies $\omega_c \pm i \cdot \omega_{\text{FSR}}$, where $i \in \mathbb{N}$ and ω_{FSR} is the so-called *Free Spectral Range** that sets the magnitude of the spectral separation between adjacent lines. Note that equation

*Note that this description continues with ring-resonator notation, in which adjacent resonator modes are spectrally separated by the quantity defined by the **FSR**. See Sections 2.1 and 5.1.2 for further details.

(4.92) is a generalisation of the single pair of Lorentzian lines considered so far, given by $\tilde{t}(\omega) \equiv \tilde{t}_1(\omega)$ (equation (4.89)) for which $i = 0$, and is therefore a good approximation of the two-photon transmission achieved with a realistic resonator filter (see Section 5.1.2). The extent to which the presence of additional filtering lines impact the photon statistics is worth investigating for the experiment presented in Chapter 5.

The action of such a multiple-line filter on the two-photon component of the scattered field is similarly (see Section 4.5.1) found by the product of the two spectra, $\tilde{\Psi}^{tn}(\omega) = \tilde{t}_n(\omega) \cdot \tilde{\Psi}(\omega)$. The parameter space to explore now also includes the number of Lorentzian lines within the filter function, n (that takes odd values only), as well as the spectral separation between them, ω_{FSR} . Appropriate restrictions on these additional parameters can be imposed by considering the desired filtering configuration. For example, the interesting scenario of suppression of the coherently scattered component while maintaining minimal modification to the incoherently scattered component would require the filtering conditions: $\omega_c = \omega_L$ with $\kappa \ll \gamma$ ($\kappa_{\text{ext}} = \kappa_0$), and that $|\omega_{\text{FSR}}| \approx 2|\Delta|$ such that $|\tilde{t}_n(\omega = \Delta)| \approx 1$. An example of this described configuration is depicted in Figure 4.23(a), which qualitatively compares the unnormalised second-order correlation function of the filtered light, $|\Psi^{tn}(\tau)|^2$, where $\Psi^{tn}(\tau) = \mathcal{F}[\tilde{\Psi}^{tn}(\omega)]$, for the considered filtering cases of $n = \{1, 3, 5\}$ with $\omega_{\text{FSR}}/2 = |\Delta| = 5\gamma$ and $\kappa = \gamma/2$. It clearly demonstrates that the inclusion of additional filtering lines, despite being well-separated from the spectral positions of the incoherent component, still have an effect on the photon statistics – due to each filtering line removing a small but finite portion of the incoherent spectrum around the spectral locations $\omega_L \pm i \cdot \omega_{\text{FSR}}$. Despite this, the fast oscillations that appear when using a $\tilde{t}_{n>1}(\omega)$ filtering always overlay the $\tilde{t}_{n=1}(\omega)$ case. This comes from the fact that all the filtering functions, as defined here, efficiently remove the coherent component, and are – like the triplet structure of the two-photon spectrum – spectrally symmetric with respect to the laser frequency (see inset of Figure 4.23(a)). The difference between the curves is displayed in Figure 4.23(b), and illustrates that it is only around a few percent in the case considered. This difference from the effect of the additional filtering lines can be minimised under an appropriate setting of the filtering parameters, i.e., $\Psi^{tn>1}(\tau) \approx \Psi^{tn=1}(\tau)$ for $\omega_{\text{FSR}} \gg |\Delta|$ (and $\kappa \ll \gamma$).

According to this analysis, the considered case of removing the coherent component from the scattered field can also be achieved with a 'realistic' notch filter (e.g., a ring-resonator) that includes multiple filtering lines. The resulting bunching behaviour in the photon statistics persists, so long as the additional lines are sufficiently separated from the spectral spread of the incoherent component. The general temporal dynamics of the second-order correlation function of the filtered light can be well captured by using a single-line filtering model ($\tilde{t}_1(\omega)$).

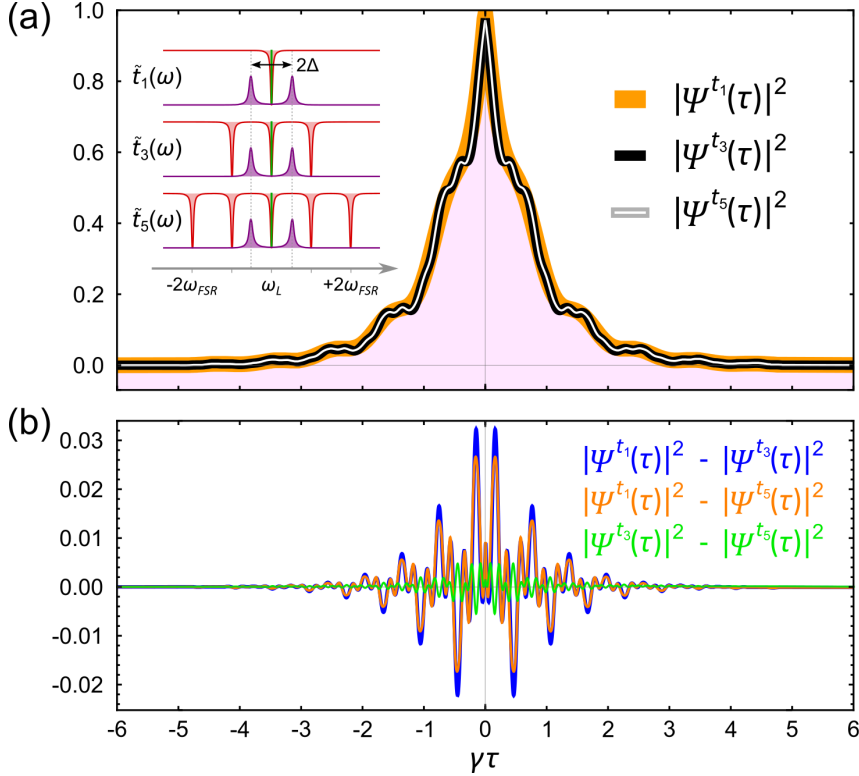


Figure 4.23. Bunched photon statistics under multiple filtering lines. (a) A comparison of $|\Psi^{t_n}(\tau)|^2$, using equation (4.92), for the $n = \{1, 3, 5\}$ (respectively $i = \{0, 1, 2\}$), displayed in orange, black, and white) filtering configuration, with $\omega_c = \omega_L$. The line separation is set to $\omega_{\text{FSR}}/2 = |\Delta| = 5\gamma$ with linewidth $\kappa = \gamma/2$ (for $\kappa_{\text{ext}} = \kappa_0$). The inset depicts the considered filtering configurations, and are overlaid with the unmodified two-photon spectrum. For visibility purposes, the curve thicknesses are decreased for increasing n . (b) The relative difference between the curves shown in (a), as $|\Psi^{t_1}(\tau)|^2 - |\Psi^{t_3}(\tau)|^2$ (blue), $|\Psi^{t_1}(\tau)|^2 - |\Psi^{t_5}(\tau)|^2$ (orange), and $|\Psi^{t_3}(\tau)|^2 - |\Psi^{t_5}(\tau)|^2$ (green).

4.6 To Conclude

This Chapter comprises a comprehensive visit to the well established, and yet presently active, subject of *resonance fluorescence*: the study of the emission emanating from a two-level system that is driven at (or close to) its transition energy. In broadly following the historical developments within this field (see Section 4.1), the treatment of resonance fluorescence in a semiclassical manner – whereby a *quantum* emitter interacts with a *classical* field – allowed to establish the optical Bloch equations (see Section 4.2) and analyse the properties of the scattered field (see Section 4.3). The former have been an essential tool for calculating the quantum properties of the latter, revealing its composition of distinct coherently and incoherently scattered components. From the solutions to the optical Bloch equations, the well-known quantum phenomenon of photon antibunching in resonance fluorescence – characterised by the second-order correlation function of the scattered field assuming a value of $g^{(2)}(0) = 0$ – can be

theoretically obtained. It demonstrates that the quantum emitter, being a saturable absorber, emits *only* a single photon at a time. Despite this fact, that is backed up by decades-old experiments, the field scattered by a two-level emitter *does* actually contain two or more photons at the same time – it’s just that different types of higher-order emission processes always exactly cancel out to preserve single photon emission. This picture was substantiated by considering the low saturation regime of resonance fluorescence, and the ways in which the scattered field contains a two-photon state using a wavefunction description (see Section 4.4). It was shown that two simultaneous photons can be scattered both coherently and incoherently with equal amplitude, but exactly out of phase, leading to a full destructive interference of their states. Both of these scattering processes feature distinct spectra and can be neatly separated by detuning the driving field with respect to the frequency of the emitter. By introducing a suitable spectral filter function into the scattered field, a strong modification of the scattered two-photon component can be achieved by selectively attenuating either the coherent or incoherent contribution to the scattered field. What remains features a drastically different second-order correlation function from the characteristic antibunching (see Section 4.5), where the limiting cases of; (i) isolating the coherent component yields a flat $g^{(2)}$, demonstrating a loss of all correlations and that the temporal dynamics of the driving field are recovered, while (ii) a full suppression of the coherent component yields a temporally-symmetric bunching in the $g^{(2)}$, demonstrating that the incoherently scattered two-photon component consists of photon pairs that appear to have been simultaneously scattered by the emitter. In particular, the cases explored in the regime of partial suppression of either component reinforces the picture that these two components interfere with each other, demonstrating that the photon statistics of the scattered field can be fully tuned by disturbing the destructive interference condition.

This Chapter has therefore posited that it should be possible to, under suitable driving along with an appropriate spectral filtering, transform the expected single photon emission in the resonance fluorescence of a two-level quantum emitter into a field consisting solely of photon pairs. The experimental confirmation of this interference picture in resonance fluorescence will be presented in the next Chapter, where the second-order correlation function of the field scattered by an isolated two-level quantum emitter – in the form of a single optically trapped ^{85}Rb atom – is measured. By introducing a spectral filter based on a **Fibre-Ring Resonator**, that can selectively attenuate the coherent component, the remaining incoherent component can be shown to exhibit a time-symmetric bunching behaviour – characteristic of simultaneously propagating photons – that has been the focus of this Chapter.

5

Observation of Two-Photon Emission from a Single Atom

When Rayleigh photons are rejected, some amplitudes vanish, leading to a bunching behaviour.

J. Dalibard and S. Reynaud, 1983 [259]

This Chapter presents a first experiment performed with the newly-constructed *CQED 2.0* set-up, concerning the optical trapping of single ^{85}Rb atoms, spectral filtering of their resonance fluorescence, and subsequent measurement of the modified photon statistics of the scattered and filtered field. An experiment of this sort is easily motivated by the fact that the characteristic triplet structure of the Mollow spectrum in resonance fluorescence – arising from the contributions of the coherently and incoherently scattered light – naturally calls for an investigation into correlations between its spectral components. Indeed, a number of studies of such frequency-resolved photon correlations in the resonance fluorescence of an isolated quantum emitter, both experimental and theoretical, have been inspired by this notion of spectrally filtering the Mollow triplet. The unfiltered Mollow spectrum always exhibits the well-known antibunching behaviour in the photon statistics (see for example [262]). Auto-correlation of the isolated central Rayleigh peak results in uncorrelated photon statistics [264, 269, 270], while that of the side peaks show antibunched statistics [261, 265, 291]. A cross-correlation between the Rayleigh peak and either side peak is also antibunched [292], whereas cross-correlation between the side peaks shows a bunched and time-ordered behaviour [260–262, 265]. Furthermore, filtering between the peaks has revealed a rich landscape of photon correlations, such as multi-photon transitions that exhibit

strong bunching [266, 293, 294]. Most of these (experimental) studies have been aided by investigating the strong driving regime, in which the fluorescence spectrum of the strongly dressed emitter is both spectrally broad and features well-separated components of the Mollow triplet. This allowed for a relatively straightforward separation of the various lines in the Mollow spectrum, either spatially or via filtering, to facilitate such frequency-resolved correlation studies.

The experiment presented in this Chapter instead investigates filtered resonance fluorescence deep in the weak driving regime, in which the Mollow spectrum is dominated by Rayleigh (coherent) scattering, but still features a vanishingly small contribution from the incoherently scattered light. It is the presence of the latter that is necessary for antibunching in the photon statistics [269, 270]. By detuning the excitation light with respect to the atomic transition, the spectral sidebands of the incoherently scattered light are split from the Rayleigh peak, and can be separated by employing a narrow-band filter. Here, the collected fluorescence is transmitted through a notch-like filter that is constructed by a **Fibre-Ring Resonator**. By appropriately setting the filter, the coherently scattered component in the collected fluorescence can be efficiently removed in order to isolate the incoherent contribution. The photon statistics of the filtered light are then studied for different suppressions of the coherent component. Performing such an experiment allows for a detailed investigation into the quantum processes underlying the light scattering by a single two-level quantum emitter, particularly for this setting of resonance fluorescence in the weak-driving regime. A complete separation of the two components that make up the scattered field – the coherently and incoherently scattered components – enables an examination of one without the other. A partial separation between the two further grants access to study their interplay, revealing how antibunched photon statistics in the scattered field relies exactly on their precise balance. The observation of time-symmetric photon bunching when suppressing the coherently scattered component of the resonance fluorescence indicates the detection of *photon pairs* that have been *simultaneously* scattered by the atom, providing insights into the nature of the incoherent component, as well as its role in resonance fluorescence. The results presented in this Chapter have been published as an article in a peer-reviewed journal:

[69] L. Masters, X.-X. Hu, M. Cordier, G. Maron, L. Pache, A. Rauschenbeutel, M. Schemmer, and J. Volz. On the simultaneous scattering of two photons by a single two-level atom. *Nature Photonics* **17**, 972–976 (2023).

Figure 5.1 depicts an artist’s [295] visualisation of this experiment [69], whereby a stream of single (antibunched) photons from the resonance fluorescence of a single quantum emitter is transformed into (bunched) photon pairs by a single spectral filter component. As shall be seen, along with being conceptually simple, the performed

experiment is straightforward to implement in practice, consisting of only a few key ingredients. Testament to this, is the fact that the idea for it was developed well on the road into the construction of the full CQED 2.0 system, and only minor modifications to the set-up had to be applied. Everything carried out was performed with a "blank" CQED system, i.e., all but the resonator fibre itself (and its two coupling nanofibres) were present. This late-stage of the experiment design process had been – in any case – initially planned for, in order to bake-out the entire system and to subsequently get the double-MOT and optical dipole trap for single atoms operational.

In this Chapter, a comprehensive view on the techniques employed in order to realise the described experiment will precede a presentation of the main measurement results and their accompanying theoretical modelling, complementary to that presented in Chapter 4. A discussion on the interpretation of the presented results will conclude this Chapter.

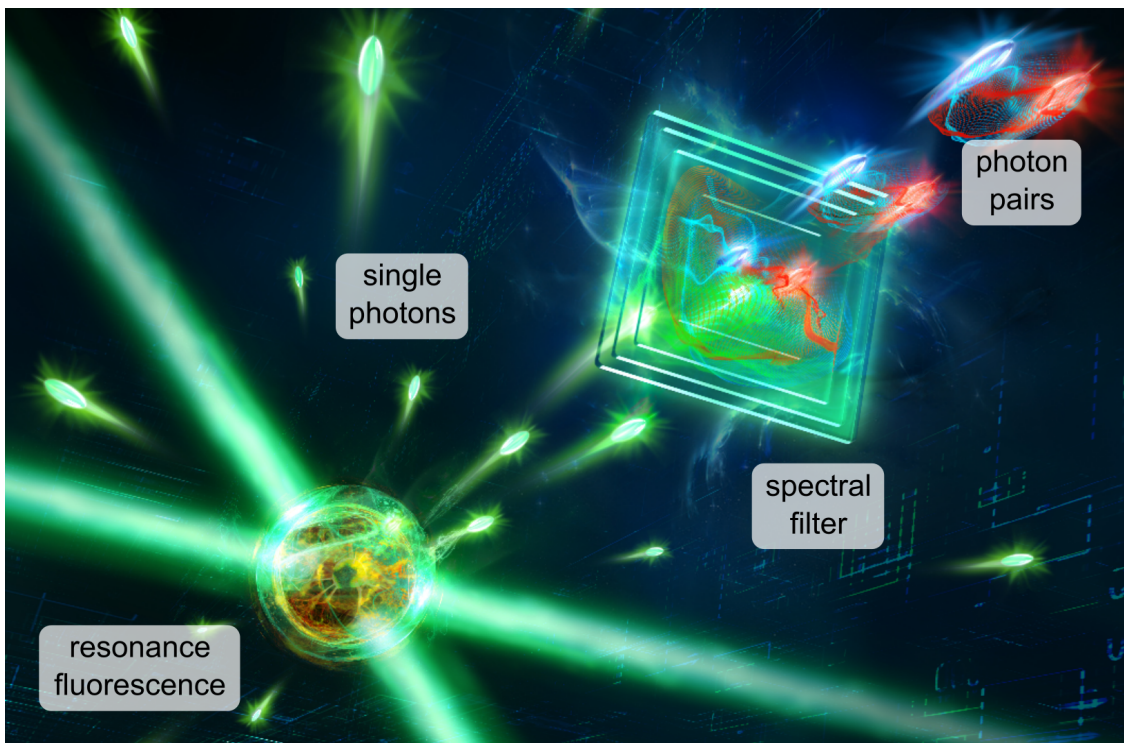


Figure 5.1. Artist's visualisation of the simultaneous scattering of two photons by a single two-level atom. Original unedited image from [295], commissioned for the press release of [69]. *A single atom is excited by laser light and scatters one photon after another. An optical filter removes certain colour components from this stream of single photons. This causes the remaining photons to become pairs that leave the filter simultaneously.* Press release image caption. Full article available at [296].

5.1 Experimental Methods

The flair of this experiment is defined not only by its conceptual simplicity of only two photons interacting with a single two-level emitter as presented in Chapter 4, but also by the few key practical ingredients that are employed. Respectively, these are; the resonance fluorescence of a single two-level quantum emitter, its appropriate spectral filtering, and its subsequent measurement and analysis. The majority of experimental techniques for realising these ingredients are well-established, with many being a common starting point in a plethora of experiments that work with cold atoms (for example). The single quantum emitter utilised here is a single ^{85}Rb atom (see Section 2.1.1) that is loaded, from the upper MOT as presented in Section 3.4.3, into an optical dipole trap generated by the in-vacuum lens system introduced in Section 3.3.3. Spectral filtering of the collected resonance fluorescence is then performed with use of a **Fibre-Ring Resonator (FRR)**, while measurements of the second-order correlation functions are performed using a **Hanbury Brown and Twiss (HBT)** set-up. Explanations of these techniques shall be outlined in the following Sections 5.1.1, 5.1.2, and 5.1.3 respectively, while the measurement results are presented and discussed in the subsequent Section 5.2.

5.1.1 Trapping and Detecting Single Atoms

In order to study the field scattered by a single quantum emitter under the setting of resonance fluorescence, a suitable two-level system must be prepared, isolated, and excited, with its emitted field then effectively collected. For this, a single, optically trapped atom is an ideal candidate. The first step in obtaining one is to generate a microscopic optical dipole trap into which – no more than one atom at a time – can be loaded and kept. As outlined in Section 3.3.3, the design of an optical system for exactly this task combines the techniques of optical dipole trapping and confocal microscopy in order to trap, detect, and eventually manipulate single ^{85}Rb atoms for their (deterministic) strong-coupling to the **WGM** of the bottle microresonator. Its design is greatly simplified by employing only a single aspheric lens inside the **UHV** chamber, which is utilised as an element to generate the optical trap in the tight focus of a red-detuned trapping laser beam, as well as for the collection of fluorescence light emitted by a trapped atom. The remaining standard optics are located outside of the vacuum chamber. The optical system built and utilised for characterising the focus achieved with this high-**NA** lens, and for all the experiments presented in this Chapter, is displayed in the main part of Figure 5.2, and is a stepping stone to the full proposed optics as presented in Section 3.6 (cf. Figure 3.21).

All optics required for the set-up are mounted on an optical breadboard (*MB3045/M, Thorlabs, Inc.*), which is placed directly in front of the Science chamber's front viewport

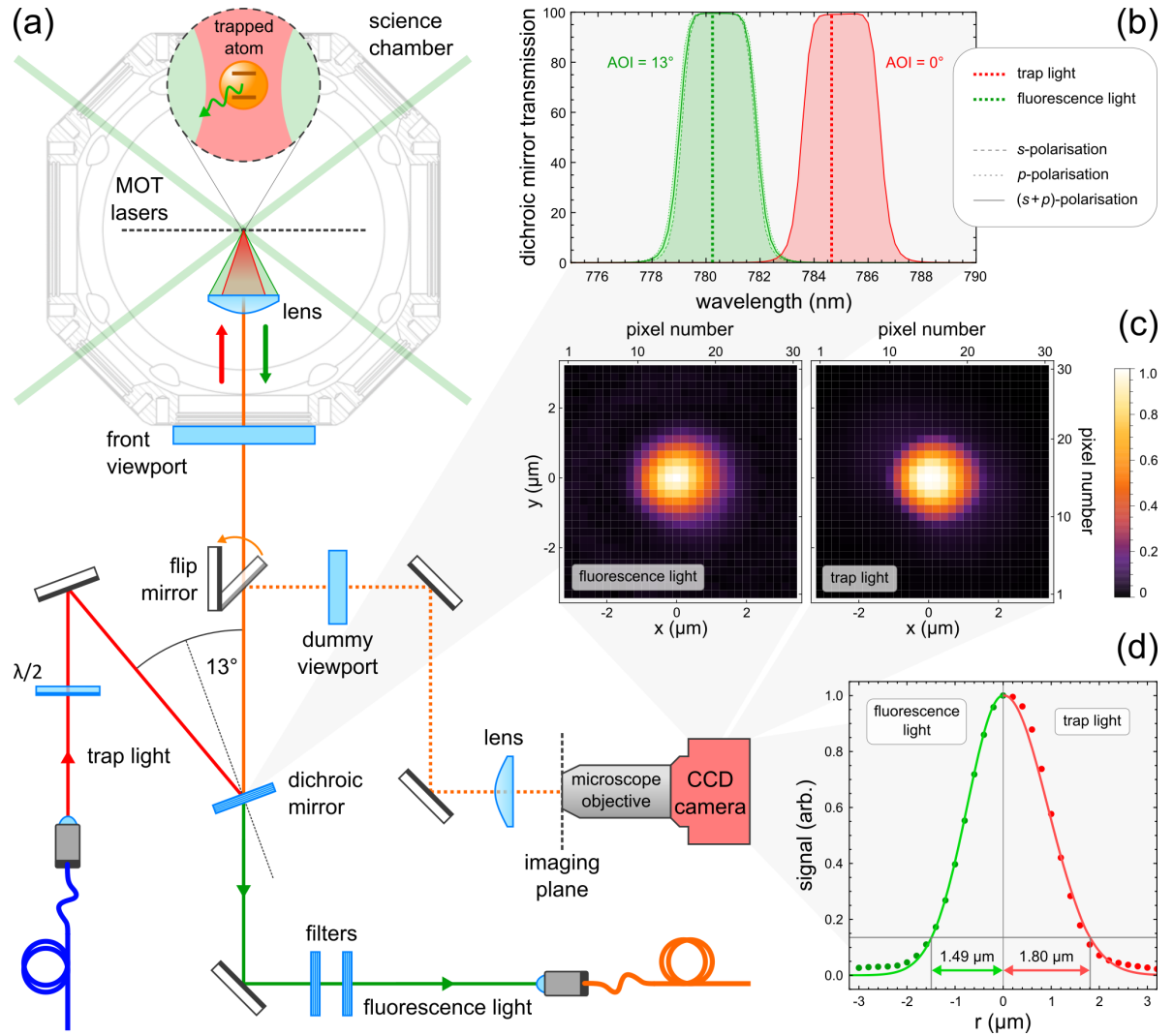


Figure 5.2. The confocal microscope. (a) Schematic representation of the constructed system for the optical trapping and imaging of single atoms. The beam paths coloured in red, green, and orange, respectively correspond to those taken by the trap light, fluorescence light, and their combination. (b) Wavelength-dependent transmission properties of the filter utilised to efficiently separate the trapping and fluorescence beam paths. The characteristic curves are displayed for an AOI of 0° (red lines) and 13° (green lines), and shown for different incident polarisations (see key). The wavelengths of the trapping ($\lambda_t = 784.65$ nm) and fluorescence ($\lambda_0 = 780.24$ nm) lights are marked. (c) A 2D intensity distribution in the focal plane of the fluorescence (left) and trap (right) beams, as measured by the objective and CCD camera in the alignment path. (d) Azimuthally integrated radial intensity distributions of the measured data in (c) (data points), and corresponding fits (solid lines). The curve to the left (right) of the origin corresponds to the fluorescence (trap) light, with the extracted $1/e^2$ waists indicated.

5. Observation of Two-Photon Emission from a Single Atom

and fastened to the raised breadboard atop the optical bench. The source of light for the optical tweezer is the trapping laser outlined in Section 3.7.4 at a wavelength of $\lambda_t = 784.65$ nm (red-detuned to the ^{85}Rb D₂ line by 4.41 nm), which is coupled into a PM fibre (*P3-780PM-FC-5*, *Thorlabs, Inc.*) and guided to the set-up. The Gaussian intensity distribution of the fibre output has a specified Mode Field Diameter (MFD) of $\phi_{\text{mfd}} \approx 3$ μm , and diverges at an angle of $\theta \approx 2\lambda_t/\pi\phi_{\text{mfd}}$ to the optical axis. It is collimated to a beam waist diameter of $d_t = 2f_c^t \tan(\theta) = 3.7$ mm by an aspheric lens (*C220TMD-B*, *Thorlabs, Inc.*) that is placed at its focal length of $f_c^t = 11$ mm away from the output facet of the fibre. The collimated beam then passes through a HWP for alignment of its linear polarisation before being appropriately steered, by a pair of mirrors prior to the vacuum viewport, towards the asphere mounted within the Science chamber. It is this last lens that is responsible for generating the optical tweezer, by tightly focussing the incident trapping laser beam to generate a spatial intensity distribution for creation of the dipole potential for single atoms (c.f. Figure 2.14). Note that this design permits beam-passage through the front vacuum viewport at normal incidence, such that the introduction of wavefront errors by the viewport's glass can be minimised. The asphere under UHV then doubles as a high-NA (= 0.55) collection optic for the fluorescence emitted by an atom trapped inside the tweezer. For this chosen lens (see Section 3.3.3), with diameter $D_l = 12.5$ mm and focal length $f_l = 10$ mm, the total fraction of fluorescence that can be collected (assuming isotropic emission into a unit sphere of 4π area), is determined by the lens' opening acceptance angle $\theta_c = \sin^{-1}(0.55) = 33^\circ$, which corresponds to a solid angle of $\Omega/4\pi = \frac{1}{2}(1 - \cos(\theta_c)) = 8.2\%$. The collected fluorescence is then coupled into a second single-mode fibre for guiding to the filtering and detection part of the experiment (see Sections 5.1.2 and 5.1.3 respectively). This single-mode fibre doubles as a narrow spatial filter. The collection efficiency of the in-vacuum lens, plus the fibre, is reduced to around 1.3%, see Section 5.1.1.2 for further details. A set of filter optics (*Semrock LL01-780-12.5*, *IDEX Corporation*) before this coupling fibre, as well as shielding along its entire length*, minimises the coupling of stray light that would otherwise significantly contribute to a high noise background. The aspheric lens used for coupling the fluorescence into the collection fibre has a focal length of $f_c^f = 25$ mm (*AL1225H-B*, *Thorlabs, Inc.*). The wavelengths of the tweezer beam and fluorescence light have a difference of around only ~ 5 nm, and so their spatial separation is achieved with the addition of a narrow-band interference filter to serve as a dichroic mirror in the combined beam path. At an AOI of 0° , the chosen filter (*Semrock LL01-785-25*, *IDEX Corporation*) features a nominal transmission bandwidth $> 90\%$ of ~ 3 nm (FWHM) centred at a wavelength of 785 nm, as displayed in Figure 5.2(b). The filter is operated as a low-loss dichroic mirror for the incident trap and

*The bare fibre has several layers of protective plastic coating included from the manufacturer. Additional layers of reflective foil and rubber tubing around the fibre were found to be necessary in order to avoid the coupling of stray light, which could originate not only from the lasers, but also from instrument displays in the lab.

collected fluorescence light fields by exploiting its spectral properties when used at a non-normal **AOI**. As the **AOI** is increased from 0° , the features of the spectrum are shifted towards lower wavelengths as well as being split into two distinct spectra – one for *s*-polarised and one for *p*-polarised light. Both of these dependencies on the **AOI** arise from the design of the filter, which is comprised of many thin-film dielectric layers of varying refractive indices and thicknesses, such that light of a defined wavelength is efficiently transmitted at normal-incidence (i.e., light reflected from the various stacked surfaces add up exactly out of phase). By increasing the **AOI**, this interference condition is modified by virtue of an increase in the optical path lengths through the dielectric stack. Additionally, birefringence and Fresnel reflectivity [297] of the media and surface boundaries begins to play a role, leading to a slight broadening (narrowing) of the transmission bandwidth for incident light that is *p*-polarised (*s*-polarised). The desired working point of the filter was found to be at an **AOI** $\simeq 13^\circ$, where the transmission (reflection) at the fluorescence (trapping) wavelength of 780.24 nm (784.65 nm) is above 99.5%. Furthermore, at this **AOI**, the transmission around 780 nm remains constant for any incident polarisation, see Figure 5.2(b).

For alignment purposes, a flip-mirror is included in the combined beam path as the last optical element before injection into the Science chamber. When operated, the flip mirror redirects beams originating from each fibre towards a calibrated imaging system* that consists of a $20\times$ microscope objective (*M Plan Apo NIR B 20X*, *Mitutoyo GmbH*) and a **CCD** camera (*F131B*, *AVT Marlin GmbH*) separated by 158 mm within a cage system. This combination, when placed at the focal plane of the high-**NA** lens, is used to characterise the intensity distribution in the focal region by measurement of the **Point Spread Function (PSF)** (see next Section 5.1.1.1). As such, the addition of it as a permanent fixture in the trap optics set-up enables alignment and overlap of the tweezer and fluorescence foci by beam walking with their respective and independent steering mirrors after each fibre outcoupling. For better accuracy, a 'dummy' viewport glass† (*10QW40-30AR.16*, *Newport Corporation*) is included to model the beams impinging on the lens under **UHV**. Note that coarse alignment of the two beam paths was initially performed by placing a fibre at the focus of the high-**NA** lens, and maximising the fibre coupling of each beam.

5.1.1.1 Focussing Lens Characterisation

A reliable optical characterisation of the in-vacuum high-**NA** lens is necessary in order to determine its working capabilities and suitability for atom trapping and fluorescence collection. Importantly, a quantified measure of the deviation from an ideal Gaussian focus provides information on the alignment and aberrations within the optical system,

*Calibration was performed with a test target (*R1DS1N*, *Thorlabs, Inc.*) yielding a resolution of 0.244 $\mu\text{m}/\text{pixel}$.

†The thickness of this optic was chosen to match the window thickness of the front viewport.

5. Observation of Two-Photon Emission from a Single Atom

which can lead to deformations of the trapping potential. As introduced in Section 3.3.3, a large body of work was carried out for selection of a lens that satisfies the mounting restrictions of the set-up, for which the details are recorded in [179]. The results of this investigation rendered a suitable candidate for the lens. Prior to placing the chosen lens under vacuum, its focus was imaged with use of the objective and CCD camera combination introduced in the preceding Section 5.1.1 that is displayed in Figure 5.2(a). Despite the fact that the collimated Gaussian trap beam profile does not uniformly fill the finite aperture of the in-vacuum lens, i.e., $d_t \sim D_l/3$, a small amount of beam clipping will occur nonetheless. The intensity at the position of the lens' focus can be calculated by Fourier optics [298], where the complex valued electric field in the plane of the focus, \mathbf{E}^{focus} , can be determined by the Fourier transform of the input field, \mathbf{E}^{lens} , at the plane of the lens. Using a cylindrical coordinate system, this is given by

$$\mathbf{E}^{focus}(\rho, \phi) = \int_0^{2\pi} \int_0^{D_l/2} \mathbf{E}^{lens}(\rho', \phi') e^{-i\frac{k}{f_l}\rho\rho' \cos(\phi-\phi')} \rho' d\phi' d\rho', \quad (5.1)$$

where ρ and ϕ are respectively the radial and azimuthal coordinates in the focal plane (ρ' and ϕ' are those in the lens plane). For the cylindrically symmetric Gaussian input field, $\mathbf{E}^{lens}(\rho') = \mathbf{E}_0 e^{-\rho'^2/d_t^2}$, the angular dependence in the above can be evaluated to yield

$$\mathbf{E}^{focus}(\rho) = 2\pi \mathbf{E}_0 \int_0^{D_l/2} e^{-\frac{\rho'^2}{d_t^2}} e^{-i\frac{k\rho\rho'}{2f_l}} J_0\left(\frac{k\rho\rho'}{f_l}\right) \rho' d\rho', \quad (5.2)$$

where the zeroth-order Bessel function of the first kind, J_0 , arises from this angular integration. The resulting intensity distribution in the focal plane, up to a normalisation constant, is determined by evaluation of equation (5.2) and taking the absolute square, i.e., $I^{focus}(\rho) \propto |\mathbf{E}^{focus}(\rho)|^2$. Due to the radial integration (up to the finite lens aperture) of the Bessel function, the focal spot then approximately follows an Airy-like pattern that is modulated by a Gaussian envelope [298]. The intensity distribution at the focal plane can then be approximated by a Gaussian function, allowing to extract the value for the $(1/e^2)$ waist radius by a fit to the measured data. This analysis is also performed for an input field originating from the fluorescence collection fibre at a wavelength of $\lambda_0 = 780.24$ nm, the results of which are displayed in Figure 5.2(d) and recorded in Table 5.1. For the constructed confocal microscope system, this yields focus spot sizes in the focal plane of the focussing lens of approximately 1.8 μm and 1.5 μm , respectively for the trap and fluorescence beams. These two spots are carefully aligned to ensure that their intensity maxima spatially coincide, such that the mode originating from the collection fibre is positioned at the location of the trap centre. Determining the collection efficiency of photons originating from the atoms in the trap centre is considered next.

input beam	wavelength	collimation lens	focus waist fit
optical dipole trap	$\lambda_t = 784.65$ nm	$f_c^t = 11$ mm	$w_t = 1.80 \pm 0.20$ μm
fluorescence light	$\lambda_0 = 780.24$ nm	$f_c^f = 25$ mm	$w_0 = 1.49 \pm 0.20$ μm

Table 5.1. Confocal microscope spot sizes. A record of the measured beam waists in the focus of the in-vacuum lens that is used for generating the optical dipole trap and for collection of the resonance fluorescence of single trapped atoms.

5.1.1.2 Collection Efficiency

Establishment of a confocal microscope for the optical trapping and detection of single atoms ensures that only light produced in the vicinity of its focal plane, i.e., at the location of the dipole trap, can be detected. This is facilitated by coupling the light collected by the focussing lens into the collection fibre, which acts as a spatial filter. An important parameter that characterises this set-up is the single photon collection efficiency, η_0 , that defines the percentage of the photons emitted by a single atom (located inside the dipole trap) that are picked up by the focussing lens and then coupled into the well-defined spatial eigenmode of the collection fibre. In order to estimate an experimentally-applicable value for this single photon collection efficiency, a calculation of the overlap between the dipole emission pattern of the single atom with the Gaussian beam profile provided by the TEM_{00} output of the collection fibre must be conducted. In order to simplify this calculation, the atom is assumed to be located at the centre of the dipole trap, with the focus of the Gaussian mode at the position of the atom. Both fields then have identical curvature of the wavefronts in the far-field, and the overlap between them can be calculated by integrating the electric field over the wavefront in spherical coordinates. This calculation is presented in the following.

It is necessary to first define the characteristics of the atomic dipole emission. Here, a semi-classical approach to describe this problem is adopted, whereby the atomic dipole is the source of quantised photons via the process of spontaneous decay from its excited to ground state, with the far-field electric field pattern described by that emitted from a Lorentz oscillator. This treatment of the problem can be justified as both quantum and classical descriptions lead to the same emission profiles [209]. In the far-field ($kr \gg 1$), the electric field emitted by such an oscillating dipole is then given by [147]

$$\mathbf{E}^{(p)}(\mathbf{r}) = E_0 \frac{e^{ikr}}{r} [(\mathbf{e}_r \times \mathbf{e}_p) \times \mathbf{e}_r], \quad (5.3)$$

where

$$\mathbf{e}_r = \begin{pmatrix} \sin \theta \cos \phi \\ \sin \theta \sin \phi \\ \cos \theta \end{pmatrix} \quad (5.4)$$

is the unit vector in the radial direction. In the above, $k = 2\pi/\lambda$ is the wavenumber, $E_0 = k^2/4\pi\epsilon_0\epsilon_r$ the field amplitude, and \mathbf{e}_p is the unit vector lying along the axis of the dipole oscillation direction. By considering the radiation emitted from atomic dipoles that are oriented along the Cartesian unit vectors \mathbf{e}_x , \mathbf{e}_y , and \mathbf{e}_z , the atomic field modes read

$$\mathbf{E}^{\sigma^\pm}(\mathbf{r}) = E_0 \frac{e^{ikr}}{r} \left[(\mathbf{e}_r \times \frac{1}{\sqrt{2}}(\mathbf{e}_y \mp i\mathbf{e}_x)) \times \mathbf{e}_r \right] \text{ and} \quad (5.5)$$

$$\mathbf{E}^\pi(\mathbf{r}) = E_0 \frac{e^{ikr}}{r} [(\mathbf{e}_r \times \mathbf{e}_z) \times \mathbf{e}_r], \quad (5.6)$$

where the three polarisation states of σ^\pm and π , defined respectively by the oscillation directions $\mathbf{e}_p = \mathbf{e}_{\sigma^\pm} = 1/\sqrt{2}(\mathbf{e}_y \mp i\mathbf{e}_x)$ and $\mathbf{e}_p = \mathbf{e}_\pi = \mathbf{e}_z$, have been used. The probability that a photon with one of these polarisations is emitted into a differential solid angle, $d\Omega$, is then given by [147]

$$\frac{dP(\sigma^\pm)}{d\Omega} = \frac{3}{8\pi} \frac{1}{2} (1 + \cos^2 \theta), \quad (5.7)$$

$$\frac{dP(\pi)}{d\Omega} = \frac{3}{8\pi} \sin^2 \theta, \quad (5.8)$$

which are the well-known dipole emission characteristics. A depiction of these dipole emission patterns, within the described photon collection set-up, are shown in Figure 5.3 for the considered case of the quantisation and optical axes lying along the z -axis.

With the possible dipole emission patterns that can originate from the atom known, the mode field structure of the Gaussian beam defined by the collection fibre must next be considered. The target fibre mode is defined by, e.g., a beam waist at its focus w_0 that is located at the position of the atom and diverges at an angle $\theta_0 = \lambda/\pi w_0$. For small divergence angles, and in the far-field ($r \gg z_R = \pi w_0^2/\lambda$), its field distribution before the in-vacuum lens is given by

$$\mathbf{E}_G = \frac{E_0}{N_G} \frac{e^{ikr}}{r} e^{-\theta^2/\theta_0^2}, \quad (5.9)$$

which is normalised by the factor N_G .

With the different atomic field modes $\mathbf{E}^{(p)}$ and the Gaussian target mode of the collection fibre \mathbf{E}_G defined and normalised across the half-sphere ($\theta = 0 \dots \pi/2$), the

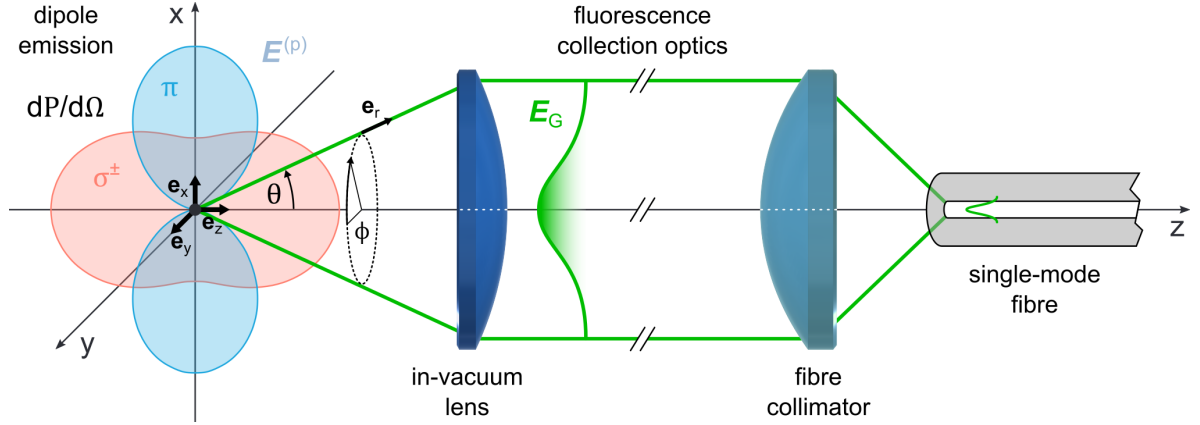


Figure 5.3. Collection of the resonance fluorescence from a single atom. The fluorescence light emitted by an atom can be described as a classical dipole radiation pattern that originates from oscillating atomic dipoles that are arranged along e_x , e_y , and e_z . Exemplary σ^\pm -polarised (red) and π -polarised (blue) emission patterns are displayed in the xz -plane, corresponding respectively to a dipole that oscillates around and along the optical axis (z -axis). Part of the total emitted fluorescence radiation is collected by the in-vacuum lens, and coupled into a single-mode fibre by a fibre collimator lens. The collection efficiency of this set-up can be estimated by evaluating the overlap between the fields of the emitted dipole radiation patterns, $\mathbf{E}^{(p)}$, and the Gaussian eigenmode of the collection fibre, \mathbf{E}_G , in the far-field.

coupling efficiency of each can be calculated by evaluating their overlap according to

$$\eta_0^{(p)} = \frac{1}{2} \left| \int_0^{2\pi} \int_0^{\pi/2} (\mathbf{E}_G \cdot \mathbf{E}^{(p)*}) d\phi \sin\theta d\theta \right|^2. \quad (5.10)$$

Evaluation of equation (5.10) can be performed for the situation sketched in Figure 5.3, where it is clear that the coupling efficiency of π -polarised light will be considerably lower than that of σ^\pm -polarised light for the depicted case of the quantisation axis lying along the optical axis (z -axis) of the confocal microscope. The overall experimental coupling efficiency is evaluated by instead assuming an average of the overlap from modes corresponding to atomic dipoles that oscillate along each of the principal axes, i.e., $\eta_0 = \frac{1}{3}(\eta_0^{(\pi)} + \eta_0^{(\sigma^+)} + \eta_0^{(\sigma^-)})$. Figure 5.4 shows this calculated average coupling efficiency into the Gaussian fibre mode as a function of its waist, w_0 , in units of the wavelength. Using the measured value for the minimum waist of the fibre mode at the plane of the atom, $w_0 = 1.49 \mu\text{m}$ (see Figure 5.2(d)), that corresponds to a divergence angle of $\theta_0 = 9.6^\circ$, an overall collection efficiency of $\eta_0 \approx 1.3\%$ is expected.

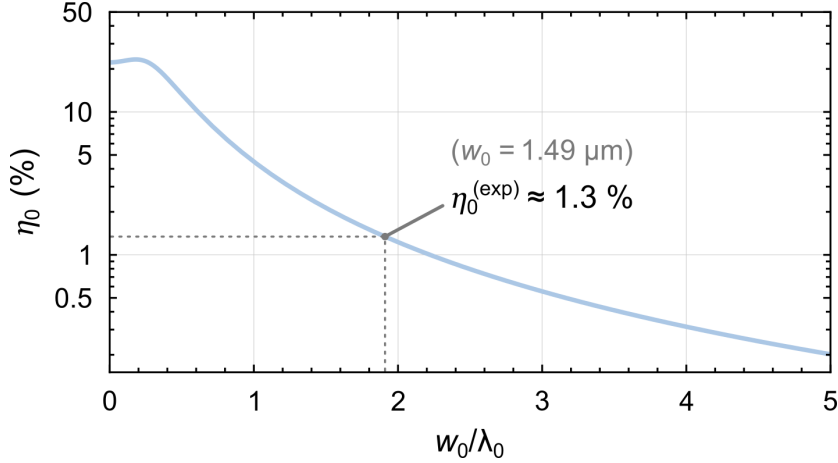


Figure 5.4. Calculated collection efficiency. η_0 is given as an average of the collection efficiencies $\eta_0^{(p \in \{\pi, \sigma^+, \sigma^-\})}$, and plotted as a function of the Gaussian waist w_0 , in units of $\lambda_0 = 780.24$ nm, at the position of the atom. At the experimental setting of $w_0 = 1.49$ μm , a collection efficiency of $\eta_0 \approx 1.3$ % is obtained (dashed lines). Note that for $w_0 < \lambda_0$, the assumption of a paraxial beam for the Gaussian target mode is no longer valid, and deviations from the calculated η_0 would be expected.

5.1.1.3 Trap Characteristics

With the confocal microscope characterised, aligned, and the photon collection efficiency satisfactorily estimated, its integration into the overall set-up enables the optical trapping and observation of single atoms. For this, the reservoir of cold ^{85}Rb atoms contained within the upper MOT is overlapped with the dipole trap located at the focal position of the in-vacuum lens, achieved by an incremental tuning of all six molasses beams, along with the bias magnetic fields, in each direction. For this challenging alignment, a high current (~ 6 A) was applied to the Rb dispensers within the Science chamber, and resonant light sent through the in-vacuum lens to observe the rough focus position by imaging the atomic fluorescence on CCD cameras from multiple directions*. Figure 5.5 depicts one such view of the tweezer beam, as observed from the left side of the in-vacuum lens.

With the tweezer position located within the upper MOT cloud, single atoms can now be cooled into the optical trap and driven to fluoresce by the cooling beams when both the upper MOT and trapping beam are permanently on. A portion of the atomic fluorescence, as previously described, is coupled into an optical fibre and guided directly to an SPCM (*Count-50N-FC, Laser Components GmbH*) that is interfaced to a timetagging unit (see Section 3.8). The parameters used for generating the optical trap are recorded in Table 5.2. With an unoccupied trap, a low countrate of 330 ± 48 s^{-1}

*Note that the focus spots of the beams originating from both the trap and fluorescence collection fibres have to be aligned in conjunction, aided by the alignment arm depicted in Figure 5.2(a).

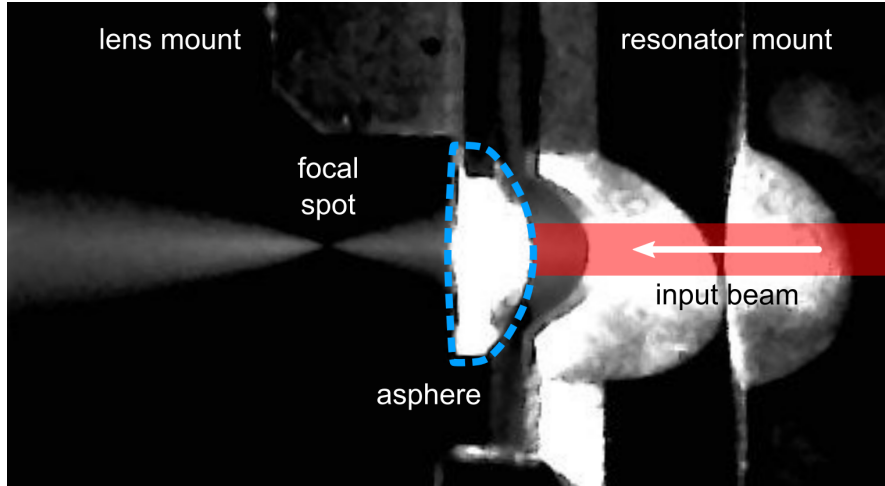


Figure 5.5. View of the tweezer beam. Resonant light (incident beam sketched in for clarity in red) is sent onto the in-vacuum aspheric lens (outlined in dashed blue), which focusses it through a high background of Rb vapour. The fluorescence highlights the free-space beam profile and its focus behind the lens, and is imaged on an infrared-sensitive camera from the left side of the Science chamber.

parameter	value
wavelength	$\lambda_t = 784.65 \text{ nm}$
detuning to D_2	$\Delta_t = 2\pi \times 2.16 \text{ THz}$
power	$P_t = 2.5 \text{ mW}$
waist	$w_t = 1.8 \text{ }\mu\text{m}$
trap depth	$U_0/k_B = 1.66 \text{ mK}$

Table 5.2. Optical dipole trap parameters.

is registered that originates from *darkcounts* of the SPCM* and stray light that is mostly from the background cloud of atoms contained within the MOT. A single atom occupying the trap is registered by a sudden jump in the detected countrate to a value of $1140 \pm 94 \text{ s}^{-1}$ due to the collection of its fluorescence. Figure 5.6(a) displays such an example measured fluorescence trace across a 10 s duration. Here, the typical single-step *telegraph* signal, featuring distinct steps in the fluorescence countrate that correspond to one or zero atoms in the trap, is clearly visible. The absence of higher fluorescence countrates corresponding to two or more simultaneously trapped atoms is verified by recording a fluorescence trace across a longer timescale, and subsequently histogramming the number of occurrences of a detected countrate. This result is displayed in Figure 5.6(b), where only two clearly separated peaks are found. The absence of a third

*For the SPCMs utilised in this experiment, darkcount rates around 50 s^{-1} are typically measured, in conformity with the specifications of the device.

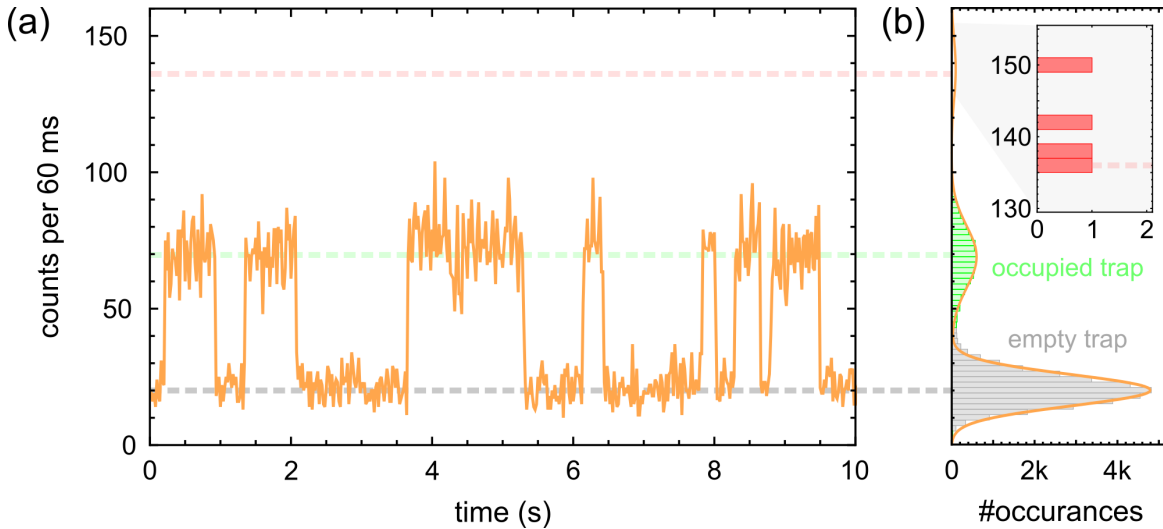


Figure 5.6. Detection of single trapped atoms. (a) A typical trace of the fluorescence countrate observed from the dipole trap region, exhibiting the single-step telegraph signal. The horizontal dashed lines indicate the countrates measured in the case of an empty trap (grey), a trap occupied by one atom (green), and the expected rate for when two atoms are trapped at the same time. (b) A histogram of the fluorescence counts, obtained from a measurement time of approximately two hours. The horizontal bars correspond to the number of occurrences of the respective countrate (shared axis from the plot in (a)), while the solid line is a fit to the first two peaks assuming Poissonian occupation statistics of the trap. This allows to extract the countrates of the empty (first grey peak centre: $19.8/60 \text{ ms}^{-1}$) and occupied (second green peak centre: $68.4/60 \text{ ms}^{-1}$) dipole trap. The inset shows a zoom at the position of the third peak at twice the countrate of the single trapped atom case (peak centre: $136.8/60 \text{ ms}^{-1}$), and demonstrates the negligible probability to trap more than one atom together, confirming the sub-Poissonian occupation statistics.

peak at twice the fluorescence countrate of a single trapped atom is a signature of the sub-Poissonian occupation statistics of the trap, where the probability to simultaneously trap multiple (two or more) atoms can be neglected. This observation confirms that the microscopic dipole trap is operating in the so-called *collisional blockade regime* [178, 299, 300] as intended, whereby inelastic collisions induced by the cooling light between a single atom within the trap volume and a second entering the trap, ensures that there is only one or zero atoms inside any one time (when neglecting the short periods in which a two-body collision occurs).

The loading rate of the trap is determined primarily by the density of the cold atom reservoir, which can be altered by changing the magnetic field gradient of the upper MOT or, alternatively, the dispenser current. It is set at an intermediate point, at a rate lower than the two-body collision rate but high enough to yield a satisfactory duty cycle of the running experiment. The lifetime of single atoms in the trap can be analysed both in the presence and absence of cooling light in order to distinguish the different loss mechanisms. With the cooling light permanently on, in a so-called *bright* trap, the blockade effect is present and losses from the trap can occur due to light-assisted inelastic

two-body collisions. This bright lifetime is found directly from the long-time fluorescence trace, by applying a suitable countrate threshold and histogramming the durations for which a single atom remains trapped. Conversely, a so-called *dark* trap configuration is realised by turning off the cooling light upon registration of a single trapped atom. To determine the corresponding dark lifetime, the cooling light is switched on again after a variable waiting time to enable a redetection of the trapped atom when the measured fluorescence countrate exceeds a threshold value if, indeed, the single atom remained trapped across this duration. In such a scenario, the limiting factor in the lifetime is mainly due to collisions with the (hot) background gas in the vacuum, but potentially also due to intensity fluctuations of the trapping light field that results in heating of the atomic motion in the trap. Figure 5.7 displays the fraction of atoms that remained trapped after a certain holding time in both the bright and dark trap arrangements. The lifetime in both cases is determined by fitting an exponential decay to the data, using a countrate threshold of ≥ 8 photons in 10 ms in order to distinguish the presence of an atom inside the trap. The fits yield $1/e$ decay constants of $t_b = 418 \pm 13$ ms for the bright trap and $t_d = 658 \pm 39$ ms for the dark trap. As expected, the lifetime in the bright trap is lower than that of the dark trap due to the additional loss mechanism from the collisional blockade effect. The measurement of sub-second lifetimes here, even in the dark trap configuration, is consistent with the relatively high background gas pressure of the vacuum environment within the Science chamber of $P_A \gtrsim 9 \times 10^{-9}$ mbar (see Section 3.5.3 for further details), which results from continuous operation of the Rb dispensers. For the experiments performed in this work, the bright lifetime is sufficiently large to yield an acceptable data collection rate.

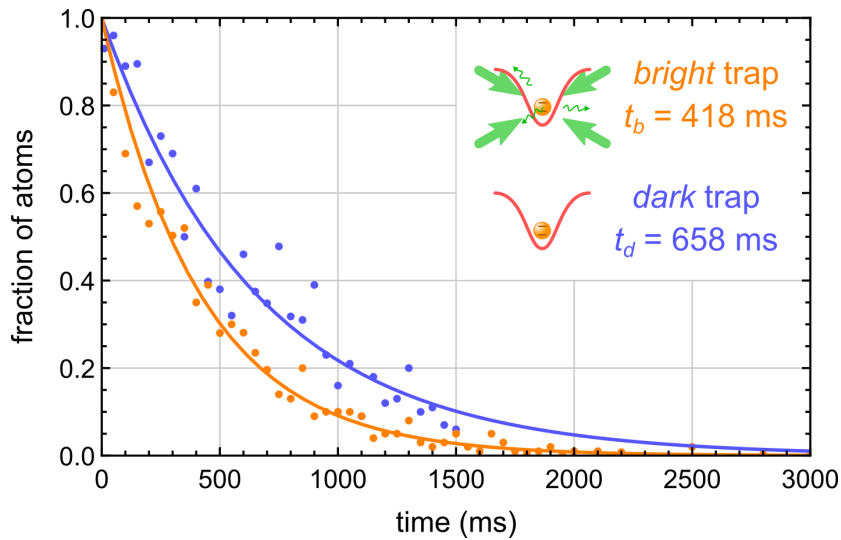


Figure 5.7. Lifetime of trapped atoms observed in both a bright and dark trap. The solid lines are exponential fits to the measured data for the two respective cases of cooling light permanently on (orange) and off (blue) during trapping. The bright and dark trapping configurations are pictorially illustrated in the inset.

An additional characterisation of the optical trap set-up is a measurement of the trapping frequencies, which can provide information on the depth and shape of the trap. There are two characteristic motional frequencies for the free-space Gaussian beam geometry adopted here: a *radial* trap frequency corresponding to oscillations of the atomic position in the transverse focal plane, and an *axial* trap frequency that corresponds to oscillations in the perpendicular plane along the beam axis. While several methods for determining these trap frequencies exist in the context of cold atomic ensembles [301], the predominant measurement technique involves the parametric excitation of oscillations to incite frequency-dependent losses from the trap, and was chosen in this case due to its relative ease of implementation [302–304]. In a time varying potential, the parametric heating effect leads to high loss rates of trapped atoms at the modulation frequencies $2\nu/n$ for integer n , with the strongest loss occurring at $n = 1$ [304]. In order to measure this, the amplitude of the RF-signal supplied to the single-pass AOM within the trapping laser set-up (see Section 3.7.4) is sinusoidally modulated at a frequency of up to 120 kHz upon detection of a single atom inside the trap, as registered by a jump in the fluorescence countrate. In doing so, the optical power of the collected AOM diffraction order is modulated at the applied frequency, which translates to a modulation of the trap’s potential depth. A modulation depth of approximately 10% was chosen, with its duration set to $t_m = 50$ ms in order to be significantly smaller (larger) than the trapping lifetime of ~ 500 ms (expected oscillation period of < 1 ms). Thus, when the modulation frequency is close to a fundamental trapping frequency or any subharmonics, the probability of redetecting the atom after the modulation is diminished due to the parametric heating effect. Figure 5.8(a) displays the results of this investigation, for which several broad dips in the redetection probability can be seen across a large and coarse scan of the applied modulation frequency. By performing finer scans across selected resonances, the spectral location of each can be more accurately determined and subsequently compared to the theoretically expected value. As shown in Figures 5.8(b) and (c), the axial and radial trap frequencies are respectively found to be $\nu_z = 16.5$ kHz and $\nu_r = 86.9$ kHz, which are in reasonable agreement with the theoretically expected values of $\nu_z^{(\text{exp.})} = 17$ kHz and $\nu_r^{(\text{exp.})} = 96$ kHz, obtained when considering confinement in a Gaussian trapping potential [145].

A final characterisation of the optical dipole trap would be to perform a measurement of the energy distribution of the trapped atoms, along the lines of [159] and [305]. One technique involves an adiabatic lowering of the trap depth to a value at which a trapped atom can potentially escape, and evaluating the survival probability as a function of the depth reduction*. Instead here, the mean energy and corresponding temperature of trapped atoms are determined in a novel method by analysis of the measured second-order correlation functions, as shall be outlined in Section 5.2.1.2. In short, since the

*Note that this method was used in determining the energy distribution of atoms trapped at the bottle microresonator, and has been described in further detail in Section 2.4.4 of Chapter 2.

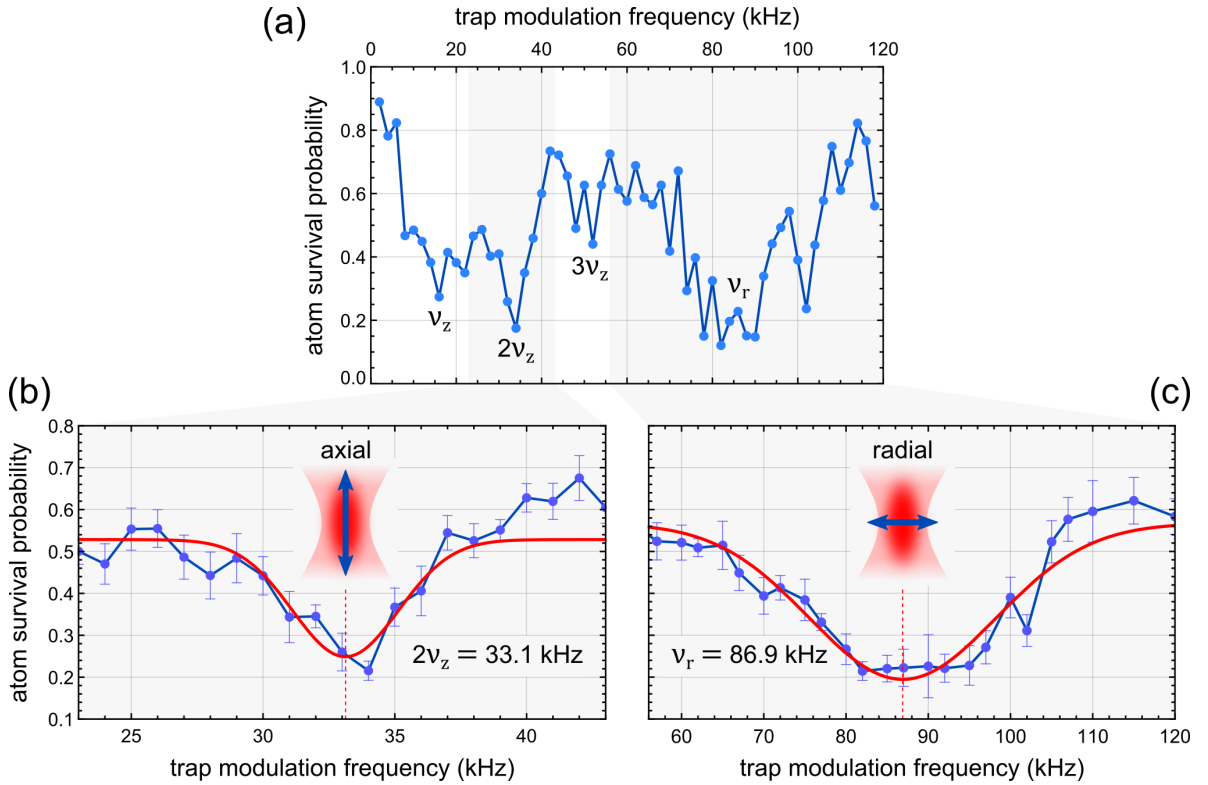


Figure 5.8. Trapping frequencies measurement. (a) A plot showing the survival probability of single trapped atoms when applying a 10 % modulation of the trap depth at an applied frequency. The approximate locations of selected loss resonances are labelled. (b) A zoom on the strong $2\nu_z$ loss resonance, corresponding to the a harmonic of the axial trap frequency. (c) A zoom on the ν_r loss resonance, corresponding to the radial trap frequency. The data points in (a)–(c) are normalised to the survival probability when no trap modulation is applied, while the solid blue lines join adjacent points as a guide to the eye. In (b) and (c), vertical error bars corresponding to the standard deviation in the measurement data have been included, while the red solid lines are Gaussian function fits to the data, used to extract the resonance centres (vertical dashed red lines). The central insets depict the considered mode of oscillation with respect to the trapping beam.

trapped ^{85}Rb atom experiences a range of detunings to the excitation cooling light as it moves around in the trap due to the position-dependent light shifts (cf. Section 2.4), a corresponding range of Rabi frequencies will occur. By fitting a thermal distribution of these frequencies to the measured second-order correlation function, an indicative figure for the average temperature of the atoms within the trap can be deduced. While further details are contained in Section 5.2.1.2, it is informative to state the obtained result of $144 \pm 47 \mu\text{K}$ here, which is approximately equal to the Doppler temperature for ^{85}Rb [96].

5.1.2 Spectral Filtering

With the fluorescence originating from a single optically trapped atom collected and coupled into a single-mode fibre, investigations into the individual coherent and incoherent components of the scattered light require their effective spatial separation. This can be achieved via the spectrum – for which an additional optical element within the detection path is necessary. As outlined in Section 4.4.2 in Chapter 4, the spectral distribution of the two-photon component of the fluorescence light consists of a triplet structure: the coherent component exhibits the same spectrum as the excitation laser and lies exactly at the excitation frequency, ω_L , while the incoherent component consists of neighbouring Lorentzian lines, each of width γ , centred at $\omega_L \pm |\Delta|$. Thus, a band-block type spectral filter centred at ω_L featuring a bandwidth much smaller than $|\Delta|$ would be the ideal candidate for removing the coherent component from the closely-spaced incoherent component. Since the magnitude of the detuning $|\Delta|$ is only on the order of several tens of megahertz (see Section 5.2.1 for details), spectral *separation* of these components becomes challenging. Spectral *isolation* on the other hand, i.e., where the incoherent component alone is selected, is reachable. Such optical filtering, where certain frequencies of light are reflected or absorbed by a suitable filter component, is common practice for the division or combination of light fields of different wavelengths – of which the confocal microscope presented in Section 5.1.1 is a prime example. However, the numerous types of commercial optical filters that are available remain unsuitable due to the broad frequency width of rejection. Interference filters, typically composed of stacked thinfilm layers of dielectric in a so-called three-cavity design [306], can be engineered to offer high spectral transmittance or reflectance over very narrow wavelength ranges by virtue of interference effects between the incident and reflected light taking place at the structure boundaries. Despite this, even the most modern effective commercially available optical filters that offer only several fractions of a nm-broad pass or block bands, with cut-off edge steepnesses (10% – 90%) approaching half a nanometre, exhibit spectral widths that are many orders of magnitude too large, rendering them also unsuitable for the task at hand.

However, the removal of a narrow spectral component of light by the principal of (destructive) interference remains intriguing, for which the immediate contender is a resonator. In following this conception, a device based on a **Fibre-Ring Resonator (FRR)** was successfully constructed and utilised. Its design, characterisation, and frequency stabilisation are the remaining topics for this Section.

5.1.2.1 The Fibre-Ring Resonator

Fibre-Ring Resonators, paired with narrow-linewidth coherent laser sources, have been valuable in many communication and sensing applications. In combination, they have been used to realise a number of devices, including high-resolution spectrum analysers

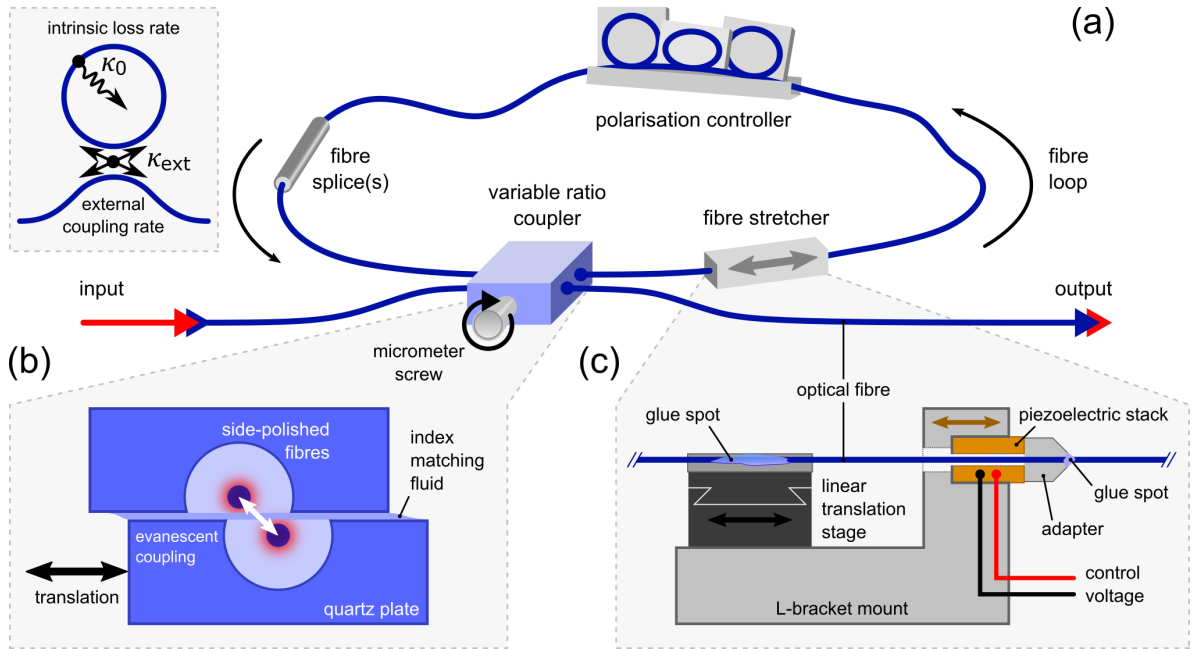


Figure 5.9. Fibre-Ring Resonator schematic. (a) An illustration of the constructed **Fibre-Ring Resonator**, showing the components needed for its operation as a tunable spectral filter. The inset (top left) depicts the intrinsic loss rate of the ring section, κ_0 , and the external coupling rate via the throughput fibre, κ_{ext} . (b) Cross-sectional illustration of the working principle behind the variable ratio coupler, whereby a controllable evanescent coupling between two side-polished fibres is achieved by mutual displacement of their cores. This is facilitated by operation of the micrometer screw, which mechanically translates the quartz plates in which the fibres are embedded. (c) A schematic illustration of the self-made piezo-based fibre stretcher, used for stabilising the length of the **FRR** ring section.

[307], discriminators [308], laser stabilisers [309, 310], and various spectral filters [311–313]. Thanks to the possibility of engineering small **FSRs**, as a component, the **FRR** with the addition of an incorporated nanofibre section has also been utilised in our group to investigate the multimode strong-coupling regime of **CQED** [314], along with the transition to **WQED** [315].

Due to their advantageous properties, an **FRR** is chosen for use as an optical filter, for which a schematic representation of its full set-up is depicted in Figure 5.9. Accordingly with its namesake, and as depicted in Figure 5.9(a), the **FRR** is simply constructed from a length of optical fibre fashioned into a ring to form the resonator itself, that is then coupled to a second optical fibre for the input (and output) of light. A commercial, all-fibre variable ratio directional coupler (*F-CPL-830-N-FA*, Newport Corporation) is used for the construction of this setting. Figure 5.9(b) displays the working principle behind this device: it features two single-mode optical fibres that each have a section embedded in a quartz plate, whereby a small portion of the bare fibre is shaved down to the core and exposed on the plate surface. By sandwiching the plates and bringing the cores into close proximity, transfer of light between the two fibres is accomplished by

5. Observation of Two-Photon Emission from a Single Atom

evanescent field coupling. The splitting ratio is controlled by an integrated micrometer screw, which adjusts the relative lateral positions of the mated fibre cores by movement of one of the glass plates. A thin layer of index matching fluid (*1806Y*, *Cargille-Sacher Laboratories Inc.*) between the plates ensures a low-loss transmission across the coupling gap*. The ends of one of these two fibres are spliced together to create the ring section (of geometrical length $l = 2.25 \pm 0.05$ m) of the full **FRR**, through which control over the coupling between the ring-resonator and remaining input fibre sections is achieved with the variable ratio coupler's micrometer screw. With this, the external coupling rate of the **FRR**, κ_{ext} , can be continuously tuned. This allows access to the three resonator regimes of the **FRR** that has an intrinsic loss rate κ_0 (see the inset of Figure 5.9(a)): undercoupled ($\kappa_{\text{ext}} < \kappa_0$), critically-coupled ($\kappa_{\text{ext}} = \kappa_0$), and overcoupled ($\kappa_{\text{ext}} > \kappa_0$). As a spectral filter, this facilitates a variable on-resonance suppression of ~ 20 dB (between 0% and ~ 100 %). A minor drawback of the device is that the fibres utilised are non-polarisation maintaining, such that the fabricated **FRR** is birefringent. Thus, light propagating through the fibre will experience polarisation-dependent phase-shifts, subject to temperature change and local stress induced on the fibre core. This results in two sets of resonances – one for each polarisation eigenmode of the resonator [316, 317]. To minimise the effects of temperature, the whole set-up is placed inside of a self-made thermally insulated environment that consists of a Styrofoam-lined double-walled wooden box (see Section 5.1.2.3 for further details). A three-paddle polarisation controller (*FPC560*, *Thorlabs, Inc.*) situated within the fibre-ring section allows for manual compensation of the resonator's stress-induced birefringence, and enables the resonance frequencies of the polarisation eigenmodes to be changed†. When setting the resonator to eigenmode degeneracy, i.e., when both polarisation eigenmodes exhibit the same resonance frequency, the **FRR** acts as a non-polarisation-selective filter that removes the spectral component from the coupling fibre that is resonant with the **FRR**. Such a setting is paramount for the consistent spectral filtering of the collected atomic fluorescence, which has no well-defined polarisation orientation due to the fact that the atom is excited from the **MOT** beams. In order to maintain a well-defined spectral resonance of the **FRR**, the length of the ring section must be stabilised. For this, a ~ 10 cm section of the ring fibre is stripped of its coating and affixed to a self-made piezo-based fibre stretcher, for which a schematic illustration is shown in Figure 5.9(c). This composite component consists of a discrete piezoelectric stack with a through hole (*PK4FA2H3P2*, *Thorlabs, Inc.*) that is bonded to a rigid L-shaped bracket, with the fibre fed concentrically through both. The input side of the bare fibre is glued to a cylindrical adapter for the piezo stack end plate while the output side is glued to a V-

*It was found that an occasional refilling of the index matching fluid (at least every six months) was required for satisfactory operation of the device.

†Note that with use of the intra-resonator polarisation controller, it is possible to fully tune the polarisation eigenmodes from degeneracy, to a point of maximum birefringence where they have a separation of half an **FSR**.

groove plate securely fastened to a compact manual linear translation stage (*M-DS25-X*, *Newport Corporation*) for pre-straining of the fibre. The piezo is driven by a dedicated amplifying module (*E-650.00*, *Physik Instrumente (PI) GmbH & Co.*) that features an amplified output voltage of $6\times$ the control input between $0 \dots 10$ V. Lengthening of the piezoelectric stack ($dL/dv \approx 50$ nm/V, with a maximum travel range of $7 \mu\text{m}$) enables a controlled axial elongation of the fibre between the two glue spots through application of a control voltage. In this way, the resonance frequency of the **FRR** can be tuned by several **FSR**, and an appropriate feedback on the piezo therefore allows for setting the length of the ring section to an external frequency reference. For this, the throughput fibre of the **FRR** is spliced to a 2×1 **MEMS** fibre-optic switch (*OS12-780-SM*, *Thorlabs, Inc.*), which allows to either direct the collected fluorescence light through the **FRR** filter during data acquisition, or to send a highly-attenuated reference light field through the **FRR** during a locking cycle. Full details and a characterisation of this locking scheme will be outlined in the upcoming Section 5.1.2.3. Finally, to minimise high-frequency acoustic noise that is transmitted through the metal-to-metal contacts between the box construction and the optical bench, the box sits atop a rubber damping mat (*Art.Nr. 8001174*, *OBI GmbH & Co.*) and is clamped down against the optical bench. It was found that this addition was necessary for a satisfactory operation of the **FRR**.

5.1.2.2 Characterisation

An optical characterisation of the constructed **FRR** is necessary in order to determine its important attributes, namely the intrinsic resonator loss rate κ_0 , which sets the linewidth of the resonance and therefore the notch bandwidth when used as a spectral filtering device. For this, transmission spectra through the coupling fibre are recorded for different settings of the resonator coupling rate κ_{ext} , as controlled by the micrometer screw of the variable ratio directional coupler. For each setting, the input light originating from the cooling laser (at a wavelength around 780 nm close to the **Rb** D_2 line, see Section 3.7.1) is scanned across several resonances of the **FRR**, while its transmission as a function of the laser-resonator detuning is recorded with a **Photodiode (PD)**. By scanning the laser frequency itself, the spectroscopy signal can be used as a frequency ruler for calibration of the measured transmission spectra along the x-axis due to its easily identifiable features [96]. Alongside calibration, this step aids the accurate measurement of the **FRR** transmission spectra by ensuring that only the data collected during the linear portion of the laser frequency scan is considered. Furthermore, all spectra are corrected for laser power fluctuations by normalising with respect to the full transmission signal (no coupling into the ring section) and the zero transmission signal (laser light blocked) to account for any offset in the **PD** signal. This step is useful for analysis of the spectra obtained in the deeply-overcoupled regime ($\kappa_{\text{ext}} \gg \kappa_0$), where adjacent resonances begin to overlap as the linewidth becomes comparable to the **FSR**. Figure 5.10(a) displays an

5. Observation of Two-Photon Emission from a Single Atom

example of such calibrated spectra obtained when the **FRR** is set operating in each of the three coupling regimes. In all cases, the centres of the visible (spectrally symmetric) transmission dips are separated by an **FSR** of $\nu_{\text{FSR}} = 89.0 \pm 0.5$ MHz, with their narrow spectral width indicating a low intrinsic field decay rate. In order to determine the latter, all recorded spectra have the resonance features fitted with an inverted Lorentzian, the linewidth from each of which is equivalent to the total field decay rate $\kappa = \kappa_0 + \kappa_{\text{ext}}$ for that setting of κ_{ext} . The field transmission through the coupling fibre around a resonance, \tilde{t} , is approximately given by

$$\tilde{t}(\omega) = \frac{\kappa_0 - \kappa_{\text{ext}} + i(\omega - \omega_0)}{\kappa + i(\omega - \omega_0)} \quad (5.11)$$

where ω is the frequency of the probe laser and ω_0 is the resonance frequency of the **FRR**. As the transmitted power, T , is the quantity measured on the **PD**, this is related to equation (5.11) by $T = |\tilde{t}|^2$. Fitting all spectra in this manner yields a list of on-resonance transmissions, T_r , and the associated total field decay rate κ . This data set is subsequently fit using equation (5.11) with κ_0 as the only free parameter, the results of which are displayed in Figure 5.10(b). The intrinsic decay rate is found to be $\kappa_0 = 2\pi \times 1.08 \pm 0.02$ MHz, yielding an unloaded resonator finesse of $\mathcal{F} = \pi\nu_{\text{FSR}}/\kappa_0 = 41.2 \pm 0.8$, and further allowing to infer a round-trip loss of $\mathcal{L} = e^{2\kappa_0 n l/c} \approx 16\%$ using $n = 1.455$ for the refractive index of silica at a wavelength of 780 nm. The cause of this loss is mainly attributed to the insertion loss of the variable ratio coupler (specified to be $\sim 3\%$ according to the manufacturer), in addition to the total of three splices that are contained within the ring section. It was found that each of the latter can contribute up to 10% transmission loss, when the reproducibility of carefully performed splices was tested in an independent measurement.

Table 5.3 contains a summary of the measured characteristics obtained with the final constructed **Fibre-Ring Resonator**.

parameter	determined value
ring length	$l = 2.25 \pm 0.05$ m
Free Spectral Range	$\nu_{\text{FSR}} = 89.0 \pm 0.5$ MHz
linewidth	$\kappa/\pi = 4.4 \pm 0.1$ MHz
intrinsic loss rate	$\kappa_0/2\pi = 1.08 \pm 0.02$ MHz
round-trip loss	$\mathcal{L} \approx 16\%$
minimum transmission	$T_r(\omega = \omega_0, \kappa_{\text{ext}} = \kappa_0) \approx 1.1\%$
finesse	$\mathcal{F} = 41.2 \pm 0.8$

Table 5.3. Summary of the **Fibre-Ring Resonator** characteristics.

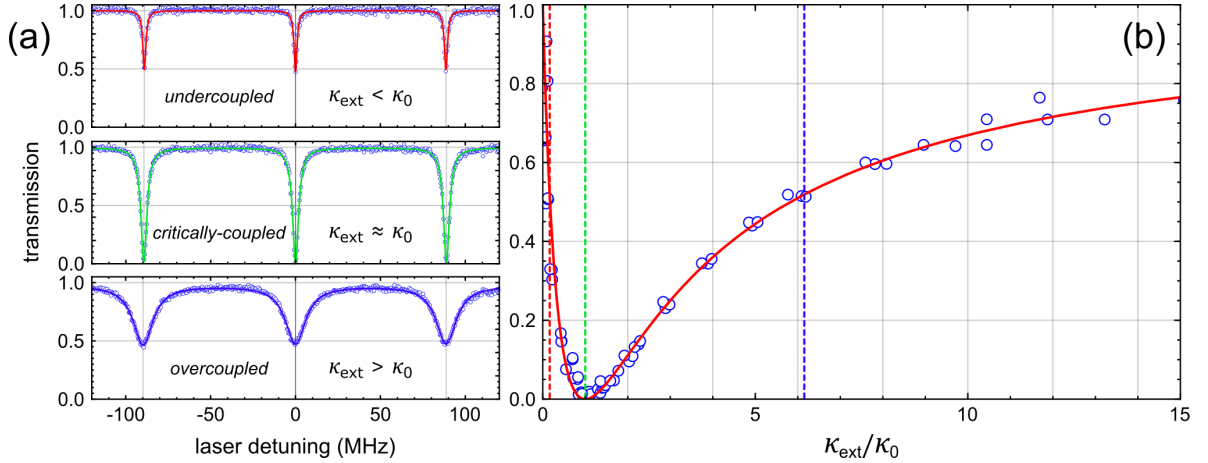


Figure 5.10. Characterisation of the Fibre-Ring Resonator. (a) Plots of the measured transmission spectrum in the throughput fibre of the FRR, as a function of the laser–resonator detuning. The solid lines are Lorentzian fits to the data. Example spectra for the three different coupling regimes are displayed and labelled accordingly. (b) Measured on-resonance transmission, plotted as a function of the external coupling rate κ_{ext} . The solid line is a fit to the data using equation (5.11), using κ_0 as the only free parameter. This yields an intrinsic loss rate of $\kappa_0 = 2\pi \times 1.08 \pm 0.02$ MHz. The vertical dashed lines relate to the spectra shown in (a).

5.1.2.3 Frequency Stabilisation

With the FRR constructed and characterised, the final step in its realisation as a narrow-band spectral filtering device is to stabilise one of its resonances to the frequency of the spectral component intended for removal – which here is the frequency of the laser used for exciting the atom. A variety of methods to implement such a *locking process* exist, including polarisation spectroscopy that takes advantage of the birefringent nature of the FRR [314, 318], and active stabilisation to a modulated laser frequency reference using the PDH technique [172, 319]. However, these locking schemes are potentially unsuitable due to the introduction of a strong and resonant light-field, or an intentional birefringence, into the FRR. In both cases, this would have detrimental effects on the signal of interest by either concealing it or improperly filtering it. After a number of iterations in the construction of a suitable thermally and acoustically insulating box, it was found that once closed up and thermalised, the passive stability of the FRR set-up was very good – a resonance frequency did not drift by more than a few linewidths on a several minutes timescale. Several such typical drift traces are displayed in Figure 5.11(a). It shows recordings of the normalised transmission through the critically-coupled FRR across a 10 s timescale, which was initially set to resonance (zero transmission) by manual adjustment of the voltage supplied to the fibre-stretching piezo. The transmission was measured using an SPCM, with the incoupling power (~ 10 pW) set to produce a few thousand counts per 20 ms binning with the FRR detuned from the probe laser by half an FSR. The resulting passive drift is demonstrated

to be much less than 1 MHz/s, and arises due to small wavelength-scale deviations in the length of the resonator, $\delta l \approx \lambda_0$, that shift the spectral locations of the resonances. Such length variations can be caused by temperature fluctuations that occur on a timescale of minutes to hours, in combination with a *creep* of the piezo actuator within the fibre-stretcher that can occur on a seconds timescale [320]. The latter – whereby a continued expansion or contraction of the piezoelectric material happens, even after an applied change in the control voltage is complete – can potentially be observed by comparing the coloured traces in Figure 5.11(a), in which a time-dependent control voltage was applied to the fibre-stretching piezo for $t < 0$, to the grey trace, in which a fixed voltage had been applied for a duration following $t \gg 0$. The grey trace exhibits almost no drift in the **FRR** resonance frequency, while a drift is clearly visible in the coloured traces, most likely due to the phenomenon of piezo creep after $t = 0$.

As the fibre-stretching piezo actuator within the ring-section is the element that can be used to tune the length, and thereby the resonance frequency, of the **FRR**, it is important to characterise its frequency response. To do so, the **FRR** is set to critical-coupling and the control voltage of the fibre-stretching piezo is adjusted to reach approximately 50% transmission. Centred at this target position, a sinusoidal modulation of the control voltage of the form $v(t) = v_0 \sin(2\pi\nu t)$ is applied to the piezo with use of a function generator. The modulation amplitude following amplification by the piezo driver is set to $v_0 = 0.3$ V, corresponding to a change in the length (resonance frequency) of up to 15 nm (1.7 MHz), and was chosen in order to roughly remain in the linear regime of the **FRR** transmission vs. the applied piezo voltage. Under this applied modulation, the response of the system can then be analysed by measuring the time-dependent transmission through the **FRR**, which will also sinusoidally oscillate at the applied frequency ν . This signal is recorded and fit with a function of the form $s(t) = s_0 \sin(2\pi\nu t + \varphi)$, in order to extract its amplitude, s_0 , and phase, φ , with respect to the input $v(t)$. Repeating this measurement for a range of applied modulation frequencies allows for the construction of a so called *Bode plot* for the system, that graphs its frequency response [321]. The Bode magnitude (purple data, left-most axis) and phase (green data, right-most axis) plots resulting from this investigation are displayed in Figure 5.11(b), with the inset pictorially depicting the described measurement. Clearly, the frequency response of the fibre-stretcher is constant up until a cut-off, after which the signal amplitude exponentially decays. A fit to the magnitude data yields a cut-off frequency of $\nu_{\text{cutoff}} \approx 1$ kHz, indicated by the intersection point of the solid red lines in the log-log scale of Figure 5.11(b). At modulation frequencies greater than 10 kHz, a peak in the data followed by a steeper roll-off (see the red dashed line) suggests a potential resonance in the system that may arise from a mechanical mode of the L-shaped holder being driven – although this was not investigated further. Note that for modulation frequencies above ~ 2 kHz, the phase data has a large error (not displayed) due to the uncertainty in the fitting procedure. This analysis shows that it can be safely assumed

that the fibre-stretching piezo suitably responds to an applied voltage change, as long as the modulation is applied at a frequency below the determined cut-off frequency of the system ν_{cutoff} . This then allows to arrange a locking protocol that enables a long-term stabilisation of the **FRR** resonance by feedback onto the characterised fibre-stretching piezo.

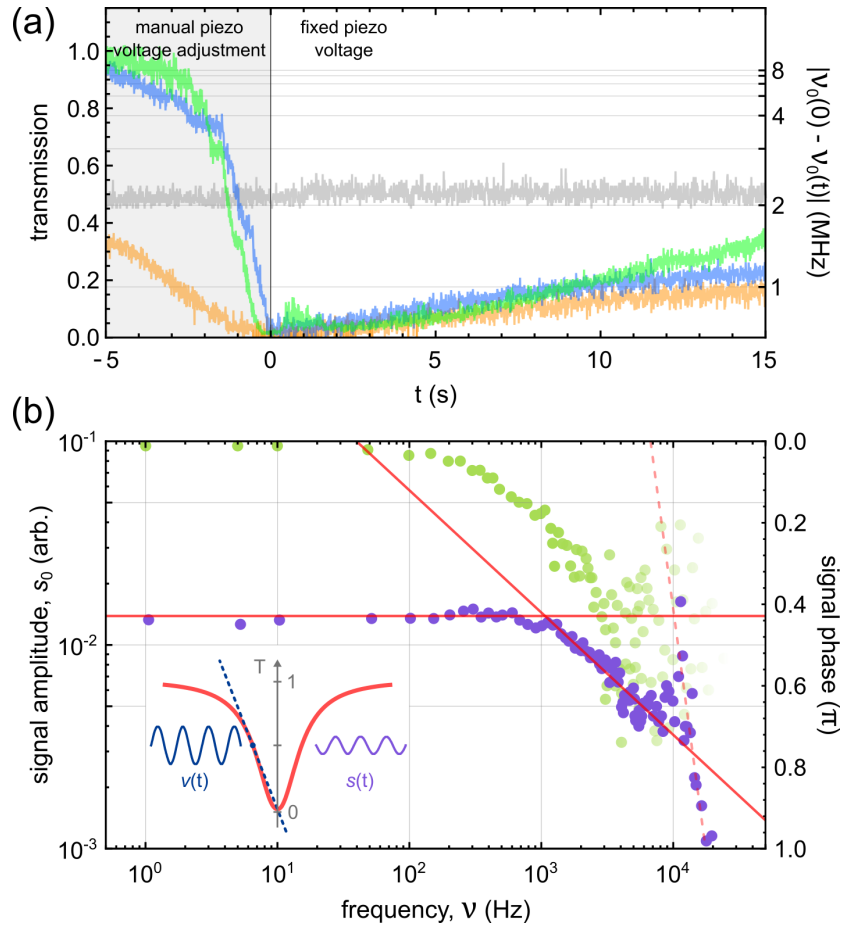


Figure 5.11. Passive stability of the Fibre-Ring Resonator. (a) Typical time traces of the measured transmission through the critically-coupled **FRR**, shown for $t > 0$ when a fixed voltage is applied to the piezo of the fibre-stretcher within the ring-section. Prior to $t = 0$ (grey shaded region), the voltage is manually adjusted to reach resonance. The grey trace is an example time-dependent transmission recorded for $t \gg 0$, following a manual piezo adjustment. The y-axis on the right displays the corresponding magnitude of the drift in the resonance frequency on a logarithmic scale. (b) A Bode plot characterising the measured frequency response of the **FRR**, in both magnitude (purple data, left-most axis) and phase (green data, right-most axis). The cut-off frequency is determined to be $\nu_{\text{cutoff}} \approx 1$ kHz at the intersection point of fits (solid red lines) to the magnitude data. Inset: an illustration of the performed measurements, where an applied modulation of the **FRR** transmission, $v(t)$, results in a frequency-dependent oscillatory response in the transmission, $s(t)$. See text for details.

5. Observation of Two-Photon Emission from a Single Atom

In order to compensate for the slow residual drifts of the resonance frequency and in knowing the response of the fibre-stretcher (see Figures 5.11(a) and (b) respectively), a simple *sample-and-hold* locking scheme was chosen and implemented. A schematic of the set-up is depicted in Figure 5.12(a). For this, a highly-attenuated light field (with a power of several pW) originating from the cooling laser is injected into the **FRR** while the length of the ring section is simultaneously linearly scanned with use of the fibre-stretching piezo. By scanning the length elongation in a small range centred

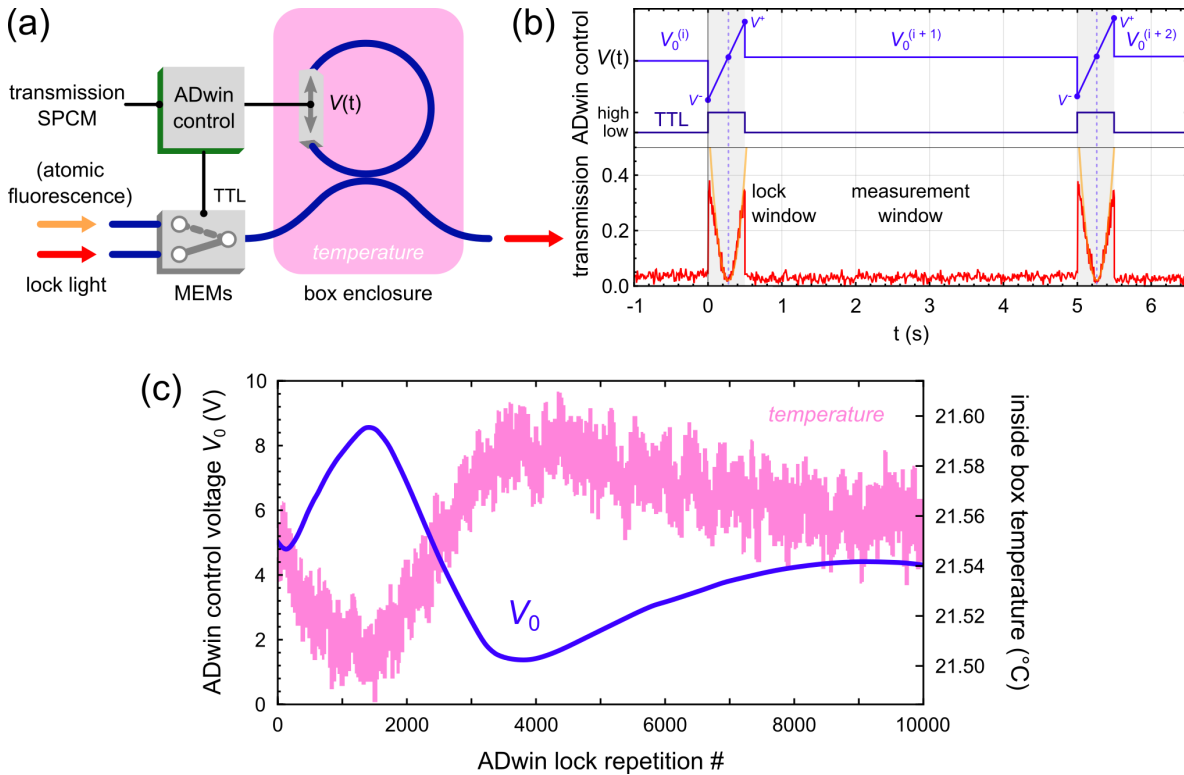


Figure 5.12. Stabilising the resonance of the Fibre-Ring Resonator. (a) A schematic of the components used for stabilising the **FRR**, with time-dependent analogue and digital voltage controls supplied by ADwin. During a locking window, lock light is injected into the **FRR** via a **MEMS** switch that receives a **TTL** high voltage from the ADwin control. During this time, ADwin supplies a linear voltage ramp to the fibre-stretching piezo within the ring section, and simultaneously measures the **FRR** transmission recorded on an **SPCM**. The voltage at which a minimum transmission was measured (corresponding to the length at which the **FRR** is resonant to the lock light) is subsequently set and held. The **FRR** is situated inside a thermally insulated enclosure at room temperature. (b) An example time-trace of two consecutive locking cycles, shaded in grey. Upper panel: the voltage outputs of ADwin, where the time-dependent voltage, $V(t)$, is supplied to the fibre-stretching piezo and the **TTL** signal to the **MEMS** switch. Lower panel: transmission of the locking light through the **FRR** measured on an **SPCM** (red line), and the parabolic fits produced by ADwin (orange lines) that extract the voltage for which a minimum count rate was measured (purple dashed lines). (c) A long-duration monitor of the ADwin control voltage set-point, V_0 , that corresponds to the **FRR** resonance (left-most axis), reveals a link to the temperature of the box in which the **FRR** is situated (right-most axis). See text for details.

around a resonance and monitoring the transmitted intensity, the length corresponding to a minimum transmission can be measured and henceforth held by a feedback onto the fibre-stretching piezo. A dedicated software was written for the ADwin control system to perform this task in its entirety, for which a detailed description is given in the following: first, a **TTL** signal is sent to the **MEMS** switch at the input side of the **FRR** to select the locking light injection port. Next, its transmission is recorded by an **SPCM** that is connected to the ADwin counter module. A trace of countrate over time is recorded during which a voltage ramp, originating from the ADwin analogue **IO** module, is supplied to the control input of the fibre-stretching piezo amplifier unit. A parabola is fit to the acquired data array, and the voltage at which the minimum countrate was measured (corresponding to resonance), is subsequently supplied to the piezo. The duration and binning of the acquisition, along with the voltage ramp and fitting parameters, are all user-defined within the program. Additionally, a small offset voltage can be manually added to the fit result in order to account for the piezo creep effect. All of these settings are important, as in order to ensure a well-running locking procedure that is consistent across measurement times of many hours, the scan around resonance must be in a suitable range in order to achieve a reliable fit. Importantly, the parameters must be adjusted depending on the κ_{ext} -dependent coupling setting of the **FRR** due to the change in lineshape (see Figure 5.10). By considering that a length change in the fibre-ring of one wavelength, λ_0 , changes the resonance frequency by one **FSR**, ν_{FSR} , the relation $d\nu/dv = dL/dv \times \nu_{\text{FSR}}/\lambda_0 \approx 5 \text{ MHz/V}$ describes the tuning ability of the fibre-stretching piezo. With this, by choosing to scan over a frequency range of half a linewidth centred on resonance, i.e., $\pm\kappa/4\pi$ around ν_0 , the voltage ramp that must be applied to the piezo sweeps across the range $V^\pm(\kappa_{\text{ext}}) = V_0 \pm \kappa/4\pi d\nu$, where V_0 is the voltage supplied at resonance. This amounts to scan ranges around a few hundred mV, and corresponding optical path length changes on the order of a few tens of nm. The duration of the locking procedure was set to 0.5 s and performed at a repetition rate of 200 mHz (i.e., once every 5 s), which were found to be an acceptable trade-off between useful measurement time and duration of a reliable and repeatable stabilisation. An example of a typical time-trace of the **FRR** transmission using this sample-and-hold locking scheme is shown in Figure 5.12(b), and includes a corresponding trace of the voltage supplied to the fibre-stretching piezo as well as the **TTL** signal supplied to the **MEMS** switch. It illustrates how the $(i + 1)^{\text{th}}$ locking cycle performs a linear ramp of the piezo voltage between the values V^\pm , using the set-point, V_0 , determined from the i^{th} lock. Finally, Figure 5.12(c) displays both the fibre-stretching piezo set-point and measured temperature inside the **FRR** containment box, monitored across 10000 lock repetitions (~ 14 hours). Clearly, the resonance of the **FRR**, and therefore the piezo set-point, is influenced by the temperature of the environment. As the temperature decreases (increases), the piezo must elongate (shorten) the length of the ring-section, likely in order to compensate for the thermal contraction (expansion) of the glass fibre.

The variation of V_0 across the measurement duration is approximately $dV_0 = 7.2$ V (minimum to maximum value), corresponding to a length change in the ring-section of $dV_0 \cdot dL/dv \approx 0.36$ μm . This value is close to a simple estimation of the absolute linear expansion of a silica fibre, as $\delta l = \alpha \cdot l \cdot \delta T \approx 0.12$ μm , where $\delta T \sim 0.1$ $^\circ\text{C}$ is the measured temperature variation and $\alpha = 5.5 \times 10^{-7}$ $^\circ\text{C}^{-1}$ is the coefficient of thermal expansion for silica glass [322]. The implemented sample-and-hold locking scheme can therefore accommodate the long-term temperature variations present in the laboratory environment, and offset the resulting μm -scale length changes of the **FRR***.

In this scheme however, the stabilisation is not active between the locking cycles, and thus the **FRR** resonance may still be subject to drifts away from the set-point found during a lock. As will be outlined in Section 5.2.1.3, this is found to be a small effect, and can be accounted for when modelling the data obtained for the second-order correlation function of the fluorescence transmitted past the **FRR** filter.

5.1.3 Measurement of the Second-Order Correlation Function

With the resonance fluorescence of a single trapped atom collected and coupled into a single-mode fibre (see Section 5.1.1), its transmission through the narrow-band **FRR** filter (see Section 5.1.2) allows for an investigation into the properties of the filtered light. As stipulated in Section 4.5, disturbing the balance of interference between the coherently and incoherently scattered two-photon components modifies the photon statistics of the scattered field. This can be experimentally verified by measuring the second-order correlation function of the fluorescence light that is transmitted past the **FRR**, for different settings of its filtering functionality. To do so requires a suitable measurement set-up placed in the transmission port of the **FRR** filter.

In general quantum optics, correlation measurements on a signal of interest are measured by spatio-temporally separated detectors, which are used to characterise its statistical and coherence properties at the two points in space or time [324]. The simplest conceivable set-up for the realisation of such measurements[†] with realistic detectors is to equally divide the signal on to two different detectors using a beamsplitter, for which the measurement outcomes of each can then be correlated. This straightforward arrangement is known as a *Hanbury Brown and Twiss (HBT)* set-up, and is named after the authors who first proposed, built, utilised, and successfully described their findings with it in the 1950s [325–327]. Their demonstrated technique for intensity correlation has become widely and commonly employed, where what was originally constructed using a pair of **PMTs** located several metres behind a half-silvered mirror, is now typically replaced respectively by **SPCMs** and high-quality optical beamsplitters.

*Note that this simple analysis neglects the effect of a temperature-dependent refractive index variation, which should be less than 10^{-5} in the measured temperature range [323].

[†]A single ideal **Photodiode**, that features a dead time much smaller than the signal of interest, is actually the simplest *conceivable* set-up – but practically not possible.

Integrating such an **HBT** set-up into the detection path following the **FRR** filter is straightforward. In order to minimise transmission losses towards a pair of detectors, an all-fibre based pathway is chosen. For this, the output fibre from the **FRR** is spliced directly to a 1×2 fibre optic coupler featuring a 50/50 splitting ratio for light at a wavelength of 780 nm (*TN785R5A1*, *Thorlabs, Inc.*). Each of its outputs are directed to an individual fibre-coupled **SPCM** (*Count-50N-FC*, *Laser Components GmbH*) that are then connected to the timetagging unit in order to record the times of photon arrivals at each detector (see Section 3.8). The fibres and **SPCMs** making up this **HBT** set-up are sealed inside a self-made blackout box in order to minimise stray light from reaching the detectors. Photon coincidences in the collected data can subsequently be analysed to yield the second-order correlation function (see Section 5.1.3.1), $g^{(2)}(\tau, \kappa_{\text{ext}})$, which is recorded for different κ_{ext} settings of the **FRR** filter.

Figure 5.13 shows (a simplified version of) the complete experimental set-up, illustrating the combination of the three main techniques discussed so far in this Chapter: the resonance fluorescence of a single trapped atom, which is collected and spectrally filtered, before being directed to an **HBT** detection set-up. A brief discussion of the processing of the raw data is given in the following, before the results obtained with this apparatus are presented and discussed throughout the remainder of this Chapter.

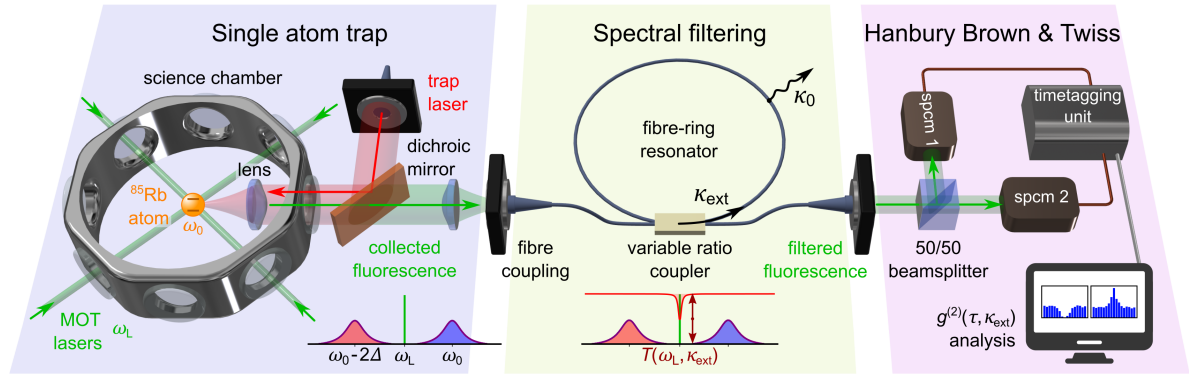


Figure 5.13. Experimental set-up. From left to right: A single ^{85}Rb atom is loaded into the optical dipole trap from the upper **MOT** and driven by the **MOT** lasers, of frequency ω_L . Fluorescence photons from the atom are collected with the lens ($\text{NA} = 0.55$), separated from the trapping laser with a dichroic mirror, and coupled into a single-mode fibre to be guided to the **FRR**-based filter. As the two-photon component of this resonance fluorescence has a triplet-like spectral structure, stabilising the filter to the excitation laser frequency allows for removal of the coherent component of the light scattered by the atom, the suppression of which is controlled by the parameter κ_{ext} . The filtered light is sent to a **Hanbury Brown and Twiss** set-up that consists of two **SPCMs** behind a 50/50 beamsplitter. The photon arrival times are recorded by a timetagging unit, from which the second-order correlation function of the filtered light, $g^{(2)}(\tau, \kappa_{\text{ext}})$, can be measured for different settings of κ_{ext} .

5.1.3.1 Treatment of the Raw Data

As shown in Figure 5.13, the photon clicks from each SPCM of the HBT set-up are sent to separate input channels on an FPGA-based timetagging unit (see Section 3.8). Its purpose is to assign a timestamp and channel number to each click, and to continuously write these timetags into a binary file stored locally on a dedicated HDD. The zeroth order of treating the collected raw data is to convert the resulting *.bin* file into a readable list of processed data, the format of which depends on the type of analysis to be performed. For example, by simply summing the clicks on the two HBT detectors and appropriately time-binning them, a list of measured photon clicks per time-bin is obtained, yielding a time-trace similar to that shown in Figure 5.6. This is used to flag the times at which the dipole trap was occupied by a single atom. In order to determine the second-order correlation function instead, the raw timetags in both channels are first grouped into 1 ns-sized time bins and discarded if less than 15 counts are registered in a 10 μ s window, as this countrate corresponds to the case of no atom present in the trap (see Figure 5.6). The remaining clicks, originating from the resonance fluorescence of a single trapped atom (plus some unavoidable background, e.g., dark counts of the SPCMs plus stray light), are sorted by their channel number and then histogrammed: in a 100 μ s window, the clicks in channel *B* surrounding a click in channel *A* are summed according to their temporal separation and repeated for every channel *A* click. The resulting file consists of a list of click-coincidences on the two SPCMs, depending on the temporal separation of that recorded on each detector, $\tau \rightarrow -50 \dots 50 \mu$ s. Coincidences in this list are typically further grouped into 2 ns-sized time bins. Using this raw data processing, a histogram of photon detection time delays between the two channels is obtained, which after normalisation (see Section 5.2.1) yields the second-order correlation functions. For all of the results presented in the rest of this Chapter, this raw data processing was carried out using a self-written multi-purpose Python program, while Mathematica was subsequently used to analyse the resulting treated data files.

5.2 Results

By combining all the of the elements previously detailed in this Chapter, an investigation into the statistics of the scattered two-photon components of the fluorescence light originating from a single two-level atom can be undertaken. Importantly, this investigation involves measurement of the second-order correlation function for *different ratios* of the incoherently to coherently scattered two-photon components, controlled by reducing the amplitude of one with respect to the other. In order to do so, the collected fluorescence from an optically trapped atom (see Section 5.1.1) is sent, via the **FRR** narrow-band filter stabilised to the frequency of the coherently scattered two-photon component (see Section 5.1.2), to the **HBT** detection set-up (see Section 5.1.3), as conceptually displayed in Figure 5.13. This experiment is repeated for different coupling settings of the **FRR** filter, which allows to tune the transmission of the coherent component of the collected fluorescence light (see equation (5.11), for $\omega = \omega_0 = \omega_L$). The control parameter responsible for setting the on-resonance transmission of the **FRR**, κ_{ext} , is tuned to reach across its three coupling regimes. The set-points are included in Table 5.4, which contains a summary of the results and parameters relevant to each measured data set. The second-order correlation function at each setting of κ_{ext} is then extracted from the raw data (see Section 5.1.3.1) and fit with a model that includes experimental imperfections. The latter will be presented in detail within Section 5.2.1.

$\kappa_{\text{ext}}/\kappa_0$	$g^{(2)}(0, \kappa_{\text{ext}})$	$T_{\text{meas.}}$ (hours)
0.00 ± 0.00	0.43 ± 0.05	67.0972
0.30 ± 0.09	1.23 ± 0.12	72.0839
0.44 ± 0.15	1.77 ± 0.40	50.3406
1.00 ± 1.45	5.73 ± 0.84	71.7961
2.23 ± 0.75	7.65 ± 1.21	63.6844
3.23 ± 0.93	2.98 ± 0.23	80.9870
5.12 ± 1.84	2.08 ± 0.23	76.9249

Table 5.4. Summary of the measurement settings and results.

Figure 5.14 displays all measured data sets (open coloured circles) along with the fitted model (solid lines of corresponding colour) as κ_{ext} is increased from zero. Firstly, the data obtained for the setting of $\kappa_{\text{ext}} = 0$ corresponds to a measurement of the unmodified (unfiltered) atomic fluorescence. As expected, the data at this setting exhibits a clear photon antibunching as evident by the signal at $\tau = 0$ dipping below $g^{(2)}(0) < 0.5$. For $|\tau| > 0$, a damped oscillatory behaviour that originates from the

5. Observation of Two-Photon Emission from a Single Atom

driven atom undergoing Rabi oscillations at an effective frequency of $\Omega_{\text{eff}} \approx \bar{\Delta}$ is observed, where $\bar{\Delta} = -57.9 \pm 3.7$ MHz is the average detuning of the light-shifted atomic resonance with respect to the excitation frequency (see Section 5.2.1.2 for a discussion of its determination). The dampening occurs on a timescale around the excited-state lifetime of $1/2\gamma$. This measurement of antibunched photon statistics illustrates the expected behaviour whereby, in the absence of spectral selection, the light scattered by the single atom does not contain more than one photon at the same time and place. However, when increasing κ_{ext} , the transmission of the coherent component of the fluorescence light past the FRR is reduced. Consequently, the delicate balance between the two scattered components of the fluorescence light is upset – they no longer fully destructively interfere at $\tau = 0$ – which results in a modified second-order correlation that does not show perfectly antibunched photon statistics. Qualitatively, the features at $\tau = 0$ and $0 < |\tau| \lesssim 1/2\gamma$ for the data sets in which $\kappa_{\text{ext}} > 0$ can be compared to those present in the case where $\kappa_{\text{ext}} = 0$. In doing so, it is clear that the value of $g^{(2)}(\tau = 0, \kappa_{\text{ext}})$ increases up to a maximum that occurs when the coherent component is maximally reduced ($\kappa_{\text{ext}} \approx \kappa_0$), before decreasing again beyond this point ($\kappa_{\text{ext}} > \kappa_0$). This observed bunching of the photon statistics, which is both symmetric in τ and maximum at zero delay, is evidence of simultaneously propagating photons (within the temporal window $0 < |\tau| \lesssim 1/2\gamma$) following the FRR filter, that originate from the atom. In the weak-driving regime of the experiment, where the saturation parameter is set to $S = 0.025 \pm 0.004$, the incoherent component should be comprised solely of pairs of photons, and the observation of maximum bunching for the data set in which it is best isolated attests to this (see Section 5.2.1.3 for a detailed discussion on the attenuation of the coherent component by the FRR, which is subject to a variable resonance frequency). Additionally, the oscillatory behaviour in the temporal window $0 < |\tau| \lesssim 1/2\gamma$ remains visible throughout each data set, although its visibility significantly decreases when strong bunching is observed, around the point of critical coupling of the FRR. As these oscillations arise from the interference between the coherent and incoherent components, the visibility is minimal for when the coherent component is maximally suppressed. For a perfect isolation (suppression) of the incoherent (coherent) component, this beating in the second-order correlation function would vanish, and it would instead exhibit a pure double-exponential decay centred at $\tau = 0$ with a decay time of $1/2\gamma$.

A quantitative analysis of the data sets presented in Figure 5.14 is required for a determination of the signal amplitude around $\tau = 0$, in order to extract the measured rate of photon-pair generation. This endeavour is aided by performing fits to the data, using a model that can account for imperfections in the measurement. These aspects, along with accompanying discussions, are respectively presented in the following Sections 5.2.1 and 5.3.

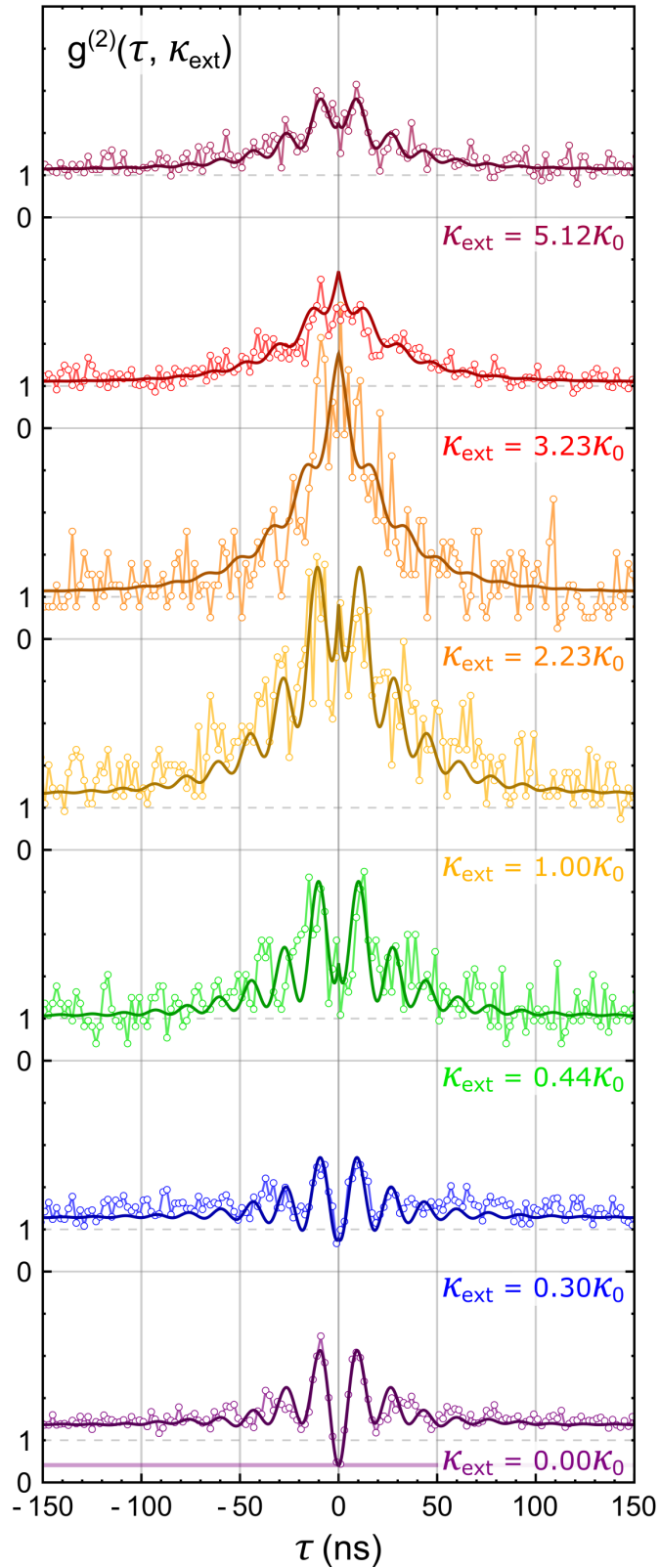


Figure 5.14. Measured second-order correlation functions $g^{(2)}(\tau)$ for different filter settings κ_{ext} . Each data set has the same vertical scale and are ordered, from bottom to top, in ascending values of κ_{ext} . The solid lines are fits of the theoretical model to the measured data points, using the temperature of the trapped atom and a residual filter–laser detuning as the only fit parameters (see Section 5.2.1). The purple horizontal line in the unfiltered data set ($\kappa_{\text{ext}} = 0$) indicates the noise floor due to background counts.

5.2.1 Modelling the Measured Second-Order Correlation Function

A number of attributes present in the imperfect (real-life) experimental platform have an impact on the quality of the data obtained, and must be taken into account when performing its analysis and fitting. These include; a finite collection efficiency of the resonance fluorescence, that is emitted by a non-stationary atom due to its finite temperature in the trap, whose signal is polluted by stray light and detector dark counts, as well as a residual detuning of the **FRR** resonance from the perfect filtering point of the coherently scattered component. These effects and their imprints on the measured second-order correlation function are discussed in the following, and accompanied by a presentation of how each was addressed when modelling the data. This Section provides details about the construction of the complete model that describes the obtained data, that is displayed alongside all data sets in Figure 5.14 of the previous Section 5.2.

When modelling the photon statistics obtained for this particular measurement, where only the coherently scattered component is filtered, a simplifying assumption can be made: that the **FRR** filter does act only on the coherently scattered light, leaving the incoherently scattered component predominantly untouched. It therefore reduces the field amplitude of the former by the κ_{ext} -dependent transmission factor $t_{\text{coh}}(\kappa_{\text{ext}}) \equiv \tilde{t}(\omega_L, \kappa_{\text{ext}})$, while the latter remains unchanged since $t_{\text{inc}}(\kappa_{\text{ext}}) \equiv \tilde{t}(\Delta, \kappa_{\text{ext}}) \approx 1$ (see equation (5.11)). The wavefunction of the light after filtering is then given by

$$|\psi_F\rangle = |t_{\text{coh}}(\kappa_{\text{ext}})\alpha\rangle + |\phi\rangle \quad (5.12)$$

and the corresponding envelope of the two-photon wavefunction then reads

$$\psi_F^{(2)}(\tau) = \frac{n_{\text{coh}}}{2} \left[t_{\text{coh}}(\kappa_{\text{ext}})^2 - e^{-(\gamma-i\Delta)|\tau|} \right]. \quad (5.13)$$

In order to analyse the collected photon statistics of this filtered field, the second-order correlation function defined by

$$g^{(2)}(\tau) = \frac{\langle a_t^\dagger a_{t+\tau}^\dagger a_{t+\tau} a_t \rangle_t}{\langle a_t^\dagger a_t \rangle_t^2} \equiv \frac{G^{(2)}(\tau)}{n^2} \quad (5.14)$$

is measured, where $\langle \dots \rangle_t$ indicates the time-averaged expectation value and $\tau = t_2 - t_1$ the temporal separation between the two photons detected on each of the **HBT SPCMs**. Here, $G^{(2)}(\tau) \propto \eta^2 |\psi_F^{(2)}|^2$ is the unnormalised second-order correlation function which, using equations (5.13) and (4.63)–(4.64), reads

$$G^{(2)}(\tau) \approx \gamma^2 S^2 \eta^2 \left| t_{\text{coh}}(\kappa_{\text{ext}})^2 - e^{-(\gamma-i\Delta)|\tau|} \right|^2, \quad (5.15)$$

while the mean photon flux after the filter is given by

$$\begin{aligned} n &= \gamma S \eta \left(|t_{\text{coh}}(\kappa_{\text{ext}})|^2 (1 - 2S) + S \right) \\ &= \eta \left(|t_{\text{coh}}(\kappa_{\text{ext}})|^2 n_{\text{coh}} + n_{\text{inc}} \right). \end{aligned} \quad (5.16)$$

The total single photon collection and detection efficiency, η , has been introduced in the previous pair of equations. It defines the probability that a photon, once emitted by the atom, will be recorded as a click by the **SPCMs** to then be included in the data set. η thus incorporates the finite **NA** of the fluorescence collection lens, propagation and coupling losses through the partly free-space and partly fibre-based detection path to and past the **FRR**, as well as the quantum detection efficiency of the **SPCMs** at the end of the chain (see Figure 5.13). In addition to the measured photon rate, n , a background countrate that originates from detector dark counts and stray light making it to the detectors must be taken into account. Including this background countrate, d , the experimentally expected second-order correlation function in the low saturation regime then reads

$$g_{\text{exp}}^{(2)}(\tau) \approx \frac{G^{(2)}(\tau) - n^2}{(n + d)^2} + 1 \quad (5.17)$$

$$= \frac{G^{(2)}(\tau) + 2nd + d^2}{(n + d)^2}, \quad (5.18)$$

which is used to model the collected data. However, accurate fits to the data are only obtained when including the remaining experimental effects present in the measurement. These are discussed in the following.

5.2.1.1 Data Normalisation

In order to accurately plot the measured second-order correlation function, the treated data that consists of a list of total number of coincidences per time-bin (set to 2 ns, see Section 5.1.3.1) must first be correctly normalised in order to obtain $g^{(2)}(\tau)$. Since all interesting correlation dynamics of the fluorescence radiation occur in a short time window (of several $1/2\gamma$ width) around $\tau = 0$, a rudimentary normalisation amounts to simply dividing everywhere by the average number of coincidences obtained at $|\tau| \rightarrow \infty$. However, doing so raises the first technical feature in the collected data, in that the baseline coincidence count is not constant in $|\tau|$, and exponentially decays on a few microseconds timescale. Clearly, there are other physical mechanisms that result in a long-timescale photon bunching. Its analysis and origin is discussed in the following.

To take this small bunching effect into account, the data (excluding $\pm 0.2 \mu\text{s}$ around $\tau = 0$) is fit with the double-exponential function

$$f(\tau) = Y + Ae^{-|\tau|/t_b} \quad (5.19)$$

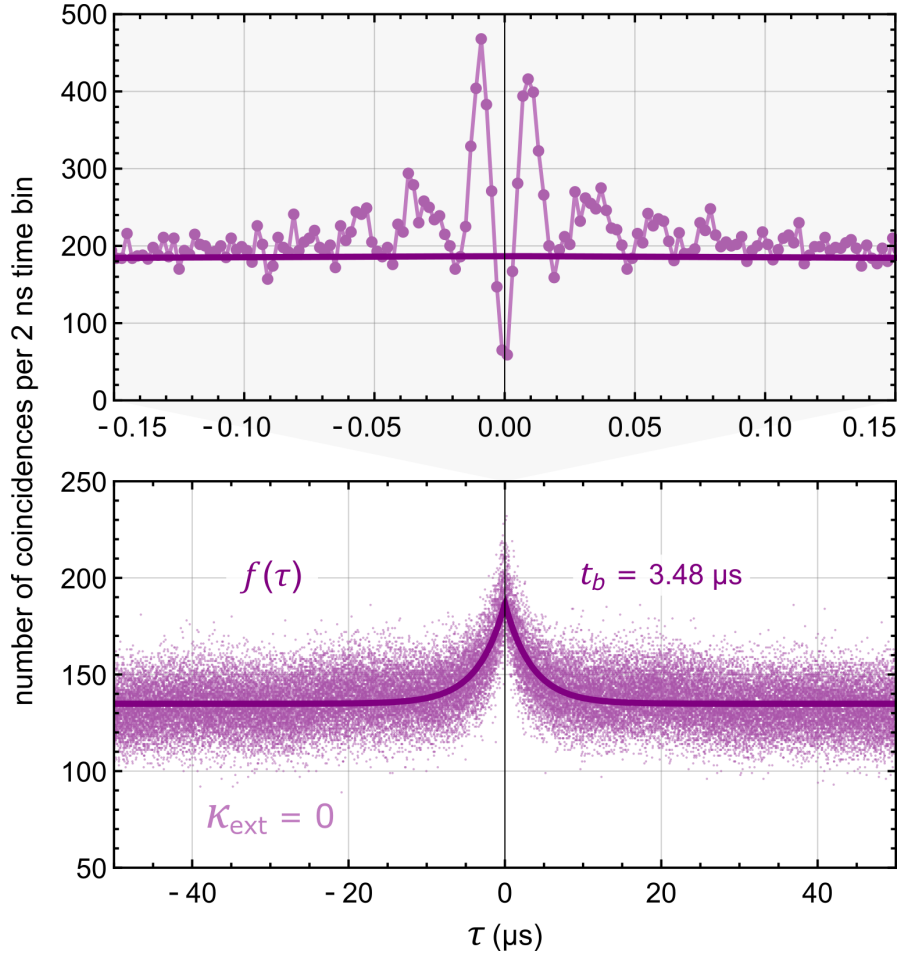


Figure 5.15. Long-term behaviour of the second-order correlation function shown exemplarily for the $\kappa_{\text{ext}} = 0$ data set. A weak bunching effect arising from diffusive atomic motion is apparent. It exhibits a decay time of $t_b = 3.48 \mu\text{s}$, which is obtained by fitting with the function $f(\tau)$ (equation (5.19)). The lower plot shows the full data set used for fitting and the upper shows a zoom on the 300 ns window centred at $\tau = 0$, where $f(\tau)$ is roughly constant.

where Y is the average coincidence count for long $|\tau|$ (at the data set limits*), with A and t_b the amplitude and time constant of the exponential. The antibunched data set ($\kappa_{\text{ext}} = 0$) and the fit result using equation (5.19) are displayed in Figure 5.15. It illustrates a weak and slowly decaying bunching effect, colloquially referred to as *technical bunching*, that originates from the diffusive motion of the trapped atoms through the complex intensity and polarisation pattern of the Upper MOT light-field topography [328]. While trapped, the atom still traverses length scales larger than the excitation wavelength λ_0 , due to the spatial extension of the trap ($w_t = 1.8 \mu\text{m}$ and $z_R \approx 13 \mu\text{m}$) and the finite temperature of the atom (see Section 5.2.1.2 for a determination and treatment of the latter). Consequently, this motion means that

*The value for this offset and its statistical distribution is determined by fitting a Gaussian function to a histogram of the number of coincidences per 2 ns bin, in a $10 \mu\text{s}$ window centred at $\tau = \pm 45 \mu\text{s}$

the atom crosses over a number of spatial nodes and antinodes* in the lattice-like excitation field, for which the position-dependent intensity distribution then gives rise to a positionally encoded intensity correlation. As such, a photon detection indicates that the atom was more likely to be located at an node of the intensity field, and the probability of a second detection event is enhanced when compared to the long time average. The characteristic timescale of this increased fluorescence probability, t_b , can be attributed to the characteristic timescale over which the atom diffuses between two neighbouring nodes that are separated by the amount $s_b \approx \lambda_0/2 = 390$ nm. From the results of the long-timescale fit using equation (5.19), the approximate centre-of-mass atomic velocity can then be computed for each data set, according to $\bar{v}_{Rb} = s_b/t_b$. These, along with the results of all fit parameters, are recorded in Table 5.5. It is clear that the decay constant obtained for each data set is in the range of only several μs , corresponding to atomic velocities in the region of 10 cm/s. The mean values and standard deviations of t_b and \bar{v}_{Rb} using all data sets are respectively found to be $\bar{t}_b = 3.26 \pm 0.14$ μs and $\bar{v}_{Rb} = 12.1 \pm 0.5$ cm/s. The uncertainty in these values are likely due to microscopic drifts in the set-up, in which the relative spatial positions of the trap with respect to the intensity topography of the excitation field varied across each measurement. This magnitude of velocity found for the trapped atoms can be related to atom temperatures on the order of $T = m_{Rb}\overline{v_{Rb}^2}/k_B \approx 150$ μK , which is in accordance with the Doppler temperature of ^{85}Rb [96].

data set $\kappa_{\text{ext}}/\kappa_0$	fit parameters of $f(\tau)$			atom velocity \bar{v}_{Rb} (cm/s)
	Y	A	t_b (μs)	
0.00	134.9 ± 8.8	51.9	3.48	11.2
0.30	55.8 ± 5.3	23.4	3.57	10.9
0.44	7.4 ± 1.9	0.5	2.94	13.3
1.00	5.5 ± 1.6	1.9	2.87	13.6
2.23	3.9 ± 1.4	0.5	3.64	10.7
3.23	26.4 ± 3.7	4.2	2.84	13.7
5.12	38.3 ± 4.4	4.3	3.49	11.2

Table 5.5. Characteristics of the slow bunching in each data set. The values for Y and A are given in number of coincidences per 2 ns time bin, where the statistical 1σ interval determines the uncertainty in Y . The fit result for the parameter t_b allows an approximate value for the average atom velocity to be obtained using $\bar{v}_{Rb} = s_b/t_b$, where $s_b = \lambda_0/2$.

*These are likely not complete antinodes with zero intensity, but rather regions of lower intensity with respect to the neighbouring nodes.

Finally, the characterised technical bunching can be removed from all data sets while simultaneously ensuring a correct normalisation, by scaling according to the inverse of equation (5.19) evaluated with the obtained fit parameters. In Figure 5.14 the technical bunching is not removed however, and the data sets are instead normalised by division with the obtained offset value, Y (see Table 5.5), to then generate the measured $g^{(2)}(\tau, \kappa_{\text{ext}})$ which is equal to unity for $|\tau| \gg 1/2\gamma$. The theoretical model for the data, discussed in the next Sections 5.2.1.2 and 5.2.1.3, is adjusted such that the value $1 + A$ serves as its baseline.

5.2.1.2 Trapped Atom Energy Distribution

With the μs -timescale exponential decay in the fluorescence probability accounted for due to diffuse atomic motion (see the preceding Section 5.2.1.1), the attention must subsequently be turned to the effects present which modify the measured dynamics on the sub- μs -timescale around $\tau = 0$. The first of these is the fact that the finite temperature of the atom in the dipole trap gives rise to a temperature-dependent distribution of atomic positions in the trap and, consequently, of the a.c. Stark shifts of the atomic transition frequency ω_0 . Correspondingly, the excitation laser detuning with respect to the Stark-shifted atomic transition, Δ , is also temperature dependent, which manifests as a quickly damped oscillatory behaviour in the second-order correlation function (for $|\tau| > 0$) at a frequency $\Omega_{\text{eff}} \approx \bar{\Delta}$, where $\bar{\Delta}$ is the mean detuning. A number of experimental methods exist to reduce such a temperature-dependent detuning, namely by employing a *magic wavelength* transition for the trapping field* [155–157], or (since one does not exist for Rb) with the addition of a second light field whose purpose is to Stark shift the excited state by the same amount as the shifted ground state to thereby realise a *dual-colour* magic wavelength trap for Rb [60, 158]. Both of these methods, with the latter in particular, are discussed in Section 2.4.3. Cooling the atom such that its spatial distribution – and thus its transition shift – is minimised is another option. Since the experiments performed here do not make use of such schemes to maintain a fixed atom–laser detuning, theoretical modelling of the data must include the effect of a temperature-dependent distribution of detunings of the atomic transition. It was found that the data obtained can be modelled well by assuming a thermal position distribution of the trapped atoms, which in turn yields a corresponding distribution of atom–laser detunings, for which the unknown width (i.e., the temperature distribution of the trapped atoms) and maximum detuning (for when the atom is in the centre of the trap) are used as fit parameters. This takes into account the complex multilevel

*A *magic wavelength* is one for which the ground and excited state of an atomic transition exhibit the same polarisability, resulting in an unperturbed transition frequency due to equal light shifts of each level. For Cs, a magic wavelength trap for the D_2 transition exists at a wavelength around ~ 935 nm [329].

structure of the atom's energy levels, for which a substantial tensor light shift results in a Zeeman state-dependent transition frequency. This model is presented in the following.

First, it is necessary to calculate ground state light shift of an atom inside the dipole trap, which, it turns out, is shifted by the scalar amount $\delta_g(\mathbf{r})$ that only depends on the atom's position in the trap \mathbf{r} . The maximum light shift of the ground state thus occurs at the region of highest intensity – the trap centre – defined by the position $\mathbf{r} = 0$ (see Figure 2.15 in Chapter 2 and the accompanying discussion). In order to determine this maximum light shift, the atom is treated as a quantum system with many hyperfine energy levels, $|(nJ)FM\rangle^*$, that interacts with a far-detuned trapping light field that can have an arbitrary polarisation. Using the formalism for this exact problem outlined in [330], the interaction energy is described by the operator

$$V_S = -\mathbf{E} \cdot \mathbf{d}, \quad (5.20)$$

so long as it remains small compared to the fine structure splitting. Here \mathbf{E} describes a classical light field (c.f. equation (2.34)), and \mathbf{d} is the operator for the electric dipole of the atom. In the basis of the hyperfine structure levels, $V_S^{FMF'M'} = \langle (nJ)FM | V_S | (nJ)F'M' \rangle$ can be expressed as

$$\begin{aligned} V_S^{FMF'M'} &= |\mathcal{E}|^2 \sum_{q=-K, \dots, K}^{K=0,1,2} \alpha_{n,J}^{(K)} \{ \mathbf{u}^* \otimes \mathbf{u} \}_{Kq} \\ &\times (-1)^{J+I+K+q-M} \sqrt{(2F+1)(2F'+1)} \\ &\times \begin{pmatrix} F & K & F' \\ M & q & -M' \end{pmatrix} \begin{Bmatrix} F & K & F' \\ J & I & J \end{Bmatrix}, \end{aligned} \quad (5.21)$$

where the notation for the sets of quantum numbers $\{F, M\}$ and $\{F', M'\}$ has been used in order to denote two different energy levels within the hyperfine manifold of the same fine structure state $|nJ\rangle$. Additionally, the Wigner 3-j and 6-j symbols respectively have notations of $\begin{pmatrix} j_1 & j_2 & j \\ m_1 & m_2 & m \end{pmatrix}$ and $\begin{Bmatrix} j_1 & j_2 & j_3 \\ j_4 & j_5 & j_6 \end{Bmatrix}$, where $K = 0, 1, 2$ respectively represents the reduced scalar, vector, and tensor dynamical polarisability of an atom in the fine structure level $|nJ\rangle$. In equation (5.21), $\alpha_{n,J}^{(K)}$ is the full dynamical polarisability of the

*Here, n and J are respectively the principal quantum number and the quantum number for the total angular momentum, \mathbf{J} , of the electron. For an atom with nuclear spin quantum number I , F is the quantum number of the total angular momentum of the atom, $\mathbf{F} = \mathbf{J} + \mathbf{I}$, while M is the quantum number of the projection F_z of \mathbf{F} onto the quantisation axis z .

fine structure state $|nJ\rangle$, and is given by

$$\begin{aligned} \alpha_{n,J}^{(K)} &= (-1)^{K+J+1} \sqrt{2K+1} \\ &\times \sum_{n'J'} (-1)^{J'} \begin{Bmatrix} 1 & K & 1 \\ J & J' & J \end{Bmatrix} |\langle n'J' | \mathbf{d} | nJ \rangle|^2 \\ &\times \frac{1}{\hbar} \operatorname{Re} \left(\frac{1}{\omega_{n'J'nJ} - \omega} + \frac{(-1)^K}{\omega_{n'J'nJ} + \omega} \right), \end{aligned} \quad (5.22)$$

while the compound tensor components $\{\mathbf{u}^* \otimes \mathbf{u}\}_{Kq}$ are defined as

$$\begin{aligned} \{\mathbf{u}^* \otimes \mathbf{u}\}_{Kq} &= \sum_{\mu, \mu' = 0, \pm 1} (-1)^{q+\mu'} u_\mu u_{-\mu'}^* \\ &\times \sqrt{2K+1} \begin{pmatrix} 1 & K & 1 \\ \mu & -q & \mu' \end{pmatrix}. \end{aligned} \quad (5.23)$$

In equation (5.22), ω and $\omega_{n'J'nJ}$ are respectively the angular frequencies of the trapping light field and the $|nJ\rangle \rightarrow |n'J'\rangle$ atomic transition, while in equation (5.23), the polarisation vector \mathbf{u} has the spherical tensor components $u_{-1} = (u_x - iu_y)/\sqrt{2}$, $u_0 = u_z$, and $u_1 = -(u_x + iu_y)/\sqrt{2}$. Furthermore, the reduced dipole matrix element $\langle n'J' | \mathbf{d} | nJ \rangle$ is related to the transition probability as

$$A_{n'J'nJ} = \frac{\omega_{n'J'nJ}^3}{3\pi\epsilon_0\hbar c^3} \frac{1}{2J'+1} |\langle n'J' | \mathbf{d} | nJ \rangle|^2, \quad (5.24)$$

where the value of $A_{n'J'nJ}$ for a specific $|nJ\rangle \rightarrow |n'J'\rangle$ transition can be found in the literature [331].

This formalism can thus be straightforwardly used to determine the spatially dependent light shift of the ^{85}Rb $5^2S_{1/2}$ ground state, by inserting the experimentally relevant parameters into equations (5.21)–(5.24). Notably, the polarisation of the trapping light field is set to linear, which brings about a simplification to the dynamical polarisability (also valid for the excited state): the polarisation vector \mathbf{u} is real, resulting in $[\mathbf{u}^* \times \mathbf{u}] = 0$, such that the contribution of the vector polarisability to the light shift is zero, i.e. $\alpha_{n,J}^{(1)} = 0^*$ [330]. The tensor contribution also vanishes for the considered ground state, i.e. $\alpha_{5,1/2}^{(2)} = 0$, as the Wigner 6-j symbol in equation (5.22) is equal to zero for $J = 1/2$ and $K = 2$. A useful consequence of the latter is that all Zeeman sublevels of the hyperfine ground state manifold, $|Fm_F\rangle$, are shifted by the same (scalar) amount for a given trapping field intensity, $I_t(\mathbf{r}) = 2\epsilon_0 c |\mathcal{E}(\mathbf{r})|^2 = 2P_t/\pi w_0^2 e^{-2(r/w_0)^2}$. By inserting this, along with the nuclear spin of $I = 5/2$, $\{\mathbf{u}^* \otimes \mathbf{u}\}_{00} = -1/\sqrt{3}$ resulting from the linear polarisation vector $\mathbf{u} = (0, 0, 1)$, considering the D_1 and D_2 contributions to $\alpha_{5,1/2}^{(0)}$ [96, 331], and the experimental trap parameters of $P_t = 2.5$ mW and $w_0 = 1.8$ μm with

*Note, however, that the effect of small longitudinal polarisation components occurring off-centre from the dipole trap axis that result in small elliptical polarisation components, is neglected.

$\Delta_t = 2.16$ THz its detuning from the $5S_{1/2} \rightarrow 5P_{3/2}$ transition (see Table 5.2), all into equation (5.21); the result

$$\delta_g(0) \approx -34 \text{ MHz} \quad (5.25)$$

is reached. Figure 5.16(a) shows the spatial dependence of $\delta_g(\mathbf{r})$ in the focal plane of the dipole trap, computed for the previously stated trapping field parameters. The dual axis plot also displays the calculated trapping potential, yielding a trap depth of $U_0 = U(\mathbf{r} = 0) = k_B \times 1.66$ mK.

In a similar fashion, it is possible to calculate the light shifts of the $5P_{3/2}$ excited state manifold [70, 330]. Although, again, the vector polarisability vanishes for a linearly polarised trapping field, for a total angular momentum of the electron of $J = 3/2$, the tensor polarisability does not. The latter leads to a complicated $m_{F'}$ sublevel-dependent light shift for each F' hyperfine state, by an amount which also depends on the position of the atom inside the trap. However, the problem can be significantly simplified by considering what occurs for the $(5S_{1/2}, F = 3, m_F = \pm 3) \rightarrow (5P_{3/2}, F' = 4, m_{F'} = \pm 4)$ transitions, where the MOT lasers are detuned (to the free-space atomic transition) by $\delta_{\text{MOT}} = \omega_L - \omega_0 = -2\pi \times 16.3$ MHz. The trap light, due to its π -polarisation, does not couple to these outermost Zeeman sublevels of the excited state. Consequently, the cycling transition of a trapped atom is only light shifted away from ω_0 by the amount $\delta_g(\mathbf{r})$. Despite this, due to interference between the three orthogonal pairs of counter-propagating excitation beams in the experiment (used to generate the Upper MOT) and the resulting presence of non-circular polarisations at the position of the trapped atom, additional $m_F \rightarrow m_{F'} = \{m_F, m_F \pm 1\}$ transitions can be driven. To take this effect into account, the total detuning between the light shifted atomic transition and the excitation frequency is taken as the sum of the MOT laser detuning and the position-dependent ground state light shift multiplied by a scaling factor c , according to $\delta(\mathbf{r}) = \omega_L - \omega_A(\mathbf{r}) = \delta_{\text{MOT}} + c \cdot \delta_g(\mathbf{r})$. As all remaining inner ($m_{F'} \neq \pm 4$) Zeeman sublevels are shifted towards higher energies with respect to the unperturbed $F' = 4$ state, c therefore takes a value between 1 (in which only the $(m_F = \pm 3) \rightarrow (m_{F'} = \pm 4)$ transitions are driven) and ~ 2 (in which the extreme case of only the $(m_F = 0) \rightarrow (m_{F'} = 0)$ transition is driven, where $\omega_A(\mathbf{r}) \approx \omega_0 + 2\delta_g(\mathbf{r})$). With this, a trapped atom experiences a maximum detuning from the excitation field of $\delta(\mathbf{r} = 0)$, to be determined by fitting the data using c as a fit parameter. Figure 5.17(a) depicts a simplified level scheme of the D_2 ($F = 3$) \rightarrow ($F' = 4$) transition when subject to the trapping field, illustrating these factors that contribute to the total detuning from the excitation frequency ω_L . As stated at the outset, the finite temperature of the atom in the trap gives rise to a temperature-dependent distribution of atomic positions in the trap and, consequently, of the light shifts. The final step in constructing the model is to obtain a suitable distribution of these detunings, using the atom temperature as an additional fit parameter alongside the maximum detuning.

5. Observation of Two-Photon Emission from a Single Atom

For simplicity, a centralised and isotropic harmonic potential generated by the dipole trap is assumed in the following, and is described by $U(\mathbf{r}) = \frac{1}{2}m\omega^2|\mathbf{r}|^2$. The normalised positional probability density function for a thermal occupation statistics of a confined **Rb** atom then reads [97, 276]

$$p(r)dr = \frac{(m\omega^2)^{3/2}}{\sqrt{2\pi}} r^2 e^{-\frac{m\omega^2 r^2}{2k_B T}} dr. \quad (5.26)$$

Here, ω is the angular frequency of the harmonic potential, $r = |\mathbf{r}|$ its radial distance from the origin (in a spherical coordinate basis), T its temperature, and m its atomic mass. Equation (5.26) is transformed into the normalised probability distribution for the potential energy of U in the trap, by substituting in $dU/dr = m\omega^2 r = \sqrt{2m\omega^2 U}$ and $r^2 = 2U/m\omega^2$, and multiplying with the normalisation prefactor $[\int_{-\infty}^{\infty} p(U)dU = \frac{1}{2}(k_B T)^{3/2}]^{-1}$. Doing so yields the Maxwell-Boltzmann distribution

$$p(U) = \frac{2}{\sigma^{3/2}} \sqrt{\frac{U}{\pi}} e^{-U/\sigma}, \quad (5.27)$$

characterised by its temperature-dependent mean $\sigma = k_B T$. Figure 5.16(b) displays an example distribution for the trapping potential shown in Figure 5.16(a), using $\sigma = k_B \times 200 \mu\text{K}$. Finally, setting $U = -2\pi\hbar \times (\Delta - \delta(r=0))$ allows for a change of variables in the above equation to provide a complementary distribution of detunings, $p(\Delta)$, that is dependent on the maximum detuning in the trap centre as well as the temperature of the trapped atoms, respectively derived from the fit parameters c and σ .

Extracting values for the fit parameters contained within $p(\Delta)$, c and σ , is achieved by a fit to the unmodified second-order correlation function obtained in the absence of filtering the resonance fluorescence (data set with $\kappa_{\text{ext}} = 0$). Practically, the fit is performed by summing over explicitly detuning-dependent $g^{(2)}(\tau, \Delta)$ functions, that are each weighted by multiplication with $p(\Delta)$ to obtain

$$g_{\Delta}^{(2)}(\tau, \kappa_{\text{ext}} = 0) = 1 + \frac{1}{N} \sum_{\Delta_{\text{min}}=\delta_{\text{MOT}}}^{\Delta_{\text{max}}=\delta(0)} p(\Delta) \cdot g^{(2)}(\tau, \Delta) \quad (5.28)$$

where the prefactor $N = \sum_{\Delta_{\text{min}}}^{\Delta_{\text{max}}} p(\Delta)$. Each second-order correlation function, $g^{(2)}(\tau, \Delta)$, is calculated according to equation (4.91), and thus contains the action of the filter transmission function – defined by a given value of κ_{ext} – on the resonance fluorescence spectrum, which in turn modifies the photon statistics of the transmitted light (see Section 4.5.3 in Chapter 4 for further details). By concentrating on the unfiltered resonance fluorescence where $\kappa_{\text{ext}} = 0$, as is the case for that presented in this Section, the spectrum of the transmission function evaluates to unity for all input frequencies. As evident in the above equation (5.28), the sum over Δ 's is performed between the limits of the **MOT** laser detuning and the maximum detuning of the light-shifted atomic

transition, with the latter varied during the fitting procedure. Furthermore, the detuning is sampled in steps of $\frac{1}{n}(\Delta_{\max} - \Delta_{\min}) \approx 0.5$ MHz for $n = 100$, and is chosen to ensure a reliable fit without excessive computational demand.

Figure 5.17(b) shows the resulting probability distribution $p(\Delta)$ as a function of Δ , using the obtained values of $c = 1.37$ and $\sigma = 176.8$ resulting from the fit. It shows that the average detuning of the trapped atoms with respect to the MOT laser frequency amounts to $\bar{\Delta}/2\pi = \int_{\delta_{\text{MOT}}}^{\delta(r=0, c=1.37)} \Delta \cdot p(\Delta, c = 1.37, \sigma = 176.8) d\Delta = -57.9 \pm 3.7$ MHz, corresponding to a temperature of $T = 144 \pm 47$ μK . This further allows for an accurate determination of the value for the saturation parameter due to the detuned driving, according to (c.f. equation (4.62) in Chapter 4)

$$S(\Delta) = \frac{I_{\text{MOT}}/I_{\text{sat}}}{1 + (2\Delta/\Gamma)^2}, \quad (5.29)$$

where $I_{\text{MOT}} = 6P/\pi R_{\text{MOT}}^2 \approx 15.3$ mW/cm² is the total intensity of the driving field at the position of the trapped atom, that uses $P = 0.5$ mW and $R_{\text{MOT}} \approx 0.25$ cm respectively as the power and waist radius of one MOT laser beam (the factor of 6 accounts for all six beams). Inserting the values of $\Gamma = 2\pi \times 6.067$ MHz for the natural linewidth of the D₂ transition and $I_{\text{sat}} = 1.66932$ mW/cm² for the saturation intensity [96] into equation (5.29), yields a saturation parameter of $S = 0.025 \pm 0.04$ for the experiment. This crucial setting of $S \ll 1$ confirms an experimental operation deep in the low saturation regime, where the resonance fluorescence can indeed be truncated at a two-photon interaction with the atom as presented throughout the latter half of Chapter 4.

The values obtained in this Section, through analysis of the second-order correlation function for the unfiltered ($\kappa_{\text{ext}} = 0$) data set (namely the atom temperature and mean detuning of the light shifted atomic transition), are used when modelling the data sets collected in the case of filtering the resonance fluorescence ($\kappa_{\text{ext}} > 0$). Importantly, the distribution of detunings resulting from this analysis demonstrates that the FRR filter, when set at the frequency of the coherently scattered component, does not significantly affect the incoherently scattered component since the latter lies within the unity transmission band* at $\bar{\Delta}/2\pi \approx \frac{2}{3}\nu_{\text{FSR}}$. Modelling the filtered data sets can therefore be performed with this simplification in mind. However, the model presented so far has to be further extended to include an additional experimental uncertainty that occurs when incorporating the FRR filter – drifts of the narrow resonator absorption line with respect to the MOT laser frequency. This is presented in the next Section 5.2.1.3, to conclude the theoretical modelling of the collected data.

*This assumption remains valid for filter settings of $\kappa \ll 2\pi \times \nu_{\text{FSR}}$.

5. Observation of Two-Photon Emission from a Single Atom

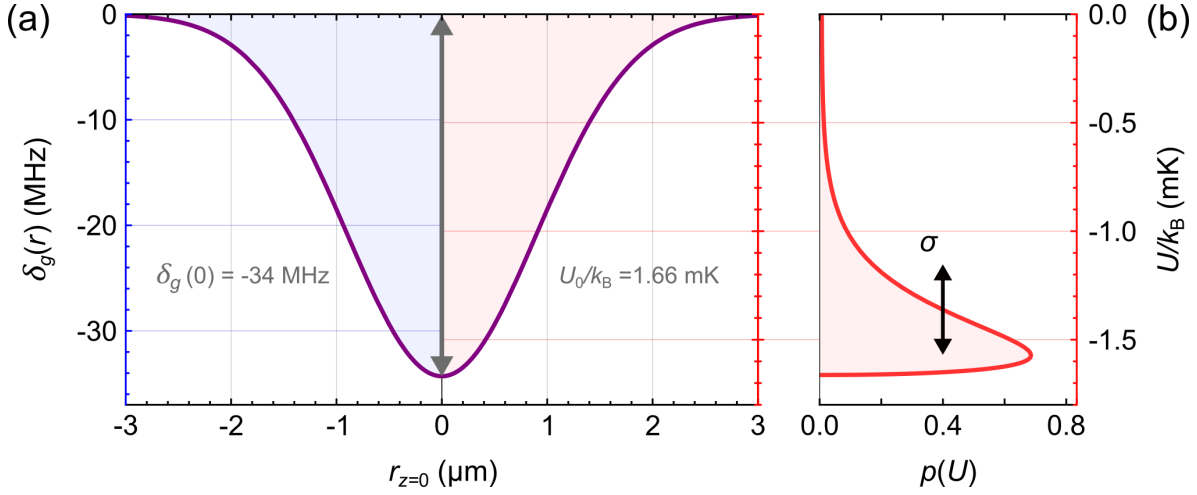


Figure 5.16. The thermally occupied dipole trap. (a) Dual axis plot of the ground state light shift $\delta_g(r)$ (left-most blue axis) and the trapping potential $U(r)$ (right-most red axis) as a function of the radial position in the trap, r . The maximum light shift of the ($5S_{1/2}, F = 3$) ground state occurs in the centre of the trap, of depth $U_0 = k_B \times 1.66$ mK, and amounts to $\delta_g(0) = -34$ MHz. Experimental parameters for the power, waist and detuning from the D_2 transition, used in the calculation: respectively $\{P_t, w_0, \Delta_t\} = \{2.5$ mW, 1.8 μm , 2.16 THz} (b) Plot of the probability distribution $p(U)$ according to equation (5.27), using a distribution width of $\sigma = k_B \times 200$ μK , that assumes thermal occupation statistics of the trap.

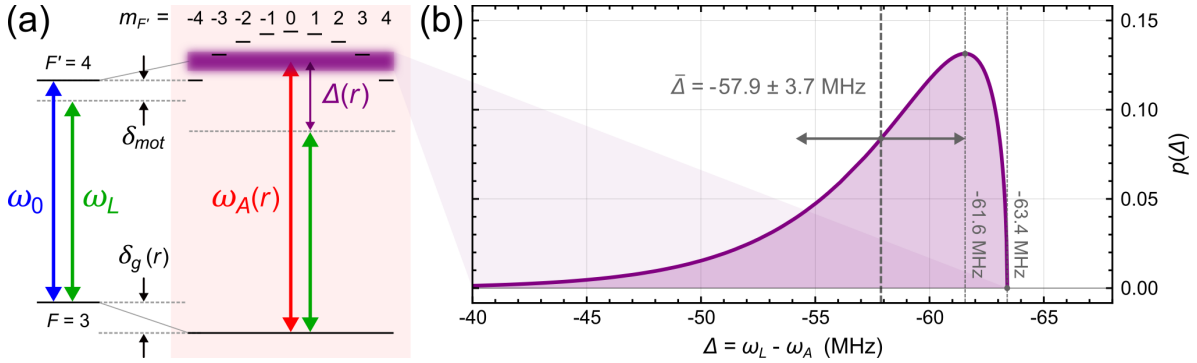


Figure 5.17. Considerations for the light-shifted atomic transition. (a) Level scheme of the ($5S_{1/2}, F = 3$) \rightarrow ($5P_{3/2}, F' = 4$) transition, that has a frequency of ω_0 in free space. The MOT lasers, of frequency ω_L , are red-detuned to this transition by the amount δ_{MOT} . When trapped, indicated by the red rectangle, the ground state of the atom is light shifted by the scalar amount $\delta_g(r)$, for a given position in the trap, r . The excited state manifold undergoes additional tensor light shifts, resulting in $m_{F'}$ -level dependent transition frequencies. The trapped atomic transition is then detuned from the driving field, on average, by a total amount $\Delta(r)$. (b) The probability distribution, $p(\Delta)$, that indicates the likelihood that a trapped atom is detuned from the driving field by the amount $\Delta = \omega_L - \omega_A$. This distribution is obtained by fitting to the second-order correlation function for the $\kappa_{\text{ext}} = 0$ data set, see text for details. It yields the following, indicated by the vertical dashed lines (from right to left): the maximum possible detuning of -63.4 MHz in the trap centre, the most probable detuning of -61.6 MHz where $p(\Delta)$ is maximised, and the average detuning of $\bar{\Delta}/2\pi = -57.9 \pm 3.7$ MHz as well as the standard deviation.

5.2.1.3 Residual Filter–Laser Detuning

The final experimental imperfection that must be accounted for during analysis of the measured second-order correlation functions is a non-negligible drift of the **FRR**'s spectral resonance, ω_{res} , that can occur between locking cycles. Such a wandering of the narrow resonator absorption line with respect to the excitation frequency set-point (see Section 5.1.2.3), incurs a variable suppression of the coherently scattered photons. This effect is particularly pronounced when using a narrow linewidth setting of the **FRR** (i.e., $\kappa_{\text{ext}} \lesssim \kappa_0$) in which even small spectral displacements of the resonance, $\delta_{\text{res}} = (\omega_{\text{res}} - \omega_{\text{L}})/2\pi$, can lead to large fluctuations in the transmission at ω_{L} . Furthermore, as explored in Chapter 4's Section 4.5.2, frequency-dependent phase shifts are imparted onto the total transmitted two-photon field when $\delta_{\text{res}} \neq 0$, which modifies the interference condition between the two components of the resonance fluorescence. This, in turn, has consequences for the dynamics present in the second-order correlation function, as investigated throughout Chapter 4's Section 4.5.3. A suitable model for the collected filtered data sets must take these effects into consideration, as well as provide information on the filter application. It is presented in the following.

As delineated in Section 5.1.2.3, the passive drift of the **FRR** resonance was found to be much less than 1 MHz/s. However, when continuously operating the experiment across a period of several days, measurements spanning this duration include times at which the resonance drift may have been significant between adjacent locking cycles (i.e., $|\delta_{\text{res}}| \gtrsim \kappa$). For the purposes of maintaining adequate statistics in the measured coincidence rates, only a loose postselection of data was performed, whereby runs in which the **FRR** was clearly not correctly locked, were discarded*. This corresponded to, on average, less than 5% of the total measurement time for each setting. Still, small residual drifts of the **FRR** that remain during data acquisition must be accounted for when modelling the measured data. To do so, it is assumed that the **FRR** filter exhibits a Gaussian probability distribution of resonance frequencies that has a width of ς centred around the average resonator–laser detuning δ_{res} , defined by the probability density function

$$p(\omega_{\text{res}}) = \frac{1}{\sqrt{2\pi\varsigma}} e^{-\frac{(\omega_{\text{res}} - \delta_{\text{res}})^2}{2\varsigma^2}}. \quad (5.30)$$

The parameters δ_{res} and ς contained within $p(\omega_{\text{res}})$ are then used for fitting each $\kappa_{\text{ext}} \neq 0$ data set, using the all-encompassing model

$$g_{\Sigma}^{(2)}(\tau, \kappa_{\text{ext}}) = \frac{1}{M} \sum_{\omega_{\text{res}}} \tilde{p}(\omega_{\text{res}}) \cdot g_{\Delta}^{(2)}(\tau, \kappa_{\text{ext}}), \quad (5.31)$$

which contains the second-order correlation function according to equation (5.28) for a given $\kappa_{\text{ext}} > 0$, evaluated with the distribution of detunings previously obtained

*This is achieved by observing the transmission of the lock light, which during a locking cycle, should appear parabolic. See Section 5.1.2.3 and Figure 5.12 in particular.

5. Observation of Two-Photon Emission from a Single Atom

for $\kappa_{\text{ext}} = 0$ (see the previous Section 5.2.1.2). In this way, the action of the filter transmission function on the two-photon component of the resonance fluorescence is thus defined by its spectral properties, which are specified by the parameters $\{\omega_{\text{res}}, \kappa_0, \kappa_{\text{ext}}\}$. In order to account for the variable suppression provided by the detuned **FRR** filter for non-constant ω_{res} , the probability density function contained within equation (5.31) is additionally weighted by the square of the total rate of photons that is expected to be transmitted at the (offset) resonance, as

$$\tilde{p}(\omega_{\text{res}}) = p(\omega_{\text{res}}) \cdot \left[n_{\text{coh}}(\bar{\Delta}) |\tilde{t}(\omega = \omega_{\text{L}}, \omega_{\text{res}})| + n_{\text{inc}}(\bar{\Delta}) |\tilde{t}(\omega = |\bar{\Delta}|, \omega_{\text{res}})| \right]^2. \quad (5.32)$$

Here, the scattering rates of the coherent and incoherent components are evaluated according to equations (4.63) and (4.64), and at the average atom–laser detuning $\bar{\Delta}$. The power transmission through the **FRR** filter at the spectral locations ω_{L} and $|\bar{\Delta}|$, for a given resonance ω_{res} , is obtained using equation (5.11). Further to this, the normalisation prefactor in equation (5.31) is $M = \sum \tilde{p}(\omega_{\text{res}})$, where the summations are performed in 25 steps across a range of $\omega_{\text{res}} = \delta_{\text{res}} \pm 5$ MHz, which together were found to yield satisfactory fits.

Upon fitting of all data sets for which $\kappa_{\text{ext}} > 0$ in this manner, an average (across all measurements) laser–**FRR** detuning of $\delta_{\text{res}} = -0.26 \pm 0.58$ MHz featuring a standard deviation of $\varsigma = 1.92 \pm 0.36$ MHz, is obtained. These values are reasonable when considering the way in which the filter resonance is stabilised (see Section 5.1.2.3), where the variation in the resonance frequency and its average offset from the set-point are in line with the spectral drift between locks and the locking procedure itself, respectively. Figure 5.18(a) displays this resulting distribution of filter resonance frequencies, according to equation (5.30), when evaluated with the found fit parameters. Alongside, in Figure 5.18(b), the transmission factor through the **FRR** filter for the field component at the driving frequency ω_{L} , are displayed for each setting of κ_{ext} . Here, the two cases of a filter with a fixed resonance at the laser frequency (dashed lines) and a variable filter resonance subject to the probability distribution shown in Figure 5.18(a) (solid lines) are compared, showcasing the difference between the ideal and realistic transmission spectra achieved with the **FRR** filter. These are calculated using equation (5.11), to yield the fixed and averaged spectra, respectively $T(\omega)$ and $\bar{T}(\omega)$. In particular, the experimentally achieved transmission of the coherently scattered component at the frequency ω_{L} is consistently larger than what would be expected using the ideal case of a fixed filter resonance at $\omega_{\text{res}} = \omega_{\text{L}}$, i.e., $\bar{T}(\omega_{\text{L}}) > T(\omega_{\text{L}}) \forall \kappa_{\text{ext}}$. This discrepancy in the transmission factor at ω_{L} is more pronounced for the cases of $\kappa_{\text{ext}} \lesssim \kappa_0$, where the narrow spectral linewidth of the filter becomes comparable to (or less than) the variation in its resonance frequency, ς . The latter is highlighted in Figure 5.18(c), where the transmission at ω_{L} across the different κ_{ext} set-points is displayed for the two considered cases of a fixed and variable filter resonance (dashed and solid green lines respectively),

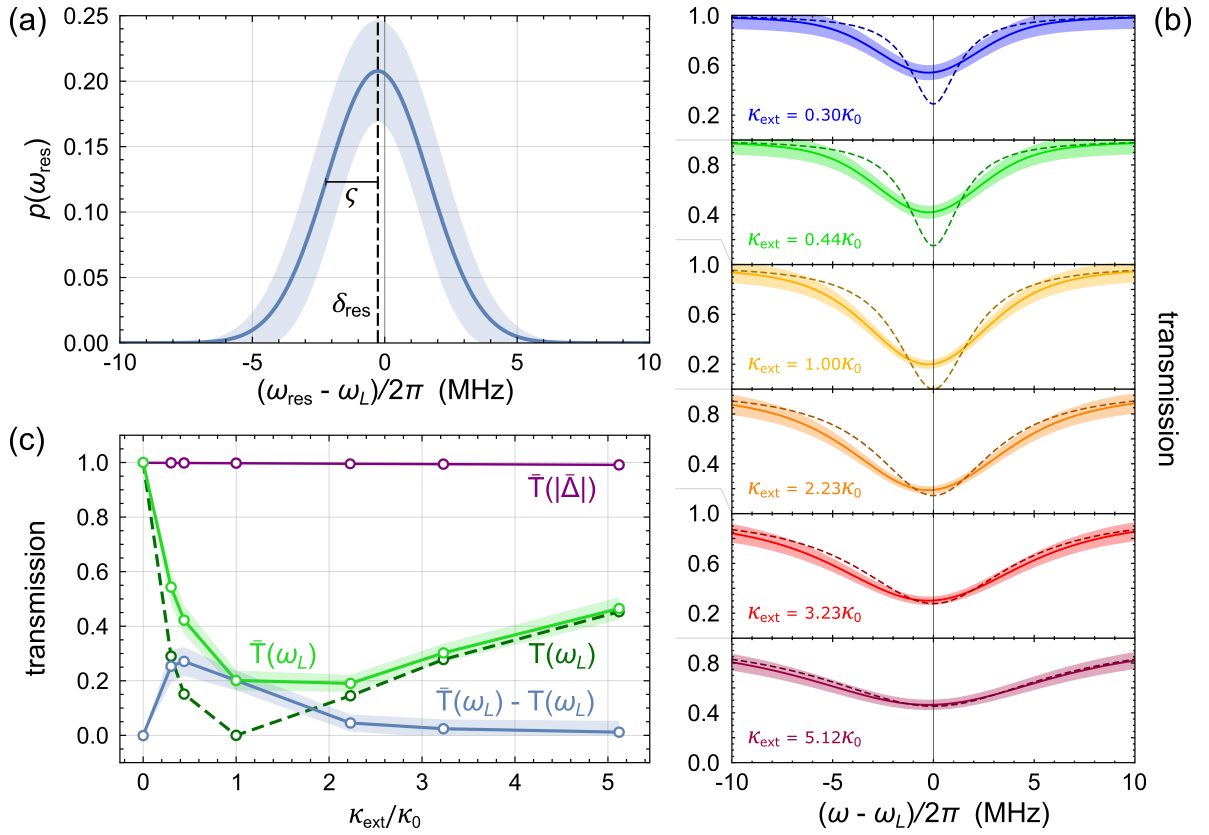


Figure 5.18. Transmission through the filter with a residual detuning from the laser. (a) The Gaussian probability distribution, $p(\omega_{\text{res}})$, that shows the likelihood that the resonance of the **FRR** filter is different from the laser frequency used for exciting the atom (ω_L). From fits to the measured second-order correlation functions in the case of filtering the resonance fluorescence, the distribution is found to be offset from the laser frequency by $\delta_{\text{res}} = -0.26 \pm 0.58$ MHz, with a standard deviation of $\zeta = 1.92 \pm 0.36$ MHz. The shaded area bounds the accumulative uncertainty in δ_{res} and ζ . (b) Plots of the **FRR** filter transmission spectrum, around the excitation laser frequency, for the different settings of κ_{ext} . The dashed lines show the expected transmission spectra according to $T = |\tilde{t}(\omega)|^2$ (equation (5.11)) for a fixed filter resonance at $\omega_{\text{res}} = \omega_L$, while the solid lines show the average transmission using the distribution of resonance frequencies shown in (a). The shaded areas bound the uncertainty in transmission arising from $p(\omega_{\text{res}})$. Each plot has the same vertical scale. (c) Plot of the filter transmission at the laser frequency for the different κ_{ext} set-points (hollow circles), for the case of a fixed resonance at $\omega_{\text{res}} = \omega_L$ (dark green, dashed line) and the distribution of resonances shown in (a) (light green, solid line). The difference in transmission between these two cases is included (blue curve), as is the averaged transmission through the filter at the spectral location of the incoherent component at $\omega_L \pm \Delta$ (purple curve). The latter remains above 99.5% for each κ_{ext} set-point.

as well as the difference between them according to $\bar{T}(\omega_L) - T(\omega_L)$ (blue solid line). Clearly, the variation of the filter resonance around the laser frequency that is present in the experiment leads to a reduction in the overall (average) suppression of the coherently scattered component across the duration of a measurement. For the filter setting of $\kappa_{\text{ext}}/\kappa_0 = 0.44$, the reduction of this suppression is most prominent and amounts to around 27% ($T(\omega_L, \kappa_{\text{ext}} = 0.44\kappa_0) = 15.1\%$ and $\bar{T}(\omega_L, \kappa_{\text{ext}} = 0.44\kappa_0) = 42.0 \pm 5.0\%$).

At the critical coupling filter setting of $\kappa_{\text{ext}} = \kappa_0$, where the expected on-resonance transmission is $T(\omega_L, \kappa_{\text{ext}} = \kappa_0) = 0\%$, variation of the filter resonance frequency limits the average suppression at ω_L to $\bar{T}(\omega_L, \kappa_{\text{ext}} = \kappa_0) = 20.0 \pm 4.0\%$. Of the different κ_{ext} filter settings used, the maximum average suppression of the coherently scattered component is achieved for $\kappa_{\text{ext}}/\kappa_0 = 2.23$, where $\bar{T}(\omega_L, \kappa_{\text{ext}} = 2.23\kappa_0) = 19.0 \pm 3.1\%$. For comparison, the average transmission at the spectral location of the incoherently scattered component is included in Figure 5.18(c) (purple solid line), which remains above 99.5% across all of the κ_{ext} set-points.

From the analysis performed in this Section, a theoretical model for the measured second-order correlation functions of the filtered resonance fluorescence has been developed and yields satisfactory fits, provided that both the variations in the atom–laser and laser–filter detunings are taken into consideration. Both of these imperfections are present in the experiment – respectively stemming from position-dependent light shifts of the optically trapped atomic transition and drifts of the filter resonance from the optimal filtering point – and the presented model provides valuable insight into their characteristics just through fitting to the data. Despite the fluctuations found in the detuning of the atomic transition with respect to the excitation frequency, alongside the sub-optimal filtering, the data and accompanying model in the obtained second-order correlation functions of the resonance fluorescence (Figure 5.14) clearly show the expected trend from antibunched to bunched photon statistics upon suppression of the coherently scattered component. An in-depth discussion of these results and their interpretation is therefore warranted, and are contained in the next penultimate Section 5.3 of this Chapter.

5.3 Discussion and Interpretation

The experimental results exhibited in Figure 5.14 confirm the interpretation of antibunching as an interference phenomenon between the coherent and incoherent two-photon components present in the light field scattered by the single atom, and are modelled well in this picture. When measuring the second-order correlation function, the expected antibunching behaviour is observed only when both of these two-photon components are scattered with equal amplitude, but opposite phase, at $\tau = 0$. In this case, the interference between them is perfectly destructive, yielding single-photon statistics that is evident by a measurement of $g^{(2)}(\tau = 0, \kappa_{\text{ext}} = 0) = 0.43 \pm 0.05$. This measured value is compatible with perfect photon antibunching when considering the background countrates of each SPCM, $d_{1,2}$, which gives rise to an accidental coincidences that do not originate from the atomic fluorescence. The accidental coincidence rate, $c_d(\tau)$, is measured during a time T_d , in which the trap was empty, within a time-bin of width t^b . The value for the normalised accidental coincidence rate is determined by

following the procedure outlined in [332], using $g_d^{(2)}(\tau) = c_d(\tau)/(d_1 d_2 t^b T_d)$. Using the ($\kappa_{\text{ext}} = 0$) measurement values of $T_d \approx 71$ hours, $d_{1,2} = \{56, 64\} \text{ s}^{-1*}$, and with $c_d = 0.76$ coincidences per $t^b = 2$ ns time-bin, the noise floor is calculated to lie at $g_d^{(2)}(\tau) \approx 0.41$. This level is indicated by the horizontal purple line shown in Figure 5.14.

As the amplitude of the coherently scattered two-photon component is then reduced by application of the **FRR** filter, which acts to attenuate light at the excitation laser frequency when increasing κ_{ext} from zero, the measured photon statistics in its transmission begin to differ from perfect antibunching. A temporally symmetric bunching behaviour is observed instead, that grows in amplitude, until the coherently scattered component is mostly removed. For the data set featuring the best suppression of the coherent component ($\kappa_{\text{ext}} = 2.23\kappa_0$), this reaches a strong value of $g^{(2)}(\tau = 0, \kappa_{\text{ext}} = 2.23\kappa_0) = 7.65 \pm 1.21$. As κ_{ext} is further increased, the coherent component is once more not fully attenuated, and what remains interferes with the unfiltered incoherent component to therefore lead to a reduction in the bunching amplitude. Antibunching would be recovered for very large values of κ_{ext} , as both components would approximately be attenuated by the same amount to once again fully destructively interfere (at $\tau = 0$). Although this was not observed due to the limited finesse of the **FRR** filter, where a κ_{ext} -dependent attenuation of the incoherent component begins to play a role for $\kappa_{\text{ext}} \gtrsim 6 \kappa_0$ (see Figure 5.10), the growing contrast visible in the beating signal as well as the gradual dip in the bunching amplitude as κ_{ext} is increased beyond $\sim 2 \kappa_0$ is indicative of a trend back towards an antibunching behaviour.

Figure 5.19(a) displays a quantitative support of these observations, showing the evolution of the measured second-order correlation function at zero delay as a function of the filter parameter κ_{ext} . For each setting, the value of $g^{(2)}(\tau = 0, \kappa_{\text{ext}})$ is obtained by averaging the data shown in Figure 5.14 within a 3 ns time window centred around $\tau = 0$. The horizontal error bars in each data point indicate the 1σ uncertainty in the setting of κ_{ext} , with the vertical error bars indicating the statistical 1σ uncertainty interval derived from fluctuations in the measured number of coincidences per time bin. The solid orange line is the theoretical prediction of $g^{(2)}(0, \kappa_{\text{ext}})$, using the approximate expression for the second-order correlation function given by equation (5.17). This contains the temperature-induced distribution of saturation parameters (see Section 5.2.1.2), the distribution of residual laser-resonator detunings (see Section 5.2.1.3), as well as the finite photon detection efficiency, η . The latter is determined by a fit to the κ_{ext} -dependent total photon countrate that is detected in the **HBT** set-up following filtering, as displayed in Figure 5.19(b). With no atom inside the trap, the average background countrate across each measurement amounts to $d = 54.9 \pm 5.9 \text{ s}^{-1}$. When

*Note that this background countrate is approximately a factor of 3 lower than that measured and displayed in Figure 5.6. This is due to an optimal alignment of the **MOT** with respect to the trap position, ensuring that the background was minimised when measuring the second-order correlation functions.

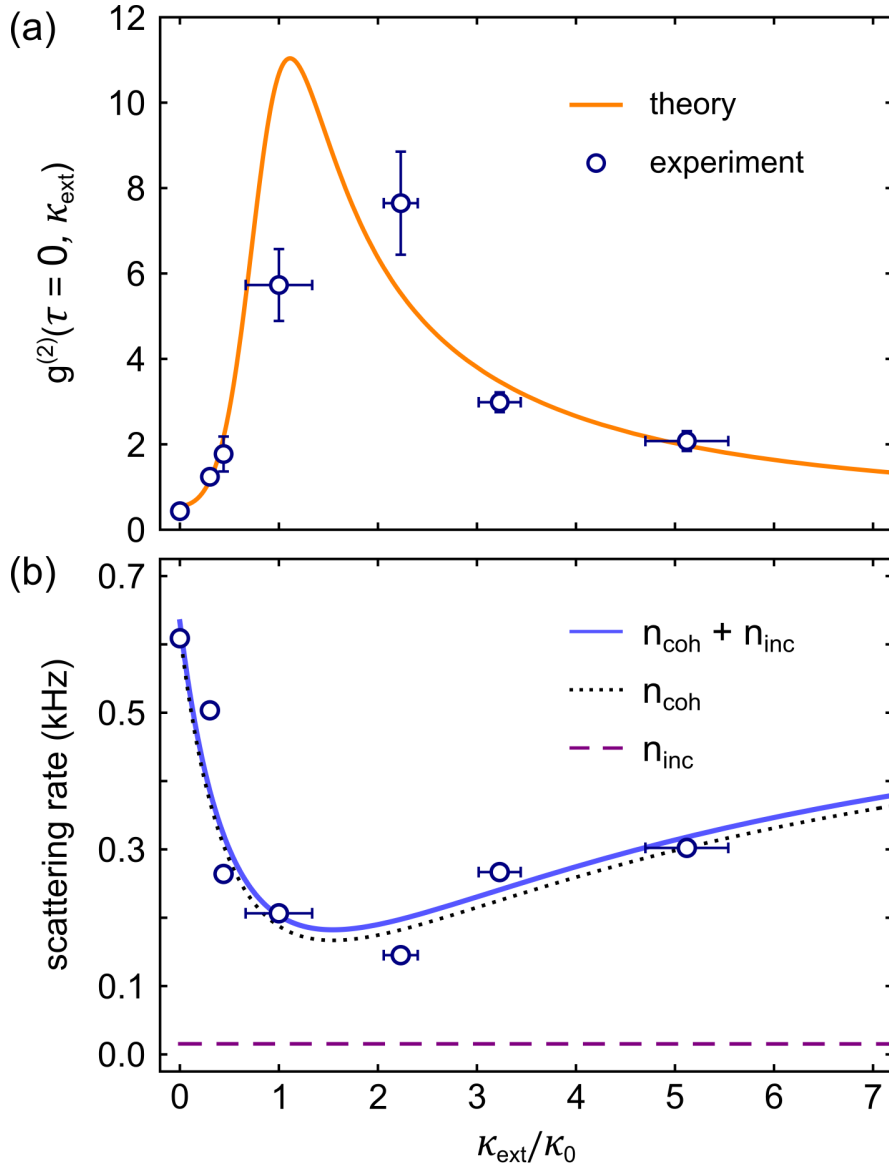


Figure 5.19. Correlations at zero time delay as a function of the filter setting. (a) The data points show the measured value of $g^{(2)}(\tau = 0, \kappa_{\text{ext}})$ averaged over a 3 ns time window centred around $\tau = 0$. The horizontal error bars indicate the 1σ uncertainty in the setting of κ_{ext} and the vertical error bars indicate the statistical 1σ uncertainty interval obtained from the number of detected photon pairs for each setting. The solid line is the theoretical prediction, that incorporates the temperature-dependent distribution of trapped atom–laser detunings as well as the distribution of laser–filter detunings. (b) The dark count corrected detected photon rate after filtering (data points), with the corresponding theory prediction (blue solid line), which contains the total single photon detection efficiency, η , as the only fit parameter. The fit yields the value $\eta = 0.136 \pm 0.002\%$. The individual contributions to the scattering rate are depicted by the black dotted (coherent) and purple dashed (incoherent) lines, calculated using the saturation parameter of the experiment $S = 0.025$. The horizontal error bars are the same as in (a), and those in the vertical direction are not visible on the scale of the Figure.

an atom is trapped, the countrate jumps to a higher value, s , that is comprised of the filtered atomic fluorescence signal, n , plus the background, d (see Figure 5.6 for example). The background subtracted data, $n = s - d$, for each setting of κ_{ext} is then fit with the function

$$n_F(\kappa_{\text{ext}}) = \frac{\eta}{N} \sum p(\omega_{\text{res}}) \cdot \left[n_{\text{coh}}(\bar{\Delta}) |\tilde{t}(\omega = \omega_L, \omega_{\text{res}})| + n_{\text{inc}}(\bar{\Delta}) |\tilde{t}(\omega = |\bar{\Delta}|, \omega_{\text{res}})| \right]^2, \quad (5.33)$$

using η as the only fit parameter. Here, $p(\omega_{\text{res}})$ is the probability density function of the **FRR** resonance frequency (equation (5.30)) evaluated with the pre-determined parameters (see Section 5.2.1.3), with the normalisation factor $N = \sum p(\omega_{\text{res}})$. Fitting in this way to the data (blue solid line in Figure 5.19(b)) yields a value of $\eta = 0.136 \pm 0.002\%$ for the total photon detection efficiency. This value agrees well with the expectation, when considering the lens collection efficiency of $\eta_0 \sim 1.3\%$ (see Section 5.1.1.2) and the **SPCM** detector efficiency of around 0.55, which would put propagation losses through the set-up at a reasonably expected $\sim 80\%*$.

Isolation of the incoherently scattered component in the resonance fluorescence of a single atom, through filtering the coherently scattered component, gives rise to a bunched photon statistics of the filtered light. In the low-saturation regime of resonance fluorescence, this results from the incoherent two-photon scattering process which distributes two incoming photons from the driving field into two outgoing photons that are respectively detuned above and below the input frequency. This scattered pair of photons propagate virtually simultaneously, within a temporal envelope bounded by the excited state lifetime of the emitter, giving rise to the characteristic symmetric bunching that is maximum at zero time delay as measured in the second-order correlation function of the filtered light. Filtering the resonance fluorescence therefore allows the single emitter to be employed as a novel type of quantum light source, that emits pairs of photons as opposed to the typical antibunched single-photon emission. The degree to which it succeeds as such a source, as well as its characteristics, can be obtained directly from the measured second-order correlation functions of the filtered light. This assessment is presented in the following Section 5.3.1.

5.3.1 A Competitive Photon-Pair Source

The resonance fluorescence of a single two-level quantum emitter is already a source of non-classical light, where its variety of applications in quantum technologies extend well beyond the testing of foundational aspects of quantum mechanics [333]. This work has demonstrated that isolating the incoherently scattered component in resonance fluorescence provides, in the low-saturation regime and under perfect removal of

*This value is likely mainly due to a non-perfect coupling of the emitted fluorescence from free-space into the collection fibre due to the atomic motion in the trap, but will also result from transmission losses across the multiple spliced fibre connections and the **MEMS** switch.

5. Observation of Two-Photon Emission from a Single Atom

the coherent component, a source of pure and energy-time entangled photon pairs. Entangled photon pairs, like their single photon constituents, are also a much-sought after commodity for burgeoning quantum technologies and tests of fundamental physics [334, 335]. Their envisioned and flourishing applications range from quantum communication via key distribution [336, 337] or teleportation protocols [338–340], to metrology [12, 341] and entanglement-enhanced microscopy [342]. Early sources of photonic entanglement were based upon the cascaded decay of atoms in experiments that demonstrated the validity of quantum mechanics [343, 344], to ultimately earn the authors a share of the Nobel Prize in 2022 [345]. Alternative sources based on nonlinear effects were then developed [346], which have become the workhorses governing the majority of photon-pair production since, falling into the categories of **Spontaneous Parametric Down-Conversion (SPDC)** [347] or **Spontaneous Four-Wave-Mixing (SFWM)** [348]. In general, the pair generation process that occurs in such sources is achieved by sending an intense pump beam through a nonlinear medium that features, in each case, a $\chi^{(2)}$ or $\chi^{(3)}$ nonlinearity. The medium’s intensity-dependent optical response then allows for the probabilistic annihilation of pump photons, with a corresponding simultaneous and energy-conserving pair creation event. In the case of **SPDC**, a single pump photon spontaneously splits into two photons of lower energies, while in **SFWM**, the interaction of two pump photons (that do not necessarily have to have the same wavelength) produce two new photons at different wavelengths. The so-called *signal* and *idler* photons that make up the generated photon-pair in these processes have frequencies that are typically (but not always) different to that of the pump photon(s), and exhibit a large spectral bandwidth. This can pose a particular challenge when interfacing these entangled photons to certain stationary quantum nodes, such as atoms. Furthermore, bulk crystals are the commonly used platforms for engineering the **SPDC** and **SFWM** processes which can limit the integrability and scalability of these sources, although recent progress has aided in overcoming this hurdle by employing on-chip or fibre-based materials [349–353]. Alternative entanglement sources that are based on single quantum emitters [354–357] are therefore an attractive avenue of investigation.

The filtering technique employed to efficiently remove the coherently scattered light that is demonstrated here, made viable by operating in the detuned regime of resonance fluorescence, lends itself to the realisation of an alternative for a photon-pair source that is based on only a single quantum emitter. Generated in this way, the pairs resulting from the filtered fluorescence are spectrally narrowband, energy-time entangled, and inherently compatible with optical transitions in quantum emitters. The crucial figure of merit that characterises the performance of any photon pair source is its *brightness*, i.e., the achievable *rate* of photon pairs*. For any source of photon pairs that has a linewidth

*Note that the exact definition for the brightness of a photon pair-source may vary depending on the experimental set-up and context [351]. For example, **SPDC** sources often define a brightness value in terms of the number of photon pairs generated per unit time, per unit pump power or pump photon flux [358].

of γ , the fundamental limit in the pair rate is bounded by $\sim \gamma/2$, as otherwise the temporal separation of subsequent pairs would be smaller than their extension in time ($\sim 1/\gamma$). Realistically, the achievable pair rate is lower than this limit, due to a finite collection efficiency of the generated photon pairs that must be taken into consideration. For the proposed source in this work, following an optical filtering of the resonance fluorescence of a single emitter, the expected photon pair rate is given by

$$n_p \lesssim \eta^2 \frac{n_{\text{inc}}}{2} = \eta^2 \frac{\gamma}{2} \frac{S^2}{(S+1)^2} \quad (5.34)$$

where η is the photon collection efficiency of the whole set-up as previously introduced. The rate $n_p \approx \eta^2 n_{\text{inc}}/2$ in the above inequality is only valid for the case of $S < 1$.

In order to determine the number of detected photon pairs within the performed experiment, the following procedure is undertaken for the data sets that feature the best suppression of the coherently scattered light ($\kappa_{\text{ext}} = \{1.00, 2.23\} \kappa_0$). First, the base level of the coincidence rate found for $|\tau| \gg 1/2\gamma$, that stems from accidental coincidences, is subtracted from the raw histogram data. All remaining coincidence events within a time window of ± 100 ns around $\tau = 0$ are then summed up, which gives the number of photon pairs detected during the entire measurement. This enables computation of the rate of detected photon pairs, $n_p^{(\text{meas.})}$, when dividing the result by the total measurement time. In doing so (using the values recorded in Table 5.4), the measured rate of photon pairs is found to be $n_p^{(\text{meas.})} = (4.91 \pm 0.47) \times 10^{-3} \text{ s}^{-1}$. Given the photon-pair detection efficiency of the set-up, $\eta^2/2 \approx 0.1\%$, this corresponds to a total rate of photon pairs that are incoherently scattered by the atom of $n_p^{(\text{tot.})} = 2n_p^{(\text{meas.})}/\eta^2 = 5.3 \pm 0.5 \text{ kHz}$. This agrees well with the rate of incoherently scattered photon pairs that is expected for the experimental setting of $S = 0.025 \pm 0.004$, as $n_p^{(\text{exp.})} = n_{\text{inc}}/2 = 5.7 \pm 1.4 \text{ kHz}$. The rate of coherently scattered photons on the other hand, $n_{\text{coh}} = 455 \pm 55 \text{ kHz}$, is larger than the rate of incoherently scattered photons, n_{inc} , by a factor S . Interestingly, despite the relative contribution of the incoherent component in one-photon observables tending to zero for a vanishing saturation, its small but finite value is still necessary for the observation of photon antibunching (a two-photon observable) when interfering with the dominating coherent component.

The theoretical description that is utilised here only considers up to the two-photon component of the scattered field, which is a valid approximation for the low-driving regime in which $S \ll 1$. Comparison to alternative theoretical models that take into account higher photon number components and consequently a stronger driving, approaching saturation [359], indicates that the two-photon theory should be valid for saturation parameters of up to $S \lesssim 0.25$, otherwise the incoherently scattered component also contains higher-order photon-scattering processes. Using this ceiling of $S = 0.25$, the performance of the filtered resonance fluorescence as a pair source can be evaluated within the ideal case of a perfectly isolated and collected incoherent component, i.e.,

$|\tilde{t}_{\text{coh}}| \approx 0$ with $\eta \approx 1$. The on-resonance transmission of the filter can indeed approach zero as demonstrated in this work, while large – or close-to-unity – collection efficiencies can be realised using high-NA optics or solid-state quantum emitters embedded in integrated structures [360–362]. Inserting these values into equation (5.34) yields a photon pair source that boasts pair rates of $n_p = \gamma/50 \approx 4 \times 10^5$ pairs per second that features a bandwidth of $\gamma = 2\pi \times 3$ MHz (for ^{85}Rb). This indicative result is substantially better than state-of-the-art photon pair-sources with a comparable bandwidth [358].

It should also be noted that this type of source also operates when dropping the assumption of a perfect filter. In the case of an imperfect filtering of the coherent light, where $|\tilde{t}_{\text{coh}}| > 0$, the pair-source would be polluted by a background of coherently scattered photons. The signal-to-noise ratio of the coherent to incoherent components after the optical filtering is given by $n_{\text{inc}}/n_{\text{coh}} = S/|\tilde{t}_{\text{coh}}|^2$. For saturation parameters around $S \approx 0.1$, the rate of incoherently scattered photons is ten times larger than the rate of coherently scattered photons when the residual filter transmission is $|\tilde{t}_{\text{coh}}|^2 \approx 1\%$. This can be readily achieved with the filtering set-up utilised in this work, with the FRR filter set to critical coupling ($\kappa_{\text{ext}} = \kappa_0$), and conditioned on its well-stabilised resonance frequency ($\omega_{\text{res}} = \omega_L$).

5.3.2 Filtering the Incoherent Component

One particular advantage of the FRR as a narrowband filtering device is its tunable resonance frequency, that allows a precise choice of both the filtering point and attenuation through a setting of the on-resonance transmission factor, $\tilde{t}(\omega_{\text{res}})$. Varying the frequency set for ω_{res} across the spectral span of the two-photon wavefunction of the resonance fluorescence allows to explore how the photon statistics of the transmitted field departs from the expected antibunching when removing other regions of the spectrum. Two examples of such studies are presented in the following, that further support the interference picture of resonance fluorescence as well as illustrating the reach of the theoretical model established for describing the data.

As a first expository example, setting $\omega_{\text{res}} = \omega_L \pm \bar{\Delta}/2$ would situate the filter line exactly between the spectral location of the coherently scattered component and one of the sidebands that make up the incoherently scattered component. For a filter linewidth much smaller than the spectral separation of the coherent and incoherent component, $\kappa \ll |\bar{\Delta}|$, the filter would have little to no effect on the photon statistics of the light transmitted past the filter as both components would experience close to unity transmission and only negligible phase shift. In this case, the filtered resonance fluorescence would still feature antibunched photon statistics. Figure 5.20 shows the results of a pair of such measurements, in which the critically-coupled FRR ($\kappa_{\text{ext}} = \kappa_0$) has its resonance set to $\omega_{\text{res}} = \omega_L \pm 35$ MHz in order that the filter line lies approximately halfway between the coherently and incoherently scattered component. The data

in both cases indeed features approximately antibunched photon statistics, whereby $g^{(2)}(\tau = 0) \lesssim 0.5$ with damped Rabi oscillations occurring at a frequency of $\Omega_{\text{eff}} \approx \bar{\Delta}$ for $0 < |\tau| \lesssim 1/2\gamma$. The theoretical model for each data set also fits well, in which the atom–laser and laser–filter detunings are taken into consideration as before (see Sections 5.2.1.2 and 5.2.1.3 respectively). The subtle difference appearing in the temporal shape of the second-order correlation function between the two measurements, in which the filter line is either situated to the red or blue side of the excitation laser, is attributed to the fact that the finite filter linewidth (together with its varying resonance frequency and temperature-dependent distribution of atom–laser detunings) imparts a different frequency-dependent phase onto the two-photon spectrum, resulting in a slightly modified interference condition between the two (see the discussion in Section 4.5.3 of Chapter 4). This difference is particularly evident around $\tau = 0$ in the data, and is highlighted further by the theoretical model.

A second example would be the case where the filter line is set exactly to lie at one of the sidebands of the incoherent component, $\omega_{\text{res}} = \omega_{\text{L}} \pm \bar{\Delta}$, to realise the complementary measurement to removal of the coherent component from the resonance fluorescence. By reducing the transmission of the incoherent component, the antibunched light would gradually lose contrast, until exhibiting a total loss of correlations upon its perfect removal (corresponding to the photon statistics of the coherent component only, which inherits that of the driving laser). This outcome has been previously experimentally observed, in which a gradual isolation of the coherently scattered component in the resonance fluorescence of a quantum dot, indeed revealed a reduction in the measured correlations [269, 270]. This was also achieved by spectrally filtering the incoherently scattered component, where reducing the width of a pass-band filter centred at the frequency of the coherently scattered component could tune the photon statistics from fully antibunched (using a filter width much broader than the fluorescence spectrum), to fully flat (using a narrow filter width that suppresses the incoherently scattered component). Such a scenario was theoretically investigated in the latter part of Section 4.5.3, see Figure 4.22. However, realising such a measurement here – when using the **FRR** filter – places stringent requirements on the relationship between the spectra of the filter and two-photon component of the resonance fluorescence: in order to fully remove the incoherent component, the filter linewidth must be much broader than the sideband width ($\kappa \gg 2\gamma$), but in order to avoid attenuation of the coherent component, the sideband must be well-separated from the driving frequency ($|\omega_{\text{L}} \pm \bar{\Delta}| \gg \kappa/2$). Furthermore, the **FSR** of the **FRR** filter must be significantly larger than the total spectral distribution of the two-photon spectrum, such that an adjacent filtering line does not play a role ($\omega_{\text{FSR}} \gg |\omega_0 - 2\bar{\Delta}|$). Performing this measurement with the current set-up is not possible without a significant re-building of the **FRR** filter which, in its current presented state, does not meet these criteria. Such requirements are however, in principle, possible to meet when using a properly designed **FRR** filter (for example,

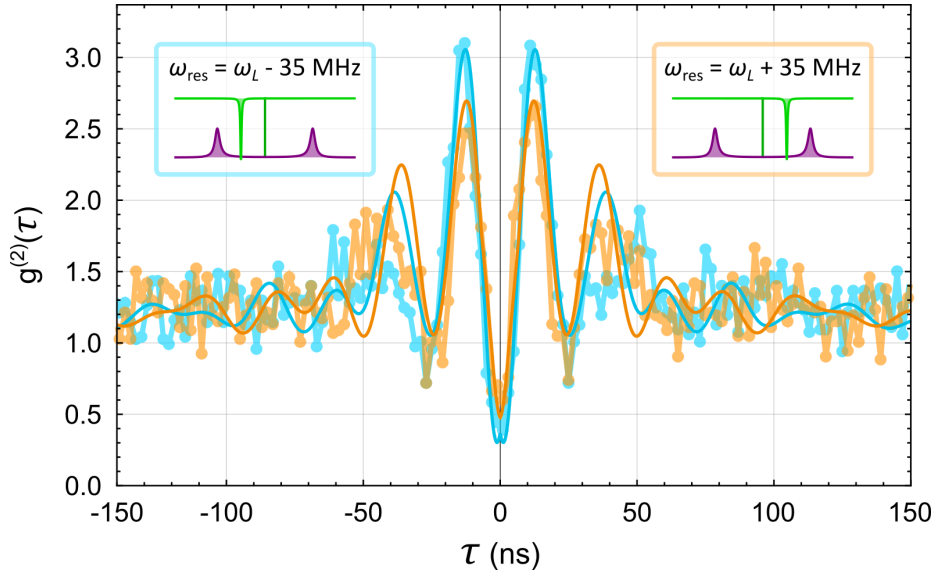


Figure 5.20. Off-resonant filtering. Measured second-order correlation functions of the filtered resonance fluorescence, when placing the filter line frequency between the spectral locations of the coherently scattered component and one of the sidebands of the incoherently scattered component. The orange (cyan) data is obtained when setting $\omega_{\text{res}} = \omega_L + (-) 35$ MHz, see the colour-coded insets. Both traces exhibit antibunching, where $g^{(2)}(0) \approx 0.5 < g^{(2)}(\tau)$, as well as damped Rabi oscillations for $|\tau| > 0$ at a frequency of $\Omega_{\text{eff}} \approx |\Delta| = 2\pi \times 57.9$ MHz. The solid lines are the theory predictions using the specific value of ω_{res} , while incorporating the distributions of atom–laser and laser–filter detunings.

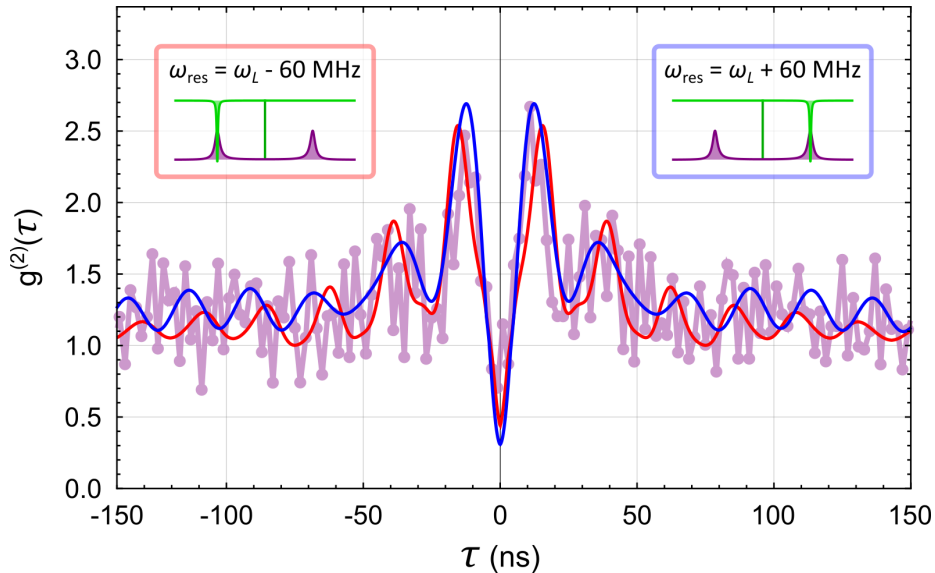


Figure 5.21. Partial filtering of the incoherent component. Measured second-order correlation function of the filtered resonance fluorescence, when placing the filter line frequency at the spectral location of one of the sidebands of the incoherently scattered component. The blue (red) solid line is the theory prediction obtained when setting $\omega_{\text{res}} = \omega_L + (-) 60$ MHz, see the colour-coded insets, while the supporting purple data is recorded for the setting of $\omega_{\text{res}} = \omega_L + 60$ MHz.

an $\mathcal{F} \sim 20$ **FRR** with a ring-section length of 1.3 m would yield a critically-coupled linewidth of $\sim 5\gamma$ for a $\nu_{\text{FSR}} = 150$ MHz **FSR**, meeting these requirements for the filtering of a two-photon spectrum with $\bar{\Delta}/2\pi \approx 30$ MHz). Still, out of curiosity, this measurement was briefly attempted using the established set-up, where the critically-coupled **FRR** was approximately placed on one sideband of the incoherent component at $\omega_{\text{res}} = \omega_{\text{L}} + 60$ MHz. The results of this investigation and comparison to the theory predictions are displayed in Figure 5.21. The data appears markedly more noisy in comparison to the previously discussed traces, as it suffers from a lack of statistics due to the limited measurement time. The overlay of the theoretical model does, however, provide some clarity to the more pronounced features. Notably, for $|\tau| \lesssim 50$ ns, it is possible to qualitatively posit that the data exhibits a reduction in the contrast of the antibunched behaviour and an increase in the value of $g^{(2)}(0)$ when compared to the unfiltered case (see Figures 5.14, 5.15, and 5.20 for example). This apparent modification of the photon statistics is only small due to the narrow filter linewidth. These observations could still indicate a step in the direction towards obtaining a flat second-order correlation function, as expected for a complete removal of the incoherently scattered component [269, 270].

These measurements further support the interference picture of resonance fluorescence, in that the narrow **FRR** filter line, when centred at different frequencies within the two-photon spectrum, still acts to control the interference between the coherent and incoherent components. This leads to a modification of the usually antibunched photon statistics achieved without filtering, which can be slight in the case of positioning the filter line between the two components, or potentially significant when partially filtering away the incoherent component. Although this Section has only presented an inexhaustive exploration into modifying the photon statistics of resonance fluorescence through filtering with the **FRR**, it demonstrates the flexibility offered by this method, as well as providing a small glimpse into its potential for further investigation. This latter remark will be elaborated upon in the final Section 5.4 of this Chapter, which is first preceded by a presentation of an alternative *time-domain interpretation* of the main results.

5.3.3 Time-Domain Interpretation

The observation of photon bunching in the second-order correlation function of the filtered resonance fluorescence (when removing the coherently scattered component) can be easily and intuitively understood as has been emphasised thus far: by exclusively considering the frequency-domain, where the two-photon spectrum of resonance fluorescence is modified by the transmission spectrum provided by the **FRR** filter. This has highlighted the picture that single photon emission in resonance fluorescence is a consequence of the emitter continuously scattering the incident two-photon component in two different

ways – coherently and incoherently – which perfectly destructively interfere to yield antibunched photon statistics. As each of these processes have distinct spectra that can also be spectrally well-separated (by detuning the excitation field with respect to the emitter’s resonance), the introduction of a spectral filter can easily disrupt the delicate balance between them, to thus spoil the antibunching. Transforming the perfectly antibunched light into a strong bunched light is achieved upon suppression of the coherently scattered component, thereby isolating the incoherently scattered component, which consists solely of pairs of simultaneously propagating photons.

An alternative – but equally valid – interpretation of these results lies in the complementary time-domain, where the atom can indeed be considered as only scattering single photons, one by one. Here, this emitted stream of antibunched photons is remarkably transformed into bunched photons by simply passing through the passive and linear notch-like **FRR** filter. While it is well established that the spectral filtering of light can alter its statistical properties, such as the transformation of coherent laser light field into a chaotic one in which the phase noise is changed into intensity fluctuations by a narrow linear filter [263], such a classical reasoning cannot be applied when the field being filtered is of a purely quantum nature. As this latter situation wholly applies to the experiment performed in this work, explaining the observed transformation of the antibunched photon statistics of resonance fluorescence to bunching by application of the filter necessitates evocation of a purely quantum phenomenon – that of a so-called *Hong-Ou-Mandel (HOM) quantum interference* [363] occurring at the incoupling beamsplitter of the **Fibre-Ring Resonator** filter.

The **HOM** effect describes how single photons behave when incident on a beamsplitter and specifically refers to the situation in which two photons, one in each input port, arrive together. Whereas each of the photons, individually, have a 50 % probability of exiting into either of the output ports*, a perfect temporal overlap between the two photons arriving at the beamsplitter ensures that they always exit together, *in the same output port*. This phenomenon results from interfering quantum amplitudes between the possible output states of the two indistinguishable input photons, where the states in which each photon is either reflected or transmitted by the beamsplitter perfectly destructively interfere [364]. This cancellation manifests, experimentally, as a drop in the number of coincidences between detectors placed in each output mode of the beamsplitter. Figure 5.22 pictorially illustrates the **HOM** effect that must occur at the beamsplitter (variable ratio coupler) that connects the ring section and input/output fibres of the **FRR** filter. The indistinguishable photons that undergo **HOM** interference are those that originate from the collected resonance fluorescence, where one comes from the input fluorescence field and the other from the stored resonator field.

In order to describe this effect, the resonator field, that is fed by the atomic fluorescence field of amplitude ψ_i , must first be defined. The fact that the **Fibre-**

*for a balanced beamsplitter.

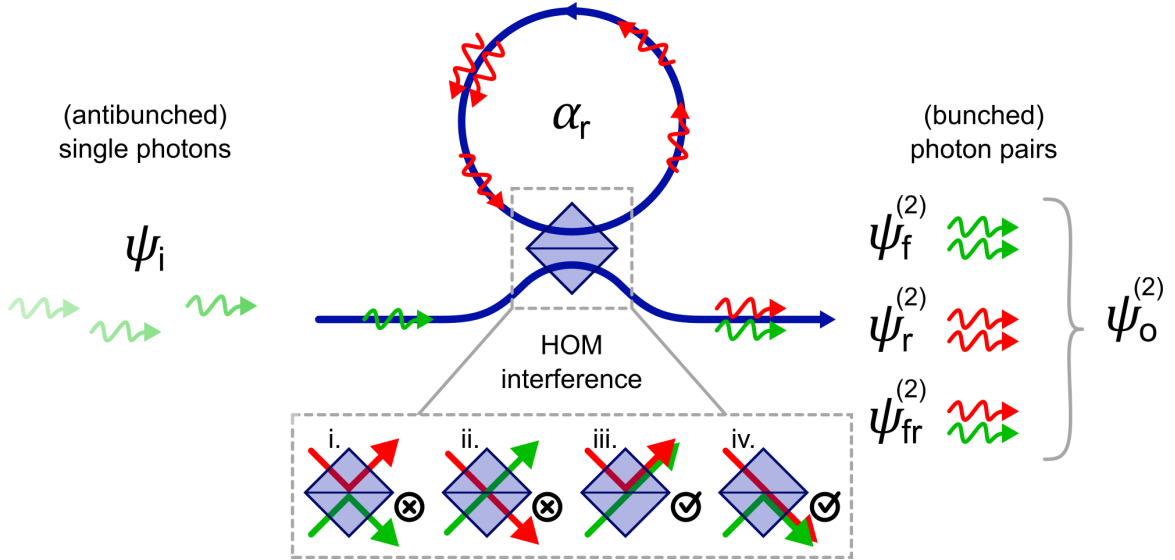


Figure 5.22. The Fibre-Ring Resonator in the time-domain. Single (antibunched) photons are transformed into (bunched) photon pairs by passing the FRR filter and interacting with the stored resonator field, α_r , with HOM interference occurring at the incoupling beamsplitter. The inset pictorially illustrates the HOM effect, where cancellation of processes i. (reflection–reflection) and ii. (transmission–transmission) for indistinguishable input photons leaves the remaining processes iii. (reflection–transmission) and iv. (transmission–reflection), in which both photons exit in the same port. The output two-photon field, $\psi_o^{(2)}$, comprises the three possible events where two photons either both originate from the fluorescence light ($\psi_f^{(2)}$) or from the resonator ($\psi_r^{(2)}$), or one from each ($\psi_{fr}^{(2)}$).

Ring Resonator has a temporal response to an input light field at a characteristic timescale of $(\kappa_0 + \kappa_{\text{ext}})^{-1}$ is used for this endeavour. It is much slower than the amplitude fluctuations in the atomic fluorescence, which are on a timescale of $\sim \bar{\Delta}^{-1}$. Consequently, the resonator averages over these fluctuations and the light stored inside the resonator, in the steady-state, can approximately be described by a coherent state that has an amplitude [105]

$$\alpha_r = \psi_f^{(1)} \cdot \frac{\sqrt{-2\kappa_{\text{ext}}}}{i(\omega - \omega_{\text{res}}) + \kappa_0 + \kappa_{\text{ext}}}. \quad (5.35)$$

Here, $\psi_f^{(1)} = \sqrt{n_{\text{coh}}}$ is the amplitude of the single photon component of the input fluorescence field (see Section 4.4), while the second term comes from the steady-state solution to the input-output relation for a resonator that couples to a waveguide via a beamsplitter-like interaction [105]. The splitting ratio of this incoupling beamsplitter is dependent on the external coupling rate parameter, κ_{ext} , which connects the transmission factor into the resonator to \tilde{t}_{coh} (see equation (5.11)). The beamsplitter is typically highly asymmetric, and features a transmission of approximately unity for the input fluorescence light. The amplitude of the outcoupled resonator field is then given by $\psi_r^{(1)} = -\alpha_r \sqrt{n_{\text{coh}}} = \sqrt{n_{\text{coh}}} (\tilde{t}_{\text{coh}}(\kappa_{\text{ext}}) - 1)$, which results in $\psi_f^{(1)} + \psi_r^{(1)} = 0$ for $\tilde{t}_{\text{coh}} = 0$.

At the output of the **FRR** filter lies the **HBT** set-up, which detects photon coincidences that occur within the time delay τ . Knowing the state of the input and outcoupled resonator fields, the amplitudes of the two-photon components in each – that would give rise to such a coincidence detection – should be considered. There are actually three possible ways in which a photon coincidence event can be registered: two photons can either originate from the input fluorescence field (amplitude $\psi_f^{(2)}$), both from the resonator field (amplitude $\psi_r^{(2)}$), or *one from each* (amplitude $\psi_{fr}^{(2)}$). The probability amplitudes of a coincidence detection from each of these processes are then given by

$$\psi_f^{(2)} = \frac{n_{\text{coh}}}{2} \left(1 - e^{-(\gamma - i\bar{\Delta})|\tau|}\right) \quad (5.36)$$

$$\psi_r^{(2)} = \frac{(-\alpha_r \sqrt{2\kappa_{\text{ext}}})^2}{2} = \frac{n_{\text{coh}}}{2} \left(\tilde{t}_{\text{coh}}(\kappa_{\text{ext}}) - 1\right)^2 \quad (5.37)$$

$$\psi_{fr}^{(2)} = -\sqrt{n_{\text{coh}}\alpha_r} \sqrt{2\kappa_{\text{ext}}} = n_{\text{coh}} \left(\tilde{t}_{\text{coh}}(\kappa_{\text{ext}}) - 1\right). \quad (5.38)$$

The total two-photon detection probability amplitude at the output of the **FRR** beamsplitter is then the coherent sum of these three contributions, following the **HOM** argument [363, 364]. In doing so, the output two-photon field after the **FRR** filter then reads

$$\begin{aligned} \psi_o^{(2)} &= \psi_f^{(2)} + \psi_r^{(2)} + \psi_{fr}^{(2)} \\ &= \frac{n_{\text{coh}}}{2} \left[\tilde{t}_{\text{coh}}(\kappa_{\text{ext}})^2 - e^{-(\gamma - i\bar{\Delta})|\tau|} \right], \end{aligned} \quad (5.39)$$

which is the same expression as equation (5.13). Here, the maximal probability for two simultaneously propagating photons ($\tau = 0$) occurs for when $|\tilde{t}_{\text{coh}}|^2 = 0$. This result demonstrates the equivalency of the spectral and temporal pictures of describing the filtered resonance fluorescence.

5.4 Final Thoughts

The experiment performed and presented in this Chapter validates an exciting – yet much overlooked – picture of resonance fluorescence. By employing the newly constructed **CQED 2.0** experimental apparatus as a setting for its study, the single optically trapped ^{85}Rb atoms that are driven to fluoresce by the near resonant **Magneto-Optical Trapping** field, could be taken advantage of for generating the well-recognised setting for single-photon emission. Here, antibunching is known to arise from the saturable nature of the quantum emitter, in that, once excited, a photon emission can only occur via a quantum jump back from the excited to ground state. The observation of transforming this antibunched light into a strongly bunched light – simply through filtering the scattered field – then helps to illuminate this most fundamental process in quantum optics: demonstrating that simultaneous multi-photon emission from a two-level quantum emitter is possible to realise, so long as the different scattering processes are separated.

This feat has been achieved here by suppressing the coherently scattered component in the resonance fluorescence from the single atom, by sending the collected antibunched light through a notch-like transmission filter constructed by a **Fibre-Ring Resonator**. As shown experimentally, the remaining incoherently scattered component consists purely of photon pairs in the investigated regime of low driving, which explains the observation of bunched photon statistics upon its isolation. The filtering ability of the **FRR**, and its imprint on the measured second-order correlation functions of the fluorescence light, has been broadly explored. Doing so has produced experimental results to verify the picture that single photon emission is only possible due to the fully destructive interference and interplay between the quantum amplitudes of the two-photon components of the coherent and incoherent emission processes.

The experiment presented in this Chapter has only just scratched the surface of single-emitter multi-photon emission through filtering, where the scattering dynamics are confined to no more than two photons at a time, and a considerable amount of possibilities for further investigation lie in the wake of its findings. On the fundamental side, continuation of the experiment in its current form – albeit with an updated and application-specific **FRR** filtering – can further map-out the correlation dynamics when sweeping the filter line across the spectrum of the scattered field and using its on-resonance transmission setting (and/or linewidth) as an additional control knob. This can be used to produce partial interference between the states of the coherently and incoherently scattered light, to engineer exotic second-order correlation functions featuring sharp bunching peaks of widths below the emitter’s lifetime, for example. Implementing an active feedback in order to improve the **FRR** frequency stabilisation, as well as a dual-colour magic wavelength dipole trap to negate temperature-dependent light shifts of the atomic transition, would aid in greatly improving the ease and quality of such investigations within this set-up. Another avenue for inquiry is that, in following a removal of the coherent component from the fluorescence light, restoration of the antibunching could be achieved by interfering the remaining incoherent component with a coherent light field of correct phase and amplitude, such as the excitation laser [365]. In general, mixing with an external laser can provide additional control and tunability of the fluorescence correlations [366], that could be used in conjunction with the pre-existing filtering scheme. Restoring antibunching in such a way is yet to be experimentally demonstrated. Beyond these suggestions for continued progression, further extensions to the current filtering set-up can be implemented in order to pursue alternative routes of investigation. For example, adding an additional variable ratio coupler into the ring-section of the **FRR** would convert the demonstrated two-port filter into a four-port (add-drop configuration) device [367], further providing access to the intra-resonator field. A pair of these in series could then be employed to each respectively remove one of the two sidebands of the incoherently scattered component, enabling measurements of a cross-correlation rather than auto-correlation when utilising

detectors in the transmission of each drop port. This kind of scheme would be one way to reveal the time-ordering between the two sidebands of the fluorescence triplet structure in the low driving regime [260]. Furthermore, the filtering linewidth tunability offered by such a device could, in principle, be used to tomographically reconstruct the two-photon state of the incoherent component: by step-wise scanning a narrow setting of the filter lines, one centred at each sideband, and monitoring the registered coincidences at each drop port output. Coincidences between the two detectors would predominantly occur only for when the filter lines are centred at the frequencies ω_R and ω_B , that meet the condition $\omega_R + \omega_B = 2\omega_L$, thus providing evidence of the energy–time entanglement between the two photons making up the incoherent component.

As the phenomenon of resonance fluorescence applies to any two-level quantum system interacting with a (quantum or classical) drive that is tuned at or close to the natural frequency of the emitter, the filtering procedure demonstrated here can straightforwardly be implemented into alternative emitter platforms in order to take advantage of particular traits that they may pose. For example, light–matter interfaces that offer higher photon collection efficiencies have been demonstrated in alternative free-space atom geometries [360] as well as in chip based architectures, where collection efficiencies in the latter class of platforms can approach close to unity [361, 362]. Implementing such a higher photon collection efficiency set-up would drastically improve the achievable photon-pair rates with respect to that shown in this work, in an effort to draw nearer the theoretical limit in brightness of a Fourier-limited pair source. Furthermore, integrated on-chip architectures that, for example, pair quantum dot emission into a waveguide with nano-fabricated ring-resonator structures [368], can significantly miniaturise the set-up for its realisation as a dedicated device for the production of entangled photon pairs. The demonstration of *simply* filtering the resonance fluorescence collected from a quantum emitter is therefore more than a curious and fundamental effect: it can be established as a strong candidate for applications in quantum technologies. As a versatile tool that is widely applicable to a variety of experimental platforms, photon pair sources that are based upon this effect are certainly a suitable resource for integration into optical quantum technologies and quantum information processing.

Beyond the exciting technological prospects that are potentially on the horizon with the employment of this effect, it is most striking to conclude by returning to its fundamental implications, answering the question *will a single two-level quantum emitter simultaneously scatter two photons?* Depending on which picture is used, the answer can be both *yes and no*, as is often the case in quantum mechanics...

6

Conclusions and Perspectives

The struggle itself towards the heights is enough to fill a man's heart.
One must imagine Sisyphus happy.

A. Camus, 1942 [369]

6.1 Summary

The contents of this thesis has been broadly two-fold. Firstly, the design and construction of a new experimental apparatus for the study of **CQED** with single atoms coupled to a **Whispering-Gallery Mode** bottle microresonator has been presented. Secondly, the results of a first experiment performed with this system, concerning the spectral filtering of the resonance fluorescence of a single atom, has also been detailed. The former paves the way for realising a fully fibre-integrated chiral interface between a single atom and a single photon, while the latter provides valuable insight into this most fundamental interaction between light and matter. Both cases additionally, beyond such fundamental interest, lend themselves to the development and implementation of novel quantum technologies, particularly for the processing or generation of highly non-classical light fields.

The new generation of the **CQED** experiment developed in this work aims to provide, first and foremost, no compromise on the capabilities offered by that of the first generation [70, 92, 93, 120]. Namely, it should consist of a **WGM** bottle microresonator that can be independently and stably interfaced by a pair of coupling nanofibres, and feature the delivery of cold atoms to – and their optical trapping within – the **WGM** of the

6. Conclusions and Perspectives

microresonator. This necessitates a sophisticated two-chamber design of the **UHV** system, in which the coupling set-up is suitably contained in one chamber, while cold atom preparation is performed in the other with use of a **Magneto-Optical Trap**. Delivery of cold atoms to the bottle microresonator is then performed with an **Atomic Fountain** via a **Differential Pumping Tube** that links the two chambers. Capture of a single atom within the microresonator's **WGM** can then be achieved with a retroreflected optical tweezer trapping scheme, that was successfully demonstrated with use of the first generation experiment [60, 70]. Further to these elements, the second generation set-up also *builds upon* certain aspects of the first. A number of minor designed-in alterations help to improve the overall experimental operation, such as a **UHV** chamber assembly that allows for a straight-forward exchange of components within the coupling set-up. The major modifications, in general, are intended to provide a route towards an advanced optical trapping scheme that should enable extended durations of strong coupling between a single atom and a **WGM** of the bottle microresonator, featuring an improved loading efficiency and atom localisation. In order to facilitate such improvements, a second **MOT** stage is added in the vicinity of the microresonator location, alongside a positionable high **Numerical Aperture** aspheric lens. Together, these additions allow for the direct loading of single atoms from the **MOT** into a microscopic optical dipole trap generated at the focus of the lens. Upon the optical capture of a single cold atom, it is envisioned that movement of the trap location towards the surface of the resonator will allow for a near-deterministic loading of the retroreflected resonator surface trap, and additionally granting an extended trapping lifetime.

The in-vacuum lens doubles as an efficient collection optic for the resonance fluorescence of single atoms in the trap, that are driven by an external coherent field operating near atomic resonance. Jumps in the photon countrate originating from the trapping volume thus signifies the presence or absence of a single trapped atom. A measurement of the second-order correlation function of the detected fluorescence photons yields an antibunching behaviour – a clear signature of single photon emission – as typically expected for the photon statistics of light originating from a single two-level quantum emitter. These observations therefore verify the successful loading of single atoms into the optical dipole trap, and its operation in the collisional blockade regime. Antibunching particularly points to the well-known interpretation that, due to its saturable nature, a quantum emitter with only a ground and excited state can never emit more than one photon at a time. However, this single photon emission can alternatively be interpreted as an interference phenomenon between higher-order photon scattering processes, whereby the quantum amplitudes of emitted photon states that contain more than one photon per time fully destructively interfere. These scattering processes can be distinguished as being coherent or incoherent, reflecting their respective ability and inability to interfere with the driving field. By examination of the properties of the two-photon components in the field scattered by the two-level atom, it becomes

evident that the coherent and incoherent components are spectrally distinct: the former is a delta function at the driving frequency while the latter populates a pair of Lorentzian sidebands positioned symmetrically around the driving frequency. This distinction allows for an individual examination of their photon statistics via a spectral separation prior to measurement of the second-order correlation function. In doing so, with the addition of a tunable notch filter based upon a **Fibre-Ring Resonator** in the detection path, removal of the coherently scattered component reveals that the incoherent component consists of photon pairs that have been simultaneously scattered the two-level atom. This is apparent by the fact that the measured second-order correlation function of the remaining incoherent component instead exhibits a time-symmetric bunching behaviour, where the probability to detect two photons is maximum when they arrive simultaneously. Furthermore, by tuning the relative amplitudes of the coherent and incoherent components by controlling the transmission of each through the filter, a clear interference between them is observed. These observations thereby validate the interference picture of resonance fluorescence, and constitute a first detection of photon pairs that have been simultaneously scattered by a single two-level quantum emitter.

6.2 Outlook

The design of the newly constructed **CQED** experiment is such that it affords a myriad of possibilities in the direction of its future explorations, which again, can be categorised as broadly two-fold. Firstly, continuing the examination of spectrally filtered resonance fluorescence originating from a single two-level atom can further refine the characterisation of the generated highly non-classical light fields. Following this, the apparatus can be used to fulfil its original purpose – to near-deterministically strongly couple single atoms to a **WGM** of the bottle microresonator for extended periods of time. The route to achieve these objectives poses opportunities to explore a plethora of new physics along the way, while the resulting **CQED** platform as a state-of-the-art nanophotonic device for quantum technologies and fundamental physics awaits as the ultimate goal.

Initially, extensions to the filtered resonance fluorescence experiment performed in this work can be relatively straightforwardly implemented. This is in part, due to the demonstrated simplicity in the generation of highly non-classical light fields, in that it only requires the resonance fluorescence of a two-level emitter in conjunction with a suitable spectral filtering. A single two-level quantum emitter undergoing resonance fluorescence – like the single optically trapped atoms demonstrated in this work – is already a single photon source, which is itself a highly sought after resource for quantum technologies [242]. Counterintuitively, appropriate spectral filtering of this resonance fluorescence transforms such a single photon source into an entangled photon pair source, which is yet another highly sought after resource. Since switching between these two

6. Conclusions and Perspectives

situations is facilitated by a simple application or removal of the filter, the demonstrated set-up constitutes a multifaceted source of highly non-classical light fields, that has a broad applicability in terms of possible implementations and platforms. Furthermore, the specific realisation of the **Fibre-Ring Resonator** that has been employed in this work as a spectral filter can be easily extended into a four-port device, to therefore gain access to the field inside the resonator. A cascade (i.e., two or three) of such devices in the fluorescence detection path, each stabilised to a different component of the fluorescence triplet structure, can be employed to perform cross-correlation measurements between the selected components to reveal their subtle time-ordering. With additional control over the suppression bandwidth of each filter, a tomographic reconstruction of the incoherent two-photon state could be used to show its energy-time entanglement. Further experimental verification of the entanglement between the incoherently scattered photon pairs can be achieved by measurement of a Bell inequality, with a successful observation of its violation. This can be realised in an interferometric measurement of the two-photon scattering response [368, 370], by sending the photon pairs through a Franson interferometer [371] and recording the time-resolved correlations.

Subsequently, or even alongside the aforementioned, the **CQED 2.0** experimental apparatus can be completed with the addition of the bottle microresonator and its two coupling nanofibres. Upon the relatively straight-forward installation of these final components into the experimental set-up, it can be reasonably expected that a characterisation of a desired **WGM** will yield a Q -factor exceeding 10^8 . Stabilising such a mode to the ^{85}Rb D_2 line enables the coupling of single atoms, in order to begin the process of their optical trapping within the **WGM**. An optional investigation would be the coupling of *free-falling* atoms to the bottle microresonator **WGM**, that can be performed in the same manner as in **CQED 1.0**: by ballistically launching the lower **MOT** in an **Atomic Fountain** such that the turning point coincides with the location of the resonator. Alternatively, a portion of the launched lower **MOT** can now be recaptured and cooled in the upper **MOT**, where its release – or slight launch towards the resonator in a second **Atomic Fountain** stage – will also couple free-falling atoms. In either of these two cases, the original retro-reflected trapping scheme based on a real-time detection of strongly coupled atoms [60] can be easily implemented, where the option for utilising the in-vacuum lens to generate the dipole trap can now be considered (as opposed to a lens located outside of the Science chamber [70]). The aforementioned alternative scheme for loading single free-falling atoms to the bottle microresonator, based upon recapturing the **AF** in a second **MOT** stage, poses the added advantage in that the loading efficiency of the resonator trap would likely be increased due to the source of atoms aligning along the dipole trap axis. Beyond these simple probabilistic loading schemes, the next natural step – taking priority – would be to implement a more deterministic method of loading atoms into the resonator surface trap. **CQED 2.0** offers the possibility to efficiently detect an atom that has been loaded into the dipole

trap directly from the upper MOT, via its fluorescence collection using the installed in-vacuum lens. Upon such a detection event, movement of the trap location from the initial loading position to the surface of the resonator can deterministically couple a trapped atom to the WGM. The movable optical tweezer in this experiment can be realised by tuning the collimation of the beam incident on the focussing lens to thereby tune the position of its focus, and thus, also the location of the optical trap. This feat is achieved by employing a so-called *Focus Tunable Lens (FTL)* as the last optical element before the in-vacuum focussing lens. In general, the FTL's most suitable for this purpose are the liquid-filled lens varieties that can vary their focal position by altering the curvature of the lens' surface profile. Their operation can be electrically controlled, where an applied mechanical compression of the liquid-filled container, and subsequent change in the lens' curvature, is achieved by supplying a current to a voice-coil actuator that encompasses the container. Preliminary tests with a commercially available FTL featuring a tuning range between $-1.5 \dots 3.5$ dpt (*EL-10-30-C-NIR-LD-MV*, *Optotune*) allows for a reproducible movement of a trapped atom over a distance of several hundred micrometres, with a survival probability across the entire motion exceeding 70%. The back-reflection from the surface of the resonator that builds up a partially modulated standing wave potential along the axis of the focussed trapping beam was previously taken advantage of in order to trap the atom in the potential minimum closest to the surface. However, the build-up of such a high-contrast standing wave can potentially inhibit the efficient transport of an atom from the initial free-space tweezer into the trap site closest to the resonator surface, as the atom can instead get trapped in an undesired potential minimum of the standing wave located further from the surface. A possible circumvention of this hindrance is to imprint an exotic spatial intensity profile onto the trapping beam, such as a flat-top or a coherent superposition of radial Laguerre-Gauss beams [225]. In such configurations, wavelength-scale dephasing of the individual components that make up the sum can be exploited to yield a strong suppression of the standing wave pattern generated in the interference between the incident and back-reflected beams around the focal region. These intensity profiles in the trapping beam can be generated by employing a *Spatial Light Modulator*, which would precede both the FTL and the final in-vacuum focussing lens. Working in conjunction, it is envisioned that these elements will lead to a near-deterministic, i.e., on-demand, loading of a trapped atom into the WGM of the bottle microresonator.

Finally, such a completion of the CQED 2.0 system would open the possibility to investigate the marriage between the two cornerstones of quantum optics broached in this thesis – that is, establishing a union of (filtered) resonance fluorescence and single emitter CQED (with WGMs) – an avenue that is yet to be fully experimentally explored. Trivially, when a sufficiently high-quality of the installed bottle microresonator is achieved, it could itself be employed as an alternative narrow-band spectral filter for the resonance fluorescence of an uncoupled trapped atom. For example, a WGM

are in stark contrast to standard Rabi oscillations in CQED (that occur between the states $|g, 1\rangle$ and $|e, 0\rangle$, which have the same energy). During each super-Rabi oscillation cycle, which is a collective process involving all N photons, any stored photon has a probability to spontaneously exit the resonator mode, which is a stochastic process defined by the oscillation period and the resonator decay rate. As soon as this occurs, the energy remaining inside the resonator is no longer enough to reach the $|e, N\rangle$ state, thereby disrupting the super-Rabi oscillation. All remaining $N - 1$ resonator photons are thus radiated within the resonator decay time – producing the N -photon bundle – and the system relaxes to the $|g, 0\rangle$ ground state. The rate at which the external laser then delivers the energy necessary to restart the oscillation cycle determines whether the source operates as a randomly firing " N -photon gun", or a continuous " N -photon laser" [373]. Both regimes of emission pose as a novel quantum light source that could be used to generate tailored multiphoton Fock states, which are an enabling technology in applied quantum science. Note that an idealised CQED 2.0 platform has been described, in which technical effects such as light shifts of the atomic transition and the coupling of excitation light into the resonator have been neglected. Intriguingly, the described system is expected to function even in the so-called *bad-cavity* regime ($\kappa \gg \{g, \gamma\}$) [375], whereby the addition of spectral filtering in the output channel can aid in selecting and purifying a desired N -photon bundle, such as an $N = 2$ "leapfrog" state corresponding to entangled pairs of photons [372]. A major benefit in the CQED 2.0 experimental apparatus, is that the channel of emission is directly realised by a fibre.

The CQED 2.0 experimental apparatus will hence provide a fully fibre-integrated interface between quanta of light and a single atom, featuring not only a deterministic principle of operation, but also a versatility in its capacity as a quantum device. It would thus be an ideal candidate for a node within a photonic quantum network, that is itself capable of processing or distributing photons in a large-scale fibre-based architecture. Such a network is suited to perform long-range quantum communication, and would greatly benefit from programmable nodes that feature a versatile functionality in their modes of operation [243]. The range of proof-of-principle devices demonstrated with this CQED experiment, along with its near-future capabilities, render it a promising solution for such applications and place it firmly as a viable contender in the current state-of-the-art [62].

References

- [1] C. Hitchens. *god Is Not Great: How Religion Poisons Everything*. McClelland & Stewart, 2008. ISBN: 9780771041433.
- [2] R. Golub and S. Lamoreaux. *The Historical and Physical Foundations of Quantum Mechanics*. Oxford University Press, 2023. ISBN: 9780198822189.
- [3] M. Planck. *Ueber das Gesetz der Energieverteilung im Normalspectrum*. Annalen der Physik **309**(3), 553–563 (1901).
- [4] A. Einstein. *Über einen die Erzeugung und Verwandlung des Lichtes betreffenden heuristischen Gesichtspunkt*. Annalen der Physik **322**(6), 132–148 (1905).
- [5] N. Bohr. *I. On the constitution of atoms and molecules*. Philosophical Magazine Series 6 **26**(151), 1–25 (1913).
- [6] E. Schrödinger. *Quantisierung als Eigenwertproblem*. Annalen der Physik **384**(4), 361–376 (1926).
- [7] Royal Swedish Academy of Sciences. *The Nobel Prize in Physics 1918*. Nobel Prize Outreach AB 2023. Available online at <https://www.nobelprize.org/prizes/physics/1918/summary/>.
- [8] Royal Swedish Academy of Sciences. *The Nobel Prize in Physics 1921*. Nobel Prize Outreach AB 2023. Available online at <https://www.nobelprize.org/prizes/physics/1921/summary/>.
- [9] Royal Swedish Academy of Sciences. *The Nobel Prize in Physics 1922*. Nobel Prize Outreach AB 2023. Available online at <https://www.nobelprize.org/prizes/physics/1922/summary/>.
- [10] Royal Swedish Academy of Sciences. *The Nobel Prize in Physics 1929*. Nobel Prize Outreach AB 2023. Available online at <https://www.nobelprize.org/prizes/physics/1929/summary/>.
- [11] D. Greenberger, K. Hentschel, and F. Weinert. *Compendium of Quantum Physics*. Springer Berlin, Heidelberg, 2009. ISBN: 9783540706229.
- [12] V. Giovannetti, S. Lloyd, and L. Maccone. *Advances in quantum metrology*. Nature Photonics **5**, 222–229 (2011).

REFERENCES

- [13] C. L. Degen, F. Reinhard, and P. Cappellaro. *Quantum sensing*. Reviews of Modern Physics **89**(3), 035002 (2017).
- [14] A. Trabesinger. *Quantum simulation*. Nature Physics **8**, 263 (2012).
- [15] N. Gisin and R. Thew. *Quantum communication*. Nature Photonics **1**, 165 (2007).
- [16] T. D. Ladd, F. Jelezko, R. Laflamme, Y. Nakamura, C. Monroe, and J. L. O’Brien. *Quantum computers*. Nature **464**, 45 (2010).
- [17] P. Ball. *Physics of life: The dawn of quantum biology*. Nature **474**, 272–274 (2011).
- [18] N. Lambert, Y.-N. Chen, Y.-C. Cheng, C.-M. Li, G.-Y. Chen, and F. Nori. *Quantum biology*. Nature Physics **9**, 10–18 (2013).
- [19] A. Marais, B. Adams, A. K. Ringsmuth, M. Ferretti, J. M. Gruber, R. Hendrikx, M. Schuld, S. L. Smith, I. Sinayskiy, T. P. J. Krüger, and F. Petruccione and R. van Grondelle. *The future of quantum biology*. Journal of The Royal Society Interface **15**, 20180640 (2018).
- [20] P. A. M. Dirac. *Quantum mechanics and a preliminary investigation of the hydrogen atom*. Proceedings of the Royal Society London A **110**, 561–579 (1926).
- [21] P. A. M. Dirac. *The quantum theory of the emission and absorption of radiation*. Proceedings of the Royal Society London A **114**, 243–265 (1927).
- [22] P. A. M. Dirac. *The quantum theory of the electron*. Proceedings of the Royal Society London A **117**, 610–624 (1928).
- [23] A. L. Schawlow and C. H. Townes. *Infrared and Optical Masers*. Physical Review **112**(6), 1940–1949 (1958).
- [24] A. Yariv and J. P. Gordon. *The laser*. Proceedings of the IEEE **51**(1), 4–29 (1963).
- [25] E. Purcell. *Spontaneous emission probabilities at radio frequencies*. Physical Review **69**, 674 (1946).
- [26] P. Goy, J. M. Raimond, M. Gross, and S. Haroche. *Observation of Cavity-Enhanced Single-Atom Spontaneous Emission*. Physical Review Letters **50**(24), 1903–1906 (1983).
- [27] D. J. Heinzen, J. J. Childs, J. E. Thomas, and M. S. Feld. *Enhanced and inhibited visible spontaneous emission by atoms in a confocal resonator*. Physical Review Letters **58**(13), 1320–1323 (1987).
- [28] F. De Martini, G. Innocenti, G. R. Jacobovitz, and P. Mataloni. *Anomalous Spontaneous Emission Time in a Microscopic Optical Cavity*. Physical Review Letters **59**(26), 2955–2958 (1987).

-
- [29] G. Gabrielse and H. Dehmelt. *Observation of inhibited spontaneous emission*. Physical Review Letters **55**(1), 67–70 (1985).
- [30] R. G. Hulet, E. S. Hilfer, and D. Kleppner. *Inhibited Spontaneous Emission by a Rydberg Atom*. Physical Review Letters **55**(20), 2137–2140 (1985).
- [31] W. Jhe, A. Anderson, E. A. Hinds, D. Meschede, L. Moi, and S. Haroche. *Suppression of spontaneous decay at optical frequencies: Test of vacuum-field anisotropy in confined space*. Physical Review Letters **58**(7), 666–669 (1987).
- [32] D. Meschede, H. Walther, and G. Müller. *One-Atom Maser*. Physical Review Letters **54**(6), 551–554 (1985).
- [33] G. Rempe, H. Walther, and N. Klein. *Observation of quantum collapse and revival in a one-atom maser*. Physical Review Letters **58**(4), 353–356 (1987).
- [34] M. Brune, J. M. Raimond, P. Goy, L. Davidovich, and S. Haroche. *Realization of a two-photon maser oscillator*. Physical Review Letters **59**(17), 1899–1902 (1987).
- [35] M. Brune, F. Schmidt-Kaler, A. Maali, J. Dreyer, E. Hagley, J. M. Raimond, and S. Haroche. *Quantum Rabi Oscillation: A Direct Test of Field Quantization in a Cavity*. Physical Review Letters **76**(11), 1800–1803 (1996).
- [36] M. Brune, E. Hagley, J. Dreyer, X. Maitre, A. Maali, C. Wunderlich, J. M. Raimond, and S. Haroche. *Observing the Progressive Decoherence of the "Meter" in a Quantum Measurement*. Physical Review Letters **77**(24), 4887–4890 (1996).
- [37] K. J. Vahala. *Optical microcavities*. Nature **424**, 839–846 (2003).
- [38] A. Reiserer and G. Rempe. *Cavity-based quantum networks with single atoms and optical photons*. Reviews of Modern Physics **87**(4), 1379–1418 (2015).
- [39] B. Hacker, S. Welte, G. Rempe, and S. Ritter. *A photon–photon quantum gate based on a single atom in an optical resonator*. Nature **536**, 193–196 (2016).
- [40] S. Daiss, S. Langenfeld, S. Welte, E. Distante, P. Thomas, L. Hartung, O. Morin, and G. Rempe. *A quantum-logic gate between distant quantum-network modules*. Science **371**(6529), 614–617 (2021).
- [41] S. Ritter, C. Nölleke, C. Hahn, A. Reiserer, A. Neuzner, M. Uphoff, M. Mücke, E. Figueroa, J. Bochmann, and G. Rempe. *An elementary quantum network of single atoms in optical cavities*. Nature **484**, 195–200 (2012).
- [42] J. P. Covey, H. Weinfurter, and H. Bernien. *Quantum networks with neutral atom processing nodes*. npj Quantum Information **9**, 90 (2023).
- [43] M. Keller, B. Lange, K. Hayasaka, W. Lange, and H. Walther. *Deterministic cavity quantum electrodynamics with trapped ions*. Journal of Physics B: Atomic, Molecular and Optical Physics **36**, 613–622 (2003).

REFERENCES

- [44] D. Najer, I. Söllner, P. Sekatski, V. Dolique, M. C. Löbl, D. Riedel, R. Schott, S. Starosielec, S. R. Valentin, A. D. Wieck, N. Sangouard, A. Ludwig, and R. J. Warburton. *A gated quantum dot strongly coupled to an optical microcavity*. Nature **675**, 622–627 (2019).
- [45] D. Wang. *Cavity quantum electrodynamics with a single molecule: Purcell enhancement, strong coupling and single-photon nonlinearity*. Journal of Physics B: Atomic, Molecular and Optical Physics **54**(13), 133001 (2021).
- [46] R. J. Thompson, G. Rempe, and H. J. Kimble. *Observation of normal-mode splitting for an atom in an optical cavity*. Physical Review Letters **68**(8), 1132–1135 (1992).
- [47] D. Yu, M. Humar, K. Meserve, R. C. Bailey, S. N. Chormaic, and F. Vollmer. *Whispering-gallery-mode sensors for biological and physical sensing*. Nature Reviews Methods Primers **1**(83) (2021).
- [48] D. W. Vernooy, A. Furusawa, N. Ph. Georgiades, V. S. Ilchenko, and H. J. Kimble. *Cavity QED with high-Q whispering gallery modes*. Physical Review A **57**(4), 2293–2296 (1998).
- [49] T. Aoki, B. Dayan, E. Wilcut, W. P. Bowen, A. S. Parkins, T. J. Kippenberg, K. J. Vahala, and H. J. Kimble. *Observation of strong coupling between one atom and a monolithic microresonator*. Nature **443**, 671–674 (2006).
- [50] C. Junge, D. O’Shea, J. Volz, and A. Rauschenbeutel. *Strong Coupling between Single Atoms and Nontransversal Photons*. Physical Review Letters **110**(21), 213604 (2013).
- [51] K. Y. Bliokh, F. J. Rodríguez-Fortuño, F. Nori, and A. V. Zayats. *Spin-orbit interactions of light*. Nature Photonics **9**, 796–808 (2015).
- [52] A. Aiello, P. Banzer, M. Neugebauer, and G. Leuchs. *From transverse angular momentum to photonic wheels*. Nature Photonics **9**, 789–795 (2015).
- [53] P. Lodahl, S. Mahmoodian, S. Stobbe, A. Rauschenbeutel, P. Schneeweiss, J. Volz, H. Pichler, and P. Zoller. *Chiral Quantum Optics*. Nature **541**, 473–480 (2017).
- [54] D. O’Shea, C. Junge, J. Volz, and A. Rauschenbeutel. *Fiber-Optical Switch Controlled by a Single Atom*. Physical Review Letters **111**(19), 193601 (2013).
- [55] I. Shomroni, S. Rosenblum, Y. Lovsky, O. Bechler, G. Guendelman, and B. Dayan. *All-optical routing of single photons by a one-atom switch controlled by a single photon*. Science **345**(6199), 903–906 (2014).
- [56] J. Volz, M. Scheucher, C. Junge, and A. Rauschenbeutel. *Nonlinear π phase shift for single fibre-guided photons interacting with a single resonator-enhanced atom*. Nature Photonics **8**, 965–970 (2014).

- [57] C. Sayrin, C. Junge, R. Mitsch, B. Albrecht, D. O’Shea, P. Schneeweiss, J. Volz, and A. Rauschenbeutel. *Nanophotonic Optical Isolator Controlled by the Internal State of Cold Atoms*. Physical Review X **5**(4), 041036 (2015).
- [58] M. Scheucher, A. Hilico, E. Will, J. Volz, and A. Rauschenbeutel. *Quantum optical circulator controlled by a single chirally coupled atom*. Science **354**(6319), 1577–1580 (2016).
- [59] O. Bechler, A. Borne, S. Rosenblum, G. Guendelman, O. E. Mor, M. Netser, T. Ohana, Z. Aqua, N. Drucker, R. Finkelstein, Y. Lovsky, R. Bruch, D. Gurovich, E. Shafir, and B. Dayan. *A passive photon–atom qubit swap operation*. Nature Physics **14**, 996–1000 (2018).
- [60] E. Will, L. Masters, A. Rauschenbeutel, M. Scheucher, and J. Volz. *Coupling a single trapped atom to a whispering-gallery-mode microresonator*. Physical Review Letters **126**, 233602 (2021).
- [61] Y. Louyer, D. Meschede, and A. Rauschenbeutel. *Tunable whispering-gallery-mode resonators for cavity quantum electrodynamics*. Physical Review A **72**(3), 031801 (2005).
- [62] A. González-Tudela, A. Reiserer, J. J. Garcíá-Ripoll, and F. J. Garcíá-Vidal. *Light–matter interactions in quantum nanophotonic devices*. Nature Reviews Physics **6**, 166–179 (2024).
- [63] M. Pöllinger, D. O’Shea, F. Warken, and A. Rauschenbeutel. *Ultrahigh- Q Tunable Whispering-Gallery-Mode Microresonator*. Physical Review Letters **103**(5), 053901 (2009).
- [64] D. O’Shea, A. Rettenmaier, and A. Rauschenbeutel. *Active frequency stabilization of an ultra-high Q whispering-gallery-mode microresonator*. Applied Physics B **99**, 623–627 (2010).
- [65] M. Pöllinger and A. Rauschenbeutel. *All-optical signal processing at ultra-low powers in bottle microresonators using the Kerr effect*. Optics Express **18**(17), 17764–17775 (2010).
- [66] D. O’Shea, C. Junge, M. Pöllinger, A. Vogler, and A. Rauschenbeutel. *All-optical switching and strong coupling using tunable whispering-gallery-mode microresonators*. Applied Physics B **105**, 129–148 (2011).
- [67] C. Junge, S. Nickel, D. O’Shea, and A. Rauschenbeutel. *Bottle microresonator with actively stabilized evanescent coupling*. Optics Letters **36**(17), 3488–3490 (2011).
- [68] M. Scheucher, J. Volz, and A. Rauschenbeutel. *Ultra-High- Q Optical Microcavities: Chapter 5, Cavity Quantum Electrodynamics and Chiral Quantum Optics*. World Scientific Publishing Co Pte Ltd, 2020. ISBN: 9789814566063.

REFERENCES

- [69] L. Masters, X.-X. Hu, M. Cordier, G. Maron, L. Pache, A. Rauschenbeutel, M. Schemmer, and J. Volz. *On the simultaneous scattering of two photons by a single two-level atom*. Nature Photonics **17**, 972–976 (2023).
- [70] E. Will. *Coupling a single trapped atom to a whispering-gallery-mode microresonator*. PhD thesis. Vienna University of Technology, 2022.
- [71] Royal Swedish Academy of Sciences. *The Nobel Prize in Physics 2012*. Nobel Prize Outreach AB 2023. Available online at <https://www.nobelprize.org/prizes/physics/2012/summary/>.
- [72] M. Fox. *Quantum Optics: An Introduction*. Oxford University Press, 2006. ISBN: 9780198566731.
- [73] B. E. A. Saleh and M. C. Teich. *Fundamentals of Photonics*. John Wiley & Sons Inc, 1991. ISBN: 9780471213741.
- [74] A. A. Savchenkov, A. B. Matsko, V. S. Ilchenko, and L. Maleki. *Optical resonators with ten million finesse*. Optics Express **15**(11), 6768–6773 (2007).
- [75] C. J. Hood, H. J. Kimble, and J. Ye. *Characterization of high-finesse mirrors: Loss, phase shifts, and mode structure in an optical cavity*. Physical Review A **64**(3), 033804 (2001).
- [76] D. Hunger, T. Steinmetz, Y. Colombe, C. Deutsch, T. W. Hänsch, and J. Reichel. *A fiber Fabry-Perot cavity with high finesse*. New Journal of Physics **12**, 065038 (2010).
- [77] D. K. Armani, T. J. Kippenberg, S. M. Spillane, and K. J. Vahala. *Ultra-high-Q toroid microcavity on a chip*. Nature **421**, 925–928 (2003).
- [78] M.-C. Tien, J. F. Bauters, M. J. R. Heck, D. T. Spencer, D. J. Blumenthal, and J. E. Bowers. *Ultra-high quality factor planar Si₃N₄ ring resonators on Si substrates*. Optics Express **19**(14), 13551–13556 (2011).
- [79] Y. Akahane, T. Asano, B.-S. Song, and S. Noda. *High-Q photonic nanocavity in a two-dimensional photonic crystal*. Nature **425**, 944–947 (2003).
- [80] J. D. Thompson, T. G. Tiecke, N. P. de Leon, J. Feist, A. V. Akimov, M. Gullans, A. S. Zibrov, V. Vuletić, and M. D. Lukin. *Coupling a Single Trapped Atom to a Nanoscale Optical Cavity*. Science **340**(6137), 1202–1205 (2013).
- [81] H. J. Kimble. *Strong interactions of single atoms and photons in cavity QED*. Physica Scripta (T76), 127 (1998).
- [82] D. A. Steck. *Quantum and Atom Optics*. (Revision 0.16.1, 16 June 2024), available online at <http://steck.us/teaching>.
- [83] P. Velha, E. Picard, T. Charvolin, E. Hadji, J. C. Rodier, P. Lalanne, and D. Peyrade. *Ultra-High Q/V Fabry-Perot microcavity on SOI substrate*. Optics Express **15**(24), 16090–16096 (2007).

- [84] T. J. Kippenberg, S. M. Spillane, and K. J. Vahala. *Demonstration of ultra-high- Q small mode volume toroid microcavities on a chip*. Applied Physics Letters **85**(25), 6113–6115 (2004).
- [85] M. H. Anderson, J. R. Ensher, M. R. Matthews, C. E. Wieman, and E. A. Cornell. *Observation of Bose-Einstein Condensation in a Dilute Atomic Vapor*. Science **269**(5221), 198–201 (1995).
- [86] C. C. Bradley, C. A. Sackett, J. J. Tollett, and R. G. Hulet. *Evidence of Bose-Einstein Condensation in an Atomic Gas with Attractive Interactions*. Physical Review Letters **75**(9), 1687–1690 (1995).
- [87] K. B. Davis, M.-O. Mewes, M. R. Andrews, N. J. van Druten, D. S. Durfee, D. M. Kurn, and W. Ketterle. *Bose-Einstein Condensation in a Gas of Sodium Atoms*. Physical Review Letters **75**(22), 3969–3973 (1995).
- [88] G. Modugno, G. Ferrari, G. Roati, R. J. Brecha, A. Simoni, and M. Inguscio. *Bose-Einstein Condensation of Potassium Atoms by Sympathetic Cooling*. Science **294**(5545), 1320–1322 (2001).
- [89] T. Weber, J. Herbig, M. Mark, H.-C. Nägerl, and R. Grimm. *Bose-Einstein Condensation of Cesium*. Science **299**(5604), 232–235 (2003).
- [90] G. Gwinner and L. A. Orozco. *Studies of the weak interaction in atomic systems: towards measurements of atomic parity non-conservation in francium*. Quantum Science and Technology **7**(2), 024001 (2022).
- [91] L. Essen and J. V. L. Parry. *An Atomic Standard of Frequency and Time Interval: A Cæsium Resonator*. Nature **176**, 280–282 (1955).
- [92] D. O’Shea. *Cavity QED experiments with a whispering-gallery-mode bottle resonator*. PhD thesis. Vienna University of Technology, 2013.
- [93] C. Junge. *Cavity quantum electrodynamics with non-transversal photons*. PhD thesis. Vienna University of Technology, 2013.
- [94] A. N. Nesmeyanov. *Vapour pressure of the chemical elements*. Journal of Chemical Education **41**(8), A590 (1964).
- [95] B. H. Bransden and C. J. Joachain. *Physics of Atoms and Molecules*. Longman Group Limited, 1983. ISBN: 0582444012.
- [96] D. A. Steck. *Rubidium 85 D Line Data*. (Revision 2.3.2, 10 September 2023), available online at <http://steck.us/alkalidata>.
- [97] H. J. Metcalf and P. Straten. *Laser Cooling and Trapping*. Springer New York, 1999. ISBN: 9780387987477.
- [98] Lord Rayleigh. *CXII. The problem of the whispering gallery*. The London, Edinburgh, and Dublin Philosophical Magazine and Journal of Science **20**(120), 1001–1004 (1910).

REFERENCES

- [99] Lord Rayleigh. *IX. Further applications of Bessel's functions of high order to the Whispering Gallery and allied problems*. The London, Edinburgh, and Dublin Philosophical Magazine and Journal of Science **27**(157), 100–109 (1914).
- [100] V. B. Braginsky, M. L. Gorodetsky, and V. S. Ilchenko. *Quality-factor and nonlinear properties of optical whispering-gallery modes*. Physics Letters A **137**(7), 393–397 (1989).
- [101] D. W. Vernooy, V. S. Ilchenko, H. Mabuchi, E. W. Streed, and H. J. Kimble. *High-Q measurements of fused-silica microspheres in the near infrared*. Optics Letters **23**(4), 247–249 (1998).
- [102] B. Gayral, J. M. Gérard, Â. Lematre, C. Dupuis, L. Manin, and J. L. Pelouard. *High-Q wet-etched GaAs microdisks containing InAs quantum boxes*. Applied Physics Letters **75**(13), 1908–1910 (1999).
- [103] S. M. Spillane, T. J. Kippenberg, K. J. Vahala, K. W. Goh, E. Wilcut, and H. J. Kimble. *Ultra-high-Q toroidal microresonators for cavity quantum electrodynamics*. Physical Review A **71**(1), 013817 (2005).
- [104] M. Sumetsky. *Whispering-gallery-bottle microcavities: the three-dimensional etalon*. Optics Letters **29**(1), 8–10 (2004).
- [105] M. L. Gorodetsky and V. S. Ilchenko. *Optical microsphere resonators: optimal coupling to high-Q whispering-gallery modes*. Journal of the Optical Society of America **16**(1), 147–154 (1999).
- [106] V. S. Ilchenko, X. S. Yao, and L. Maleki. *Pigtailing the high-Q microsphere cavity: a simple fiber coupler for optical whispering-gallery modes*. Optics Letters **24**(11), 723–725 (1999).
- [107] J. C. Knight, G. Cheung, F. Jacques, and T. A. Birks. *Phase-matched excitation of whispering-gallery-mode resonances by a fiber taper*. Optics Letters **22**(15), 1129–1131 (1997).
- [108] F. Warken. *Ultradünne Glasfasern als Werkzeug zur Kopplung von Licht und Materie*. PhD thesis. Rheinische Friedrich-Wilhelms-Universität Bonn, 2007.
- [109] A. W. Snyder and J. D. Love. *Optical Waveguide Theory*. Springer New York, 1983. ISBN: 9780412099502.
- [110] F. Le Kien, J. Q. Liang, K. Hakuta, and V. I. Balykin. *Field intensity distributions and polarization orientations in a vacuum-clad subwavelength-diameter optical fiber*. Optics Communications **242**(4), 445–455 (2004).
- [111] C. Lutzler. *Fabrication of Optical Microfibers*. Master's thesis. Rheinische Friedrich-Wilhelms-Universität Bonn, 2012.

- [112] P. Solano, J. A. Grover, J. E. Hoffman, S. Ravets, F. K. Fatemi, L. A. Orozco, and S. L. Rolston. *Optical Nanofibers: A New Platform for Quantum Optics*. Advances In Atomic, Molecular, and Optical Physics **66**, 439–505 (2017).
- [113] E. Vetsch, D. Reitz, G. Sagué, R. Schmidt, S. T. Dawkins, and A. Rauschenbeutel. *Optical Interface Created by Laser-Cooled Atoms Trapped in the Evanescent Field Surrounding an Optical Nanofiber*. Physical Review Letters **104**(20), 203603 (2010).
- [114] S. Kato and T. Aoki. *Strong Coupling between a Trapped Single Atom and an All-Fiber Cavity*. Physical Review Letters **115**(9), 093603 (2015).
- [115] L. Liebermeister, F. Petersen, A. v. Münchow, D. Burchardt, J. Hermelbracht, T. Tashima, A. W. Schell, O. Benson, T. Meinhardt, A. Krueger, A. Stiebeiner, A. Rauschenbeutel, H. Weinfurter, and M. Weber. *Tapered fiber coupling of single photons emitted by a deterministically positioned single nitrogen vacancy center*. Applied Physics Letters **104**(3), 031101 (2014).
- [116] A. Stiebeiner, O. Rehband, R. Garcia-Fernandez, and A. Rauschenbeutel. *Ultra-sensitive fluorescence spectroscopy of isolated surface-adsorbed molecules using an optical nanofiber*. Optics Express **17**(24), 21704–21711 (2009).
- [117] S. M. Spillane, T. J. Kippenberg, O. J. Painter, and K. J. Vahala. *Ideality in a Fiber-Taper-Coupled Microresonator System for Application to Cavity Quantum Electrodynamics*. Physical Review Letters **91**(4), 043902 (2003).
- [118] M. Pöllinger. *Bottle microresonators for applications in quantum optics and all-optical signal processing*. PhD thesis. Johannes Gutenberg-Universität Mainz, 2010.
- [119] A. N. Oraevsky. *Whispering-gallery waves*. Quantum Electronics **32**(5), 377 (2002).
- [120] M. Scheucher. *Single-atom cavity quantum electrodynamics with whispering-gallery-modes: Single-photon nonlinearity and nonreciprocity*. PhD thesis. Vienna University of Technology, 2017.
- [121] E. T. Jaynes and F. W. Cummings. *Comparison of quantum and semiclassical radiation theories with application to the beam maser*. Proceedings of the IEEE **51**(1), 89–109 (1963).
- [122] C. Gerry and P. Knight. *Introductory Quantum Optics*. Cambridge University Press, 2004. ISBN: 9780511791239.
- [123] J.J. Sanchez-Mondragon, N. B. Narozhny, and J. H. Eberly. *Theory of Spontaneous-Emission Line Shape in an Ideal Cavity*. Physical Review Letters **51**(7), 550–553 (1983).

REFERENCES

- [124] H. Carmichael. *An Open Systems Approach to Quantum Optics*. Springer Berlin, Heidelberg, 1991. ISBN: 9783662139264.
- [125] M. Tavis and F. W. Cummings. *Exact Solution for an N -Molecule—Radiation-Field Hamiltonian*. Physical Review **170**(2), 379–384 (1968).
- [126] H.-I. Yoo and J. H. Eberly. *Dynamical theory of an atom with two or three levels interacting with quantized cavity fields*. Physics Reports **118**(5), 239–337 (1985).
- [127] A. Messina, S. Maniscalco, and A. Napoli. *Interaction of bimodal fields with few-level atoms in cavities and traps*. Journal of Modern Optics **50**(1), 1–49 (2003).
- [128] M. Blaha, A. Johnson, A. Rauschenbeutel, and J. Volz. *Beyond the Tavis-Cummings model: Revisiting cavity QED with ensembles of quantum emitters*. Physical Review A **105**(1), 013719 (2022).
- [129] H. Carmichael. *Statistical Methods in Quantum Optics 1: Master Equations and Fokker-Planck Equations*. Springer Berlin, Heidelberg, 2002. ISBN: 9783642081330.
- [130] T. J. Kippenberg, S. M. Spillane, and K. J. Vahala. *Modal coupling in traveling-wave resonators*. Optics Letters **27**(19), 1669–1671 (2002).
- [131] M. J. Collett and C. W. Gardiner. *Squeezing of intracavity and traveling-wave light fields produced in parametric amplification*. Physical Review A **30**(3), 1386–1391 (1984).
- [132] B. Dayan, A. S. Parkins, T. Aoki, E. P. Ostby, K. J. Vahala, and H. J. Kimble. *A photon turnstile dynamically regulated by one atom*. Science **319**(5866), 1062–1065 (2008).
- [133] J. L. Hall, M. Zhu, and P. Buch. *Prospects for using laser-prepared atomic fountains for optical frequency standards applications*. Journal of the Optical Society of America B **6**(11), 2194–2205 (1989).
- [134] M. A. Kasevich, E. Riis, S. Chu, and R. G. DeVoe. *Atomic fountains and clocks*. Optics News **15**(12), 31–32 (1989).
- [135] P. Münstermann, T. Fischer, P. W. H. Pinkse, and G. Rempe. *Single slow atoms from an atomic fountain observed in a high-finesse optical cavity*. Optics Communications **159**(1), 63–67 (1999).
- [136] K. Friebe. *Strong coupling of single atoms to a whispering-gallery-mode resonator of ultrahigh quality*. Master’s thesis. Johannes Gutenberg-Universität Mainz, 2011.
- [137] V. S. Ilchenko and A. B. Matsko. *Optical resonators with whispering-gallery modes—part II: applications*. IEEE Journal of Selected Topics in Quantum Electronics **12**(1), 15–32 (2006).
- [138] R. Raussendorf and H. J. Briegel. *A One-Way Quantum Computer*. Physical Review Letters **86**(22), 5188–5191 (2001).

- [139] V. S. Letokhov. *Doppler line narrowing in a standing light wave*. Soviet Journal of Experimental and Theoretical Physics **7**(9), 348–351 (1968).
- [140] A. Ashkin. *Acceleration and Trapping of Particles by Radiation Pressure*. Physical Review Letters **24**, 156 (1970).
- [141] Royal Swedish Academy of Sciences. *The Nobel Prize in Physics 2018*. Nobel Prize Outreach AB 2023. Available online at <https://www.nobelprize.org/prizes/physics/1918/summary/>.
- [142] A. Ashkin and J. M. Dziedzic. *Optical Trapping and Manipulation of Viruses and Bacteria*. Science **235**, 1517–1520 (1987).
- [143] A. Ashkin. *Laser in Life Sciences*. Berichte der Bunsen-Gesellschaft für Physikalische Chemie **93**, 255 (1988).
- [144] S. Chu, J. E. Bjorkholm, A. Ashkin, and A. Cable. *Experimental Observation of Optically Trapped Atoms*. Physical Review Letters **57**, 314 (1986).
- [145] R. Grimm, M. Weidemüller, and Y. B. Ovchinnikov. *Optical dipole traps for neutral atoms*. Advances In Atomic, Molecular, and Optical Physics **42**, 95 (2000).
- [146] D. Griffiths. *Introduction to Electrodynamics*. Cambridge University Press, 2017. ISBN: 9781108420419.
- [147] J. D. Jackson. *Classical Electrodynamics*. John Wiley & Sons Inc, 1962. ISBN: 9780471309321.
- [148] J. Dalibard and C. Cohen-Tannoudji. *Dressed-atom approach to atomic motion in laser light: the dipole force revisited*. Journal of the Optical Society of America B **2**(11), 1707–1720 (1985).
- [149] C. Cohen-Tannoudji. *Laser cooling and trapping of neutral atoms: theory*. Physics Reports **219**(3), 153–164 (1992).
- [150] R. J. Cook and R. K. Hill. *An electromagnetic mirror for neutral atoms*. Optics Communications **43**(4), 258–260 (1982).
- [151] Y. B. Ovchinnikov, S. V. Shul’ga, and V. I. Balykin. *An atomic trap based on evanescent light waves*. Journal of Physics B: Atomic, Molecular and Optical Physics **24**(14), 3173 (1991).
- [152] H. Mabuchi and H. J. Kimble. *Atom galleries for whispering atoms: binding atoms in stable orbits around an optical resonator*. Optics Letters **19**(10), 749–751 (1994).
- [153] A. Goban, K. S. Choi, D. J. Alton, D. Ding, C. Lacroûte, M. Pototschnig, T. Thiele, N. P. Stern, and H. J. Kimble. *Demonstration of a State-Insensitive, Compensated Nanofiber Trap*. Physical Review Letters **109**(3), 033603 (2012).

REFERENCES

- [154] M. E. Kim, T.-H. Chang, B. M. Fields, C.-A. Chen, and C.-L. Hung. *Trapping single atoms on a nanophotonic circuit with configurable tweezer lattices*. Nature Communications **10**(1647) (2019).
- [155] J. McKeever, J. R. Buck, A. D. Boozer, A. Kuzmich, H.-C. Nägerl, D. M. Stamper-Kurn, and H. J. Kimble. *State-Insensitive Cooling and Trapping of Single Atoms in an Optical Cavity*. Physical Review Letters **90**(13), 133602 (2003).
- [156] H. Katori, T. Ido, and M. Kuwata-Gonokami. *Optimal Design of Dipole Potentials for Efficient Loading of Sr Atoms*. Journal of the Physical Society of Japan **68**(8), 2479–2482 (1999).
- [157] J. Ye, H. J. Kimble, and H. Katori. *Quantum State Engineering and Precision Metrology Using State-Insensitive Light Traps*. Science **320**(5884), 1734–1738 (2008).
- [158] A. P. Hilton, C. Perrella, A. N. Luiten, and P. S. Light. *Dual-Color Magic-Wavelength Trap for Suppression of Light Shifts in Atoms*. Physical Review Applied **11**(2), 024065 (2019).
- [159] W. Alt, D. Schrader, S. Kuhr, M. Müller, V. Gomer, and D. Meschede. *Single atoms in a standing-wave dipole trap*. Physical Review A **67**(3), 033403 (2003).
- [160] K. P. Nayak, J. Wang, and J. Keloth. *Real-Time Observation of Single Atoms Trapped and Interfaced to a Nanofiber Cavity*. Physical Review Letters **123**(21), 213602 (2019).
- [161] K. Jousten. *Handbook of Vacuum Technology*. John Wiley & Sons Inc, 2016. ISBN: 9783527413386.
- [162] J. D. Barrow. *The Book of Nothing: Vacuums, Voids, and the Latest Ideas about the Origins of the Universe*. Vintage. Knopf Doubleday Publishing Group, 2009. ISBN: 9780375420993.
- [163] I. J. R. Aitchison. *Nothing’s plenty. The vacuum in modern quantum field theory*. Contemporary Physics **26**(4), 333–391 (1985).
- [164] P. W. Milonni. *The Quantum Vacuum: An Introduction to Quantum Electrodynamics*. Academic Press, 1994. ISBN: 9780080571492.
- [165] M. Knudsen. *Die Molekularströmung der Gase durch Öffnungen und die Effusion*. Annalen der Physik **333**(5), 999–1016 (1909).
- [166] D. R. Scherer, D. B. Fenner, and J. M. Hensley. *Characterization of alkali metal dispensers and non-evaporable getter pumps in ultrahigh vacuum systems for cold atomic sensors*. Journal of Vacuum Science & Technology A **30**(6), 061602 (2012).

- [167] T. Aoki, A. S. Parkins, D. J. Alton, C. A. Regal, B. Dayan, E. Ostby, K. J. Vahala, and H. J. Kimble. *Efficient Routing of Single Photons by One Atom and a Microtoroidal Cavity*. Physical Review Letters **102**(8), 083601 (2009).
- [168] R. Kitamura, L. Pilon, and M. Jonasz. *Optical constants of silica glass from extreme ultraviolet to far infrared at near room temperature*. Applied Optics **46**(33), 8118–8133.
- [169] J. Rezac and A. Rosenberger. *Locking a microsphere whispering-gallery mode to a laser*. Optics Express **8**(11), 605–610 (2001).
- [170] A. Chiba, H. Fujiwara, J. Hotta, S. Takeuchi, and K. Sasaki. *Resonant Frequency Control of a Microspherical Cavity by Temperature Adjustment*. Japanese Journal of Applied Physics **43**(9R), 6138 (2004).
- [171] D. Armani, B. Min, A. Martin, and K. J. Vahala. *Electrical thermo-optic tuning of ultrahigh-Q microtoroid resonators*. Applied Physics Letters **85**(22), 5439–5441 (2004).
- [172] E. D. Black. *An introduction to Pound–Drever–Hall laser frequency stabilization*. American Journal of Physics **69**(1), 79–87 (2001).
- [173] ASTM International. *E595-15, Standard Test Method for Total Mass Loss and Collected Volatile Condensable Materials from Outgassing in a Vacuum Environment*. American Society for Testing and Materials (ASTM) (2021).
- [174] A. A. Becker. *An Introductory Guide to Finite Element Analysis*. John Wiley & Sons Inc, 2003. ISBN: 9781860584107.
- [175] A. Rettenmaier. *Aktive Frequenzstabilisierung eines durchstimmbaren Flüstergaleriemoden-Mikroresonators ultrahoher Güte*. Master’s thesis. Johannes Gutenberg-Universität Mainz, 2009.
- [176] E. R. I. Abraham and E. A. Cornell. *Teflon feedthrough for coupling optical fibers into ultrahigh vacuum systems*. Applied Optics **37**(10), 1762–1763 (1998).
- [177] Y. R. P. Sortais, H. Marion, C. Tuchendler, A. M. Lance, M. Lamare, P. Fournet, C. Armellin, R. Mercier, G. Messin, A. Browaeys, and P. Grangier. *Diffraction-limited optics for single-atom manipulation*. Physical Review A **75**(1), 013406 (2007).
- [178] N. Schlosser, G. Reymond, I. Protsenko, and P. Grangier. *Sub-poissonian loading of single atoms in a microscopic dipole trap*. Nature **411**, 1024–1027 (2001).
- [179] L. Pache. *Set-up, Characterization of an optical system to trap and transport single atoms in a cavity quantum electrodynamics experiment*. Master’s thesis. Humboldt-Universität zu Berlin, 2022.

REFERENCES

- [180] J. M. Khosrofian and B. A. Garetz. *Measurement of a Gaussian laser beam diameter through the direct inversion of knife-edge data*. Applied Optics **22**, 3406–3410 (1983).
- [181] M. A. de Araújo, R. Silva, E. de Lima, D. P. Pereira, and P. C. de Oliveira. *Measurement of Gaussian laser beam radius using the knife-edge technique: improvement on data analysis*. Applied Optics **48**(2), 393–396 (2009).
- [182] C. Robens, S. Brakhane, W. Alt, F. Kleißler, D. Meschede, G. Moon, G. Ramola, and A. Alberti. *High numerical aperture ($NA = 0.92$) objective lens for imaging and addressing of cold atoms*. Optics Letters **42**(6), 1043–1046 (2017).
- [183] D. Wang, Y. Guo, E. Zhang, X. Chao, L. Yu, J. Luo, W. Zhang, and M. Yin. *Synthesis and NIR-to-violet, blue, green, red upconversion fluorescence of Er^{3+} :LaOBr*. Journal of Alloys and Compounds **397**, 1–4 (2005).
- [184] Technical Report. *Measured curve for StockOptics and BeamTuning*. asphericon GmbH (2010).
- [185] N. M. Wereley. *Magnetorheology: Advances and Applications*. The Royal Society of Chemistry, 2013. ISBN: 9781849736671.
- [186] K. Bian, C. Gerber, A. J. Heinrich, D. J. Müller, S. Scheuring, and Y. Jiang. *Scanning probe microscopy*. Nature Reviews Methods Primers **1**, 36 (2021).
- [187] Sodano H. A., Bae J. S., Inman D. J., and Belvin W. K. *Concept and model of eddy current damper for vibration suppression of a beam*. Journal of Sound and Vibration **288**, 1177–1196 (2005).
- [188] A. D. Nashif, D. I. G. Jones, and J. P. Henderson. *Vibration Damping*. John Wiley & Sons Inc, 1985. ISBN: 9780471867722.
- [189] N. W. Hagood and A. Von Flotow. *Damping of structural vibrations with piezoelectric materials and passive electrical networks*. Journal of Sound and Vibration **146**(2), 243–268 (1991).
- [190] J. W. Humbeeck and S. Kustov. *Active and passive damping through shape memory alloys: applications and mechanisms*. Journal of Smart Materials and Structures **14**, 171–185 (2005).
- [191] S. Chikkamaranahalli, R. Vallance, B. Damazo, and R. Silver. *Damping mechanisms for precision applications in UHV environment*. American Society for Precision Engineering 2006 Spring Topical Meeting: Challenges at the Intersection of Precision Engineering and Vacuum Technology, Pittsburgh, PA (2006).
- [192] W. D. Callister Jr. and D. G. Rethwisch. *Materials Science and Engineering: An Introduction*. John Wiley & Sons Inc, 2018. ISBN: 9781119453918.

- [193] I. Rajagopal, K. S. Rajam, and S. R. Rajagopalan. *Gold plating of critical components for space applications: Challenges and solutions*. Gold Bulletin **25**, 55–66 (1992).
- [194] A. I. Oliva, M. Aguilar, and V. Sosa. *Low- and high-frequency vibration isolation for scanning probe microscopy*. Measurement Science and Technology **9**(3), 383 (1998).
- [195] A. I. Oliva, V. Sosa, R. de Coss, R. Sosa, N. López Salazar, and J. L. Peña. *Vibration isolation analysis for a scanning tunneling microscope*. Review of Scientific Instruments **63**(6), 3326–3329 (1992).
- [196] Kurt J. Lesker Company. *CF Flanged Quartz (Fused Silica) Laser Transmission Viewports*. Available online at <https://www.lesker.com/viewports/viewports-cf-flanged-quartz-fused-silica-laser-transmission.cfm>.
- [197] Kurt J. Lesker Company. *CF Flanged Exotic Lens Viewports*. Available online at <https://www.lesker.com/viewports/viewports-cf-flanged-exotic-lens.cfm>.
- [198] Royal Swedish Academy of Sciences. *The Nobel Prize in Physics 1997*. Nobel Prize Outreach AB 2023. Available online at <https://www.nobelprize.org/prizes/physics/1997/summary/>.
- [199] N. F. Ramsey. *History of atomic clocks*. Journal of Research of the National Institute of Standards and Technology **88**(5), 301–320 (1983).
- [200] E. L. Raab, M. Prentiss, A. Cable, S. Chu, and D. E. Pritchard. *Trapping of Neutral Sodium Atoms with Radiation Pressure*. Physical Review Letters **59**(23), 2631–2634 (1987).
- [201] K. Dieckmann, R. J. C. Spreeuw, M. Weidemüller, and J. T. M. Walraven. *Two-dimensional magneto-optical trap as a source of slow atoms*. Physical Review A **58**(5), 3891–3895 (1998).
- [202] R. Folman, P. Krüger, D. Cassettari, B. Hessmo, T. Maier, and J. Schmiedmayer. *Controlling Cold Atoms using Nanofabricated Surfaces: Atom Chips*. Physical Review Letters **84**(20), 4749–4752 (2000).
- [203] S. Wildermuth, P. Krüger, C. Becker, M. Brajdic, S. Haupt, A. Kasper, R. Folman, and J. Schmiedmayer. *Optimized magneto-optical trap for experiments with ultracold atoms near surfaces*. Physical Review A **69**(3), 030901 (2004).
- [204] K. I. Lee, J. A. Kim, H.-R. Noh, and W. Jhe. *Single-beam atom trap in a pyramidal and conical hollow mirror*. Optics Letters **21**(15), 1177–1179 (1996).
- [205] M. Vangeleyn, P. F. Griffin, E. Riis, and A. S. Arnold. *Single-laser, one beam, tetrahedral magneto-optical trap*. Optics Express **17**(16), 13601–13608 (2009).

REFERENCES

- [206] M. Vangeleyn, P. F. Griffin, E. Riis, and A. S. Arnold. *Laser cooling with a single laser beam and a planar diffractor*. Optics Letters **35**(20), 3453–3455 (2010).
- [207] C. C. Nshii, M. Vangeleyn, J. P. Cotter, P. F. Griffin, E. A. Hinds, C. N. Ironside, P. See, A. G. Sinclair, E. Riis, and A. S. Arnold. *A surface-patterned chip as a strong source of ultracold atoms for quantum technologies*. Nature Nanotech **8**, 321–324 (2013).
- [208] L. Chen, C.-J. Huang, X.-B. Xu, Y.-C. Zhang, D.-Q. Ma, Z.-T. Lu, Z.-B. Wang, G.-J. Chen, J.-Z. Zhang, H. X. Tang, C.-H. Dong, W. Liu, G.-Y. Xiang, G.-C. Guo, and C.-L. Zou. *Planar-Integrated Magneto-Optical Trap*. Physical Review Applied **17**(3), 034031 (2022).
- [209] C. J. Foot. *Atomic Physics*. Oxford University Press, 2004. ISBN: 9780198506966.
- [210] D. J. Wineland and W. M. Itano. *Laser cooling of atoms*. Physical Review A **20**, 1521–1540 (1979).
- [211] R. J. Cook. *Quantum-Mechanical Fluctuations of the Resonance-Radiation Force*. Physical Review Letters **44**, 976–979 (1980).
- [212] J. Dalibard and C. Cohen-Tannoudji. *Laser cooling below the Doppler limit by polarization gradients: simple theoretical models*. Journal of the Optical Society of America B **6**, 2023–2045 (1989).
- [213] C. Hauswald. *Aufbau und Charakterisierung eines Atom-Springbrunnens für ein Resonator-QED-Experiment mit Flüstergaleriemoden-Mikroresonatoren*. Master’s thesis. Johannes Gutenberg-Universität Mainz, 2010.
- [214] T. Bergeman, G. Erez, and H. J. Metcalf. *Magnetostatic trapping fields for neutral atoms*. Physical Review A **35**(4), 1535–1546 (1987).
- [215] Scientific Software Developed by the ID Group at ESRF. *Radia*. Available online at <http://www.esrf.eu/Accelerators/Groups/InsertionDevices/Software/Radia>.
- [216] C. Chubar, P. Elleaume, and J. Chavanne. *A 3D Magnetostatics Computer Code for Insertion Devices*. Journal of Synchrotron Radiation **5**, 481–484 (1998).
- [217] A. M. Steane, M. Chowdhury, and C. J. Foot. *Radiation force in the magneto-optical trap*. Journal of the Optical Society of America B **9**(12), 2142–2158 (1992).
- [218] I. Serre, L. Pruvost, and H. T. Duong. *Fluorescence imaging efficiency of cold atoms in free fall*. Applied Optics **37**(6), 1016–1021 (1998).
- [219] J. R. Buck. *Cavity-QED in Microsphere and Fabry-Perot Cavities*. PhD thesis. California Institute of Technology, 2003.
- [220] K. M. Birnbaum. *Cavity QED with Multilevel Atoms*. PhD thesis. California Institute of Technology, 2005.

- [221] A. P. Burgers, L. S. Peng, J. A. Muniz, A. C. McClung, M. J. Martin, and H. J. Kimble. *Clocked atom delivery to a photonic crystal waveguide*. Proceedings of the National Academy of Sciences **116**(2), 456–465 (2019).
- [222] D. Schrader, S. Kuhr, W. Alt, M. Müller, V. Gomer, and D. Meschede. *An optical conveyor belt for single neutral atoms*. Applied Physics B **73**(8), 819–824 (2001).
- [223] X. Zhou, H. Tamura, T.-H. Chang, and Chen-Lung C.-L. Hung. *Coupling Single Atoms to a Nanophotonic Whispering-Gallery-Mode Resonator via Optical Guiding*. Physical Review Letters **130**(10), 103601 (2023).
- [224] J. Léonard, M. Lee, A. Morales, T. M. Karg, T. Esslinger, and T. Donner. *Optical transport and manipulation of an ultracold atomic cloud using focus-tunable lenses*. New Journal of Physics **16**, 093028 (2014).
- [225] J.-B. Béguin, J. Laurat, X. Luan, A. P. Burgers, Z. Qin, and H. J. Kimble. *Reduced volume and reflection for bright optical tweezers with radial Laguerre–Gauss beams*. Proceedings of the National Academy of Sciences **117**(42), 26109–26117 (2020).
- [226] M. Padgett and R. Bowman. *Tweezers with a twist*. Nature Photonics **5**, 343–348 (2011).
- [227] S. Franke-Arnold. *Optical angular momentum and atoms*. Philosophical Transactions of the Royal Society A: Mathematical, Physical and Engineering Sciences **375**(2087), 20150435 (2017).
- [228] M. Babiker, D. L. Andrews, and V. E. Lembessis. *Atoms in complex twisted light*. Journal of Optics **21**(1), 013001 (2019).
- [229] R. W. Boyd. *Intuitive explanation of the phase anomaly of focused light beams*. Journal of the Optical Society of America **70**(7), 877–880 (1980).
- [230] O. Steuernagel, E. Yao, K. O’Holleran, and M. Padgett. *Observation of Gouy-phase-induced transversal intensity changes in focused beams*. Journal of Modern Optics **52**(18), 2713–2721 (2005).
- [231] T. Ando, Y. Ohtake, N. Matsumoto, T. Inoue, and N. Fukuchi. *Mode purities of Laguerre–Gaussian beams generated via complex-amplitudemodulation using phase-only spatial light modulators*. Optics Letters **34**(1), 34–36 (2009).
- [232] J. A. Davis, D. M. Cottrell, J. Campos, M. J. Yzuel, and I. Moreno. *Encoding amplitude information onto phase-only filters*. Applied Optics **38**(23), 5004–5013 (1999).
- [233] E. Bolduc, N. Bent, E. Santamato, E. Karimi, and R. W. Boyd. *Exact solution to simultaneous intensity and phase encryption with a single phase-only hologram*. Optics Letters **38**(18), 3546–3549 (2013).

REFERENCES

- [234] D. McGloin, G. C. Spalding, H. Melville, W. Sibbett, and K. Dholakia. *Applications of spatial light modulators in atom optics*. Optics Express **11**(2), 158–166 (2003).
- [235] D. Preece, S. Keen, E. Botvinick, R. Bowman, M. Padgett, and J. Leach. *Independent polarisation control of multiple optical traps*. Optics Express **16**(20), 15897–15902 (2008).
- [236] J. Lee, G. Vrijsen, I. Teper, O. Hosten, and M. A. Kasevich. *Many-atom-cavity QED system with homogeneous atom-cavity coupling*. Optics Letters **39**(13), 4005–4008 (2014).
- [237] A. Donley, T. P. Heavner, F. Levi, M. O. Tataw, and S. R. Jefferts. *Double-pass acousto-optic modulator system*. Review of Scientific Instruments **76**(6), 063112 (2005).
- [238] T. Grove, V. Sanchez-Villicana, B. C. Duncan, S. Maleki, and P. L. Gould. *Two-photon two-color diode laser spectroscopy of the Rb $5D_{5/2}$ state*. Physica Scripta **52**(3), 271 (1995).
- [239] A. Yu. Kalatskiy, A. E. Afanasiev, P. N. Melentiev, and V. I. Balykin. *Frequency stabilization of a diode laser on the $5P \rightarrow 5D$ transition of the Rb atom*. Laser Physics **27**(5), 055703 (2017).
- [240] A. Prasad. *Generating correlations between photons via interaction with nanofiber-trapped atoms*. PhD thesis. Vienna University of Technology, 2020.
- [241] E. Z. Casalengua, E. del Valle, and F. P. Laussy. *Two-photon correlations in detuned resonance fluorescence*. Physica Scripta **98**(5), 055104 (2023).
- [242] I. A. Walmsley. *Quantum optics: Science and technology in a new light*. Science **348**, 525–530 (2015).
- [243] H. J. Kimble. *The Quantum Internet*. Nature **453**, 1023 (2008).
- [244] M. D. Eisaman, J. Fan, A. Migdall, and S. V. Polyakov. *Invited Review Article: Single-photon sources and detectors*. Review of Scientific Instruments **82**, 071101 (2011).
- [245] I. Aharonovich, D. Englund, and M. Toth. *Solid-state single-photon emitters*. Nature Photonics **10**, 631 (2016).
- [246] V. Weisskopf. *Zur Theorie der Resonanzfluoreszenz*. Annalen der Physik **401**(1), 23–66 (1931).
- [247] V. Weisskopf. *Die Streuung des Lichts an angeregten Atomen*. Zeitschrift für Physik **85**, 451–481 (1933).
- [248] W. Heitler. *The Quantum Theory of Radiation*. Oxford University Press, 1954. ISBN: 9780486645582.

- [249] C. R. Stroud. *Quantum-Electrodynamic Treatment of Spontaneous Emission in the Presence of an Applied Field*. Physical Review A **3**(3), 1044–1052 (1971).
- [250] F. Schuda, C. R. Stroud Jr, and M. Hercher. *Observation of the resonant Stark effect at optical frequencies*. Journal of Physics B: Atomic and Molecular Physics **7**(7), L198 (1974).
- [251] F. Y. Wu, R. E. Grove, and S. Ezekiel. *Investigation of the Spectrum of Resonance Fluorescence Induced by a Monochromatic Field*. Physical Review Letters **35**(21), 1426–1429 (1975).
- [252] W. Hartig, W. Rasmussen, R. Schieder, and H. Walther. *Study of the frequency distribution of the fluorescent light induced by monochromatic radiation*. Zeitschrift für Physik A Atoms and Nuclei **278**, 205–210 (1976).
- [253] B. R. Mollow. *Power Spectrum of Light Scattered by Two-Level Systems*. Physical Review **188** (1969).
- [254] H. J. Carmichael and D. F. Walls. *A comment on the quantum treatment of spontaneous emission from a strongly driven two-level atom*. Journal of Physics B: Atomic and Molecular Physics **8**(6), L77 (1975).
- [255] M. E. Smithers and H. S. Freedhoff. *QED calculation of the resonant Stark effect*. Journal of Physics B: Atomic and Molecular Physics **7**(16), L432 (1974).
- [256] B. R. Mollow. *Pure-state analysis of resonant light scattering: Radiative damping, saturation, and multiphoton effects*. Physical Review A **12**(5), 1919–1943 (1975).
- [257] C. Cohen-Tannoudji and S. Reynaud. *Dressed-atom description of resonance fluorescence and absorption spectra of a multi-level atom in an intense laser beam*. Journal of Physics B: Atomic, Molecular and Optical Physics **10**, 345 (1977).
- [258] C. Cohen-Tannoudji and S. Reynaud. *Atoms in strong light-fields: photon antibunching in single atom fluorescence*. Philosophical Transactions of the Royal Society of London. Series A, Mathematical and Physical Sciences **293**, 223–237 (1979).
- [259] J. Dalibard and S. Reynaud. *Correlation signals in resonance fluorescence: interpretation via photon scattering amplitudes*. Journal de Physique **44**, 1337–1343 (1983).
- [260] A. Aspect, G. Roger, S. Reynaud, J. Dalibard, and C. Cohen-Tannoudji. *Time Correlations between the Two Sidebands of the Resonance Fluorescence Triplet*. Physical Review Letters **45**, 617 (1980).
- [261] A. Ulhaq, S. Weiler, S. M. Ulrich, R. Roßbach, M. Jetter, and P. Michler. *Cascaded single-photon emission from the Mollow triplet sidebands of a quantum dot*. Nature Photonics **6**, 238–242 (2012).

REFERENCES

- [262] B. L. Ng, C. H. Chow, and C. Kurtsiefer. *Observation of the Mollow triplet from an optically confined single atom*. Physical Review A **106**, 063719 (2022).
- [263] R. C. Neelen, D. M. Boersma, M. P. van Exter, G. Nienhuis, and J. P. Woerdman. *Spectral filtering within the Schawlow-Townes linewidth of a semiconductor laser*. Physical Review Letters **69**, 593 (1992).
- [264] H. F. Arnoldus and G. Nienhuis. *Photon correlations between the lines in the spectrum of resonance fluorescence*. Journal of Physics B: Atomic, Molecular and Optical Physics **17**, 963–977 (1984).
- [265] C. A. Schrama, G. Nienhuis, H. A. Dijkerman, C. Steijsiger, and H. G. M. Heideman. *Intensity correlations between the components of the resonance fluorescence triplet*. Physical Review A **45**, 8045 (1992).
- [266] E. del Valle, A. Gonzalez-Tudela, F. P. Laussy, C. Tejedor, and M. J. Hartmann. *Theory of Frequency-Filtered and Time-Resolved N-Photon Correlations*. Physical Review Letters **109**, 183601 (2012).
- [267] J. C. López Carreño, E. Zubizarreta Casalengua, F. P. Laussy, and E. del Valle. *Joint subnatural-linewidth and single-photon emission from resonance fluorescence*. Quantum Science and Technology **3**, 045001 (2018).
- [268] E. Z. Casalengua, J. C. López Carreño, F. P. Laussy, and E. del Valle. *Conventional and Unconventional Photon Statistics*. Laser & Photonics Reviews **14**, 1900279 (2020).
- [269] L. Hanschke, L. Schweickert, J. C. López Carreño, E. Schöll, K. D. Zeuner, T. Lettner, E. Z. Casalengua, M. Reindl, S. F. C. da Silva, R. Trotta, J. J. Finley, A. Rastelli, E. del Valle, F. P. Laussy, V. Zwiller, K. Müller, and K. D. Jöns. *Origin of Antibunching in Resonance Fluorescence*. Physical Review Letters **125**, 170402 (2020).
- [270] C. L. Phillips, A. J. Brash, D. P. S. McCutcheon, J. Iles-Smith, E. Clarke, B. Royall, M. S. Skolnick, A. M. Fox, and A. Nazir. *Photon Statistics of Filtered Resonance Fluorescence*. Physical Review Letters **125**, 043603 (2020).
- [271] H.-R. Noh and W. Jhe. *Analytic solutions of the optical Bloch equations*. Optics Communications **283**(11), 2353–2355 (2010).
- [272] P. J. Colmenares and J. L. Paz. *On the analytical solution of the optical Bloch equations*. Optics Communications **284**(21), 5171–5176 (2011).
- [273] H. C. Torrey. *Transient Nutations in Nuclear Magnetic Resonance*. Physical Review **76**(8), 1059–1068 (1949).
- [274] M. Lax. *Formal Theory of Quantum Fluctuations from a Driven State*. Physical Review **129**(5), 2342–2348 (1963).

-
- [275] M. Lax. *Quantum Noise. X. Density-Matrix Treatment of Field and Population-Difference Fluctuations*. Physical Review **157**(2), 213–231 (1967).
- [276] C. Cohen-Tannoudji, J. Dupont-Roc, and G. Grynberg. *Atom–Photon Interactions: Basic Processes and Applications*. John Wiley & Sons Inc, 1998. ISBN: 9780471293361.
- [277] H. J. Kimble and L. Mandel. *Theory of resonance fluorescence*. Physical Review A **13**(6), 2123–2144 (1976).
- [278] R. Loudon. *The Quantum Theory of Light*. Oxford University Press, 2000. ISBN: 9780198501763.
- [279] L. Ortiz-Gutiérrez, R. Celistrino Teixeira, A. Eloy, D. Ferreira da Silva, R. Kaiser, R. Bachelard, and M. Fouché. *Mollow triplet in cold atoms*. New Journal of Physics **21**(9), 093019 (2019).
- [280] G. Wrigge, I. Gerhardt, J. Hwang, G. Zumofen, and V. Sandoghdar. *Efficient coupling of photons to a single molecule and the observation of its resonance fluorescence*. Nature Physics **4**, 60–66 (2008).
- [281] E. B. Flagg, A. Muller, J. W. Robertson, S. Founta, D. G. Deppe, M. Xiao, W. Ma, G. J. Salamo, and C. K. Shih. *Resonantly driven coherent oscillations in a solid-state quantum emitter*. Nature Physics **5**, 203–207 (2009).
- [282] M. Baur, S. Filipp, R. Bianchetti, J. M. Fink, M. Göppl, L. Steffen, P. J. Leek, A. Blais, and A. Wallraff. *Measurement of Autler-Townes and Mollow Transitions in a Strongly Driven Superconducting Qubit*. Physical Review Letters **102**(24), 243602 (2009).
- [283] B. Pigeau, S. Rohr, L. Mercier de Lépinay, A. Gloppe, V. Jacques, and O. Arcizet. *Observation of a phononic Mollow triplet in a multimode hybrid spin-nanomechanical system*. Nature Communications **6**, 8603 (2015).
- [284] J. Kim and H.-R. Noh. *Analytical Solution of the Second-Order Correlation Function in Resonance Fluorescence for Two-level Systems*. Journal of the Korean Physical Society **76**, 463–468 (2020).
- [285] J.-T. Shen and S. Fan. *Strongly correlated multiparticle transport in one dimension through a quantum impurity*. Physical Review A **76**, 062709 (2007).
- [286] S. Mahmoodian, M. Čepulkovskis, S. Das, P. Lodahl, K. Hammerer, and A. S. Sørensen. *Strongly correlated photon transport in waveguide quantum electrodynamics with weakly coupled emitters*. Physical Review Letters **121**, 143601 (2018).

REFERENCES

- [287] A. S. Prasad, J. Hinney, S. Mahmoodian, K. Hammerer, S. Rind, P. Schneeweiss, A. S. Sørensen, J. Volz, and A. Rauschenbeutel. *Correlating photons using the collective nonlinear response of atoms weakly coupled to an optical mode*. Nature Photonics **14**, 719–722 (2020).
- [288] J. Hinney, A. S. Prasad, S. Mahmoodian, K. Hammerer, A. Rauschenbeutel, P. Schneeweiss, J. Volz, and M. Schemmer. *Unraveling two-photon entanglement via the squeezing spectrum of light traveling through nanofiber-coupled atoms*. Physical Review Letters **127**, 123602 (2021).
- [289] K. Laiho, T. Dirmeier, M. Schmidt, S. Reitzenstein, and C. Marquardt. *Measuring higher-order photon correlations of faint quantum light: A short review*. Physics Letters A **435**, 128059 (2022).
- [290] P. Schneeweiss, S. Zeiger, T. Hoinkes, A. Rauschenbeutel, and J. Volz. *Fiber ring resonator with a nanofiber section for chiral cavity quantum electrodynamics and multimode strong coupling*. Optics Letters **42**, 85–88 (2017).
- [291] S. Weiler, D. Stojanovic, S. M. Ulrich, M. Jetter, and P. Michler. *Postselected indistinguishable single-photon emission from the Mollow triplet sidebands of a resonantly excited quantum dot*. Physical Review B **87**(24), 241302 (2013).
- [292] C. A. Schrama, G. Nienhuis, H. A. Dijkerman, C. Steijsiger, and H. G. M. Heideman. *Destructive interference between opposite time orders of photon emission*. Physical Review Letters **67**(18), 2443–2445 (1991).
- [293] M. Peiris, B. Petrak, K. Konthasinghe, Y. Yu, Z. C. Niu, and A. Muller. *Two-color photon correlations of the light scattered by a quantum dot*. Physical Review B **91**(19), 195125 (2015).
- [294] Y. Nieves and A. Muller. *Third-order frequency-resolved photon correlations in resonance fluorescence*. Physical Review B **98**(16), 165432 (2018).
- [295] H. Ritsch. *Illustration für Pressemitteilung*. Artist’s website available at <http://quantum-physics-illustration.com/>.
- [296] K. A. Kirstein. *Aus Singles werden Paare: Neue Erkenntnisse über die Lichtstreuung von Atomen*. Pressemitteilung. Department of Physics, Humboldt-Universität zu Berlin. Available online at <https://idw-online.de/en/news818813>.
- [297] M. Born and E. Wolf. *Principles of Optics*. Cambridge University Press, 1999. ISBN: 9781139644181.
- [298] J. W. Goodman. *Introduction to Fourier Optics*. Roberts & Co., 2005. ISBN: 9780974707723.
- [299] N. Schlosser, G. Reymond, and P. Grangier. *Collisional Blockade in Microscopic Optical Dipole Traps*. Physical Review Letters **89**(2), 023005 (2002).

- [300] A. Fuhrmanek, R. Bourgain, Y. R. P. Sortais, and A. Browaeys. *Light-assisted collisions between a few cold atoms in a microscopic dipole trap*. Physical Review A **85**(6), 062708 (2012).
- [301] B. M. Henson, K. F. Thomas, Z. Mehdi, T. G. Burnett, J. A. Ross, S. S. Hodgman, and A. G. Truscott. *Trap frequency measurement with a pulsed atom laser*. Optics Express **30**(8), 13252–13262 (2022).
- [302] J. Joykuty, V. Mathur, V. Venkataraman, and V. Natarajan. *Direct Measurement of the Oscillation Frequency in an Optical-Tweezers Trap by Parametric Excitation*. Physical Review Letters **95**(19), 193902 (2005).
- [303] S. Friebel, C. D’Andrea, J. Walz, M. Weitz, and T. W. Hänsch. *CO₂-laser optical lattice with cold rubidium atoms*. Physical Review A **57**(1), 20–23 (1998).
- [304] J. Wu, R. Newell, M. Hausmann, D. J. Vieira, and X. Zhao. *Loading dynamics of optical trap and parametric excitation resonances of trapped atoms*. Journal of Applied Physics **100**(5), 054903 (2006).
- [305] C. Tuchendler, A. M. Lance, A. Browaeys, Y. R. P. Sortais, and P. Grangier. *Energy distribution and cooling of a single atom in an optical tweezer*. Physical Review A **78**(3), 033425 (2008).
- [306] M. Bass. *Handbook of Optics*. McGraw-Hill, Inc., 1995. ISBN: 9780071498890.
- [307] K. Kalli and D. A. Jackson. *Ring resonator optical spectrum analyzer with 20-kHz resolution*. Optics Letters **17**(15), 1090–1092 (1992).
- [308] G. Chen, J. U. Kang, and J. B. Khurgin. *Frequency discriminator based on ring-assisted fiber sagnac filter*. IEEE Photonics Technology Letters **17**(1), 109–111 (2005).
- [309] P.-H. Merrer, O. Llopis, and G. Cibiel. *Laser Stabilization on a Fiber Ring Resonator and Application to RF Filtering*. IEEE Photonics Technology Letters **20**(16), 1399–1401 (2008).
- [310] B. Merkel, D. Repp, and A. Reiserer. *Laser stabilization to a cryogenic fiber ring resonator*. Optics Letters **46**(2), 444–447 (2021).
- [311] Y. H. Chew, T.-T. Tjhung, and F. V. C. Mendis. *An optical filter of adjustable finesse using an amplified fiber ring resonator*. Journal of Lightwave Technology **15**(2), 364–370 (1997).
- [312] M. Seifouri, V. Fallahi, and S. Olyaei. *Ultra-high-Q optical filter based on photonic crystal ring resonator*. Photonic Network Communications **35**, 225–230 (2018).
- [313] O. Schwelb. *Transmission, group delay, and dispersion in single-ring optical resonators and add/drop filters—a tutorial overview*. Journal of Lightwave Technology **22**(5), 1380–1394 (2004).

REFERENCES

- [314] A. Johnson, M. Blaha, A. E. Ulanov, A. Rauschenbeutel, P. Schneeweiss, and J. Volz. *Observation of Collective Superstrong Coupling of Cold Atoms to a 30-m Long Optical Resonator*. Physical Review Letters **123**(24), 243602 (2019).
- [315] D. Lechner, R. Pennetta, M. Blaha, P. Schneeweiss, A. Rauschenbeutel, and J. Volz. *Light-Matter Interaction at the Transition between Cavity and Waveguide QED*. Physical Review Letters **131**(10), 103603 (2023).
- [316] R. C. Jones. *A New Calculus for the Treatment of Optical Systems*. Journal of the Optical Society of America **31**(7), 488–493 (1941).
- [317] M. Blaha. *Multimode strong coupling of cold atoms to a fiber ring resonator including a nanofiber-based optical interface*. PhD thesis. Vienna University of Technology, 2021.
- [318] A. Libson, N. Brown, A. Buikema, C. C. López, T. Dordevic, M. Heising, and M. Evans. *Simple method for locking birefringent resonators*. Optics Express **23**, 3809–3817 (2015).
- [319] R. W. P. Drever, J. L. Hall, F. V. Kowalski, J. Hough, G. M. Ford, A. J. Munley, and H. Ward. *Laser phase and frequency stabilization using an optical resonator*. Applied Physics B **31**, 97–105 (1983).
- [320] H. Jung and D.-G. Gweon. *Creep characteristics of piezoelectric actuators*. Review of Scientific Instruments **71**(4), 1896–1900 (2000).
- [321] H. J. M. T. S. Adriaens, W. L. De Koning, and R. Banning. *Modeling piezoelectric actuators*. IEEE/ASME Transactions on Mechatronics **5**(4), 331–341 (2000).
- [322] N. P. Bansal and R. H. Doremus. *Handbook of Glass Properties*. Academic Press, 1986. ISBN: 9780120781409.
- [323] C. Wuttke. *Thermal excitations of optical nanofibers measured with a fiber-integrated Fabry-Pérot cavity*. PhD thesis. Johannes Gutenberg-Universität Mainz, 2014.
- [324] R. J. Glauber. *The Quantum Theory of Optical Coherence*. Physical Review **130**(6), 2529–2539 (1963).
- [325] R. Hanbury Brown and R. Q. Twiss. *LXXIV. A new type of interferometer for use in radio astronomy*. The London, Edinburgh, and Dublin Philosophical Magazine and Journal of Science **45**(366), 663–682 (1954).
- [326] R. Hanbury Brown and R. Q. Twiss. *Correlation between Photons in two Coherent Beams of Light*. Nature **177**, 27–29 (1956).
- [327] R. Hanbury Brown and R. Q. Twiss. *A Test of a New Type of Stellar Interferometer on Sirius*. Nature **178**, 1046–1048 (1956).

- [328] V. Gomer, B. Ueberholz, S. Knappe, F. Strauch, D. Frese, and D. Meschede. *Decoding the dynamics of a single trapped atom from photon correlations*. Applied Physics B **67**, 689–697 (1998).
- [329] T. Yoon and M. Bajcsy. *Laser-cooled cesium atoms confined with a magic-wavelength dipole trap inside a hollow-core photonic-bandgap fiber*. Physical Review A **99**(2), 023415 (2019).
- [330] F. Le Kien, P. Schneeweiss, and A. Rauschenbeutel. *Dynamical polarizability of atoms in arbitrary light fields: general theory and application to cesium*. The European Physical Journal D **67**(92) (2013).
- [331] J. E. Sansonetti. *Wavelengths, Transition Probabilities, and Energy Levels for the Spectra of Rubidium (RbI through RbXXXVII)*. Journal of Physical and Chemical Reference Data **35**(1), 301–421 (2006).
- [332] A. Beveratos, S. Kühn, R. Brouri, T. Gacoin, J.-P. Poizat, and P. Grangier. *Room temperature stable single-photon source*. The European Physical Journal D **18**, 191–196 (2002).
- [333] U. Sinha, S. Ranjan Behera, and M. Layal. *Chapter One - Photon sources and their applications in quantum science and technologies*. Progress in Optics, Elsevier **68**, 1–65 (2023).
- [334] L. K. Shalm, E. Meyer-Scott, B. G. Christensen, P. Bierhorst, M. A. Wayne, M. J. Stevens, T. Gerrits, S. Glancy, D. R. Hamel, M. S. Allman, K. J. Coakley, S. D. Dyer, C. Hodge, A. E. Lita, V. B. Verma, C. Lambrocco, E. Tortorici, A. L. Migdall, Y. Zhang, D. R. Kumor, W. H. Farr, F. Marsili, M. D. Shaw, J. A. Stern, C. Abellán, W. Amaya, V. Pruneri, T. Jennewein, M. W. Mitchell, P. G. Kwiat, J. C. Bienfang, R. P. Mirin, E. Knill, and S. W. Nam. *Strong Loophole-Free Test of Local Realism*. Physical Review Letters **115**, 250402 (2015).
- [335] M. Giustina, M. A. M. Versteegh, S. Wengerowsky, J. Handsteiner, A. Hochrainer, K. Phelan, F. Steinlechner, J. Kofler, J. Larsson, C. Abellán, W. Amaya, V. Pruneri, M. W. Mitchell, J. Beyer, T. Gerrits, A. E. Lita, L. K. Shalm, S. W. Nam, T. Scheidl, R. Ursin, B. Wittmann, and A. Zeilinger. *Significant-Loophole-Free Test of Bell’s Theorem with Entangled Photons*. Physical Review Letters **115**(25), 250401 (2015).
- [336] N. Gisin, G. Ribordy, W. Tittel, and H. Zbinden. *Quantum cryptography*. Reviews of Modern Physics **74**(1), 145–195 (2002).
- [337] R. Ursin, F. Tiefenbacher, T. Schmitt-Manderbach, H. Weier, T. Scheidl, M. Lindenthal, B. Blauensteiner, T. Jennewein, J. Perdigues, P. Trojek, B. Ömer, M. Fürst, M. Meyenburg, J. Rarity, Z. Sodnik, C. Barbieri, H. Weinfurter, and A. Zeilinger. *Entanglement-based quantum communication over 144km*. Nature Physics **3**, 481–486 (2007).

REFERENCES

- [338] C. H. Bennett, G. Brassard, C. Crépeau, R. Jozsa, A. Peres, and W. K. Wootters. *Teleporting an unknown quantum state via dual classical and Einstein-Podolsky-Rosen channels*. Physical Review Letters **70**(13), 1895–1899 (1993).
- [339] D. Bouwmeester, J.-W. Pan, K. Mattle, M. Eibl, H. Weinfurter, and A. Zeilinger. *Experimental quantum teleportation*. Nature **390**, 575–579 (1997).
- [340] D. Boschi, S. Branca, F. De Martini, L. Hardy, and S. Popescu. *Experimental Realization of Teleporting an Unknown Pure Quantum State via Dual Classical and Einstein-Podolsky-Rosen Channels*. Physical Review Letters **80**(6), 1121–1125 (1998).
- [341] S. Slussarenko, M. M. Weston, H. M. Chrzanowski, L. K. Shalm, V. B. Verma, S. W. Nam, and G. J. Pryde. *Unconditional violation of the shot-noise limit in photonic quantum metrology*. Nature Photonics **11**, 700–703 (2017).
- [342] T. Ono, R. Okamoto, and S. Takeuchi. *An entanglement-enhanced microscope*. Nature Communications **4**, 2426 (2013).
- [343] S. J. Freedman and J. F. Clauser. *Experimental Test of Local Hidden-Variable Theories*. Physical Review Letters **28**(14), 938–941 (1972).
- [344] A. Aspect, J. Dalibard, and G. Roger. *Experimental Test of Bell’s Inequalities Using Time-Varying Analyzers*. Physical Review Letters **49**, 1804–1807 (1982).
- [345] Royal Swedish Academy of Sciences. *The Nobel Prize in Physics 2022*. Nobel Prize Outreach AB 2023. Available online at <https://www.nobelprize.org/prizes/physics/2022/summary/>.
- [346] P. G. Kwiat, K. Mattle, H. Weinfurter, A. Zeilinger, A. V. Sergienko, and Y. Shih. *New High-Intensity Source of Polarization-Entangled Photon Pairs*. Physical Review Letters **75**(24), 4337–4341 (1995).
- [347] C. Couteau. *Spontaneous parametric down-conversion*. Contemporary Physics **59**(3), 291–304 (2018).
- [348] T. Schneider. *Nonlinear Optics in Telecommunications*. Springer Berlin, Heidelberg, 2004, 167–200. ISBN: 9783642057724.
- [349] C. Xiong, L. G. Helt, A. C. Judge, G. D. Marshall, M. J. Steel, J. E. Sipe, and B. J. Eggleton. *Quantum-correlated photon pair generation in chalcogenide As₂S₃ waveguides*. Optics Express **18**(15), 16206–16216 (2010).
- [350] M. A. Hall, J. B. Altepeter, and P. Kumar. *Drop-in compatible entanglement for optical-fiber networks*. Optics Express **17**(17), 14558–14566 (2009).
- [351] S. D. Dyer, B. Baek, and S. W. Nam. *High-brightness, low-noise, all-fiber photon pair source*. Optics Express **17**(12), 10290–10297 (2009).

- [352] B. Fang, O. Cohen, and V. O. Lorenz. *Polarization-entangled photon-pair generation in commercial-grade polarization-maintaining fiber*. Journal of the Optical Society of America B **31**(2), 277–281 (2014).
- [353] J. Wang, S. Paesani, Y. Ding, R. Santagati, P. Skrzypczyk, A. Salavrakos, J. Tura, R. Augusiak, L. Mancinska, D. Bacco, D. Bonneau, J. W. Silverstone, Q. Gong, A. Acín, K. Rottwitt, L. K. Oxenløwe, J. L. O’Brien, A. Laing, and M. G. Thompson. *Multidimensional quantum entanglement with large-scale integrated optics*. Science **360**(6386), 285–291 (2018).
- [354] O. Benson, C. Santori, M. Pelton, and Y. Yamamoto. *Regulated and Entangled Photons from a Single Quantum Dot*. Physical Review Letters **84**(11), 2513–2516 (2000).
- [355] N. Akopian, N. H. Lindner, E. Poem, Y. Berlatzky, J. Avron, D. Gershoni, B. D. Gerardot, and P. M. Petroff. *Entangled Photon Pairs from Semiconductor Quantum Dots*. Physical Review Letters **96**(13), 130501 (2006).
- [356] B. Srivathsan, G. K. Gulati, B. Chng, G. Maslennikov, D. Matsukevich, and C. Kurtsiefer. *Narrow Band Source of Transform-Limited Photon Pairs via Four-Wave Mixing in a Cold Atomic Ensemble*. Physical Review Letters **111**(12), 123602 (2013).
- [357] M. Rezaei, J. Wrachtrup, and I. Gerhardt. *Polarization-entangled photon pairs from a single molecule*. Optica **6**(1), 34–40 (2019).
- [358] A. Moqanaki, F. Massa, and P. Walther. *Novel single-mode narrow-band photon source of high brightness tuned to cesium D2 line*. APL Photonics **4**, 090804 (2019).
- [359] K. J. Kusmierik, S. Mahmoodian, M. Cordier, J. Hinney, A. Rauschenbeutel, M. Schemmer, P. Schneeweiss, J. Volz, and K. Hammerer. *Higher-order mean-field theory of chiral waveguide QED*. SciPost Physics Core **6**, 041 (2023).
- [360] M. Fischer, M. Bader, R. Maiwald, A. Golla, M. Sondermann, and G. Leuchs. *Efficient saturation of an ion in free space*. Applied Physics B **117**, 797 (2014).
- [361] M. Arcari, I. Söllner, A. Javadi, S. Lindskov Hansen, S. Mahmoodian, J. Liu, H. Thyrrerstrup, E. H. Lee, J. D. Song, S. Stobbe, and P. Lodahl. *Near-Unity Coupling Efficiency of a Quantum Emitter to a Photonic Crystal Waveguide*. Physical Review Letters **113**, 093603 (2014).
- [362] H. Abudayyeh, B. Lubotzky, A. Blake, J. Wang, S. Majumder, Z. Hu, Y. Kim, H. Htoon, R. Bose, A. V. Malko, J. A. Hollingsworth, and R. Rapaport. *Single photon sources with near unity collection efficiencies by deterministic placement of quantum dots in nanoantennas*. APL Photonics **6**, 036109 (2021).

REFERENCES

- [363] C. K. Hong, Z. Y. Ou, and L. Mandel. *Measurement of subpicosecond time intervals between two photons by interference*. Physical Review Letters **59**, 2044 (1987).
- [364] H. Fearn and R. Loudon. *Theory of two-photon interference*. Journal of the Optical Society of America B **6**(5), 917–927 (1989).
- [365] E. Z. Casalengua, F. P. Laussy, and E. del Valle. *Two photons everywhere*. Philosophical Transactions of the Royal Society A: Mathematical, Physical and Engineering Sciences **382**(2281), 20230315 (2024).
- [366] J. C. López Carreño, E. del Valle, and F. P. Laussy. *Frequency-resolved Monte Carlo*. Scientific Reports **8**(6975) (2018).
- [367] C. J. Kaalund. *Critically coupled ring resonators for add-drop filtering*. Optics Communications **237**(4), 357–362 (2004).
- [368] S. Liu, O. August Dall’Alba Sandberg, M. Lai Chan, B. Schrintski, Y. Anyfantaki, R. B. Nielsen, R. G. Larsen, A. Skalkin, Y. Wang, L. Midolo, S. Scholz and A. D. Wieck, A. Ludwig, A. S. Sørensen, A. Tiranov, and P. Lodahl. *Violation of Bell inequality by photon scattering on a two-level emitter*. Nature Physics **20**, 1429–1433 (2024).
- [369] A. Camus. *The Myth of Sisyphus, and Other Essays*. Vintage, 1991. ISBN: 9780679733737.
- [370] M. Peiris, K. Konthasinghe, and A. Muller. *Franson Interference Generated by a Two-Level System*. Physical Review Letters **118**, 030501 (2017).
- [371] J. D. Franson. *Bell inequality for position and time*. Physical Review Letters **62**(19), 2205–2208 (1989).
- [372] E. del Valle. *Distilling one, two and entangled pairs of photons from a quantum dot with cavity QED effects and spectral filtering*. New Journal of Physics **15**, 025019 (2013).
- [373] C. Sánchez Muñoz, E. del Valle, A. González Tudela, K. Müller, S. Lichtmannecker, M. Kaniber, C. Tejedor, J. J. Finley, and F. P. Laussy. *Emitters of N-photon bundles*. Nature Photonics **8**, 550–555 (2014).
- [374] J. C. López Carreño, E. del Valle, and F. P. Laussy. *Photon Correlations from the Mollow Triplet*. Laser & Photonics Reviews **11**(5), 1700090 (2017).
- [375] C. Sánchez Muñoz, F. P. Laussy, E. del Valle, C. Tejedor, and A. González-Tudela. *Filtering multiphoton emission from state-of-the-art cavity quantum electrodynamics*. Optica **5**(1), 14–26 (2018).

A

Documenting images

This Appendix contains a selection of images that chronologically document various stages of the **CQED** 2.0 experiment, as described throughout this thesis. These are included in the following.



Figure A.1. From Vienna to Berlin. (a) Deconstruction of the **CQED** 1.0 experiment in Vienna. (b) Unpacking the transportation boxes in Berlin. (c) Reconstruction of the experiment in Berlin.

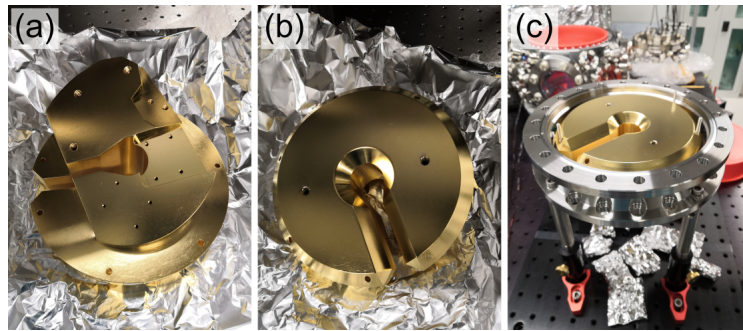


Figure A.2. Gold-plated copper block. (a) A view of its underside. (b) A view of its topside. (c) The copper block situated inside the closed coupler piece.

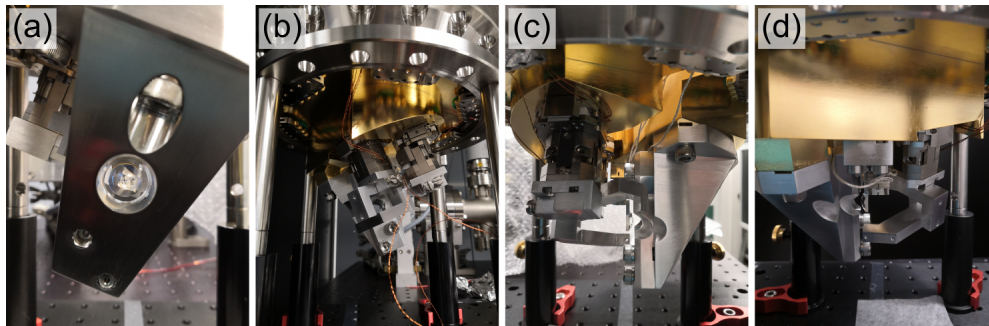


Figure A.3. Coupling set-up. (a) Front view. The in-vacuum lens is visible through the hole in the resonator mount. (b) Back view. (c) Left view. (d) Right view.

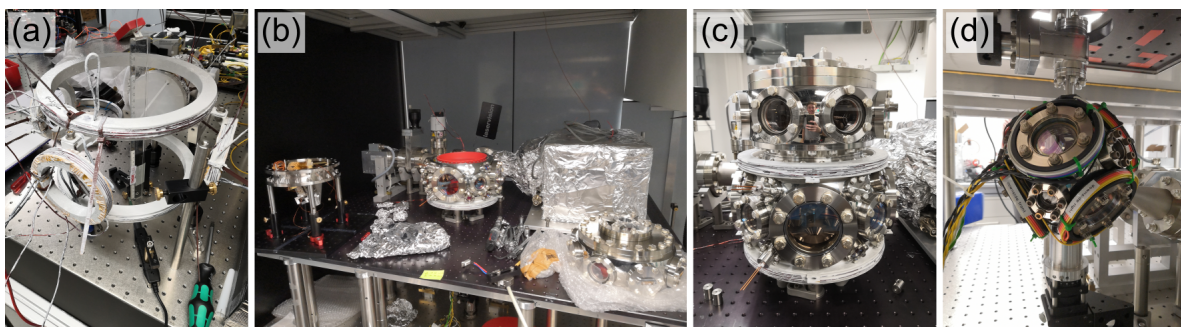


Figure A.4. Construction of CQED 2.0. (a) Test set-up for the upper MOT coil system. (b) Prior to the full construction of the Science chamber. (c) Front view of the assembled Science chamber, containing the coupling set-up. (d) Right view of the Mot chamber without the cage system.

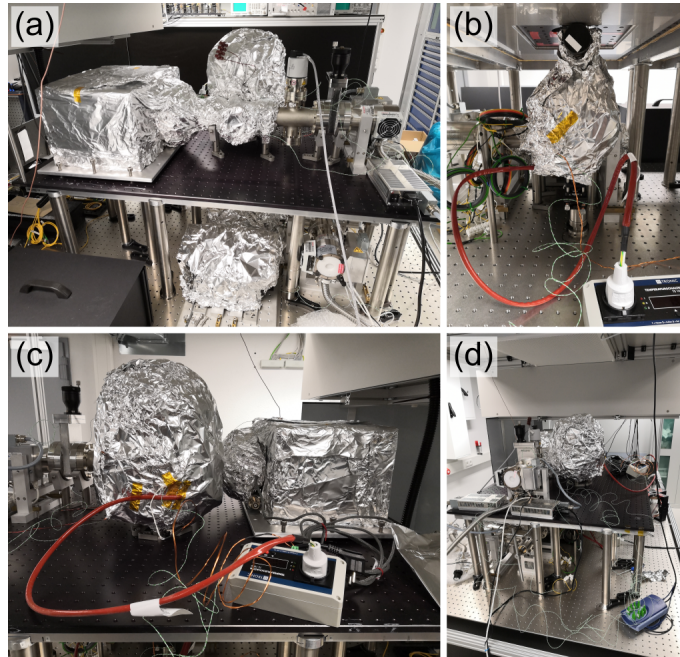


Figure A.5. System bake-out. (a) Back view of the experiment, in preparation for the bake-out procedure. (b) Front view of the Mot chamber. (c) Front view of the Science chamber. (d) Left view of the experiment.

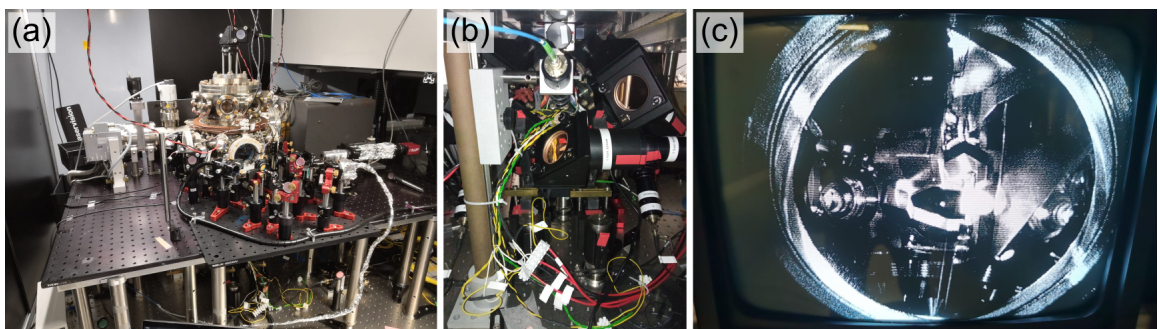


Figure A.6. Double MOT construction. (a) Front view of the assembled upper system. The trap optics are situated in front of the Science chamber, that is itself surrounded by the field coils and optomechanics required for the upper MOT. (b) Front view of the completed Mot chamber, surrounded by the cage system that houses the cooling beam optomechanics and field coils for the lower MOT. (c) A first creation of a MOT inside the Science chamber, afforded by its completed construction.

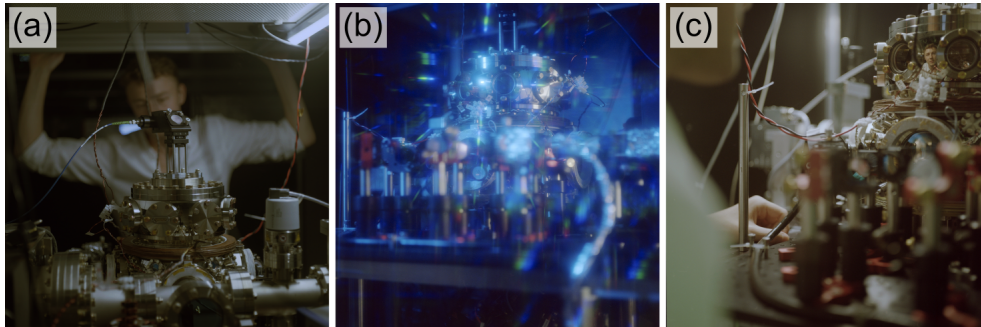


Figure A.7. A view on the Science chamber. (a) From the rear. (b) Through a pair of diffraction glasses, from the front. (c) Close-up from the front-right.

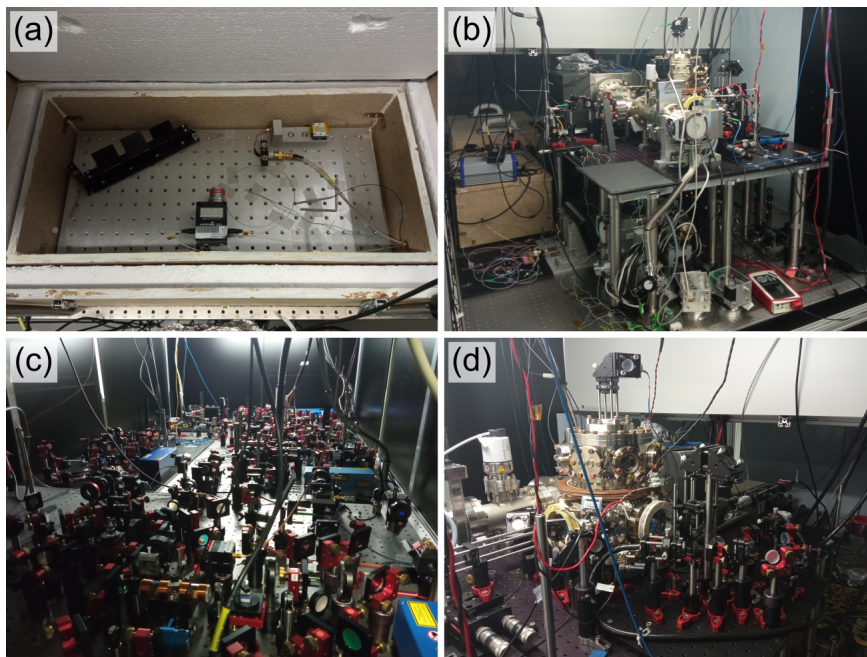


Figure A.8. The operational lab. (a) A view of the **FRR** set-up, situated inside its insulating box. (b) The main experimental apparatus on the Science table. (c) A view into the laser table. (d) A view on the current status of the Science chamber and trapping optics, as of Summer 2024.

B

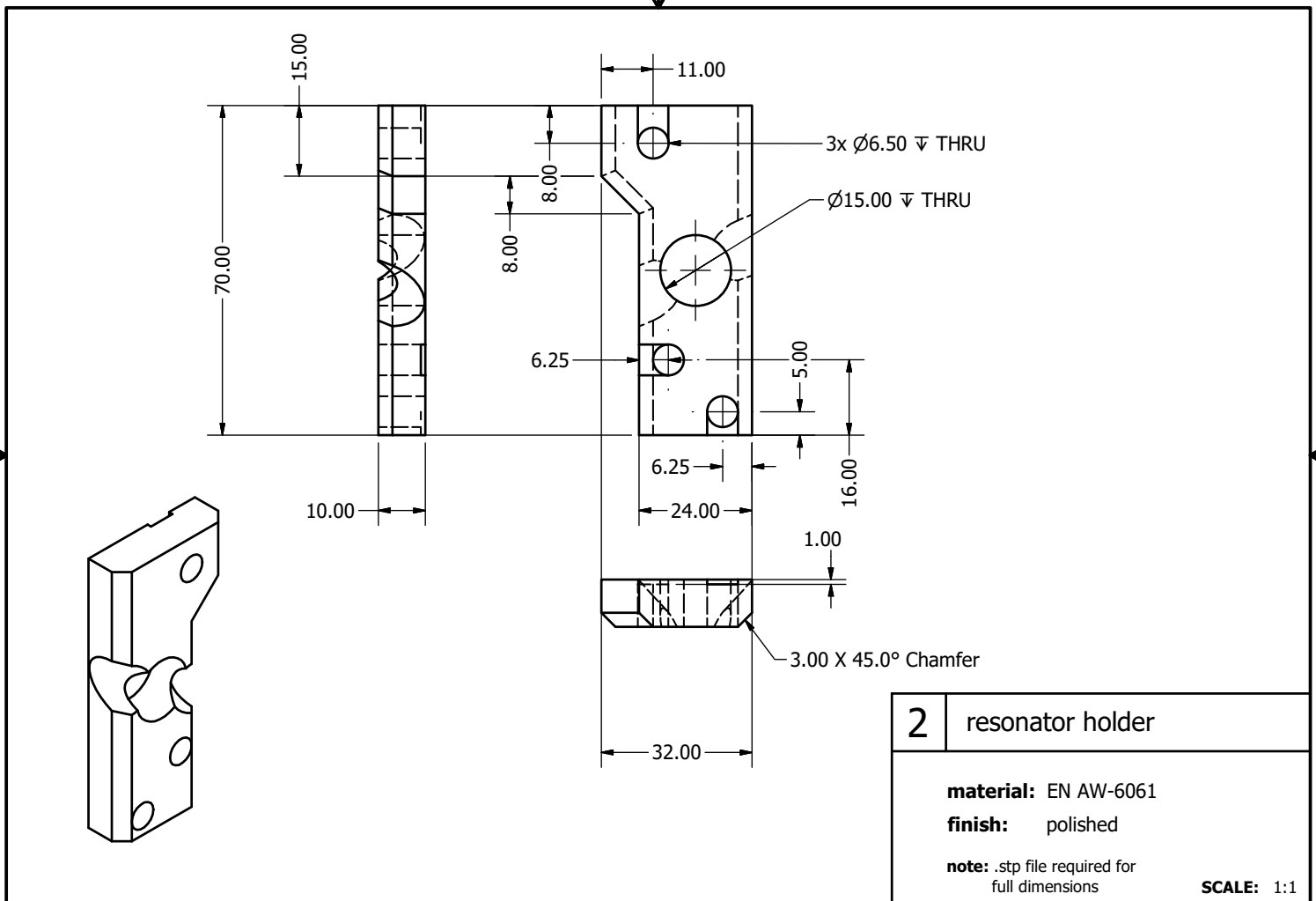
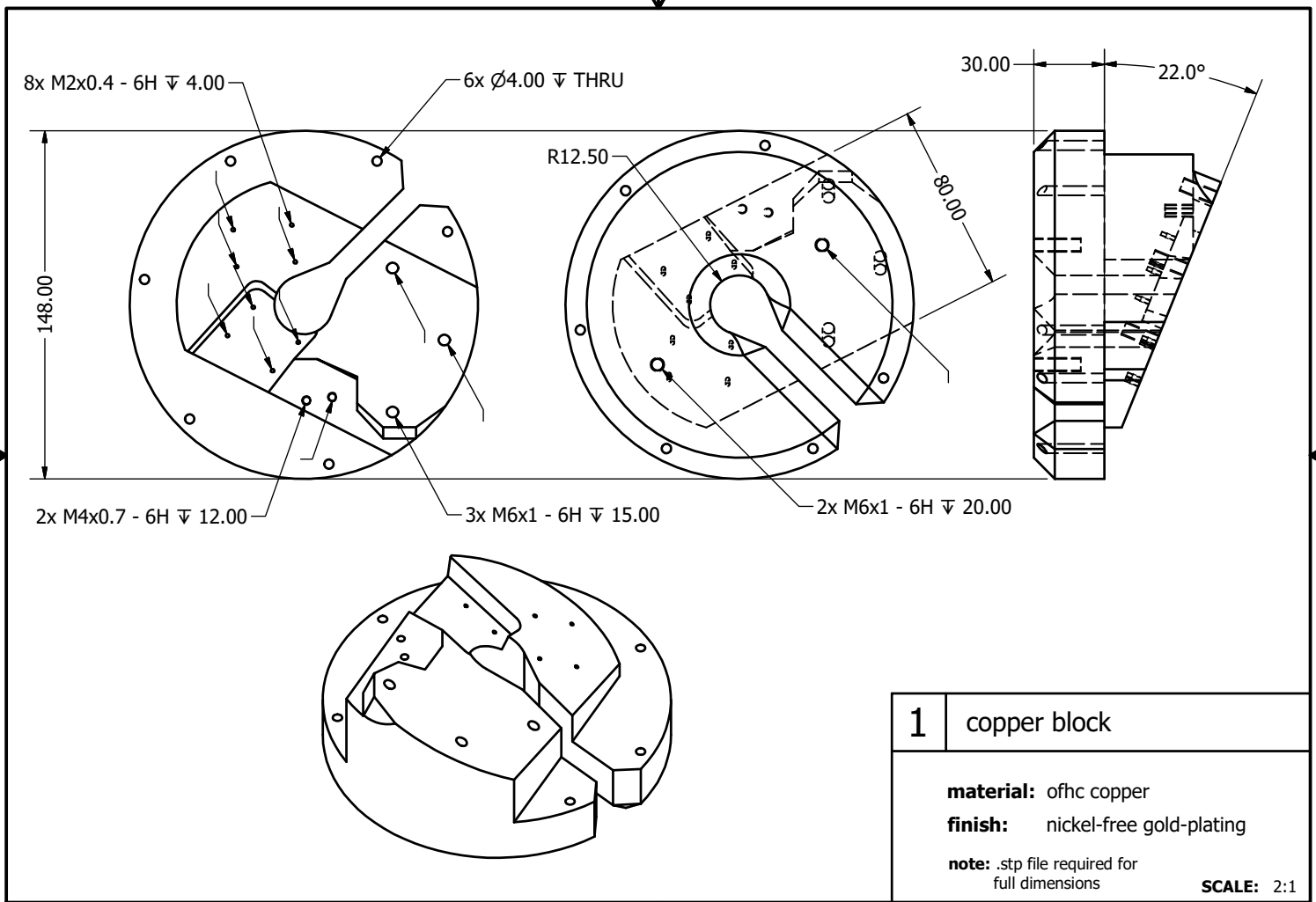
Part drawings

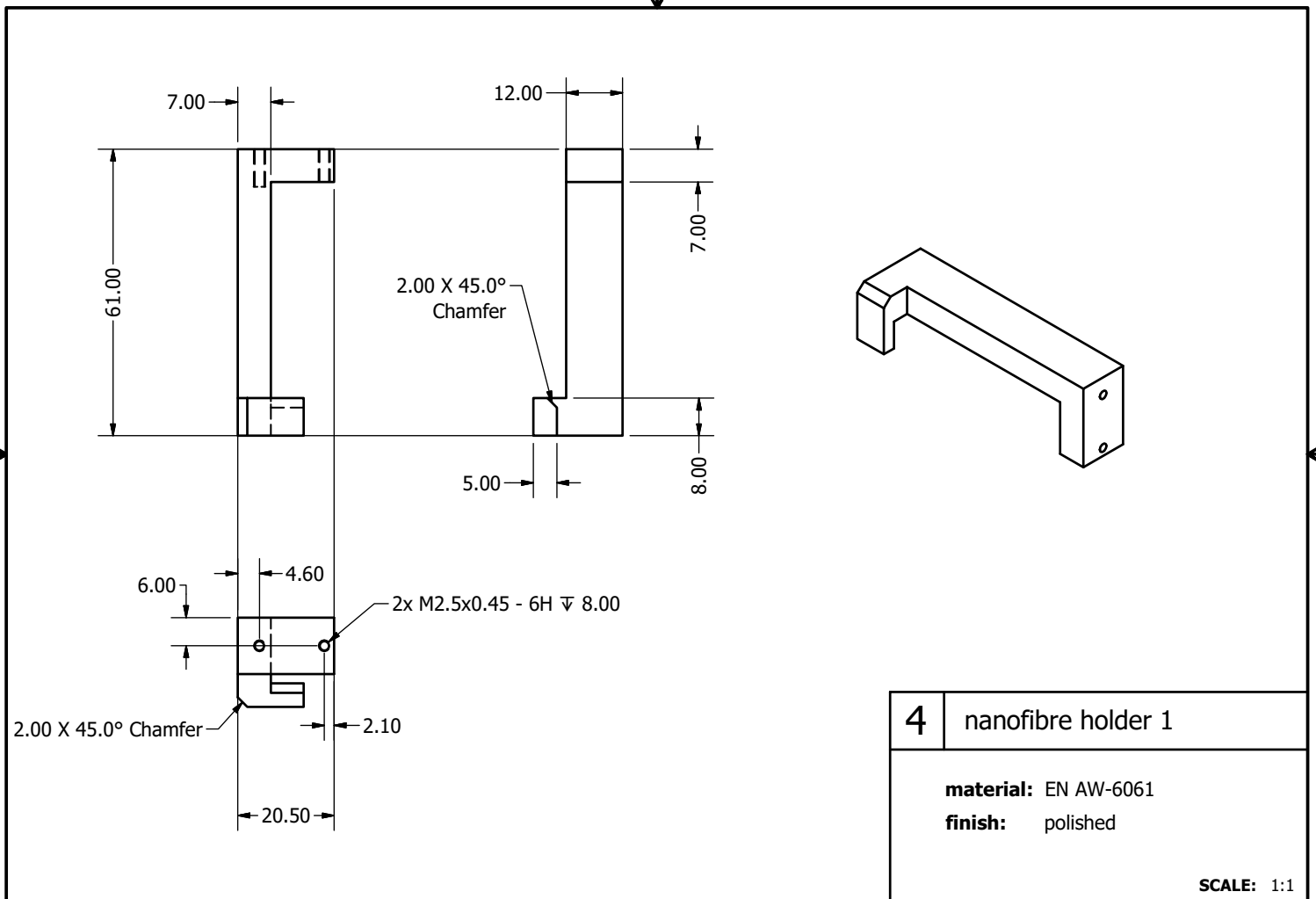
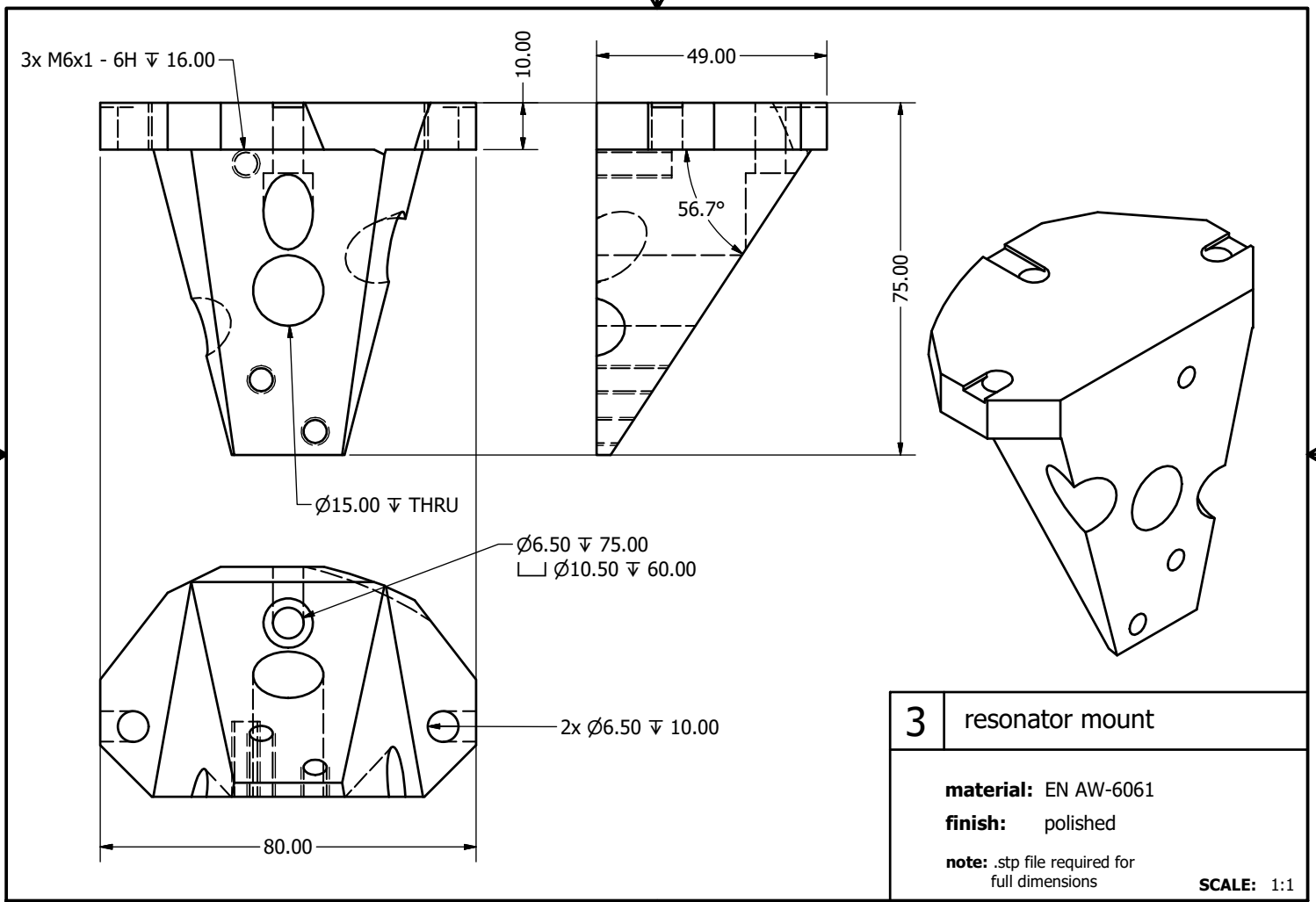
In this Appendix, a complete series of technical drawings for the custom pieces used in the construction of the **CQED** experiment is provided. A documenting summary is first given in Table **B.1**, that contains the assigned number of each drawn part, its naming description, as well as its chosen material and finish. The drawings are split between the two categories of pieces used *inside* or *outside* of the **UHV** environment, which influences the chosen material and required finish (and manufacturing precision). Note that all technical drawings (aside from numbers **13** and **14**) are not professionally produced, and therefore do not conform to any standardised style. All units are given in mm unless stated otherwise. The indicated scale for each refers to an A4 paper size.

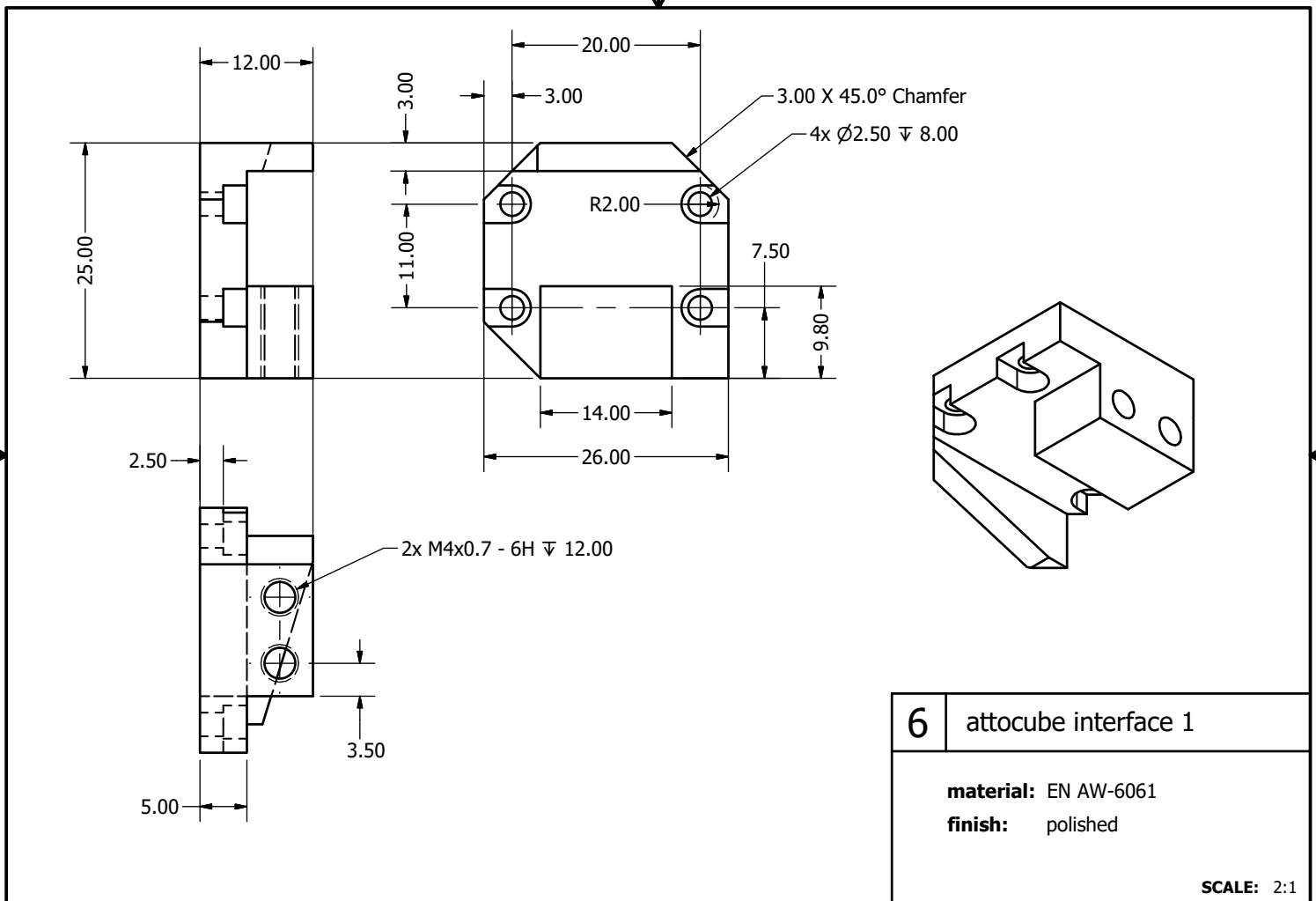
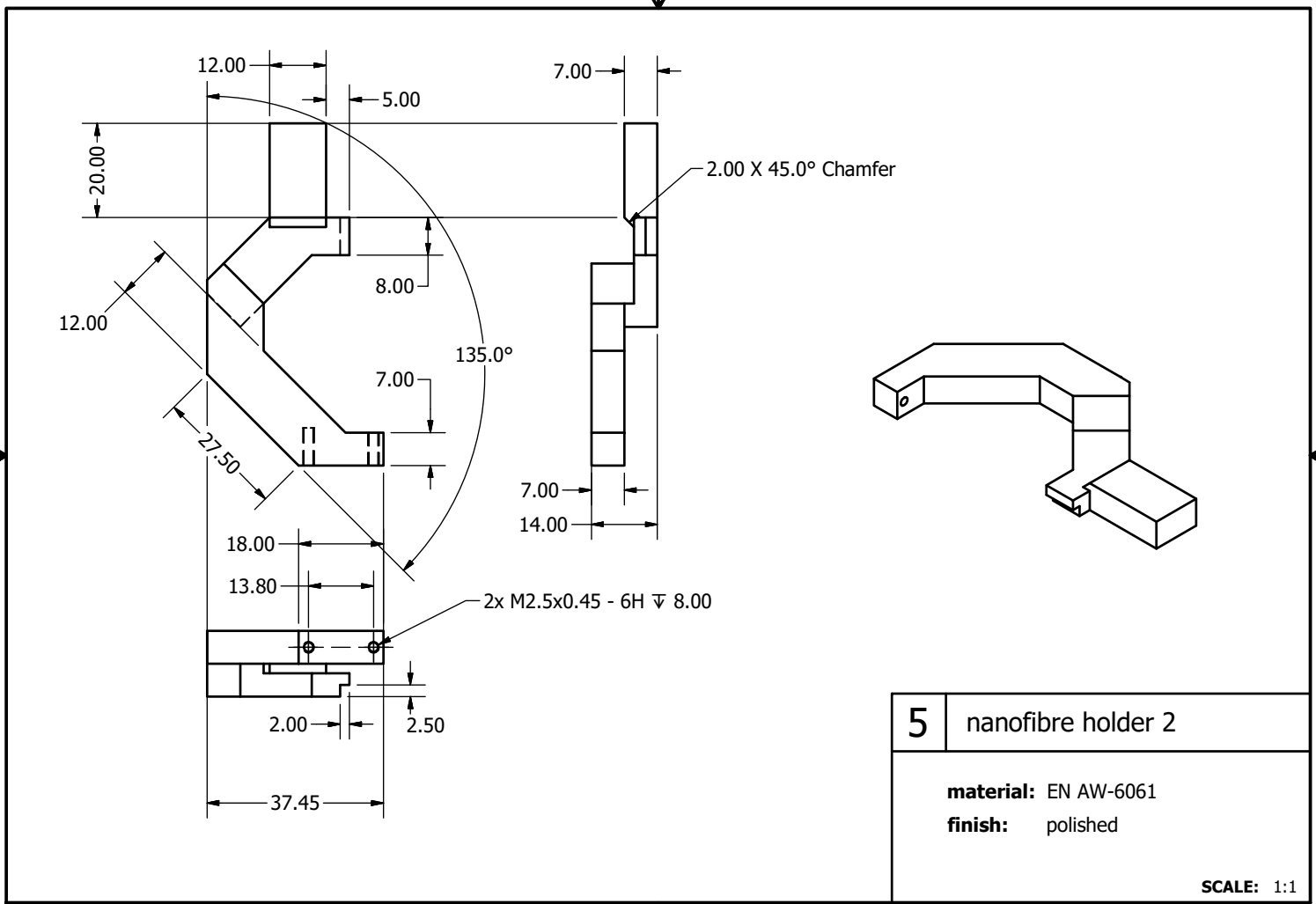
B. Part drawings

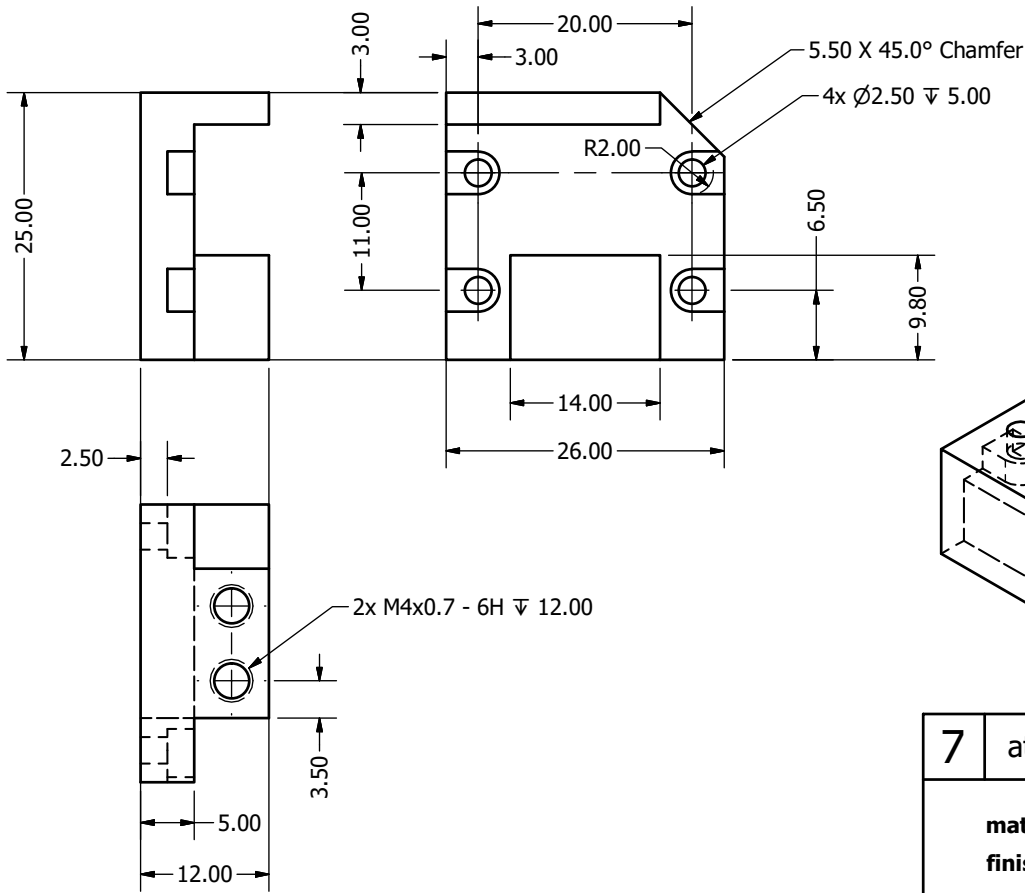
part no.	description	material	finish
1	copper block	OFHC copper	nickel-free gold-plating
2	resonator holder	aluminium EN AW-6061	polished
3	resonator mount	— —	— —
4	nanofibre holder 1	— —	— —
5	nanofibre holder 2	— —	— —
6	attocube interface 1	— —	— —
7	attocube interface 2	— —	— —
8	lens frame	— —	— —
9	lens mount	— —	— —
10	fibre plate	— —	— —
11	bending piezo clamp	PTFE	machined
12	Differential Pumping Tube	316LN stainless steel	— —
13	custom flange	— —	— —
14	custom fibre feedthrough	— —	— —
<hr/>			
15	Science chamber support	— —	— —
16	Mot chamber support	— —	— —
17	viewport cage adaptor	aluminium	— —
18	UHV pipe support	— —	sand-blasted
19	MOT cage cross	— —	black-anodised
20	MOT cage bar	— —	— —
21	MOT cage bracket	— —	— —
22	MOT coil holder 1	aluminium	machined
23	MOT coil holder 2	— —	— —
24	fibre stretcher	— —	— —

Table B.1. List of part drawings. A naming description of each designed and manufactured component, alongside its chosen material and finish, is reported. Parts 1–14 (above the horizontal line) are utilised inside the UHV environment, while parts 15–24 (below the horizontal line) are externally used.







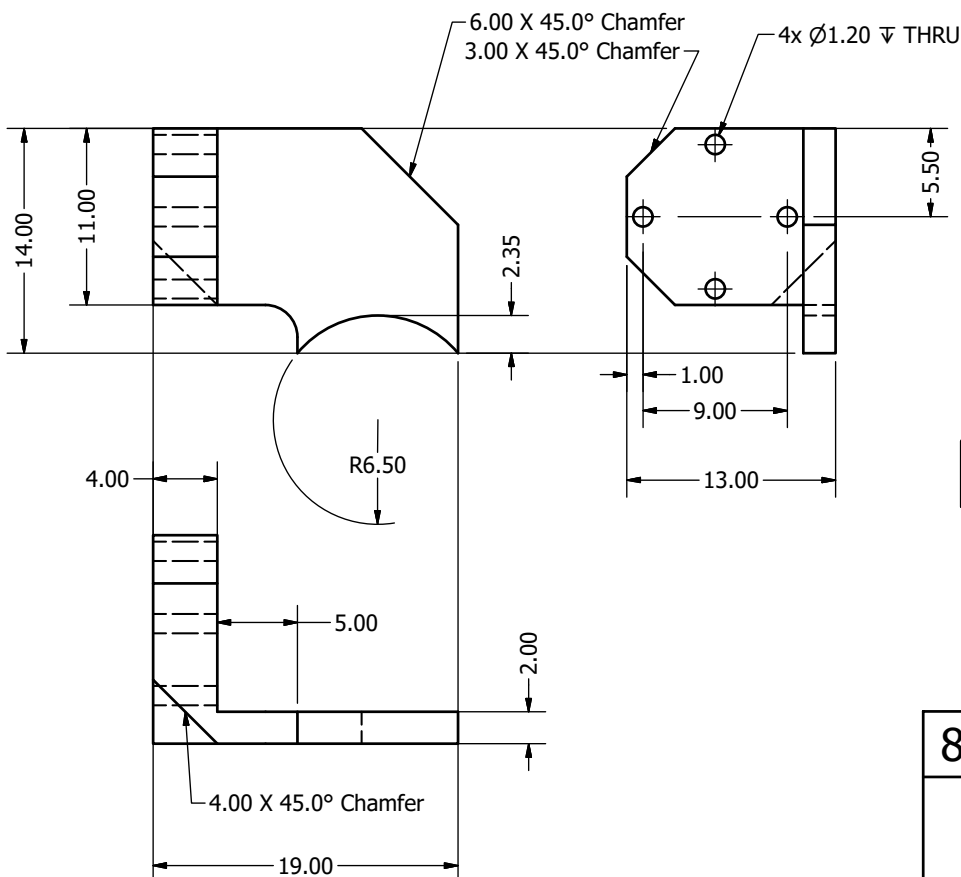


7 attocube interface 2

material: EN AW-6061

finish: polished

SCALE: 2:1

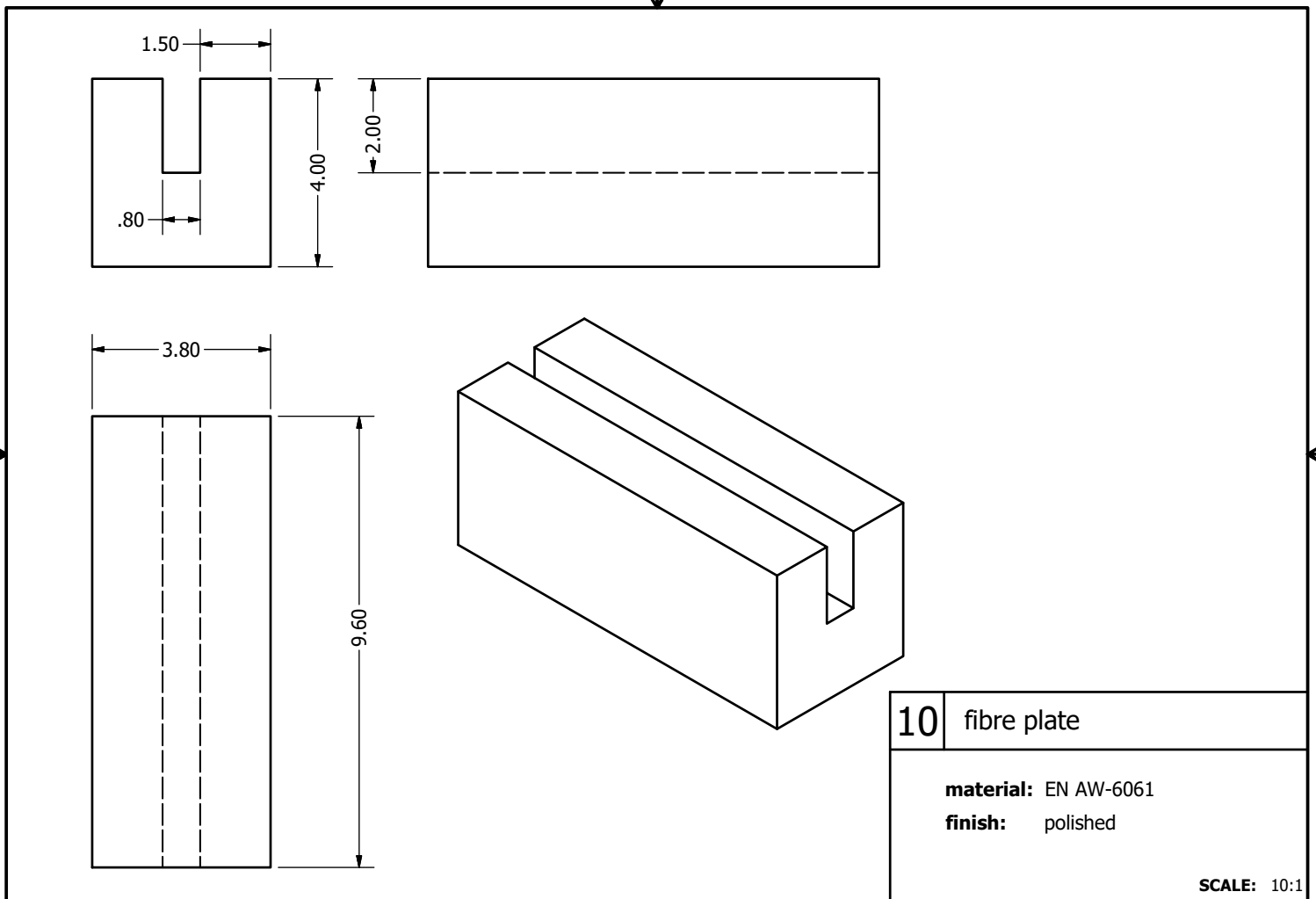
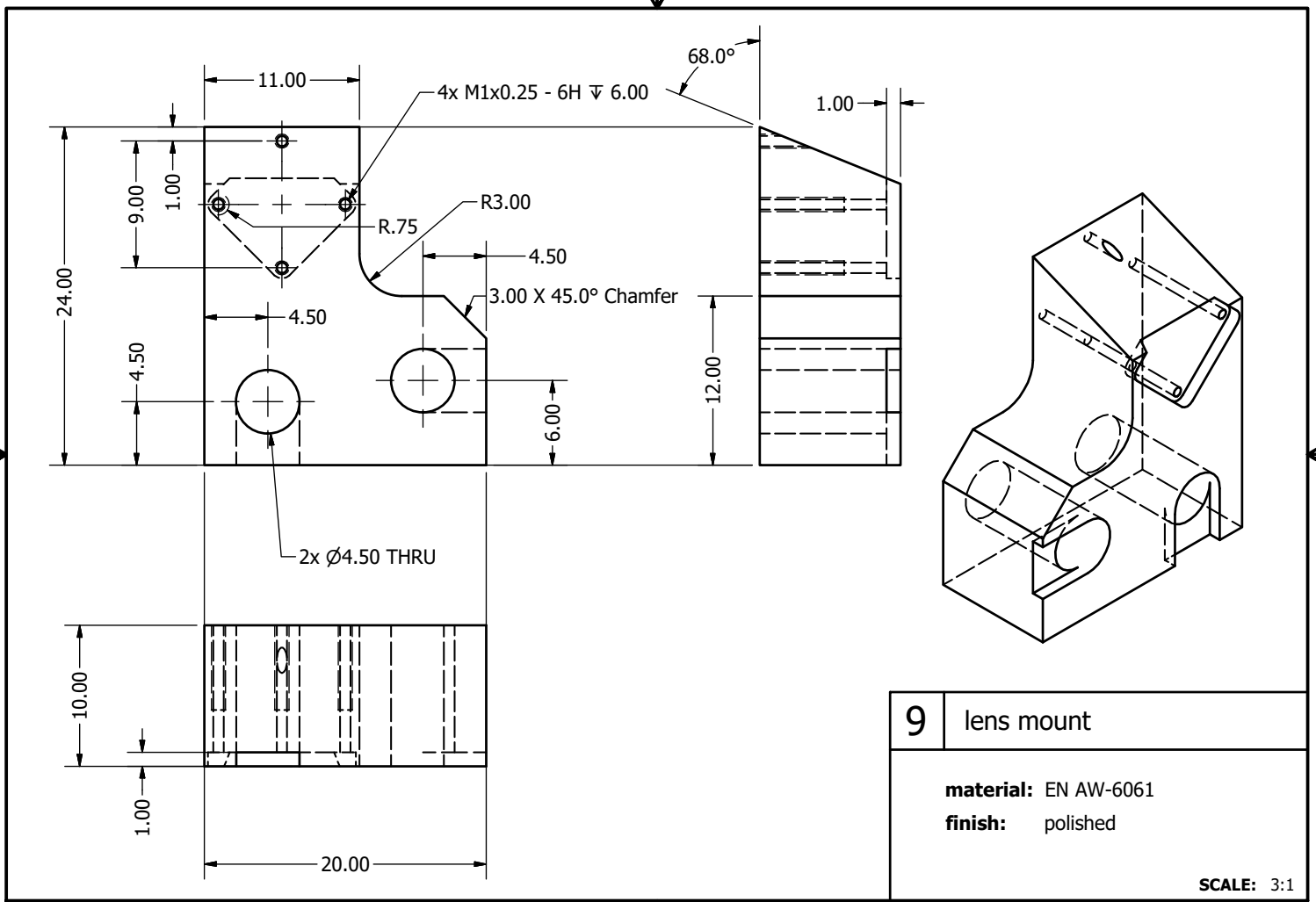


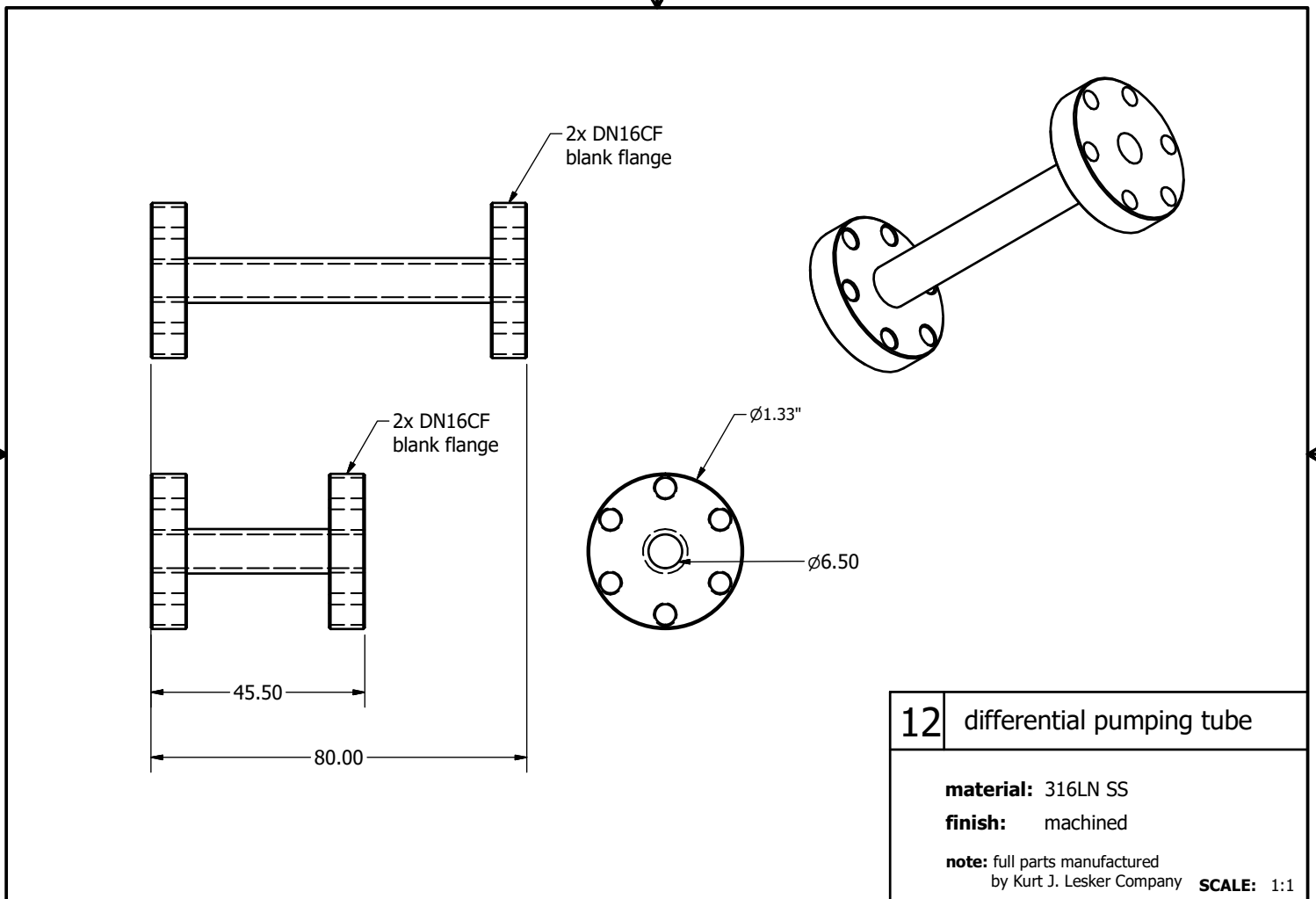
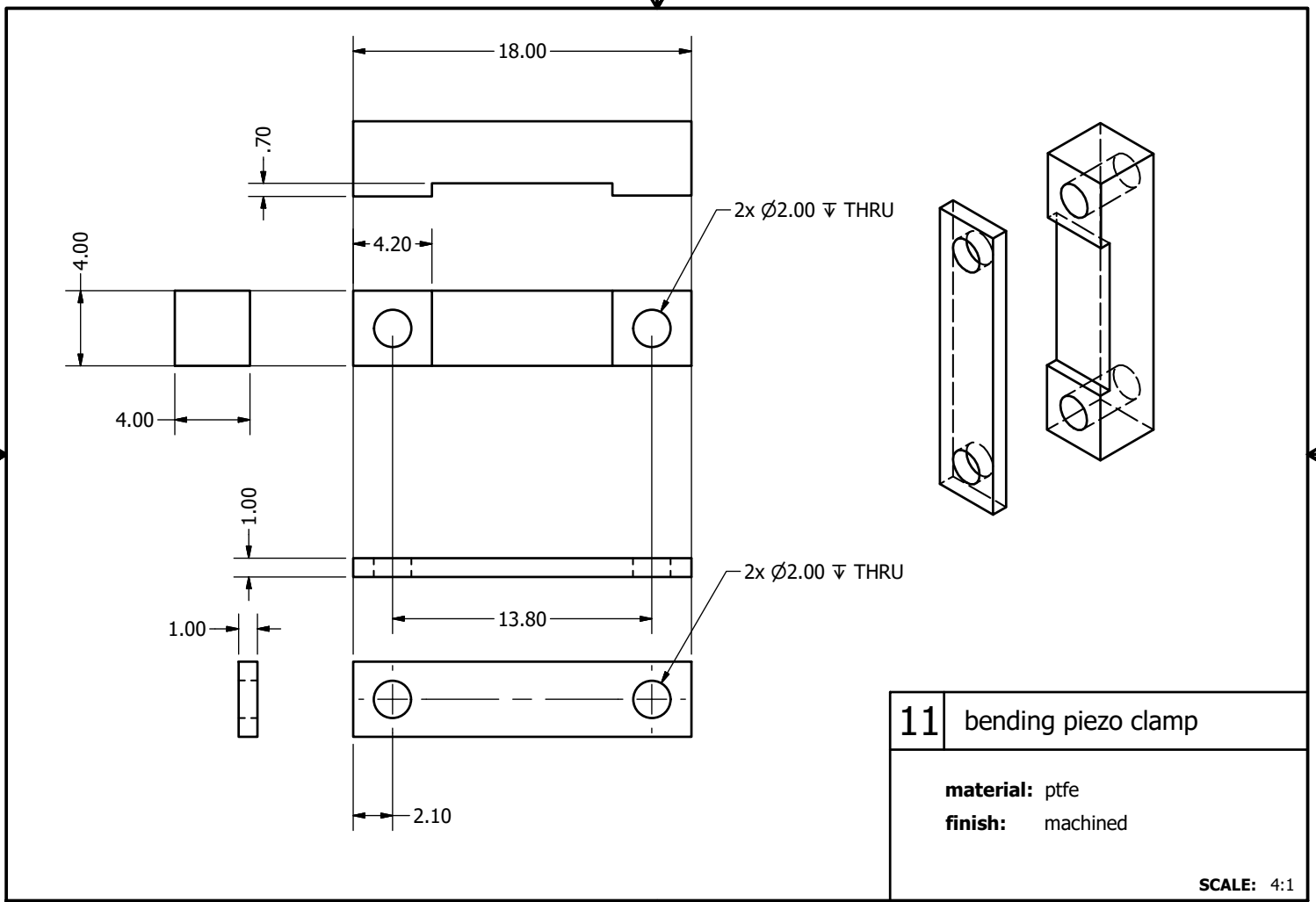
8 lens frame

material: EN AW-6061

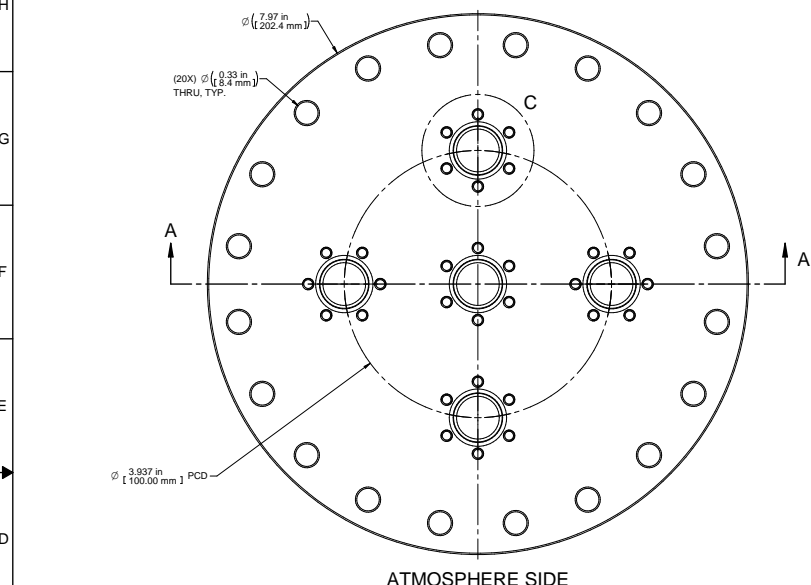
finish: polished

SCALE: 3:1



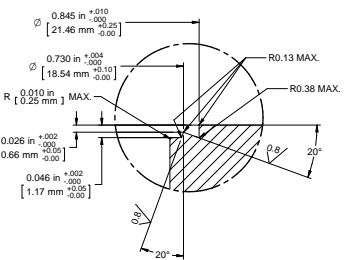


BILL OF MATERIALS					
NO.	PART NUMBER	DRAWING NUMBER	DESCRIPTION	QTY	UM
01	F0800X00N	P0000265	FLANGE,UHV,SS,BLANK,FXD,5"OD	1	EA
02	F0800CAP		PROTECTIVE COVER FOR 8" FLANGE	1	EA

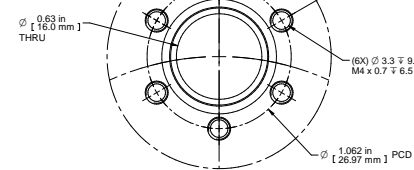


ACKNOWLEDGEMENT REQUEST

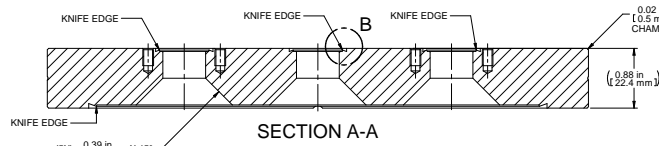
The attached drawings are related to your current order and are provided for your review. No work will begin until we have received your approval. Please contact your sales representative as soon as possible. Please note that changes to the drawing package (that are determined to be out of scope) may result in chargeable expenses, a delay in the project schedule, and ultimately a delayed delivery. Your acknowledgment authorizes KJLC to manufacture the components as described in the drawing package.



DETAIL B
1.33" KNIFE EDGE (5) PLCS
4:1



DETAIL C
TYPICAL (5) PLCS
2:1



SECTION A-A

SYMBOL	LEGEND	MATERIAL LEVEL	WELDING PROCEDURE	ALL	RELIEF FOR CUSTOMER APPROVAL	17/04/2020	MAL
REVISION	MSW-DCP-116, LEVEL 3	MSW-DCP-100, LEVEL II	MSW-DCP-100, LEVEL II				
ITEM BALLON	UNLESS OTHERWISE SPECIFIED, MACHINE FINISH SHALL BE 1.6µm/63µin Ra	AS SUPPLIED	OTHER SURFACE FINISHES SHALL BE AS SPECIFIED				
FOCAL POINT							
INSPECTION BALLON							
WATER TRACE IDENTIFICATION							
ANALYSIS IDENTIFICATION							

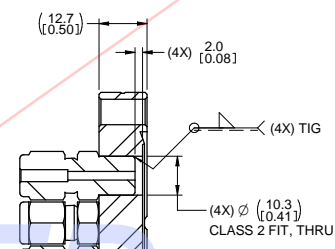
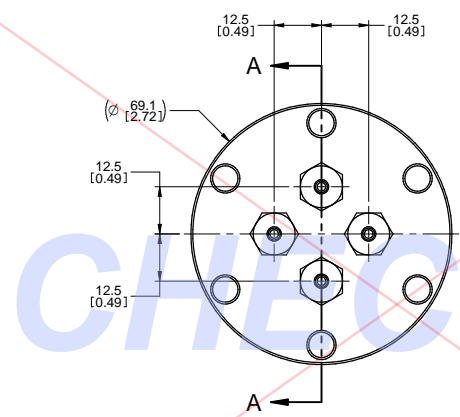
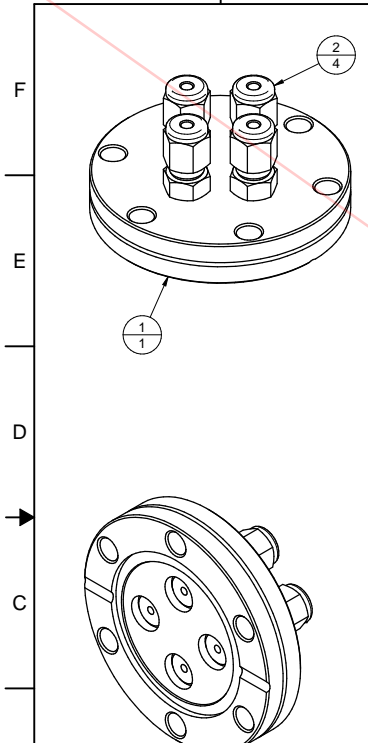
DATE	16/03/2020	DRAWN BY	DW
DATE	16/03/2020	APPROVED BY	MAL

TITLE	CUSTOM SS MULTI-PORT ZERO LENGTH REDUCER FLANGE DN200CF
MATERIAL SPECIFICATION	A2 304L STAINLESS STEEL
FINISHING NO.	FLG-SPL708
APPROX. WEIGHT	4.998 kg
SHEET	1 OF 1

NOTES:

- ALL DIMENSIONS ARE IN MILLIMETERS, REFER TO TABLE 1 FOR STANDARD TOLERANCING INFORMATION.
- IF DUAL DIMENSIONS ARE USED MILLIMETERS TAKE PRECEDENCE EVEN IN BRACKETS.

POSN	ITEM ID	NAME	DESCRIPTION	QTY	UM
1	SKU0123145	F0275X000N	EUDF-SUPP FLANGE, UHV, SS, BLANK, FXD, 2.75"	1	EA
2	SKU0146899	SS-200-1-2W	EUDF-SUPP FITTING, SWAGELOK, .125 TUBE OD,	4	EA



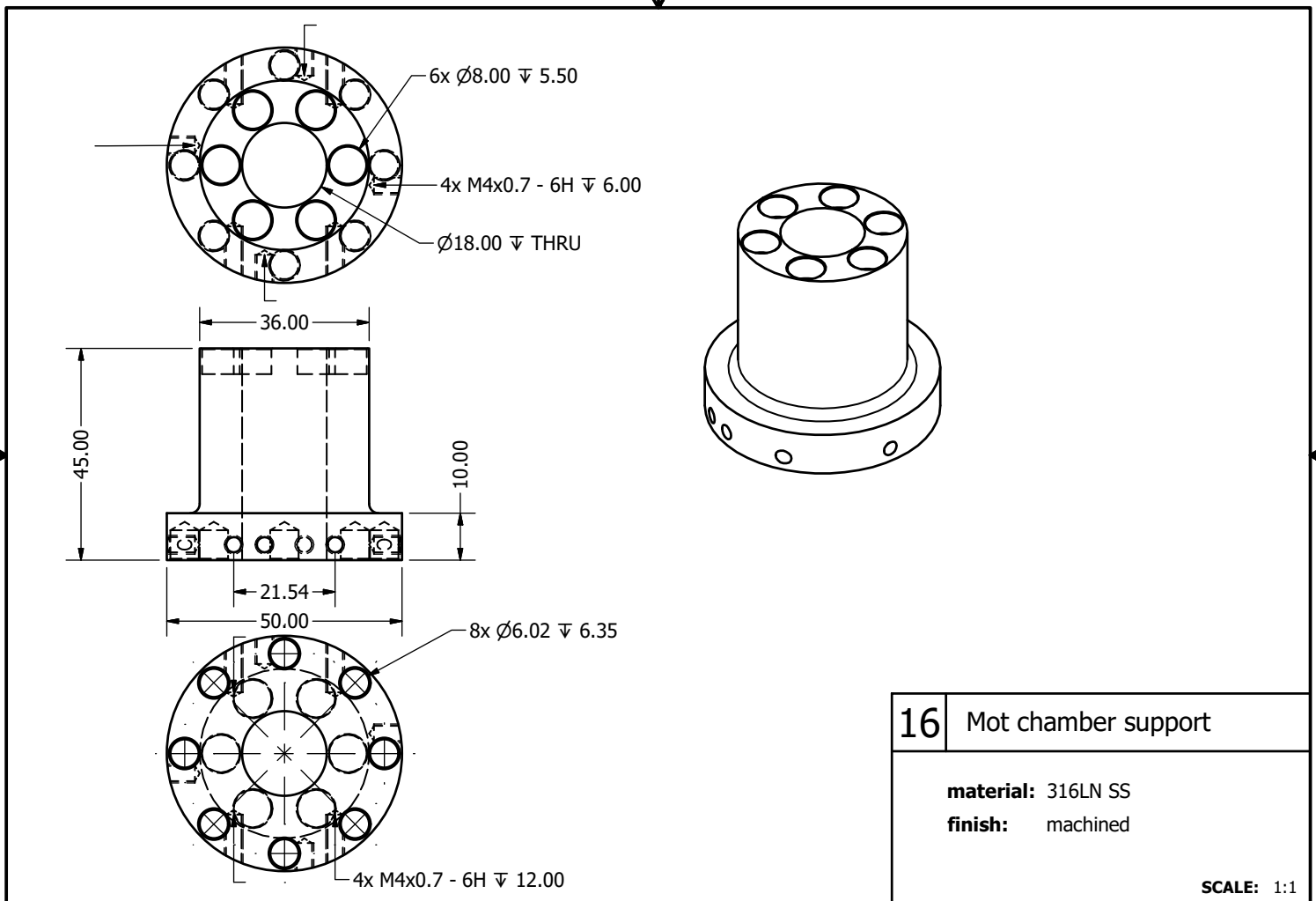
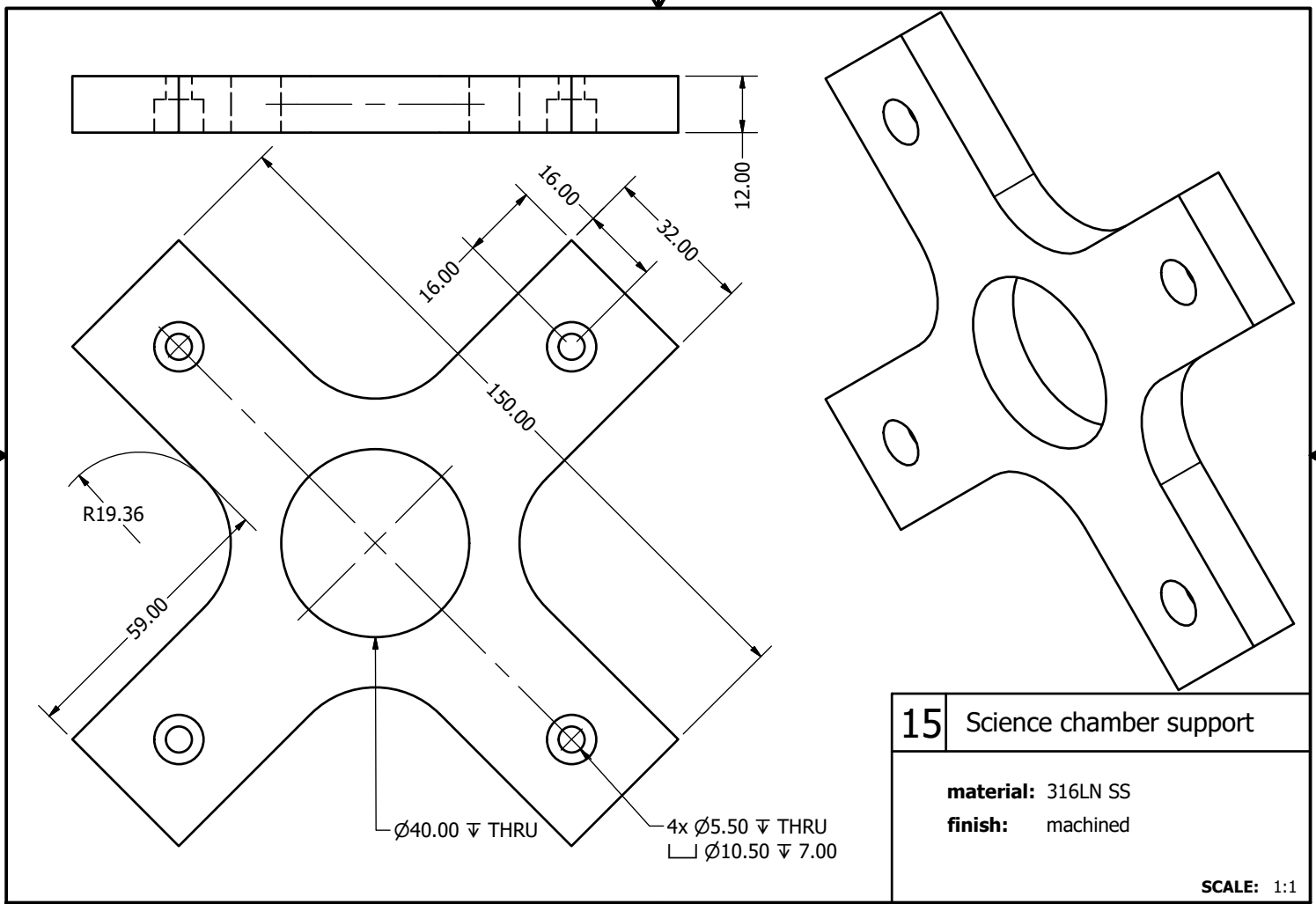
SECTION A-A

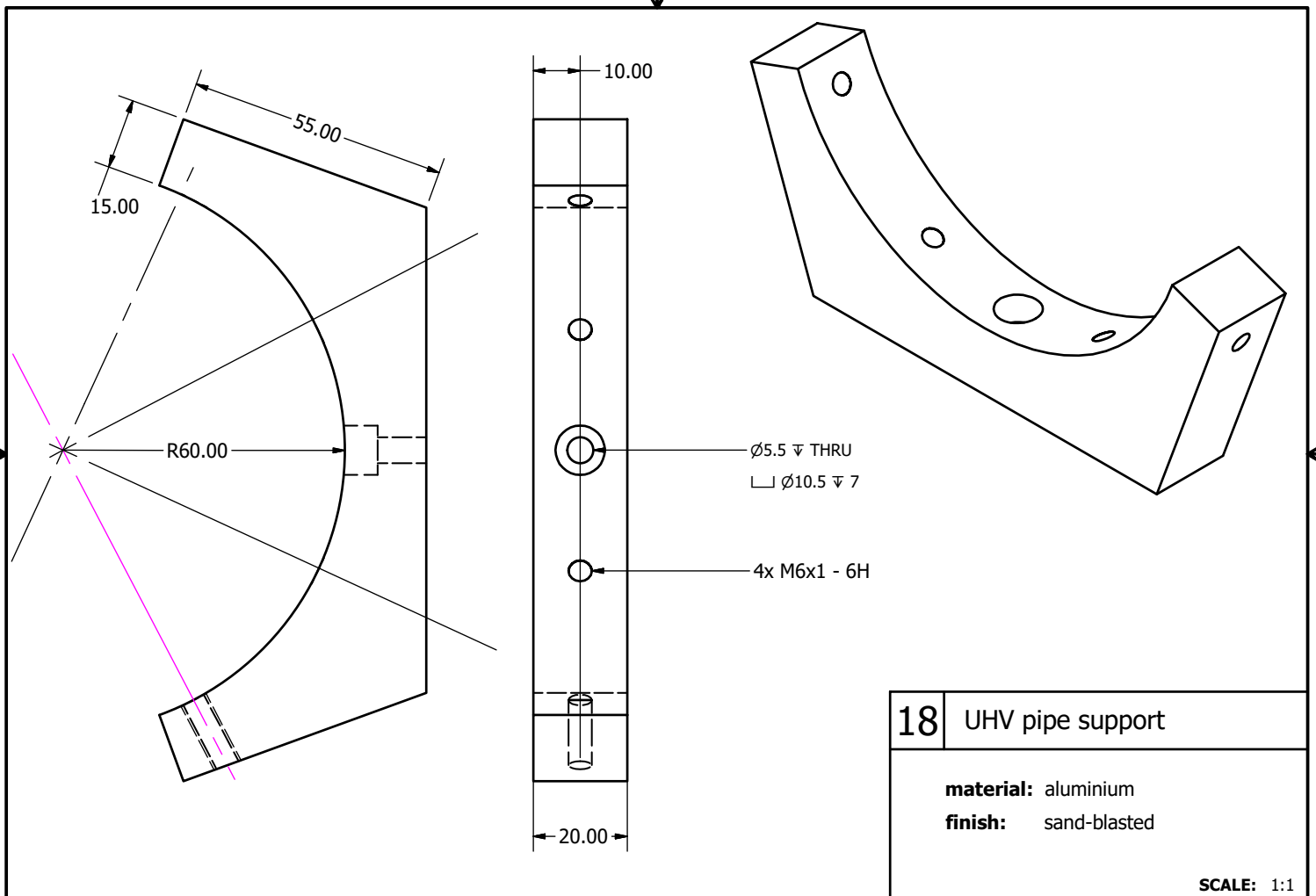
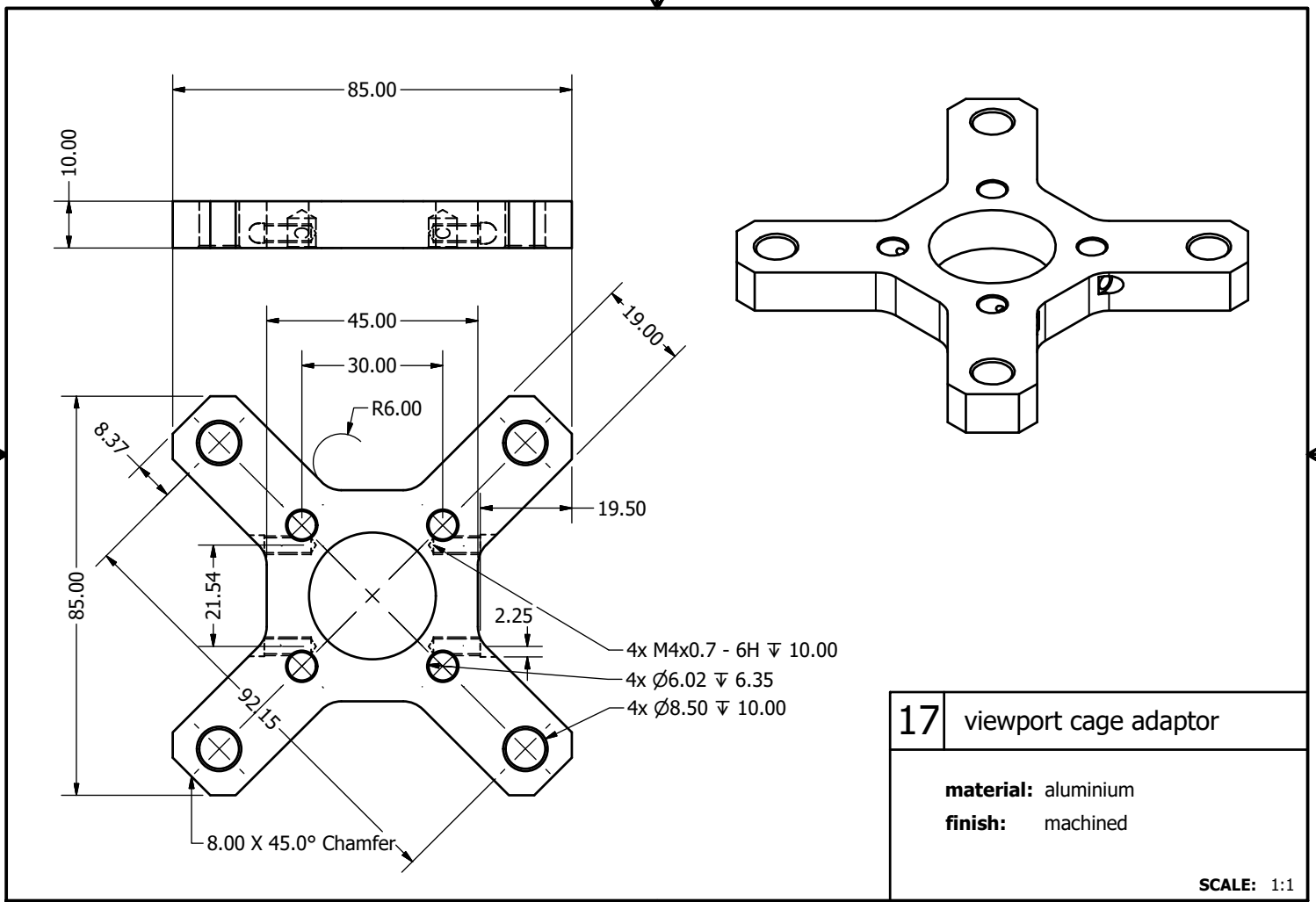
NOTES:

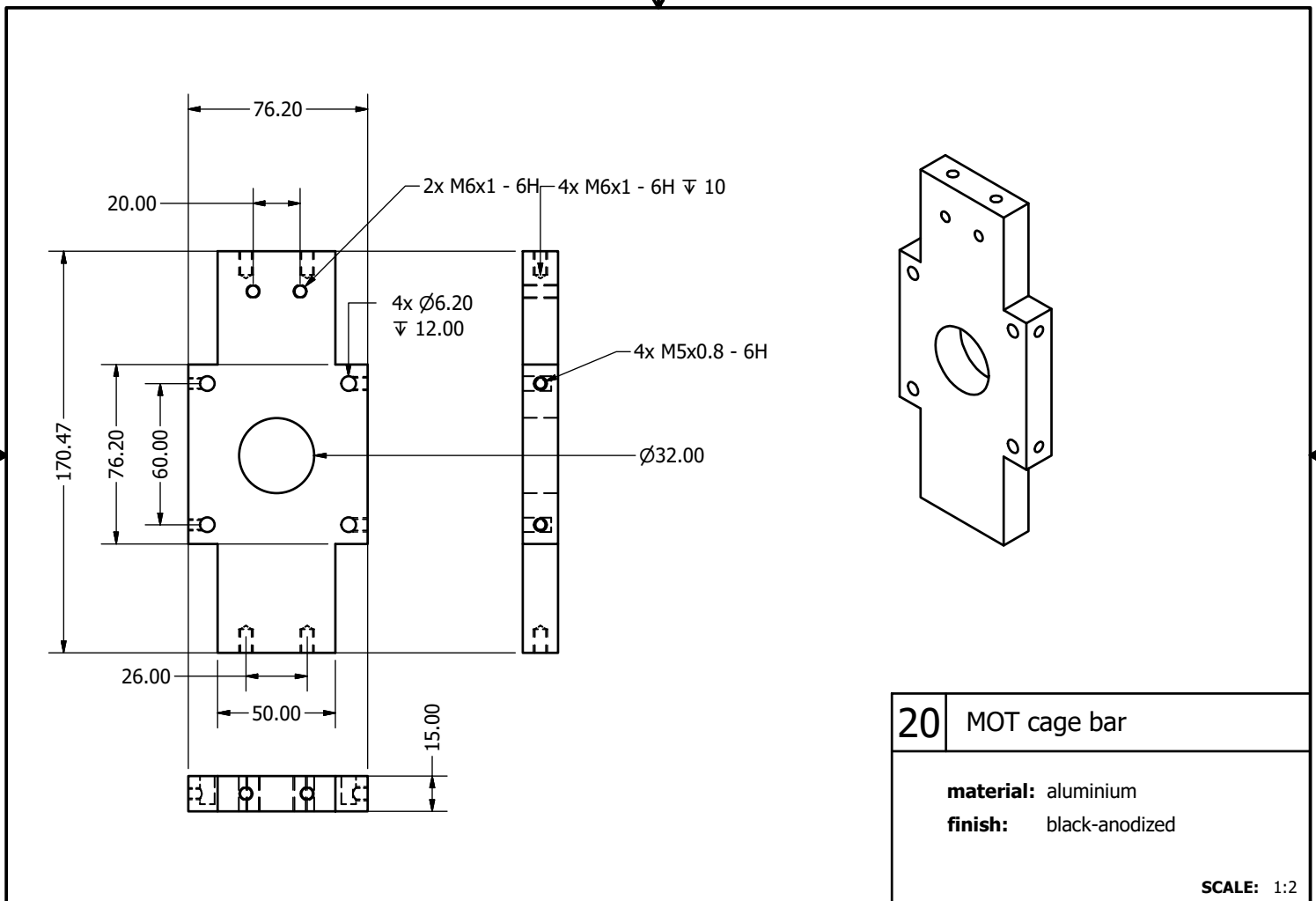
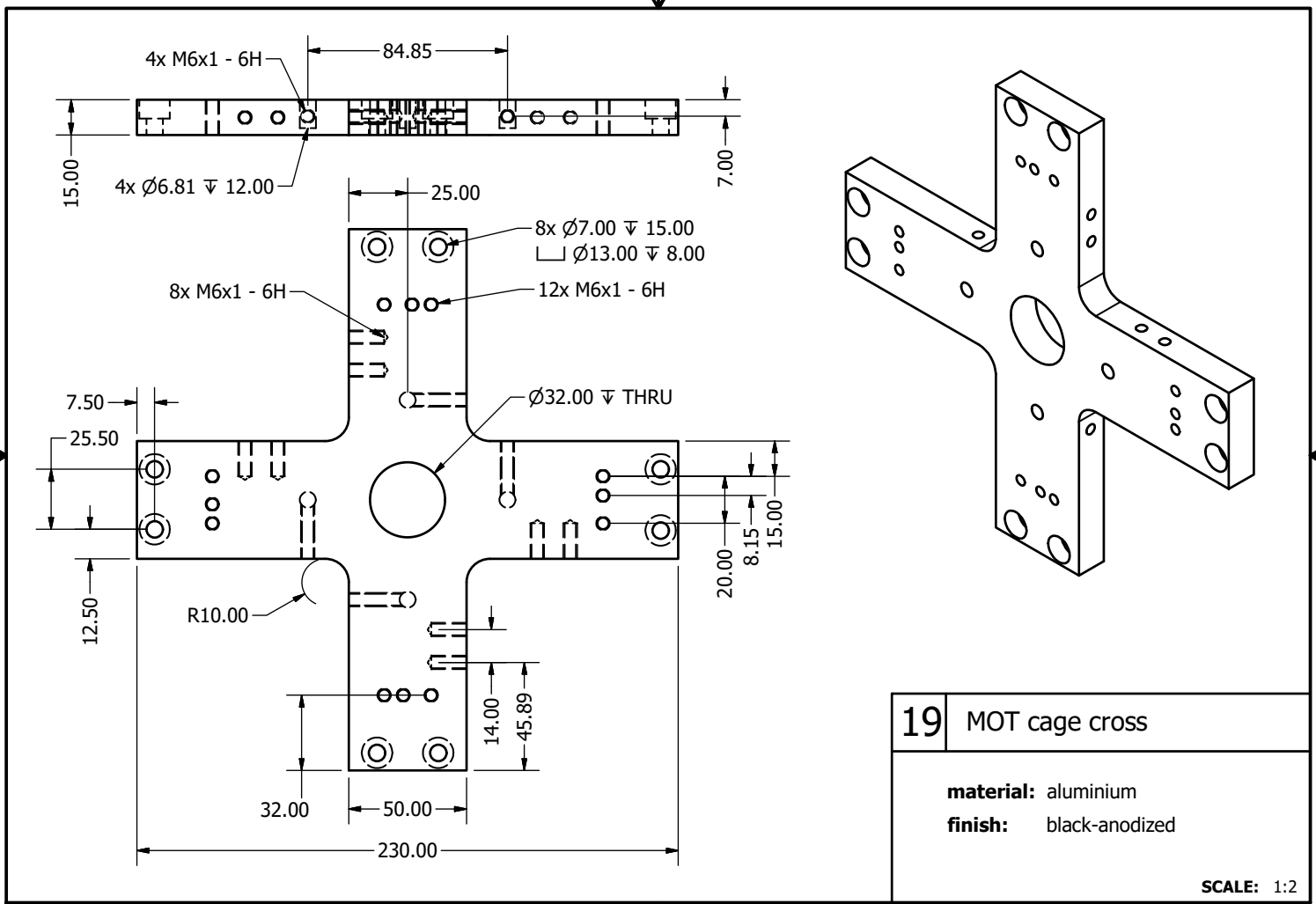
- ALL DIMENSIONS ARE IN MILLIMETERS (INCHES), REFER TO TABLE 2 FOR STANDARD TOLERANCING INFORMATION.
- DETAIL LEVEL: MSW-DCP-116, LEVEL 3
- CLEANING PROCEDURE: MSW-DCP-100, LEVEL II
- UNLESS OTHERWISE SPECIFIED, MACHINE FINISH: 1.6µm/63µin Ra
- UNLESS OTHERWISE SPECIFIED, SURFACE FINISH: AS SUPPLIED
- VACUUM WELDS TO BE LEAK CHECKED WITH A HELIUM MASS SPECTROMETER TO A LEAK RATE OF 5 X 10⁻⁹ atm-cc/sec OF HELIUM (5 X 10⁻⁹ mbar l/sec) OR BETTER.

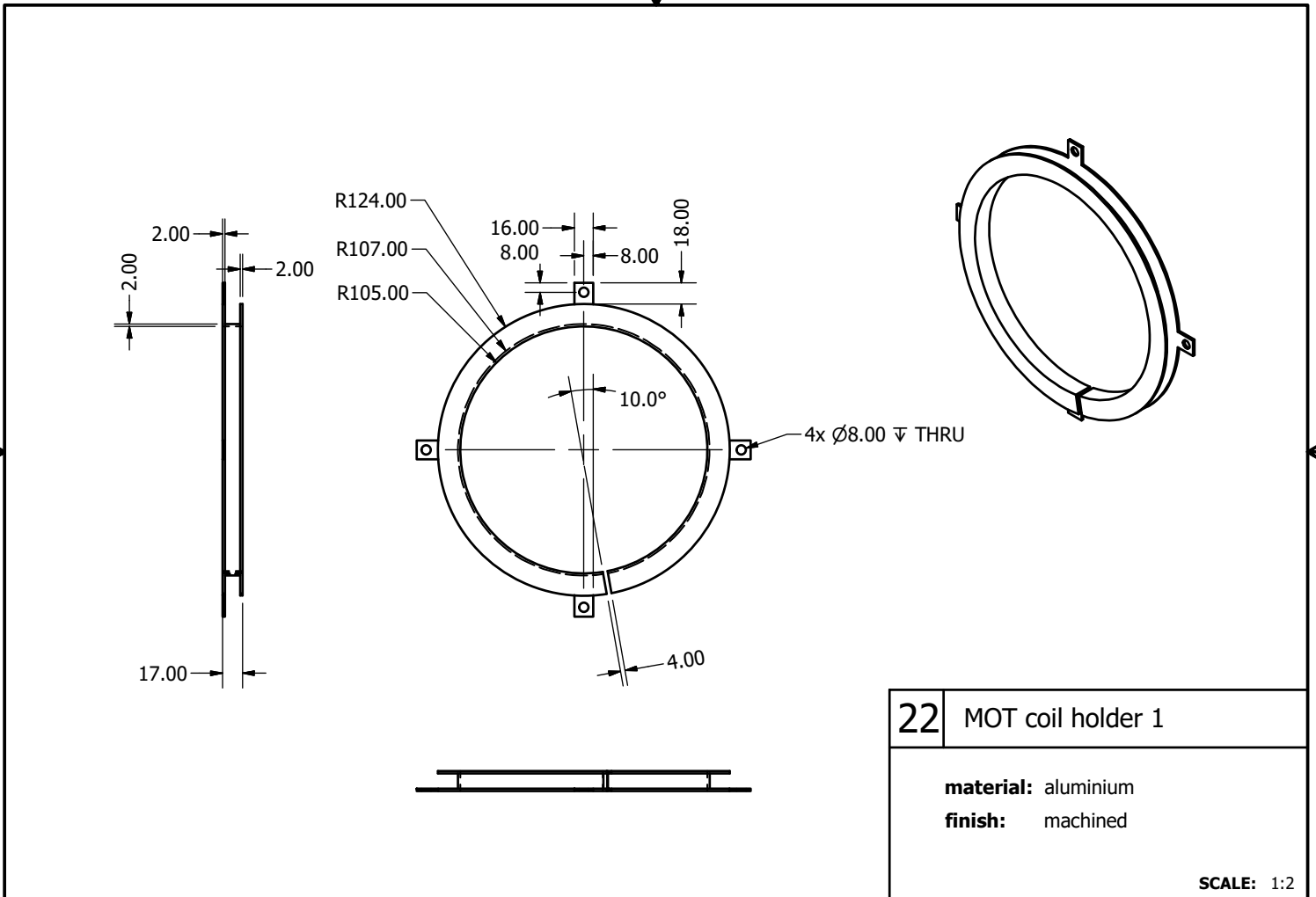
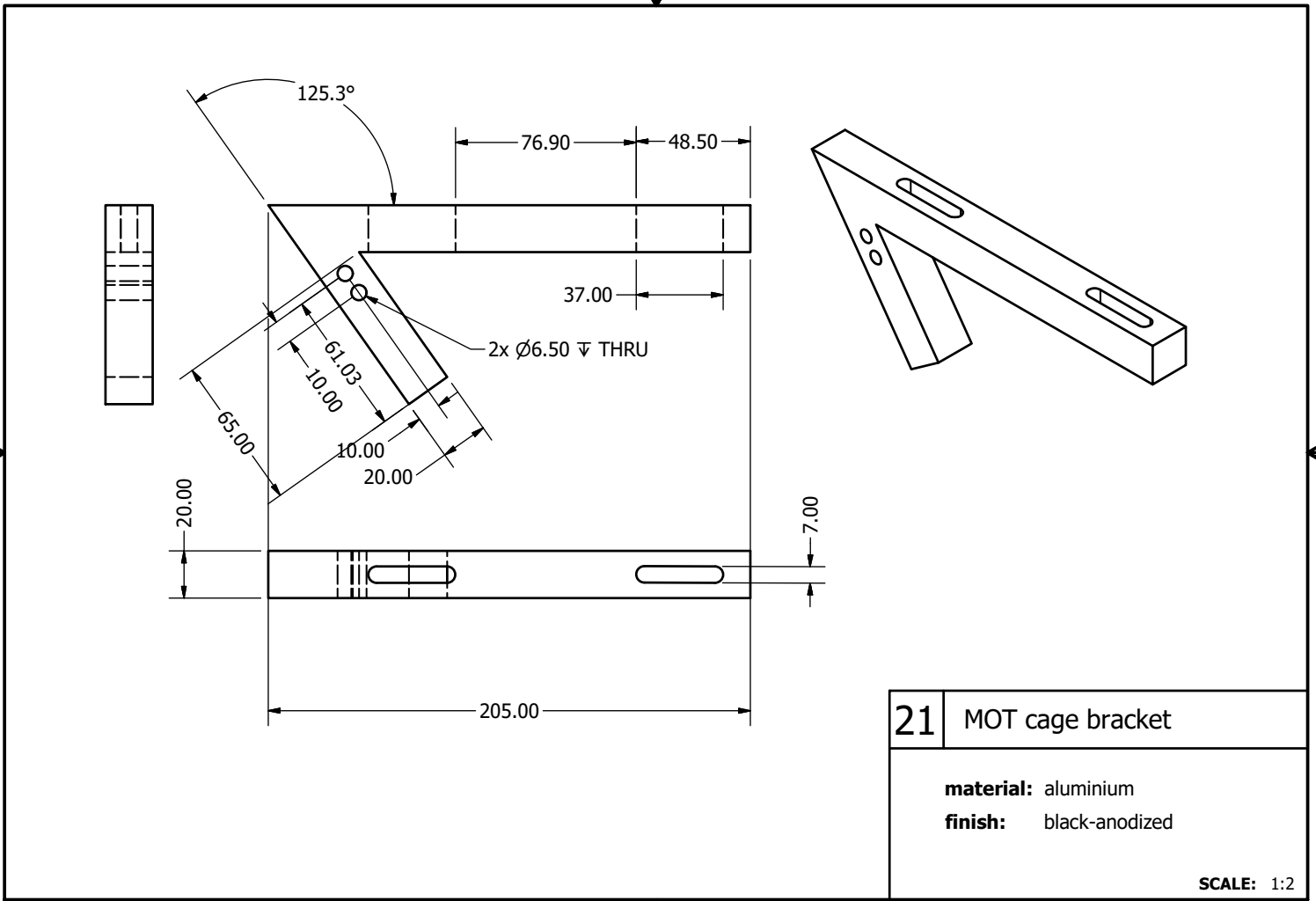
SYMBOL	LEGEND	UNLESS OTHERWISE SPECIFIED, REFER TO DOCUMENT ENW-1201, KJLC STANDARD TOLERANCES AND MANUFACTURING PRACTICES	1925 Route 51 Jefferson Hills PA 15025-5681 USA Phone: 1-800-245-6656 Web: www.lesker.com
REVISION		MACHINED TOLERANCES (UNLESS OTHERWISE NOTED)	<p>Kurt J. Lesker Company Enabling Technology for a Better World</p> <p>NOTE: THIS DRAWING AND ITS CONTENT IS THE CONFIDENTIAL AND PROPRIETARY INFORMATION OF KURT J. LESKER COMPANY AND CAN NOT BE DISCLOSED OR USED EXCEPT WITH THE EXPRESS WRITTEN PERMISSION OF KURT J. LESKER COMPANY.</p>
ITEM BALLON		FABRICATION/WELDMENT TOLERANCES (UNLESS OTHERWISE NOTED)	
FOCAL POINT			<p>DESCRIPTION: DN40CF BLANK THRU HOLE FIXED FLANGE WITH 4 OFF SS-200-1-2W</p> <p>PRODUCT NAME: FLG-SPL809</p> <p>ITEM NUMBER: SKU0341205</p> <p>DESIGN: A3</p> <p>SCALE: 1:1</p> <p>WELDMENT: MFG ME</p> <p>MATERIAL SPECIFICATION: STAINLESS STEEL, 304L</p> <p>APPROX. WEIGHT: 4 kg</p> <p>SHEET: 1 OF 1</p>
INSPECTION BALLON			<p>DATE: 01/12/2020</p> <p>DRAWN BY: MAL</p> <p>APPROVED BY: MAL</p>

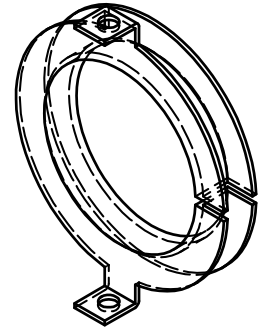
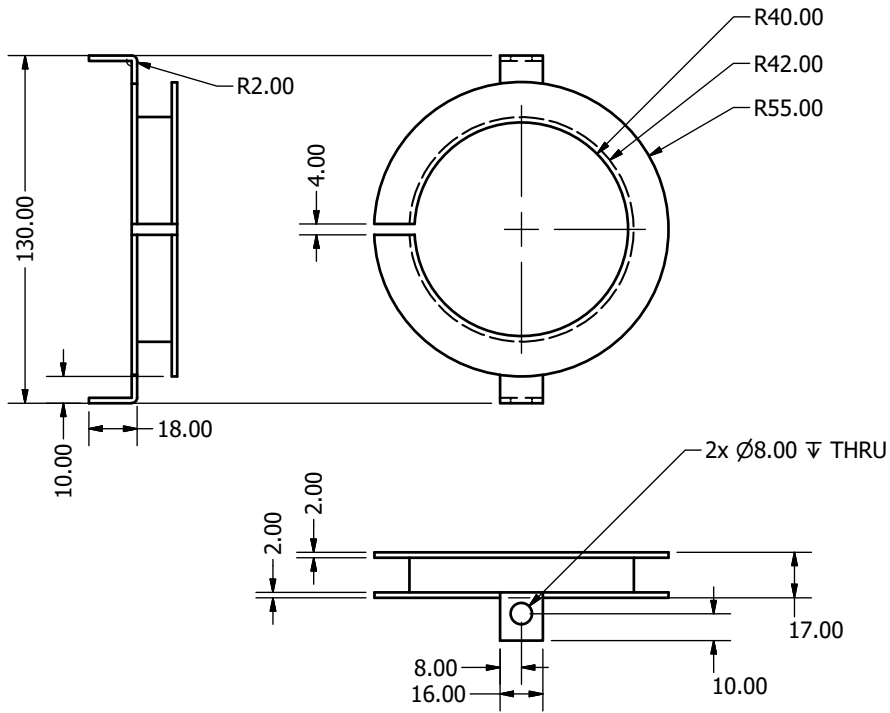
APPROVAL REQUEST







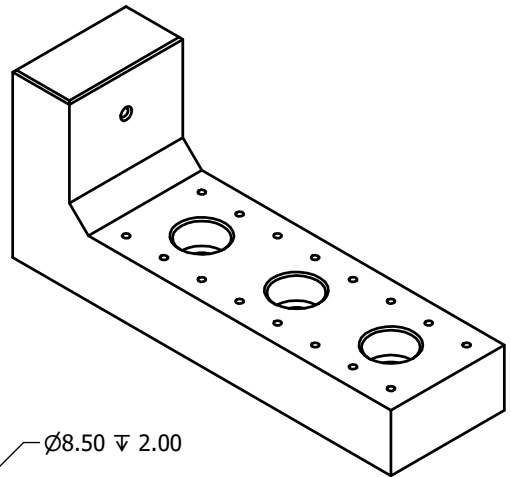
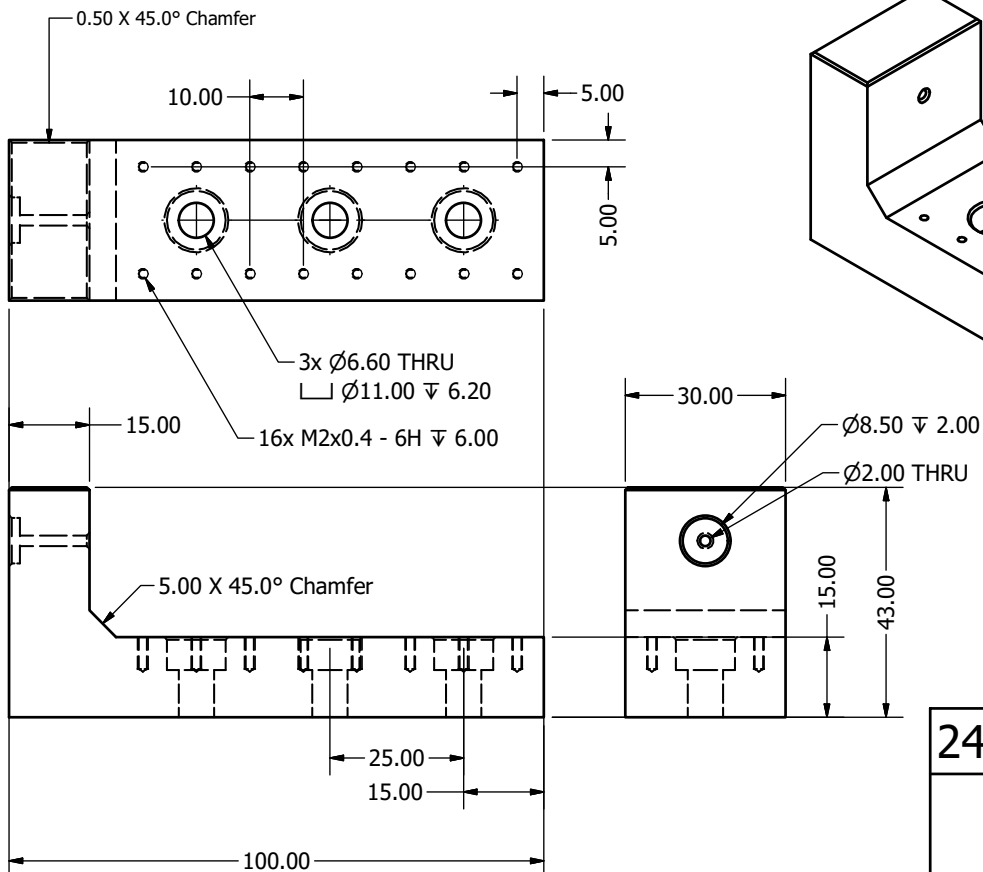




23 MOT coil holder 2

material: aluminium
finish: machined

SCALE: 1:2



24 fibre stretcher

material: aluminium
finish: machined

SCALE: 1:1



Procedure for exchanging in-vacuum components

This Appendix acts as a pre-checklist and thorough guide for placing and/or replacing any element located inside the **CQED** 2.0 science chamber – the procedure of which requires an argon venting of the entire (upper) **UHV** system, before a controlled removal of the gold-plated “copper block” from within the chamber can be carried out. With a minimum of two people involved, it is possible to complete the entire procedure in only a few hours (when neglecting the time required to pump the system back to **UHV**).

C.1 Important Guidelines

- Organise all that is required for this procedure *before* breaking the vacuum!
- Clean the environment around the Science chamber (i.e., remove any tools, unnecessary devices etc.).
- Ensure that the laminar flow above the Science chamber is active.
- Adorn appropriate protection for working with **UHV** equipment (i.e., powder-free gloves, hair-nets, face masks, lab coats).
- Any component to be placed under **UHV** should be suitably prepared by, for example, immersing in a sonic bath.
- All components and/or tools that will come into contact with **UHV** material must also be cleaned prior to their use. A wipe down with isopropanol or acetone suffices, but a sonic bath is preferable.

C. Procedure for exchanging in-vacuum components

- For preservation of the **UHV**-seal on the flange to be opened, be aware of the correct method for the loosening or tightening of the sealing bolts. Incremental torques should be applied up to the maximum value following a star-shaped pattern.
- *Beware of the knife edges at each flange seal!*

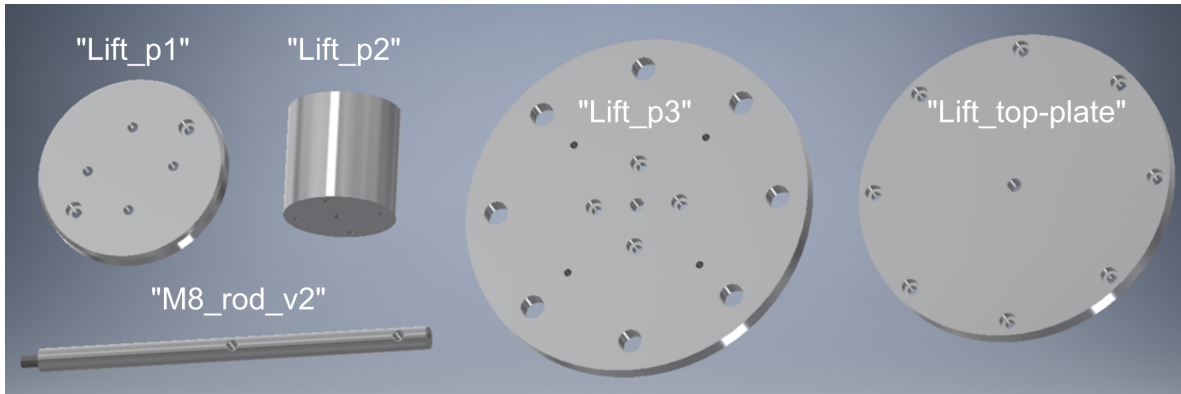


Figure C.1. Parts required for the experiment lift structure.

C.2 Required Tools and Parts

- Vacuum foil (for storage and/or protection of components)
- Adjustable torque wrench with M8 hex-head bolt fitting (for releasing or tightening the sealing bolts)
- New 8.00" copper gasket (to replace the old)
- A source of ultra-pure argon gas (for chamber flooding)
- **UHV**-compatible wiring (for securing feedthrough cabling)
- Various cleaned tools (at least: M2.5, M4, M6, M8 screw drivers and hex keys)
- Cleaned and prepared lift structure (see Figure C.1)
- Cleaned screws for procedure (8× M6×18 mm, 8× M6×20 mm, 2× M6×30 mm, 1× M8×50 mm)
- Dowels with a diameter of 6 mm, or similar (for holding the raised lift structure in place)
- Any finished replacement parts (that have been processed for **UHV**)
- All required KF vacuum components (see Figure C.2)

C.3 Procedure

1. Venting the vacuum (Carefully refer to Figure C.2)
 - 1.1 *Important:* wear powder-free gloves when handling KF vacuum hardware, clean each component before using, and store within UHV foil
 - 1.2 Take note of the pressure values for System 1 (upper) and System 2 (lower) from the Ion pump controller before starting
 - 1.3 Fully close Gate Valve 3 to separate System 1 and System 2
 - 1.4 Now System 1 is isolated: Connect all various cables of the Full range gauge 1 and Turbo pump 1 to the “Science” Pre-pump and turbo pump control 1 via the TPS 100 1 (see Figure C.2)
 - 1.5 Check the Full range gauge 1 pressure on the controller (see Table C.1)
 - 1.6 Connect a KF Tee with KF valve 1a to KF valve 1b (do not open yet)
 - 1.7 Connect a KF needle valve to the same KF Tee
 - 1.8 Put the standalone pre-pump 1 on damping material (foam padding etc.) and connect it to KF valve 1a (via a second KF Tee with needle valve)
 - 1.9 Connect a clean dry Argon source to the needle valve installed in 1.5.
 - 1.10 Close all needle and KF valves
 - 1.11 Turn OFF System 1’s (upper) ion pump (for its protection)
 - 1.12 Turn ON the standalone pre-pump 1 to purge the installed KF tubing
 - 1.13 Fully open the KF valves 1a and 1b to purge up to gate valve 1
 - 1.14 Close the KF valve 1a and then switch off the pre-pump
 - 1.15 Have a play with the Argon supply and its needle valve to get a feel for the flowrates (which should be as low as possible)
 - 1.16 Repeat Steps 1.10. – 1.12. to remove the ‘test’ Argon
 - 1.17 Gently and slightly open gate valve 1 – monitor the pressure

channel number	channel function
340	pressure
707	speed level (%)
309	rotor speed (Hz)
023	turbo pump ON/OFF
010	pumping station ON/OFF

Table C.1. Important controller channels.

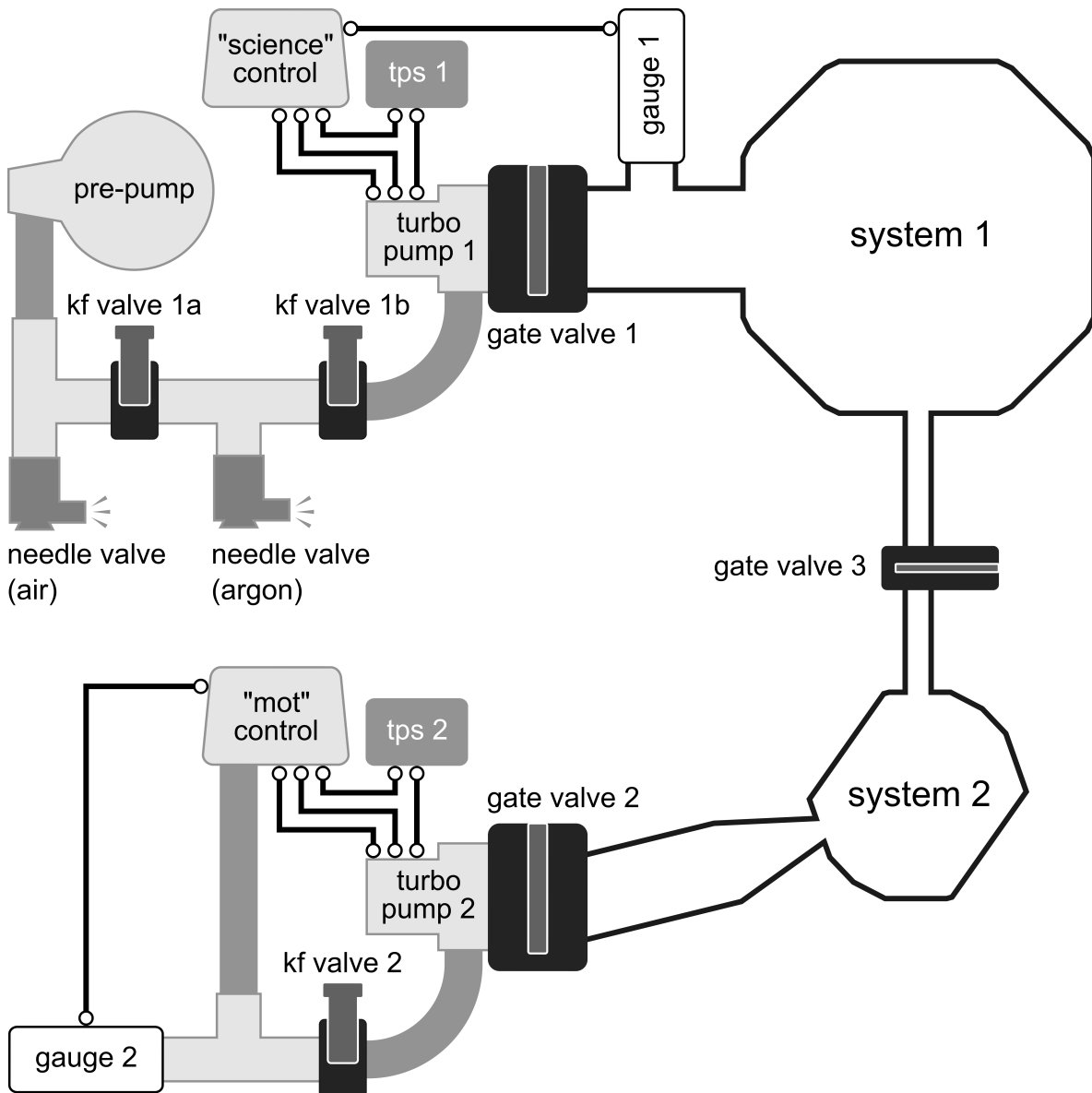


Figure C.2. Schematic for venting and pumping the entire experiment.

- 1.18 Begin backfilling with the Argon through a controlled opening of the corresponding needle valve
- 1.19 Once ambient pressure is reached, close KF valve 1b, the Argon needle valve, and the Argon supply.
2. Opening the Science chamber (Figure C.3)
 - 2.1 Correct flange: Zero-length reducer from DN160CF to DN63CF that has a DN63CF viewport and Upper MOT upper vertical beam optics
 - 2.2 Take note of the flange orientation and mark it
 - 2.3 Incrementally loosen the M8 hex-head bolts with the torque wrench little by little in a star-pattern

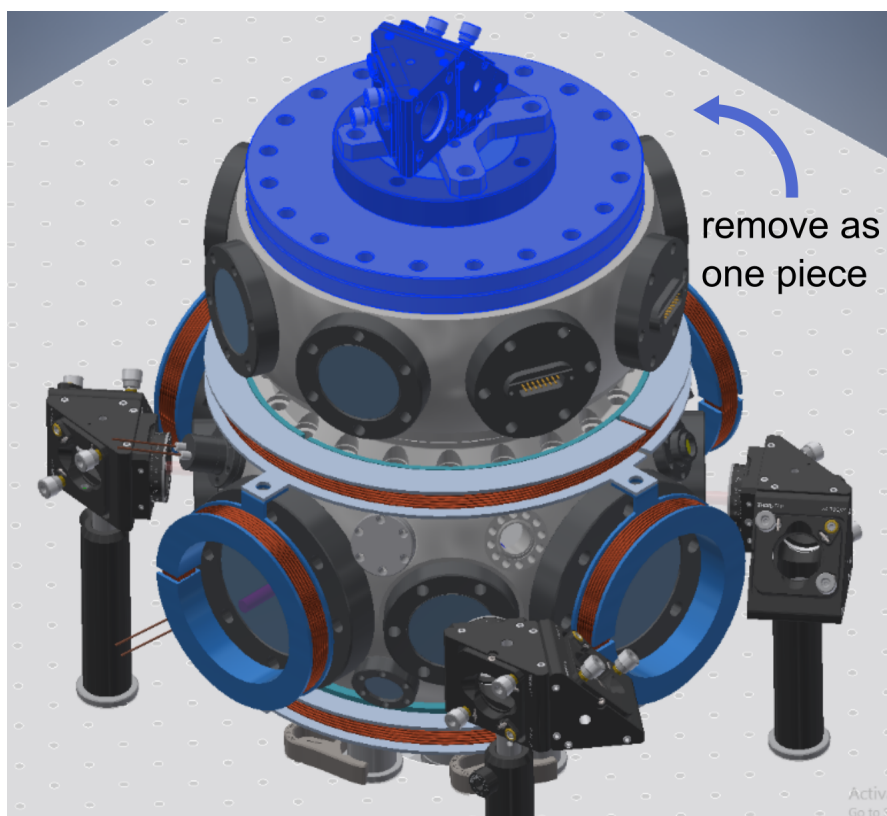


Figure C.3. Science chamber top flange.

- 2.4 Once fully loosened, completely remove all ($\times 20$) bolts and washers and store in foil
 - 2.5 Carefully lift the flange upwards and then place knife-edge down on a foil bed – watch out for the viewport, attached optics, and patch fibre cable
 - 2.6 Remove the used copper gasket (do not damage knife-edge!). If additional force is needed, use a cleaned pair of grips to grab the gasket
3. Organising the cabling I
 - 3.1 Beware of the Spherical Octagon chamber's knife-edge
 - 3.2 Take note of where each cable is plugged
 - 3.3 Carefully unplug all feedthroughs on the inside
 - 3.4 Remove all cables from the upper surface of the copper block and tie them together with UHV-compatible wiring
 4. Attaching partial lift structure (Figure C.4)
 - 4.1 Clean all the parts: Especially surfaces/screws that touch the copper block
 - 4.2 Screw together Lift_p1 and Lift_p2 with $4 \times M6 \times 20$ mm (leave M8 thread exposed)
 - 4.3 Carefully place Lift_p1 on the top surface of the copper block inside the chamber

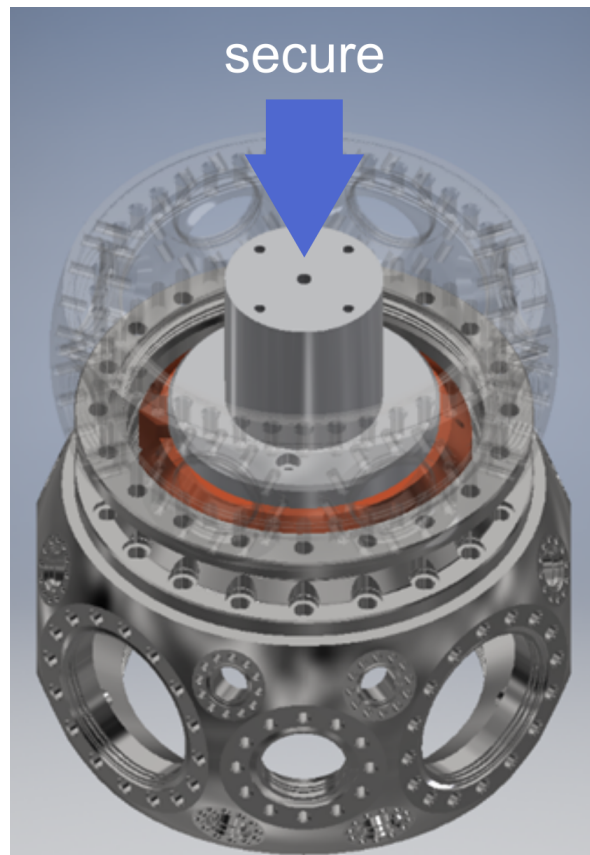


Figure C.4. Partial lift structure to copper block.

- 4.4 Adjust its orientation and secure with $2 \times$ (UHV-compatible) M6 \times 30 mm
- 4.5 Wind the vacuum cables around the Lift_p2 and secure in place
5. Completing lift structure assembly (Figure C.5)
 - 5.1 *Beware of the knife edge!*
 - 5.2 Fully screw in (at least) $4 \times$ M8_rod_v2 guide rods directly into the Spherical Octagon chamber – front, back, left, right
 - 5.3 Additional M8_rod_v2 guide rods fit halfway between two adjacent primary guide rods
 - 5.4 Check orientation of Lift_p3 with respect to Lift_p2, i.e. ensure screw holes are aligned
 - 5.5 Lower Lift_p3 along the guide rods to Lift_p2
 - 5.6 Screw together Lift_p3 and Lift_p2 with $4 \times$ M6 \times 20 mm
 - 5.7 Screw Lift_top-plate to all installed guide rods with M6 \times 18 mm
6. Extracting the experiment
 - 6.1 Slowly lift the experiment out of the chamber by holding Lift_p3
 - 6.2 Ensure slow, guided, vertical motion to the Lift_top-plate

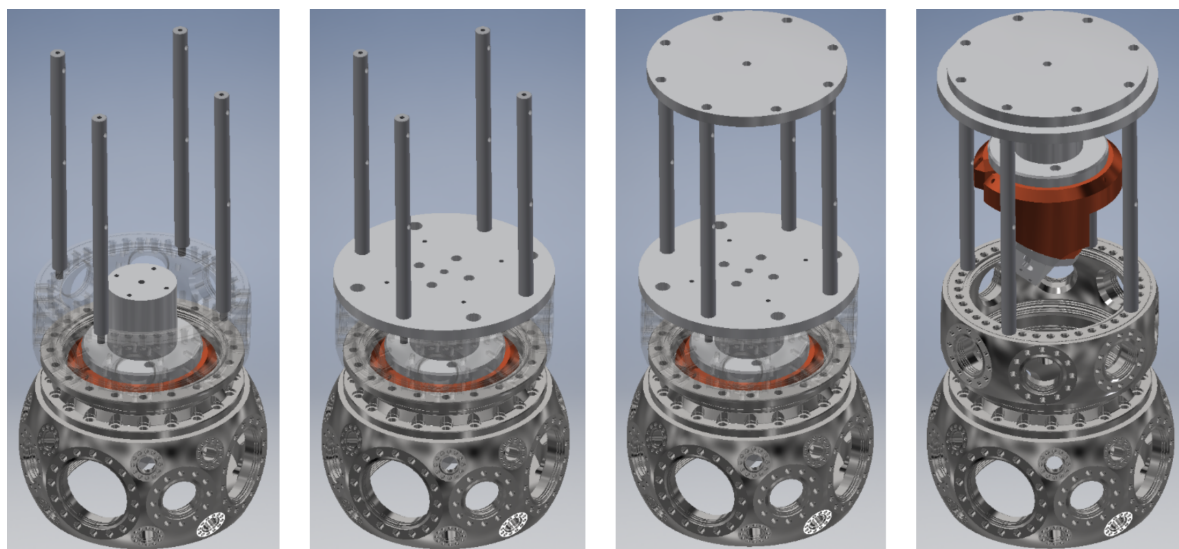


Figure C.5. Removing the coupling set-up with the lift structure.

- 6.3 Have a second person secure the lift by adding $\text{Ø}6\text{mm}$ dowels into the thru-holes of the guide rods (underneath Lift_p3) - don't drop the dowels!
- 6.4 A single $\text{M}8 \times 50\text{ mm}$ can be added through the Lift_top-plate, which screws into Lift_p2 for additional security

7. Pre-replacement checks

- 7.1 Check that each viton ring ($\times 6$) is resting on a groove-grabber in the closed-coupler, and is lightly pushed against the chamber wall
- 7.2 Find any viton rings that may have fallen into the chamber and remove

8. Exchanging parts (Figure C.6)

- 8.1 Take care when fixing mounts into the attocube stacks – do not apply too much torque to the positioners!
- 8.2 When finished, take some time to arrange the cables/fibres/etc. such that they freely pass upwards without obscuring any optical paths

9. Lowering experiment

- 9.1 Unscrew top $\text{M}8$ screw and remove (if present)
- 9.2 Lift up with Lift_p3 and have a second person remove the dowels from the guide rods – *take care not to drop them!*
- 9.3 Slowly lower the experiment back into the chamber – a slight rotation may be required to feed the copper block onto its own guide rails
- 9.4 Check correct positioning by looking through the front **DN63CF** viewport: one should observe the resonator mount through hole (and lens) is concentric with the viewport

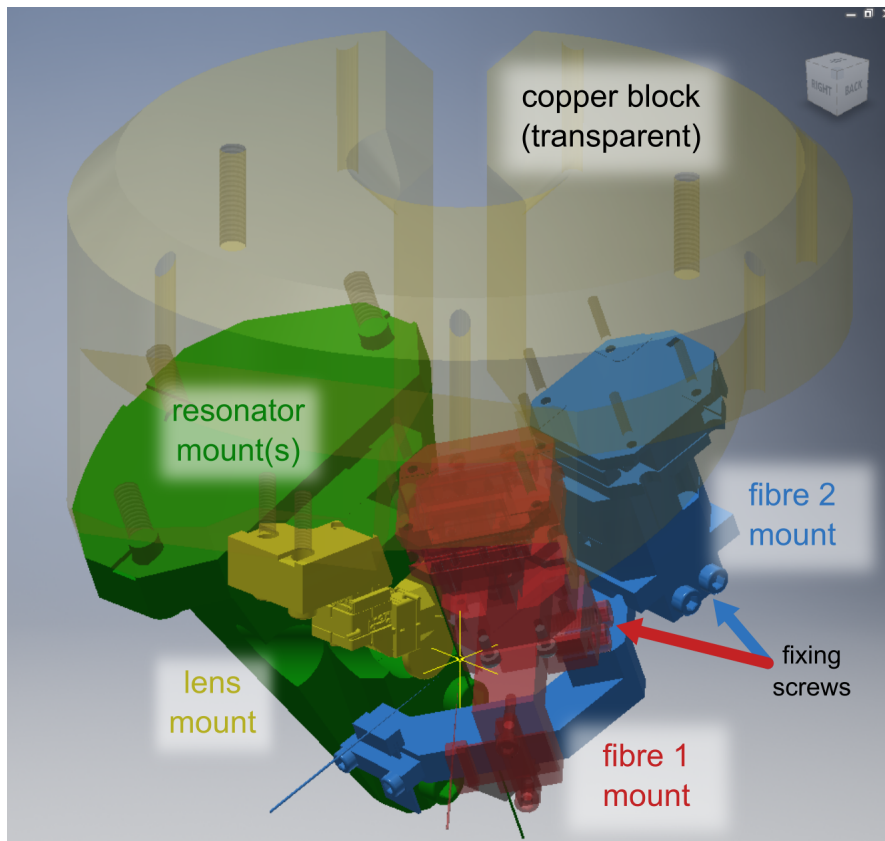


Figure C.6. Colour-coded view of the coupling set-up assembly.

10. Removing lift structure

- 10.1 Unscrew Lift_top-plate from the guide rods and remove
- 10.2 Unscrew Lift_p3 from Lift_p2 and remove
- 10.3 Remove all guide rods from the chamber – *beware of the knife edge!*
- 10.4 Unscrew Lift_p1 from the copper block, and remove it together with Lift_p2 – *do not drop the screws into the open chamber!*

11. Organising the cabling II

- 11.1 Untangle cables and plug them back to the correct feedthroughs
- 11.2 Ensure that no cables are hanging down into the science chamber (look through all the viewports)
- 11.3 Ensure cables do not block the centre hole of the copper block
- 11.4 For fibres: feed each end through an open Swagelok tube, then thread (from the outside) a cleaned single-hole conical Teflon ferrule, followed by the Swagelok thread cap onto each bare fibre, up to the feedthrough. Hand tighten the Swagelok cap. (Approximately two further full-revolutions will ensure **UHV**-tightness, but this should be carried out during the pump down in Step 13.)

12. Sealing the chamber

- 12.1 Place a new 8.00” copper gasket onto the knife edge of the spherical octagon chamber – check first that it isn’t scratched or damaged
- 12.2 Carefully replace the top flange onto the chamber with the original orientation (recorded in Step 2.2.)
- 12.3 Hand-tighten all bolts (with a washer) into the chamber
- 12.4 Use the torque wrench to tighten the bolts in a star-pattern, with incremental torque values until 20 N m is reached (DN160CF flange)

13. Pumping down (Figure C.2)

13.1 *Important Info:* Pumping down has to be carried out carefully when nanofibres are installed inside the chamber – pumping too fast with the roughing pump can generate currents within the chamber, which increases the chance of depositing dust (etc.) on the waist region (thereby decreasing or destroying the fibre transmission). The idea is to bypass this ‘turbulent’ regime by decreasing the pumping speed of the pre pump, manually, by adding an air-intake with use of a needle valve. In addition, the Swagelok fibre feedthroughs have to be properly tightened during the pump down without damaging the fibres. The transmission of all present nanofibres should be continuously monitored.

13.2 The set-up should still look like that shown in Fig. 2.

13.3 Gate valve 1 should still only be slightly open – this is advantageous for the following steps;

13.4 Fully open the Air-inlet needle valve and turn on the pre-pump 1

13.5 Gradually close the Air-inlet needle valve to begin the roughing of System 1 – the timescale until fully closing should be ~hours

13.6 Gate valve 1 can be gradually fully opened at the same time

13.7 When the pressure reaches the limit of what the pre-pump can achieve (around 10^{-2} mbar), switch ON the Turbo pump 1 (refer to Table 1)

13.8 For absolute caution, the Turbo pump rotor speed can be gradually ramped up over several hours

13.9 Leave this pumping configuration for several days – the pressure should ‘quickly’ reach 10^{-6} mbar – i.e. **High Vacuum**

13.10 Fully close gate valve 1 and turn ON System 1’s (upper) ion pump

13.11 Close KF valve 1b and turn OFF the turbo and pre-pumps

13.12 Dismantle the KF hardware up to KF valve 1b and store safely

13.13 ***Have a well-deserved drink!***

14. (Optional) Baking: see Chapter 3, Section 3.5.3

D

Calculation of the UHV system conductances

In this Appendix, the calculations performed for determination of the conductance values for each connection piece within the UHV system are presented, according to the schematic assembly shown in Figure 3.15 (Section 3.5.1 of Chapter 3). The following formulas are those with relevance to the system under consideration, and are approximately valid within the molecular flow regime and assuming smooth inner surfaces of the container.

The conductance of a straight cylindrical pipe with internal radius r and overall length l can be approximated by [161]

$$C_{\text{cyl}} = \frac{2\pi r^3}{3} \frac{\bar{v}}{l}, \quad (\text{D.1})$$

where $\bar{v} = \sqrt{\frac{8RT}{\pi M}}$ is the average speed of the contained particles with molar mass M at a temperature T , where R denotes the gas constant.

For a straight conical pipe of length l , with opening and closing radii r_1 and r_2 , the conductance is given by [161]

$$C_{\text{con}} = \frac{\pi \bar{v} (r_1 r_2)^2}{4r_2^2 + (r_1 + r_2)l}. \quad (\text{D.2})$$

Finally, equation (D.1) can be further used to obtain the conductance through a cylindrical pipe this is bent in half at a right-angle, where the parameter l must be replaced by an effective length, given by

D. Calculation of the UHV system conductances

$$l_{\text{eff}} = l_1 + l_2 + \frac{2d}{3} \quad (\text{D.3})$$

where $l_1 = l_2$ is the axial length of each straight section of the pipe and $d = 2r$ its internal diameter.

Table D.1 contains the calculation results performed with use of these equations, including values of the relevant parameters that were used. Connections in series are calculated according to equation (3.10) as outlined in Section 3.5.1.

piece	air conductance (L/s)	Rb conductance (L/s)
C_1	259.8	151.6
C_2	125.4	73.2
C_{12}	84.6	49.4
C_3	0.2	0.1
C_4	9.4	5.5
C_5	39.6	23.1
C_{45}	7.6	4.4

Table D.1. Conductance values: calculated for air ($M_{\text{air}} = 0.029$ kg/mol) or Rb ($M_{\text{Rb}} = 0.085$ kg/mol) at room temperature ($T = 296$ K) using equations (D.1), (D.2) and (3.10). The piece number is according to Figure 3.15, while the relevant dimensions for each are extracted from CAD models obtained from the manufacturer.

Considering the flow Q_B as depicted in Figure 3.15, rearrangement of equation (3.9) yields the following equations, respectively for the pressure and suction power in the Mot chamber as

$$P'_B = \frac{(P_{PB} - P_B^0)S_{PB} + P_{PB}C_{45}}{C_{45}} \quad (\text{D.4})$$

$$S'_B = C_{45} \frac{P'_B - P_{PB}}{P'_B - P_B^0}. \quad (\text{D.5})$$

E

Calculating the second-order correlation function in the wavefunction description

This Appendix provides supplementary information to the theory presented in the latter half of Chapter 4, specifically Section 4.4. In the following, the experimental situation of filtering the coherent component of the resonance fluorescence, in the low-saturation regime, is considered. In this low-saturation limit, only the two-photon components of the incident light field can give rise to a two-photon detection event. Accessing these photon statistics of the light is performed by measurement of the second-order correlation function, defined as

$$g^{(2)}(\tau) = \frac{\langle a_t^\dagger a_{t+\tau}^\dagger a_{t+\tau} a_t \rangle_t}{\langle a_t^\dagger a_t \rangle_t^2}, \quad (\text{E.1})$$

where $\langle \dots \rangle_t = 1/T \int dt \langle \dots \rangle$ indicates the time-averaged expectation value. In order to calculate this, the state of the filtered resonance fluorescence must first be defined, by considering the action of the applied filter on the incident light. Close to resonance, the **FRR** filter is described by the complex frequency-dependent transmission coefficient $\tilde{t}(\omega)$, given by equation (4.89) in Chapter 4. Following this, equation (E.1) can be determined by calculating the expectation values that appear in the numerator and denominator. This calculation is performed, and evaluated, in this Appendix.

E.1 Calculation

The effect of the filter on the coherent component of the input atomic fluorescence is to reduce its complex amplitude factor, α , by the transmission coefficient $\tilde{t}(\omega_L)$. The transmitted state then reads

$$|\alpha'\rangle = e^{-|\alpha'|^2/2} \left(1 + \alpha' a_\omega^\dagger + \frac{\alpha'^2}{2} a_\omega^\dagger a_\omega^\dagger + \dots \right) |0\rangle \quad (\text{E.2})$$

where $\alpha' = \tilde{t}(\omega_L)\alpha$. For the incoherent component of the light, $|\phi\rangle$, the two-photon state transmitted past the filter is given by

$$|\phi'\rangle = \frac{-\alpha^2}{\sqrt{2}} \int_{-\infty}^{\infty} \tilde{t}(\omega_L - \omega) \tilde{t}(\omega_L + \omega) \tilde{\phi}(\omega) a_{\omega_L - \omega}^\dagger a_{\omega_L + \omega}^\dagger |0\rangle d\omega. \quad (\text{E.3})$$

In addition to this, there is the possibility that either one or both of the incoherently scattered photons are absorbed by the filter, which has the probability $|\langle\phi|\phi\rangle|^2 - |\langle\phi'|\phi'\rangle|^2$. In the case where only one of the photons is absorbed, the transmitted light can no longer be described by a pure quantum state and instead requires a density matrix description. This can be avoided by making some simplifying assumptions.

Making use of the experimental situation, where the resonance of the **FRR** filter is placed close to the frequency of the coherently scattered light, allows to assume that the filter does not significantly affect the incoherently scattered photons. Thus, $|\phi'\rangle \approx |\phi\rangle$, and the light after the **FRR** filter is described by the quantum state

$$|\psi'\rangle = |\alpha'\rangle + |\phi\rangle \quad (\text{E.4})$$

which is assumed to be approximately normalised. A justification for this assumption is given in Section [E.2.3](#).

In order to calculate the expected $g^{(2)}(\tau)$ for the state $|\psi'\rangle$, equation [\(E.1\)](#) must be evaluated using the full state. To do so, the two expectation values $\langle a_t^\dagger a_t \rangle_t$ and $\langle a_t^\dagger a_{t+\tau}^\dagger a_{t+\tau} a_t \rangle_t$ are calculated. This is performed in the following.

E.1.1 Calculating $\langle a_t^\dagger a_t \rangle_t$

The first of the expectation values is comprised of four terms, according to

$$\begin{aligned} \langle a_t^\dagger a_t \rangle_t &= (\langle\alpha'| + \langle\phi|) n_t (|\alpha'\rangle + |\phi\rangle) \\ &= \langle\alpha'| n_t |\alpha'\rangle_t + \langle\phi| n_t |\phi\rangle_t + \langle\alpha'| n_t |\phi\rangle_t + \langle\phi| n_t |\alpha'\rangle_t. \end{aligned} \quad (\text{E.5})$$

The first of these terms yields

$$\langle\alpha'| a_t^\dagger a_t |\alpha'\rangle_t = \frac{|\alpha'|^2}{T}, \quad (\text{E.6})$$

while the second results in

$$\begin{aligned}
 \langle \phi | a_t^\dagger a_t | \phi \rangle_t &= \langle 0 | \frac{|\alpha|^4}{4T^3} e^{-|\alpha|^2} \int^{(5)} \phi^*(t_1, t_2) \phi(t_3, t_4) \underbrace{a_{t_1} a_{t_2} a_t^\dagger a_t a_{t_3}^\dagger a_{t_4}^\dagger}_{a_{t_1} a_{t_2} (\delta_{t_1, t_3} + \delta_{t_1, t_4}) a_{t_3}^\dagger a_{t_4}^\dagger} | 0 \rangle \\
 &= \frac{|\alpha|^4}{2T^3} e^{-|\alpha|^2} \int^{(4)} \phi^*(t_1, t_2) \phi(t_3, t_4) \underbrace{\langle 0 | a_{t_1} a_{t_2} a_{t_3}^\dagger a_{t_4}^\dagger | 0 \rangle}_{\delta_{t_1, t_3} \delta_{t_2, t_4} + \delta_{t_1, t_4} \delta_{t_2, t_3}} \\
 &= \frac{|\alpha|^4}{T^3} e^{-|\alpha|^2} \int^{(2)} \phi^*(t_1, t_2) \phi(t_1, t_2) \\
 &= \frac{|\alpha|^4}{T^3} e^{-|\alpha|^2} \int_{-T/2}^{T/2} dt \int_{-\infty}^{\infty} \phi^*(\tau) \phi(\tau) d\tau \\
 &= \frac{2|\alpha|^4}{T^2} e^{-|\alpha|^2} \int_0^{\infty} e^{-2\gamma\tau} d\tau \\
 &= \frac{|\alpha|^4}{\gamma T^2} e^{-|\alpha|^2}
 \end{aligned} \tag{E.7}$$

where the shorthand notation of $\int^{(n)}$ denotes the n -dimensional time integral and $\delta_{t_j, t_k} = \delta(t_j - t_k)$. Furthermore, the assumption of $T \gg 1/\gamma$ (equivalently $T \rightarrow \infty$) was used in evaluating the integral over $\phi(\tau)$. The final two terms in equation (E.5) are calculated in a similar way, yielding

$$\begin{aligned}
 \langle \alpha' | a_t^\dagger a_t | \phi \rangle_t &= \langle \phi | a_t^\dagger a_t | \alpha' \rangle_t \\
 &= \langle 0 | \frac{-\tilde{t}(\omega_L)^2 |\alpha|^4}{4T^3} e^{-|\alpha|^2} \int^{(5)} \phi^*(t_1, t_2) \underbrace{a_{t_1} a_{t_2} a_t^\dagger a_t a_{t_3}^\dagger a_{t_4}^\dagger}_{a_{t_1} a_{t_2} (\delta_{t_1, t_3} + \delta_{t_1, t_4}) a_{t_3}^\dagger a_{t_4}^\dagger} | 0 \rangle \\
 &= \frac{-2\tilde{t}(\omega_L)^2 |\alpha|^4}{T^3} e^{-|\alpha|^2} \int_{-T/2}^{T/2} dt \int_0^{\infty} \phi^*(\tau) d\tau \\
 &= \frac{-2\tilde{t}(\omega_L)^2 |\alpha|^4}{T^2} e^{-|\alpha|^2} \int_0^{\infty} e^{-(\gamma+i\Delta)\tau} d\tau \\
 &= -\frac{2\tilde{t}(\omega_L)^2 |\alpha|^4}{(\gamma+i\Delta)T^2} e^{-|\alpha|^2}.
 \end{aligned} \tag{E.8}$$

Putting these results together provides the expectation value of

$$\langle a_t^\dagger a_t \rangle_t = \frac{|\alpha|^2}{T} \left(|\tilde{t}(\omega_L)|^2 + \frac{|\alpha|^2}{\gamma T} e^{-|\alpha|^2} - 4 \frac{|\alpha|^2}{T} e^{-|\alpha|^2} \operatorname{Re} \left[\frac{\tilde{t}(\omega_L)^2}{\gamma + i\Delta} \right] \right). \tag{E.9}$$

In the case when $\tilde{t}(\omega) = 1$, the above expectation value corresponds to the total number of photons scattered by the atom per time, i.e., $\langle a_t^\dagger a_t \rangle_t = \gamma S / (1 + S)$. Using this equality, and up to second order in α^2 and S , gives

$$\alpha^2 = \gamma S T + 2\gamma S^2 T \frac{\gamma^2 - \Delta^2}{\gamma^2 + \Delta^2}, \tag{E.10}$$

E. Calculating the second-order correlation function in the wavefunction description

which allows to finally write the photon number expectation value as

$$\langle a_t^\dagger a_t \rangle_t = |\tilde{t}(\omega_L)|^2 \gamma S + \gamma S^2 \frac{\gamma - 2\gamma \tilde{t}^*(\omega_L)^2 + 2i\Delta \tilde{t}(\omega_L)^2 - i\Delta}{\gamma - i\Delta}. \quad (\text{E.11})$$

E.1.2 Calculating $\langle a_t^\dagger a_{t+\tau}^\dagger a_{t+\tau} a_t \rangle_t$

For the second expectation value, only the two-photon components of the scattered field contribute, which again gives an expression consisting of four terms according to

$$\begin{aligned} \langle a_t^\dagger a_{t+\tau}^\dagger a_{t+\tau} a_t \rangle_t &= (\langle \alpha'^{(2)} | + \langle \phi |) a_t^\dagger a_{t+\tau}^\dagger a_{t+\tau} a_t (|\alpha'^{(2)}\rangle + |\phi\rangle) \\ &= \langle \alpha'^{(2)} | a_t^\dagger a_{t+\tau}^\dagger a_{t+\tau} a_t | \alpha'^{(2)} \rangle_t + \langle \phi | a_t^\dagger a_{t+\tau}^\dagger a_{t+\tau} a_t | \phi \rangle_t \\ &\quad + \langle \alpha'^{(2)} | a_t^\dagger a_{t+\tau}^\dagger a_{t+\tau} a_t | \phi \rangle_t + \langle \phi | a_t^\dagger a_{t+\tau}^\dagger a_{t+\tau} a_t | \alpha'^{(2)} \rangle_t. \end{aligned} \quad (\text{E.12})$$

Each of the terms are calculated as outlined before (see the previous Section E.1.1), for which the first gives

$$\langle \alpha'^{(2)} | a_t^\dagger a_{t+\tau}^\dagger a_{t+\tau} a_t | \alpha'^{(2)} \rangle_t = \frac{|\alpha'|^4}{T^2} \quad (\text{E.13})$$

and the second gives

$$\begin{aligned} \langle \phi | a_t^\dagger a_{t+\tau}^\dagger a_{t+\tau} a_t | \phi \rangle_t &= \frac{|\alpha|^4}{2T^3} e^{-|\alpha|^2} \int^{(5)} \phi^*(t_1, t_2) \phi(t_3, t_4) \underbrace{\langle 0 | a_{t_1} a_{t_2} a_t^\dagger a_{t+\tau}^\dagger a_{t+\tau} a_t a_{t_3} a_{t_4}^\dagger | 0 \rangle}_{(\delta_{t_1, t} \delta_{t_2, t+\tau} + \delta_{t_1, t+\tau} \delta_{t_2, t}) (\delta_{t, t_3} \delta_{t+\tau, t_4} + \delta_{t, t_4} \delta_{t+\tau, t_3})} \\ &= \frac{|\alpha|^4}{T^3} e^{-|\alpha|^2} \int^{(2)} \phi^*(\tau) \phi(\tau) dt \\ &= \frac{|\alpha|^4}{T^2} e^{2\gamma\tau} e^{-|\alpha|^2}. \end{aligned} \quad (\text{E.14})$$

Similarly, the remaining terms yield

$$\begin{aligned} \langle \alpha'^{(2)} | a_t^\dagger a_{t+\tau}^\dagger a_{t+\tau} a_t | \phi \rangle_t &= \langle \phi | a_t^\dagger a_{t+\tau}^\dagger a_{t+\tau} a_t | \alpha'^{(2)} \rangle_t \\ &= \frac{-\tilde{t}(\omega_L)^2 |\alpha|^4}{T^2} e^{-(\gamma+i\Delta)\tau} e^{-|\alpha|^2}. \end{aligned} \quad (\text{E.15})$$

These results can all be combined to give

$$\begin{aligned} \langle a_t^\dagger a_{t+\tau}^\dagger a_{t+\tau} a_t \rangle_t &= \frac{|\alpha|^4}{T^2} e^{-|\alpha|^2} \left(|\tilde{t}(\omega_L)|^4 e^{|\alpha|^2} + e^{-2\gamma\tau} - 2e^{-\gamma\tau} e^{-|\alpha|^2} [\tilde{t}(\omega_L)^2 e^{i\Delta\tau} + \tilde{t}^*(\omega_L)^2 e^{-i\Delta\tau}] \right) \\ &= \frac{|\alpha|^4}{T^2} e^{-|\alpha|^2} \left| \tilde{t}(\omega_L)^2 - e^{-(\gamma-i\Delta)\tau} \right|^2 + \frac{|\alpha|^4}{T^2} |\tilde{t}(\omega_L)|^4 (1 - e^{-|\alpha|^2}), \end{aligned} \quad (\text{E.16})$$

and, when using the expression for S given in equation (E.10),

$$\langle a_t^\dagger a_{t+\tau}^\dagger a_{t+\tau} a_t \rangle_t = \gamma^2 S^2 \left| \tilde{t}(\omega_L)^2 - e^{-(\gamma-i\Delta)\tau} \right|^2 \left(1 + 2S \frac{\gamma^2 - \Delta^2}{\gamma^2 + \Delta^2} \right)^2. \quad (\text{E.17})$$

In reaching this last expression, an expansion up to fourth order in S was performed, where terms containing γTS were neglected.

E.1.3 Calculating $g^{(2)}(\tau)$

The pair of expectation values previously calculated, respectively given in equations (E.11) and (E.17), can now be inserted into equation (E.1) in order to yield an expression for the second-order correlation function of the filtered resonance fluorescence. Doing so, and taking care to square the expectation value appearing in the denominator, results in the expression

$$g^{(2)}(\tau) = \frac{|\tilde{t}(\omega_L)^2 - e^{-(\gamma-i\Delta)\tau}|^2}{\left(|\tilde{t}(\omega_L)|^2 + \frac{S^2}{\gamma+i\Delta}(\gamma - 2\gamma^2\tilde{t}^*(\omega_L)^2 + 2i\Delta\tilde{t}(\omega_L)^2 - i\Delta)\right)^2} \underbrace{\left(1 + 2S\frac{\gamma^2 - \Delta^2}{\gamma^2 + \Delta^2}\right)^2}_{\approx 1}. \quad (\text{E.18})$$

In the case considered, where $S \ll 1$, the second factor in the above equation is approximately equal to one as indicated. Using this, and further assuming that $\tilde{t}(\omega_L)$ is real for simplicity, allows to simplify the second-order correlation function to

$$g^{(2)}(\tau) = \frac{|\tilde{t}(\omega_L)^2 - e^{-(\gamma-i\Delta)\tau}|^2}{\left(\tilde{t}(\omega_L)^2 + S(1 - 2\tilde{t}(\omega_L)^2)\right)^2}. \quad (\text{E.19})$$

This function has the following properties:

$$g^{(2)}(\infty) = \frac{|\tilde{t}(\omega_L)|^4}{S^2} \quad \text{for } \tilde{t}(\omega_L) \rightarrow 0 \quad (\text{E.20})$$

$$g^{(2)}(0) = \frac{1}{S^2} \quad \text{for } \tilde{t}(\omega_L) \rightarrow 0 \quad (\text{E.21})$$

$$g^{(2)}(\tau) = \frac{|\tilde{t}(\omega_L)^2 - e^{-(\gamma-i\Delta)\tau}|^2}{\tilde{t}(\omega_L)^4} \quad \text{for } S \rightarrow 0. \quad (\text{E.22})$$

It is clear that the second-order correlation function is well-defined everywhere and has an amplitude that decreases with S^2 as expected, thus illustrating the validity of the approach and approximations used in reaching equation (E.19). However, it is still only valid in the low-saturation regime: as S increases, the normalisation is such that the function no longer approaches unity for $\tau \rightarrow \infty$. This is expected, as only the two-photon components in the light were considered as the source of coincidences in the presented treatment. For larger S , coincidences from higher-photon number components would have to be taken into account.

E.2 Some Sanity Checks

In the following, the validity of this presented description is briefly examined. By calculating the expectation value $\langle a_t \rangle_t$ using the state of the filtered light, a comparison of the scattering rates obtained with this method – to those that are expected – can be performed. The normalisation of the filtered state of the light is also discussed.

E.2.1 Calculating $\langle a_t \rangle_t$

In order to check whether this treatment predicts the correct power dependence of the coherent and incoherent scattering rates, the expectation value $\langle a_t \rangle_t$ must first be calculated. These rates are most easily compared in the case without the filter, and so for simplicity, $\tilde{t}(\omega_L) = 1$ is set throughout the following. Then,

$$\begin{aligned} \langle a_t \rangle_t &= \langle \alpha' | a_t | \alpha' \rangle + \langle \phi | a_t | \phi \rangle + \langle \alpha' | a_t | \phi \rangle + \langle \phi | a_t | \alpha' \rangle \\ &= \frac{\alpha}{\sqrt{T}} + \langle \alpha'^{(1)} | a_t | \phi \rangle + \langle \phi | a_t | \alpha'^{(3)} \rangle, \end{aligned} \quad (\text{E.23})$$

where in the second line, only the one- and three- photon components of the coherent state with the incoherent state respectively give non-zero values. These are calculated as

$$\begin{aligned} \langle \alpha'^{(1)} | a_t | \phi \rangle &= -\frac{\alpha^* |\alpha|^2}{2T^{5/2}} e^{-|\alpha|^2} \int^{(4)} \phi(t_2, t_3) a_{t_1} a_t a_{t_3}^\dagger a_{t_1}^\dagger \\ &= -\frac{\alpha^* |\alpha|^2}{T^{3/2}} e^{-|\alpha|^2} \int_{-\infty}^{\infty} \phi(\tau) d\tau \\ &= -\frac{2\alpha^* |\alpha|^2}{T^{3/2}(\gamma - i\Delta)} e^{-|\alpha|^2} \end{aligned} \quad (\text{E.24})$$

and

$$\begin{aligned} \langle \phi | a_t | \alpha'^{(3)} \rangle &= -\frac{\alpha |\alpha|^4}{6T^{7/2}} e^{-|\alpha|^2} \int^{(6)} \phi^*(t_1, t_2) \langle 0 | a_{t_1} a_{t_2} a_t a_{t_3}^\dagger a_{t_4}^\dagger a_{t_5}^\dagger | 0 \rangle \\ &= -\frac{\alpha |\alpha|^4}{T^{3/2}} e^{-|\alpha|^2} \int_{-\infty}^{\infty} \phi^*(\tau) d\tau \\ &= -\frac{2\alpha |\alpha|^4}{T^{3/2}(\gamma + i\Delta)} e^{-|\alpha|^2}. \end{aligned} \quad (\text{E.25})$$

These previous two results can be inserted into equation (E.23) to yield

$$\begin{aligned} \langle a_t \rangle_t &= \frac{\alpha}{\sqrt{T}} \left(1 - \frac{2|\alpha|^2 e^{-|\alpha|^2}}{T(\gamma - i\Delta)} - \frac{2|\alpha|^4 e^{-|\alpha|^2}}{T(\gamma + i\Delta)} \right) \\ &\approx -\sqrt{\gamma S} \frac{(S-1)(\gamma^2 + \Delta^2) + 2i\gamma S\Delta}{\gamma^2 + \Delta^2} \end{aligned} \quad (\text{E.26})$$

where the form of α^2 in terms of S , given by equation (E.10), has been used in reaching the second line. This result can be used for calculating the scattering rates, allowing for a comparison to expectation.

E.2.2 Comparison to the Expected Scattering Rates

The total, coherent, and incoherent scattering rates that are expected in resonance fluorescence are respectively given by

$$n_{\text{tot}} = \gamma \frac{S}{1+S} \quad (\text{E.27})$$

$$n_{\text{coh}} = \gamma \frac{S}{(1+S)^2} \quad (\text{E.28})$$

$$n_{\text{tot}} = n_{\text{tot}} - n_{\text{coh}} = \gamma \frac{S^2}{(1+S)^2}. \quad (\text{E.29})$$

Using equations (E.11) and (E.26), the above expressions can be compared to the scattering rates obtained under the presented description, which respectively are

$$\langle a_t^\dagger a_t \rangle = \gamma S - \gamma S^2 + \mathcal{O}[S]^3 \quad (\text{E.30})$$

$$|\langle a_t \rangle|^2 = \gamma S - 2\gamma S^2 + \mathcal{O}[S]^3 \quad (\text{E.31})$$

$$\langle a_t^\dagger a_t \rangle - |\langle a_t \rangle|^2 = \gamma S^2 + \mathcal{O}[S]^3 \quad (\text{E.32})$$

up to second order in S . These results, given in equations (E.30), (E.31), and (E.32), are respectively equivalent to the expectations in equations (E.27), (E.28), and (E.29), when also expanding the latter up to second order in S . The fact that the coherent part of the scattered light has the correct power dependence as expected ($\propto S - 2S^2$), indicates that the performed calculations are valid, but only in the low-saturation regime where $\mathcal{O}[S]^3$ can be neglected.

E.2.3 State Normalisation

A final check is to consider the normalisation of the filtered state of light, which in the end, will justify why it has been considered to be approximately normalised thus far. For this, the state $|\psi'\rangle$ must satisfy the condition $|\langle \psi' | \psi' \rangle|^2 = 1$. The norm of the considered state is obtained as

$$\langle \psi' | \psi' \rangle = \langle \alpha' | \alpha' \rangle + \langle \phi | \phi \rangle + 2 \text{Re} [\langle \phi | \alpha' \rangle] \quad (\text{E.33})$$

with

$$\langle \alpha' | \alpha' \rangle = 1 \quad (\text{E.34})$$

E. Calculating the second-order correlation function in the wavefunction description

and

$$\begin{aligned}
\langle \phi | \phi \rangle &= \frac{|\alpha|^4}{4T^2} e^{-|\alpha|^2} \int^{(4)} \phi^*(t_1, t_2) \phi(t_3, t_4) \langle 0 | a_{t_1} a_{t_2} a_{t_3}^\dagger a_{t_4}^\dagger | 0 \rangle \\
&= \frac{|\alpha|^4}{2T} e^{-|\alpha|^2} \int |\phi(\tau)|^2 d\tau \\
&= \frac{|\alpha|^4}{2\gamma T} e^{-|\alpha|^2}
\end{aligned} \tag{E.35}$$

together with

$$\begin{aligned}
\langle \phi | \alpha' \rangle &= -\frac{\tilde{t}(\omega_L)^2 |\alpha|^4}{4T^2} e^{-|\alpha|^2} \int^{(4)} \phi^*(t_1, t_2) \langle 0 | a_{t_1} a_{t_2} a_{t_3}^\dagger a_{t_4}^\dagger | 0 \rangle \\
&= -\frac{\tilde{t}(\omega_L)^2 |\alpha|^4}{2T} e^{-|\alpha|^2} \int \phi^*(\tau) d\tau \\
&= \frac{\tilde{t}(\omega_L)^2 |\alpha|^4}{(\gamma + i\Delta)T} e^{-|\alpha|^2},
\end{aligned} \tag{E.36}$$

to give the final result

$$\langle \psi' | \psi' \rangle = \left(1 + |\alpha|^4 e^{-|\alpha|^2} \left[\frac{1}{2\gamma T} - \frac{\tilde{t}^*(\omega_L)^2}{T(\gamma - i\Delta)} - \frac{\tilde{t}(\omega_L)^2}{T(\gamma + i\Delta)} \right] \right)^{-\frac{1}{2}}. \tag{E.37}$$

Substituting α^2 in terms of S (equation (E.10)) into the above yields

$$\begin{aligned}
\frac{1}{|\langle \psi' | \psi' \rangle|^2} &= 1 + \left(\frac{\gamma T}{2} - \frac{\tilde{t}^*(\omega_L)^2 \gamma^2 T}{\gamma - i\Delta} - \frac{\tilde{t}(\omega_L)^2 \gamma^2 T}{\gamma + i\Delta} \right) S^2 + \mathcal{O}[S]^3 \\
&\approx 1,
\end{aligned} \tag{E.38}$$

where in the last line, the terms of order $S^2 \gamma T$ are neglected. Consequently, under the $S \ll 1$ assumption, renormalisation of the quantum state is unnecessary.

Acknowledgements

Undertaking successful scientific research is, at its core, a collaborative endeavour. The achievements documented in this thesis are a testament to this fact. I offer my heartfelt gratitude towards those who have been instrumental in its completion, and all who have supported me throughout this journey – both scientifically and personally.

Thank you first and foremost to my Supervisor, Prof. Dr. Arno Rauschenbeutel, whose superlative breadth of knowledge and motivating force has been a constant source of inspiration and encouragement over the years. Thank you for providing a research environment that values freedom of exploration, supporting the pursuit of new ideas, and for allowing me to be a part of it. Under his supervision, I have had the rare opportunity to live and work in two vibrant capital cities during my **PhD** – an experience that has been further enriched by numerous opportunities to present our work internationally – for which I am equally thankful, and appreciative of the trust bestowed upon me.

I am deeply indebted to Dr. Jürgen Volz, for whom words of thanks hardly suffice. I have greatly benefited from his seemingly boundless expertise, that is always combined with a limitless patience, and studded with humour and humility. It has been a pleasure and a privilege to interact with and learn from him. Thank you in particular for assistance with the theory sections, and in general for the numerous(!) iterative rounds of proofreading, that – despite the rumours – were not necessitated by excessive bribery.

My sincere appreciation goes especially to members of the **CQED** team, with whom I have had the pleasure to work alongside throughout the pursuit of scientific discovery within the confines of our windowless lab(s). Thank you for sharing the challenges of taming the experimental beast. To the Vienna team, I am grateful for the smooth transition into the world of **WGM** bottle microresonators strongly coupled to single atoms, and to the Berlin team, thank you for the unwavering support as we ventured into filtered resonance fluorescence and back again. I would like to extend this gratitude to all members of the *Grundlagen der Optik und Photonik* Forschungsgruppe, both past and present, for fostering a diverse and stimulating atmosphere. I would like to further acknowledge the **CoQuS** Doctoral School, for providing a foundational social hub that extended far beyond the lecture hall during the early stages of my **PhD**. The people I encountered during this time were truly formative in my journey. Vielen Dank an Steffen, dass er mich hierher gebracht hat. Ich bin Ihnen für Ihre selbstlose Unterstützung zu großem Dank verpflichtet.

With that: *To dear friends along the way, no matter how far that I may stray, in my mind and my heart you will all remain.* Vielen Dank, meine Lieben.

These final, and most significant words, are dedicated to my loving family. Yet ironically, there is nothing that I could ever write to adequately convey the depth of my gratitude. This was for you. Mum, Dad, and Freya – thank you for believing in me for each and every tread of this arduous ascent, for sustaining the harness onto which I have held.

List of Publications

During the course of this thesis, the following articles have been published – or are currently under review – in a peer-reviewed journal.

1. Elisa Will, Luke Masters, Arno Rauschenbeutel, Michael Scheucher, and Jürgen Volz.
[Coupling a Single Trapped Atom to a Whispering-Gallery-Mode Microresonator](#)
Physical Review Letters **126**, 233602 (2021)
2. Luke Masters, Xin-Xin Hu, Martin Cordier, Gabriele Maron, Lucas Pache, Arno Rauschenbeutel, Max Schemmer, and Jürgen Volz.
[On the simultaneous scattering of two photons by a single two-level atom](#)
Nature Photonics **17**, 972–976 (2023)
3. Gabriele Maron, Anton Bölian, Xin-Xin Hu, Luke Masters, Arno Rauschenbeutel, and Jürgen Volz.
[Few-MHz bandwidth tunable optical filter based on a fiber-ring resonator](#)
arXiv:2506.11953 (2025)
4. Xin-Xin Hu, Gabriele Maron, Luke Masters, Arno Rauschenbeutel, and Jürgen Volz.
[Transforming Resonance Fluorescence into Maximally Entangled Photon Pairs Using Minimal Resources](#)
arXiv:2504.11294 (2025)

Academic Curriculum Vitae

Luke Masters

Birth 11th April 1994, Barnstaple, United Kingdom
Address 19 White Street, Devizes, Wiltshire, UK SN10 4NZ
E-Mail luke.masters@physik.hu-berlin.de
Mobile +49 152 09043820

Education

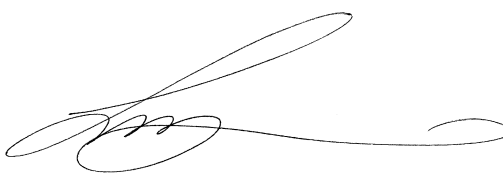
2020 – Present **Humboldt-Universität zu Berlin, Germany**
Doctoral Candidate in Physics
Thesis: *One Atom, One to Two Photons*

2017 – 2020 **Technische Universität Wien, Austria**
PhD Student
The Vienna Doctoral Program on Complex Quantum Systems

2012 – 2016 **University of St Andrews, Scotland**
Master in Physics (Honours)
Thesis: *The Scattering of Light from Optical Event Horizons*

2005 – 2012 **Queen Victoria School, Scotland**
Advanced Highers

Berlin, 01.12.2024

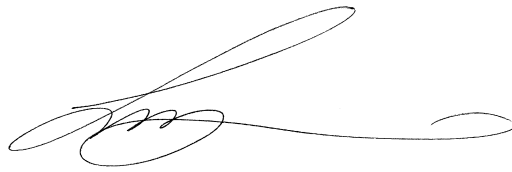


Luke Masters

Selbstständigkeitserklärung

Ich erkläre, dass ich die Dissertation selbständig und nur unter Verwendung der von mir gemäß § 7 Abs. 3 der Promotionsordnung der Mathematisch-Naturwissenschaftlichen Fakultät, veröffentlicht im Amtlichen Mitteilungsblatt der Humboldt-Universität zu Berlin Nr. 42/2018 am 11.07.2018 angegebenen Hilfsmittel angefertigt habe.

Berlin, 01.12.2024

A handwritten signature in black ink, consisting of a large, stylized initial 'L' followed by a cursive name, all written over a horizontal line.

Luke Masters

